DOE/MC/23075 -- 5031
(DE96000577)
Vol. I, Part 1

Measurement and Modeling of Advanced Coal Conversion Processes Volume I, Part 1

Final Report
September 1986 - September 1993

Peter R. Solomon
Michael A. Serio
David G. Hamblen
L. Douglas Smoot
B. Scott Brewster
Predrag T. Radulovic

September 1995

Work Performed Under Contract No.: DE-AC21-86MC23075

For
U.S. Department of Energy
Office of Fossil Energy
Morgantown Energy Technology Center
Morgantown, West Virginia

By
Advanced Fuel Research, Inc.
East Hartford, Connecticut
and
Brigham Young University
Provo, Utah

DISCLAIMER

DOE/MC/23075 -- 5031
(DE96000577)
Vol. I, Part 1
Distribution Category UC-109

Measurement and Modeling of Advanced Coal Conversion Processes Volume I, Part 1

Final Report
September 1986 - September 1993

Peter R. Solomon
Michael A. Serio
David G. Hamblen
L. Douglas Smoot
B. Scott Brewster
Predrag T. Radulovic

Work Performed Under Contract No.: DE-AC21-86MC23075

For
U.S. Department of Energy
Office of Fossil Energy
Morgantown Energy Technology Center
P.O. Box 880
Morgantown, West Virginia 26507-0880

By
Advanced Fuel Research, Inc.
87 Church Street
East Hartford, Connecticut 06108
and
Brigham Young University
Provo, Utah 84602

September 1995

ACKNOWLEDGEMENTS

The authors gratefully acknowledge the support for the work provided by the Morgantown Energy Technology center of the Department of Energy under contract No. DE-AC21-86MC23075. The contract monitors were Mr. Justin Beeson, Dr. Richard Johnson and Dr. Norman Holcombe and we are grateful for their advice and technical guidance. We wish to acknowledge the significant contributions of Professor Eric M. Suuberg of Brown University in the areas of char reactivity, pyrolysis modeling and pyrolysis kinetics. Prof. Philip E. Best of the University of Connecticut made significant contributions in the areas of coal and char optical properties, modeling of coal viscosity and swelling, and FT-IR emission/transmission (E/T) tomography. In addition to the authors listed on the title page, the Senior Investigators at Advanced Fuel Research, Inc. (AFR) included Ms. Sylvie Charpenay, Dr. Zhen-Zhong Yu, and Dr. Yuxin Zhao for subtask 2.a., Mr. James R. Markham for subtask 2.c., and Dr. Marek A. Wójtowicz for subtask 2.d. The preparations of the manuscript and illustrations was ably performed at AFR by Karin Dutton, Margaret Lane, and Lori Bellone.

For Brigham Young University (BYU), the other Senior Investigators included Prof. Geoffrey Germane and Prof. Angus Blackham for subtasks 2.b. and 2.f. and Dr. Paul Hedman for subtask 2.h. The student Research Assistants at BYU included Charles Monson, Gary Pehrson, and Kenneth Bateman for subtask 2.b., Kenneth Bateman, Gary Pehrson, Layne Pincock, Wade Riser, and Parvin Yousefi for subtask 2.f., Richard D. Boardman for subtask 2.g., and David Braithwaite, Aaron Huber, Laren Huntsman, and Gregg Shipp for subtask 2.h. The other Research Assistants at BYU were Ziaul Huque and Susana K. Berrondo for subtask 3.a., M. Usman Ghani, Michael Hobbs, and Sung-Chul Yi for subtask 3.b., Ziaul Huque for subtask 4.a, and M. Usman Ghani and Michael Hobbs for subtask 4.b. The work performed at BYU also included cost sharing provided by the Advanced Combustion Engineering Research Center (ACERC) at Brigham Young University. Funds for this center are provided by the U.S. National Science Foundation, the State of Utah, the U.S. Department of Energy, industrial participants, Brigham Young University and the University of Utah.

"MEASUREMENT AND MODELING OF COAL CONVERSION PROCESSES"
Contract No. DE-AC21-86MC23075

Table of Contents

List of Figures

List of Figures (Continued)

List of Figures (Continued)

List of Figures (Continued)

List of Figures (Continued)

List of Figures (Continued)

List of Figures (Continued)

List of Figures (Continued)

List of Figures (Continued)

List of Figures (Continued)

List of Tables

List of Tables (Continued)

List of Tables (Continued)

EXECUTIVE SUMMARY

The overall objective of this program was the development of a predictive capability for the design, scale up, simulation, control and feedstock evaluation in advanced coal conversion devices. This technology is important to reduce the technical and economic risks inherent in utilizing coal, a feedstock whose variable and often unexpected behavior presents a significant challenge. This program merged significant advances made at Advanced Fuel Research, Inc. (AFR) in measuring and quantitatively describing the mechanisms in coal conversion behavior, with technology developed at Brigham Young University (BYU) in comprehensive computer codes for mechanistic modeling of entrained-bed gasification. Additional capabilities in predicting pollutant formation were implemented and the technology was expanded to fixed-bed reactors.

The foundation to describe coal-specific conversion behavior was AFR's Functional Group (FG) and Devolatilization, Vaporization and Crosslinking (DVC) models, developed under previous and on-going METC sponsored programs. These models have demonstrated the capability to describe the time dependent evolution of individual gas species, and the amount and characteristics of tar and char. The combined FG-DVC model was integrated with BYU's comprehensive two-dimensional reactor model for combustion and gasification, PCGC-2, and a one-dimensional model for fixed-bed gasifiers, FBED-1. The program included: i) validation of the submodels by comparison with laboratory data obtained in this program, ii) extensive validation of the modified comprehensive codes by comparison of predicted results with data from bench-scale and process scale investigations of gasification, mild gasification and combustion of coal or coal-derived products, and iii) development of well documented user friendly software applicable to a "workstation" environment.

The progress during the program is summarized below.

For Subtask 2.a., the processes described were: 1) tar formation mechanisms and kinetics; 2) gas formation mechanisms and kinetics; 3) sulfur and nitrogen evolution mechanisms and kinetics; 4) coal and char fluidity (viscosity); 5) char swelling; 6) optical properties of coal and char; 7) the behavior of polymethylenes; 8) crosslinking; 9) char reactivity. These processes were embodied in the Functional Group - Depolymerization, Vaporization, Crosslinking (FG-DVC) model for coal conversion behavior. To provide the data for model development and for model parameters, several experimental methods were developed. These included: TG-FTIR (Thermogravimetric Analysis with analysis of evolved products by Fourier Transform Infrared spectroscopy) to determine coal composition, volatile evolutions, kinetics, and char reactivity and a transparent wall reactor (TWR) with in-situ FT-IR diagnostics to study rapid pyrolysis and combustion phenomenon. In addition, experiments were performed where coal was pyrolyzed in the inlet of a Field Ionization Mass Spectrometer (FIMS) apparatus.

The work has resulted in a successful method to characterize coal in the laboratory and predict its behavior over a wide variety of temperatures (100 to 1500°C), heating rates (10°/million years to 10^5°/sec), and pressures (vacuum to 10 atm). The work is described in a number of publications which were written as a result of this contract.

For Subtask 2.b., a high pressure facility (HPCP) was designed and constructed and char oxidation experiments were conducted at both atmospheric and elevated pressures. Approximately 100 oxidation experiments were performed with two sizes of Utah and Pitt. bituminous coal chars at 1, 5, 10, and 15 atm total pressure. Reactor temperatures were varied between 1000 and 1500 K and bulk gas compositions ranged from 5 to 21%, resulting in average particle temperatures ranged from 1400 to 2100 K with burnouts from 15 to 96%. Individual particle temperature, size and velocity were determined for approximately 75 particles at each test condition and overall reaction rates were independently determined from mass loss measurements.

The major findings of the study are as follows: 1) in spite of careful size classification and char preparation, the resulting particle population exhibited substantial variations in combustion behavior; 2) increasing total pressure in an environment of constant gas composition leads to modest increases in the

reaction rate and particle temperature; 3) significant kinetic control of the char oxidation process is exhibited at elevated pressures; 4) the global model kinetic parameters were found to be strongly dependent on the total pressure; 5) CO_2 formation must be accounted for at particle temperatures below about 1700 K; 6) independent particle temperature and mass loss measurements are both experimental necessities to fully describe combustion behavior.

For Subtask 2.c., studies of ignition, soot formation, and char burnout were performed in a Transparent Wall Reactor (TWR) which included in-situ FT-IR diagnostics. Experiments were done with several coal and char samples and the flame characteristics were compared to TGA measurements on the same samples. A comparison of the ignition of several samples suggested that the rate of ignition in the laminar flame correlated with the initial rate of weight loss in air in a TGA experiment at lower temperatures. Ignition of chars was heterogeneous; ignition of the high rank coals was homogeneous; but low rank coals exhibited both homogenous and heterogeneous contributions to ignition. Soot formation in combustion correlated well with tar yields in pyrolysis, suggesting that tar is the chief precursor to soot.

For a Montana Rosebud flame, tomographic reconstruction techniques were applied to line-of-sight FT-IR Emission/Transmission (E/T) measurements to derive spectra that correspond to small volumes within a coal flame. From these spectra, spatially resolved point values for species temperatures and relative concentrations can be determined. The spectroscopic data are in good agreement with visual observations and thermocouple measurements. The data present a picture of the coal burning in a shrinking annulus which collapses to the center at the tip of the flame. It has been found that the preheated air velocity has a significant effect on the shape of the flame. Two cases were done for the Montana Rosebud coal (low velocity and high velocity) and a low velocity case for the Pittsburgh Seam coal was completed. The three flames showed both coal and flow dependent phenomena. Simulations of these results were done at BYU, as discussed under subtask 3.a. In addition, submodels for ignition, soot formation, and soot radiation were formulated.

For Subtask 2.d., work was performed in four areas: 1) laboratory studies of mineral-matter transformations; 2) laboratory studies of catalytic effects of minerals on char reactivity; 3) modeling of mineral effects on char reactivity; 4) literature review of mineral-matter transformations. The results for each of these areas are summarized below.

1) Argonne premium coal samples were characterized using a Scanning Electron Microscope (SEM) with dispersive energy x-ray analysis. In most cases, good agreement with elemental analysis data was obtained. Sampling of char/fly ash and subsequent TGA and SEM analyses were also performed. It was found that ash spheres present on the char surface were rich in Ca, moderately rich in Al and Si, and had varying amounts of Fe, K, and Mg. Many of the pure mineral particles were found to be of the same size as the starting coal particles.

2) The reactivity of chars prepared from raw and demineralized coals was measured. Above 10% oxygen, the mineral matter dominates the char reactivity through the catalytic effect of alkali metals, especially Ca.

3) The modeling of mineral effects on char reactivity was integrated into the overall char-reactivity model.

4) The relevant literature on mineral matter in coal as well as ash formation and deposition was reviewed. Emphasis was placed on research carried out at EERC, MIT and PSI. Several key areas have been identified and discussed. Application of advanced mineral-matter characterization techniques, such as CCSEM and chemical fractionation, is advocated. The review also includes modeling of ash formation and deposition.

For Subtask 2.e., a literature review of heat and mass transport effects in coal pyrolysis was completed. In addition, calculations were done to define regimes of internal and external heat and mass transport control for conditions of interest. This was done to define the boundary regions where such

considerations become important.

A single particle FG-DVC model was developed for use in the fixed bed reactor code. This version of the model is based on an ordinary differential equation (ODE) version of the 2-σ percolation FG-DVC model. The code was delivered to BYU for integration into the FBED-1 Model.

A model for the destruction of tar in fixed bed gasifiers was developed in order to account for the relatively low yield of tar from these systems. According to the predictions of the FBED-1 model, the tar evolution occurs in a relatively small region near the top of the reactor where the gas and particle temperatures are changing rapidly. While the coal particles are entering at room temperature, the exit gas temperature is close to 1000 K and is 1300 K in the region where tar evolves. Some experiments were done to assess the relative importance of tar gasification and tar cracking reactions. It was found that, while the thermal cracking effects were significant, the addition of CO_2 did not have much effect on the yield or composition of tar. Consequently, it was concluded that the tar destruction in the top part of a fixed-bed gasifier can probably be attributed primarily to thermal cracking rather than gasification reactions.

For Subtask 2.f., atmospheric char oxidation runs in platinum and porcelain crucibles were made. Char particles were prepared and oxidized from Utah bituminous, North Dakota lignite, Wyoming subbituminous, Illinois #6, Pittsburgh #8, and Colorado bituminous coals. In these tests, large particles (0.5-1 cm) were oxidized, one at a time, over 5-15 minutes for time periods up to two hours, in incremental steps. The cube root of particle mass declined linearly with time during the first 80-90% burnout. Ash layers formed and usually remained in place around the decreasing volume of carbon. Average mass reactivities increased with decreasing initial char particle mass. These observations are consistent with oxidation being controlled by diffusion of oxygen. However, some chemical kinetic control is indicated at lower temperatures.

The extension of the experimental char oxidation tests to include the variable of pressure was accomplished with the design and construction of a cantilever beam balance unit which was attached to the HPCP reactor of Subtask 2b. The mass loss of a reacting coal particle was followed continuously by the changing response of a force transducer connected to the reacting particles with a long-small-bore ceramic tube. Here also the cube root of particle mass declined linearly with time during the first 80-90% of char burnout. A significant influence of pressure was observed between one and five atmospheres but the burning characteristics at 5 and 7.5 atmospheres were about the same.

For Subtask 2.g., The fuel NO_x submodel in an existing 2-D comprehensive model for pulverized coal gasification and combustion (PCGC-2) was revised and extended to include thermal NO and to be applicable to fuel-rich systems. The effect of two different expressions for oxygen atom concentration was investigated. The fuel NO mechanism was revised to include parallel reaction paths through HCN or NH_3. An alternative global mechanism from the literature involving NH_3 was also investigated. The resulting model was evaluated by comparing model predictions with experimental data.

For Subtask 2.h., The cross-flow injection and mixing of sorbent were studied in a cold-flow facility, and the results were used to modify an existing entrained-flow gasifier for sorbent injection. Sulfur-capture studies were then carried out at pressure with limestone and four coals of varying sulfur content. Three methods were used to investigate the sorbent mixing in cold-flow. The results at relatively low jet-to-free-stream momentum ratios showed that such flows are slower to mix with the free stream than flows with sufficient energy to impinge on the opposite wall. In such cases, increasing the number of cross-flow injectors was found to enhance the mixing. Sight windows were installed to permit optical access, and FT-IR temperature data were obtained with the assistance of AFR. There was no significant sulfur capture for three of the coals, and only a small effect with the highest-sulfur coal. The major cause of the low capture is believed to be the high temperature in the gasifier.

For Subtask 3.a., a 2-D comprehensive model for pulverized coal gasification and combustion (87-PCGC-2) was extended to include the FG-DVC model as an option for predicting weight loss and volatiles enthalpy. Other improvements in the code include laminar flow effects, gas buoyancy, a user-friendly and reliable energy equation option, and a condensed-phase equilibrium algorithm. The improved model was extensively evaluated by comparing model predictions with experimental data from several reactors. A clear advantage of the FG-DVC submodel was shown to be coal generality. Needed model improvements were identified. User-friendly graphics options were developed for code input and output. A user's manual was prepared, documenting code theory and use. Under a closely related, but independent study, improvements were made to the radiation submodel and enthalpy balance closure was realized.

For Subtask 3.b., the principal objective was to develop, evaluate and apply an advanced, steady-state, one-dimensional model of countercurrent, fixed-bed coal combustion and gasification. Improvements included advanced treatment of devolatilization, separate gas and coal temperatures, axially variable solid and gas flow rates, variable bed void fraction, generalized treatment of gas phase chemistry, and SO_x/NO_x pollutants. The initial fixed-bed model, MBED-1, was evaluated through sensitivity analysis and comparisons to experimental data. The predicted temperature and pressure profiles were found to agree reasonably well with the measured values. In MBED-1, gas evolution rates are determined by the functional group (FG) submodel and the tar evolution rate is determined by the semi-empirical tar (SET) correlation. The MBED-1 results brought out the significant effect of tar yield on predictions and the need for a more rigorous devolatilization model.

The most important improvement in the final version of the fixed-bed model, FBED-1, is the inclusion of the advanced devolatilization submodel, FG-DVC. In this submodel, gas evolution rates are determined by the functional group (FG) submodel and the tar evolution rate by the depolymerization-vaporization-crosslinking (DVC) submodel. The final version of the fixed-bed code, FBED-1, provides also: improved predictions of product gas composition and temperature; improved prediction of tar production; modifications in the iteration scheme to satisfy the gas phase boundary conditions at the bottom of the gasifier; improved modularity, code structure, and use friendliness; and improved graphics output. The final fixed-bed model, FBED-1, was also evaluated through sensitivity analysis and comparisons to experimental data. The predicted effluent composition and temperature as well as the predicted temperature and pressure profiles were found to agree very well with the measured values.

For Subtask 3.c., the fuels feedstock submodel in PCGC-2 was generalized to feed particles in any inlet, and to feed sorbent particles as well as coal particles. The generalized feedstock submodel was tested with the sorbent reactions submodel developed under Subtask 2.g.

For Subtask 4.a., the applicability of 93-PCGC-2 to practical-scale processes of commercial interest was demonstrated by simulating two such reactors. One is the Coal Tech Corp. advanced, air-cooled cyclone combustor, and the other is the Solar Turbines, Inc. combustor. The latter simulation was performed under an independent study and is reported separately. The code was shown to be a useful tool for reactor design and simulation. A user's manual was prepared, the final code was installed at METC and a short course was given.

For Subtask 4.b., the fixed-bed coal combustion, gasification, and devolatilization codes, MBED-1 and FBED-1, developed in Subtask 3.b, were successfully demonstrated by simulating the four dry-ash, fixed-bed gasifiers of interest to METC: the high-pressure, oxygen-blown Lurgi gasifier, the medium-pressure, air-blown METC gasifier, the atmospheric-pressure, air-blown Wellman-Galusha gasifier, and the high-pressure, air-blow, PyGas™ staged gasifier. The most comprehensive test data, including the temperature and the pressure profiles, were available for the atmospheric-pressure Wellman-Galusha gasifier. The Wellman-Galusha test data were used to validate the fixed-bed codes and the corresponding simulations were presented in Subtask 3.b. The simulations of the high-pressure Lurgi gasifier, the medium-pressure METC gasifier, and the high-pressure, air-blow, PyGas™ staged gasifier were presented as part of this subtask.

The user's manual was prepared for the FBED-1 code. The code was ported to a Silicon Graphics workstation and the sample case was successfully executed. The code, the user's manual, and the installation instructions were sent to METC. A short course on the use of the FBED-1 code was conducted at METC.

SECTION I. INTRODUCTION

I.A. Program Background and Description

During the past several years, significant advances have been made at Brigham Young University (BYU) in comprehensive two-dimensional computer codes for mechanistic modeling of entrained-bed gasification and pulverized coal combustion. During the same time period, significant advances have been made at Advanced Fuel Research, Inc. (AFR) in the mechanisms and kinetics of coal pyrolysis and secondary reactions of pyrolysis products. This program provided an opportunity to merge the technology developed by each organization in order to provide a detailed predictive capability for advanced coal characterization techniques in conjunction with comprehensive computer models to provide accurate process simulations.

The program streamlined submodels existing or under development for coal pyrolysis chemistry, volatile secondary reactions, tar formation, soot formation, char reactivity, and SO_x-NO_x pollutant formation. Submodels for coal viscosity, agglomeration, tar/char secondary reactions, sulfur capture, and ash physics and chemistry were developed or adapted. The submodels were first incorporated into the BYU entrained-bed gasification code and subsequently, into a fixed-bed gasification code, which was developed at BYU. These codes were validated by comparison with small scale laboratory and PDU-scale experiments. The validated codes can now be employed to simulate and to develop advanced coal conversion reactors of interest to METC.

I.B. Objectives

The objectives of this study were to establish the mechanisms and rates of basic steps in coal conversion processes, to integrate and incorporate this information into comprehensive computer models for coal conversion processes, to evaluate these models and to apply them to gasification, mild gasification and combustion in heat engines.

I.C. Approach

This program was a closely integrated, cooperative effort between AFR and BYU. The program consisted of four tasks: 1) Preparation of Research Plans, 2) Submodel Development and Evaluation, 3) Comprehensive Model Development and Evaluation, and 4) Applications and Implementation.

I.D. Critical Technical Issues

To achieve the goals of the program, the computer models must provide accurate and reliable descriptions of coal conversion processes. This required the reduction of very complicated and interrelated physical and chemical phenomena to mathematical descriptions and, subsequently, to operational computer codes. To accomplish this objective, a number of technical issues were addressed as noted below.

- Separation of Rates for Chemical Reaction, Heat Transfer, and Mass Transfer
- Particle Temperature Measurements Using FT-IR E/T Spectroscopy
- Functional Group Descriptions of Coal, Char and Tar
- Tar Formation Mechanisms
- Char Formation Mechanisms
- Viscosity/Swelling
- Intraparticle Transport
- Pyrolysis of Volatiles and Soot Formation
- Secondary Reaction of Tar
- Particle Ignition
- Char Reactivity
- Ash Chemistry and Physics

- Particle Optical Properties
- Coupling of Submodels with Comprehensive Codes
- Comprehensive Code Efficiency
- Turbulence
- SO_x and NO_x
- Generalized Fuels Models
- Fixed-Bed Model

These technical issues were addressed in three main tasks as described in Sections II-IV.

I.E. Summary

Subtask 2.a. Coal to Char Chemistry Submodel Development and Evaluation

The processes described in this work were: 1) tar formation mechanisms and kinetics; 2) gas formation mechanisms and kinetics; 3) sulfur and nitrogen evolution mechanisms and kinetics; 4) coal and char fluidity (viscosity); 5) char swelling; 6) optical properties of coal and char; 7) the behavior of polymethylenes; 8) crosslinking; 9) char reactivity. These processes were embodied in the Functional Group - Depolymerization, Vaporization, Crosslinking (FG-DVC) model for coal conversion behavior. To provide the data for model development and for model parameters, several experimental methods were developed. These included: TG-FTIR (Thermogravimetric Analysis with analysis of evolved products by Fourier Transform Infrared spectroscopy) to determine coal composition, volatile evolutions, kinetics, and char reactivity and a transparent wall reactor (TWR) with in-situ FT-IR diagnostics to study rapid pyrolysis and combustion phenomenon. In addition, experiments were performed where coal was pyrolyzed in the inlet of a Field Ionization Mass Spectrometer (FIMS) apparatus.

The work has resulted in a successful method to characterize coal in the laboratory and predict its behavior over a wide variety of temperatures (100 to 1500 °C), heating rates (10°/million years to 10^{5}°/sec), and pressures (vacuum to 10 atm). The work is described in a number of publications which were written as a result of this contract.

Subtask 2.b. Fundamental High-Pressure Reaction Rate Data

A high pressure facility was designed and constructed and char oxidation experiments were conducted at both atmospheric and elevated pressures. Approximately 100 oxidation experiments were performed with two sizes of Utah and Pitt. bituminous coal chars at 1, 5, 10, and 15 atm total pressure. Reactor temperatures were varied between 1000 and 1500 K and bulk gas compositions ranged from 5 to 21%, resulting in average particle temperatures ranged from 1400 to 2100 K with burnouts from 15 to 96%. Individual particle temperature, size and velocity were determined for approximately 75 particles at each test condition and overall reaction rates were independently determined from mass loss measurements. The results from the 1 atm Utah char oxidation results were shown to be consistent with results obtained by other researchers using the same coal. The chars were found to be burning mainly in a reducing density mode in a regime intermediate between the kinetic and pore diffusion zones, irrespective of total pressure. While the global model was used to correlate the results of the study, the extrapolation of the n^{th} order rate equation to pressures higher than atmospheric was found to be invalid.

The effect of increasing total pressure on char oxidation at a constant gas composition can be summarized as follows. Raising total pressure also necessarily increases the bulk gas O_2 pressure, leading to an increase in the reaction rate. However, this increase is tempered by the decrease in oxygen diffusivity that also accompanies increases in pressure. The overall result is a slight increase in rate with increasing total pressure. Most of this change occurred by 10 atm and further increases in total pressure produce little effect on the rate.

The major findings of the study are as follows:

1. In spite of careful size classification and char preparation, the resulting particle population exhibited substantial variations in combustion behavior.

2. Increasing total pressure in an environment of constant gas composition leads to modest increases in the reaction rate and particle temperature.

3. Significant kinetic control of the char oxidation process is exhibited at elevated pressures.

4. The global model kinetic parameters were found to be strongly dependent on the total pressure. This indicates that the empirical n^{th} order equation is not completely valid over the range of pressures covered in the experiments.

5. CO_2 formation must be accounted for at particle temperatures below about 1700 K. This is true regardless of the pressure.

6. Independent particle temperature and mass loss measurements are both experimental necessities to fully describe combustion behavior.

Subtask 2.c. Secondary Reaction of Pyrolysis Products and Char Burnout

Studies of ignition, soot formation and char burnout were performed in a Transparent Wall Reactor (TWR) which included in-situ FT-IR diagnostics. Experiments were done with several coal and char samples and the flame characteristics were compared to TGA measurements on the same samples. A comparison of the ignition of several samples suggested that the rate of ignition in the laminar flame correlated with the initial rate of weight loss in air in a TGA experiment at lower temperatures. Ignition of chars was heterogeneous; ignition of the high rank coals was homogeneous; but low rank coals exhibited both homogenous and heterogeneous contributions to ignition. Soot formation in combustion correlated well with tar yields in pyrolysis, suggesting that tar is the chief precursor to soot.

A series of pyrolysis experiments was also done with Zap lignite and Pittsburgh seam bituminous coal in the TWR. These experiments included FT-IR gas and particle temperature measurements, thermocouple measurements of the gas temperature and collection of char samples with a probe at six different heights. The particle temperature measurements were used to reconstruct the particle time-temperature history. The pyrolysis yields were then simulated with the FG-DVC model and the results were consistent with kinetic rates measured previously at AFR and Sandia for experiments where particle temperature measurements were made.

For a Montana Rosebud flame, tomographic reconstruction techniques were applied to line-of-sight FT-IR Emission/Transmission (E/T) measurements to derive spectra that correspond to small volumes within a coal flame. From these spectra, spatially resolved point values for species temperatures and relative concentrations can be determined. The spectroscopic data are in good agreement with visual observations and thermocouple measurements. The data present a picture of the coal burning in a shrinking annulus which collapses to the center at the tip of the flame. It has been found that the preheated air velocity has a significant effect on the shape of the flame. Two cases were done for the Montana Rosebud coal (low velocity and high velocity) and a low velocity case for the Pittsburgh Seam coal was completed. The three flames showed both coal and flow dependent phenomena. Simulations of these results were done at BYU, as discussed under subtask 3.a.

In addition, submodels for ignition and soot formation were formulated. Work was also done on developing a radiative model for soot as part of the soot submodel. The inputs are the volume fraction of soot and the temperature. The output is the average soot emissivity. The main difficulty is to correct for the presence of CO_2 and H_2O. This work was done jointly with BYU since the radiation model is an

integral part of PCGC-2.

Subtask 2.d. Ash Physics and Chemistry Submodel

Under this subtask, work was performed in four areas:

1) laboratory studies of mineral-matter transformations
2) laboratory studies of catalytic effects of minerals on char reactivity
3) modeling of mineral effects on char reactivity
4) literature review of mineral-matter transformations

The results are summarized below.

1) Argonne premium coal samples were characterized using a Scanning Electron Microscope (SEM) with dispersive energy x-ray analysis. In most cases, good agreement with elemental analysis data was obtained. Sampling of char/fly ash and subsequent TGA and SEM analyses were also performed. It was found that ash spheres present on char surface were rich in Ca, moderately rich in Al and Si, and had varying amounts of Fe, K, and Mg. Many of the pure mineral particles were found to be of the same size as the starting coal particles. Small-particle shedding (< 10μm was also observed. Sodium was nearly completely lost from the char, while magnesium was retained up to 30-50% burn-off. Sulfur was progressively lost as burn-off increased.

2) The reactivity of chars prepared from raw and demineralized coals was measured. For the raw-coal samples, an increase in reactivity with increasing coal-oxygen content was observed. Above 10% oxygen, the mineral matter dominates the char reactivity through the catalytic effect of alkali metals, especially Ca. This was confirmed by lower reactivities observed for demineralized samples. Loading demineralized samples with Ca and Mg ions restored the originally high reactivity.

3) The modeling of mineral effects on char reactivity was integrated into the overall char-reactivity model and is reported in section II.A.10

4) The relevant literature on mineral matter in coal as well as ash formation and deposition was reviewed. Emphasis was placed on research carried out at EERC, MIT and PSI. The following key areas have been identified and discussed: 1) the chemical and physical characterization of inorganic matter in coal; 2) the mechanisms of mineral-matter transformation into inorganic vapors, liquids and solids; 3) the physical properties of the intermediate ash species as a function of temperature, atmosphere, and residence time; 4) The mechanisms of ash transport to heat-transfer surfaces as a function of particle size and flow patterns in the combustor; 5) the heat-transfer characteristics coupled with the reactivity and melting behavior of the deposited ash material; 6) the characteristics of the liquid components in the deposit with respect to deposit growth and strength development; and 7) the physical characteristics of the deposit that influence its ability to be removed by conventional processes (e.g., by soot blowing). Application of advanced mineral-matter characterization techniques, such as CCSEM and chemical fractionation, is advocated. The review also includes modeling of ash formation and deposition.

Subtask 2.e. Large Particle/Thick Bed Submodels

A literature review of heat and mass transport effects in coal pyrolysis was completed. In addition, calculations were done to define regimes of internal and external heat and mass transport control for conditions of interest. This was done to define the boundary regions where such considerations become important.

A single particle FG-DVC model was developed for use in the fixed bed reactor code. This version of the model is based on an ordinary differential equation (ODE) version of the 2-σ percolation FG-DVC model. The code was delivered to BYU for integration into the FBED-1 Model.

Under this subtask, a model for the destruction of tar in fixed bed gasifiers was developed in order to account for the relatively low yield of tar from these systems. A compilation was made of literature data from laboratory reactors and full-scale moving bed gasifiers to help validate the model. The focus was on data for the Pittsburgh seam coal which shows the change in tar yield and/or compostion with variations in heating rate, bed depth, flow rate, pressure, particle size, and reactor type.

According to the predictions of the FBED-1 model, the tar evolution occurs in a relatively small region near the top of the reactor where the gas and particle temperatures are changing rapidly. While the coal particles are entering at room temperature, the exit gas temperature is close to 1000 K and is 1300 K in the region where tar evolves. Consequently, the contribution of tar cracking and tar gasification (by CO_2) must also be accounted for and could be the dominant mode of tar loss under some conditions. Some experiments were done to assess the relative importance of tar gasification and tar cracking reactions. It was found that, while the thermal cracking effects were significant, the addition of CO_2 did not have much effect on the yield or composition of tar. Consequently, it was concluded that the tar destruction in the top part of a fixed-bed gasifier can probably be attributed primarily to thermal cracking rather than gasification reactions. A recommendation was made to assume that the rates of tar pyrolysis and gasification were the same as that for the coal and this feature was incorporated into the FBED-1 model.

Subtask 2.f. Large Char Particle Oxidation at High Pressure

Atmospheric Char Oxidation in Simple Devices - Atmospheric char oxidation runs in platinum and porcelain crucibles were made. Char particles were prepared and oxidized from Utah bituminous, North Dakota lignite, Wyoming subbituminous, Illinois #6, Pittsburgh #8, and Colorado bituminous coals.

Approximately 150 tests were made at atmospheric pressure in two different simple experimental devices using heat from Meker burners or a muffle furnace. In these tests, large particles (0.5-1 cm) were oxidized, one at a time, over 5-15 minutes for time periods up to two hours, in incremental steps. The cube root of particle mass declined linearly with time during the first 80-90% burnout. Ash layers formed and usually remained in place around the decreasing volume of carbon. Average mass reactivities increased with decreasing initial char particle mass. These observations are consistent with oxidation being controlled by diffusion of oxygen. However, some chemical kinetic control is indicated at lower temperatures.

Oxidation at Elevated Pressures in the HPCP Reactor - The extension of the experimental char oxidation tests to include the variable of pressure was accomplished with the design and construction of a cantilever beam balance unit which was attached to the HPCP reactor of Subtask 2b. The mass loss of a reacting coal particle was followed continuously by the changing response of a force transducer connected to the reacting particles with a long-small-bore ceramic tube. Here also the cube root of particle mass declined linearly with time during the first 80-90% of char burnout. A significant influence of pressure was observed between one and five atmospheres but the burning characteristics at 5 and 7.5 atmospheres were about the same.

Subtask 2.g. SO_x - NO_x Submodel Development

NO_x Submodel - The fuel NO_x submodel in an existing 2-D comprehensive model for pulverized coal gasification and combustion (PCGC-2) was revised and extended to include thermal NO and to be applicable to fuel-rich systems. The effect of two different expressions for oxygen atom concentration was investigated. The fuel NO mechanism was revised to include parallel reaction paths through HCN or NH_3. An alternative global mechanism from the literature involving NH_3 was also investigated. The resulting model was evaluated by comparing model predictions with experimental data.

SO_x/Sorbent Submodel - An existing sulfation submodel was integrated into PCGC-2 and used to predict the reaction of injected sorbents with SO_2 and H_2S. The equilibrium approach for predicting sulfur species was evaluated. The use of the submodel was demonstrated by simulating a fuel-lean and a fuel-rich case. A sensitivity analysis of the sulfation submodel was performed.

Subtask 2.h. SO_x/NO_x Submodel Evaluation

The cross-flow injection and mixing of sorbent were studied in a cold-flow facility, and the results were used to modify an existing entrained-flow gasifier for sorbent injection. Sulfur-capture studies were then carried out at pressure with limestone and four coals of varying sulfur content. Three methods were used to investigate the sorbent mixing in cold-flow: 1) Smoke injection for visualization, 2) tracer gas injection and sampling, and 3) laser-Doppler anemometry (LDA). The results at relatively low jet-to-free-stream momentum ratios showed that such flows are slower to mix with the free stream than flows with sufficient energy to impinge on the opposite wall. In such cases, increasing the number of cross-flow injectors was found to enhance the mixing. Three injection ports were therefore used in the gasifier. Sight windows were installed to permit optical access, and FT-IR data were obtained with the assistance of AFR. There was no significant sulfur capture for three of the coals, and only a small effect with the highest-sulfur coal. The major cause of the low capture is believed to be the high temperature in the gasifier. Temperature determined by FT-IR ranged from approximately 1510 to 2480 K. Also, slag samples taken at various axial locations indicated that interactions between the slag, sulfur, and sorbent were occurring, probably reducing the amount of sorbent available for sulfur capture.

Subtask 3.a. Integration of Advanced Submodels into Entrained-Flow Code, with Evaluation and Documentation

A 2-D comprehensive model for pulverized coal gasification and combustion (87-PCGC-2) was extended to include the FG-DVC model as an option for predicting weight loss and volatiles enthalpy. Other improvements in the code include laminar flow effects, gas buoyancy, a user-friendly and reliable energy equation option, and a condensed-phase equilibrium algorithm. The improved model was extensively evaluated by comparing model predictions with experimental data from several reactors. A clear advantage of the FG-DVC submodel was shown to be coal generality. Needed model improvements were identified. User-friendly graphics options were developed for code input and output. A user's manual was prepared, documenting code theory and use. Under a closely related, but independent study, improvements were made to the radiation submodel and enthalpy balance closure was realized.

Subtask 3.b. Comprehensive Fixed-Bed Modeling Review, Development, Evaluation, and Implementation

The principal objective of this project was to develop, evaluate and apply an advanced, steady-state, one-dimensional model of countercurrent, fixed-bed coal combustion and gasification. Improvements included advanced treatment of devolatilization, separate gas and coal temperatures, axially variable solid and gas flow rates, variable bed void fraction, generalized treatment of gas phase chemistry, and SO_x/NO_x pollutants. The initial fixed-bed model, MBED-1, was evaluated through sensitivity analysis and comparisons to experimental data. The predicted temperature and pressure profiles were found to agree reasonably well with the measured values. In MBED-1, gas evolution rates are determined by the functional group (FG) submodel and the tar evolution rate is determined by the semi-empirical tar (SET) correlation. The MBED-1 results brought out the significant effect of tar yield on predictions and the need for a more rigorous devolatilization model.

The most important improvement in the final version of the fixed-bed model, FBED-1, is the inclusion of the advanced devolatilization submodel, FG-DVC. In this submodel, gas evolution rates are determined by the functional group (FG) submodel and the tar evolution rate by the depolymerization-vaporization-crosslinking (DVC) submodel. The final version of the fixed-bed code, FBED-1, provides also:

improved predictions of product gas composition and temperature; improved prediction of tar production; modifications in the iteration scheme to satisfy the gas phase boundary conditions at the bottom of the gasifier; improved modularity, code structure, and use friendliness; and improved graphics output. The final fixed-bed model, FBED-1, was also evaluated through sensitivity analysis and comparisons to experimental data. The predicted effluent composition and temperature as well as the predicted temperature and pressure profiles were found to agree very well with the measured values.

Subtask 3.c. Generalized Fuels Feedstock Submodel

The fuels feedstock submodel in PCGC-2 was generalized to feed particles in any inlet, and to feed sorbent particles as well as coal particles. The generalized feedstock submodel was tested with the sorbent reactions submodel developed under Subtask 2.g.

Subtask 4.a. Application of Generalized Pulverized Coal Comprehensive Code

The applicability of 93-PCGC-2 to practical-scale processes of commercial interest was demonstrated by simulating two such reactors. One is the Coal Tech Corp. advanced, air-cooled cyclone combustor, and the other is the Solar Turbines, Inc. combustor. The latter simulation was performed under an independent study and is reported separately. The code was shown to be a useful tool for reactor design and simulation. A user's manual was prepared, the final code was installed at METC and a short course was given on June 29-30, 1993.

Subtask 4.b. Application of Fixed-Bed Code

The fixed-bed coal combustion, gasification, and devolatilization codes, MBED-1 and FBED-1, developed in Subtask 3.b, were successfully demonstrated by simulating the four dry-ash, fixed-bed gasifiers of interest to METC: the high-pressure, oxygen-blown Lurgi gasifier, the medium-pressure, air-blown METC gasifier, the atmospheric-pressure, air-blown Wellman-Galusha gasifier, and the high-pressure, air-blow, PyGas™ staged gasifier. The most comprehensive test data, including the temperature and the pressure profiles, were available for the atmospheric-pressure Wellman-Galusha gasifier. The Wellman-Galusha test data were used to validate the fixed-bed codes and the corresponding simulations were presented in Subtask 3.b. The simulations of the high-pressure Lurgi gasifier, the medium-pressure METC gasifier, and the high-pressure, air-blow, PyGas™ staged gasifier were presented as part of this subtask.

The user's manual was prepared for the FBED-1 code. The code was ported to a Silicon Graphics workstation and the sample case was successfully executed. The code, the user's manual, and the installation instructions were sent to METC. A short course on the use of the FBED-1 code was conducted at METC.

SECTION II. TASK 2. SUBMODEL DEVELOPMENT AND EVALUATION

Objectives

The objectives of this task were to develop or adapt advanced physics and chemistry submodels for the reactions of coal in an entrained-bed and a fixed-bed reactor and to validate the submodels by comparison with laboratory scale experiments.

Task Outline

The development of advanced submodels for the entrained-bed and fixed-bed reactor models was organized into the following categories: a) Coal Chemistry (including coal pyrolysis chemistry, char formation, particle mass transfer, particle thermal properties, and particle physical behavior); b) Char Reaction Chemistry at high pressure; c) Secondary Reactions of Pyrolysis Products (including gas-phase cracking, soot formation, ignition, and char burnout); d) Ash Physics and Chemistry (including mineral characterization, evolution of volatile, molten and dry particle components, and ash fusion behavior); e) Large Coal Particle Effects (including secondary reactions within the particle and in multiple particle layers; f) Large Char Particle Effects (including oxidation); g) SO_x-NO_x Submodel Development (including the evolution and oxidation of sulfur and nitrogen species); and h) SO_x and NO_x Model Evaluation.

II.A. SUBTASK 2.a. - COAL TO CHAR CHEMISTRY SUBMODEL DEVELOPMENT AND EVALUATION

Senior Investigators - David G. Hamblen, Michael A. Serio and Peter R. Solomon
Advanced Fuel Research, Inc.
87 Church Street, East Hartford, CT 06108
(203) 528-9806

Objective

The objective of this subtask is to develop and evaluate, by comparison with laboratory experiments, an integrated and compatible submodel to describe the organic chemistry and physical changes occurring during the transformation from coal to char in coal conversion processes.

Accomplishments

The processes described in this work were:

- tar formation mechanisms and kinetics
- gas formation mechanisms and kinetics
- sulfur and nitrogen evolution mechanisms and kinetics
- coal and char fluidity (viscosity)
- char swelling
- optical properties of coal and char
- the behavior of polymethylene
- crosslinking
- char reactivity

These processes were embodied in the Functional Group - Depolymerization, Vaporization, Corsslinking (FG-DVC) model for coal conversion behavior.

To provide the data for model development and for model parameters, several experimental methods were developed. These included:

- TG-FTIR (Thermogravimetric Analysis with analysis of evolved products by Fourier Transform Infrared spectroscopy) to determine coal composition, volatile evolutions, kinetics, and char reactivity.
- Transparent wall reactor (TWR) with in-situ FT-IR diagnostics to study rapid pyrolysis and combustion phenomenon.
- Pyrolysis of coal in a Field Ionization Mass Spectrometer (FIMS) apparatus.

The work has resulted in a successful method to characterize coal in the laboratory and predict is behavior over a wide variety of temperatures (100 to 1500°C), heating rates (10^0/million years to 10^{5}°/sec), and pressures (vacuum to 10 atm).

The work is described in a number of publications which were written for this contract.

Serio, M.A., Solomon, P.R., and Carangelo, R.M., Pyrolysis of the Argonne Premium Coals under Slow Heating Conditions, ACS Div of Fuel Chem. Preprints **33**, (2), 295, (1988).

Serio, M.A., Solomon, P.R., Yu, Z.Z., Desphande, G.V., and Hamblen, D.G., Pyrolysis Modeling of Argonne Premium Coals, ACS Div. of Fuel Chem. Preprints, **33**, (3), 91, (1988).

Solomon, P.R. and Carangelo, R.M., FT-IR Analysis of Coal 2. Aliphatic and Aromatic Hydrogen Concentration, Fuel, **67**, 949, (1988).

Solomon, P.R., Chien, P.L., Carangelo, R.M., Best, P.E., and Markham, J.R., Application of FT-IR Emission/Transmission (E/T) Spectroscopy to Study Coal Combustion Phenomena, The 22nd Symposium (Int) on Combustion, The Combustion Institute, Pittsburgh, PA, p. 211, (1988).

Solomon, P.R., Hamblen, D.G., Carangelo, R.M., Serio, M.A. and Deshpande, G.V., Models of Tar Formation During Coal Devolatilization, Combustion and Flame, **71**, 137, (1988).

Solomon, P.R., Hamblen, D.G., Carangelo, R.M., Serio, M.A., and Deshpande, G.V., A General Model of Coal Devolatilization, Energy and Fuel, **2**, 405, (1988).

Serio, M.A., Solomon, P.R., Bassilakis, R., and Suuberg, E.M., The Effects of Minerals and Pyrolysis Conditions on Char Gasification Rates, ACS Div. of Fuel Chem. Preprints, **34**, (1), 9, (1989).

Serio, M.A., Solomon, P.R., Yu, Z.Z., Bassilakis, R., The Effect of Rank on Coal Pyrolysis Kinetics, ACS Div. of Fuel Chem. Preprints, **34**, (4), 1324, (1989).

Khan, M.R., Serio, M.A., Malhotra, R., and Solomon, P.R., A Comparison of Liquids Produced from Coal by Rapid and Slow Heating Pyrolysis Experiments, ACS Div. of Fuel Chem. Preprints, **34**, (4), 1054, (1989).

Solomon, P.R., Serio, M.A., and Markham, J.R., Kinetics of Coal Pyrolysis, Int. Conference on Coal Science Proceedings, IEA, Tokyo, Japan, p. 575, (October 23-27, 1989).

Solomon, P.R., Best, P.E., Markham, J.R., and Klapheke, J., The Study of Coal Flames using FT-IR Emission/Transmission Tomography, Int. Conference on Coal Science Proceedings, IEA, Tokyo, Japan, p. 329, (October 23-27, 1989).

Solomon, P.R., Serio, M.A., and Carangelo, R.M., Coal Analysis by TG-FTIR, Int. Conference on Coal Science Proceedings, IEA, Tokyo, Japan, p. 67, (October 23-27, 1989).

Serio, M.A., Solomon, P.R., Bassilakis, R., and Suuberg, E.M., The Effects of Minerals on Coal Reactivity, Int. Conference on Coal Science Proceedings, IEA, Tokyo, Japan, p. 341, (October 23-27, 1989).

Serio, M.A., Solomon, P.R., Yu, Z.Z., and Deshpande, G.V., An Improved Model of Coal Devolatilization, Int. Conference on Coal Science Proceedings, IEA, Tokyo, Japan, p. 209, (October 23-27, 1989).

Solomon, P.R., Hamblen, D.G., Yu, Z.Z., and Serio, M.A., Network Models of Coal Thermal Decomposition, Fuel, **69**, 754, (1990).

Solomon, P.R., "On-Line Fourier Transform Infrared Spectroscopy in Coal Research", in Advances in Coal Spectroscopy, (H.L.C. Meuzelaar, Ed.), Plenum Publishing Corp., pp 341 - 371, (1992).

Solomon, P.R., Serio, M.A., Deshpande, G.V., and Kroo, E., Crosslinking Reactions During Coal Conversion, Energy & Fuels, **4**, (1), 42, (1990).

Solomon, P.R. and Best, P.E., "Fourier Transform Infrared Emission/Transmission Spectroscopy in Flames", in Combustion Measurements, (N. Chigier, Ed.), Hemisphere Publishing Corp., pp. 385-344, (1991).

Solomon, P.R., Serio, M.A., Carangelo, R.M., Bassilakis, R., Gravel, D., Baillargeon, M., Baudais, F., and Vail, G., Analysis of the Argonne Premium Coal Samples by TG-FTIR", Energy & Fuels, **4**, (3), 319, (1990).

Carangelo, R.M., Solomon, P.R., Bassilakis, R., Gravel, D., Baillargeon, M., Baudais, F., and Vail, G., Applications of TG-FTIR in the Analytical Lab, American Laboratory, p. 51, (1990).

Solomon, P.R., Serio, M.A., Hamblen, D.G., Yu, Z.Z., and Charpenay, S., Advances in the FG-DVC Model of Coal Devolatilization, ACS Div. of Fuel Chem. Preprints, **35**, (2), 479, (1990).

Solomon, P.R., Chien, P.L., Carangelo, R.M., Serio, M.A., and Markham, J.R., New Ignition Phenomenon in Coal Combustion, Combustion & Flame, **79**, 214, (1990).

Markham, J.R., Zhang. Y.P., Carangelo, R.M., and Solomon, P.R., FT-IR Emission/Transmission Tomography of a Coal Flame, 23rd Symposium (Int) on Combustion, The Combustion Institute, Orleans, France, pp 1869-1875, (1990).

Brewster, B.S., Smoot, L.D., and Solomon, P.R., Structure of a Near Laminar Coal Jet Diffusion Flame, Poster Session, 23rd Symposium (Int) on Combustion, The Combustion Institute, Orleans, France, (1990).

Serio, M.A., Solomon, P.R., Charpenay, S., Yu, Z.Z., and Bassilakis, R., Kinetics of Volatile Product Evolution from the Argonne Premium Coals, ACS Div of Fuel Chem. Preprints, **35**, (3), 808, (1990).

Solomon, P.R., Markham, J.R., Zhang, Y.P., Carangelo, R.M., Brewster, B.S., and L.D. Smoot, The Study of a Coal Flame by FT-IR Emission/Transmission Tomography and Comprehensive Modeling, Sci - Mix Poster Session, American Chemical Society, Meeting, Washington, DC (1990).

Solomon, P.R., Fletcher, T.H., and Pugmire, R.J., Progress in Coal Pyrolysis, Pittsburgh Coal Conference, (Sept. 10-14, 1990).

Solomon, P.R., Serio, M.A., and Suuberg, E.M., Coal Pyrolysis: Experiments, Kinetic Rates, and Mechanisms, Progress in Energy and Combustion Science, **18**, pp 133-220, (1992).

Solomon, P.R., Serio, M.A., Carangelo, R.M., Bassilakis, R., Yu, Z.Z., Charpenay, S., and Whelan, J., Analysis of Coal by TG-FTIR and Pyrolysis Modeling, presented at the Pyrolysis '90 Meeting in Holland, June 1990, also published in Journal of Analytical and Applied Pyrolysis, **19**, 1, (1991).

Solomon, P.R., Can Coal Science be Predictive, Presented at the Fourth Annual Australian Coal Science Conf., Brisbane, Australia, (Dec. 3-5, 1990).

Serio, M.A., Solomon, P.R., Yang, Y.P., and Suuberg, E.M., The Use of TG-FTIR Analysis to Determine Char Combustion Properties, presented at the AIChE Annual Meeting, Chicago, IL, (Nov. 11-16, 1990).

Solomon, P.R., Hamblen, D.G., Serio, M.A., Yu, Z.Z., Charpenay, S., Can Coal Science be Predictive, Storch Award Symposium Lecture, ACS Div. of Fuel Chemistry Preprints, **36** (1) 267, (1991).

Carangelo, R.M., Serio, M.A., Solomon, P.R., Charpenay, S., Yu, Z.Z., and Bassilakis, R., Coal Pyrolysis: Measurements and Modeling of Product Evolution Kinetics and Char Properties, ACS Div. of Fuel Chem. Preprints, **36** (2), 796, (1991).

Solomon, P.R., Hamblen, D.G., Serio, M.A., Yu, Z.Z., and Charpenay, S., A Characterization Method and Model for Predicting Coal Conversion Behavior, Fuel, **72** (4), 469 (1993).

Solomon, P.R., Charpenay, S., Yu, Z.Z., Serio, M.A., Kroo, E., Solum, M.S., and Pugmire, R.J., Network Changes During Coal Pyrolysis: Experiment and Theory, presented at the 1991 Int. Conf. on Coal Science, New Castle, England (Sept. 1991).

Solomon, P.R., Best, P.E., Yu, Z.Z., and Charpenay, S., An Empirical Model for Coal Fluidity Based on a Macromolecular Network Pyrolysis Model, Energy & Fuel, **6**, 143 (1992).

Serio, M.A., Solomon, P.R,. Yu, Z.Z., and Charpenay, S., Modeling of Mild Gasification Processes, proceedings of the 8th Annual Int. Pittsburgh Coal Conference, pp 183-188 (Oct. 14-18, 1991).

Solomon, P.R., Fletcher, T.H., and Pugmire, R.J., Progress Coal Pyrolysis, Fuel, **72**, (5), 587 (1992).

Charpenay, S., Serio, M.A., and Solomon, P.R., The Production of Coal Char Reactivity under Combustion Conditions, 24th Symposium (Int) on Combustion, The Combustion Institute, Pittsburgh, PA, 1189-1197 (1992).

Charpenay, S., Serio, M.A., Teng, H., and Solomon, P.R., The Influence of Char Structure on Low Temperature Combustion Reactivity, ACS Div. of Fuel Chem Preprints, **37** (4), 1937 (1992).

Bassilakis, R., Serio, M.A., and Solomon, P.R., Sulfur and Nitrogen Evolution in The Argonne Coals, ACS Div. of Fuel Chem. Preprints, **37**, (4), 1712 (1992).

Brewster, B.S., Smoot, L.D., Solomon, P.R., and Markham, J.R., Structure of a Near-Laminar Coal Jet Flame, submitted to Combustion Science and Technology (1992).

dela Rosa, L., Pruski, M., Lang, D., Gerstein, B., and Solomon, P.R., Characterization of the Argonne Premium Coals by Using ^{1}H and ^{13}C NMR and FT-IR Spectroscopies, Energy and Fuels, **6**, 460 (1992).

Bassilakis, R., Zhao, Y., Solomon, P.R., and Serio, M.A., Sulfur and Nitrogen Evolustion in the Argonne Coals: Experiment and Modeling, submitted to Energy and Fuel (1993).

These topics are discussed in the sections that follow.

II.A.1. Coal Characterization

Characterization of the coal samples for this program was performed by quantitative FT-IR analysis, pyrolysis, and char reactivity. Analyses were run on ampoules of Argonne samples 1-7 and 9, listed in Tables II.A.1-1 and II.A.1-2. Also, six jars containing bulk samples of coal were received from the Argonne National Laboratory for coals 1, 2, and 4-7. Due to the broad particle distribution, each jar was well mixed and a small representative sample was removed, handground and sieved to obtain the 200 x 325 mesh fractions. Additional samples of these six coals were obtained from BYU after grinding. For Rosebud subbituminous coal, samples have been obtained from METC. Bulk samples of the Beulah lignite were obtained from UNDERC. Bulk samples of Illinois #6 have been ordered from the Illinois State Geological Survey. Measurements have been made on raw coals and coals demineralized in HCl and HF.

Quantitative FT-IR Analysis

The coal samples were subjected to FT-IR analysis using approximately 1 mg of dry ground sample in approximately 300 mg of alkali halide. To obtain optical properties for the coals, CsI pellets were prepared in addition to the KBr pellets. Figures II.A.1-1a and 1b to II.A.1-9a and 9b show the dry

Table II.A.1-1. AFR/BYU Program Coal Samples.

Coal Name	Rank	Mine/Location	Source
1. Upper Freeport	Medium Volatile Bituminous	Pennsylvania	ANL
2. Wyodak	Subbituminous	Wyoming	ANL
3. Illinois #6	High Volatile Bituminous	Macoupin, Illinois	ANL
4. Pittsburgh #8	High Volatile Bituminous	Washington, Penn	ANL
5. Pocahontas #3	Low Volatile Bituminous	Virginia	ANL
6. Utah Blind Canyon	High Volatile Bituminous	Utah	ANL
7. Utah Blind Canyon	Medium Volatile Bituminous	Eastern, WV	ANL
8. Zap	Lignite	Mercer, N. Dakota	UND
9. Rosebud	Subbituminous	Montana	METC

Table II.A.1-2.

ELEMENTAL COMPOSITION (MAF)

COAL	NAME	C	H	O	S*	ASH*
1.	Upper Freeport (UF)	87	5.5	4	2.8	13
2.	Wyodak (WY)	74	5.1	19	0.5	8
3.	Illinois #6 (Ill. #6)	77	5.7	10	5.4	16
4.	Pittsburgh #8 (Pitt #8)	83	5.8	8	1.6	9
5.	Pocahontas #3 (Poc #3)	91	4.7	3	0.9	5
6.	Utah Blind Canyon (UT)	79	6.0	13	0.5	5
7.	Upper Knawha (WV)	81	5.5	11	0.6	20
9.	North Dakota (Zap)	73	5.3	21	0.8	6
10.	Rosebud	72.1	4.7	20.3	1.2	10

* Dry Basis

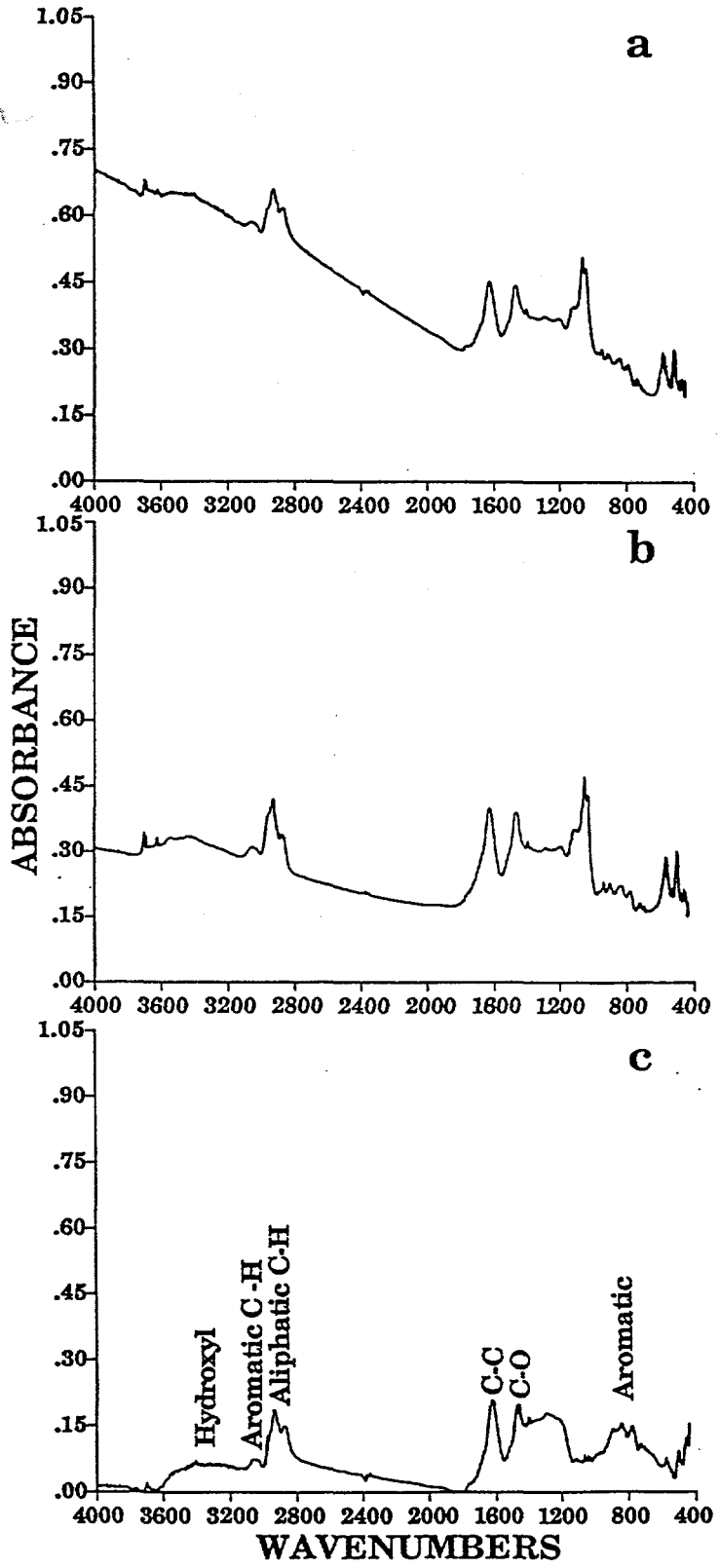

Figure II.A.1-1. FT-IR Spectra of Bulk Upper Freeport Bituminous Coal. a) KBr, b) CSI, and c) KBr Pellet, Mineral Matter Corrected.

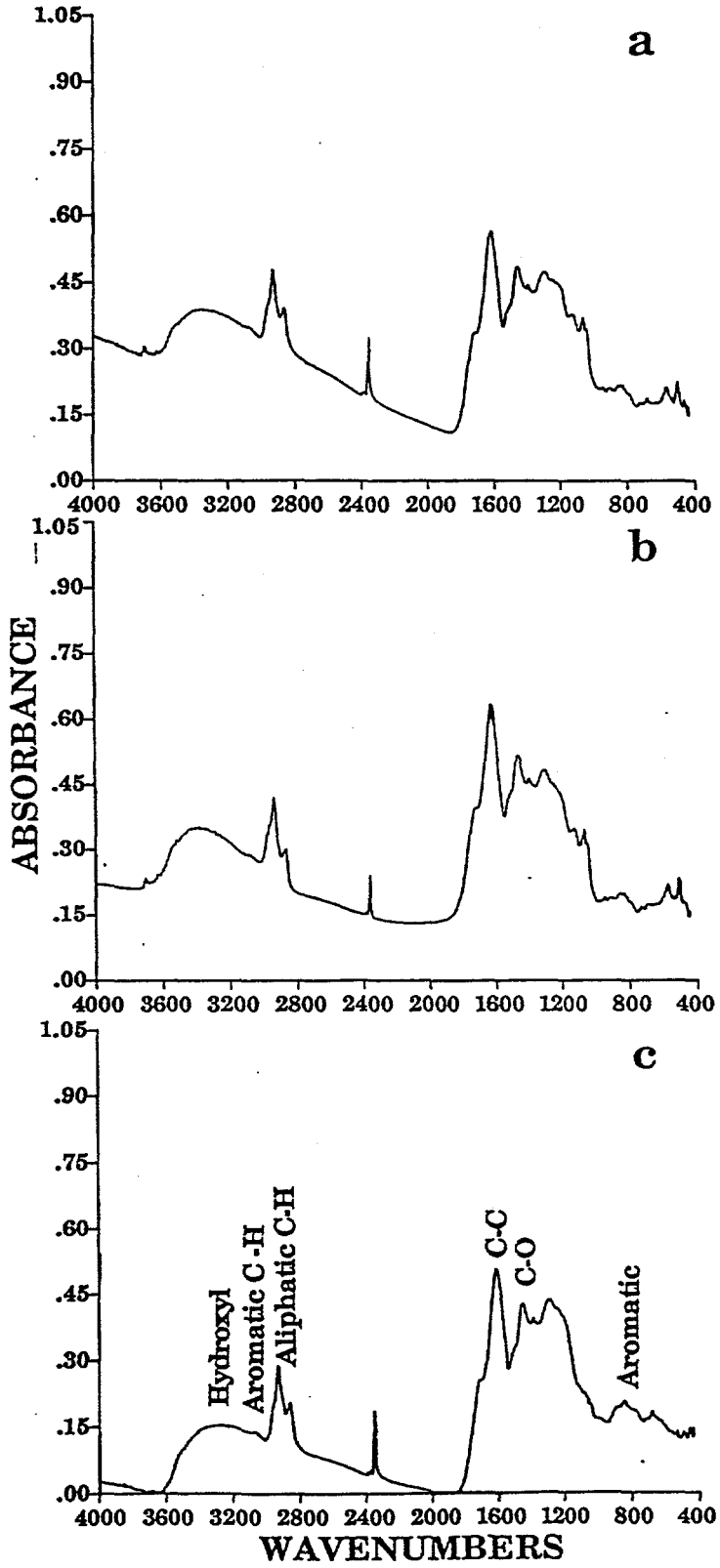

Figure II.A.1-2. FT-IR Spectra of Bulk Wyodak Subbituminous Coal. a) KBr, b) CSI, and c) KBr Pellet, Mineral Matter Corrected.

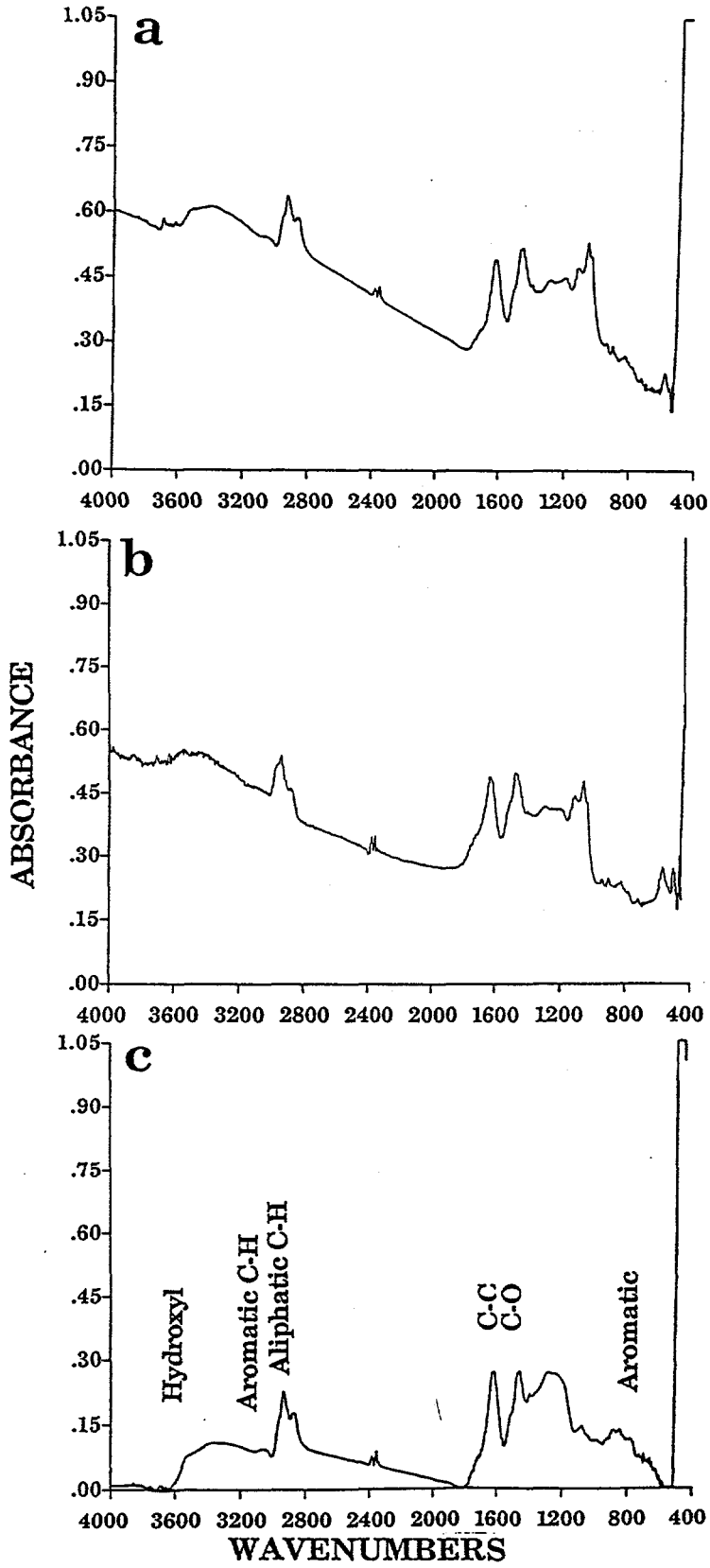

Figure II.A.1-3. FT-IR Spectra of Bulk Illinois #6 Bituminous Coal. a) KBr, b) CSI, and c) KBr Pellet, Mineral Matter Corrected.

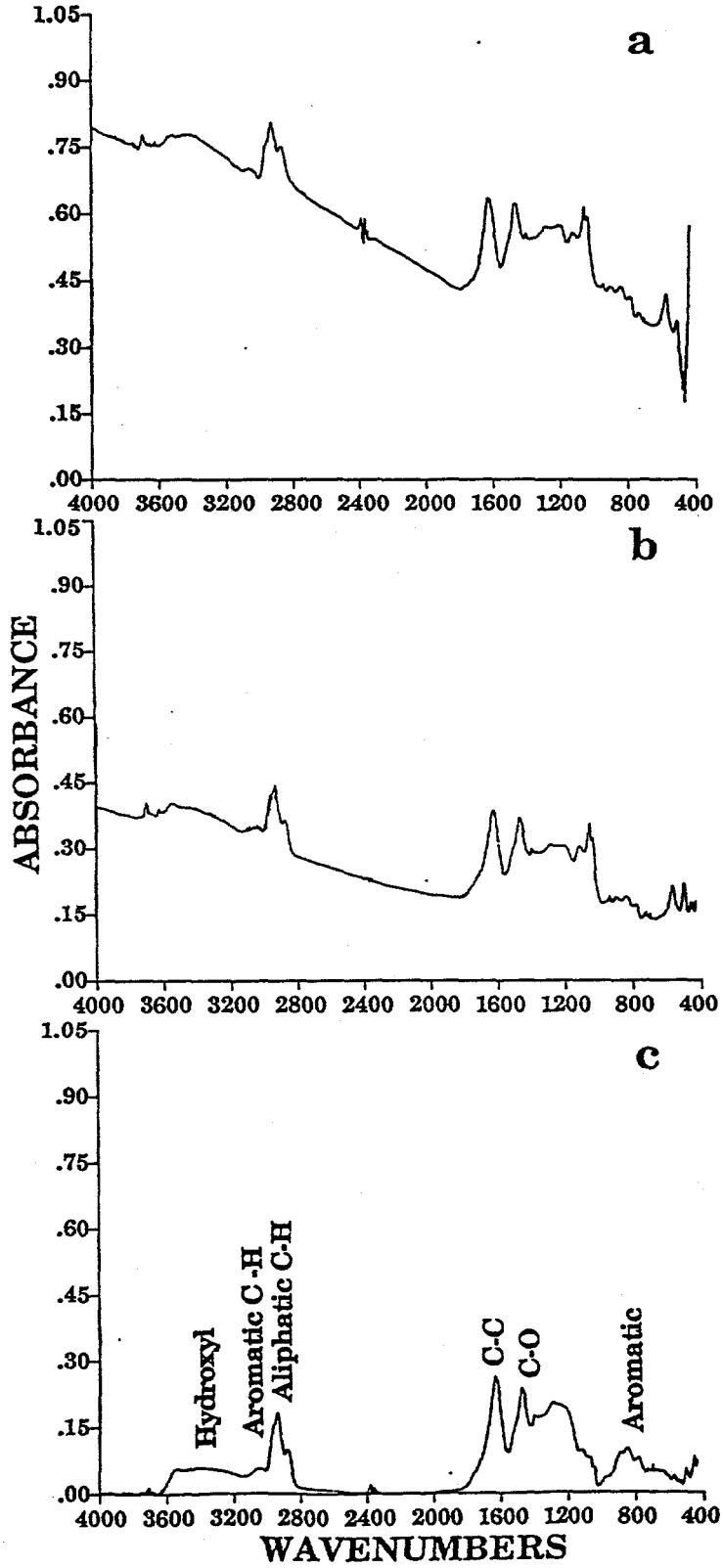

Figure II.A.1-4. FT-IR Spectra of Bulk Pittsburgh Seam Bituminous Coal. a) KBr, b) CSI, and c) KBr Pellet, Mineral Matter Corrected.

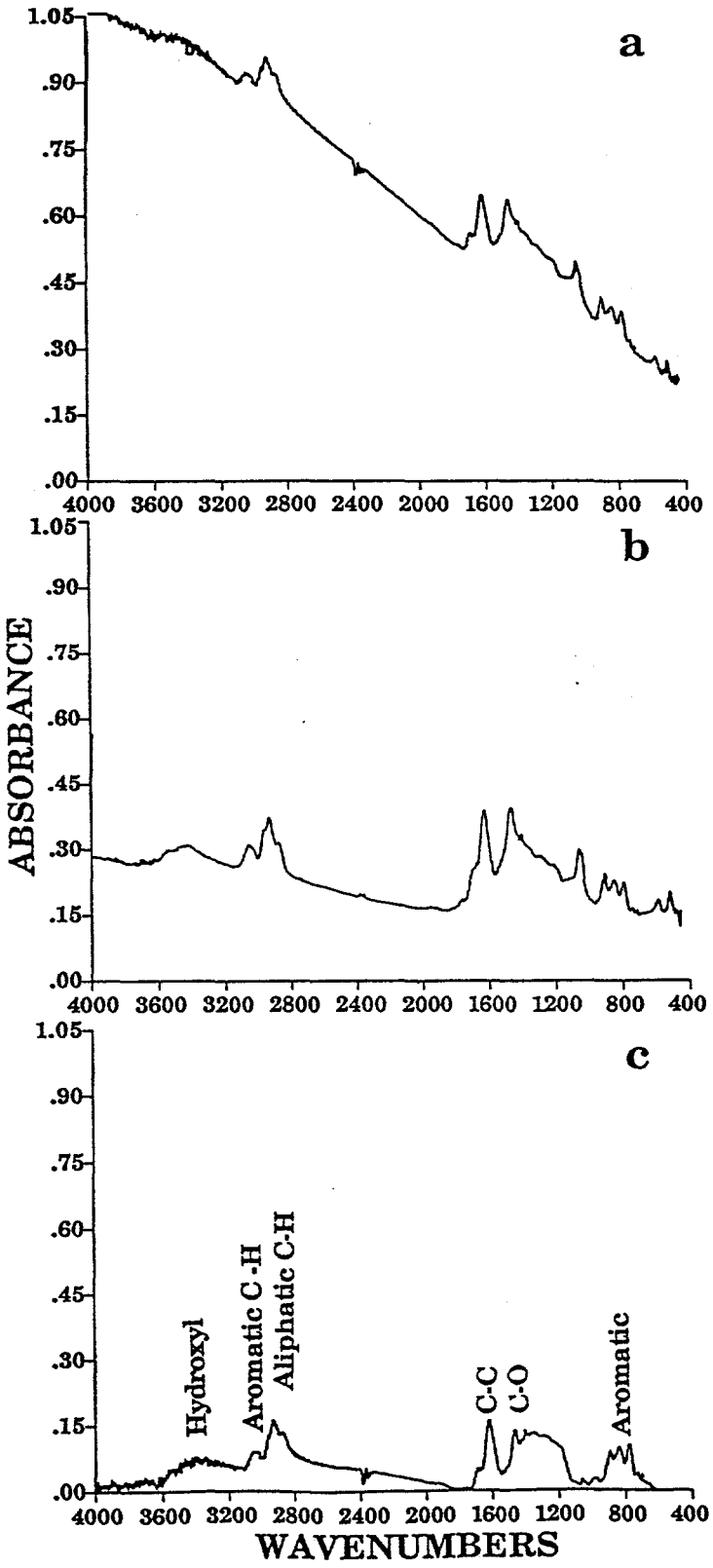

Figure II.A.1-5. FT-IR Spectra of Bulk Pocahontas Bituminous Coal. a) KBr, b) CSI, and c) KBr Pellet, Mineral Matter Corrected.

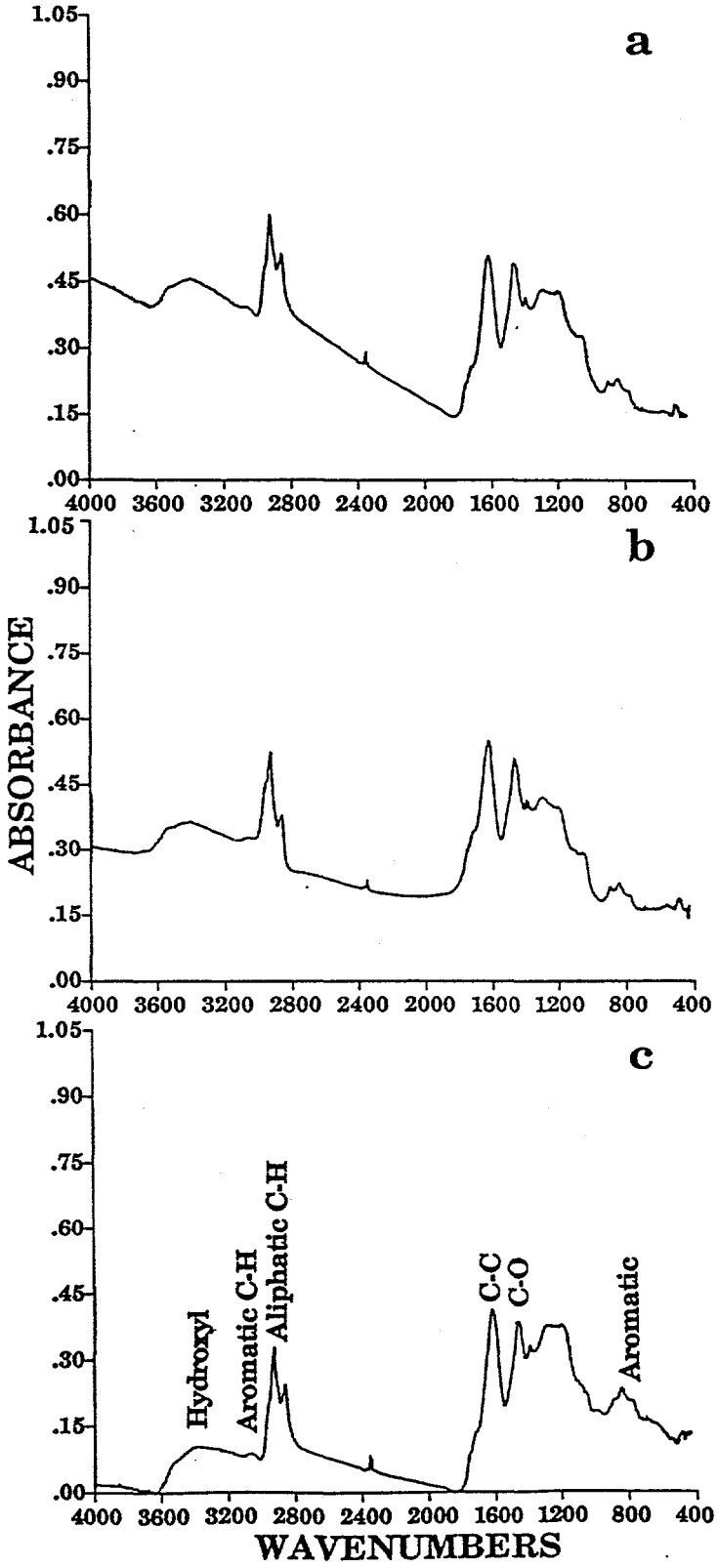

Figure II.A.1-6. FT-IR Spectra of Bulk Blind Canyon Bituminous Coal. a) KBr, b) CSI, and c) KBr Pellet, Mineral Matter Corrected.

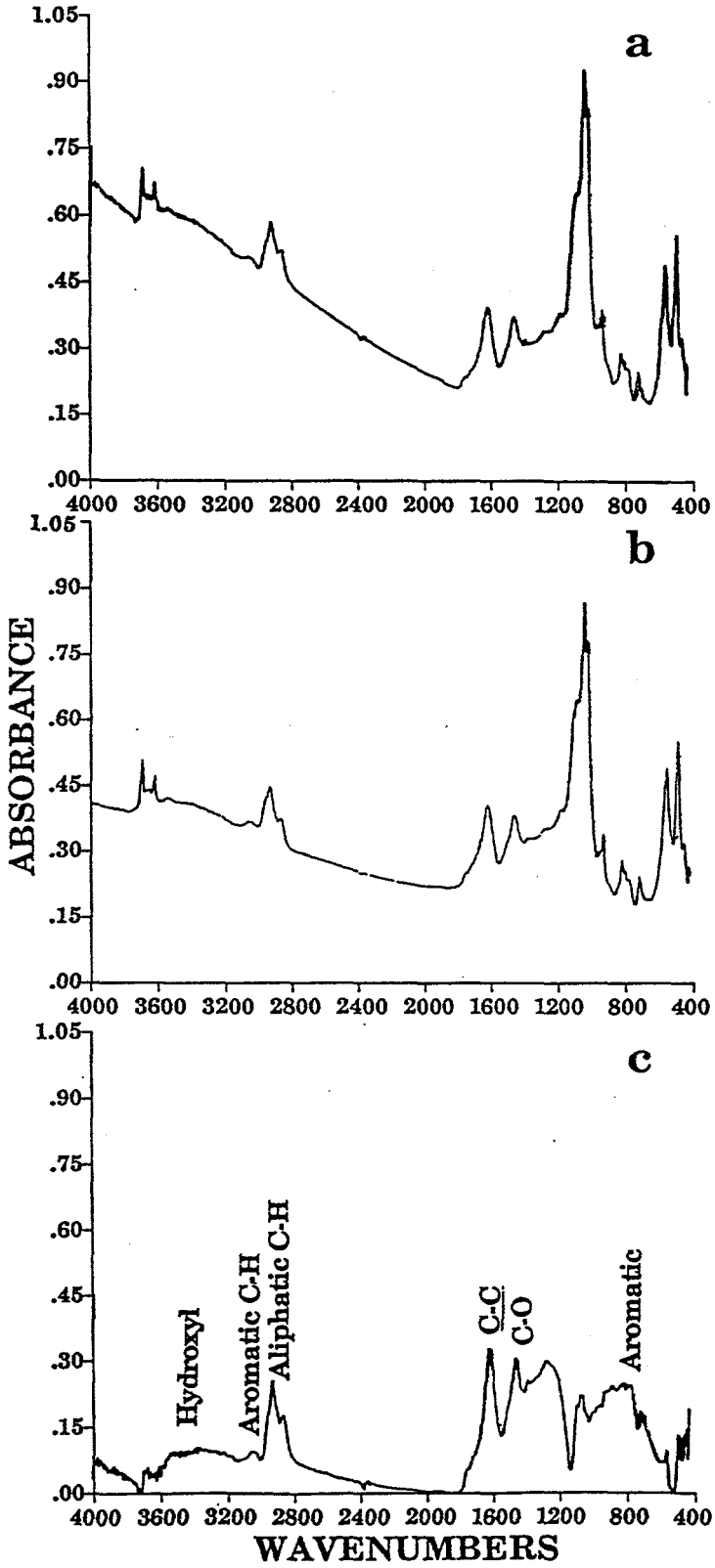

Figure II.A.1-7. FT-IR Spectra of Bulk Upper Knawha Bituminous Coal. a) KBr, b) CSI, and c) KBr Pellet, Mineral Matter Corrected.

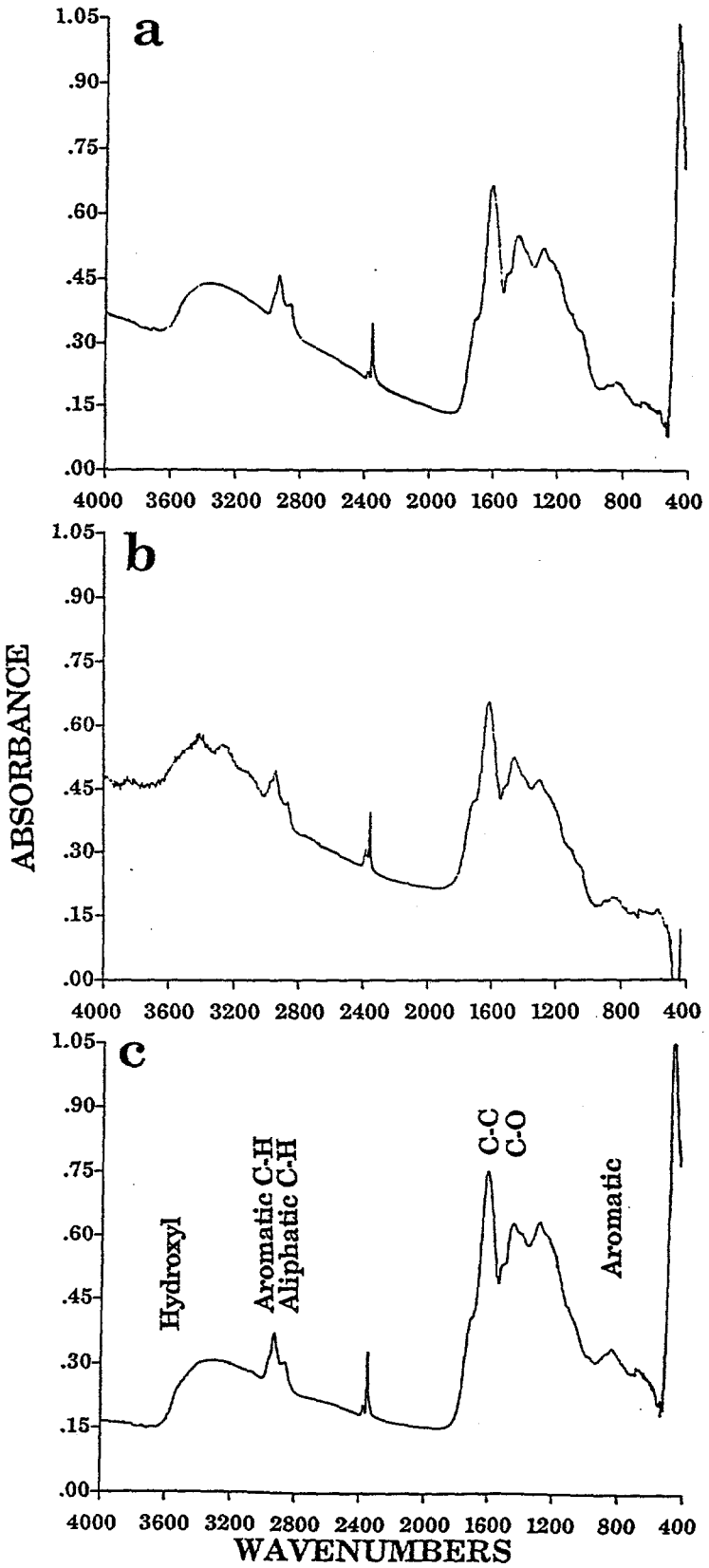

Figure II.A.1-8. FT-IR Spectra of Bulk North Dakota Zap Lignite. a) KBr, b) CSI, and c) KBr Pellet, Mineral Matter Corrected.

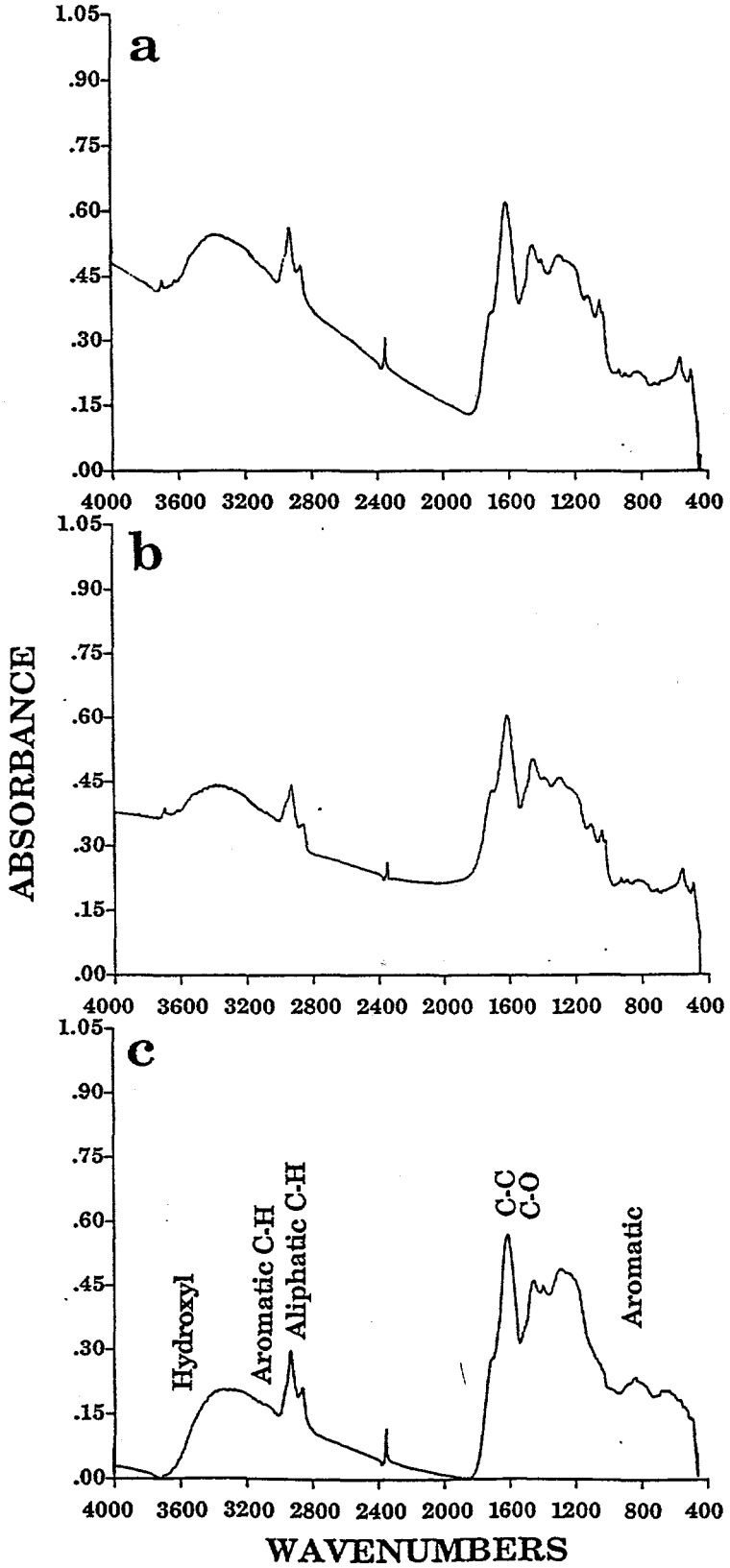

Figure II.A.1-9. FT-IR Spectra of Bulk Montana Rosebud Subbituminous Coal. a) KBr, b) CSI, and c) KBr Pellet, Mineral Matter Corrected.

uncorrected KBr and CsI pellet spectra for the nine coals. Seven of the spectra are for bulk samples and two are for amouple samples. In general, the bulk and ampoule samples are quite similar as shown in Figs. II.A.1-10 to II.A.1-16. The exception is the Upper Knawha which was a much higher mineral concentration in the bulk sample.

To obtain quantitative functional group and mineral matter data, a spectral synthesis routine was applied to the dry mineral matter and baseline corrected spectra (see Figs. II.A.1-1c to II.A.1-9c). The organic functional group data are shown in Tables II.A.1-3 and II.A.1-4 for bulk and ampoule samples, respectively. Tables II.A.1-5 and II.A.1-6 list the mineral matter data for the bulk and ampoule samples, respectively. The two sets of samples are similar except for the Upper Freeport and Pittsburgh No. 8 where the bulk samples are poorer in hydrogen and the Upper Knawha in which the bulk sample has a higher clay and quartz content.

Pyrolysis in Thermogravimetric Analyzer (TGA)

Pyrolysis experiments on the ampoule and bulk samples were performed using the TGA. With a N_2 flow of 400 cc/min and a N_2 purge flow of 20 cc/min, the coal particle temperatures reached 900°C with heating rates of 30°C/min. Plots of the TGA pyrolysis runs are shown in Figs. II.A.1-17 to II.A.1-21. The bulk samples and ampoules are similar except for some differences in moisture and mineral content for Wyodak, Upper Knawha, and North Dakota (Zap) lignite.

Char Reactivity in TGA

The reactions in chars prepared from both raw and demineralized coals were measured. The chars were prepared by pyrolysis as described above. The char reactivity measurements were made by employing a non-isothermal technique using the TGA. With an air flow of 40 cc/min and a N_2 purge flow of 40 cc/min, the samples were heated at a rate of 30°C/min until 900°C was reached. The resulting critical temperatures (defined as the temperature at which the derivative of the weight loss reaches 0.11 weight fraction/min) are listed in Table II.A.1-7 and are also plotted in Fig. II.A.1-22 as functions of oxygen in the parent coal.

Figure II.A.1-22a compares the bulk and ampoule sample. There is a good agreement between the two and the trend is an increase in reactivity (decreasing T_{cr}) with increasing oxygen.

Figure II.A.1-22b compares the raw bulk samples with the demineralized samples. The reactivities show interesting trends. Above 15% O_2, the ash content of the coal dominates the char reactivity, increasing the char's reactivity (lower T_{cr}) compared to the demineralized samples. The reason for this increase appears to be the catalytic activity of the organically bound alkali metals as will be discussed in Section II.D. Below 10% O_2, the raw coals have a lower reactivity (higher T_{cr}) than the demineralized samples. The reason for this is not known and is being investigated.

Determination of Percent Ash

Ash percent values ascertained through three different analytical techniques are listed in Table II.A.1-8. The values are in good agreement for the Argonne ampoule samples. These samples (excluding Montana sample) which were from amber borosilicate glass ampoules flame sealed under nitrogen were subjected to x-ray analysis, TGA analysis and Argonne's proximate analysis. There is more scatter for the bulk samples and the Montana Rosebud subbituminous which were not as well homogenized as the Argonne ampoule samples. The ash in the bulk sample of the Upper Knawha coal is much higher than in the ampoules.

Pyrolysis in Entrained Flow Reactor (EFR)

The 200 x 325 mesh sieved fractions of 6 of the Argonne coals were pyrolyzed in the entrained flow reactor. The coals were vacuum dried at 105°C for 1 hour prior to the pyrolysis runs. The coal was

Table II.A.1-3.

Data on Bulk Coals (weight Percent dmmf)*

	Hydrogen				Aromatic Hydrogen				Carbon	Carbonyl	Oxygen	
Sample	H_{al}	H_{oh}	H_{ar}	H_{total}	H_{ar}/H_{total}	1 Adj	2 Adj	3 or More	C_{al}	Units (Abs. x cm $^{-1}$)	O_{oh}	O_{ether}
UF	2.84	0.14	1.59	4.57	0.35	0.50	0.59	0.50	18.93	1.69	2.23	1.11
WY	3.10	0.34	1.74	5.18	0.34	0.54	0.78	0.42	20.67	26.65	5.50	4.53
PITT#8	3.02	0.11	1.57	4.70	0.33	0.54	0.63	0.40	20.13	8.38	1.75	1.44
POC#3	1.96	0.13	2.19	4.28	0.51	0.68	0.75	0.76	13.06	1.09	2.06	0.40
UT	4.65	0.20	1.96	6.81	0.29	0.52	0.89	0.55	31.00	11.17	3.25	4.00
WV	3.77	0.19	1.59	5.55	0.29	---	---	---	25.13	7.35	3.09	2.48
ZAP	2.31	0.33	1.66	4.30	0.39	0.50	0.69	0.46	15.40	25.59	5.25	5.5
ROSEBUD	2.79	0.45	1.62	4.86	0.33	0.48	0.71	0.43	18.60	26.64	7.22	6.31

* Except Carbonyl: Relative Peak Area

Table II.A.1-4.

Data on Ampoule Samples (weight Percent dmmf)*

	Hydrogen				Aromatic Hydrogen				Carbon	Carbonyl	Oxygen	
Sample	H_{al}	H_{oh}	H_{ar}	H_{total}	H_{ar}/H_{total}	1 Adj	2 Adj	3 or More	C_{al}	Units (Abs. x cm $^{-1}$)	O_{oh}	O_{ether}
UF	3.43	0.11	2.08	5.62	0.37	0.66	0.71	0.71	22.87	0.63	1.75	0.75
WY	3.03	0.33	1.73	5.09	0.34	0.52	0.78	0.43	20.20	23.86	5.25	5.0
ILL#6	3.41	0.23	2.07	5.71	0.36	0.69	0.78	0.60	22.73	4.48	3.75	2.25
PITT#8	3.60	0.16	2.07	5.83	0.36	0.67	0.80	0.60	24.00	0.86	2.5	1.88
POC#3	1.97	0.06	2.19	4.22	0.52	0.60	0.73	0.86	13.93	1.92	1.0	1.25
UT	4.79	0.16	1.90	6.85	0.28	0.51	0.80	0.58	31.93	8.70	2.5	4.0
WV	3.48	0.23	2.12	5.83	0.36	0.67	0.67	0.79	23.20	3.59	3.75	1.75
ZAP	2.02	0.34	1.58	3.94	0.40	0.46	0.74	0.37	13.47	24.67	5.5	5.0

* Except Carbonyl: Relative Peak Area

Table II.A.1-5.

Data on Bulk Coals (dry weight percent)

Minerals

Sample	Mixed Clay	Quartz	Calcite	Kaolin	Total
UF	9.06	0.86	1.98	2.63	14.53
WY	3.52	1.34	0.59	2.00	7.45
PITT#8	5.65	0.64	1.49	2.90	10.68
POC#3	4.91	0.53	3.88	0.45	9.76
UT	3.31	0.48	2.23	0.24	6.26
WV	21.40	4.79	1.08	8.44	35.71
ZAP					
ROSEBUD	3.42	1.00	1.92	2.51	8.86

Table II.A.1-6.

Data on Ampoule Samples (dry weight percent)

Minerals

Sample	Mixed Clay	Quartz	Calcite	Kaolin	Total
UF	10.40	0.93	2.97	3.60	17.90
WY	2.57	0.76	1.04	2.11	6.48
ILL#6	8.50	2.26	3.98	2.29	17.02
PITT#8	7.74	1.00	2.01	2.72	13.47
POC#3	4.28	0	4.83	0.99	10.11
UT	2.90	0.12	2.40	0.17	5.59
WV	15.50	1.24	1.46	7.74	25.95
ZAP	2.36	0.73	1.38	0.71	5.18

Table II.A.1-7.
Data on Char Reactivity

Coal Name	Abbreviation	Rank	Wt. % Oxygen in Original Coal Sample by Difference (DMMF)	0-900°C N_2 Char					
				Ampoules		Bulk Sample		Demineralized Bulk Sample	
				T_{cr}	%Ash	T_{cr}	%Ash	T_{cr}	%Ash
1. Upper Freeport	UF	Medium Volatile Bituminous	4	644	13.81	641	11.63	513	1.93
2. Wyodak	WY	Subbituminous	19	436	8.07	440	11.13	503	0.40
3. Illinois #6	ILL	High Volatile Bituminous	10	519	15.02	---	---	---	---
4. Pittsburgh #8	PITT	High Volatile Bituminous	8	586	9.61	600	9.01	542	1.44
5. Pocahontas #3	POC	Low Volatile Bituminous	3	607	5.10	611	4.83	564	---
6. Utah Blind Canyon	UT	High Volatile Bituminous	13	527	4.45	528	4.68	516	0.80
7. Upper Knawha	WV	Medium Volatile Bituminous	11	529	19.49	544	26.44	498	1.24
9. North Dakota	ZAP	Lignite	21	443	8.98	434	7.54	550	0.26
10. Rosebud		Subbituminous	20	---	---	478	14.72	508	3.47

*HF/HCL demineralized.

Table II.A.1-8. Ash in Dry Weight Percent

Analysis Type	Upper Freeport	Wyodak	Illinois No.6	Pittsburgh No.8	Pocohontas No.3	Utah Blind Canyon	Upper Knawha	North Dakota Lignite	Montana Rosebud
TGA Ampoule	13.81	8.07	15.02	9.61	5.00	4.45	19.49	8.98	---
TGA Bulk	11.63	11.13	--	9.01	4.83	4.68	26.44	7.54	14.72
X-Ray Ampoule	12.49	9.02	16.14	8.51	4.40	3.41	21.48	9.60	12.33
Argonne Proximate (ampoule)	13.16	8.95	17.76	9.44	4.90	4.68	19.81	6.53	--

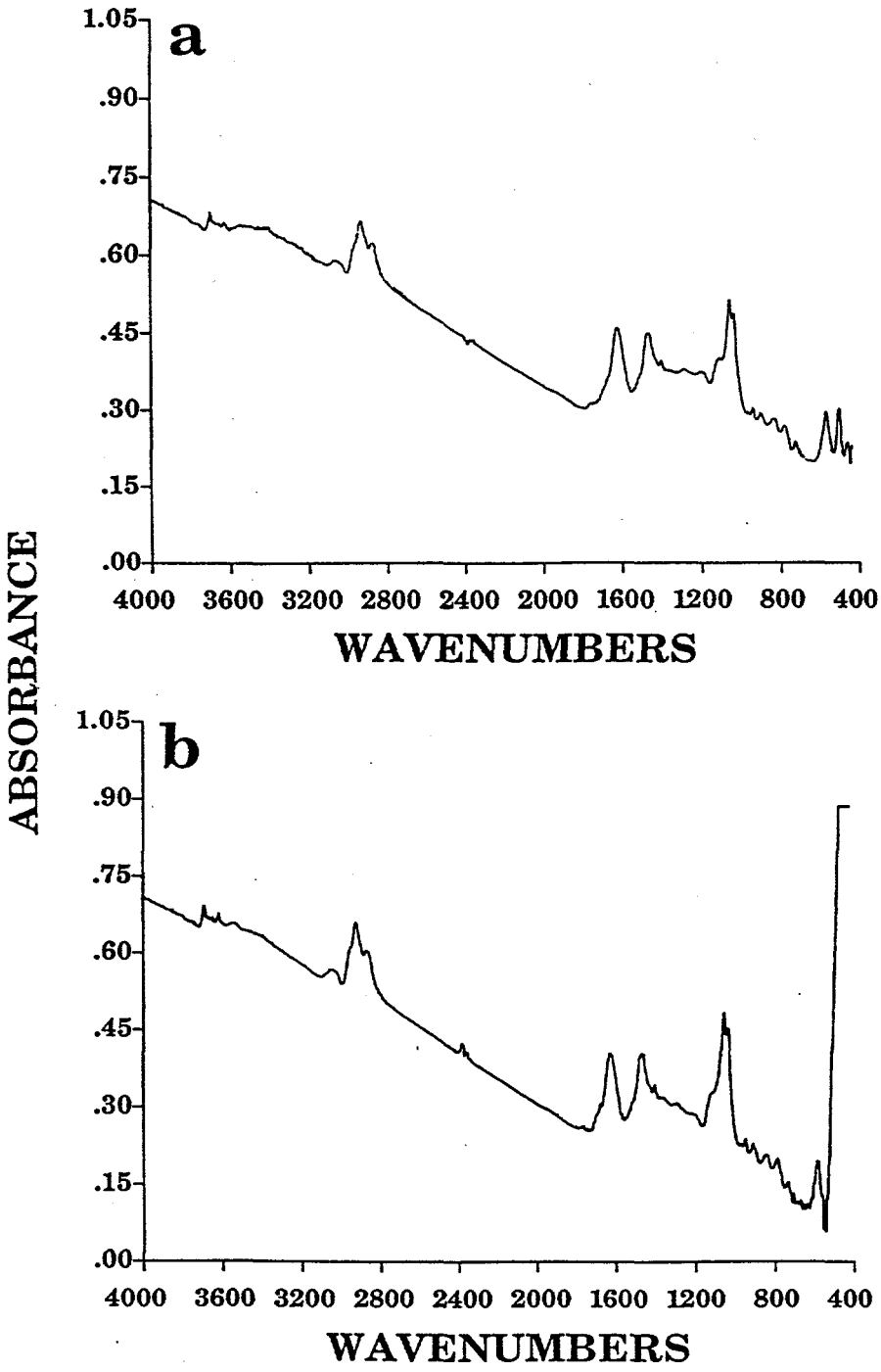

Figure II.A.1-10. Dry Uncorrected FT-IR Spectra of Upper Freeport Bituminous Coal. a) Bulk Sample and b) Ampoule Sample.

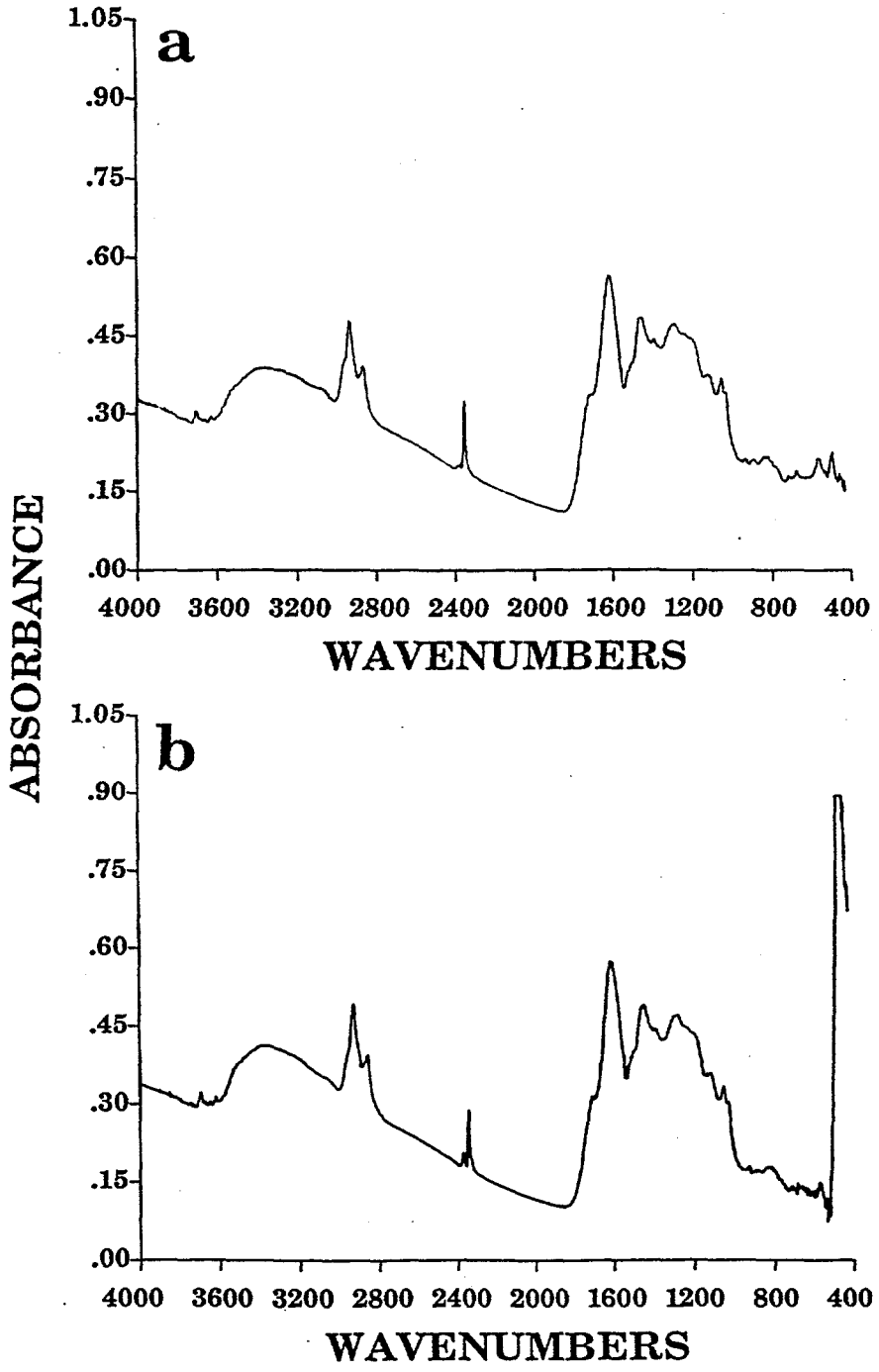

Figure II.A.1-11. Dry Uncorrected FT-IR Spectra of Wyodak Subbituminous Coal. a) Bulk Sample and b) Ampoule Sample.

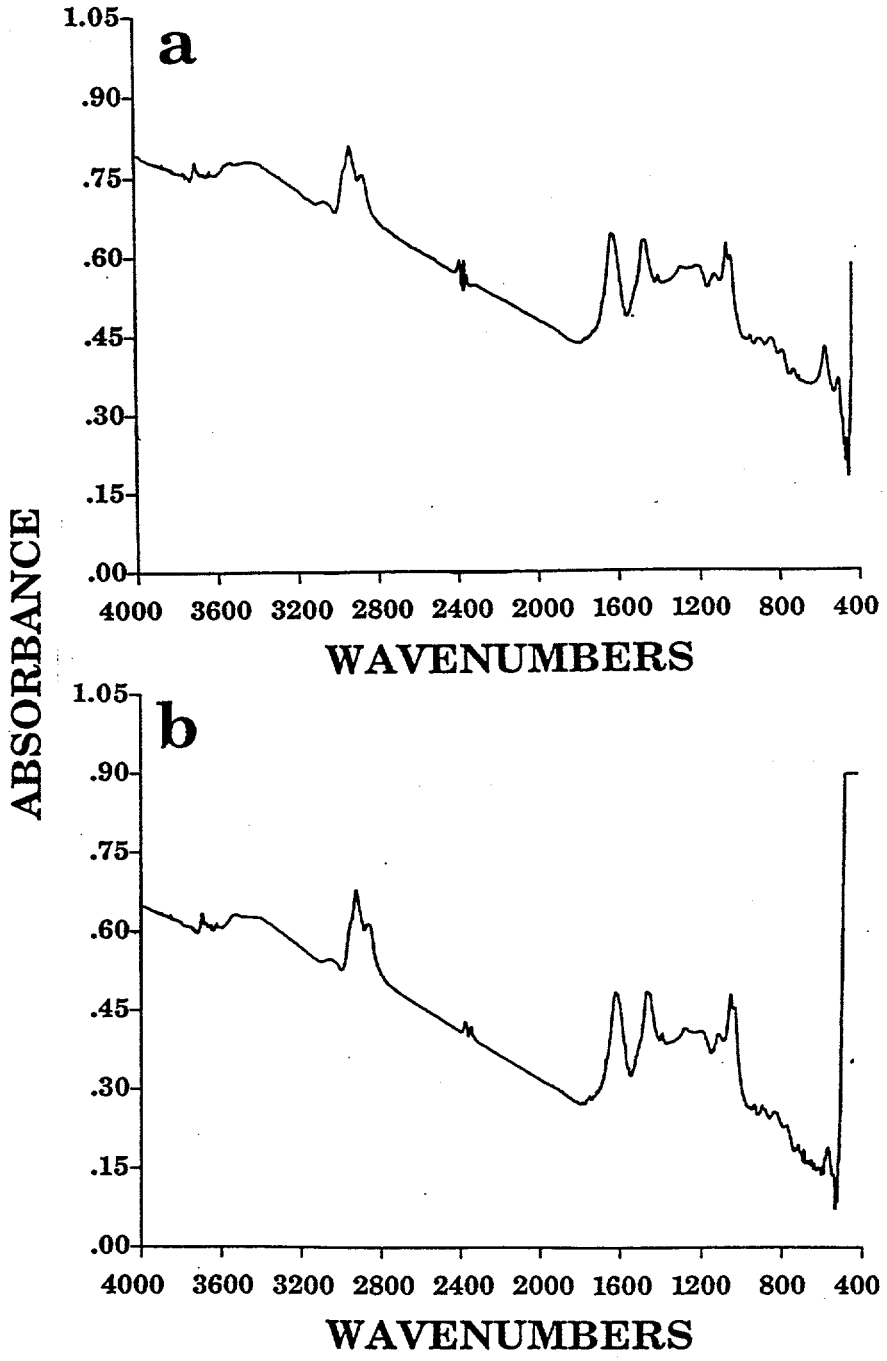

Figure II.A.1-12. Dry Uncorrected FT-IR Spectra of Pittsburgh Seam #8 Bituminous Coal. a) Bulk Sample and b) Ampoule Sample.

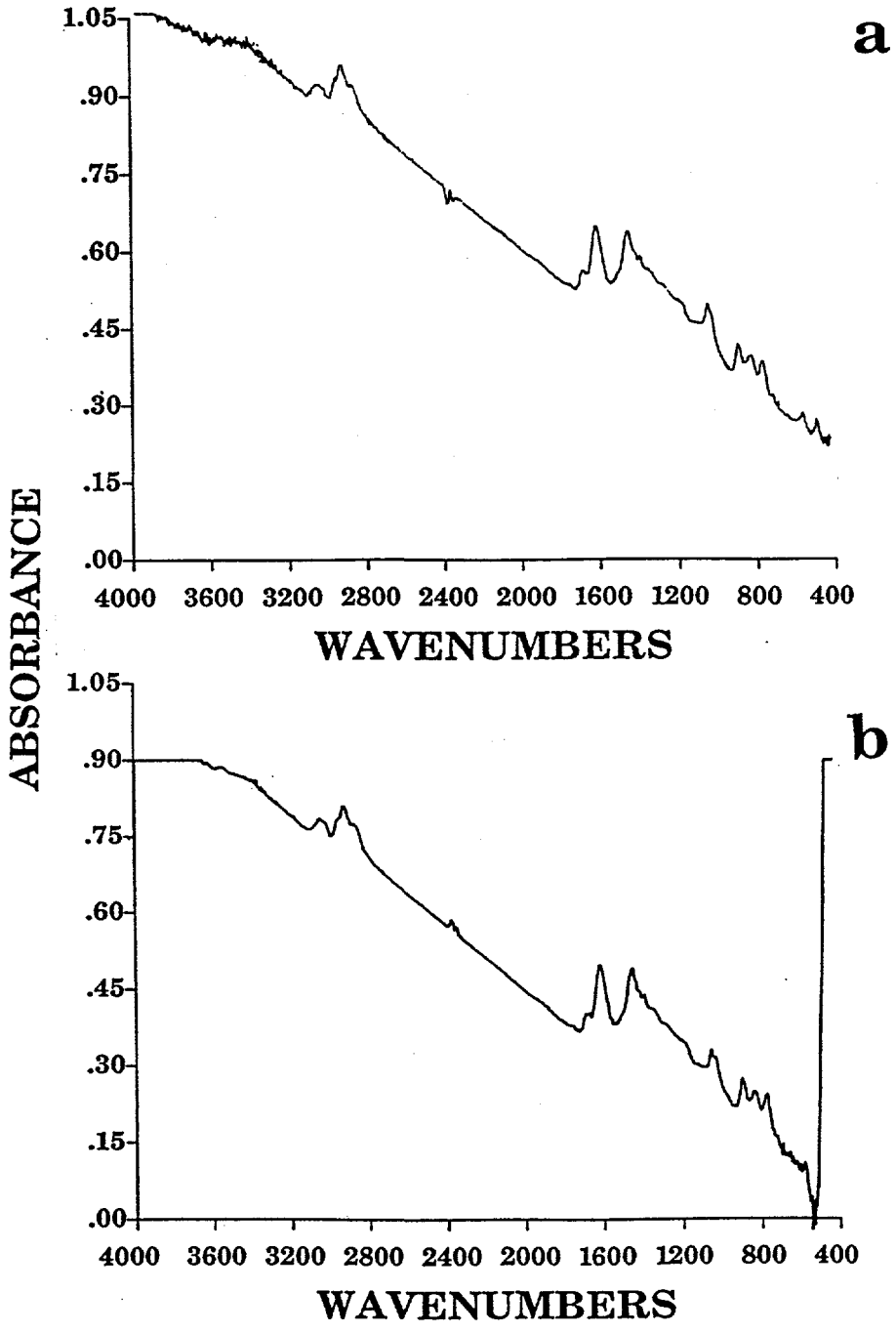

Figure II.A.1-13. Dry Uncorrected FT-IR Spectra of Pocahontas #3 Bituminous Coal. a) Bulk Sample and b) Ampoule Sample.

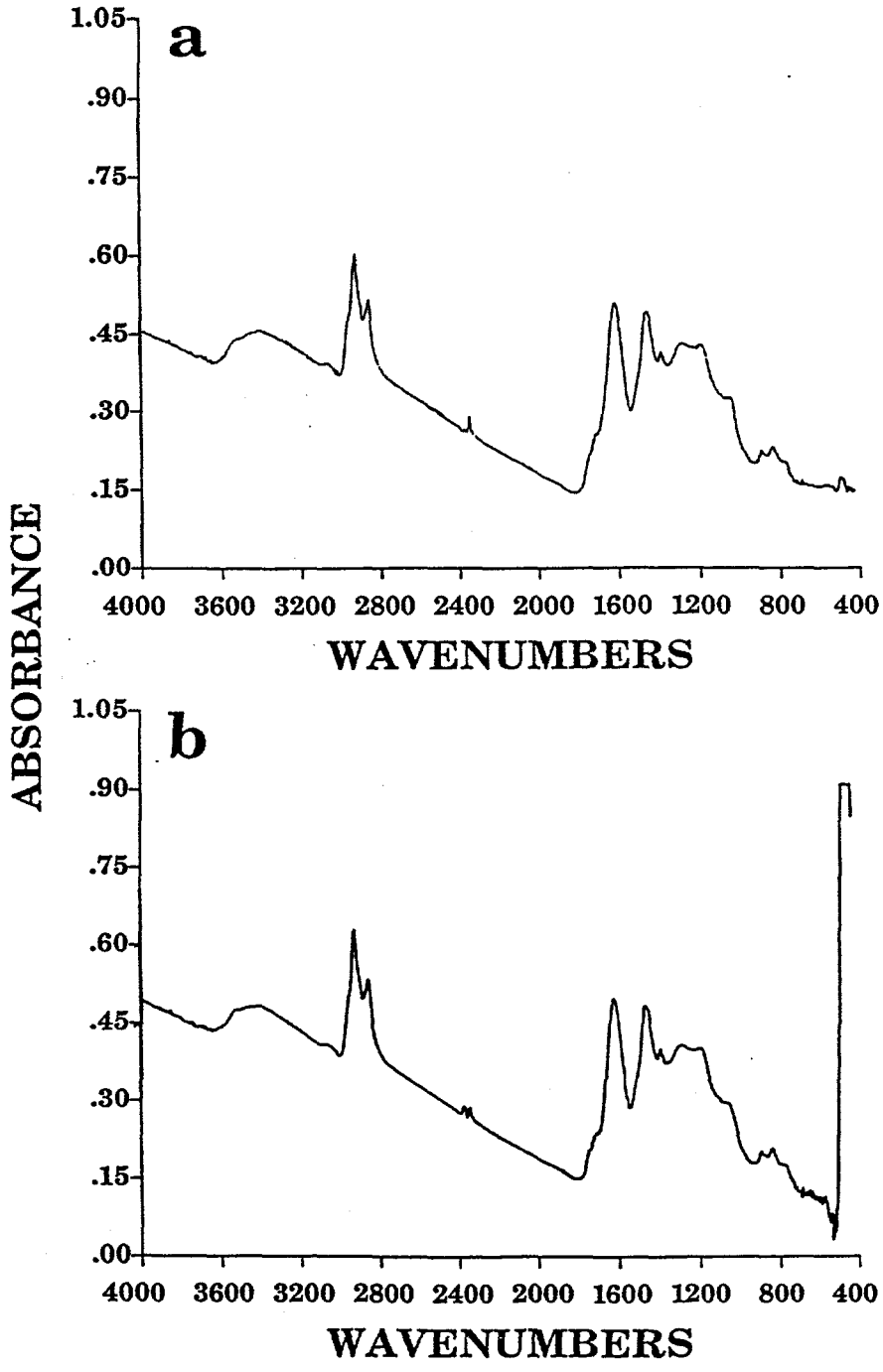

Figure II.A.1-14. Dry Uncorrected FT-IR Spectra of Utah Blind Canyon Bituminous Coal. a) Bulk Sample and b) Ampoule Sample.

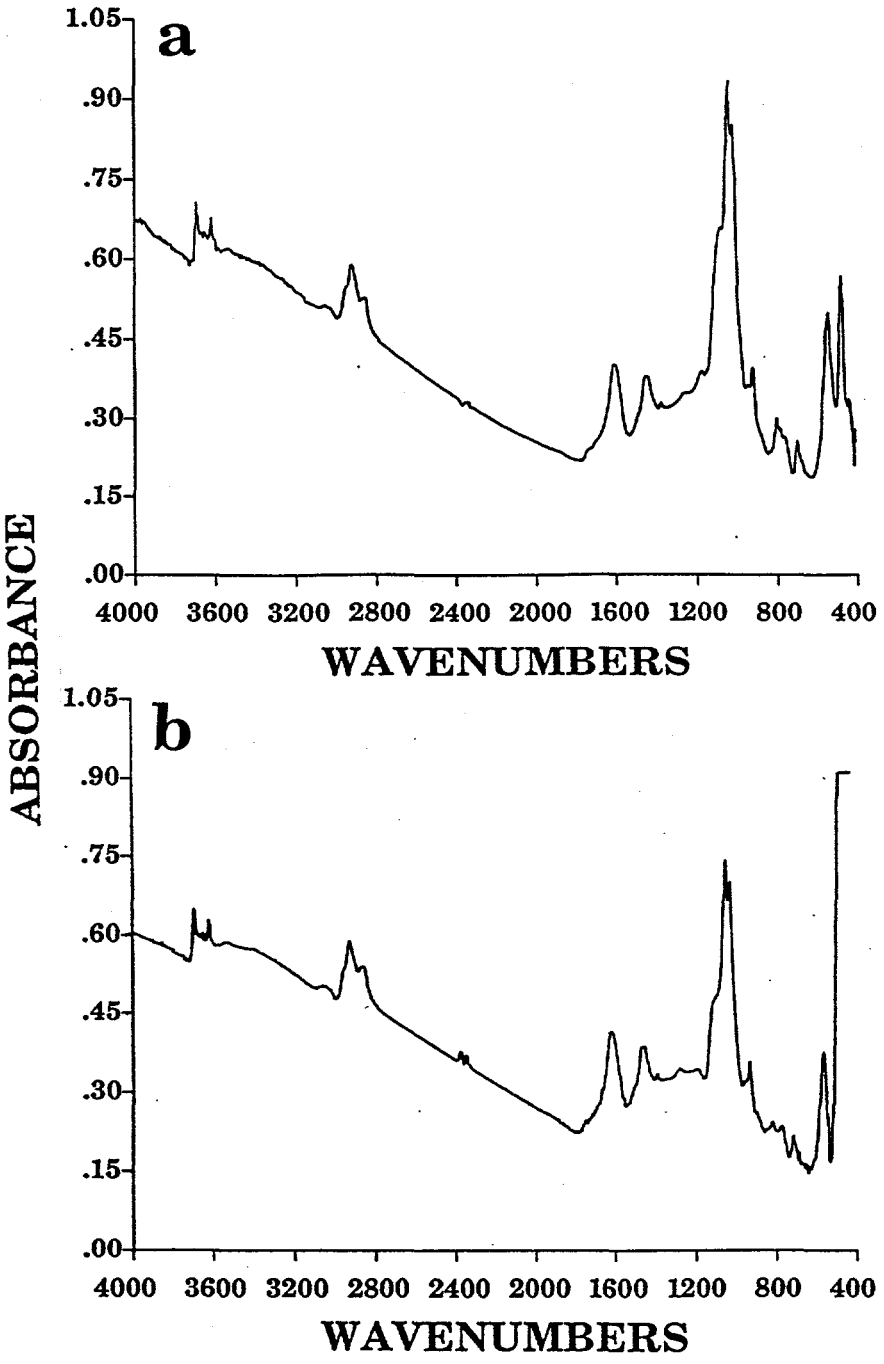

Figure II.A.1-15. Dry Uncorrected FT-IR Spectra of Upper Knawha Bituminous Coal. a) Bulk Sample and b) Ampoule Sample.

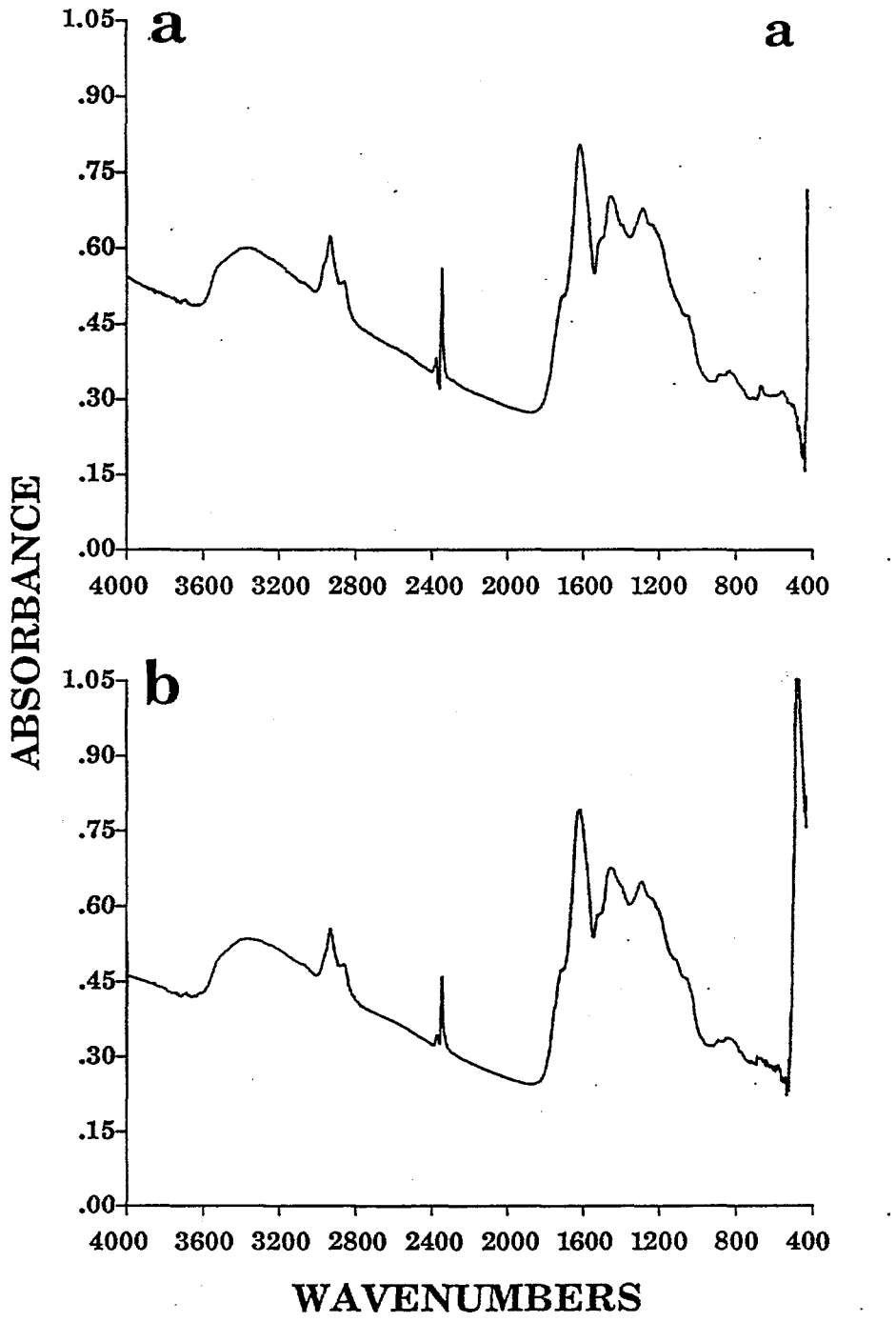

Figure II.A.1-16. Dry Uncorrected FT-IR Spectra of Beulah Zap Lignite. a) Bulk Sample and b) Ampoule Sample.

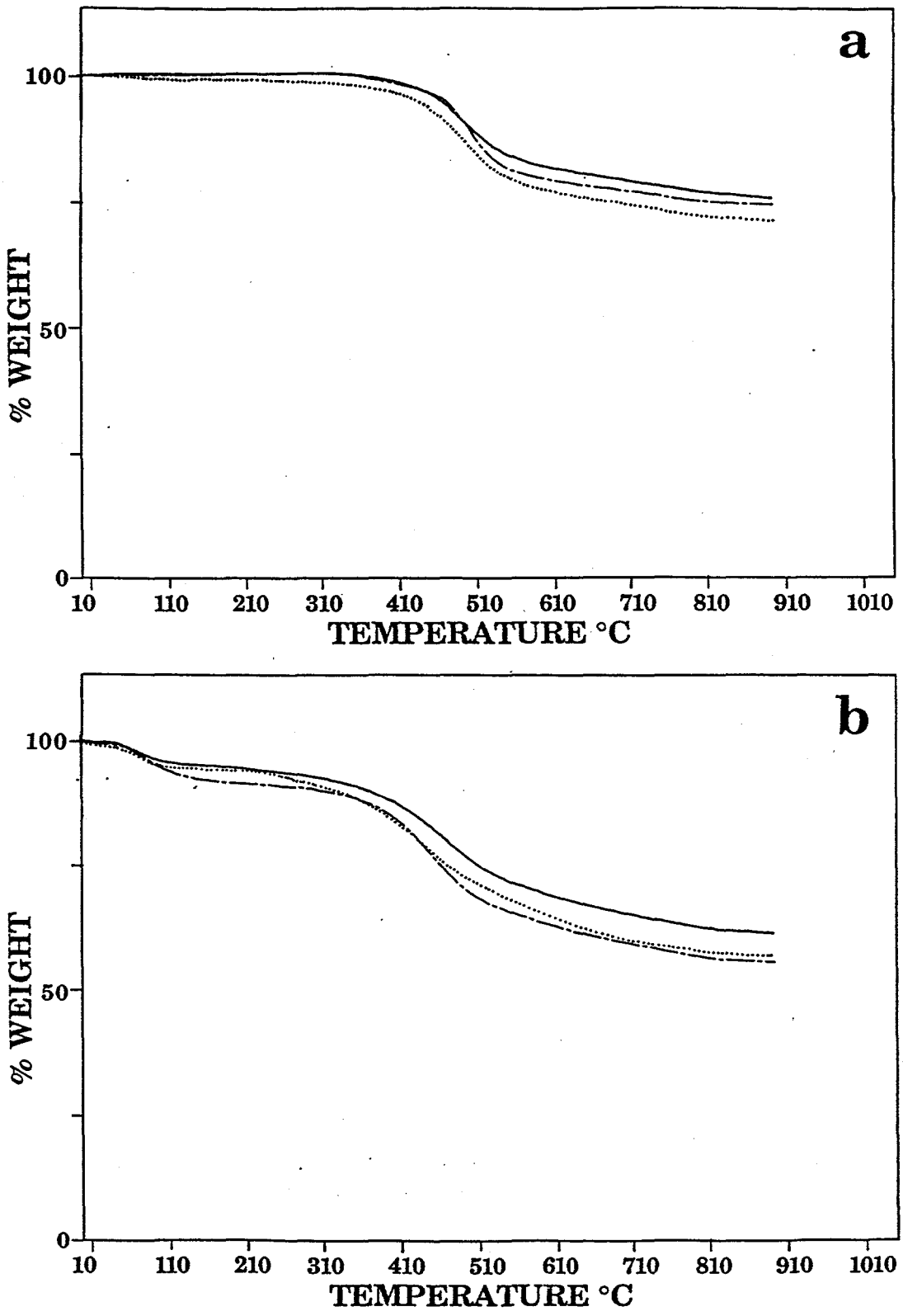

Figure II.A.1-17. Pyrolysis of a) Upper Freeport Bituminous Coal and b) Wyodak Subbituminous Coal in TGA at 30°C/min in N_2. Solid, Dashed, and Dotted Lines Represent Bulk, Ampoule and Demineralized Samples, Respectively.

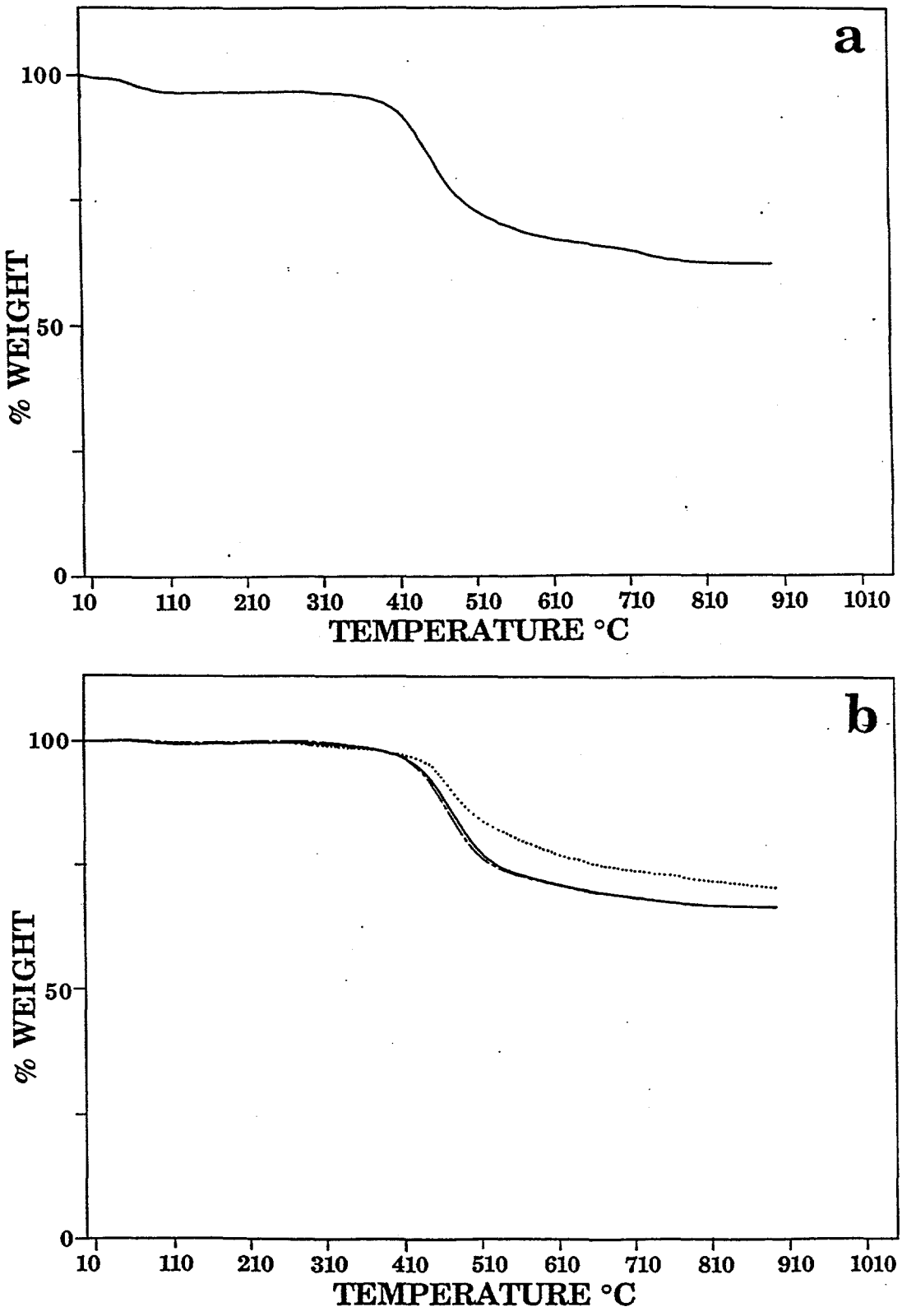

Figure II.A.1-18. Pyrolysis of a) Illinois #6 Bituminous Coal and b) Pittsburgh Seam Bituminous Coal in TGA at 30°C/min in N_2. Solid, Dashed, and Dotted Lines Represent Bulk, Ampoule and Demineralized Samples, Respectively.

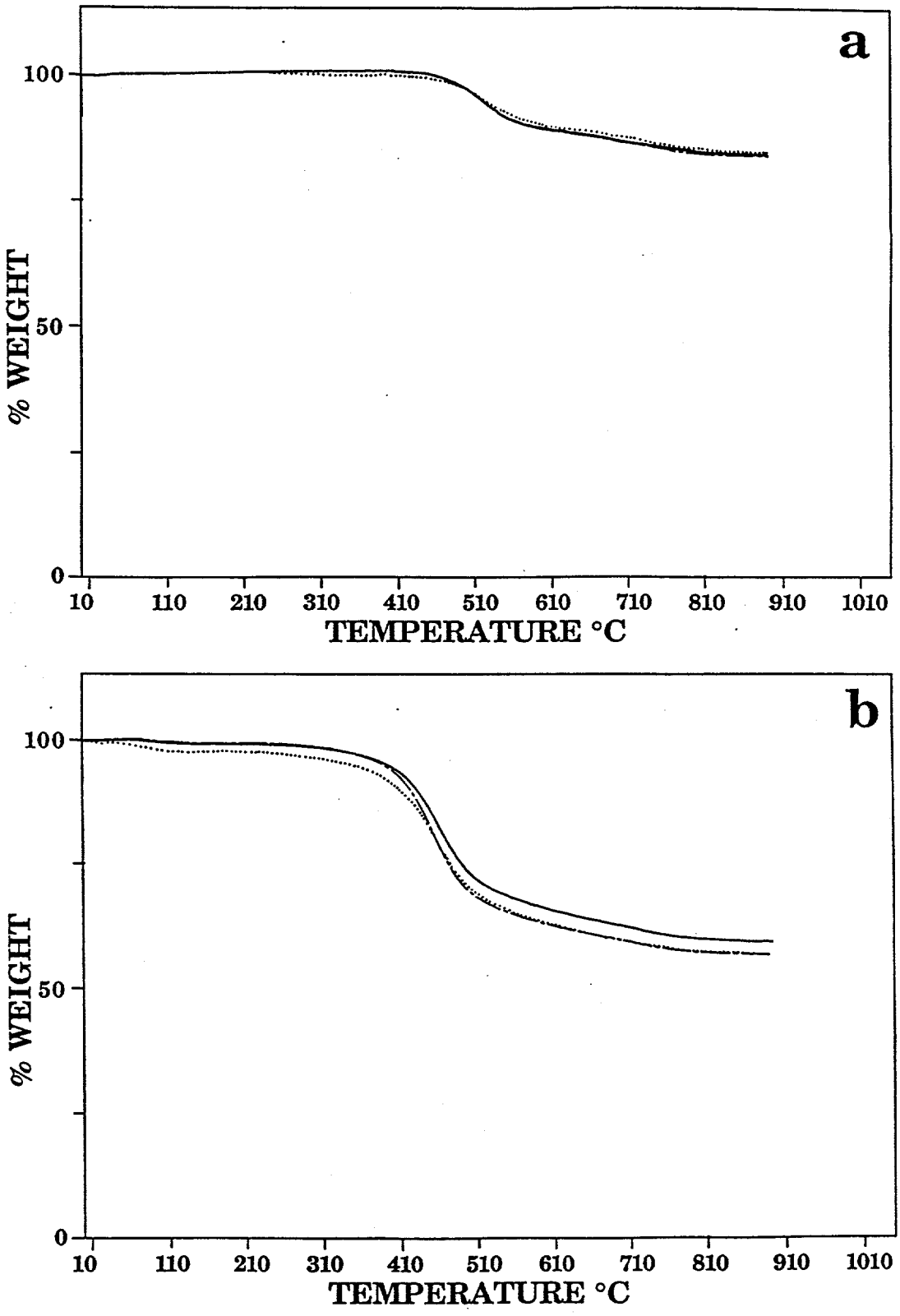

Figure II.A.1-19. Pyrolysis of a) Pocahontas #3 Bituminous Coal and b) Utah Blind Canyon Bituminous Coal in TGA at 30°C/min in N_2. Solid, Dashed, and Dotted Lines Represent Bulk, Ampoule and Demineralized Samples, Respectively.

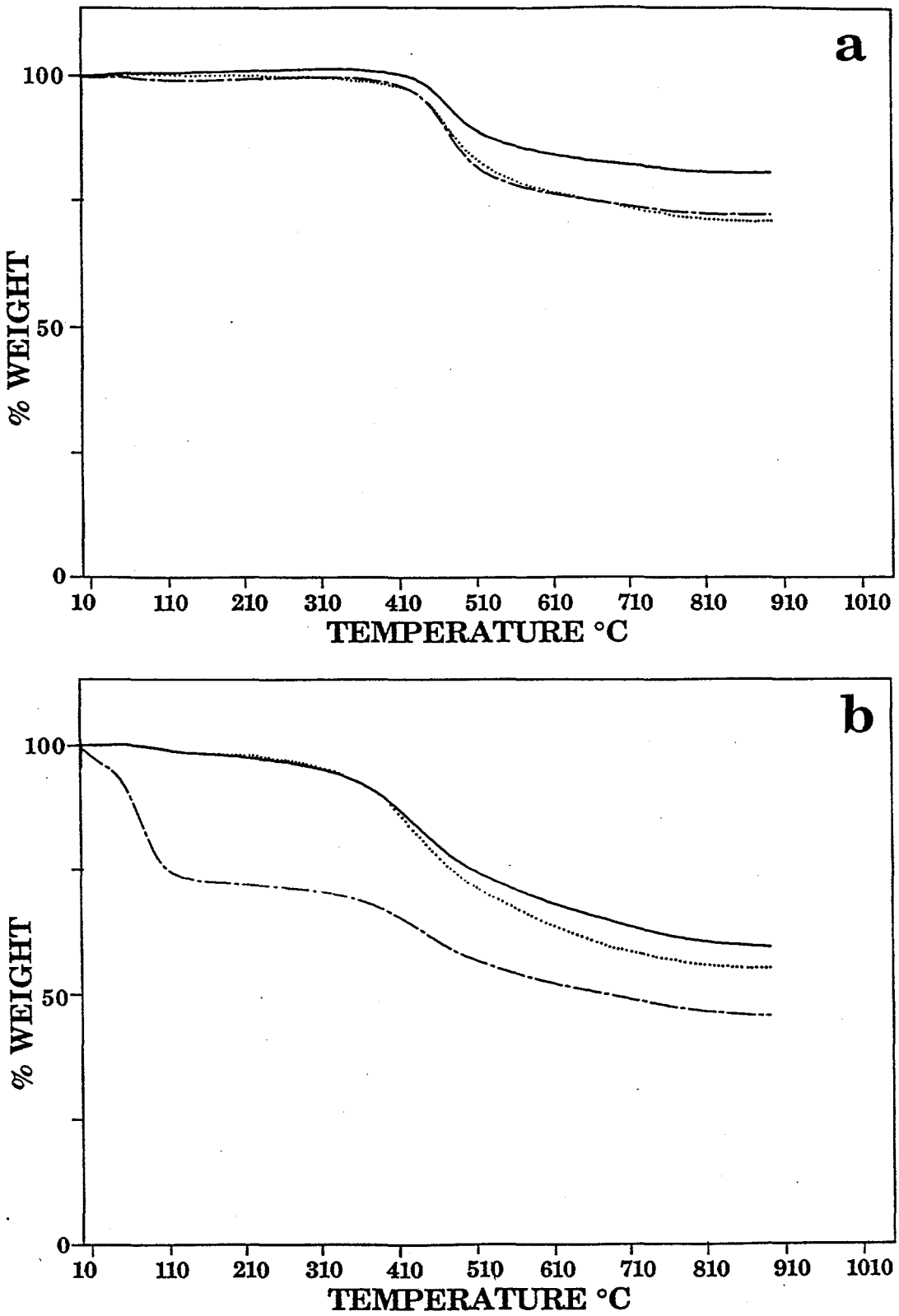

Figure II.A.1-20. Pyrolysis of a) Upper Knawha Bituminous Coal and b) Zap North Dakota Lignite in TGA at 30°C/min in N_2. Solid, Dashed, and Dotted Lines Represent Bulk, Ampoule and Demineralized Samples, Respectively.

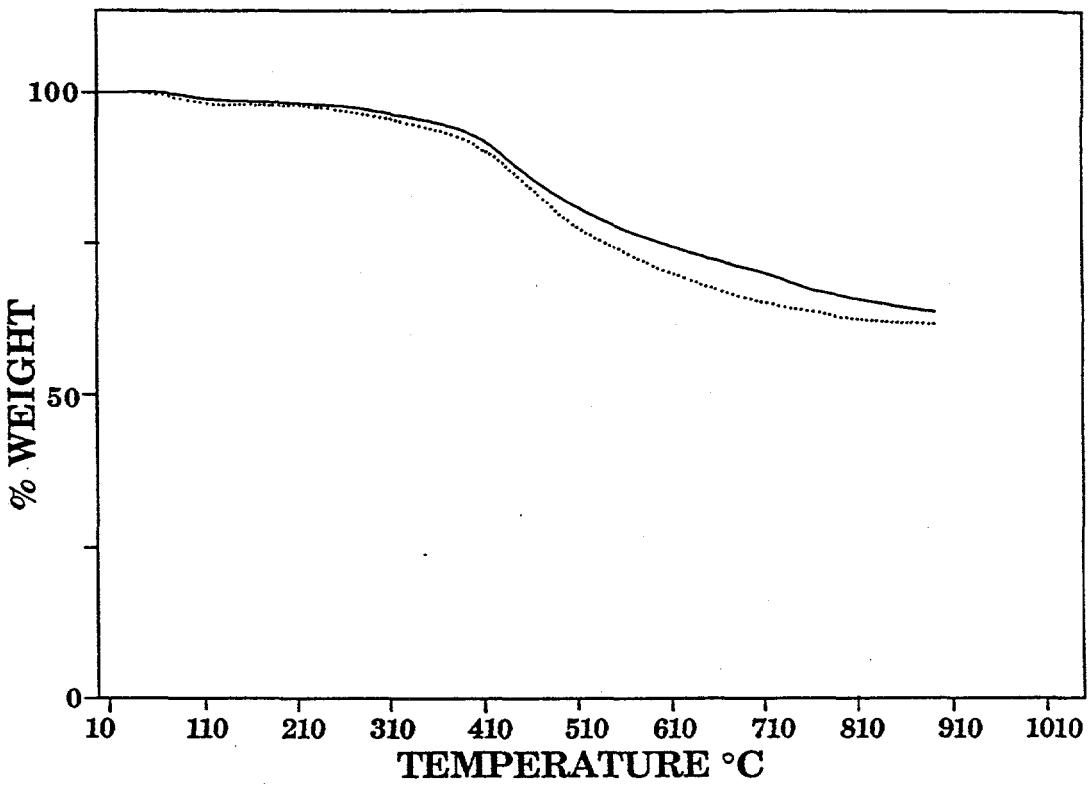

Figure II.A.1-21. Pyrolysis of Upper Montana Rosebud Subbituminous Coal in TGA at 30°C/min in N_2. Solid, Dashed, and Dotted Lines Represent Bulk, Ampoule and Demineralized Samples, Respectively.

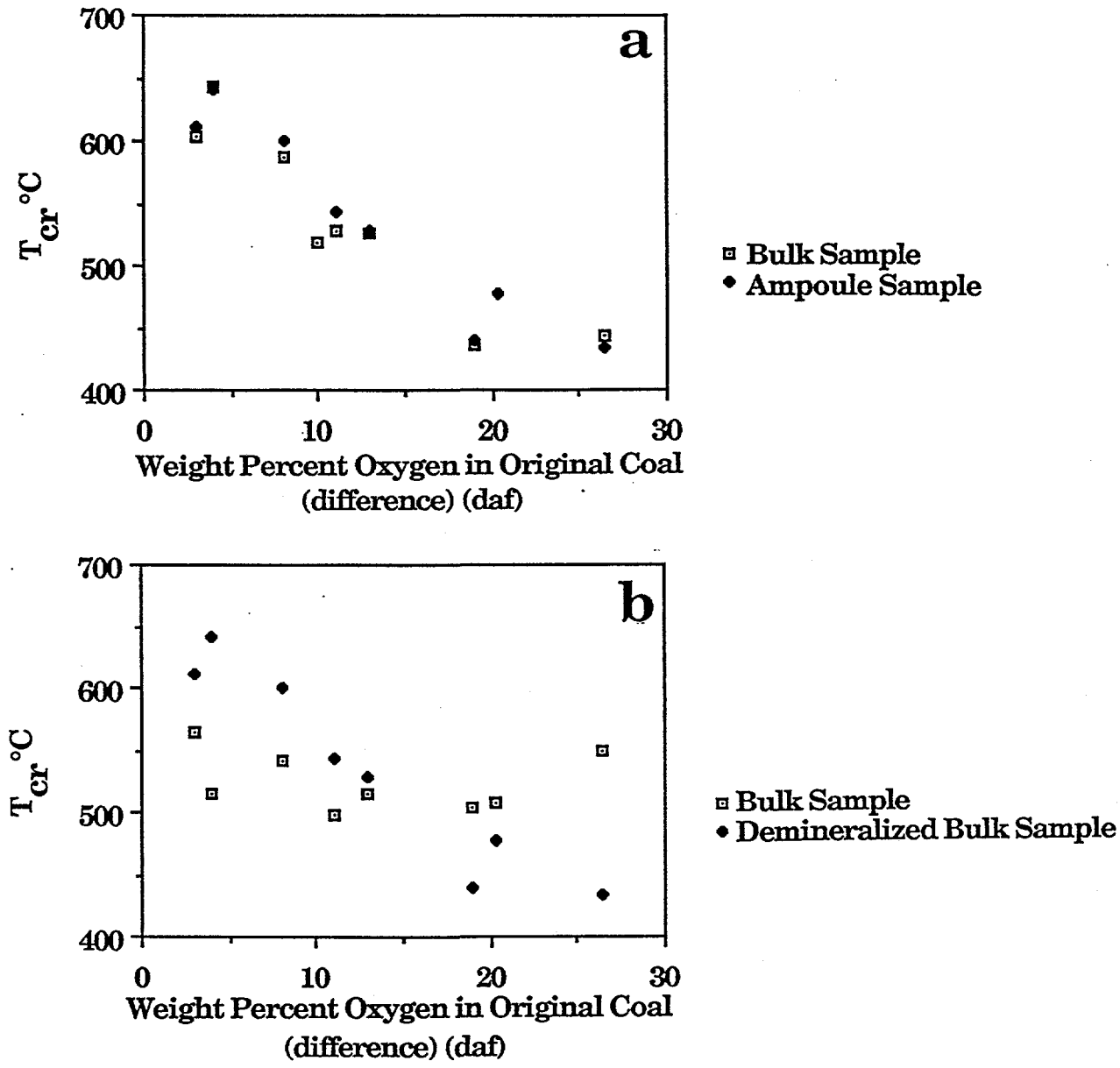

Figure II.A.1-22. Variation of Reactivity with Coal Rank for Chars Prepared by Heating in Nitrogen at 30°C/min to 900°C.

fed at rates of 1½ to 2 g/min with a N_2 carrier. Particle residence time was approximately 0.66 seconds with the injector height position adjusted to 24" and the furnace operated at 1400°C. 1100°C, and 700°C. The gas analyses were performed using two analytical techniques: 1) FT-IR calibration program and 2) Gas Chromatograph.

The data are presented in Tables II.A.1-9 to II.A.1-11. The data are plotted for each coal as a function of temperature in Figs. II.A.1-23 to II.A.1-28. The yields show the expected dependence on temperature. These data, as well as data from the TG-FTIR will be modeled using the FG/DVC model during the next year.

II.A.2. FG-DVC Model

The FG-DVC model has been developed as a stand alone PC-based predictive model as well as a submodel for comprehensive combustion and gasification codes. FG-DVC is a general model for coal pyrolysis which predicts the coal's decomposition into tar, char, and gas, given the ambient pressure and the time-temperature history of an isothermal coal particle. The model predicts the amount, functional group composition, elemental composition, and molecular weight distribution of tar and char and the amount and composition of the gas.

The FG model considers certain functional groups in the coal which decompose to form the light gas species. At the same time, the DVC model describes the overall depolymerization of the macromolecular network which combines bridge breaking and crosslinking to produce fragments of the coal macromolecule. These fragments are then subjected to transport behavior, specifically the vaporization of the lightest fragments to form tar. The tar fragmentation process provides a second mechanism for the removal of functional groups from the coal. The model, whose parameters are determined in the laboratory at moderate temperatures and one atmosphere, can then be used to extrapolate away from the laboratory conditions to predict pyrolysis and combustion in high temperature reactions, or liquefaction at high pressure. Recently, we have explored extrapolation of the kinetics and reactions to low temperature geological transformations in coal beds.

The model for coal thermal decomposition has six basic concepts.

- Functional Groups (decompose to produce light gases)
- Macromolecular Network (decomposes to produce tar and metaplast)
- Network Coordination Number (possible number of attachments per cluster)
- Bridge Breaking (limited by hydrogen availability)
- Crosslinking (related to gas evolution)
- Mass Transport of Tar (evaporation of light network fragments into light gases)

The first concept is that light gases are formed by the decomposition of certain functional groups in the coal. For example, methyl groups can lead to the formation of methane, carboxyl groups can lead to the formation of CO_2, etc. The second concept is that coal consists of a macromolecular network. This network is made up of fused aromatic ring clusters (which are described by their molecular weight) linked by bridges, some of which are relatively weak. There are some unattached parts of the network which can be extracted. Sometimes, there is also a second component of high polymethylene content. When heated, this network decomposes to produce smaller fragments. The lightest of the fragments evaporate to produce tar and the heavier fragments form the metaplast. These heavier molecules are the primary liquid fragments in liquefaction or the fragments that make coal fluid.

The third concept is that one of the most important properties of the network is its coordination number ($1 + \sigma$). The coordination number describes the geometry of the network, and specifies how many possible attachments there are per aromatic ring cluster. For example, a linear polymer chain has a coordination number of 2, because each fused aromatic ring has two possible attachments to link it in the chain. On the other hand, a square "fish net" has a coordination number of 4, because there are four possible attachments at each ring cluster. The coordination number controls the molecular weight

Table II.A.1-9.

Pyrolysis in the Entrained Flow Reactor in Nitrogen at 700°C, 24".

Values in Ash Free Weight Percent.

AFR/BYU Run # / Species	19 Upper Freeport	20 Upper Knawha	21 Pittsburgh #8	22 Wyodak	23 Pocahontas #3	24 Utah Blind Canyon
Char	64.88	66.95	57.49	59.56	80.64	54.8
Tar & Soot	22.07	17.22	30.5	13.09	10.29	25.8
Gas	5.85	6.95	7.44	13.46	3.83	13.62
H_2O	6.68	3.62	5.96	2.27	2.71	.95
Missing	.53	5.27	-1.4	11.62	2.52	4.83
CH_4	.92	.678	1.1	.696	.784	1.25
CO	.122	.449	.506	2.44	.118	1.04
H_2	0	0	0	0	0	0
CO_2	.408	1.16	.331	4.82	.81	3.47
C_2H_2	.021	.002	.006	.007	1.4×10^{-4}	0.1
C_2H_4	.372	.271	.433	.452	.095	.623
C_2H_6	.373	.169	.393	.198	.201	.66
C_3H_6	.305	.591	.589	.703	.106	.83
C_6H_6	.002	.609	.217	.406	.338	.24
CS_2	.145	.107	.108	.134	.074	.07
SO_2	.024	0	.014	.01	0	.01
HCN*	.094	0	0	0	0	.12
Paraffins	1.93	2.17	2.46	1.73	1.09	3.54
Olefins	1.57	.744	1.32	1.77	.208	1.77

* HCN values not included in gas totals or missing totals.

Table II.A.1-10.

Pyrolysis in the Entrained Flow Reactor in Nitrogen at 1100°C, 24".

Values in Ash Free Weight Percent.

AFR/BYU Run #	10	11	12	13	14	15	16
Species	Upper Freeport	Wyodak	Upper Freeport	Upper Knawha	Utah Blind Canyon	Pittsburgh #8	Pocahontas #3
Char	52.50	43.16	52.14	56.52	40.94	47.91	73.50
Tar & Soot	21.65	7.71	16.59	14.35	13.40	21.84	11.69
Gas	25.99	40.14	24.94	21.49	39.28	28.62	14.17
H_2O	1.73	2.85	3.40	5.64	7.02	4.58	3.58
Missing	-1.88	6.14	2.93	2.60	-.64	-2.95	-2.94
CH_4	4.37	1.86	4.01	3.80	5.34	5.55	3.23
CO	5.46	12.27	5.40	4.16	8.85	6.04	1.82
H_2	1.38	.99	1.22	.77	1.5	1.21	1.04
CO_2	1.91	9.29	2.02	1.02	6.07	1.62	1.03
C_2H_2	1.49	2.09	1.21	.73	2.01	1.06	1.23
C_2H_4	1.95	2.27	1.76	1.84	2.84	2.29	.96
C_2H_6	.005	.006	.009	.15	.05	.08	.08
C_3H_6	.15	.24	.15	.20	.24	.25	.06
C_6H_6	3.32	5.26	3.45	3.23	3.97	3.98	2.08
CS_2	.18	.24	.25	.14	.164	.16	0.097
SO_2	.03	.012	.029	--	.002	.018	---
HCN *	2.16	1.49	1.93	1.36	2.98	2.07	.70
Paraffins	.56	.44	.59	.83	.55	.61	.33
Olefins	3.05	3.66	2.89	3.26	4.68	3.68	1.51

* HCN values not included in gas totals or missing totals.

Table II.A.1-11.

Pyrolysis in the Entrained Flow Reactor in Nitrogen at 1400°C, 24".

Values in Ash Free Weight Percent

AFR/BYU Run #	1	2	3	4	5	6	8	9
Species	Pocahontas #3	Pocahontas #3 Re-run of Run #1	Upper Knawha	Wyodak	Upper Freeport	Utah Blind Canyon	Wyodak Re-run of Run #4	Pittsburgh #8
Char	70.03	70.19	51.22	44.82	46.64	35.24	42.82	37.38
Tar & Soot	13.54	13.22	20.05	15.54	25.85	28.52	13.44	29.75
Gas	14.22	15.34	22.28	43.0	21.91	33.49	45.18	30.64
H_2O	.58	2.23	1.37	2.40	.64	.85	1.46	1.80
Missing	1.23	-.99	5.08	-3.36	4.94	1.90	-2.90	.43
CH_4	.24	.19	.16	.16	.14	.28	.41	.19
CO	7.21	8.27	15.80	30.25	12.95	22.72	31.12	18.92
H_2	4.38	4.11	4.22	4.17	4.55	5.19	4.0	4.82
CO_2	.49	.70	1.80	5.75	1.28	1.42	6.74	1.96
C_2H_2	1.83	1.87	.03	2.36	2.59	3.72	2.59	4.33
C_2H_4	.56	.04	.06	.04	.05	.12	.054	.10
C_2H_6	1.73×10^{-5}	.02	4.86×10^{-6}	.01	.01	6.34×10^{-4}	.001	2.91×10^{-3}
C_3H_6	.03	.01	.02	.04	.03	.03	.01	-1.14×10^{-2}
C_6H_6	.01	.01	.01	.01	.01	.01	.006	1.25×10^{-2}
CS_2	.08	.17	.17	.20	.26	.11	.183	.28
SO_2	.00	.01	.01	.01	.01	.01	.009	1.11×10^{-2}
HCN *	2.22	2.20	3.96	3.30	4.36	5.65	3.56	5.54
Paraffins	0	.109	0	0	0	0	.06	.00
Olefins	0	0	0	0	0	.03	0	-.07

* HCN values not included in gas totals or missing totals.

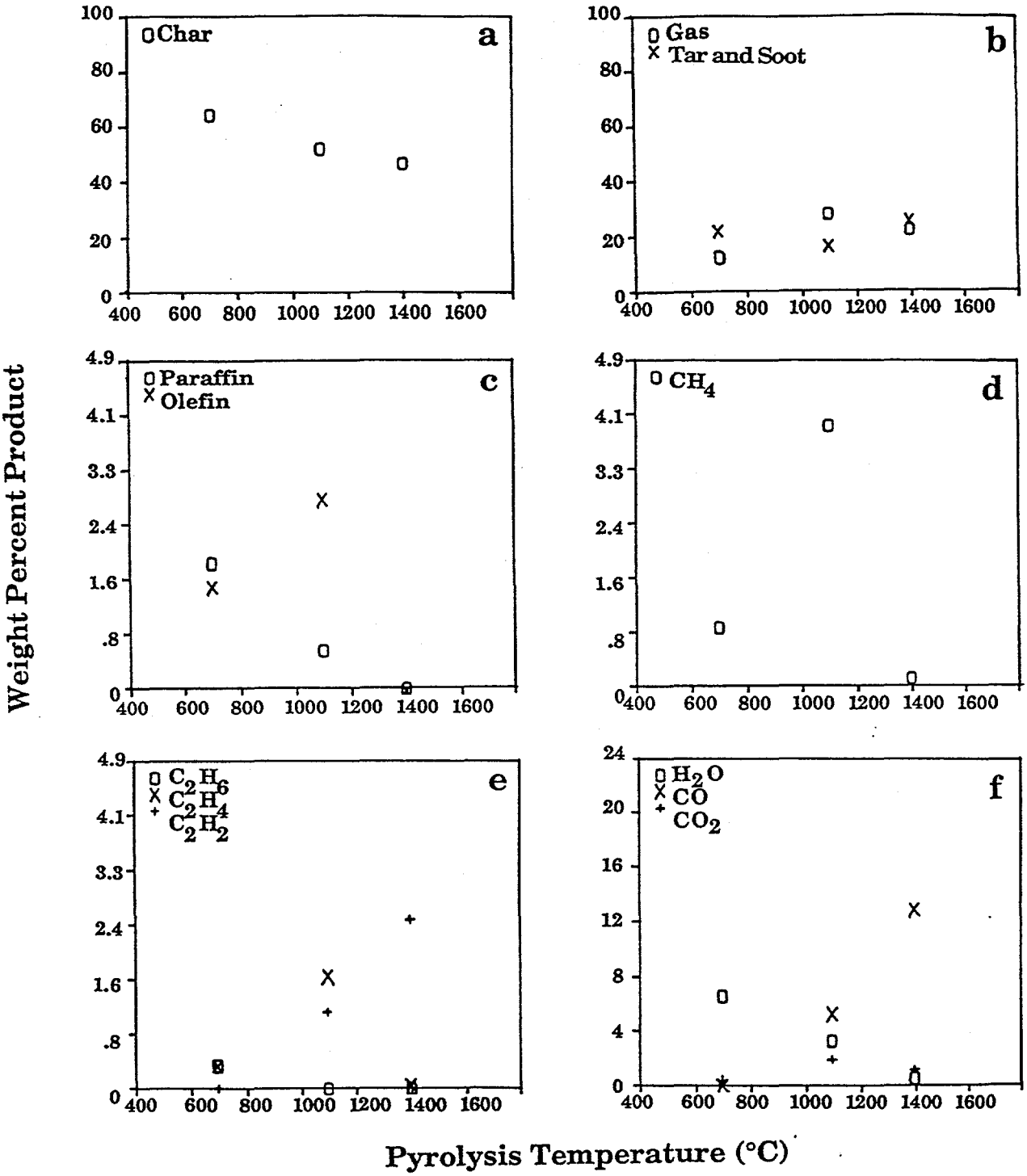

Figure II.A.1-23. Pyrolysis Results for Upper Freeport Bituminous Coal, 200 x 325 Mesh, in the Entrained Flow Reactor at a Reaction Distance of 24". The Coal was Fed at Rates of 1-1/2 - 2 g/min with an N_2 Carrier. Particle Residence Time was Approximately 0.66 Seconds.

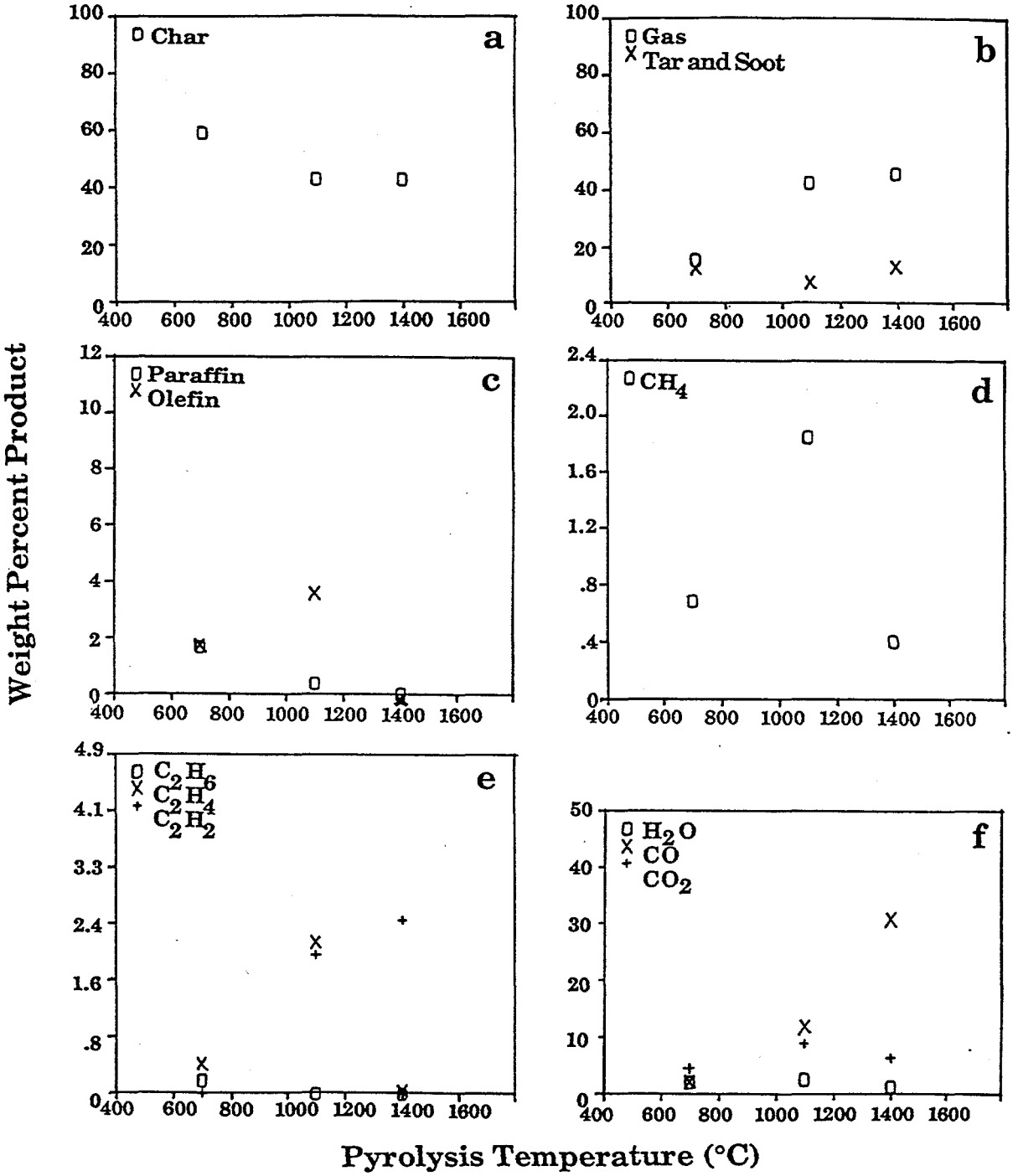

Figure II.A.1-24. Pyrolysis Results for Wyodak Subbituminous Coal, 200 x 325 Mesh, in the Entrained Flow Reactor at a Reaction Distance of 24". The Coal was Fed at Rates of 1-1/2 - 2 g/min with an N_2 Carrier. Particle Residence Time was Approximately 0.66 Seconds.

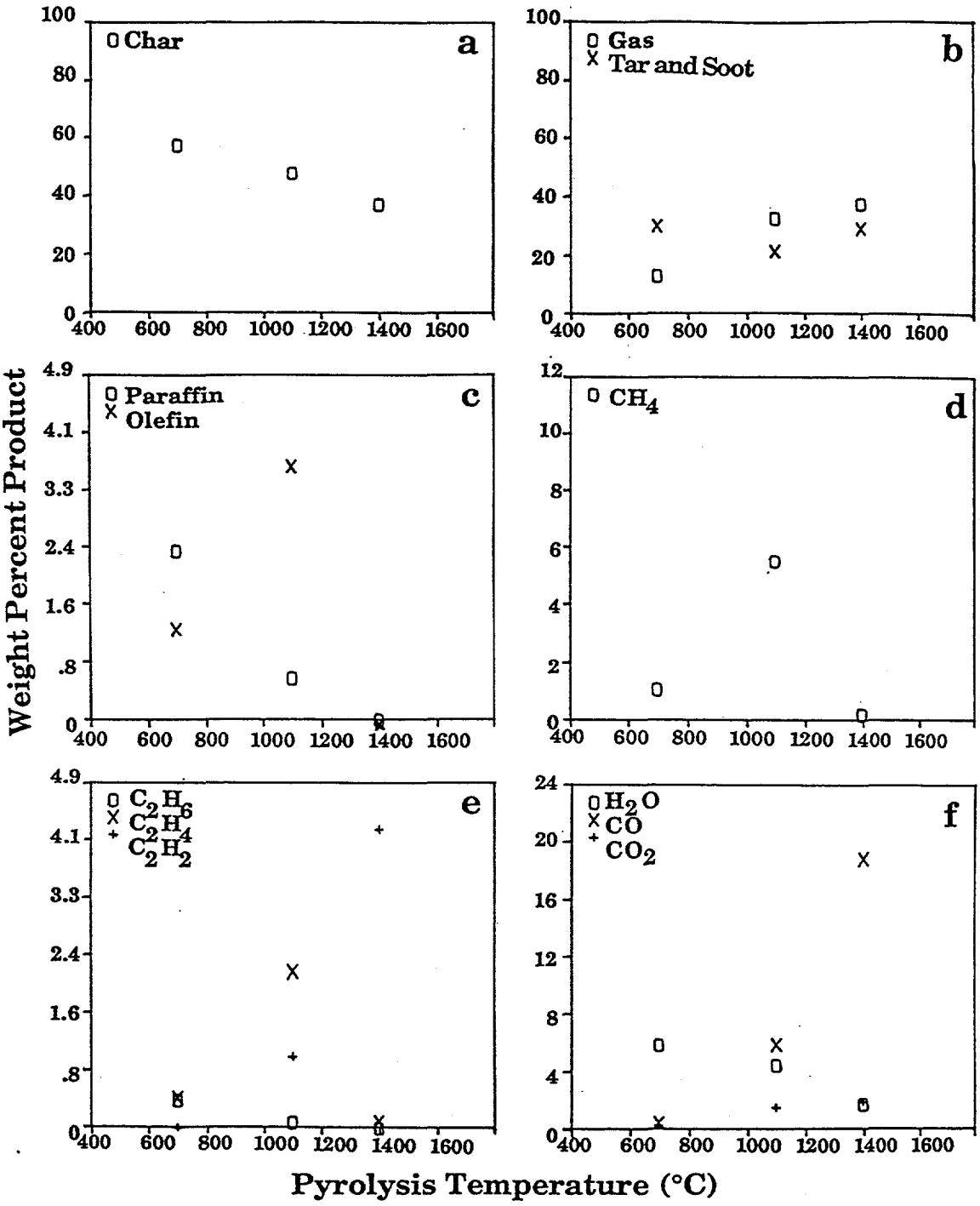

Figure II.A.1-25. Pyrolysis Results for Pittsburgh Seam Bituminous Coal, 200 x 325 Mesh, in the Entrained Flow Reactor at a Reaction Distance of 24". The Coal was Fed at Rates of 1-1/2 - 2 g/min with an N_2 Carrier. Particle Residence Time was Approximately 0.66 Seconds.

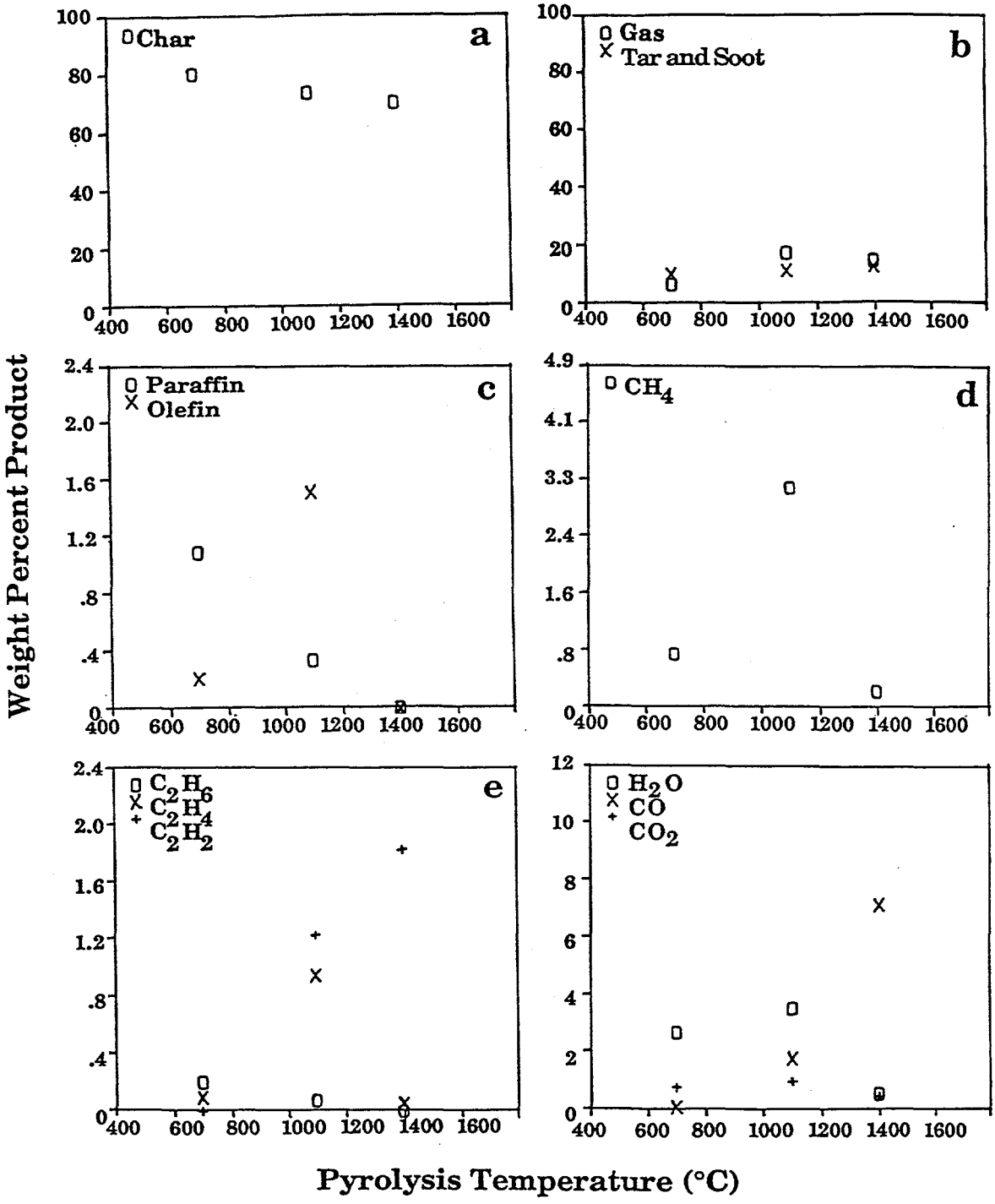

Figure II.A.1-26. Pyrolysis Results for Pocahontas Bituminous Coal, 200 x 325 Mesh, in the Entrained Flow Reactor at a Reaction Distance of 24". The Coal was Fed at Rates of 1-1/2 - 2 g/min with an N_2 Carrier. Particle Residence Time was Approximately 0.66 Seconds.

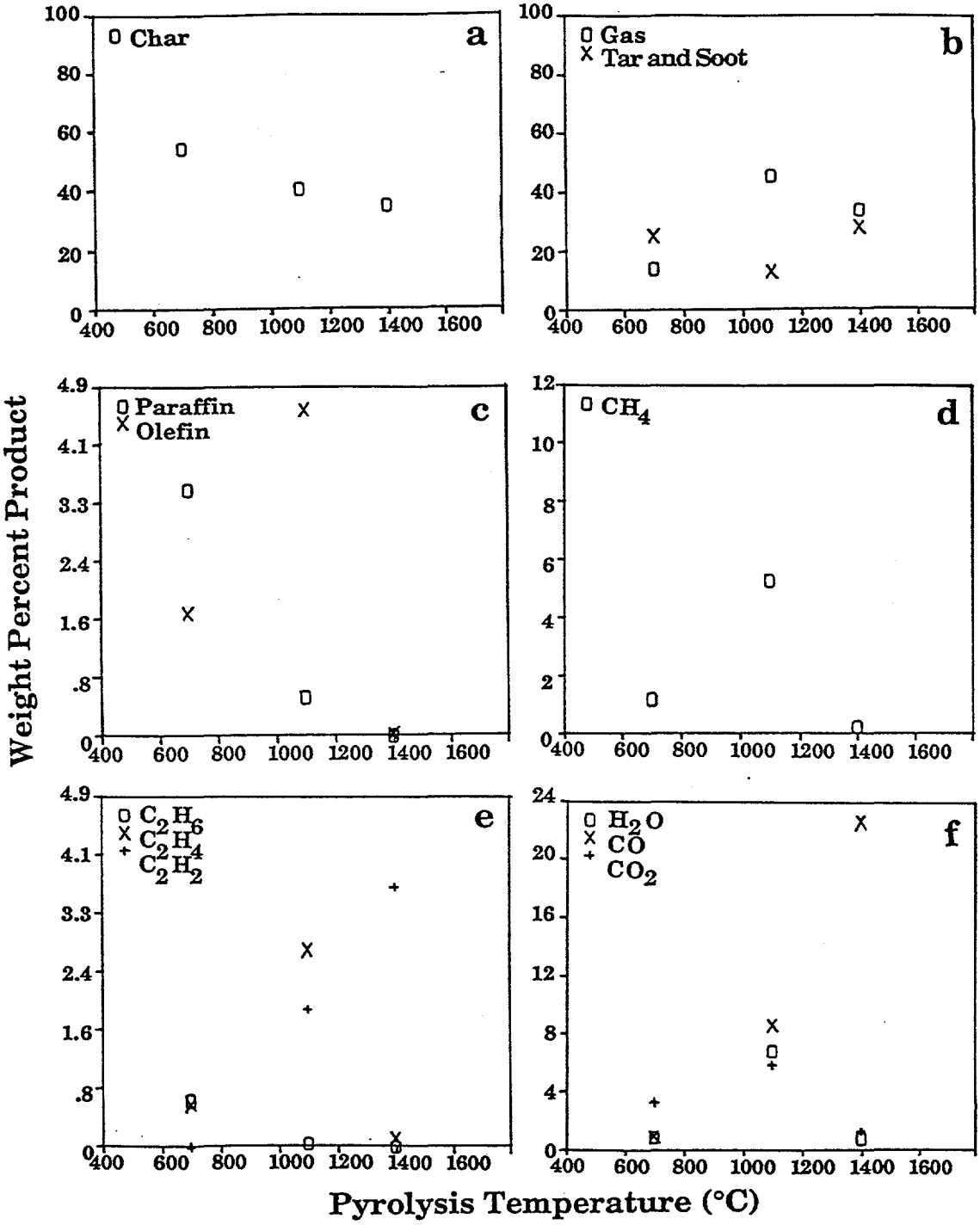

Figure II.A.1-27. Pyrolysis Results for Utah Blind Canyon Bituminous Coal, 200 x 325 Mesh, in the Entrained Flow Reactor at a Reaction Distance of 24". The Coal was Fed at Rates of 1-1/2 - 2 g/min with an N_2 Carrier. Particle Residence Time was Approximately 0.66 Seconds.

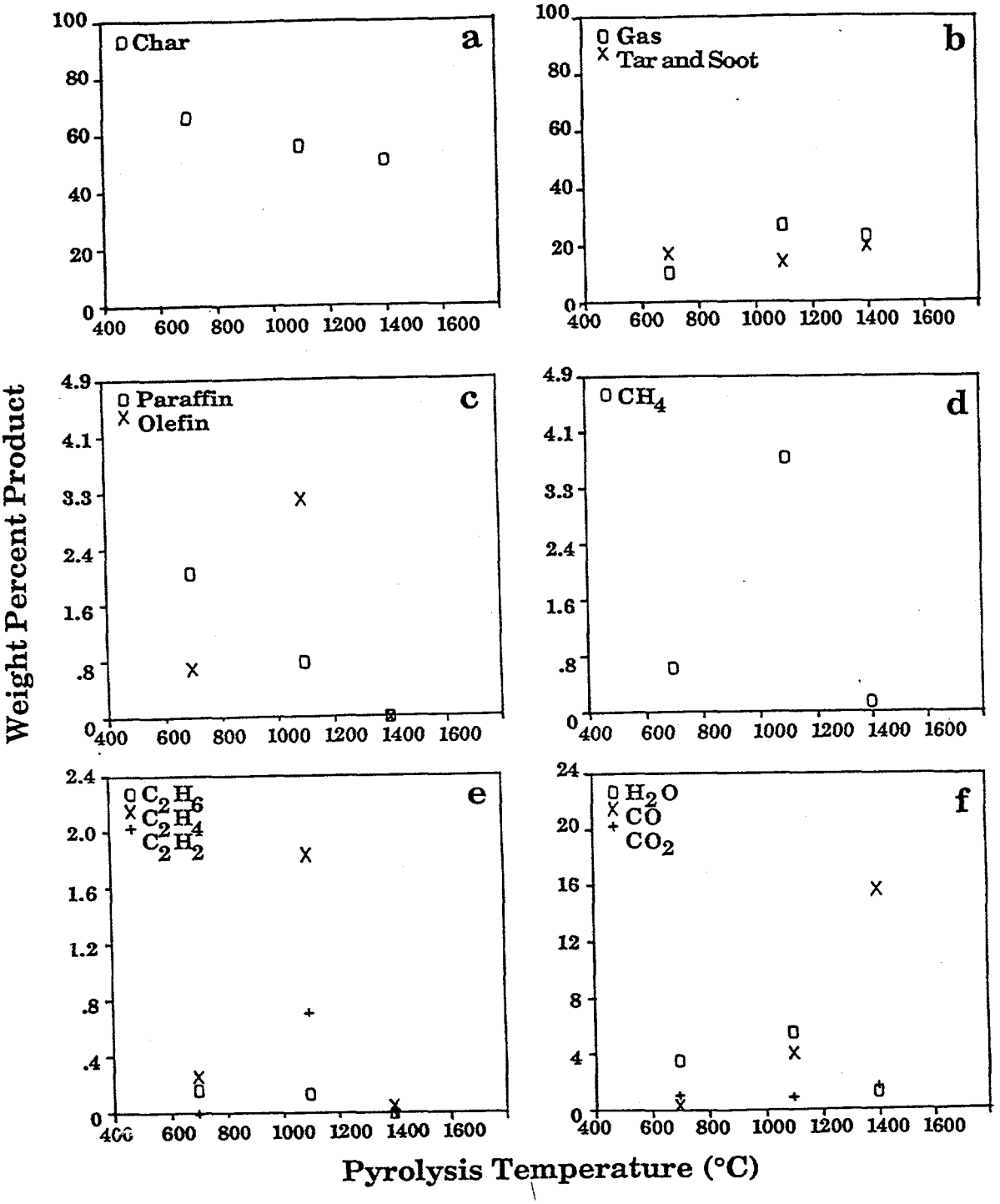

Figure II.A.1-28. Pyrolysis Results for Upper Knawha Bituminous Coal, 200 x 325 Mesh, in the Entrained Flow Reactor at a Reaction Distance of 24". The Coal was Fed at Rates of 1-1/2 - 2 g/min with an N_2 Carrier. Particle Residence Time was Approximately 0.66 Seconds.

distribution of the network fragments at a given extent of decomposition. The extent of decomposition is specified by the probability, p, that the possible attachments are made. For example, for 20% of broken bridges (p = 0.8), a linear chain is totally fragmented, while a "fish net" will have some holes but is almost totally connected. In describing the network, a crosslink is defined to occur at a branch point where there are more than two attachments on a ring cluster. The coordination number is thus related to the crosslink density. With no possible crosslinks, the coordination number is two. With increasing crosslink density the coordination number increases.

The second important property of the network is the fraction of possible attachments, p, which are actually present. During thermal decomposition, this fraction is determined by the rates of bridge breaking. The factors which control how many of the weak links can break are the rate constant and the amount of hydrogen that can be donated from the coal to stabilize the free radicals which form when the links break.

A competitive process with the bond breaking is the retrogressive process of crosslinking. Crosslinking reactions appear to be related to the evolution of certain gases. Specifically, for low rank coals, crosslinking at low temperature (prior to bridge breaking) seems to be related to the evolution of carbon dioxide. For coals of all rank, a higher temperature crosslinking event (following bridge breaking) seems to be related to the evolution of methane. At high temperatures, the evolution of hydrogen is also related to crosslinking.

The final concept is that the tar evolution is controlled by mass transport. Bridge breaking and crosslinking produce a set of fragments with a molecular weight distribution. The lightest fragments can leave the coal melt by evaporation into the light gas species. The heavier fragments remain, forming the metaplast which controls the coal's fluidity.

It is described fully in Solomon et al. (1988a) and is described in the abstract as follows.

Abstract

A general model for coal devolatilization, which combines a functional group model for gas evolution and a statistical model for tar formation, has been presented. The tar formation model includes depolymerization, crosslinking, external transport, and internal transport. The crosslinking is related to the evolutions of CO_2 and CH_4, with one crosslink formed per molecule evolved. The model predictions compare favorably with a variety of data for the devolatilization of Pittsburgh Seam coal and North Dakota (Beulah) lignite, including volatile yields, extract yeilds, crosslink densities, and tar molecular weight distributions. The variations with pressure, devolatilization temperature, rank, and heating rate were accurately predicted. Comparison of the model with several sets of data employing alterative assumptions on transport suggests that assuming that the particle is well mixed (i.e., the surface concentration of tar molecules is the same as the bulk) overpredicts the transport rate. For 50 μm particles, assuming that the internal transport limitation dominates (i.e., neglecting the external transport) provides a good fit to the data. The rank dependence of tar formation, extract yields, crosslinking, and viscosity appears to be explained by the rank dependence of CO_2 yields and its associated crosslinking. High CO_2 yields in low rank coals produce rapid crosslinking at low temperatures and hence thermosetting behavior, low tar yields, low extract yields, loss of solvent swelling properties, and high viscosities. The relative importance of crosslinking compared to bond breaking is, however, sensitive to heating rate. and this effect is predicted by the model. Areas for improving the model include: 1) refinement of the internal and external transport assumptions; 2) accounting for hydroaromatic structures and bridge structures besides ethylene; and 3) including polymethylene "guest" molecules.

Recently, the model characterization methods and kinetics for the Argonne premium coal collection were published (Solomon et al. 1993). The abstract for this paper is as follows.

Abstract

The paper considers the development of a predictive macromolecular network decomposition

model for coal conversion which is based on a variety of modern analytical techniques for coal characterization. Six concepts which are the foundation of the Functional Group, Depolymerization, Vaporization, Crosslinking (FG-DVC) model are considered: 1) The decomposition of functional group sources in the coal yields the light gas species in thermal decomposition. The amount and evolution kinetics can be measured by TG-FTIR, the functional group changes by FT-IR and NMR. 2) The decomposition of a macromolecular network yields tar and metaplast. The amount and kinetics of the tar evolution can be measured by TG-FTIR and the molecular weight by FIMS. The kinetics of metaplast formation and destruction can be determined by solvent extraction, by Geissler plastometer measurements and by proton magnetic resonance thermal analysis (PMRTA). 3) The molecular weight distribution of the metaplast depends on the network coordination number (average number of attachments on aromatic ring clusters). The coordination number can be determined by solvent swelling and NMR. 4) The network decomposition is controlled by bridge breaking. The number of bridges broken is limited by the available donatable hydrogen. 5) The network solidification is controlled by crosslinking. The changing crosslink density can be measured by solvent swelling and NMR. Crosslinking appears to occur with evolution of both CO_2 (before bridge breaking) and CH_4 (after bridge breaking). Thus, low rank coals (which evolve much CO_2) crosslink before bridge breaking and are thus thermosetting. High volatile bituminous coals (which form little CO_2) undergo significant bridge breaking before crosslinking and become highly fluid. Weathering, which increases the CO_2 yield, causes increased crosslinking and lowers fluidity. 6) The evolution of tar is controlled by mass transport in which the tar molecules evaporate into the light gas or tar species and are carried out of the coal at rates proportional to their vapor pressure and the volume of light species. High pressures reduce the volume of light species and hence reduce the yield of heavy molecules with low vapor pressures. These changes can be studied with FIMS. The paper describes how the coal kinetic and composition parameters are obtained by TG-FTIR, solvent swelling, solvent extraction, and Geissler plastometer data. The model is compared to a variety of experimental data in which heating rate, temperature, and pressure are all varied. There is good agreement with theory for most of the data available from our laboratory and in the literature.

Modeling of Mild Gasification

The FG-DVC coal devolatilization model was used to simulate mild gasification processes. The model was applied to data obtained from pyrolysis of Illinois #6 coal in the IGT mild gasification Process Research Unit (PRU) under essentially isothermal conditions. The PRU is a combination of a fluidized-bed and an entrained-bed reactor operated at temperatures from 1000 to 1400°F (550 to 750°C) and pressures close to atmospheric. Simulations were also done of pyrolysis data from a two-stage circulating bed reactor at Battelle obtained at temperatures from 1200 to 1650°F (650 to 900°C), ~ 1 atm pressure, also for Illinois #6 coal. In general, good agreement was obtained for the effect of temperature on the yields of char and gas. In the case of the tar, the model did not predict the fall-off in the tar yield at high temperature (> 1200°F) for the IGT data. However, the Battelle data did not show this fall-off in the tar yield and were in good agreement with the model predictions for tar, gas, and char.

Introduction - In recent years, there has been a growing interest in so-called "mild" gasification processes in which coal is converted using a pyrolysis process into a mixture of gaseous, liquid, and solid products. Work supported by the U.S. DoE includes projects at Battelle (Litt, et al., 1990) and IGT (Knight, et al., 1990). The Battelle project is based on a Multi-Solid Fluidized-Bed (MSFB) reactor system to produce high quality liquid and gaseous products. The MSFB reactor uses a circulating burden of fine particles to transport heat between an exothermic char combustion stage and an endothermic coal pyrolysis stage. Additional benefits of the circulation of these solid particles is the ability to use catalysts or sulfur capture agents. Preliminary tests of this concept have been done in small (2 inch diameter) circulating bed gasifier coupled to a 12 inch diameter bubbling bed combustor.

The IGT project incorporates an integration of fluidized-bed and entrained-bed reactors. The Process Research Unit (PRU) consists of an 8 inch ID x 8 foot long fluidized-bed reactor closely coupled to a 4 inch ID x 13 foot long entrained-bed reactor (Knight, et al. 1990). The feed rate of coal is approximately 100 lb/hr. This reactor is designed to be able to process caking coals of a wide range of particle sizes without oxidative pretreatment. In the full scale unit, the process heat would be provided by

recycled hot char or high temperature flue gases. The heat requirements for the PRU were supplied by external electrical heaters.

Model - The results from these two pyrolysis reactors were modeled with the FG-DVC coal devolatilization model (Solomon, et al., 1988a). This model combines a functional group (FG) description of gas evolution (Solomon, 1981) with a depolymerization, vaporization, crosslinking (DVC) model of tar formation (Solomon, 1988b). The model is able to predict the correct trends for the variations of pyrolysis yields and tar molecular weight distributions with pressure, temperature, rank and heating rate (Solomon et al., 1988a). The model is general in that it can predict pyrolysis behavior for coals of wide range of ranks.

For the prediction of mild gasification processes, a version of the model was used which has the following features: 1) a secondary reaction model which includes the vapor phase cracking of tar to produce light gases using the same functional group approach that is used for coal; 2) a hydrocarbon cracking model which describes the gas phase pyrolysis of paraffinic and olefinic hydrocarbon species; 3) an optional equilibrium model which is used to treat reactions involving the major C, H, O containing species at high temperatures. The set of reactions used in the equilibrium model is as follows:

$$CO + H_2O = CO_2 + H_2 \qquad \text{(II.A.2-1)}$$

$$CH_4 + H_2O = CO + 3H_2 \qquad \text{(II.A.2-2)}$$

$$C + H_2O = CO + H_2 \qquad \text{(II.A.2-3)}$$

The equilibrium model is used by assuming that equilibrium of the char and the major gaseous species occurs at the highest temperature reached in a pyrolysis experiment, after which the products are "frozen". Of course, this is only an approximation which improves as the temperature and residence time increase. The coal char is assumed to have the properties of graphite and the gases are assumed to be ideal. Details of these submodels can be found in Serio et al. (1987).

An additional change to the model was the ability to have separate residence times for the gas and solid phases which is necessary to simulate fluidized-bed reactors.

Results - The model was applied to data obtained from pyrolysis of Illinois #6 coal in the IGT mild gasification Process Research Unit (PRU) under essentially isothermal conditions at temperatures from 1000 to 1400°F (550 to 750°C) and pressures close to atmospheric.

A comparison of the FG-DVC mild gasification model predictions and experimental data from the IGT PRU is shown in Fig. II.A.2-1. This is an adaption of a figure shown in Knight et al., 1990 which includes the plotting of data as solid circles where good material balances were obtained. The open circles are for runs where the material balances were suspect. The solid lines in Fig. II.A.2-1 are the results of a regression analysis on the "good" IGT data. Also shown in Fig. II.A.2-1 for comparison purposes are pilot-plant data from the COED (Scotti, et al., 1975) and Occidental flash pyrolysis processes (Che, et al., 1978) and laboratory data from CSIRO (Tyler, 1980) for similar coals. The FG-DVC model predictions are the dashed lines in Fig. II.A.2-1. The model does a reasonable job in predicting the variation in the yields of char, gas, and water with temperature. It does not, however, predict the maximum observed in the tar yield with pyrolysis temperature (~ 1200°F) for the IGT data.

Simulations were also done of pyrolysis data from the 2 inch circulating-bed reactor at Battelle obtained at temperatures from 1200 to 1650°F (650 to 900°C), ~ 1 atm pressure, also for Illinois #6 coal. The experimental results for the yields of tar and gas are shown in Fig. II.A.2-2 (open circles). The predictions for the standard FG-DVC mild gasification model are shown as closed circles connected by lines in Fig. II.A.2-2. The predictions of FG-DVC model with the added assumption that the gaseous pyrolysis products are in equilibrium with the char is shown in Fig. II.A.2-2 as the solid lines connected by solid squares. The equilibrium model does not include the tar species. The predictions of the standard

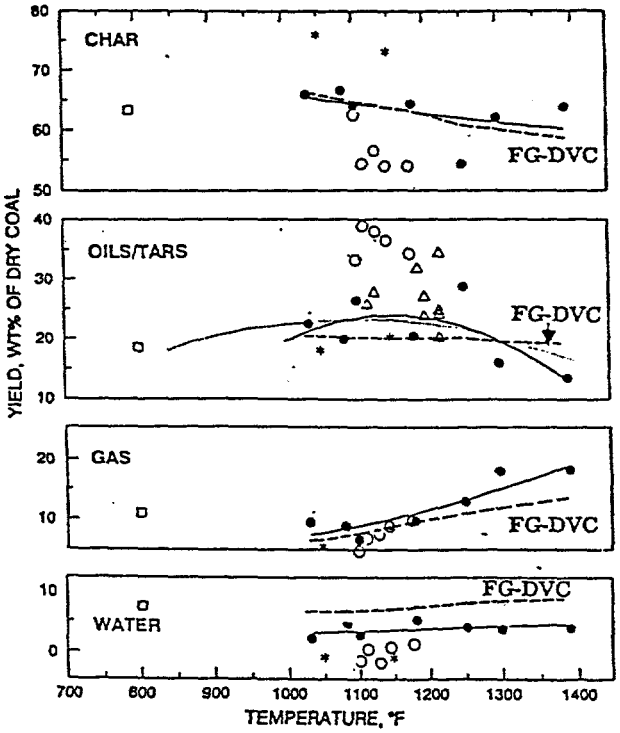

Figure II.A.2-1. Comparison of FG-DVC Mild Gasification Model Predictions (---) and Experimental Data from IGT for Overall Product Yields ● IGT PRU , Illinois Coal; ○ IGT PRU Data, Illinois coal (not included in regression curve); * IGT PRU Data, West Virginia Coal; ▵ Occidental Flash Pyrolysis; ■ COED Second Stage; (...) CSIRO Fluidized Bed, LiddellB Coal.

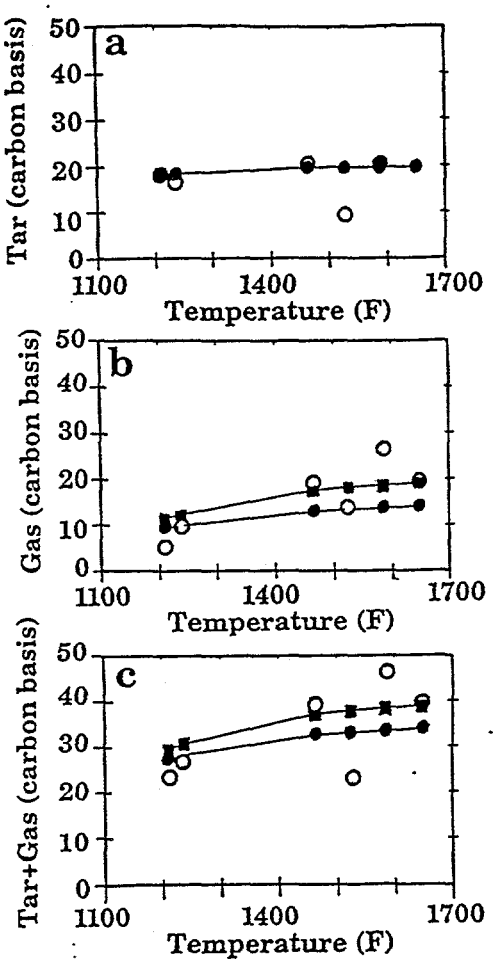

Figure II.A.2-2. Comparison of Standard (● - ●) and Equilibrium (■ - ■) FG-DVC Mild Gasification Model Predictions and Experimental Data from Battelle (○).

model are in good agreement with the tar data, except for one data point. It is interesting that the tar yield data from the Battelle reactor do not show the maximum in tar yield despite the relatively high temperatures used. This difference is probably due to the fact that the mean gas phase residence time is relatively small for the Battelle unit (see below).

The data for the total gas yields are more scattered. It appears that the assumption of equilibrium of the volatile products gives a better prediction. However, it is unlikely that the system would be close to equilibrium under conditions where the reactor severity is so low that tar cracking does not occur.

A parameter in the model was the gas-phase residence time. A value of 2 sec was used for the IGT reactor; while a value of 0.8 sec was used for the Battelle reactor. These values were based on estimates of the gas hold up in the system provided by the respective organizations. The average solids residence time was in the range of 20 to 30 minutes for the IGT system and ~ 1 sec for the Battelle reactor.

In the case of individual gases, good agreement was obtained for H_2, CH_4, C_2's and CO data from the IGT PRU (see Fig. II.A.2-3). The amount of CO_2 was somewhat under predicted (see Fig. II.A.2-3b). Better agreement was obtained using a partial equilibrium model for the gas phase. Data on individual gas species yields were not available from the Battelle study.

Conclusions - A coal devolatilization model has been adopted for simulation of mild gasification process. Good agreement has been obtained for the prediction of char and gas yields from mild gasification processes. The model does not yet predict the maximum observed in the tar yield for the IGT data. This may require an improved description of tar cracking and/or the residence time of the tar species.

II.A.3. Coal and Char Fluidity

The FG-DVC model predicts the amount of detached molecules or liquids (tar, extracts, and liquids) produced in pyrolysis. This quantity can be directly related to the coal's fluidity or viscosity. The fluidity model is presented in Solomon, et al. 1992. The abstract for this publication is as follows.

Abstract

We have developed a phenomenological model for coal fluidity based on a macromolecular network model for the decomposition and condensation of the network under the influence of bond breaking and crosslinking reactions. The macromolecular network model is the previously published FG-DVC model of coal pyrolysis. It employs a network consisting of aromatic ring clusters linked by bridges. The bond scissions are described by a single first order reaction with a distribution of activation energies. Crosslinking is related to CO_2 and CH_4 formation which are described in multiple first order reactions with distributions of activation energies. The fluidity is described by an empirical equation which depends on the relative amounts of the liquid (molecules detached from the network), and solid (the remaining network) and on the fluidity of the liquid component. The FG-DVC model predicts the yield of liquids. The fluidity of the liquid component is described by a second phenomonological equation which depends only on the temperature. The advantage of this model is that it is based on a previously demonstrated methodology which allows the incorporation of rank dependent kinetics, crosslinking, weathering, and extraction phenomena into the fluidity predictions. Excellent agreement has been obtained between the model predictions and low temperature fluidity measurements of Oxley and Pitt, van Krevelen, and Gieseler plastometer measurements for the Argonne premium coal samples. The trends for changes in the fluidity with weathering or extraction are predicted as well. Good agreement has been obtained at high temperatures between the model predictions and measurements of Fong for the onset of the fluidity. The loss of fluidity, however, is predicted to occur sooner than is indicated by the data and the maximum value of fluidity is over predicted. The data cover over five orders of magnitude in fluidity, and eight coals with carbon concentration between 80 and 90%. This agreement is obtained using coal independent equations for the dependence of the fluidity on the liquid fraction and the liquid fluidity. The coal dependent variables are the kinetic rates for bond breaking and crosslinking and the extent of crosslinking as determined from

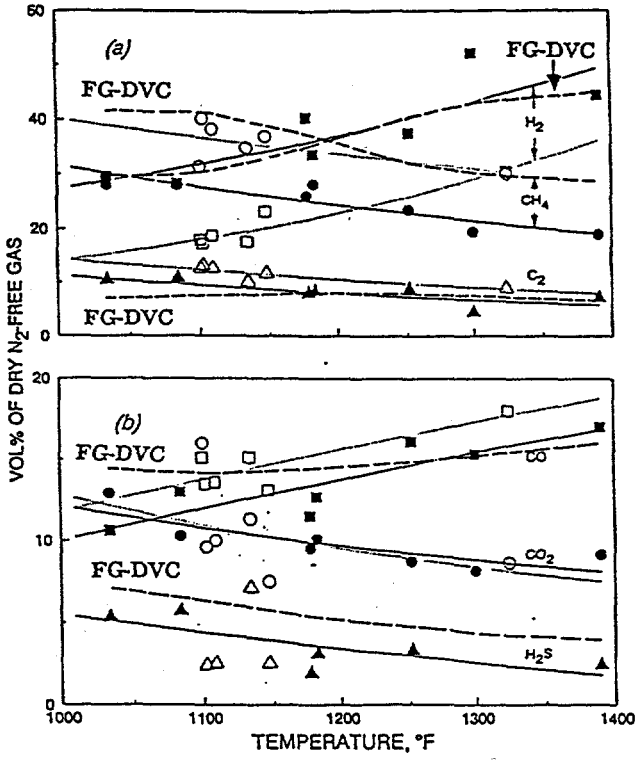

Figure II.A.2-3. Comparison of FG-DVC Mild Gasification Model Predictions (----) and Experimental Data from IGT for Individual Gas Product Yields. (.....) Regression Model for Open Symbols: Steam/Coal Ratio = 0.0 to 0.5 (—) Regression Model for Filled Symbols: Steam/Coal Ratio = 0.7 to 1.4.

laboratory pyrolysis measurements using a TG-FTIR (Thermogravimetric analyzer with Fourier Transform Infrared analysis of evolved products). There are only two adjustable parameters of the model.

II.A.4. Char Swelling Model

Introduction

Under certain conditions, coals which become fluid when heated also swell, due to the internal pressure of trapped, evolved gases. Experimental observations of the swelling in the absence of oxygen are made both on single particles which have swollen in essential isolation, and on agglomerates, as in a measurement of the free-swelling index. Although the same basic phenomena are involved in both cases, only the swelling of individual particles of pulverized coal (radius < 100 μm, say) has been modeled to date. These particles are treated as being isothermal.

When microscopic observations of swollen coal particles are made it becomes apparent that the particles do not behave in an identical fashion. At average heating rates, between 10^2 and 10^4 K s^{-1}, the swollen particles of a typical swelling coal, Pittsburgh No. 8, can be categorized into one of three types: a small fraction (~ 10%) which shows virtually no sign of fluidity, and hence no swelling; the majority (~ 80%) which experience swelling of about the same magnitude; and another small fraction (~ 10%) which exhibits behavior that can be associated with a much higher fluidity (lower viscosity) than the majority. We have associated the three behaviors with the three main maceral types of the coal; inertinite, vitrinite, and exinite, respectively. In the model the properties only of average particles are described, and this must be recognized when comparing predictions with microscopic observations. It is for average particles that the FG-DVC model is applicable.

The range of "swelling" behaviors encompassed by our model includes the swelling which is observed for moderate heating, but also the behaviors at the extremes of heating rate. At very low heating rates ($\leq$ 10 K s^{-1}) there is virtually no swelling: gas production by pyrolysis is only marginally greater than out-diffusion of gas. At extremely high rates ($\geq$ 5 x 10^4 K s^{-1}), the liquid walls surrounding the gas-filled internal voids rupture, allowing the gas to escape. Minimal swelling is observed in this case.

Because the modeling is driven by observation, the various swelling behaviors will be introduced by scanning electron microphotographs, all of which were recorded in METC supported research. In Figs. II.A.4-1a and II.A.4-1b (close-up) we show single-cell cenospheres. What we term multi-cell or multi-bubble swollen particles are shown in Figs. II.A.4-2a and II.A.4-2b (close-up). Typically each particle appears to have between 10 and 20 internal cells. We believe that the rope-like structures which appears on the inside of the wall is the residue of internal walls between adjacent bubbles of the swollen particle. Popped or ruptured particles are shown in Figs. II.A.4-3a, II.A.4-3b and in II.A.4-3c, where the internal surface of a cracked particle is shown. In contrast to the cases of Figs. II.A.4-1 and II.A.4-2, these particles have not undergone significant swelling. Finally, in Figs. II.A.4-4a and II.A.4-4b, two "no-model" particles are shown. Like the single and multi-cell particles, these are thin-walled structures, but are characterized by a myriad of internal cells. These no-model particles exhibit the greatest swelling. Unlike the case for the other particles, however, we have not made sufficient observations to assert that the no-model behavior occurs for the vitrinite component of the coal. We do not quantitatively predict the swelling of the no-model particles. It is believed that the above behaviors represent the swelling types, although variants of these are observed.

Qualitative Discussion

The different swelling (or non-swelling) behaviors can be accounted for qualitatively. To begin with a discussion based on dimensional analysis is presented.

a

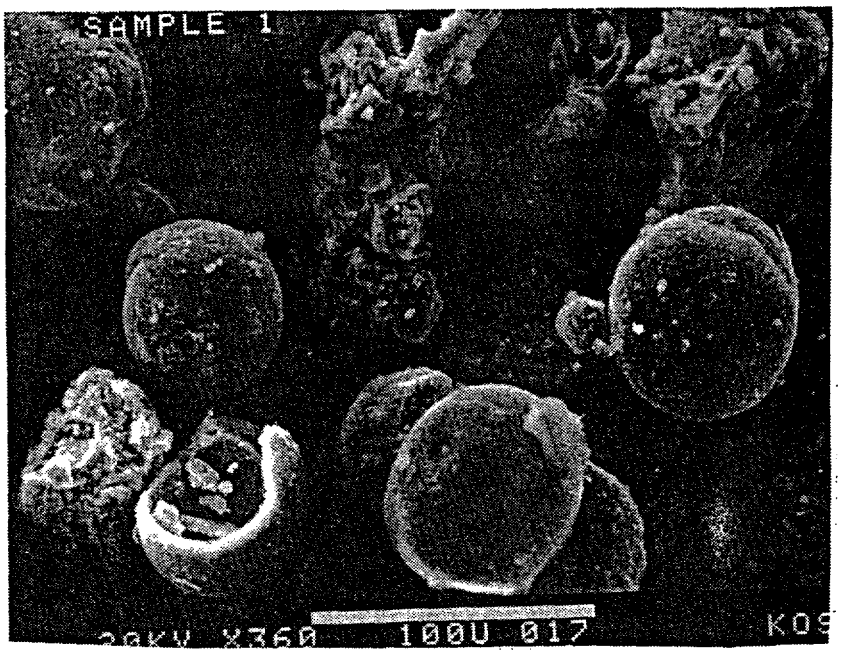

b

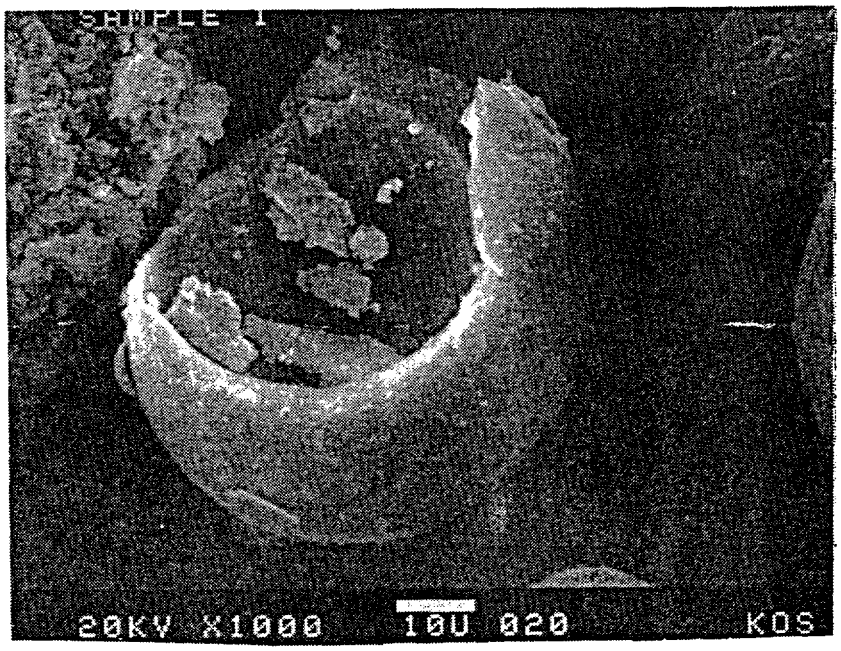

Figure II.A.4-1 a) Cenospheres Formed from PDU Coal Heated in Helium at ~$5x10^3$ K/s to 800° C. Residence Time ~360 ms. b) Close-Up of Fractured Cenosphere.

a

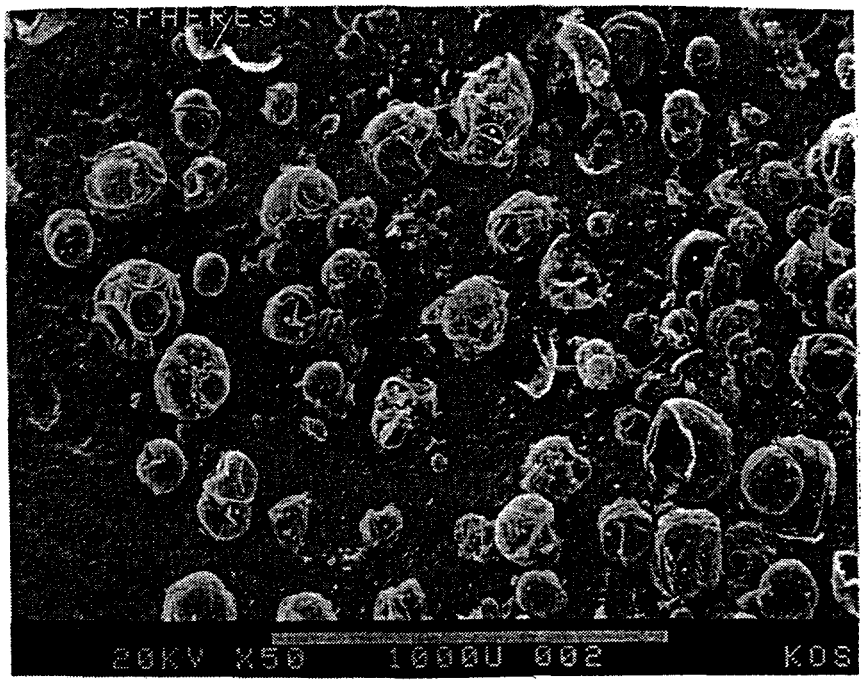

b

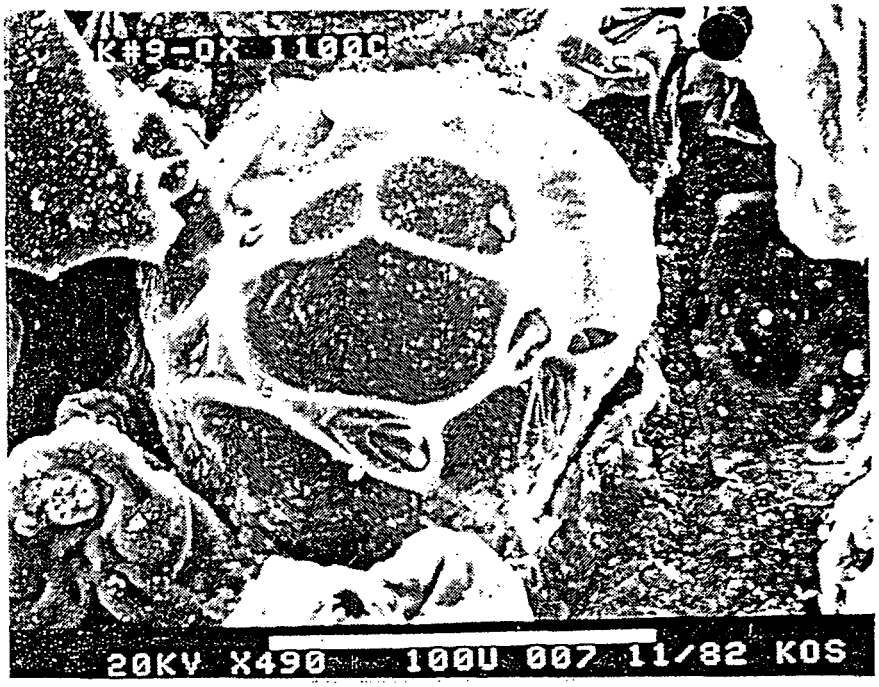

Figure II.A..4-2 a) Multi-Cell Swollen Particles Formed When Kentucky #9 Butuminous Coal was Heated in 99% Nitrogen/1% Oxygen, at 1100° C. b) Close-Up of One of These Particles.

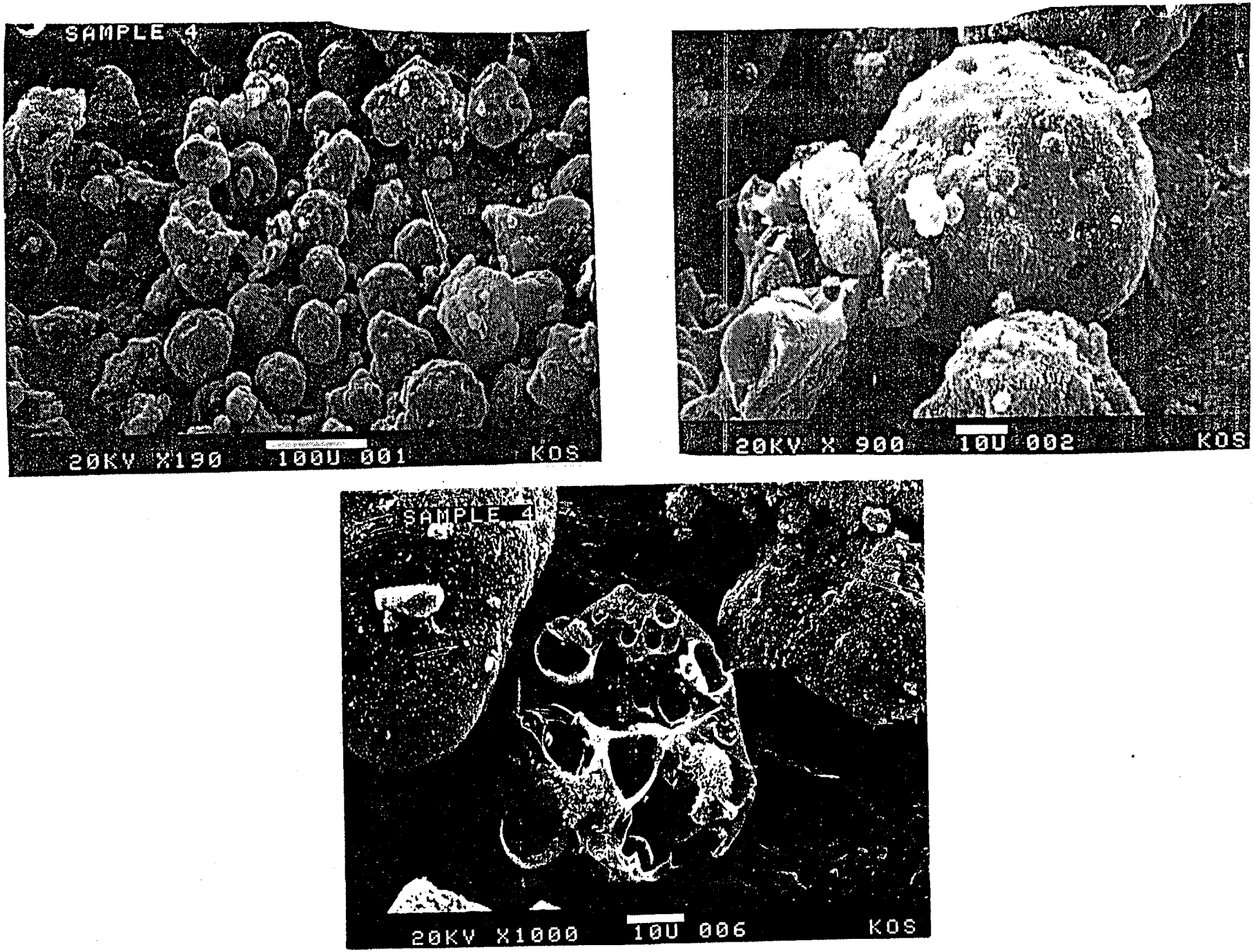

Figure II.A.4-3 a) Field of "Popped" Particles, Formed when PDU Coal was Heated in Helium at ~3 x 10^4 K/s to 1504° C. b) Close-Up of a Popped Particle. c) Internal Surface of a Fractured, Popped Particle.

a

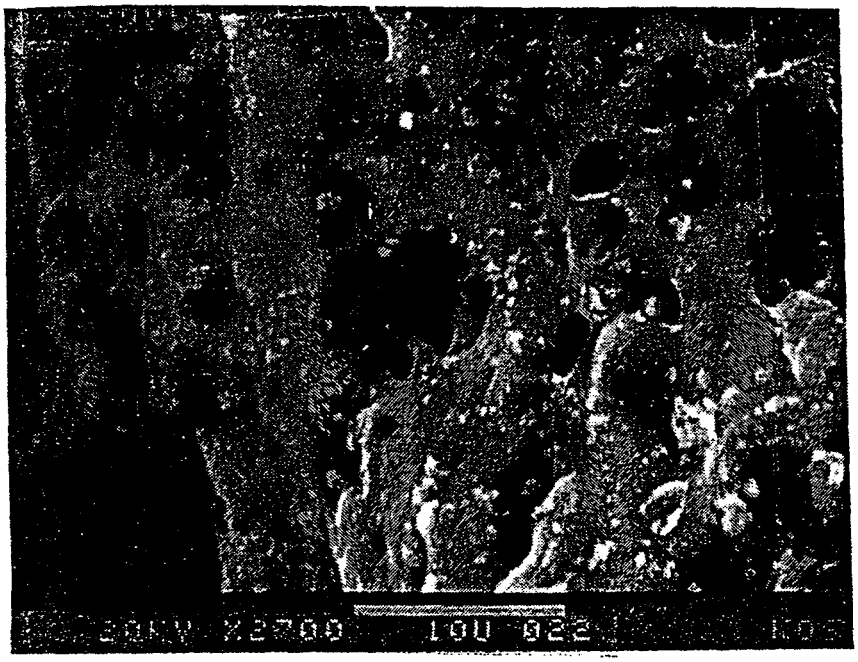

b

Figure II.A.4-4 a, b. "No- Model" Particles.

An internal pore of radius r will collect gas, n, at a rate proportional to its surface area:

$$\frac{dn}{dt} \propto r^2 \qquad \text{(II.A.4-1)}$$

The internal pressure will be proportional to (collected gas)/volume:

$$P \propto \int \frac{r^2}{r^3} dt \propto \int \frac{1}{r} dt \qquad \text{(II.A.4-2)}$$

The contracting force of surface tension also behaves as 1/r, therefore, for heating rates high enough so that there is insufficient time for appreciable inter-bubble transport, the time at which the outward gas pressure exceeds the inward surface-tension pressure, is the same for all bubbles. In that case a multitude of pores above micro-pore size will simultaneously swell: the no-model case. For longer times, the greater internal pressure in smaller bubbles (Eq. II.A.4-2), will cause the transfer of gas from small to larger bubbles. It is in this heating rate domain that the "single" and multi-bubble models apply.

In general, a slower heating rate will favor single-cell formation. Slower heating also allows more time for gas to escape by diffusion. Therefore, single-cell cenospheres will tend to be less swollen than multi-cell particles, which in turn are less swollen than no-model particles. Another factor which enhances the above trends in size is the ratio of internal to external surface area. Gas is evolved from the wall material, and the lowest internal to external surface area ratio of the single-cell particle marks it as the lowest swelling one.

In the modeling, the multi-cell particles are considered to be made up of a collection of single-cell cenospheres. The value of r_2', the radius of coal material which contains only one bubble, is found to be 20μm to fit the data for most of the coals. The extrapolation of this single bubble model to large particles needs to be further investigated. The current model assumes that the number of bubbles in a particle of radius R is $(R/r_2')^3$.

The ruptured particles appear to follow a temperature history slower that that of the no-model particles. Inspection of cracked surfaces of these particles shows a number of internal bubbles not unlike that of the multi-cell particles. There is apparently time for coalescence for the smaller bubbles. Subsequent rapid gas evolution leads to cell wall rupture.

Quantitative Model

The starting point for our quantitative model is the equation described by Chiou and Levine who considered the swelling rate of a pulverized coal particle of external radius r_2, with a single void of radius r_1, with spherical symmetry. The swelling they depict is due to the pressure, ΔP_t, of trapped evolved gases, doing work against viscous forces (viscosity = η). Their equation was further modified in our work to take account of the pyrolysis weight loss.

For this single bubble model, the equation for the velocity of expansion of the outer wall is given by:

$$\frac{dr_2}{dt} = \frac{r_1^3 r_2 \, \Delta P_t}{4\eta(r_2^3 - r_1^3)} + \frac{r_2}{3(r_2^3 - r_1^3)} \frac{d(r^3)}{dt} \qquad \text{(II.A.4-3)}$$

Where r_1 and r_2 are the radius of the inner and outer surfaces, respectively.

In our model, the temperature-dependent viscosity is supplied by the viscosity model. The accounting of excess internal pressure begins at t = 0, considering the gas gain from trapped, evolved gas, and loss due to out-diffusion. The number of moles of gas, n_g, evolved in one second, by the particle walls of volume, Δv, is obtained from the FG-DVC model, Δv being updated to account for pyrolysis. Of the evolved gas, a fraction $r_1^2/(r_1^2 + r_2^2)$ is captured within the void, so that the captured gas is given by:

$$dn_c = n_g \, r_1^2 / (r_1^2 + r_2^2) \bullet dt \qquad \text{(II.A.4-4)}$$

In this same period an amount of gas diffuses out:

$$dn_d = \frac{4\pi D_l \, c_1 dt}{(1/r_1 - 1/r_2)} \qquad \text{(II.A.4-5)}$$

where D_l is the diffusivity of the gas in the coal liquid, $c_1 = 3\, n_d / 4\pi\, r_1^3$, and the total gas within the cenosphere, n_t, is the "sum" of Eqs. 2 and 3.

$$\frac{dn_t}{dt} = \frac{dn_c}{dt} - \frac{dn_d}{dt} \qquad \text{(II.A.4-6)}$$

The excess of internal over external pressure, ΔP_g, due to the trapped gas is given by:

The calculation of the amount of the trapped ambient gas n_a follows a similar argument:

$$\Delta P_g = \frac{3 n_t \, RT}{4\pi \, r_1^3} \qquad \text{(II.A.4-7)}$$

$$\frac{dn_a}{dt} = \frac{4\pi \, D_a}{1/r_1 - 1/r_2} \left[\frac{P_0}{RT} - \frac{n_a}{4\pi \, r_1^3/3} \right] \qquad \text{(II.A.4-8)}$$

where P_0 is the ambient pressure and D_a the diffusivity of ambient gas. The pressure difference is then:

$$\Delta P'_t = \frac{3\,(n_t + n_a)RT}{4\pi r_1^3} - P_0 \qquad \text{(II.A.4-9)}$$

where P_0 is the external pressure. The outward pressure is reduced by the effective negative pressure due to the surface tension, σ; so that the total outward pressure differential, ΔP_t, is:

$$\Delta P_t = \frac{3\,(n_t + n_a)\,RT}{4\pi\, r_1^3} - \sigma\left(\frac{1}{r_1} + \frac{1}{r_2}\right) - P_0 \qquad \text{(II.A.4-10)}$$

This is the pressure difference used in Eq. II.A,4-3, to calculate swelling.

If $\Delta P'_t$ is sufficiently large, the stress in the wall will exceeded the strength of the wall S_c. Cell rupture is defined to occur when:

$$S_c \leq -P_0 + \frac{1.5\, r_1^3\, \Delta P'_t}{(r_2^3 - r_1^3)} \qquad \text{(II.A.4-11)}$$

The parameters of the model are: D_l, D_a, σ, and S_c, which are listed in Table II.A.4-1.

Table II.A.4-1. Swelling Model Parameters

Apparent Pyrolysis Gas Diffusity, cm^2/sec	$7.5e\text{-}5(T/773)^{1.8}$
Apparent Ambient Gas Diffusivity, cm^2/sec	7.5e-4
Critical Bubble Wall Stress, atm	1.0
Surface Tension	30 dyne cm^{-1}

Another input to the model is the temperature history of the particle. For the modeling of some experiments on coal pyrolysis in the entrained flow reactor, we used particle temperature histories which were furnished by an experimentally verified model. For other situations we used a two straight-line segment temperature history representation in the model. The first segment represents the heating rate, the second segment the final particle temperature.

For monodisperse coal particles, we expect to be able to draw a "phase diagram" such as depicted in Fig. II.A.4-5. From drop tube experiments we determined the value of Tmin to be 520 °C. In conjunction with the swelling model results this observation was used to fix the diffusivity at $7.5x10^{-5}$ cm^2 sec. We later incorporated a temperature dependence into D_1.

In quantitative exercising of the model, the swelling of P.S.C. particles of small and intermediate size were predicted to within ±25%, for a wide range of heating rates. The effect of external pressure on the swelling of an Illinois #6 coal was predicted to the same level of accuracy (Fig. II.A.4-6). In looking at reasons for that behavior it was seen that with increasing pressure the more volatile components of tar were held in the particles for longer times, decreasing viscosity at the critical time of gas evolution. With further increase in pressure the compressive external environment made itself felt, and swelling was reduced (Fig. II.A.4-6).

In parallel calculations it was found that for a range of (model imposed) maximum fluidities the swelling of P.S.C. #8 coal particles did not change until a value of 4.3 DDMP (Fig. II.A.4-7). These results, at first, appear to contradict the stated swelling behaviors of the Illinois #6 coal described in Fig. II.A.4-6: increased swelling with decreased viscosity. Agreement does exist, however, as the maximum fluidity of Illinois #6 coal at one atmosphere is 2.9 DDMP, which is in the region of the curve of Fig. II.A.4-7 where swelling is viscosity dependent.

SWELLING MAP

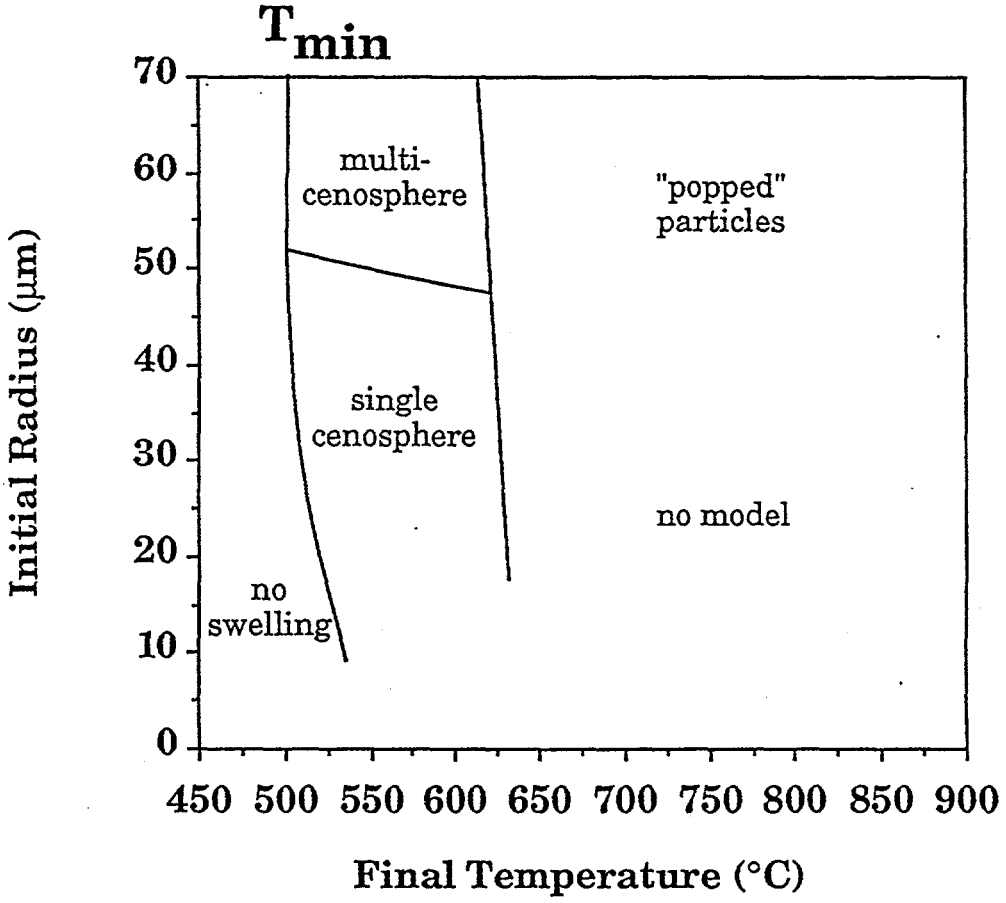

Figure II.A.4-5. Schematic Swelling Map Showing Dependence of Swelling Type on Initial Particle Radius and Final Temperature, High Heating Rate (~10^4 K/s). Heating Rates and Maceral Type are Also Important Factors in Swelling Behaviour.

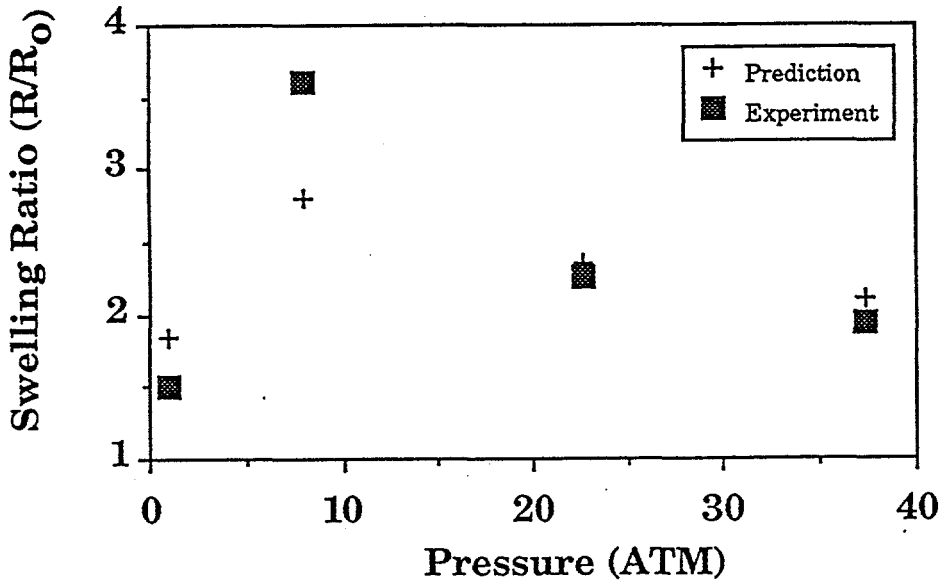

Figure II.A.4-6. Comparison of Model Prediction and Experiment (Lee et al.) for Swelling Ratio Versus Ambiant Pressure, for Illinois #6 (Nominal Rad = 31μm), at a Heating Rate of Between 1000 and 1150 K/s.

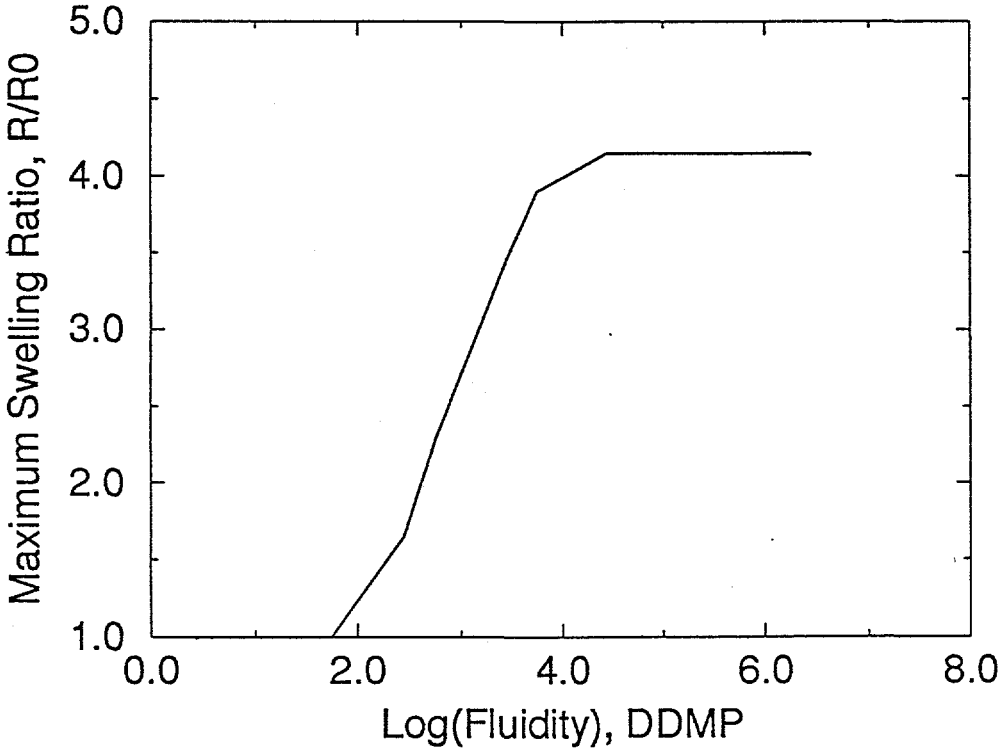

Figure II.A.4-7. Calculated Maximum Swelling Ratio for Model Imposed Maximum Fluidities, as Shown.

Other Considerations

In the swelling model work, analysis other than that based on swelling calculations was made. This section deals with the question of the relationship between swelling and reactivity, via surface area. It is a chronicle of reasons why a thorough knowledge of char swelling will not lead to predictions of reactivity.

Zygourakis (1989) has examined sectioned chars microscopically, using image processing techniques to deduce porosity, swelling, and surface area. His optical technique has resolution only down to O.5 μm, and with this he deduces a maximum surface area of about 0.08 m^2/cc of particle. But this is two orders of magnitude less than areas measured by BET and other gas adsorption techniques (Gan, et al., 1972). Consequently, it is concluded that most of the surface area of a char is in micropores. However, the swelling model predicts no swelling for pores as small as micropores, as gas collection is low and the surface tension is high. Therefore, swelling cannot be a direct major factor in the development of pore surface area or reactivity. On the other hand, it has been shown that swelling can effect the access of gas to the reactive areas. A study of this relationship has not been made.

Also, during the course of this work, we checked Simon's pore-tree model with the swelling calculations, as follows. The model includes an empirically chosen constant, which represents the number density of cavity "nuclei" in the coal. An investigation was made to relate the predictions made by Simon's pore-tree model to our observations of swelling particles. If successful, the pore-tree model would serve as a basis for choosing the number density of cavities.

To begin with, we used Suuberg's adaption of Simon's pore-tree model for this study. Suuberg found that the excess internal pressure is inversely proportional to diameter, as in Eq. II.A.4-2. This means that as temperature, and hence, pressure increases, a point will be reached at which all internal pores begin to swell, more or less at the same time. This is the condition for the "no-model" expansion, described in the qualitative discussion, above. With this model, and input from the FG-DVC model, it was calculated that for low and moderate heating rates the internal excess pressure never exceeded 1% of the effective pressure due to surface tension, at a temperature at which heated vitrinite particles are observed to swell.

This result implies that the pore-tree model is not appropriate to use for the swelling phase of heated coal particles. The results of the calculation were checked by going back to Simon's original work, but changing the bulk density value, and r_{min}, in accordance with Suuberg's observations. Again, predicted pressures were always too low by about one and a half orders of magnitude when compared with the observed swelling of small particles of Pittsburgh seam coal The narrowest conclusion that we can draw here is that the pore tree model should not be used to predict the swelling of bituminous coals at low and medium heating rates.

An application of the swelling model could be in the description of the interception of flame radiation by swollen particles. Such an estimate would be more realistic if the swelling were performed in an oxidizing atmosphere, rather than the inert gas environment used for the model so far.

Conclusions

A viable model for the swelling of pyrolyzing pulverized coal particles has been developed and refined. The model semiquantitatively predicts swelling behavior for all cases considered, to within $\pm$ 25%. In principle, the model is applicable to all of the Argonne coals, at heating rates between 1 and $5x10^4$ °C per second, and for a variety of ambient pressures. Further refinements of the model depend on obtaining a greater array of data.

II.A.5. Sulfur and Nitrogen Evolution

Sulfur and nitrogen evolution from the Argonne premium coals has been studied using

Thermogravimetric Analysis with measurement of evolved products by Fourier Transform Infrared spectroscopy (TG-FTIR). The method combines temperature programmed pyrolysis and combustion. H_2S and tar sulfur were monitored by measuring SO_2 after oxidation of volatile products. The SO_2 evolution curves produced with volatile oxidation exhibit two main evolution peaks and one smaller high temperature evolution peak. For each peak, the temperature of the maximum evolution rate (T_{max}) increases with increasing rank. The individual evolution curves of the organic and pyritic sulfur were identified, and their evolution kinetics were derived. The overall SO_2 evolution curves were modeled by using the FG-DVC coal pyrolysis model. The evolution curves for both NH_3 and HCN show an increase in T_{max} with increasing rank. NH_3 is the dominant product at low heating rate. Results from previous high heating rate experiments show that HCN is the dominant product. Experiments show that tar cracking at high temperatures is not a major contributor to HCN formation. The heating rate dependence of the conversion of coal nitrogen to HCN and NH_3 is believed to be due to the secondary reaction of HCN and coal hydrogen in the char pores to produce NH_3. This reaction can be completed with enough gas residence time within the char pores. At high temperature, the residence time is reduced and HCN conversion does not occur. Such a reaction sequence was added to the FG-DVC model and the kinetics were derived.

Introduction

Although sulfur and nitrogen are small contributors to the mass of coal, their oxides are significant contributors to environmental pollution. Understanding the mechanism of the transition from coal sulfur and nitrogen to the pollutant gas species is crucial for more efficient and cleaner coal utilization. The objective of this work was to study the evolution of sulfur and nitrogen from the Argonne Premium coals during pyrolysis and to employ the data to develop a model for sulfur and nitrogen evolution during pyrolysis.

To develop the model, sulfur and nitrogen reactions are being added to the FG-DVC model of coal pyrolysis which describes the evolution of tar and carbon, hydrogen, and oxygen gas species. The FG-DVC model combines a functional group (FG) model for gas evolution and a statistical depolymerization, vaporization and crosslinking (DVC) model for tar formation (Solomon, et al., 1988a; 1990a). The FG model describes the evolution of gases from sources in the coal, char and tar. The DVC model describes the decomposition and condensation of a macromolecular network representation of coal under the influence of bond breaking and crosslinking to predict the molecular weight distribution of the network fragments. The network is composed of fused aromatic rings connected by aliphatic bridges. Previous work (Solomon, et al., 1993) with the FG-DVC model has derived the functional group compositions and evolution kinetics for C, H and O volatile species in the Argonne Premium coals.

The pyrolysis instrument employed in this study couples thermogravimetric (TG) analysis with quantitative fourier transform infrared (FT-IR) analysis (TG-FTIR). In a previous study using this TG-FTIR programmed temperature pyrolysis and combustion technique, the major volatile products evolving from the Argonne Premium coals were investigated (Solomon, et al., 1990b).

The forms of sulfur in coal have been studied by a number of investigators (Kelemen, et al., 1991; Huffman, et al., 1991; LaCount, et al., 1992; Boudou, et al., 1987; and Calkins, 1987). Sulfur exists in coal in three forms: organic sulfur, pyritic sulfur and sulfates. Organic sulfur exists in the coal structure, either in aromatic rings or in aliphatic functional groups. Pyrite exists in coal as dispersed particles, but interactions with the coal structure during pyrolysis are expected. Sulfate is only a very small part of the total sulfur in most coals, especially in the Argonne Premium coals (Vorres, 1989). The recent application of XPS and XANES (Kelemen, et al., 1991) and XAFS (Huffman, et al., 1991) to the study of organic sulfur forms has identified the amounts of aliphatic and aromatic sulfur in the Argonne Premium coals.

During coal devolatilization, the various forms of sulfur decompose into gas species including H_2S, COS, SO_2, and CS_2. A large amount of sulfur remains in the char and some of the sulfur is evolved with the tar. Among all the volatile sulfur containing species, H_2S and tar sulfur are the most abundant during coal pyrolysis. Since H_2S is a very weak IR absorber and tar sulfur is difficult to quantify, a post oxidation technique (Solomon, et al., 1990b) has been employed to oxidize H_2S and the other sulfur containing gas

species to SO_2 which is easily detected by FTIR.

Most of the coal nitrogen is in pyrrole and pyridine structures, which are aromatic. There is very little evidence of amine groups in coal (Burchill, 1987; Wallace, et al., 1989). The most significant evolution gases are HCN and NH_3. Both HCN and NH_3 are strong IR absorbers, and can be easily observed in pyrolysis. There is evidence (Wallace, et al., 1989) showing that the relative abundance of HCN and NH_3 depends on the pyrolysis temperature. Some workers (Baumann and Moller, 1991; Usman and Wendt, 1990; and Bose, et al., 1988) believe that HCN precedes the NH_3 formation during combustion and that secondary conversion of HCN to NH_3 is possible. Since amounts of HCN and NH_3 are the main factors in NO_x formation (Bose, et al., 1988), their evolution kinetics need to be investigated.

In this paper the experimental section presents a description of the TG-FTIR apparatus and the techniques for determining kinetics and pyrolysis mechanisms. Next, sulfur results are presented followed by sulfur modeling. The paper then presents nitrogen results and modeling.

Experimental

The TG-FTIR system employed in this study was the TG/plus from Bomem, Inc., and its details have been presented elsewhere (Solomon, et al., 1990b; Carangleo, et al., 1987; and Whelan, et al., 1988). Its components are as follows: a DuPont 951 TGA, a hardware interface, an Infrared Analysis 16 pass gas cell with transfer optics, and a Bomem Michelson 110 FT-IR (resolution, 4 cm^{-1}; detector, MCT). A helium sweep gas (250 cm^3/min) is employed to bring evolved products from the TGA directly into the gas cell. The system is operated at atmospheric pressure.

The programmed temperature pyrolysis and combustion profile is as follows: A 20 mg sample loaded in the platinum sample pan of the DuPont 951 is taken on a 30°C/min temperature excursion in helium first to 150°C to dry for 4 minutes and then to 900°C at 30°C/min for pyrolysis. Upon reaching 900°C and holding the temperature for 3 minutes, the sample is cooled to 250°C over a 20 minute period. After cooling, a small flow of O_2 (20 cm^3/min) is added to the helium sweep gas and the temperature is ramped to 900°C in order to combust the remaining char. Infrared spectra are obtained once every 41 seconds.

A post oxidation method was employed to collectively study sulfur evolution. In this procedure, heat (approximately 900°C) and oxygen (10 cm^3/min) is added to the volatile product stream after the furnace but before the gas analysis cell. This added step allows detection of H_2S, a very weak infrared absorber; elemental sulfur; and tar sulfur by monitoring SO_2 evolution rate. Details of this post oxidation method appear elsewhere (Solomon, et al., 1990b).

The samples studied in this work were the Argonne Premium Coal samples. The effects of pyrite were examined through the analysis of depyritized Argonne Premium Illinois #6 and Pittsburgh #8 coals as well as a pure pyrite sample from Custer, South Dakota.

Figure II.A.5-1 presents the DAF weight percent sulfur values determined by the TG-FTIR in comparison with those values provided by Argonne National Laboratory (Vorres, 1989). With the exception of Zap lignite and Wyodak coal, the TG-FTIR results are within 16 % of Argonne's data. For Zap lignite and Wyodak coal, the TG-FTIR data is 36 % and 45 % respectively lower than the Argonne data. Possible explanations for this large discrepancy are that sulfur is being incorporated in the ash or evolving as gaseous SO_3. Examination of the TG-FTIR absorbance spectra, however, show no SO_3 evolving during combustion.

Sulfur Results and Discussion

The Argonne premium coals were subjected to regular pyrolysis and pyrolysis with the post oxidizer. Presented in Figure II.A.5-2 are the COS and SO_2 evolution curves from regular pyrolysis of Zap lignite and Wyodak, Illinois #6, and Utah Blind Canyon coals. The COS is formed by reaction of pyrite or

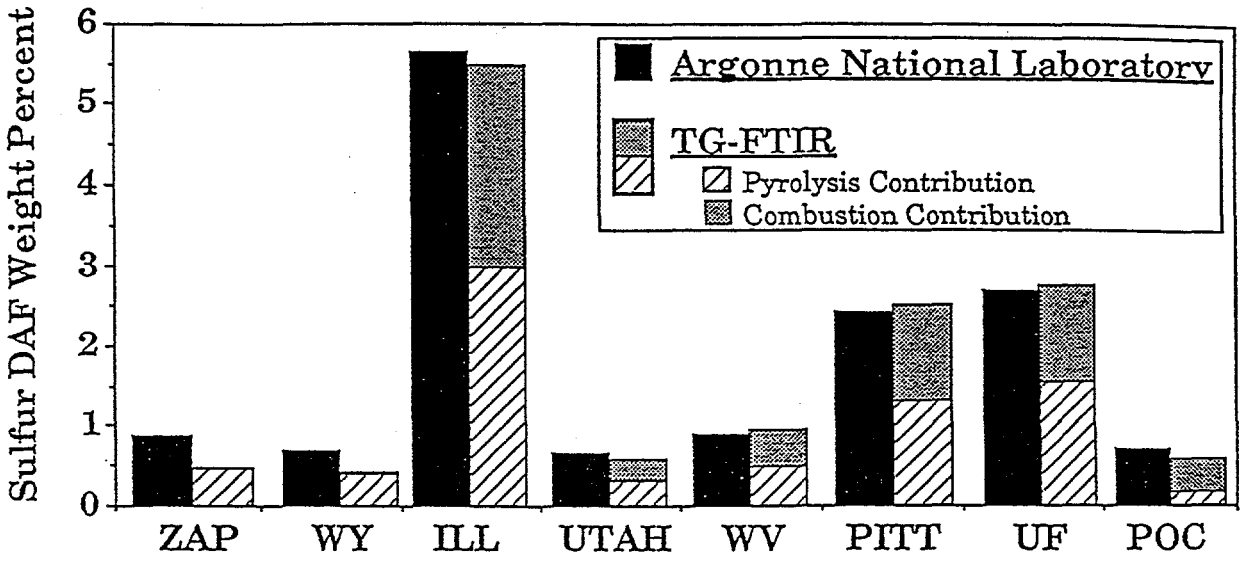

Figure II.A.5-1. DAF Sulfur Weight Percent Values Determined by TG-FTIR Compared with those Provided by Argonne National Laboratory (Vorres, 1989)

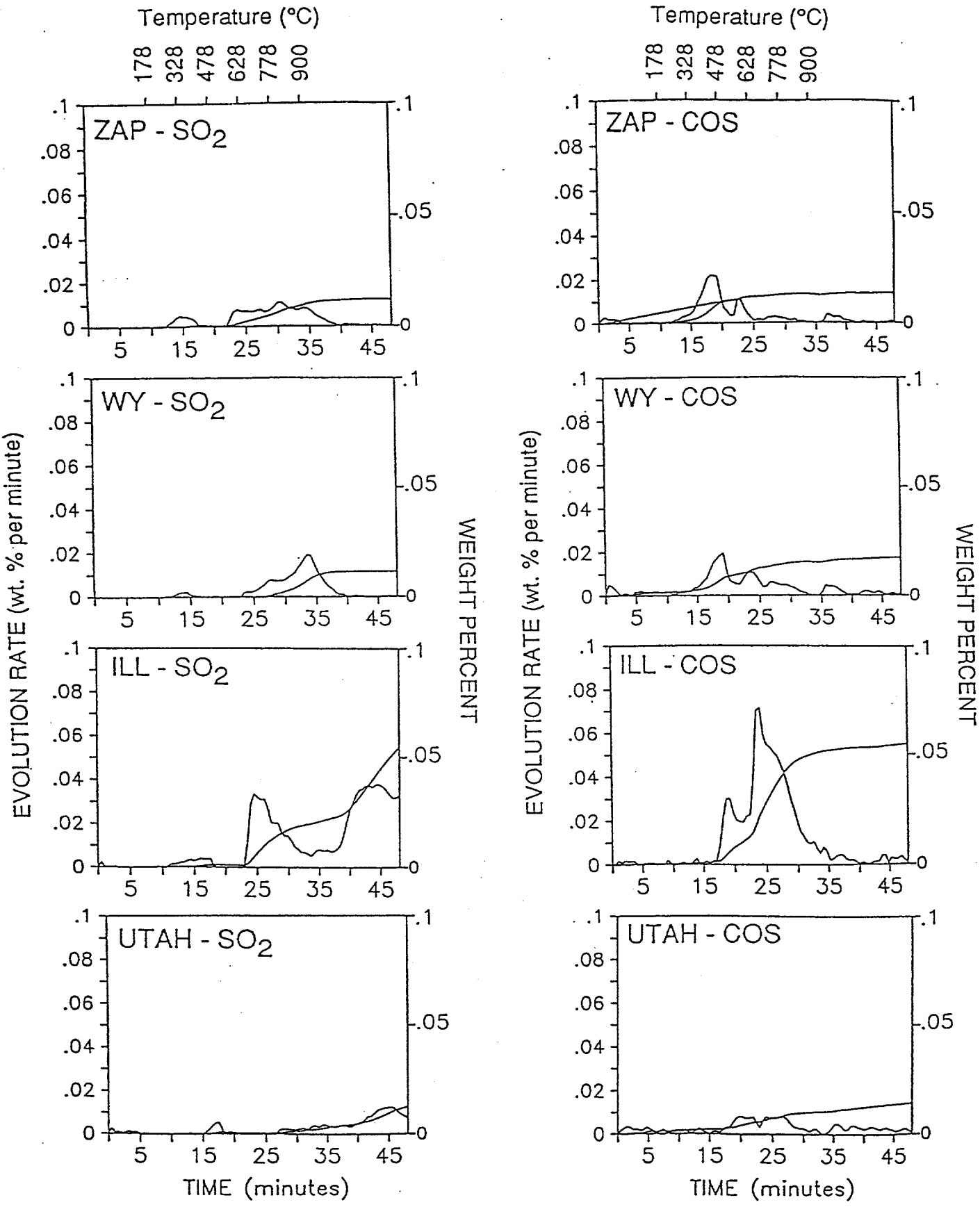

Figure II.A.5-2. COS and SO_2 Evolution Curves from Regular Pyrolysis of Zap Lignite and Wyodak, Illinois #6 and Utah Blind Canyon Coals.

sulfur formed during pyrite decomposition with CO (Calkins, 1987). The SO_2 is formed from sulfates which can be present in small amounts in some coals, particularly weathered ones (Calkins, 1987). Presented in Figure II.A.5-3 are the SO_2 evolution and weight curves from pyrolysis of all eight of the Argonne Premium coals with post oxidation of volatile products. Compared with the post oxidized SO_2 evolution curves, the contributions of COS and pyrolysis SO_2 to the total sulfur evolution are minute. It is obvious that H_2S is the major sulfur containing gas specie evolving during coal pyrolysis and consequently, only H_2S gas evolution has been included in modeling. Furthermore, subsequent discussion of pyrolysis SO_2 evolution will refer to the collective SO_2 evolution formed from post oxidation of pyrolysis products.

The SO_2 evolution curves presented in Figure II.A.5-3 exhibit two main evolution peaks and one smaller high temperature evolution peak, although each peak is more precisely a collection of smaller peaks. For each main evolution peak, the temperature of the maximum evolution rate (T_{max}) increases with increasing rank. Similar rank dependance has been reported by Kelemen et al., 1991 and Oh et al., 1988. Furthermore, the low temperature SO_2 evolution peak coincides with the coal's tar evolution peak.

With the post oxidation apparatus installed on the TG-FTIR instrument, small amounts of oxygen were able to diffuse from the post oxidation chamber to the remaining char sample resulting in mild oxidation at high temperatures. In Figure II.A.5-3, the SO_2 evolution seen beyond 37 minutes is believed to be from decomposition of the pyrrhotite (FeS).

Fraction of Volailte Sulfur - The SO_2 weight curves in Figure II.A.5-3 offer the quantitative amounts of sulfur volatilized during pyrolysis. By dividing the volatile sulfur values by the amount of total sulfur in the parent coals, the volatile sulfur fractions for each coal were generated and are presented in Fig. II.A.5-4 on a DAF basis. For all the coals except Pocahontas #3, the volatile sulfur fractions are from 0.5 to 0.6. For Pocahontas #3, only 34% of total coal sulfur is volatile. This may be attributed to its high aromaticity, low tar yields, and low aliphatic sulfur content. More discussion of the rank dependence of sulfur evolution is to be presented below.

Aliphatic Sulfur Contribution - Figure II.A.5-5 presents data concerning the origin of the low temperature SO_2 evolution peak. In this figure, the fraction of total organic sulfur evolved during the first SO_2 peak is plotted as a function of the oxygen content in the parent coal (Vorres, 1989) using oxygen as a simplified measurement of rank. A very interesting rank correlation can be seen where, with the exception of Zap lignite, the low rank coals release a much larger fraction of their organic sulfur during the low temperature peak than the high rank coals. Since low rank coals are more aliphatic by nature, the plot suggests that the main contributor to the low temperature SO_2 peak is aliphatic sulfur. This idea is supported by the work of Mehldi Taghiei et al. (1991) which indicates that the aliphatic sulfur is much less stable than the aromatic sulfur, consistent with its evolution under the low temperature evolution peak.

Pyritic Sulfur Contribution - As mentioned in the introduction, pyrite exists in coal as dispersed particles. The mechanism for thermal decomposition should be similar to that for pure pyrite, although some coal/pyrite interactions are expected.

To understand the pyritic sulfur contribution to the SO_2 evolution curves, Illinois #6 and Pittsburgh #8 coals were subjected to ASTM D-2492 (ASTM, 1985) under a nitrogen atmosphere. In this method, sulfate sulfur is extracted from the coal with dilute hydrochloric acid and pyrites (FeS_2) are removed using dilute nitric acid. Results from temperature programmed pyrolysis and combustion of raw and ASTM D-2492 modified Illinois #6 coal are presented in Figures II.A.5-6 and II.A.5-7 respectively. Figures II.A.5-6a and II.A.5-7a are the balance and thermocouple curves and Figures II.A.5-6b and II.A.5-7b are the SO_2 evolution and weight curves. The tar evolution curve for the raw Illinois #6 coal (obtained without the post oxidizer) is included in Figure II.A.5-6a to demonstrate how the tar peak overlays the low temperature SO_2 peak. The ASTM D-2492 procedure removed the second SO_2 pyrolysis peak as well as the "sharp" portion of the combustion cycle SO_2 peak. The pyrite (FeS_2) is believed to decompose during pyrolysis to form pyrrhotite (FeS) and sulfur. The pyrrhotite then remains relatively stable until O_2 is added to the helium sweep gas and the char is heated to 900°C for combustion of the remaining char. During the harsh

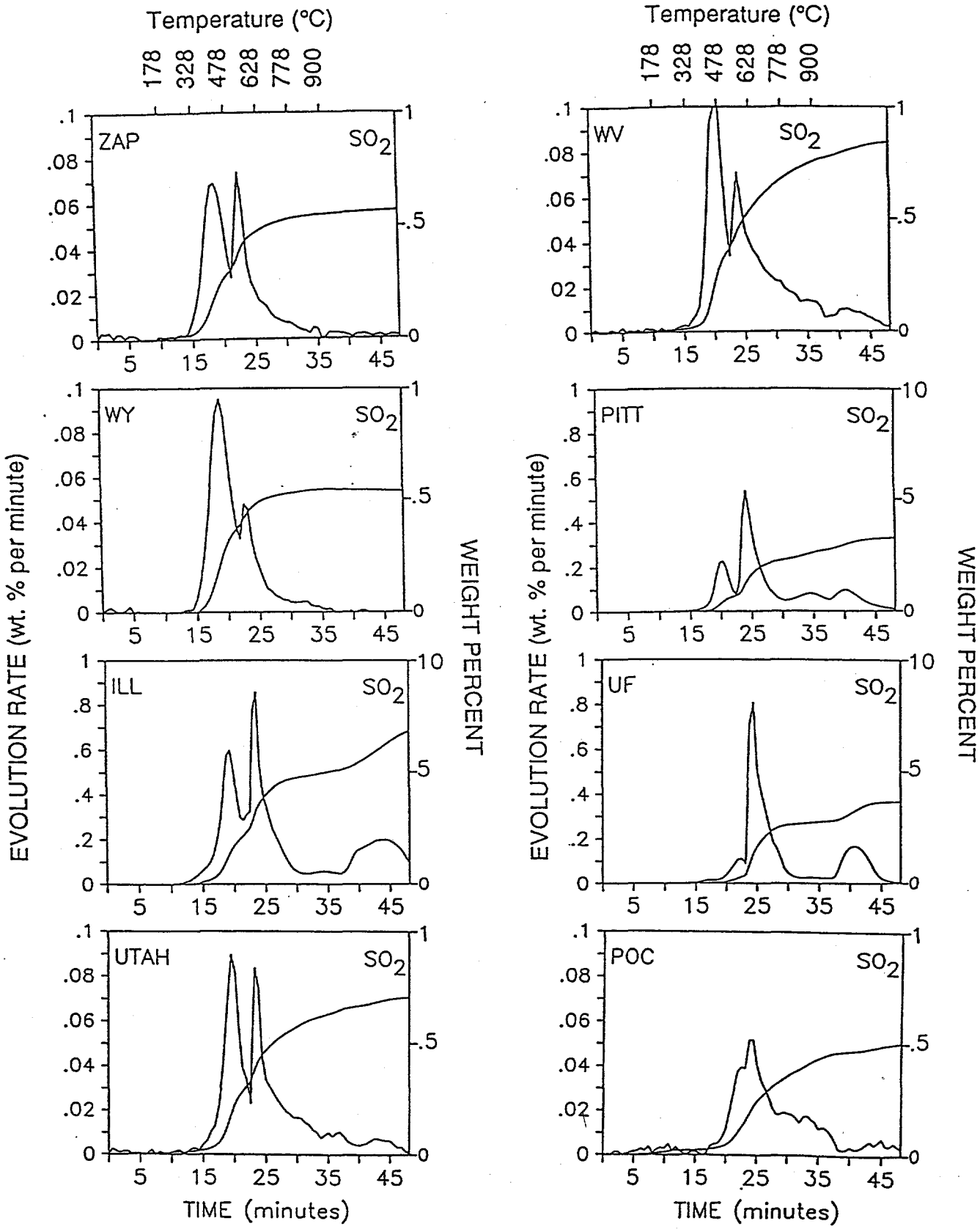

Figure II.A.5-3. SO_2 Evolution and Weight Curves from Post Oxidized Pyrolysis of the Argonne Coals.

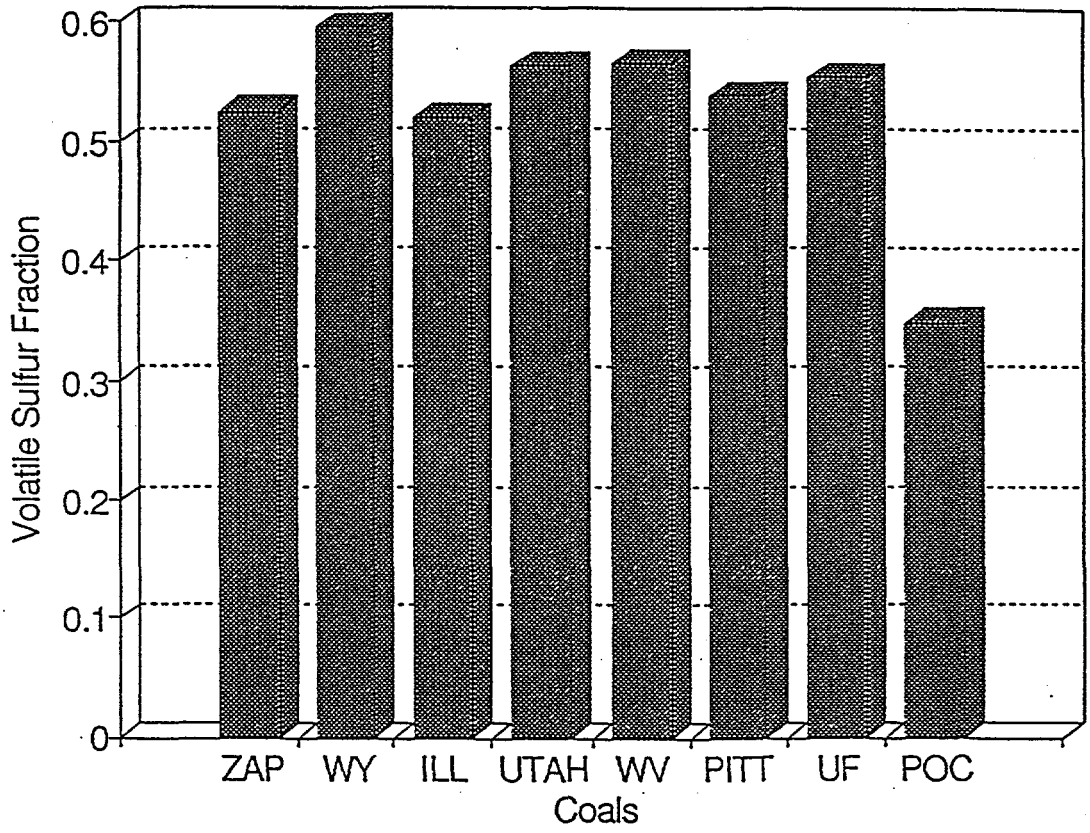

Figure II.A.5-4. Fraction of Volatile Sulfur in the Argonne Coals Determined by Post Oxidized Pyrolysis in the TG-FTIR.

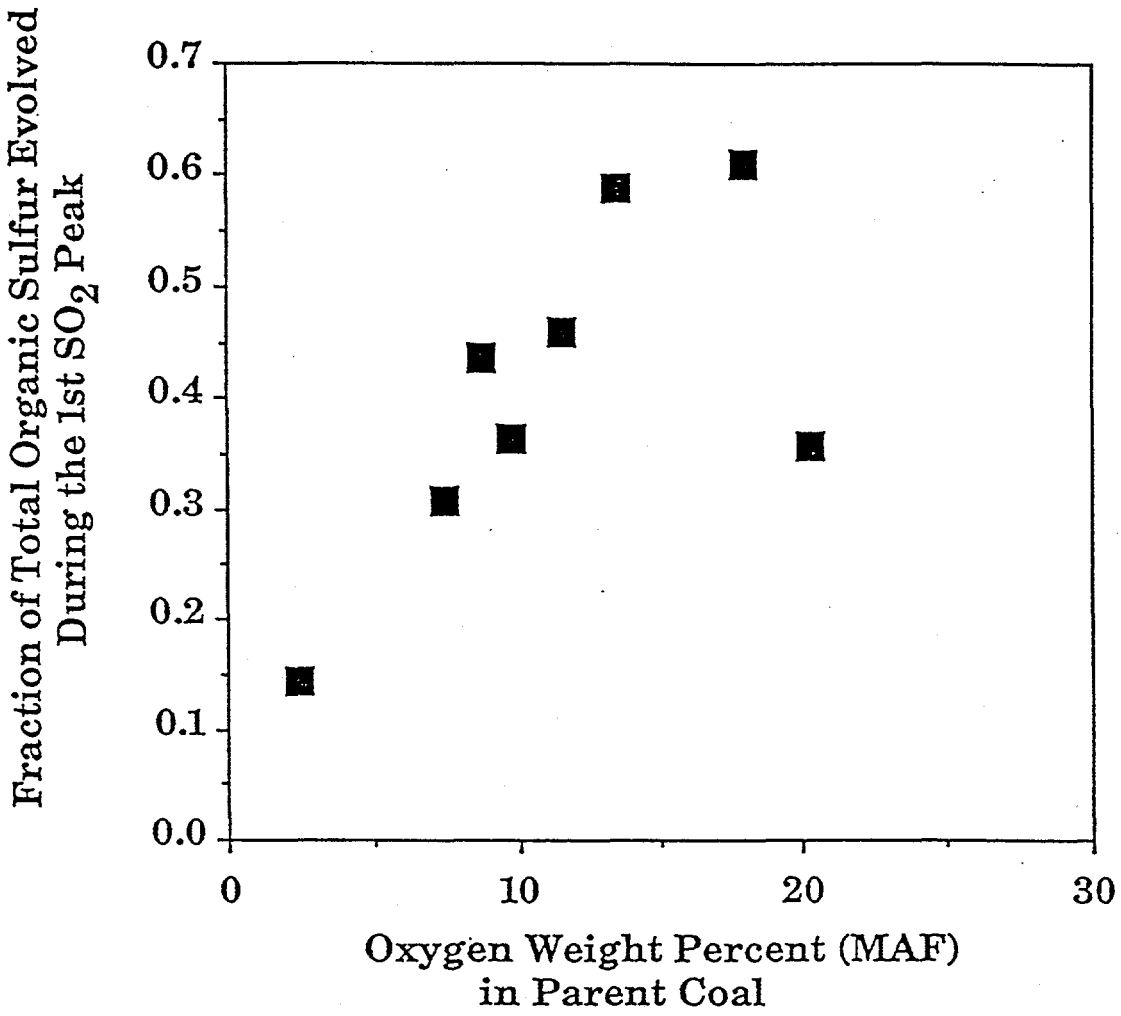

Figure II.A.5-5. Fraction of Organic Sulfur Evolved from the Argonne Coals During the First SO_2 Evolution Peak (Post Oxidized Pyrolysis) Plotted as a Function of Oxygen in the Parent Coal.

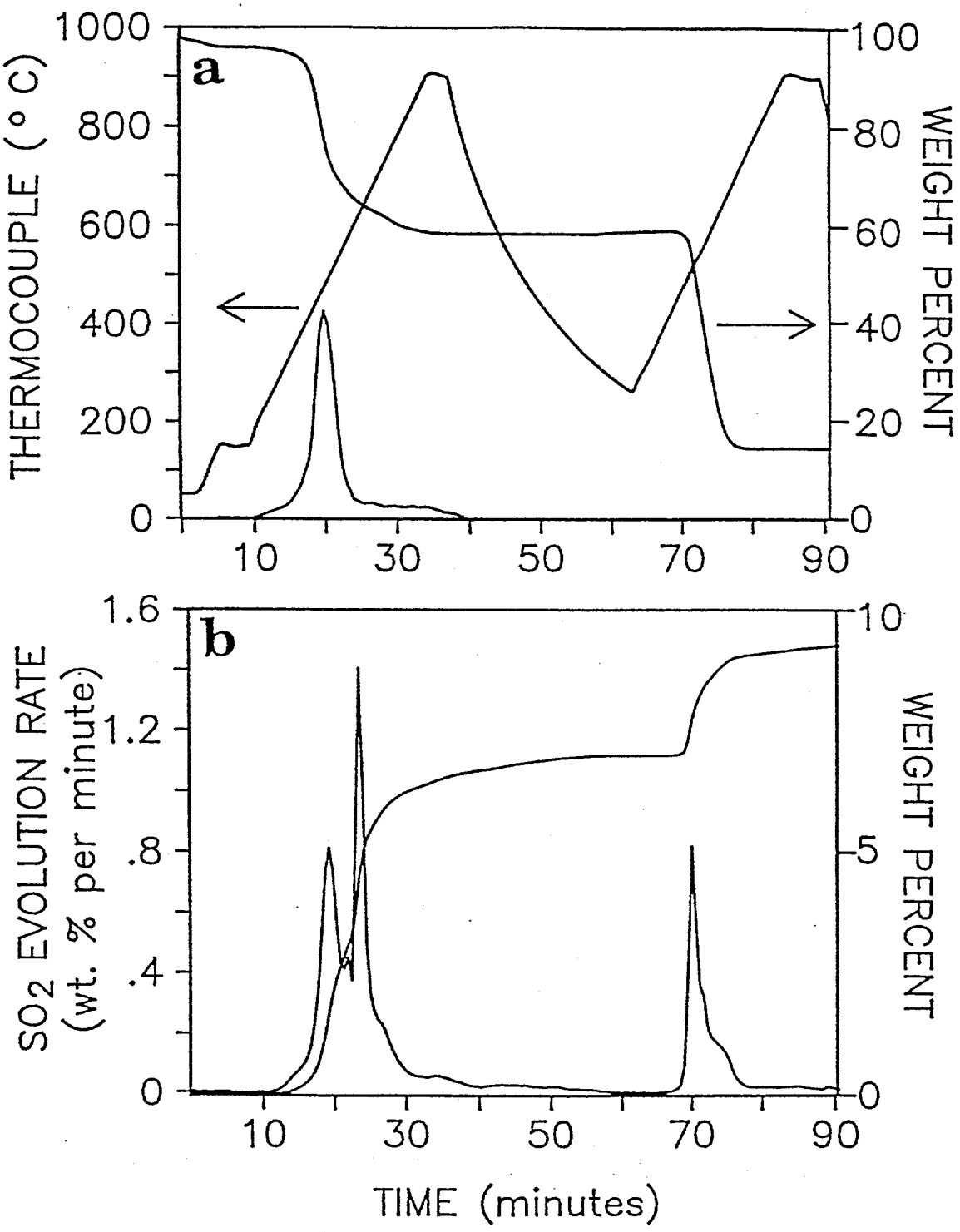

Figure II.A.5-6. Results from Post Oxidized Pyrolysis of Illinois #6 Coal. a) Balance, Thermocouple and Tar Evolution Curves and b) SO_2 Evolution and Weight Curves.

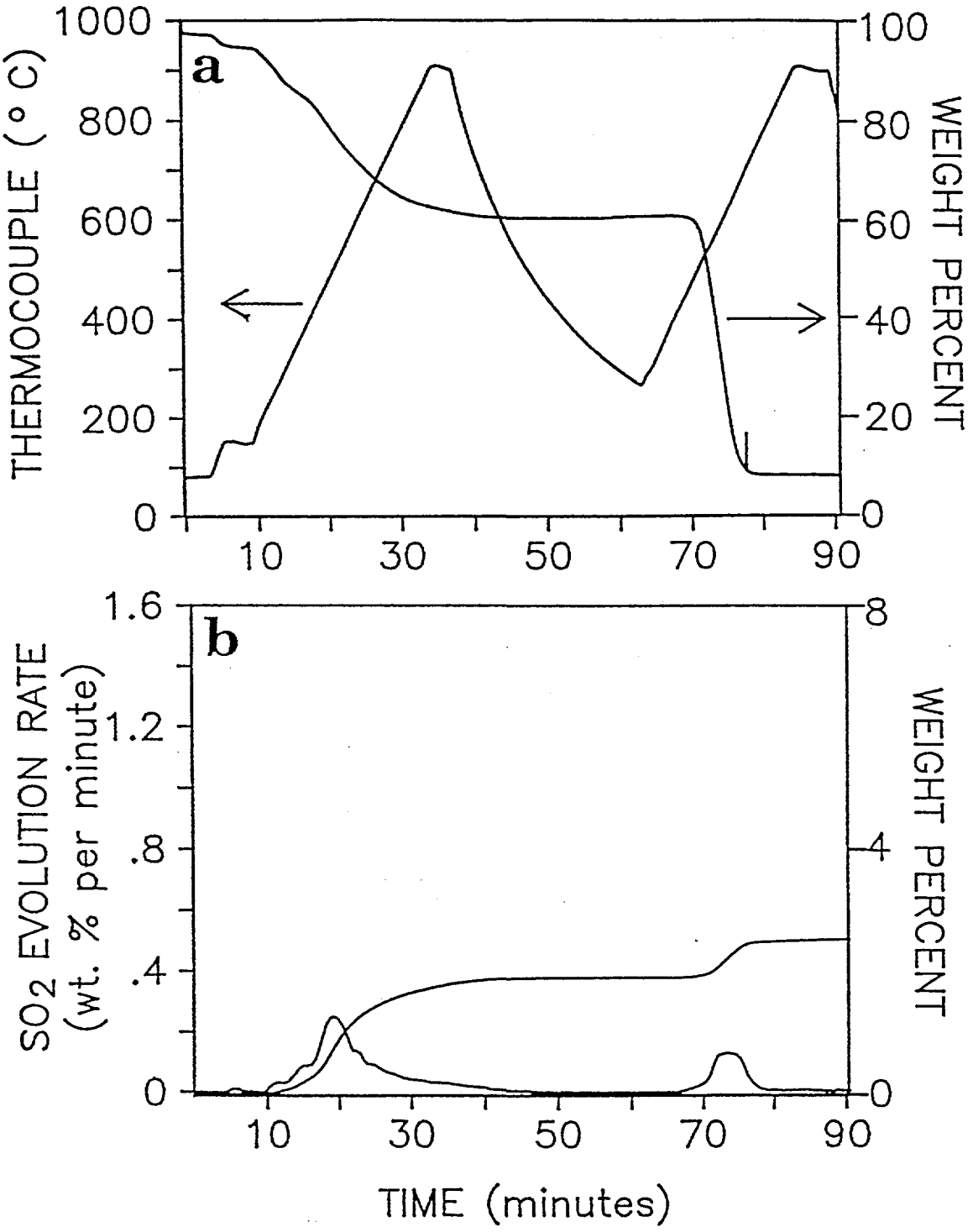

Figure II.A.5-7. Results from Post Oxidized Pyrolysis of ASTM D-2492 Modified Illinois #6 Coal. a) Balance and Thermocouple Curves and b) SO_2 Evolution and Weight Curves.

conditions of combustion, the pyrrhotite decomposes to form Fe_2O_3 and SO_2. To compare the behavior of coal pyrite with pure pyrite, a pure pyrite sample from Custer, South Dakota was subjected to temperature programmed pyrolysis and combustion. The pyrite evolution curve (not shown) has a single SO_2 T_{max} at 610°C which is slightly higher than that of Upper Freeport coal (603°C). The study by Mehldi Taghiei et al., (1991) shows that after pyrolysis, the decomposition of coal pyrite is complete and that FeS sulfur represents half of the retained sulfur in an Illinois #6 coal. Since Illinois #6 has about 50% of the total coal sulfur in pyrite and it lost about 50% of the total sulfur in pyrolysis (Figure II.A.5-4), it can be deduced that the retention of FeS is almost 100% and that it is stable throughout the pyrolysis. Consequently, 50% of the pyritic sulfur evolves and the other half remains in coals as FeS.

In addition to removing the peaks indicative of pyrite, the ASTM D-2492 procedure also removed a substantial portion of the low temperature SO_2 pyrolysis peak. In recent work, Gorbaty et. al. (1992) found that the aliphatic sulfur in coals subjected to 125°C in air for 5 days was selectively transformed to oxidized organic sulfur forms and that most of these oxidized sulfur forms were retained in the char after 400°C pyrolysis as either sulfur oxides or aromatic sulfur. Since nitric acid is a strong oxidizing agent, the majority of the decrease in the low temperature SO_2 evolution peak is probably due to the oxidation of the coal's aliphatic sulfur. It is possible however that a small amount of FeS_2 in coal does decompose during the low temperature SO_2 evolution peak, as low and high temperature FeS_2 decomposition has been reported by others (Oh, et al., 1988; Khan, 1989). Temperature programmed pyrolysis and combustion of raw and ASTM D-2492 modified Pittsburgh #8 coal showed trends similar to the Illinois #6 coal.

As noted from Figure II.A.5-3, the SO_2 T_{max} which is a result of pyrite decomposition demonstrates rank dependence. The SO_2 T_{max} increases from 555°C in the case of Zap lignite, to 603°C in the case of Upper Freeport coal. It is unclear as to why pyrite in coal is rank dependent. Pyrolysis experiments were done with pyrite/coal mixtures and with pure pyrite with small flows of CO_2, CO, H_2O, H_2, and C_2H_6 added to the helium sweep gas with no success in lowering the pyrite decomposition temperature. In all the experiments, the pyrite decomposition temperatures showed little variation. Pyrite decomposition in coal occurs at a time when there is an abundance of free radical formation. Consequently, the pyrite dispersion throughout the coal matrix and the coal/pyrite interaction is probably the key factor which causes earlier decomposition of pyrite during coal pyrolysis.

Sulfur Modeling

Modeling of coal sulfur evolution was performed by employing our FG-DVC coal pyrolysis model (Solomon, et al., 1988a; 1990a; and 1993). FG-DVC terminology divides the total coal sulfur into a number of precursor pools that would evolve during the pyrolysis with different kinetics. The evolution of each pool is modeled using a distributed activation energy approach (Solomon et al., 1988a) to represent the diversity of the chemical structure of coals. The pool composition and kinetics were determined by fitting the model to the data collected in this work. The procedure was based on the physics and understanding of coal sulfur established previously by the work of Gorbaty and the coworkers (1992), Calkins and the coworkers (1987), Huffman and coworkers (1991), and LaCount and the coworkers, (1992). It needs to be noted that our model, as all engineering models, represents a simplified picture of the complicated processes involved in the coal sulfur evolution. However, efforts were made to maintain the basic physics for the pool assignment so that the model contains the minimum set of processes that are needed for it to be physically significant.

Figure II.A.5-3 has shown that sulfur pyrolysis evolution spans continuously over a wide temperature range of 400°C to 800°C at 30°C/min. We classify the evolution sequence into three groups of peaks, i.e., low temperature, intermediate temperature and high temperature groups. The low temperature group consists of peaks that evolve at temperature lower than that of the sharp pyrite peak. The intermediate temperature group has only one member which is the sharp pyrite peak. The high temperature group is located at temperatures higher than the pyrite decomposition temperature and is a broad shoulder. Each group of peaks have contributions from the evolving organic and pyritic sulfur. Sulfatic sulfur contributes an insignificant amount of the total sulfur and was not modeled here. Besides the gaseous sulfur species, another contributor is the tar sulfur that is chemically part of the tar when it

evolves. This type of mechanism is contained in the FG-DVC tar evolution algorithm (Solomon, et al., 1988a), and does not need to be addressed here. As indicated above (Figure II.A.5-6), the tar evolution peak coincides with the low temperature group of peaks. The sulfur evolution was modeled as H_2S evolution, since it is known that H_2S is the major component in the sulfur gases evolved in the pyrolysis. Although the model also has COS and SO_2 pools, they are treated as background to the H_2S peaks and are only of trace amount.

As identified by the direct measurements of sulfur forms in coal (Kelemen, et al., 1991; Huffman, et al., 1991), organic coal sulfur can be aromatic and aliphatic. It is understood that the aliphatic sulfur is less stable than the aromatic sulfur during pyrolysis and that aliphatic sulfur evolves at lower temperature (Mehldi Taghiei, et al., 1991). The aromatic sulfur which is in the coal aromatic ring structure is more stable to thermal exposure. This leads to classifying the organic sulfur into two precursor pools, i.e., the aliphatic sulfur (loose) and the volatile aromatic sulfur (tight) pools, and one char sulfur pool. The aliphatic pool contains all the aliphatic sulfur and is the major contributor of the low temperature group. The volatile aromatic pool has the volatile portion of the aromatic sulfur which evolves at high temperature. The char pool has the rest of the organic sulfur that does not evolve during pyrolysis.

According to the work by Khan (1989), the pyritic sulfur decomposes mainly through the reaction $FeS_2 \rightarrow FeS + S$. The FeS remains stable during pyrolysis. This suggests that 50% of the pyritic sulfur is volatile and will evolve as H_2S mainly under the sharp spike shown in Figure II.A.5-3. Although there is no direct evidence showing that coal pyrite evolves at temperature other than its intrinsic temperature, we tentatively use three pyrite pools, i.e., low temperature (loose), intrinsic (tight), and high temperature (extra tight) pools to enable us to model the alternative routes of pyrite decomposition. The tight pool corresponds to the pyrite spike and should contain most of the volatile pyritic sulfur. The model sketched above is schematically shown in Figure II.A.5-8. The overall sulfur evolution is now modeled with one tar sulfur peak, two H_2S peaks from organic sulfur, three H_2S peaks from pyritic sulfur. Finally COS and SO_2 peaks (organic and inorganic) are treated as background of H_2S peaks and no effort was made to fit their evolutions.

Assuming that all of the aliphatic sulfur evolves at low temperature during the pyrolysis, the amount of the first organic sulfur peak was obtained from the direct measurements of coal aliphatic sulfur (Kelemen, et al., 1991; Huffman, et al., 1991). To verify this assumption, Figure II.A.5-9 compares the gaseous sulfur amount evolved under the first SO_2 peak group with the direct measurement of the sulfur forms in coal (Kelemen, et al., 1991; Huffman, et al., 1991). This gaseous sulfur amount was determined by the difference between the total sulfur evolved in the first peak group measured in this work and the tar sulfur as calculated with FG-DVC. For the 6 high rank coals, the amount of aliphatic sulfur matches well the gaseous sulfur amount in the first peak group in the range of experimental uncertainty. The difference for the Wyodak and Illinois #6 coals indicates contributions from other sulfur sources to the first peak group. Since the aromatic sulfur is quite stable, it is more likely that part of the pyritic sulfur decomposes at this temperature range for these two low rank coals. This low temperature pyrite decomposition was supported by a reaction pathway proposed by Khan where the pyrite reacts with hydrogen gas a temperatures as low as 230°C. The lack of this decomposition in high rank coals however is still not explained. Also unexplainable is the Zap lignite coal, for which the gaseous sulfur evolved in the first peak group is much less than the aliphatic sulfur amount.

As discussed previously, the second peak group corresponds to the pyritic sulfur decomposition. After the amount of sulfur in this peak group was determined from Figure II.A.5-3, it was found that the amount is lower than that of volatile pyritic sulfur which is 50% of the total pyritic sulfur, indicating that part of the pyritic sulfur decomposed is retained by the coal matrix. The retained pyritic sulfur is believed to evolve at higher temperature in the third peak group. Finally, the volatile aromatic sulfur is assumed to evolve in the third peak group and the amount was determined by matching the total amount of the volatile sulfur.

Although derivation of kinetic data needs at least three different heating rate experiments, this requirement is relaxed by the fact that the pre-exponential factors of the gas pools are all in the range of

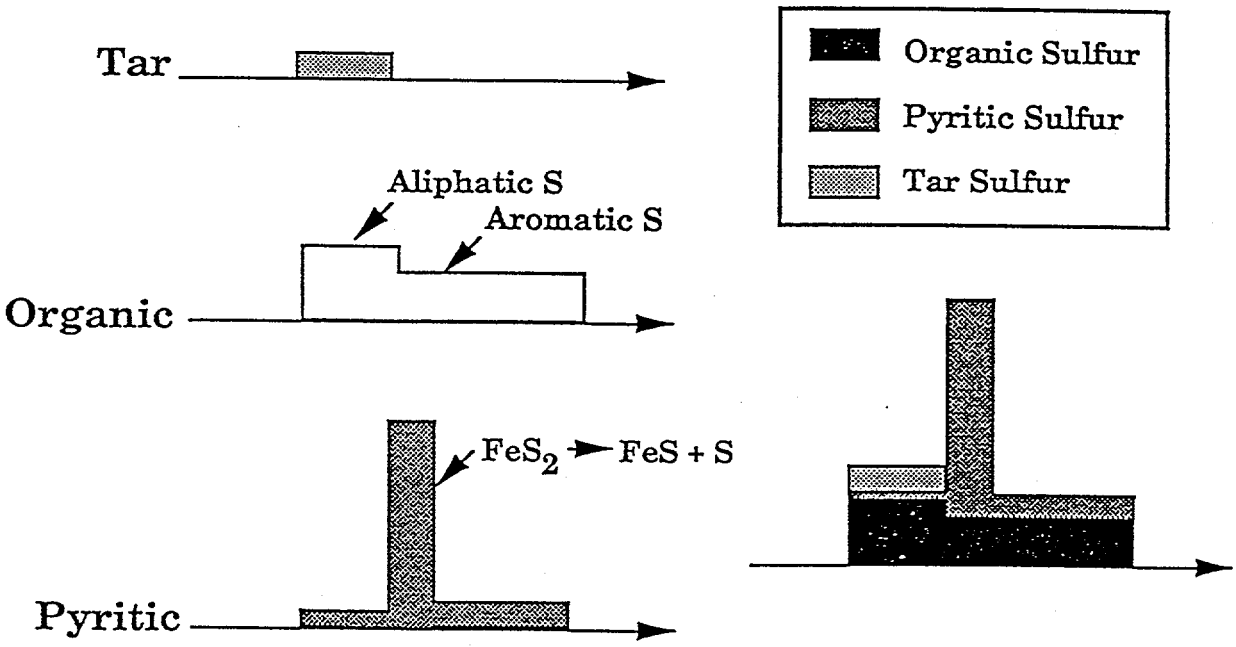

Figure II.A.5-8. Schematic Representation of the Proposed Component Peaks for Sulfur Evolution.

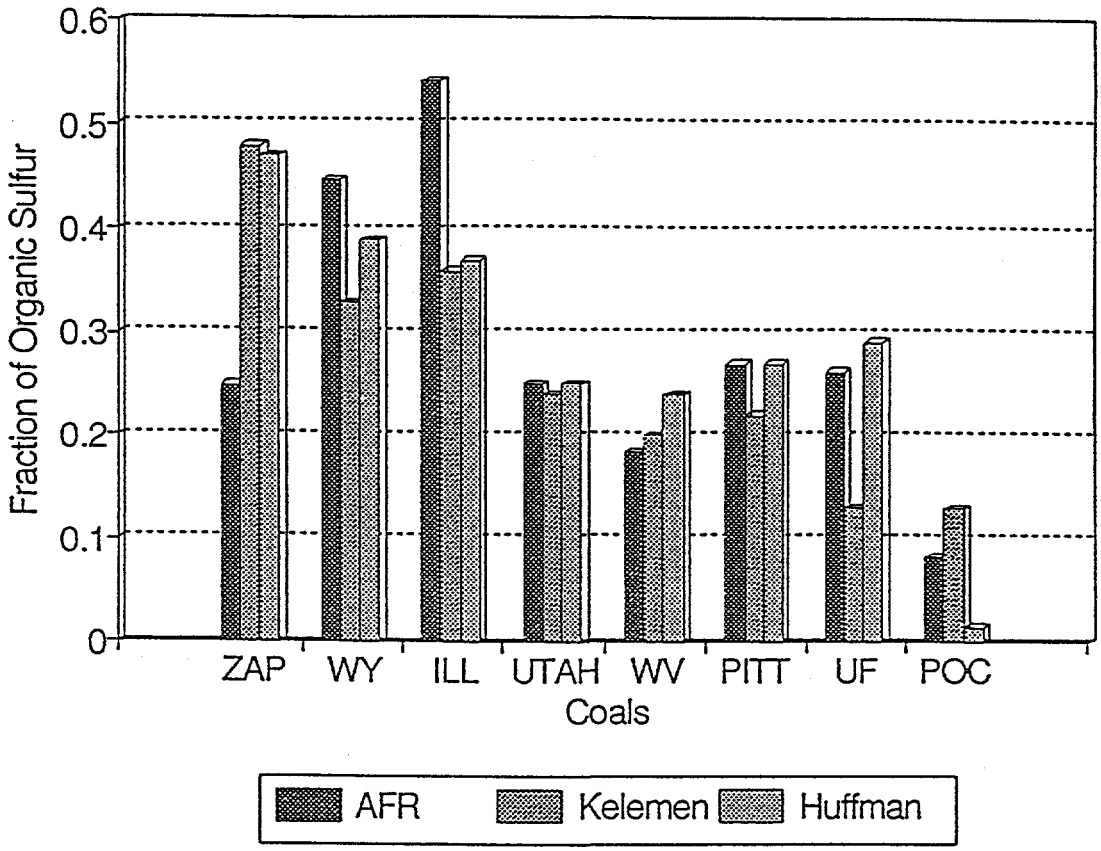

Figure II.A.5-9. Comparison of the Amount of the Sulfur Evolved under the First SO_2 Peak During Post Oxidized Pyrolysis and the Direct Measurements of the Aliphatic Sulfur. (Kleeman et. al., 1991 and Huffman et al., 1991)

10^{12} to 10^{14} (Solomon, et al., 1993). Moreover, the distributed activation energy adopted in the FG-DVC model has the advantage that kinetic data derived at one heating rate can be used more reliably at other heating rates (Solomon, et al., 1993). Therefore, the same pre-exponential factor of 5×10^{12} was used for all sulfur gas pools, and the activation energy and the σ are the fitting kinetic parameters. The activation energy was chosen to match the peak evolution temperature, and the σ was chosen to fit the shape of the evolution curve. More detail on FG-DVC gas kinetics can be found in Solomon, et al., (1988a and 1993).

A typical fit obtained by the procedure described above is given in Figure II.A.5-10 for Illinois #6 coal. The symbols are the TG-FTIR data points. The curves are the overall fit and the resolved component curves. For simplicity, the component curves plotted are the tar sulfur, organic sulfur and pyritic sulfur curves. Further division of these curves into individual species peaks would be too visually complicated. It is still quite clear in Fig. II.A.5-10 that the tar sulfur, the aliphatic sulfur and the pyritic sulfur decomposing at low temperatures constitute the first SO_2 peak group, while the pyritic sulfur is responsible primarily for the second peak group, and the aromatic sulfur and the rest of the volatile pyritic sulfur comprise the third peak group.

Figure II.A.5-11 displays the fractions of three types of organic sulfur for eight Argonne coals and Figure II.A.5-12 plots the fractions of four types of pyritic sulfur. As stated before, the organic sulfur is classified into three pools, among which the aliphatic is the least stable and evolves at low temperature while the nonvolatile aromatic sulfur is the most stable and dose not decompose in pyrolysis. There are three volatile and one non-volatile pyritic sulfur pools. The volatile pyritic sulfur results from the FeS_2 to FeS + S decomposition. The fate of the decomposed S from this reaction splits it into three volatile sulfur types. Most of the decomposed S evolves immediately in gaseous form and they constitute the intrinsic volatile pyrite peak. Part of the S from the FeS_2 decomposition would be retained in the coal matrix and is released at higher temperature. This results in the high temperature type of volatile pyritic sulfur. The low temperature pyritic sulfur would be due to the interaction between the coal matrix and pyrite which would de-stabilize the pyrite. Although Figures II.A.5-11 and II.A.5-12 show some information on the rank dependence of coal sulfur stability, it would be too speculative to draw further conclusions from the plots at this stage.

The sulfur pyrolysis evolution of eight Argonne coals are fitted with the FG-DVC and the sulfur model explained above, and the fits are plotted in Figure II.A.5-13. The pyrolysis evolution kinetic data for sulfur evolution from the Argonne coals are presented in Table II.A.5-1.

Nitrogen Results and Discussion

The NH_3 and HCN evolutions from pyrolysis of the Argonne Premium coals are presented in Figures II.A.5-14 and II.A.5-15 respectively. The NH_3 evolution curves exhibit two main evolution peaks. For each peak, the T_{max} increases with increasing rank, although the majority of the shift in T_{max} for the high temperature NH_3 peak occurs between Wyodak and Illinois #6 coals. The HCN evolution curves exhibit only one main evolution peak. With the exception of Zap lignite and Wyodak coal, the HCN evolution curves overlay the high temperature NH_3 evolution peak suggesting that a common source is responsible for their formation. In the cases of Zap lignite and Wyodak coal, HCN evolves at a lower temperature than the high temperature NH_3 peak.

Fraction of Volatile Nitrogen - The fraction of nitrogen released from the Argonne Coals during pyrolysis displays rank dependance. In Figure II.A.5-16, the fraction of nitrogen evolved as HCN and NH_3 during pyrolysis is plotted as a function of oxygen content in the parent coal. There is a trend where the lower rank coals release a larger fraction of their nitrogen during pyrolysis as HCN and NH_3 than the higher rank coals.

Heating Rate Dependence - Table II.A.5-2 compares the TG-FTIR measured weight percents for NH_3 and HCN to previously obtained values generated during rapid heating rate pyrolysis in an entrained flow reactor (EFR) (Solomon, et al., 1982). Also included in this table are some data concerning the

Table II.A.5-1. Pyrolysis Evolution Kinetics of Sulfur Gases. The Frequency Factors Are 5.0×10^{12} (1/seconds) for All the Pools. AE– Activation Energy in Kelven. Sigma is in Kelven.

	ZAP	WY	ILL	UTAH	WV	PITT	UF	POC
H2S-L								
AE	23500	23700	24300	24500	25300	25500	28000	27500
Sigma	1500	1000	1000	700	800	800	1000	1000
H_2S-T								
AE	29000	28000	29500	31000	31000	30000	32000	34000
Sigma	3000	3000	2500	4000	4000	3000	2000	4000
SO_2								
AE	24000	24000	24000	24500	25000	25500	26000	26000
Sigma	1000	1000	1000	1000	1000	1000	1000	1000
COS								
AE	24000	24000	24000	24500	25000	25500	26000	26000
Sigma	1000	1000	1000	1000	1000	1000	1000	1000
FeS_2. low temp. decomp.								
AE	-	24000	23500	-	-	-	-	-
Sigma	-	4000	4000	-	-	-	-	-
FeS_2, the intrinsic peak								
AE	27700	27700	28500	28500	28500	29300	29500	29500
Sigma	100	100	100	100	100	100	100	100

Table II.A.5-2. NH_3 and HCN Weight Percents from Pyrolysis in TG-FTIR and Entrained Flow Reactor

	TG-FTIR			EFR 1100°C, 24"		
	(DAF wt.%)		Total Volatile Nitrogen Fraction	(DAF wt.%)		Total Volatile Nitrogen Fraction
	HCN	NH_3		HCN	NH_3	
Pocahontas	0.036	0.07	---	0.28	0	0.11
Upper Freeport	0.032	0.13	---	0.78	0	0.26
Pittsburgh	0.043	0.16	0.31	0.84	0	0.27
Stockton	0.065	0.15	---	0.55	0	0.18
Utah Blind Canyon	0.110	0.16	---	1.21	0	0.40
Illinois	0.083	0.15	0.43	---	---	---
Wyodak	0.049	0.11	---	0.60	0	0.27
Zap	0.110	0.14	---	---	---	---

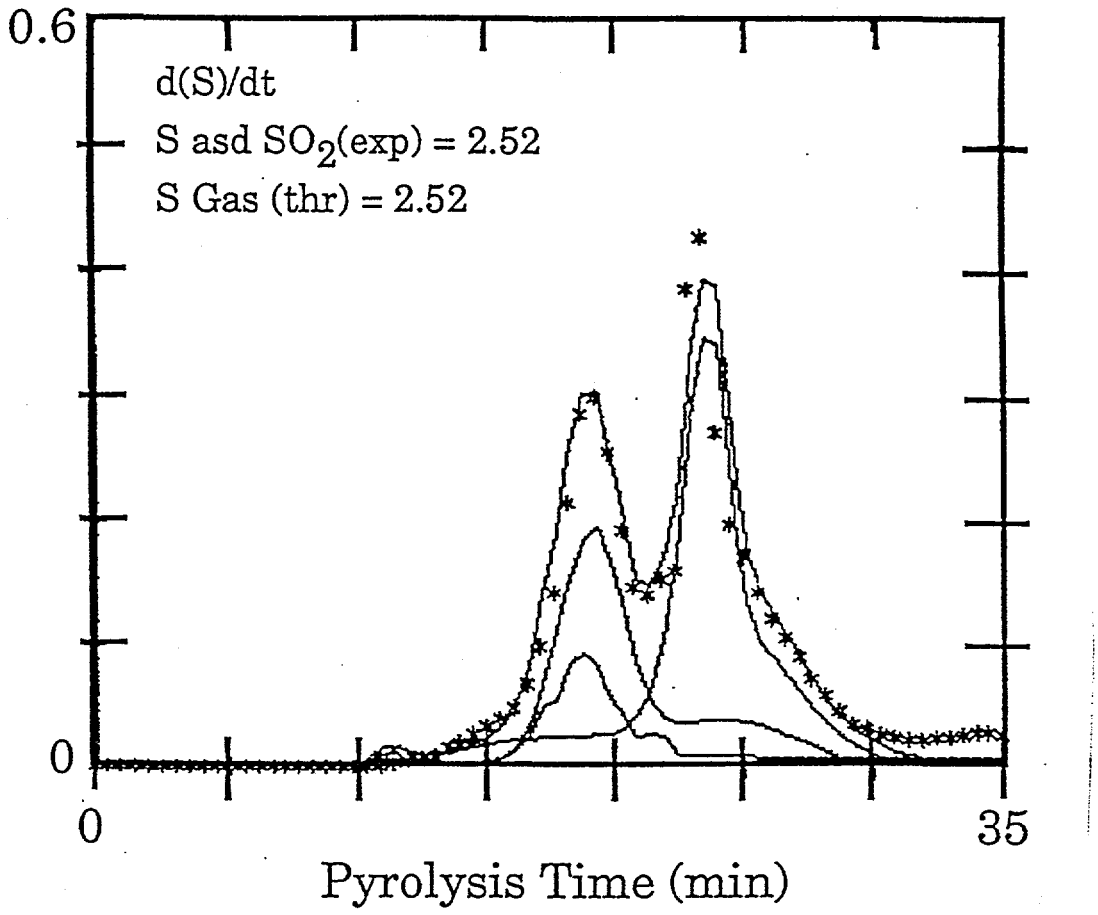

Figure II.A.5-10. Peak Resolutions of Sulfur Evolution for Illinois #6 Coal.

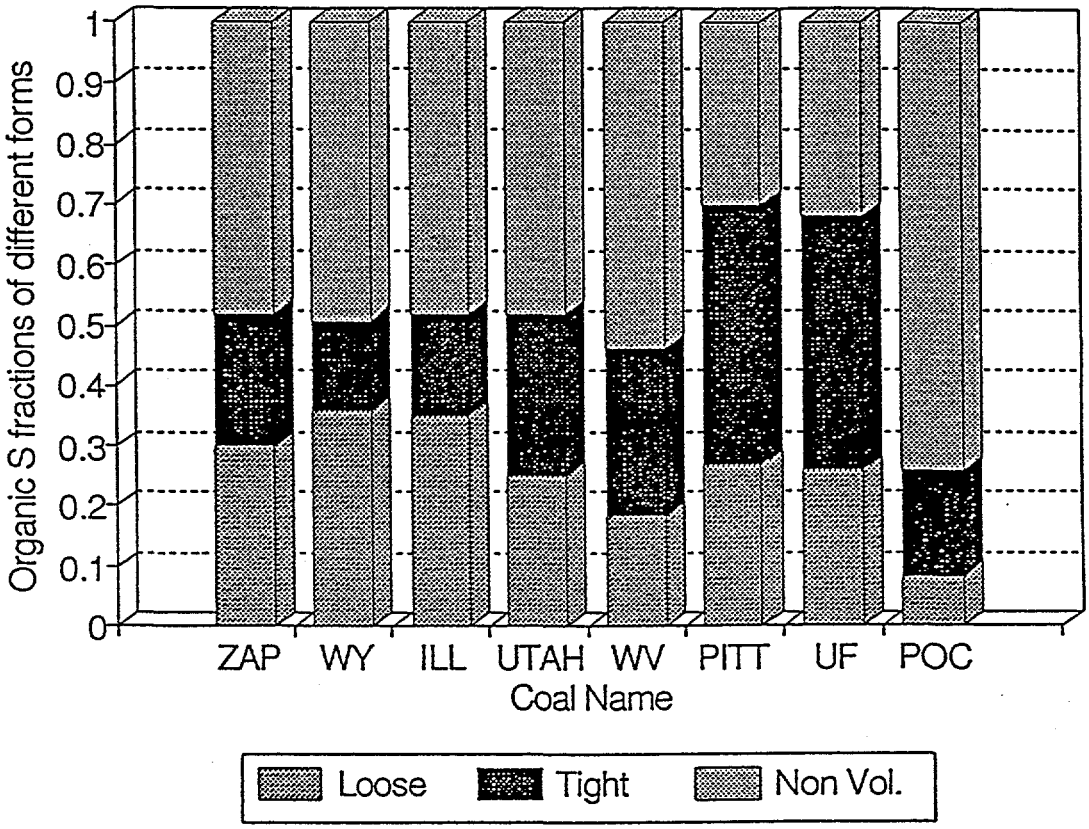

Figure II.A.5-11. Organic Sulfur Fractions of Different Forms for the Argonne Coals, Determined in this Work.

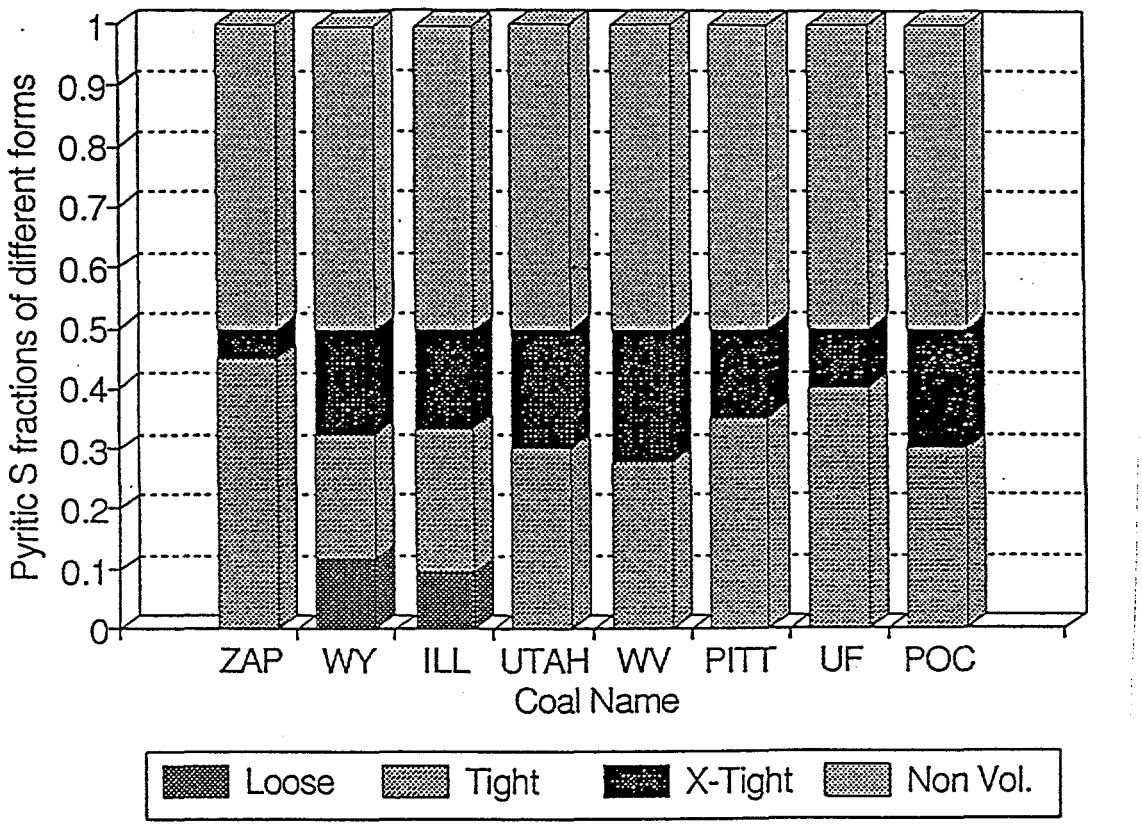

Figure II.A.5-12. Pyritic Sulfur Fractions of Different Forms for the Argonne Coals, Determined in this Work.

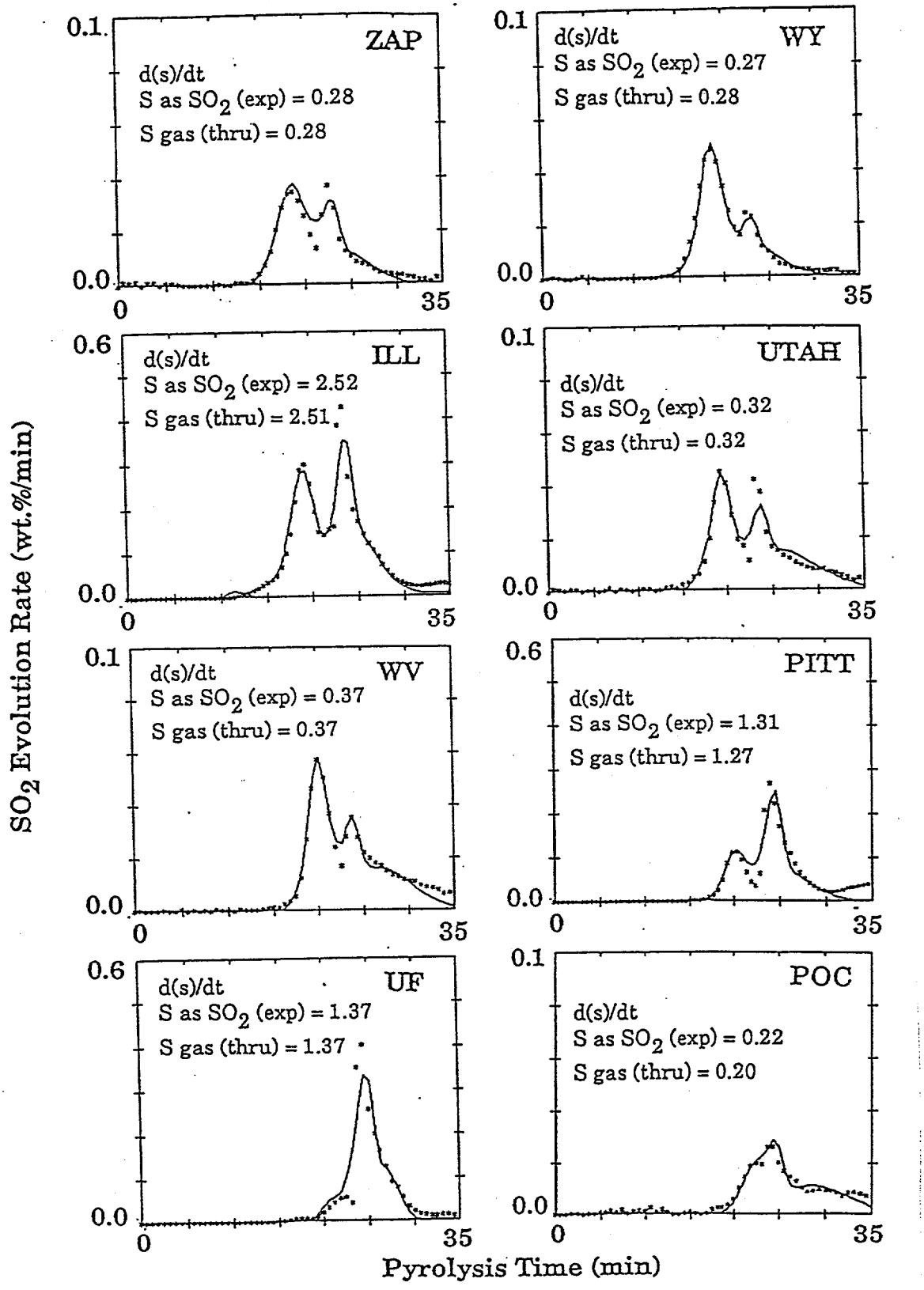

Figure II.A.5-13. SO_2 Evolution Curves Measured in Post Oxidized Pyrolysis (symbols), and the Fitted Curves by FG-DVC Model with Sulfur Evolution Kinetics Developed in this Work. Heating Rate is 30°C/sec.

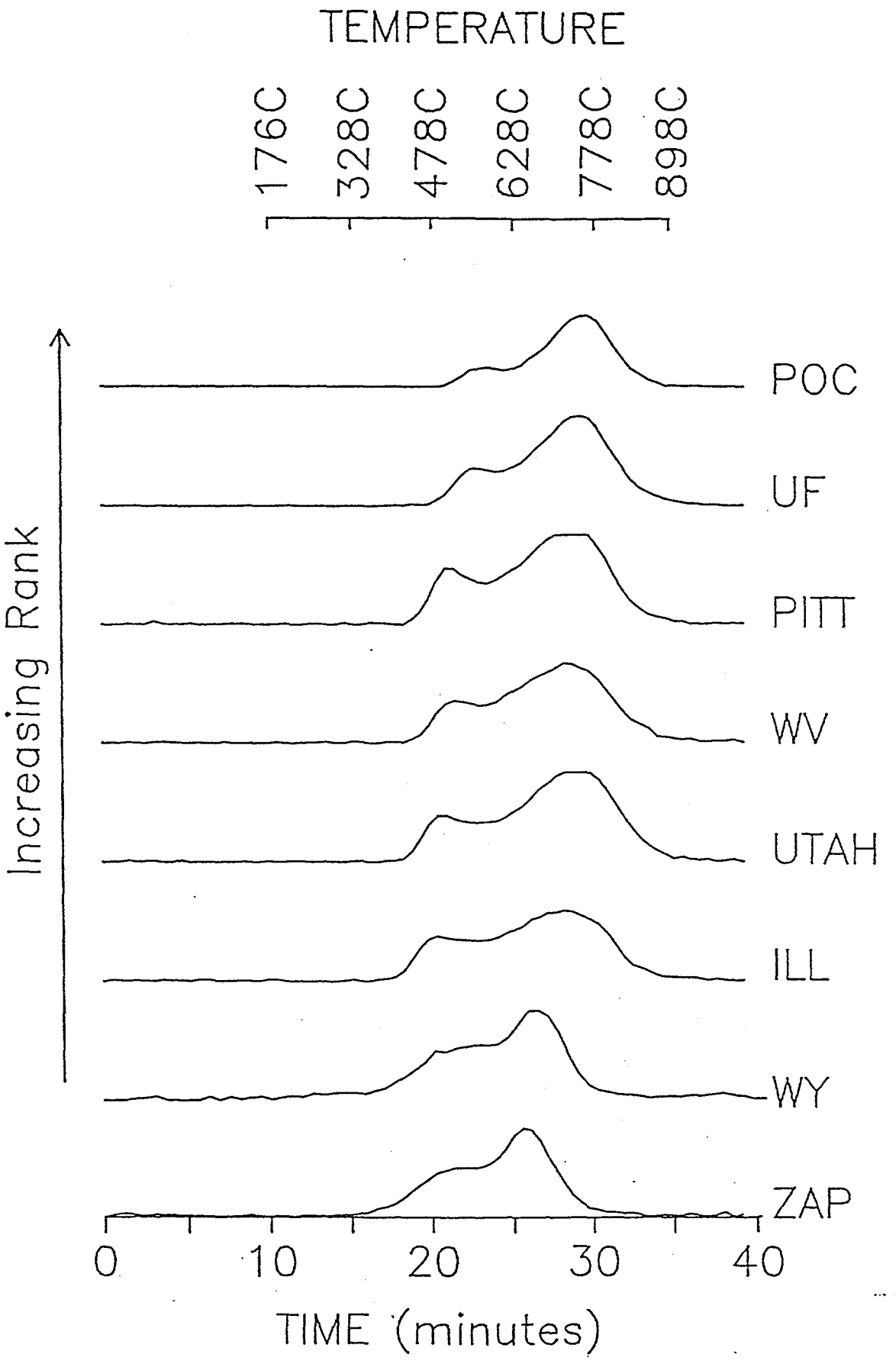

Figure II.A.5-14. NH_3 Evolution Curves from Pyrolysis of the Argonne Coals.

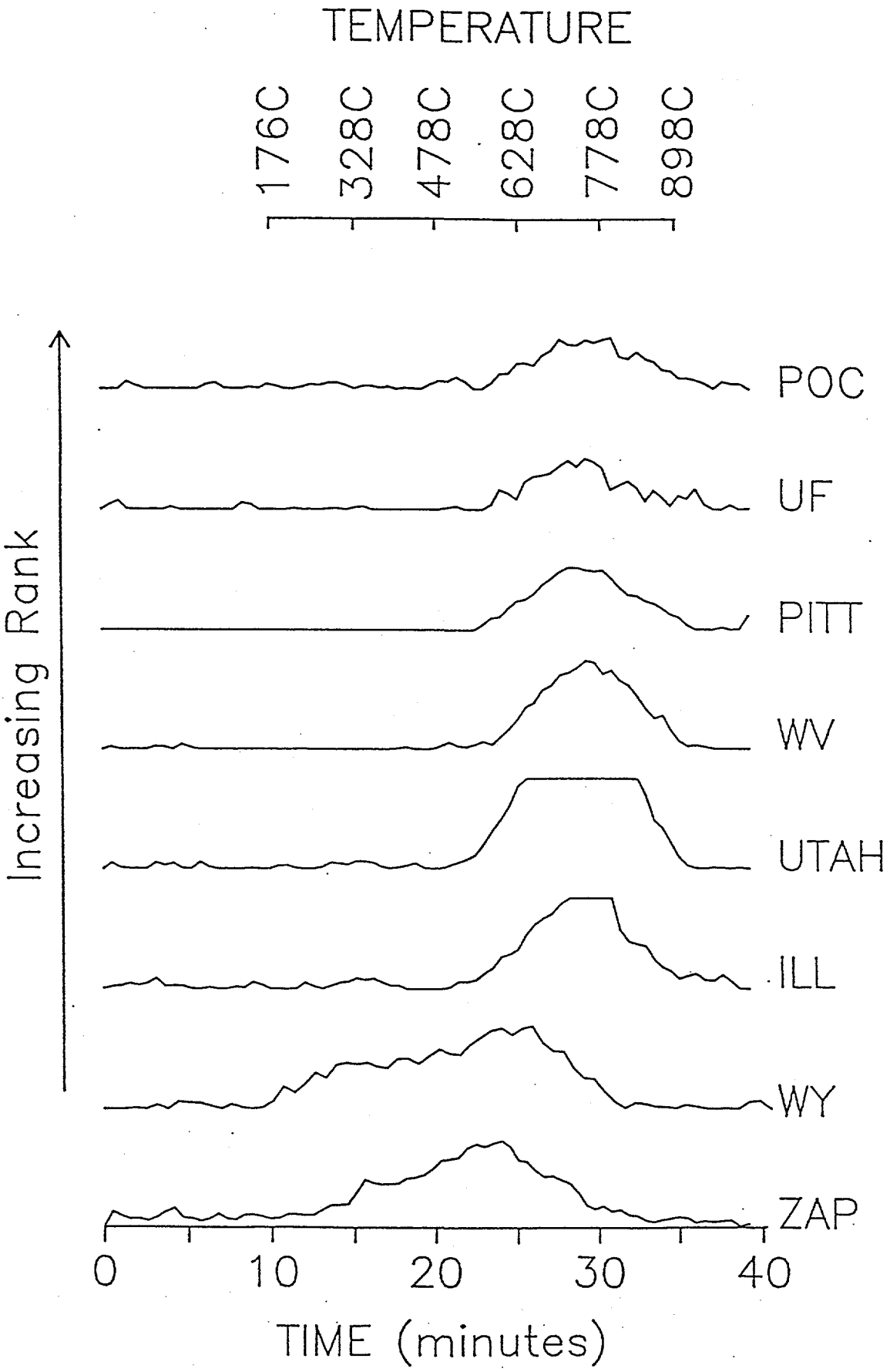

Figure II.A.5-15. HCN Evolution Curves from Pyrolysis of the Argonne Coals.

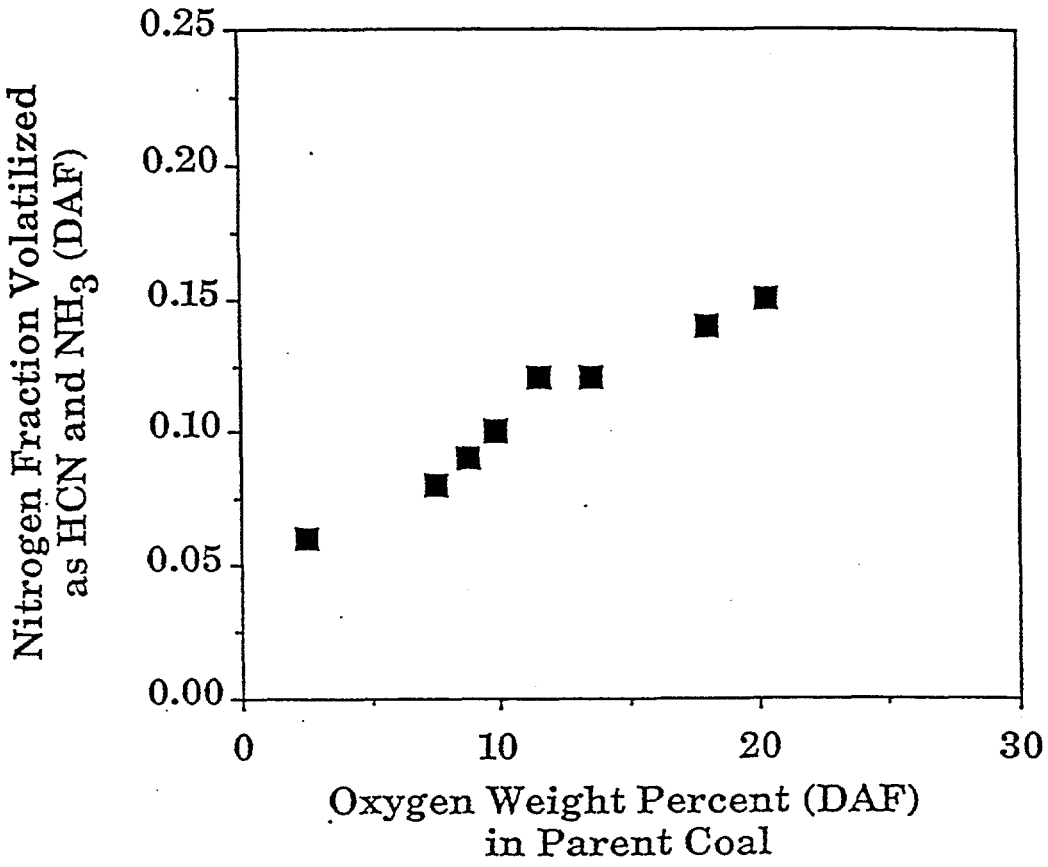

Figure II.A.5-16. Fraction of Nitrogen Evolved as NH_3 and HCN from the Argonne Coals During Pyrolysis in the TG-FTIR Plotted as a Function of Oxygen in the Parent Coal.

volatile nitrogen fractions inclusive of tar nitrogen for the two systems. The volatile nitrogen fraction data for the TG-FTIR is incomplete as only the Illinois #6 and Pittsburgh #6 coal tars were collected and subjected to nitrogen determination. Furthermore the tar nitrogen contribution in the TG-FTIR is overpredicted as the TG-FTIR apparatus includes paraffins and olefins in the tar amount. For the Pittsburgh #8 coal, the total amount of nitrogen evolved during pyrolysis in both experiments is similar. The ratio of HCN to NH_3, however, differs significantly. The dominant product during slow heating rate pyrolysis in the TG-FTIR is NH_3 while the only product during rapid pyrolysis in the EFR is HCN. Possible explanations for these results are as follows: 1) A secondary reaction process leads to the formation of NH_3 at the expense of HCN at low pyrolysis heating rates; 2) In the entrained flow reactor, secondary pyrolysis reactions, especially tar cracking, lead to the formation of HCN and the destruction of NH_3; 3) NH_3 is removed in the collection system of the entrained flow reactor (e.g., dissolution into water which condenses on the walls of the gas collection apparatus). Explanation #3 does not account for the order of magnitude difference in HCN weight percent in the two systems.

To test hypothesis #2, an experiment was preformed to increase the tar cracking in a slow heating rate pyrolysis run. Utah Blind Canyon coal was pyrolyzed in the TG-FTIR and the pyrolysis products were passed through a hot quartz tube heated to approximately 900°C just prior the gas analysis cell. This post pyrolysis method utilizes the same apparatus as the post oxidization method; however, helium is added to the sample stream rather than oxygen. The post pyrolysis results are presented in Figure II.A.5-17. Figure II.A.5-17a displays the HCN evolution curves while Figure II.A.5-17b shows the NH_3 evolution curves. In the post pyrolysis experiment, the HCN evolution peak at the 20 minute mark indicates an increase in tar cracking which resulted in a 0.04 weight percent increase in HCN. Although this is consistent with hypothesis #2, the 0.04 weight percent increase in HCN is not enough to account for the order of magnitude difference in the two systems. Furthermore post-pyrolysis did not show significant reductions in NH_3 evolution. These results suggest that hypothesis #1 is the most likely explanation.

Nitrogen Modeling

What makes the nitrogen evolution difficult to model is the heating rate dependency discussed above. In the literature, most of the investigations of the coal nitrogen conversion to nitrogenous gases were conducted in the combustion conditions, which normally feature high heating rates, short coal particle residence time, and high temperature. Although the presence of oxygen produces NO and could alter the conversion pathways, a brief look at these results is worthwhile. In general, coal devolatilization produces more HCN than NH_3 for bituminous coals, while more NH_3 evolves in subbituminous coals and lignites (Chen, et al., 1982). In the cases where the time evolution profile were provided (Baumann, and Moller, 1991 and Usman Ghani and Wendt, 1990), it is observed that for coals of all ranks HCN evolves before the NH_3 gas evolution. Based on this observation, several investigators (Baumann, and Moller, 1991; Usman Ghani and Wendt, 1990; and Bose et al., 1988) suggested that NH_3 is produced in a secondary reaction involving the HCN gas, but it is not clear whether this reaction is in the gas or solid phase. Also, the source of the needed hydrogen atoms is unknown.

Baumann and Moller (1991) studied the coal nitrogen evolution during pyrolysis under fluidized bed combustor conditions for coals of a wide range of ranks. They discovered that HCN starts to evolve at lower temperature than does NH_3 for all the coals. With addition of small amount of oxygen, the NH_3 amount is reduced, because, as they explained, the hydrogen that was available for hydrogenation of HCN to form NH_3 is consumed by the formation of H_2O.

The importance of hydrogen in the conversion of the coal nitrogen to nitrogen gases was demonstrated by the studies of Mackie et. al., (1990 and 1991) which shows that the decomposition products of aromatic compounds containing nitrogen in heterocyclic structures do not include NH_3 at all. The model compounds differ from the coals in that they are pure aromatic and do not contain any aliphatic structure which has a large potential to donate hydrogen. The absence of NH_3 from the pyrolysis products of these compounds could thus be explained by the lack of donatable hydrogen atoms.

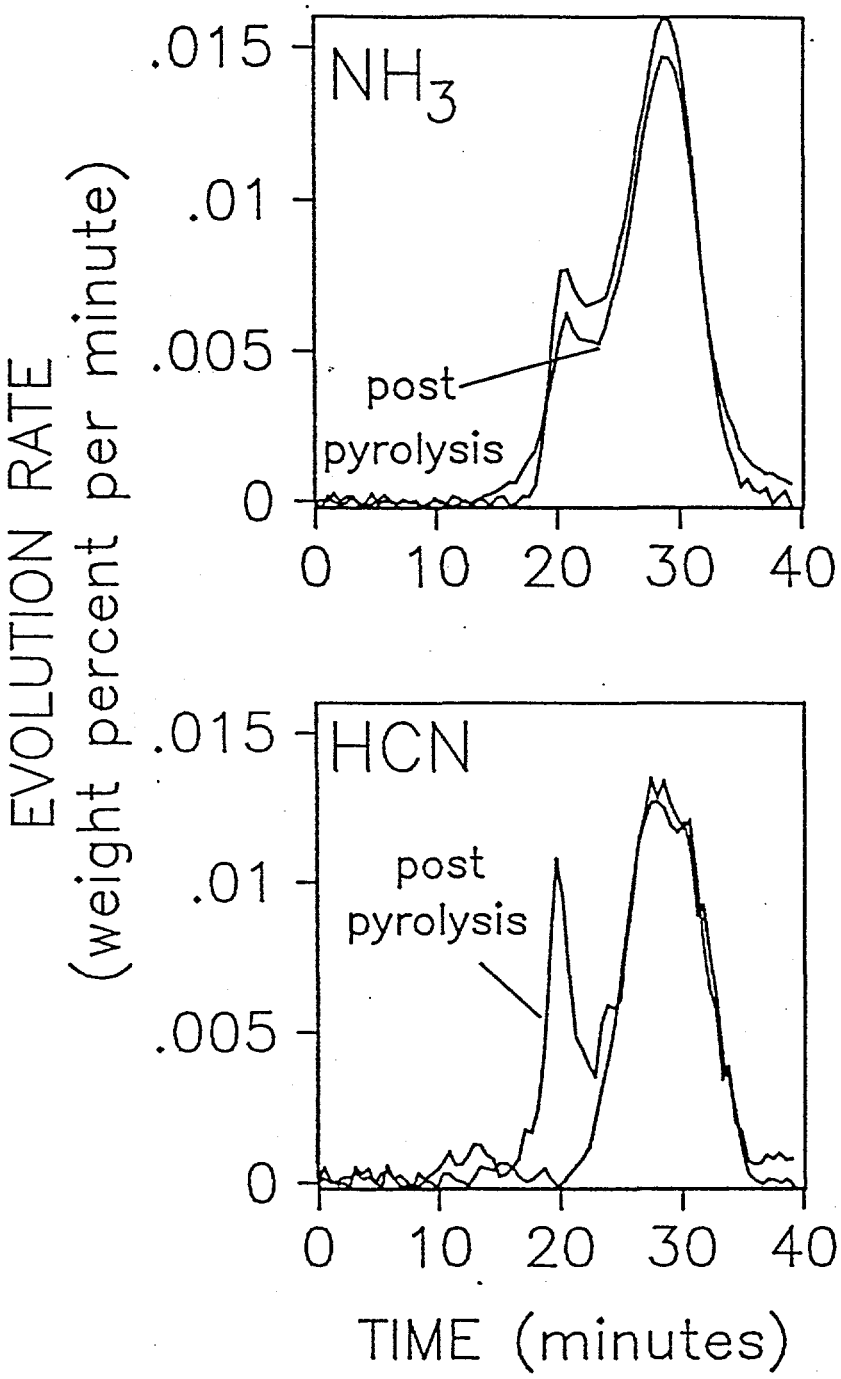

Figure II.A.5-17. NH_3 and HCN Evolution Curves from Pyrolysis and Post Pyrolysis of Utah Blind Canyon.

Although the existence of the secondary reaction that produces NH_3 from HCN seems apparent, the details of the reaction path have not been identified. In principle, this reaction could occur either in the gas or solid phase. If the HCN reacts with H_2 in the gas phase, the reaction kinetics ought to be coal rank independent and the gas phase reaction will only proceed with high enough rate when the reactants are sufficiently concentrated. In a study of modeling the nitrogenous gas productions during the fuel-rich combustion, Bose, et. al., (1988) found that the homogeneous gas reaction mechanism failed because the reaction kinetics seems to be coal rank dependent. Considering these arguments, the reaction of HCN with coal hydrogen is more probable.

One of the reasons for the heating rate dependence of the coal nitrogen evolution exhibited in our experimental results could be that the HCN to NH_3 conversion is depended on the length of the contact time between the evolving HCN gas and the coal or char solid. The pyrolysis gas leaves the coal particle more slowly at low heating rate than at high heating rate, allowing enough time for the HCN and coal or char hydrogen to react. The other limiting factor is the availability of the donatable coal hydrogen since hydrogen is needed to convert HCN to NH_3. As the tar cracking at high temperatures consumes more hydrogen, the completeness of this conversion could be reduced due to the deficit of hydrogen at this condition. FG-DVC needs to be further refined in the direction of hydrogen evolution and tar cracking before we can describe the effect of the hydrogen availability on the nitrogen evolution.

Three possible mechanisms for HCN and NH_3 formation are plotted in Figure II.A.5-18. Based on the above discussion we have chosen mechanism b. HCN evolves directly from its pool precursors. NH_3 gas comes from two sources: the direct evolution from coal nitrogen (pools) and the secondary conversion from evolved gaseous HCN to NH_3. The former contributes only a small amount, while the later is the major reaction pathway. The conversion is assumed via the reaction of the gaseous HCN with the coal hydrogen in the pore structure of coals. The completeness of this reaction is obviously dependant upon the HCN to NH_3 conversion rate, the gas residence time in the pore structure, the coal reaction residence time in reactors, and the coal devolatilization rate. For a constant conversion rate, the longer the gas residence time in the pore, the higher the conversion fraction. This residence time is highly dependent on the pyrolysis or combustion conditions. A high coal devolatilization rate sweeps the gas out of the coal particle very quickly, leading to a very short gas residence time in coal. In general, a longer gas-coal contact time could be expected in fluidized-bed and fixed-bed conditions than in a drop tube or an entrained flow reactor, since in a fluidized-bed the gas continuously maintains contact with other coal particles after it leaves its parent coal particles. In other words, more conversion could occur in the former conditions than in the later.

Since nitrogen evolves at higher temperatures than other gases, the gas residence time depends on the char structure instead of the coal structure. The precise determination of the gas residence time is difficult as the char structure is a complicated function of the pyrolysis process. It can be more complicated if bed conditions can affect the gas conversion reactions.

This model uses a simplified single cell structure to estimate the gas residence time. Consider a spherical coal particle with an original radius r_0. The radius changes to r_2 in the pyrolysis due to the weight loss and swelling. The particle has a single inner bubble of radius r_1. During pyrolysis, the evolution gas flux in this particle is always positively outward. At a point inside this particle of distance r from the origin of the sphere, the residence time, Δt_n, of the evolution gas before leaving the particle is

$$\Delta t_n(r) = \Delta t_{n0} \ln \frac{r_2}{r} \qquad \text{(II.A.5-1)}$$

and

$$\Delta t_{n0} = \frac{3P^* \phi_v}{\rho n_{tot} RT} \qquad \text{(II.A.5-2)}$$

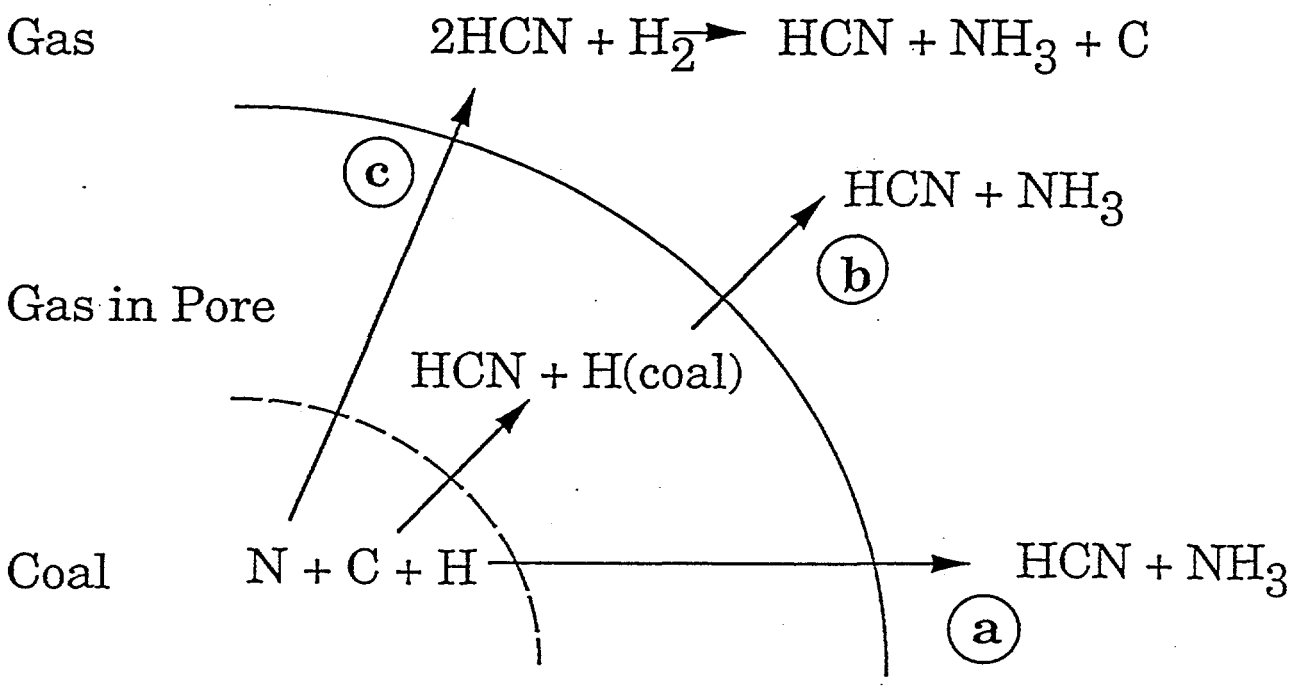

Figure II.A.5-18. Three Possible Mechanisms of HCN and NH_3 Evolution.

where P* is the gas pressure in the coal pores, n_{tot} is the total gas evolution rate per unit weight coal, R is the gas constant, T is the temperature, ρ is the coal solid density, and ϕ_v is the volume swelling ratio that can be calculated by a swelling model (Users Guide, 1992). The HCN gas that is generated within the shell $4\pi r^2 dr$ has a time period of Δt_n to react to NH_3. The modified HCN evolution rate is then

$$\frac{dW^*_{HCN}(gas)}{dt}\Big|_r = \frac{dW_{HCN}(gas)}{dt} e^{(-k_n \Delta t_{n0} \ln(\frac{r_2}{r}))} \qquad \text{(II.A.5-3)}$$

where k_n is the reaction constant of HCN to NH_3 conversion, and $dW_{HCN}(gas)/dt$ is the HCN evolution rate given by FG-DVC gas evolution equation

$$\frac{dW_{HCN}(gas)}{dt} = k_{HCN} W_{HCN}(char) \qquad \text{(II.A.5-4)}$$

Averaging over the whole particle leads to

$$\frac{dW^*_{HCN}(gas)}{dt} = f_n \frac{dW_{HCN}(gas)}{dt} \qquad \text{(II.A.5-5)}$$

where

$$f_n = (1 - f_{n0}) \frac{1 - e^{(-k_n \Delta t_{n0} \ln(\frac{r_2}{r_1}))} (r_1/r_2)^3}{(1 - (r_1/r_2)^3)(1 + k_n \Delta t_{n0}/3)} + f_{n0} \qquad \text{(II.A.5-6)}$$

where f_{n0} is a non-zero residue fraction of HCN rate. $(1-f_n)$ is the HCN to NH_3 conversion factor. And

$$\frac{dW^*_{NH_3}(gas)}{dt} = \frac{M_{NH_3}}{M_{HCN}} (1 - f_n) \frac{dW_{HCN}(gas)}{dt} \qquad \text{(II.A.5-7)}$$

where M_{HCN} and M_{NH_3} are the molecular weights of HCN and NH_3, respectively.

To extend this single cell structure model to the generally heterogeneous coal/char structure, the residue HCN rate fraction, f_{n0}, the coal volume swelling ratio, ϕ_v, and coal particle-bubble radius ratio, r_1/r_2, are the model parameters.

A non zero f_{n0} is employed to retain a small fraction of HCN after the most of it has been converted to NH_3, even at very low heating rate. f_{n0} is affected by the char particle size and the char structure, which in turn are affected by the heating rate. f_{n0} is also a function of reaction bed conditions that could alter Δt_n evaluated above by affecting the length of the evolution gas/particle contact time. The model suggested f_{n0} value is 0.1. It is only important for low heating rate, while for very high heating rate cases in which the conversion has no time to complete, f_{n0} is not important.

Although the char volume swelling ratio, ϕ_v, and the ratio of the inner bubble size to the char particle size, r_1/r_2, can be calculated directly from the swelling model, (Users Guide, 1992) we would rather treat them as model parameters, because the single cell swelling model (Users Guide, 1992) is too primitive to describe the heterogeneity of the char structure. For most of the combustion cases, swelling is not significant due to the very high heating rate and the presence of oxygen. Therefore, ϕ_v is set to 4 and r_1/r_2 to 0.8.

By fitting our experimental data of the pyrolysis nitrogen gas evolutions, the coal nitrogen gas evolution kinetics were obtained in the same way as for the C, H and O volatile species (Solomon, et al., 1988a; 1990a; and 1993), and are listed in Table II.A.5-3. Figure II.A.5-19 shows the experimental evolutions and model predictions of HCN and NH_3 for Stockton Seam coal: (a and b) at 30°C/min and (c and d) during high heating rate pyrolysis in an entrained flow reactor of furnace temperature 1100°C. As shown, our model maintains reasonable agreement consistently with nitrogen evolution data at both low and high heating rates. The time evolution curves of HCN and NH_3 in the entrained flow reactor are not available due to the extremely high heating rate. The comparison is then made on the ultimate yields of these two gases in this case. As mention above in the Results Section, the experimental NH_3 value in the EFR may be too low because NH_3 is being removed from the system prior to the gas analysis.

Recently Nelson, et al. (1992) published their experimental results on the splitting of coal nitrogen into HCN and NH3 in a fluidized bed condition. The yields of these two nitrogen gases have very interesting temperature dependence. Our model was used to model the nitrogen evolution under the conditions given by Nelson, et al. The model prediction compares reasonably well with the data (Nelson et al., 1992), as displayed in Figure II.A.5-20. The basic trends of the gas yields are correctly predicted and, most importantly, the predicted transition temperature at which the yield of NH_3 starts to decline is in good agreement of the data (Nelson, et al., 1992).

Summary and Conclusions

The total SO_2 evolution from the Argonne Premium Coals during pyrolysis measured by post oxidation of volatile products demonstrated two main peaks and one small high temperature peak. These overall evolution peaks are composed of several component peaks that are formed by the different forms of sulfur existing in coals. By applying the FG-DVC model and literatures data and suggested mechanisms, these peaks were resolved and the evolution sequences of coal sulfur of all forms were identified. The experimental data coupled with the FG-DVC model offered the following conclusions: the first SO_2 peak was from aliphatic sulfur and possibly pyrite in Wyodak and Illinois #6 coals. The second peak was primarily pyrite and the third peak was aromatic sulfur and small amounts of pyrite. The evolution kinetics of coal sulfur of all forms were obtained and incorporated in FG-DVC.

NH_3 evolutions exhibited two main evolution peaks whose T_{max}'s showed rank dependence. HCN evolution curves coincided with the high temperature NH_3 evolution curves except in the cases of Wyodak coal and Zap lignite. At low heating rates, NH_3 is the dominant product while during rapid heating rate pyrolysis HCN was the only product. The main pathway to NH_3 formation is believed to be from the secondary reaction of gaseous HCN with coal hydrogen in the pores of coal. A model was developed that describes the direct evolution of HCN and the secondary reaction to form NH_3. The effects of heating rate and the char structure on the relative abundance of pyrolysis HCN and NH_3 gases were considered. This model provides consistent agreement between the prediction and experiment data on the HCN and NH_3 evolutions at both low and high heating rates.

II.A.6. Optical Properties of Char

Emissivities

In gasification, the determination of spectral emittance is important for two reasons. First, knowledge of the spectral emittance is necessary for the measurement of particle temperatures. Second, the spectral emittance or the emissivity (the average emittance over wavelength) must be known to

Table II.A.5-3. Pyrolysis Evolution Kinetics of Nitrogen Gases. The Frequency Factors Are 5.0×10^{12} (1/seconds) for All the Pools. AE-- Activation Energy in Kelven. Sigma is in Kelven.

	ZAP	WY	ILL	UTAH	WV	PITT	UF	POC
HCN-L								
AE	24000	25000	26000	26000	26000	26000	26000	26000
Sigma	3000	3000	3000	3000	3000	3000	3000	3000
HCN-T								
AE	31000	32000	34000	36000	34000	34000	35000	35000
Sigma	2500	2000	3000	3000	2500	2500	2500	2200
NH_3-L								
AE	25000	26000	26000	26500	26500	27000	27300	27700
Sigma	1500	1500	1500	1500	1500	1200	1500	1500
HCN to NH_3 conv.								
AE	15000	15000	15000	15000	15000	15000	15000	15000
Sigma	3000	3000	3000	3000	3000	3000	3000	3000

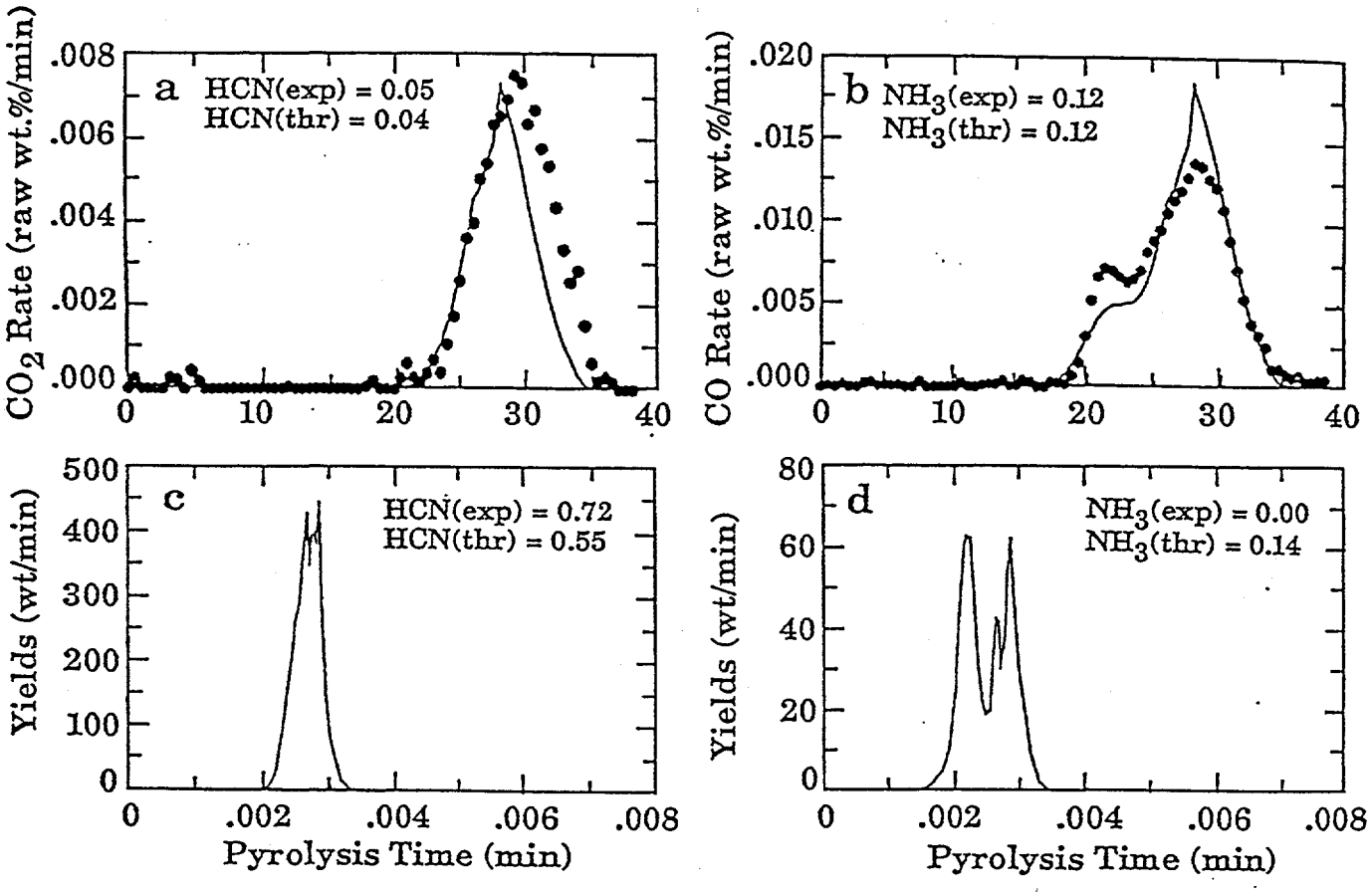

Figure II.A.5-19. a) and b) HCN and NH_3 Evolution Curves at 30°C/min, the Experimental Data (symbols) and the Fitted curves by FG-DVC. c) and d) Comparison of the 1100°C Entrained Flow Reactor Experimental Data and the FG-DVC Model Predictions.

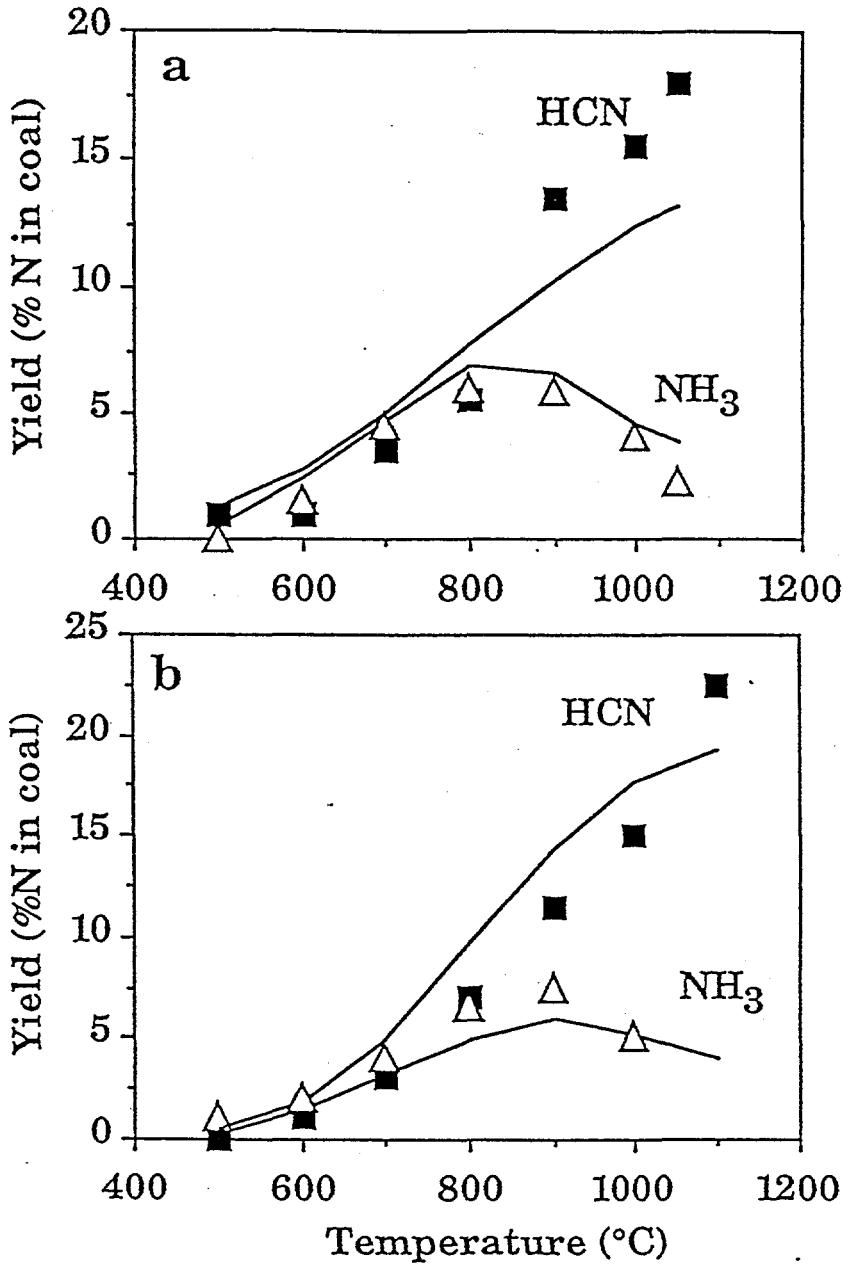

Figure II.A.5-20. Comparison of Model Predictions and Experimental Data (Nelson et al., 1992) for two Australian Coals: a) Yallourn and b) Blair. Lines-Prediction; Symbols-Data.

calculate the rate of particle heat up, and the power radiated by the particle during combustion.

We have recently developed a new method for on-line, in-situ monitoring of particle streams to determine their spectral emittance, chemical composition, size, and temperature (Best, et al., 1986; Solomon, et al., 1985a; Best, et al., 1984; Solomon, et al., 1986a; 1986b; 1986c; and 1987a). The technique uses a Fourier Transform Infrared (FT-IR) spectrometer to perform both emission and transmission (E/T) spectroscopy for a stream of gas suspended particles.

The technique has been applied to measure spectral emittance of coal. Measurements on a variety of samples show that coal of pulverized particle size is not gray, having values of emittance near 0.9 for some regions of the spectrum, but values substantially less than 0.9 in many regions. The spectral emittance is dependent on rank, particle size, and the extent of pyrolysis, approaching a gray-body for chars, anthracite, and large particles. Recent measurements (Solomon, et al., 1987a) show that pulverized coal particles of the size used in entrained gasification undergo a transition from highly non-gray coal to highly gray char ($\epsilon \approx 0.9$), and finally to moderately gray char ($\epsilon = 0.7$ to 0.8). An example of the non-gray to gary transition is illustrated in Fig. II.A.6-1 which shows the radiance per unit surface area from char particles. Here a gray-body with $\epsilon = 0.9$ would emit at the theoretical lines marked BB (883), etc. The char is least gray at low temperatures, but increase in grayness as the temperatures (and exposure time) increases.

To provide understanding of this process and to develop a predictive theory for the emissivity as a function of particle size, rank and extent of pyrolysis, a theoretical analysis has been performed of emissivity during the coal to char transformation. Emissivities were calculated using the frequency dependent complex index of refraction, $m_\nu = n_\nu - ik_\nu$, from the standard equations of electromagnetic theory. For spherical particles these calculations can be performed using Mie theory (Bohren and Huffman, 1983).

The property of coal which determines its non-gray behavior and its variations with rank is primarily the imaginary part of the index of refraction, k_ν. As discussed in (Solomon, et al., 1986b; 1986d; and Solomon, 1987a), n_ν and k_ν can be determined from the infrared spectra of coal and chars prepared in both KBr and CsI pellets. In Fig. II.A.6-2 are KBr pellet spectra recorded for chars of a Zap North Dakota lignite in differing states of pyrolysis, formed in the heated tube reactor (Best, et al., 1986) at an asymptotic tube temperature of 800°C. The 1200 to 1600 cm^{-1} region is one in which scattering is small in the pellet spectra, so the absorption coefficient can be accurately determined from these data. At higher frequencies (wavenumbers) the determination is less accurate when only KBr pellet spectra are employed, and in this case only provide rough estimates of k.

In Fig. II.A.6-3 we have plotted (open circles) an average value of k in the 1200 to 1600 cm^{-1} region measured from the char spectra (Fig. II.A.6-2), as a function of distance, D, traveled in the tube reactor. Here, the extent of pyrolysis increases monotonically with increase in D. Also plotted is the value for k at 2000 wavenumbers (closed circle in Fig. II.A.6-3a) and k at the absorbance minimum near 1500 cm^{-1} (squares).

Taking a constant value of 1.6 for the real part of the index of refraction, n, we have used the Mie theory program (Bohren and Huffman, 1983) to calculate the emittance of particles of different size, and different k values (Fig. II.A.6-3b).

Using Figs. II.A.6-3a and II.A.6-3b it can be seen that for all states of pyrolysis, the value of k determined for the chars in the region between 1200 and 1600 cm^{-1} are such that the value of the emittance, ϵ_ν, is constant and is within 10% of 1.05 for particle diameter, d, greater than 20 μm. The actual value depends slightly on particle size, but is practically independent of pyrolysis state. This is the region which has been used for temperature measurements.

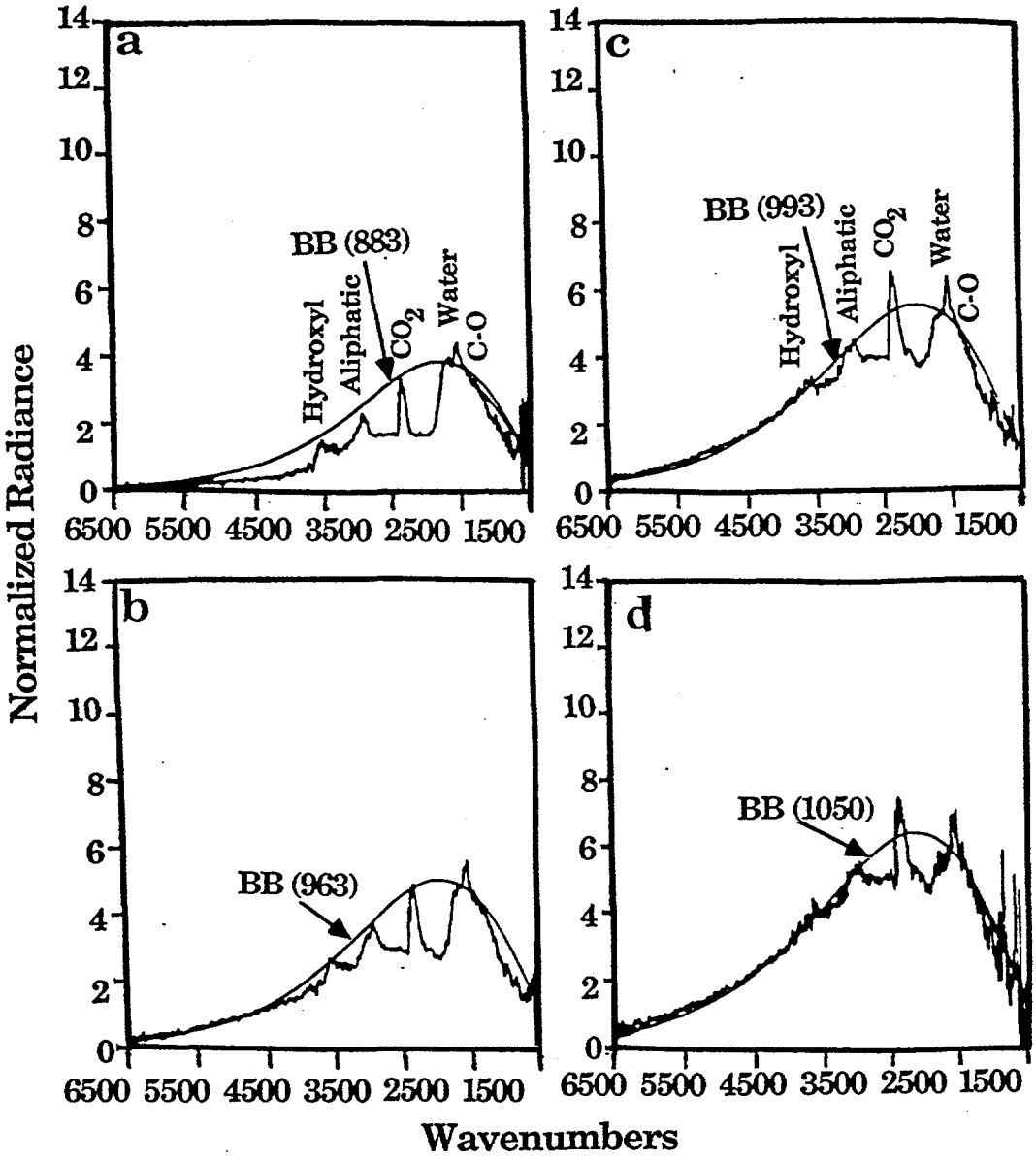

Figure II.A.6-1. Comparison of Normalized Radiance with Theoretical Grey-body Curves ($\varepsilon = 0.9$) for Chars at Increasing Extents of Pyrolysis (200x325 mesh).

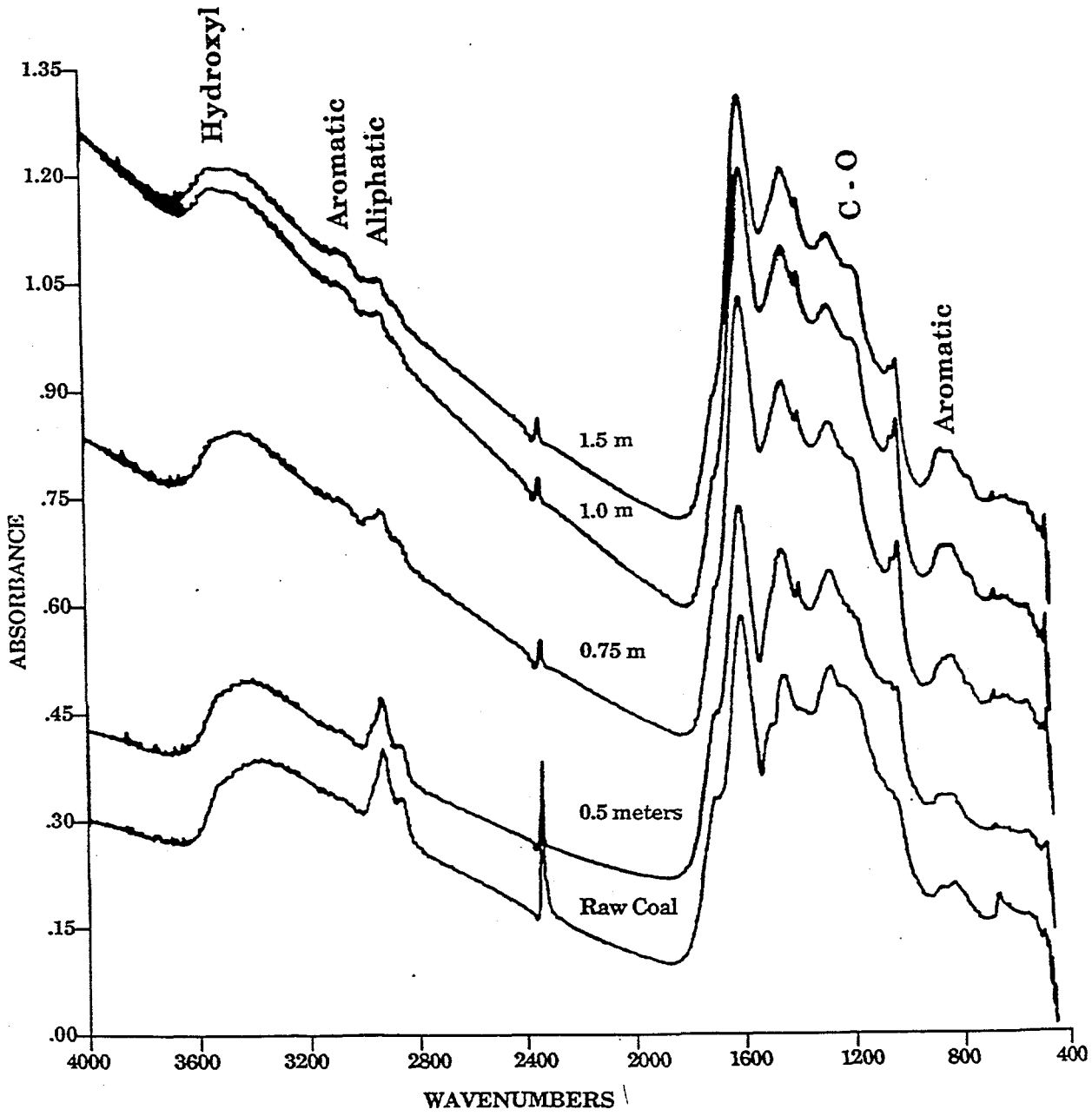

Figure II.A.6-2. Absorbance Spectra of Coal and Char in KBr-Pellets, as a Function of Distance in the Furnace at 800°C.

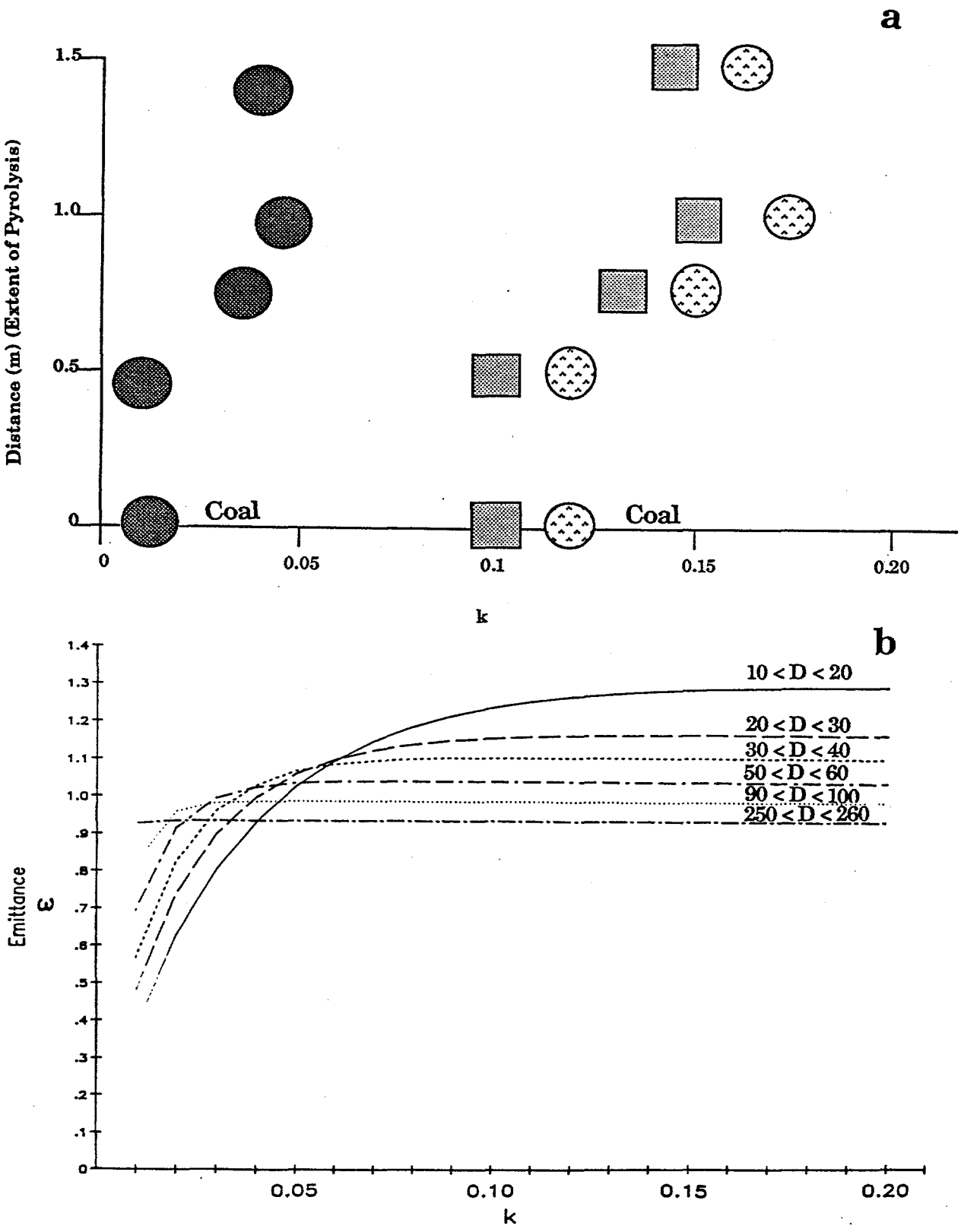

Figure II.A.6-3. a) Average Value of k in the 1200 to 1600 cm^{-1} Region Measured from the Char Spectra of Figure II.A.6-2 , as a Function of Distanced Traveled in the Tube Reactor (open circles): Value of k at the Absorbance Minimum Between 1200 and 1600 cm^{-1} (squares): k for the Raw Lignite at 2000 cm^{-1} (closed circles): b) Calculated Emittance as a Function of k, for Spheres of Various Diameters, with n = 1.6.

At 2000 cm^{-1} the values of ϵ_ν for coals are particle size dependent and significantly less than unity for small particle sizes. As can be seen in Fig. II.A.6-3b, an increase in k with extent of pyrolysis will affect ϵ_ν at 2000 cm^{-1}. The estimated values of k at 2000 cm^{-1} for the chars of Fig. II.A.6-2 suggest that ϵ_ν for a 50 micron particle increases from 0.6 to 0.7 to a value of 1.0 during pyrolysis. This is in reasonable agreement with the observed emittance in Fig. II.A.6-1 which are for comparable conditions to those for which the chars were obtained.

There is a stage in pyrolysis beyond which ϵ_ν in the 1200 to 1600 cm^{-1} regions starts to vary. This occurs when the coal starts to graphitize and both the real and imaginary parts of the complex index of refraction ($m_\nu = n_\nu + ik_\nu$) start to increase. In Fig. II.A.6-4 we display contour plots of emittance in the n-k plane for 55 μm diameter spheres. That part of the figure which contains the n and k values appropriate to coals in the infrared region of the spectrum is cross-hatched, on the left hand side of the figure. The region for graphite is cross-hatched on the upper right hand side of the figure. During pyrolysis, the emittance in the 1200 to 1600 cm^{-1} region (where $k \approx 0.1$) drops from a value greater than 1, towards the value for graphite. In other regions of the spectrum where k = 0.01, ϵ_ν first increases and then decreases as k increase i. Our experimental observations suggest that for residence time on the order of 1 sec, n and k increase significantly only above 1000°C, and it is above this temperature that ϵ_ν is observed to decrease. For a highly graphitized char ϵ_ν can be as low as 0.7.

Besides the calculation of the emissivity, the Mie theory program can be used to calculate the total extinction cross section F^t_ν. F^t_ν determines the shape of the transmittance, τ_ν where N, A, and L are the particle number density, particle area, and path length through the particle stream, respectively.

$$\tau_\nu = \exp(-NA\, F^t_\nu L) \qquad \text{(II.A.6-1)}$$

Some calculations of F^t_ν are presented in Fig. II.A.6-5. In Fig. II.A.6-5a we show calculations of F^t_ν for a Nicolet 7199 FT-IR, using the optical constants we have derived for a Montana subbituminous coal (Solomon, et al., 1986d). The Nicolet 7199 FT-IR spectrometer, with a 4" diameter, 9.5" focal length collection mirror, has a semi-cone acceptance angle of 12° which was used for the calculations in Fig. II.A.6-5a. It can be seen that F^t_ν is a smooth function of wavenumber, even though k changes substantially across the spectrum. For swelling coals, F^t_ν must be measured at each temperature because it varies with particle size. Indeed, the shape of the F^t_ν spectrum has been made the basis for the method of particle size determination (Solomon, et al., 1987a). The shape of F^t_ν can, however, be determined from measurement with the use of the above equation. For particles above 40 μm diameter, F^t_ν at 6500 cm^{-1} is relatively insensitive to size, being equal to 1.1 ± 0.10. The temperature measurement can therefore be made on swelling coals as well. The sensitivity of the spectral shape of F^t_ν to particle size distribution makes the measured F^t_ν spectral useful monitors of the size distribution. Particle break-up, or swelling can be easily detected.

Variations of Emittance with Coal Reactivity and Particle Size

Recent measurements (Solomon, et al., 1987a; 1987b) show that pulverized coal particles of the size used in entrained gasification are on-gray with emissivities which depend on size and rank. Also coal undergoes a transition from highly non-gray moderately pyrolyzed coal to highly gray char. Here we present measurements on non-pyrolyzing, warm coal particles of different rank and particle sizes.

The coal particles were entrained in He through the HTR for a distance of 90 cm at a nominal tube temperature of 350°C. A radial temperature profile of the gas stream taken with a 0.005" thermocouple where it passes through the FT-IR beam focus is shown in Fig. II.A.6-6. The average of this profile across the distance of the stream diameter is 568 K.

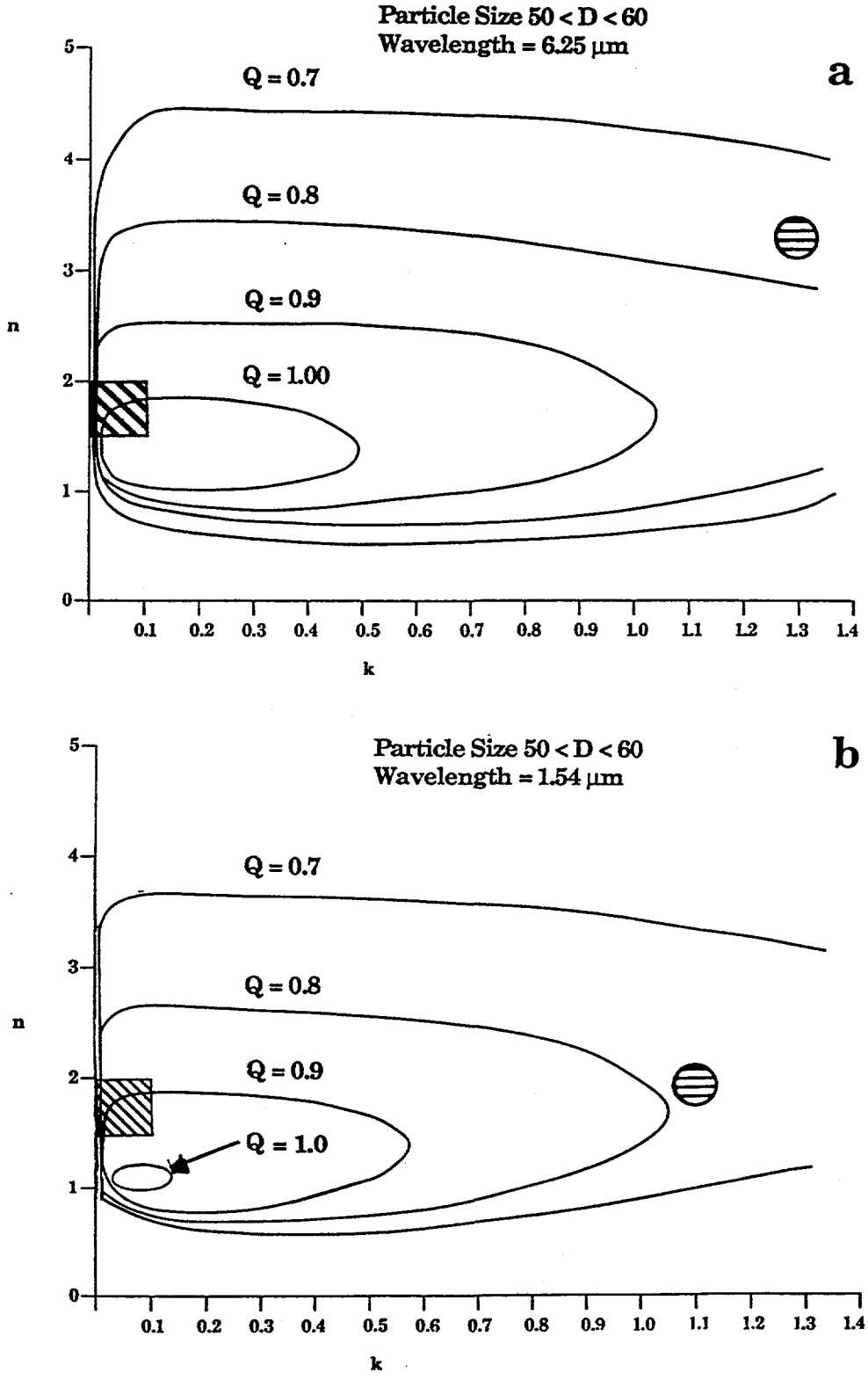

Figure II.A.6-4. Contour Plots of Constant Emittance, Q, Calculated by Mie Theory for Spheres of Various Values of n and k, for 55 μm Diameter Particles. The Combinations of n and k found for Coal in the Infrared are Shown Shaded on the Left Hand Side of the Diagram: Those for Graphite are Shaded on the Right (the values for graphite are taken from Foster and Howarth, 1968). The Calculations are for Radiation of two Wavelengths, as Shown.

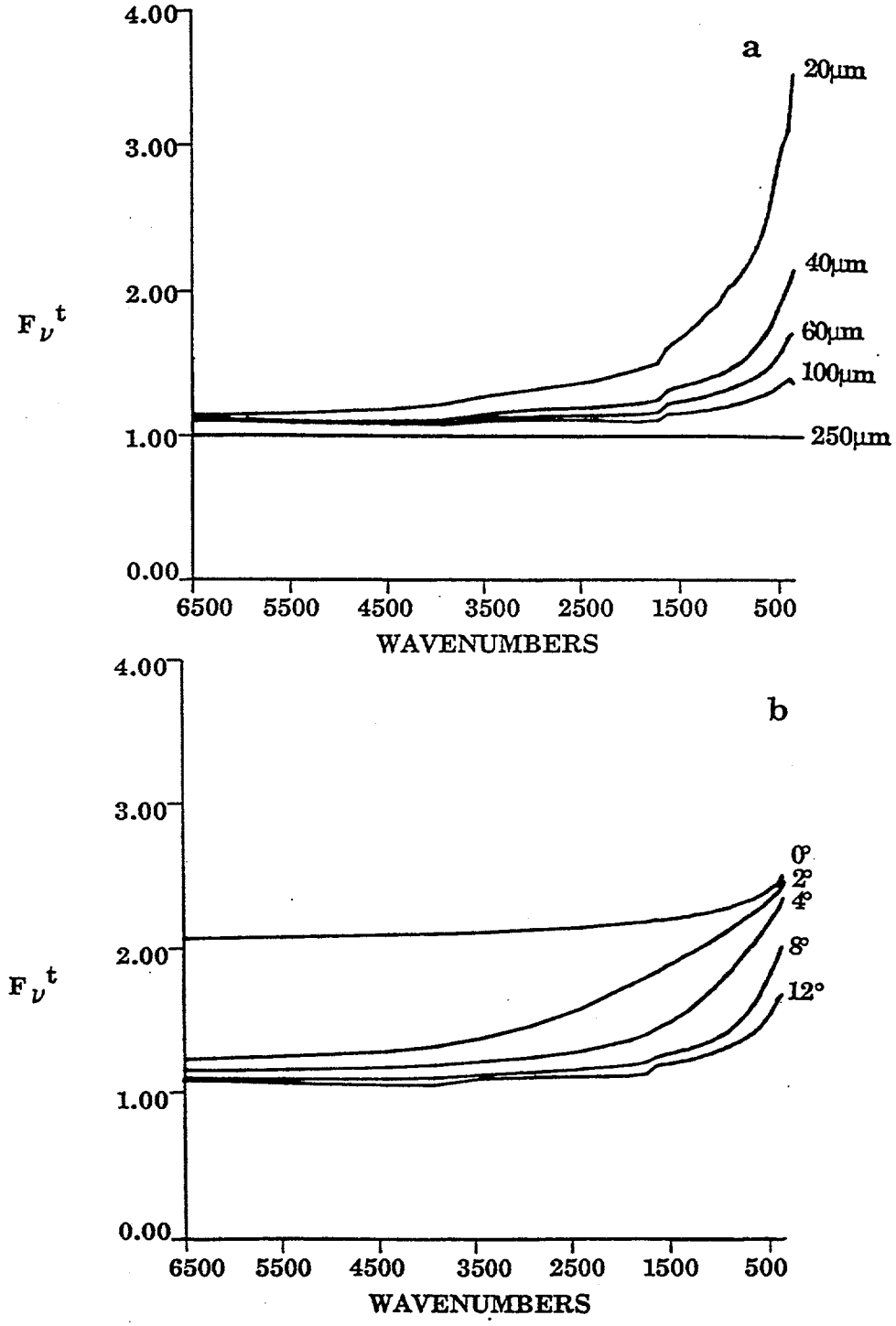

Figure II.A.6-5. a) Calculations of $F_\nu{}^t$ Spectra for our Instrument, for Particles of Various Diameters, and Having the Wavelength Dependent Optical Properties of a Montana Rosebud Subbituminous Coal (2). The Calculation for the 250 μm Diameter Particle was done with Raleigh Large Particle Theory. b) Calculations of $F_\nu{}^t$ Spectra for Instruments of Differing Half-Acceptance Angles, for Particles of Mean Diameter 60 μm.

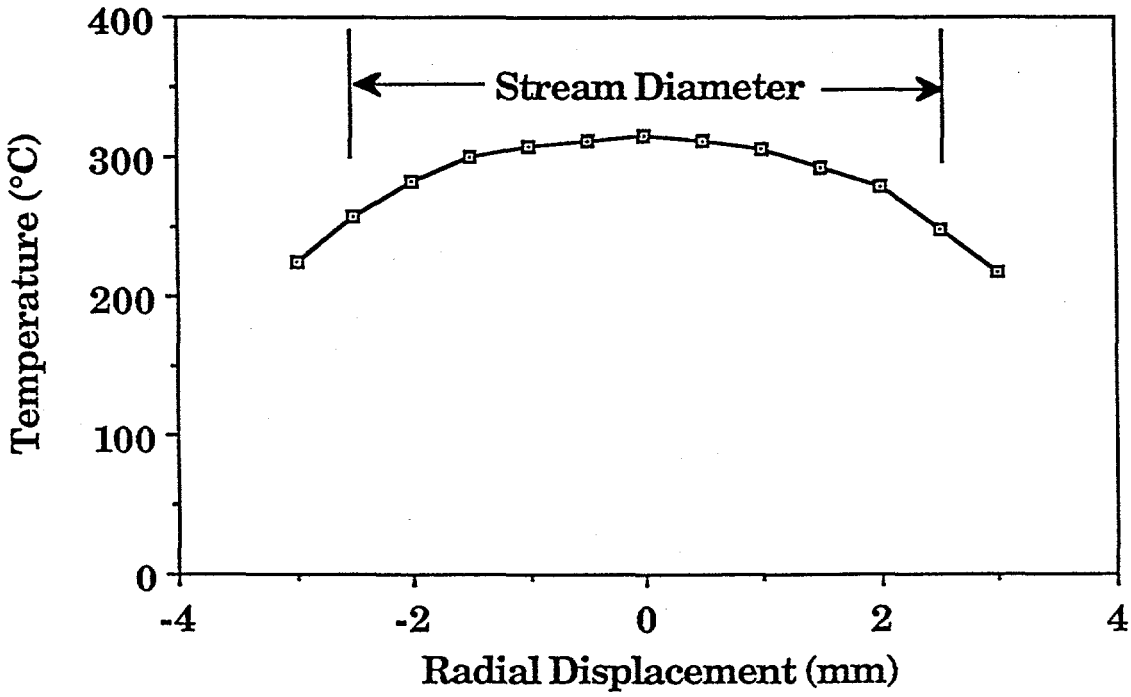

Figure II.A.6-6. Radial Thermocouple Temperature of Gas Stream Exiting the HTR at FT-IR Focus (.005" bead). Nominal HTR Temperature = 350°C. Radial Average = 295°C (568K).

To determine the spectral emittance for coal at a known temperature, measurements are made of the transmittance, τ_v, and the radiance, R_v, from which the normalized radiance $R^n_v = R_v / (1-\tau_v)$ is calculated.

For the geometry of the HTR, the sample consists of hot or warm particles surrounded by cold walls. The spectral emittance is then given by (Best, et al., 1986)

$$\epsilon_v = F^t_v R^n_v / R^b_v (T_p) \qquad \text{(II.A.6-2)}$$

where $R^b_v(T_p)$ is the theoretical blackbody radiance at the particle temperature, T_p, and F^t_v is the total extinction efficiency for the particles to scatter radiation our of the angular acceptance aperture of our instrument plus absorption. If T_p and F^t_v are known, then ϵ_v can be determined. Conversely, if ϵ_v and F^t_v are known, T_p can be determined.

Prior to each coal particle experiment presented here, a gas temperature determination was performed on a trace amount of CO_2 added to the particle stream to track fluctuations in the HTR nominal temperatures. The accuracy of this measurement is illustrated in Fig. II.A.6-7 which presents R_v, $1 - \tau_v$, and the normalized radiance for a mixture of carbon dioxide, butane, and acetylene passed through the HTR. For this non-scattering, gaseous sample, excellent agreement is observed between the thermocouple average temperature (568 K) and FT-IR line-of-sight determined average temperature 565 K). Figure II.A.6-8 indicates the sensitivity of this method to small shifts in temperature.

The coal samples used in this study (Table II.A.6-1) were obtained from the AFR/BYU sample bank (bulk samples) or from the Pittsburgh Energy Technology Center (PETC) of the Department of Energy. All samples having more then 3% moisture were dried before measurements were taken.

The transmittance spectra used to calculate the normalized radiance for the samples used in this study are presented in Figs. II.A.6-9 to II.A.6-12. The spectra are presented as $1 - \tau_v$ so that increased amplitude is proportional to increased attenuation.

The characteristics of large particles are that they scatter or absorb essentially all of the light incident on them. Any radiation hitting the particle which is not absorbed will be scattered. Consequently, the attenuation is proportional to the area of the particle and no absorption effects can be seen.

Figure II.A.6-9 to II.A.6-12 illustrate the effect of particle size on the shape of $1 - \tau_v$. As the particle size distribution is decreased, there is an increase in attenuation (sloping of the spectra) from short (6500 cm^{-1}) to long (500 cm^{-1}) wavelengths of incident radiation. This particle dependent change in the scattering (diffraction) component of F^t_v indicates that the longer wavelengths of light have a higher efficiency of scattering out of the angular acceptance aperture of our instrument than the shorter wavelengths of light. As the particles get smaller, the higher efficiency to scatter extends further towards the short wavelength end of the spectrum.

Below a particle size of 20 μm, a drop in attenuation is observed at the long wavelength end of the spectrum. This effect is caused by the particles being smaller than the wavelength of incident radiation (1000 to 500 cm^{-1} = 10 to 20 μm) and will allow this radiation to pass through without any scattering or absorption effects.

To see trends in emissivity with varying particle size and composition, $(1 - \tau_v)$ 6500 cm^{-1} was used for the percent attenuation in the following analysis. Figures II.A.6-13 to II.A.6-15 are the normalized radiance, $R^n_v(T) = R_v / (1- \tau_v)$ 6500 cm^{-1}, for three coals with different size distributions. Overlayed on the experimental data is the theoretical blackbody curve $R^b_v(T)$, corresponding to the temperature determined from the CO_2 tracer test, multiplied by a constant (ϵ_v / F^t_{6500}) to give the best

Table II.A.6-1.
SAMPLE DATA FOR OPTICAL PROPERTIES MEASUREMENTS

Coal Name	Rank	Particle Size Distribution (μm)	%C (DAF)	%Ash (Dry Basis)	%Moisture	Source
Pocahontas #3	LVB	75-45	91	4.83	0.61	AFR/BYU
Upper Freeport	MVB	75-45	87	11.63	0.83	AFR/BYU
Pittsburgh #8	HVAB	75-45	83	9.02	1.80	AFR/BYU
Upper Kanawha	MVB	75-45	81	26.44	2.60	AFR/BYU
Utah Blind Canyon	HVCB	75-45	79	4.68	4.71	AFR/BYU
Illinois #6	HCVB	75-45	77	23.42	2.94	AFR/BYU
Smith Roland	SUBC	250-210	72.97	9.23	24.51	PETC
Smith Roland	SUBC	106-75	73.26	12.27	20.97	PETC
Smith Roland	SUBC	63-45	72.38	18.29	13.26	PETC
Smith Roland	SUBC	30-20	73.67	12.87	9.96	PETC
Smith Roland	SUBC	20-10	73.24	14.03	9.10	PETC
Smith Roland	SUBC	-10	73.17	15.64	8.23	PETC
Lower Kittaning	LVB	106-75	88.65	19.31	0.62	PETC
Lower Kittaning	LVB	36-45	87.73	17.43	0.64	PETC
Lower Kittaning	LVB	30-20	90.53	9.17	0.83	PETC
Lower Kittaning	LVB	20-10	90.55	8.03	0.91	PETC
Lower Kittaning	LVB	-10	89.82	7.68	0.93	PETC
Beulah N.D.	Lignite	250-210	69.48	8.86	28.49	PETC
Beulah N.D.	Lignite	106-750	69.82	15.23	22.63	PETC
Beulah N.D.	Lignite	63-45	71.25	32.81	13.41	PETC

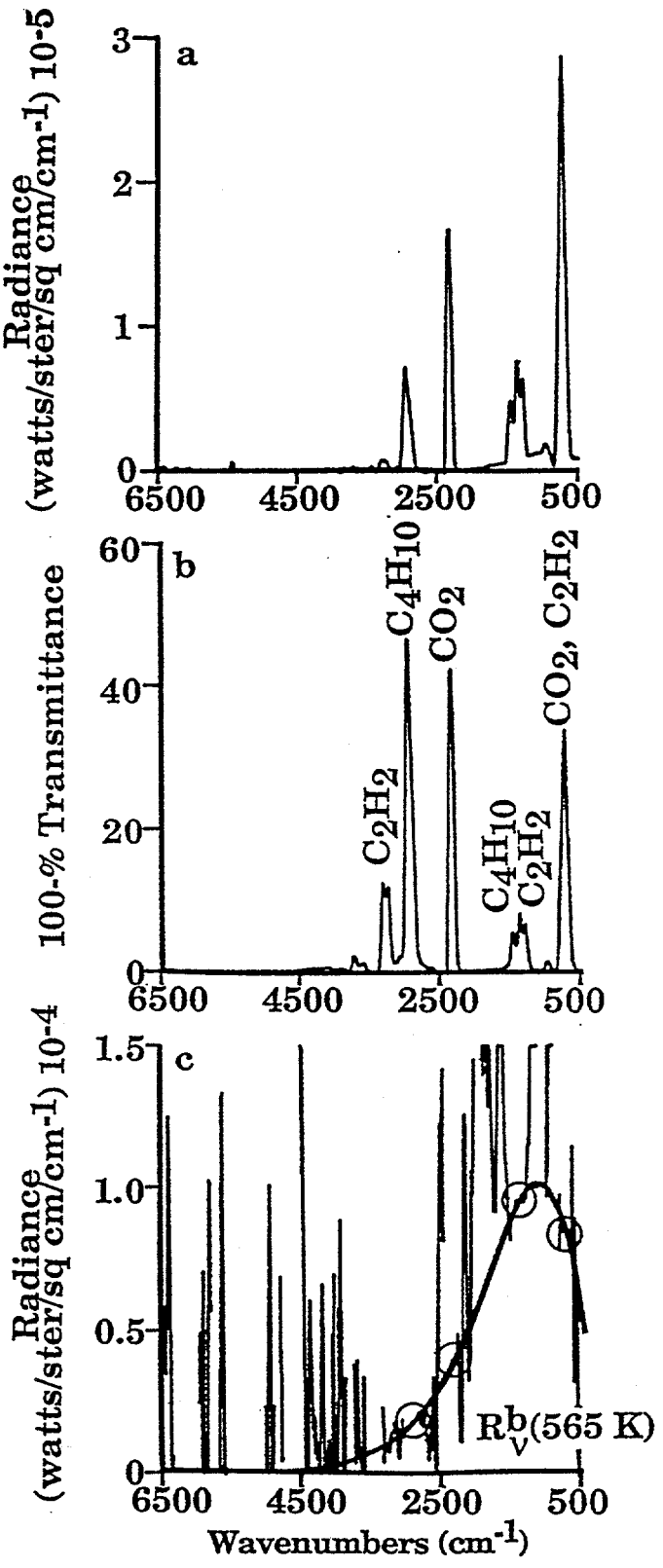

Figure II.A.6-7. FT-IR E/T Spectra for a Mixture of CO_2, C_4H_{10}, and C_2H_2 Exiting the HTR. a) Raw Radiance (R_ν), b) 100%-Transmittance ($1-\tau_\nu$), and c) Normalized Radiance, $R^n_\nu = R_\nu/(1-\tau_\nu)$. R^b_ν(565K) Represents Theoretical Black Body Distribution Best Fit to Regions of Absorption/Emission for the Mixture (circled regions).

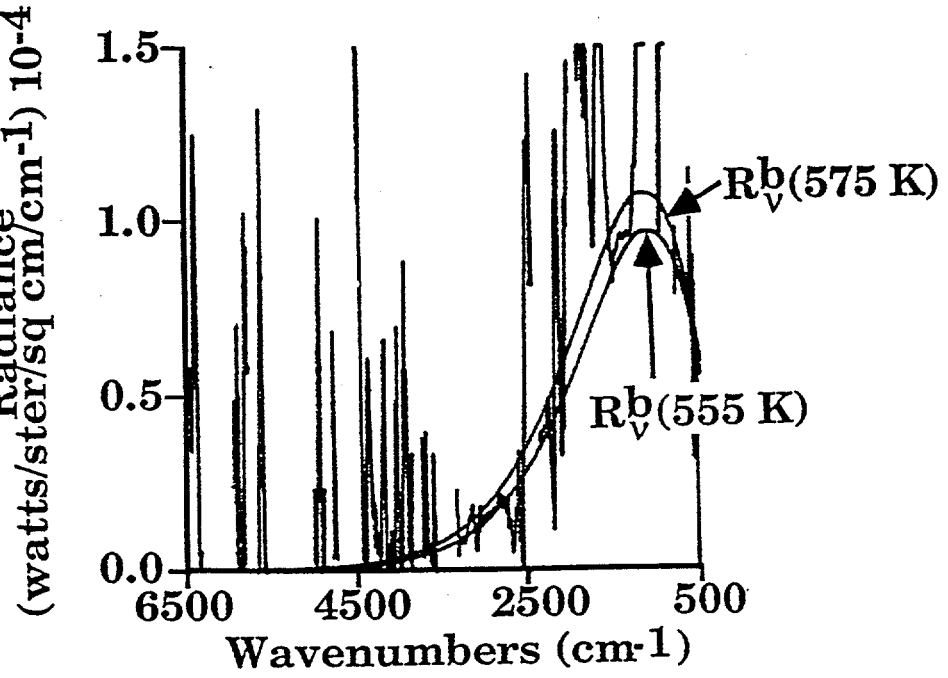

Figure II.A.6-8. Normalized Radiance Spectrum with ±10K Shift from the Best Fit $R_v^b(T)$.

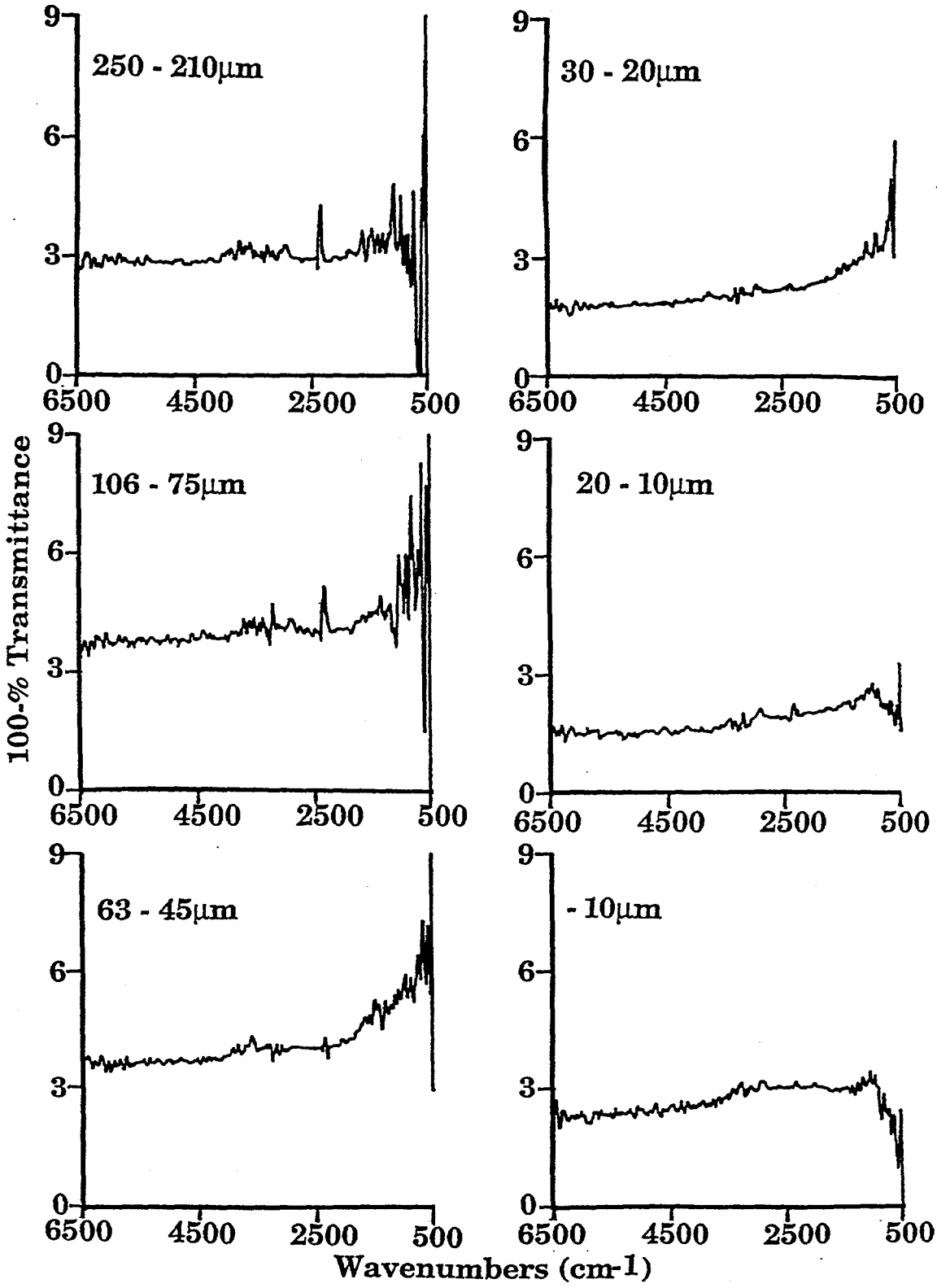

Figure II.A.6-9. 100-% Transmittance Spectra for Different Particle Size Distributions of Smith Roland Subbituminous Coal.

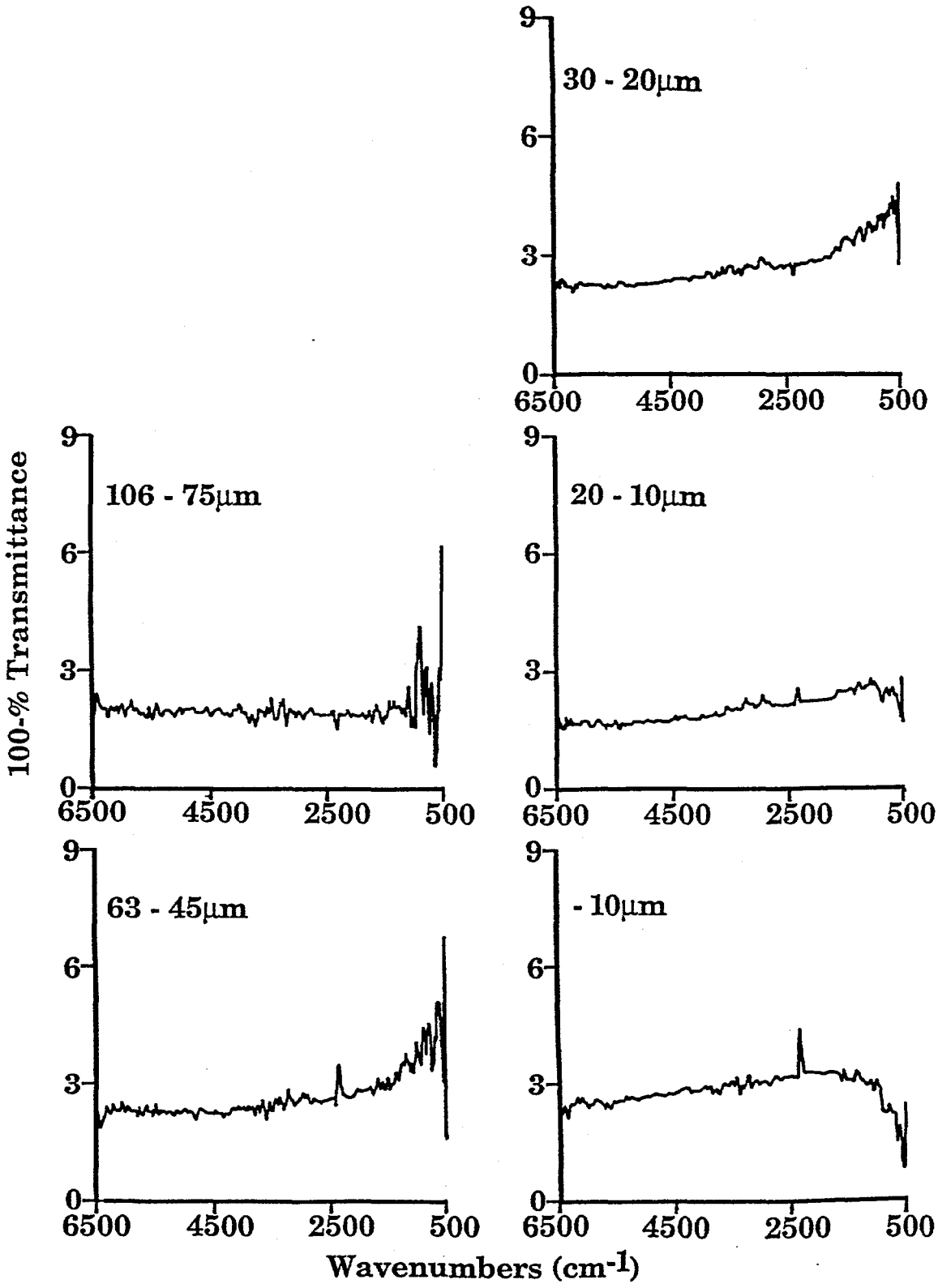

Figure II.A.6-10. 100-% Transmittance Spectra for Different Particle Size Distributions of Lower Kittaning Bituminous Coal.

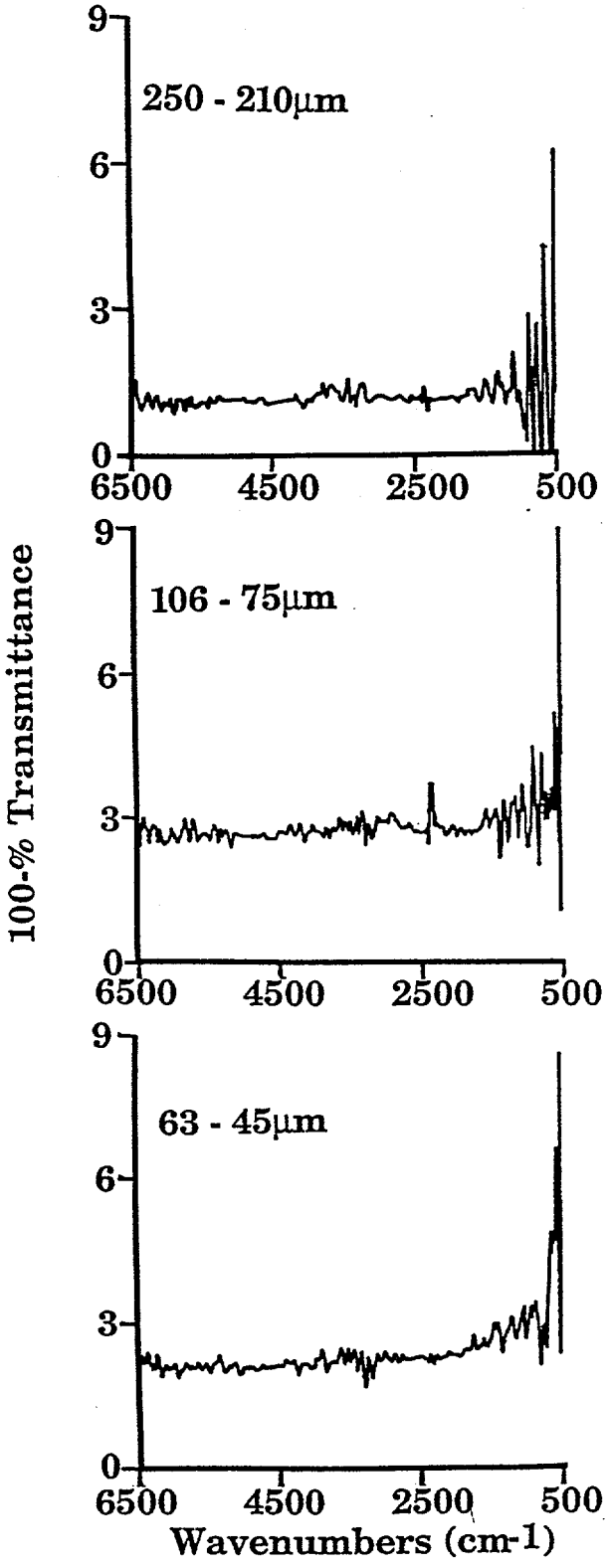

Figure II.A.6-11. 100-% Transmittance Spectra for Different Particle Size Distributions of Beulah North Dakota Lignite.

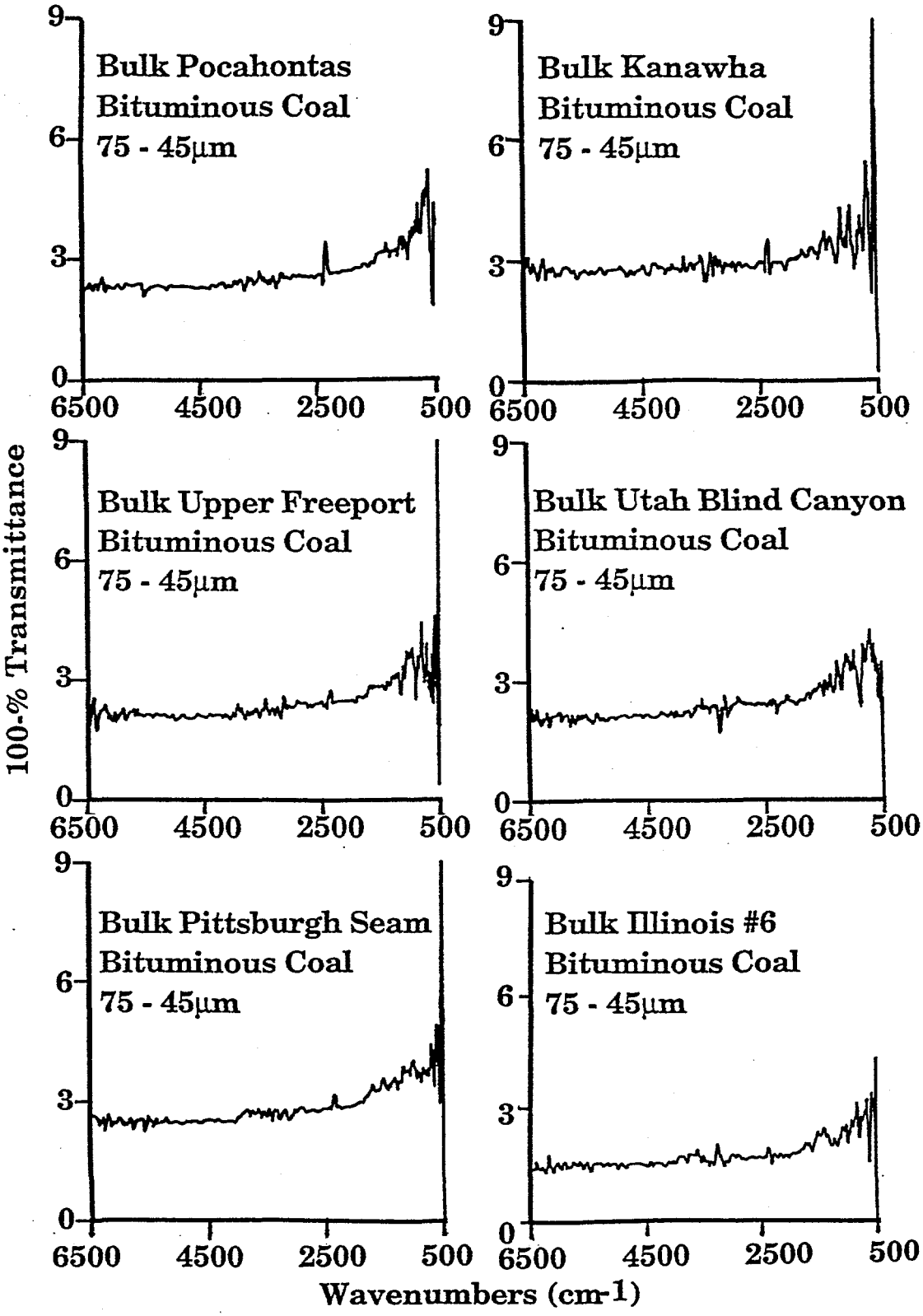

Figure II.A.6-12. 100-% Transmittance Spectra for Bituminous Coals from the AFR/BYU Sample Bank (bank bulk samples).

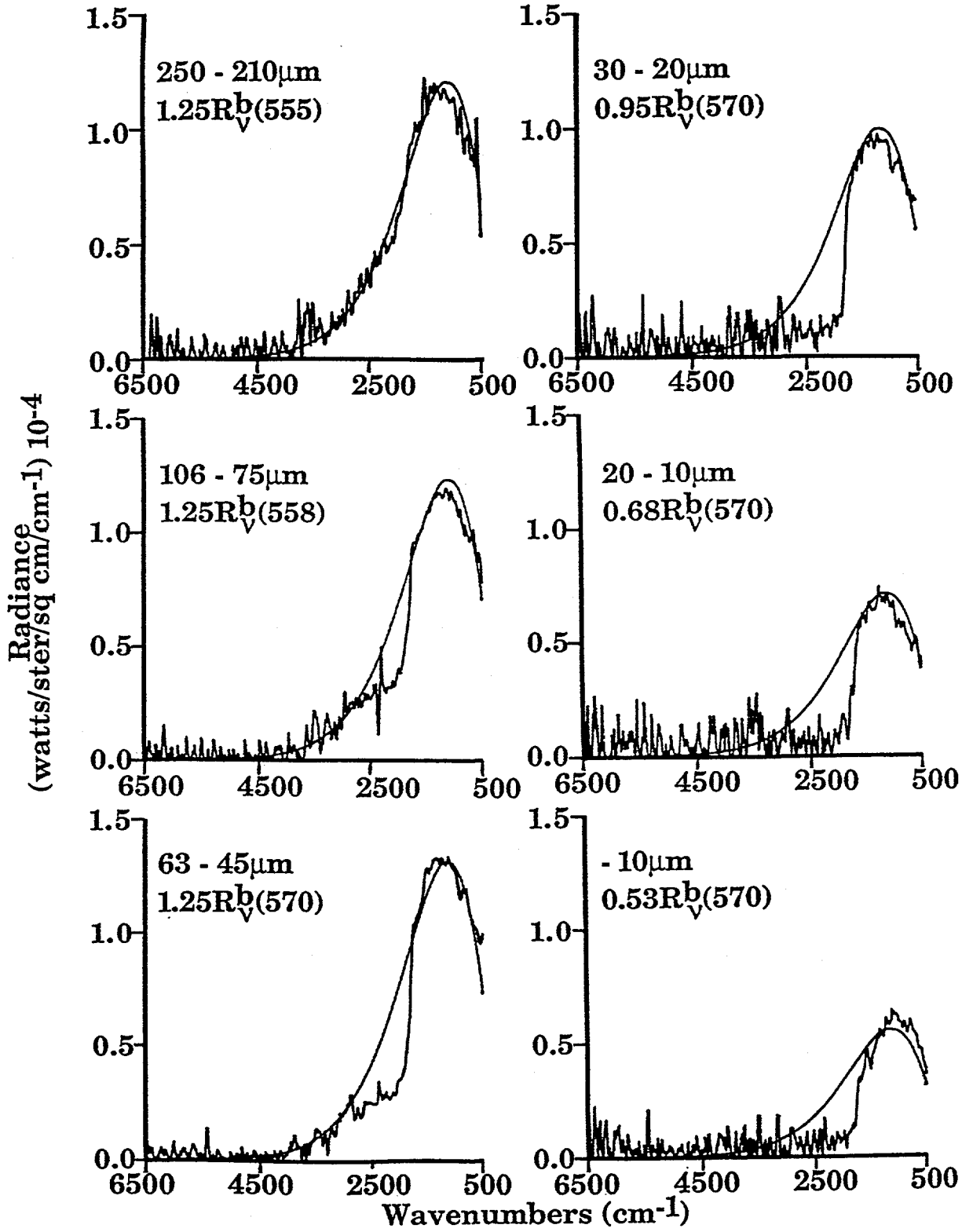

Figure II.A.6-13. Normalized Radiance Spectra for Different Particle Size Distributions of Smith Roland Subbituminous Coal. $R_v^b(T)$ is in Degrees Kelvin.

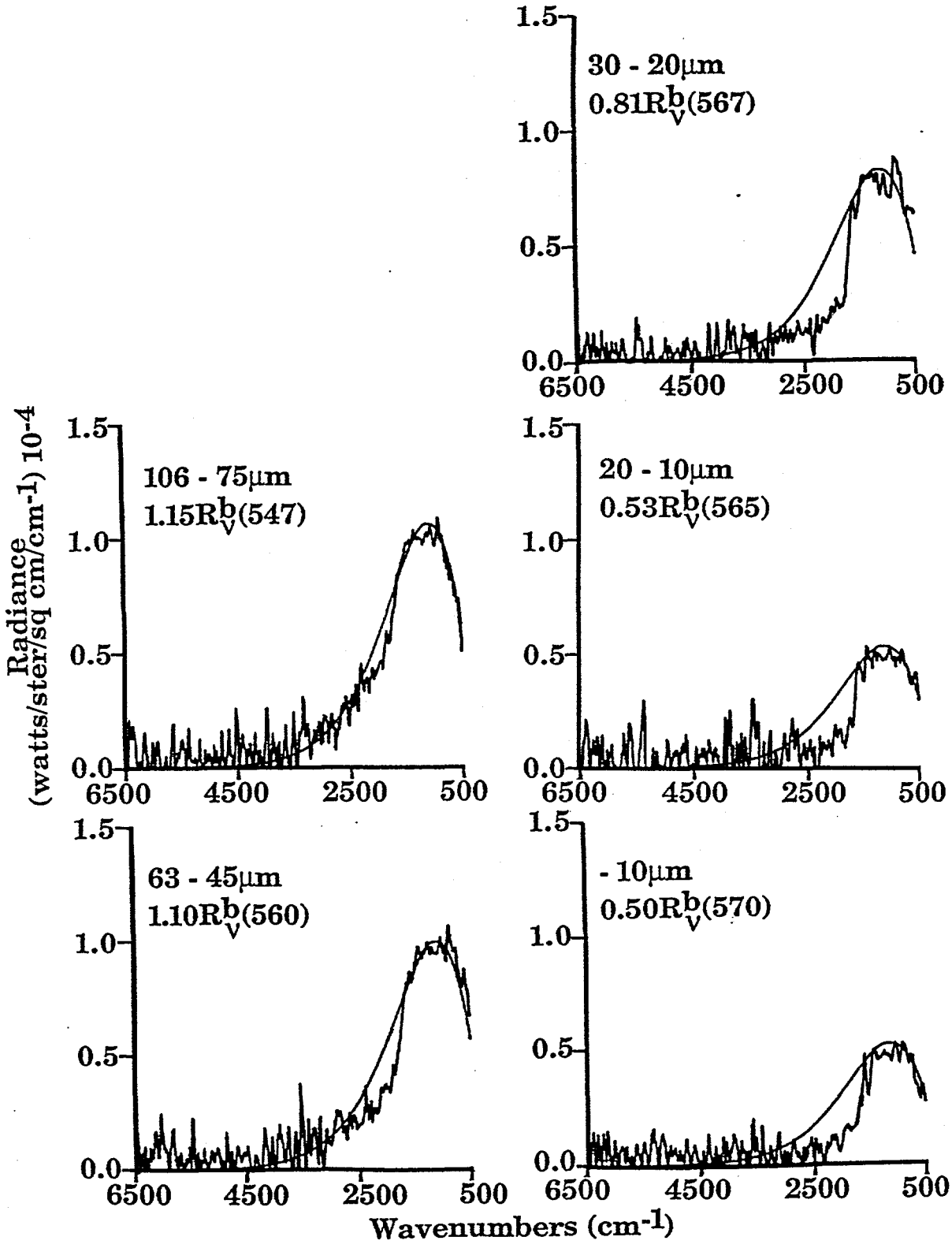

Figure II.A.6-14. Normalized Radiance Spectra for Different Particle Size Distributions of Lower Kittaning Bituminous Coal.

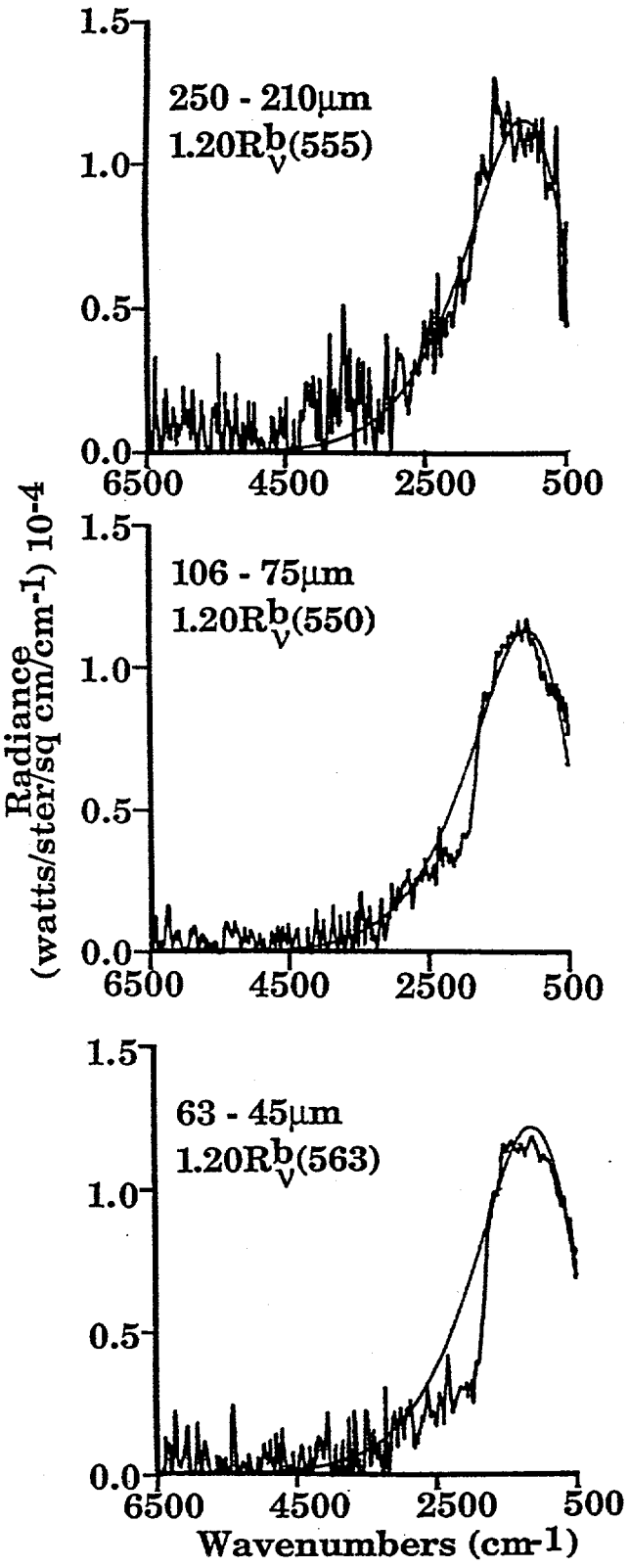

Figure II.A.6-15. Normalized Radiance Spectra for Different Particle Size Distributions of Beulah North Dakota Lignite.

fit to the coal spectrum in the strong absorption region ($\nu < 1700$ cm^{-1}) for coal.

The trend with particle size is consistent for all three coals. The largest particle size (250 to 210 μm) shows agreement close to the overall blackbody over all of the spectrum. The smaller particles sizes continue this agreement for $\nu < 1700$ cm^{-1}, but the emittance decreases for $\nu > 1700$ cm^{-1}. The smaller the particle size, the larger is the decrease. The trend with rank is that the lower rank Beulah lignite and Smith Roland subbituminous coals show a slightly larger decrease above 1700 cm^{-1} than does the higher rank Lower Kittaning bituminous coal.

Figure II.A.6-16 compares six bituminous coals from the bulk AFR/BYU samples obtained for this program. For these similar size fractions (75 to 45 μm), again there is agreement with the overlayed blackbody curve below 1700 cm^{-1}. The decrease above 1700 cm^{-1} does appear to become slightly more drastic with decreasing carbon content of the coals.

The spectral emissivity (ϵ_ν) for coal particles larger than 10 μm at wavelengths which coincide with strong infrared absorption bands should be approximately equal to 1. Therefore, F^t_{6500} is changing with particle size and rank as indicated by the different multiplier values used to fit $R^b_\nu(T)$ to the observed normalized radiance spectra. An attempt was made to determine the surface area of the particle stream by using a light source with an incident radiation that is well out of the diffraction and absorption regime for coal particles ($F^t_\nu = 1$). A He-Ne laser, 0.633 μm radiation, ~ 16,000 cm^{-1} was directed through the coal stream to a photo-sensitive resistor. The output of this visible light detector was checked for linearity by partially blocking the laser beam with several different area sized light choppers. The source was also modulated (chopped) when directed through the coal to avoid room light interferences. The coal should be opaque to the laser radiation.

A plot of percent FT-IR beam attenuation at 6500 cm^{-1}, vs percent He-Ne laser beam attenuation is presented in Fig. II.A.6-17 for the size fractions of Smith Roland subbituminous coal. For the three large size fractions, where $\epsilon_\nu / F^t_{6500} > 1$ in Fig. II.A.6-13, the laser indicates that a larger value of $(1 - \tau)$ 6500 cm^{-1} should be used (i.e., the FT-IR is indicating a low amount of beam attenuation due to scattering of incident radiation back into the collection angle of our instrument, $F^t_{6500} < 1$). For the three smaller size fractions, where $\epsilon_\nu / F^t_{6500} < 1$ in Fig. II.A.6-13, the laser indicates that a smaller value of $(1-\tau)$ 6500 cm^{-1} should be used (i.e., the FT-IR is indicating a high amount of beam attenuation due to a high efficiency of scattering incident radiation out of the collection angle of our instrument, $F^t_{6500} > 1$).

Although the He-Ne laser measurements begin to converge the spectral emittance for $\nu < 1700$ cm^{-1} towards 1 for the different particle sizes, it was observed that the moving particles contributed their own modulated signal to the visible light detector. This contribution, along with laser power and detector drift, did not allow this laser beam attenuation technique to be as accurate as desired in determining the surface area of the particle stream. Work is in progress on an accurate optical geometry for this determination.

Trends in the spectral emittance (R^n_ν / R^b_ν) as a function of particle size and rank re plotted in Fig. II.A.6-18. The value at 2500 cm^{-1} was calculated since it is out of the functional group emission region ($\nu < 1700$ cm^{-1}) but still within the broad band emission region for coal particles at 300°C. The trends with rank and particle size are clearly shown. Figure II.A.6-19 compares the spectral emittance for one particle size distribution for nine different coals. The emittance remains fairly constant (~ 0.55) until above 85% carbon (DAF), at which point an increase in emittance is observed.

Conclusions

Although we can determine the trends in the spectral emissivity (ϵ_ν) for coal with varying particle size and rank, accurate values of F^t_ν (the total extinction efficiency for scattering out of the angular acceptance aperture of our instrument plus absorption) must be determined for particles and experimental geometry used before accurate ϵ_ν can be determined. By choosing a light source (He-Ne laser) that

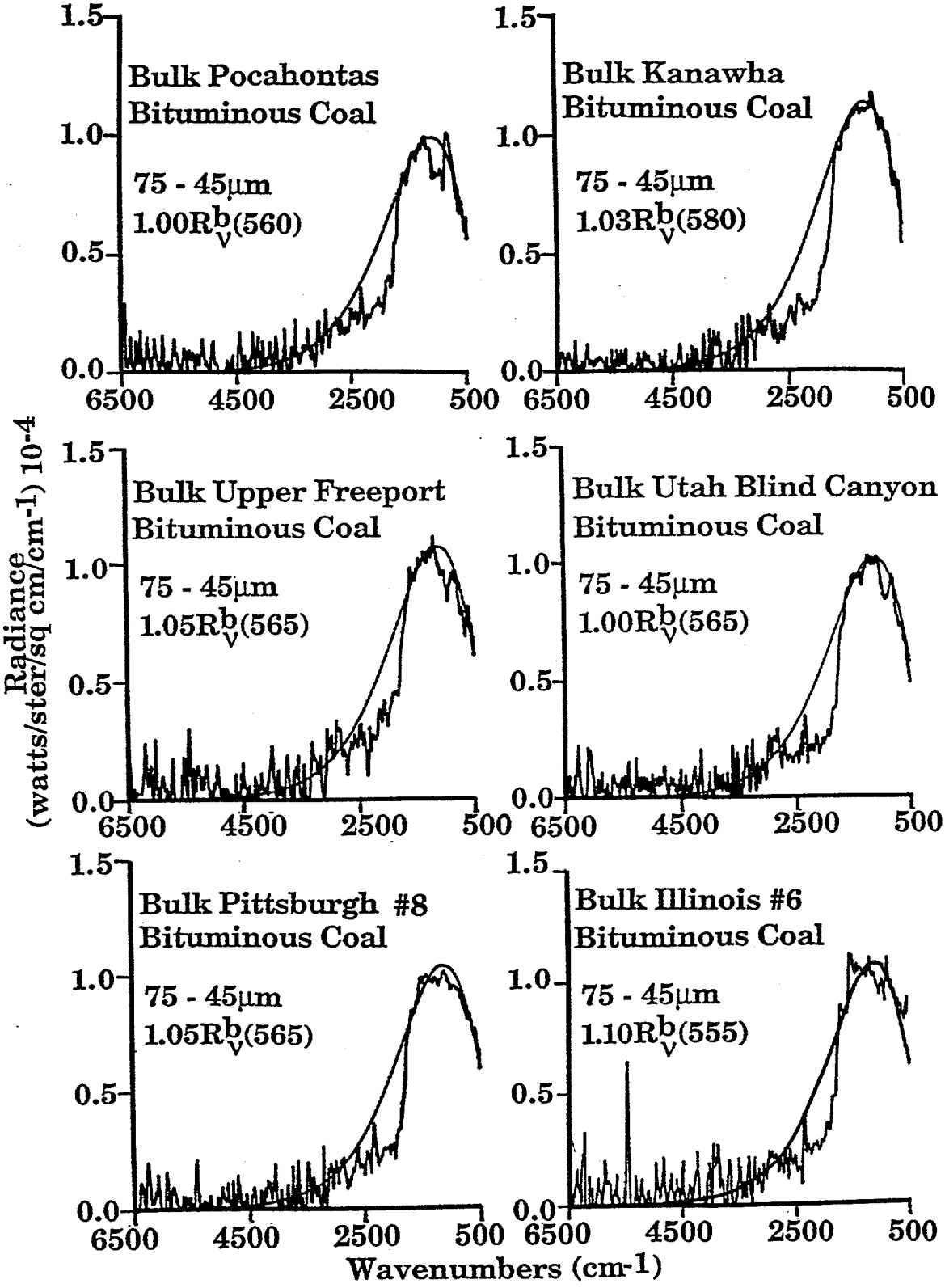

Figure II.A.6-16. Normalized Radiance Spectra for Bituminous Coals from the AFR/BYU Sample Babk (bulk samples). $R_v^b(T)$ is in Degrees Kelvin.

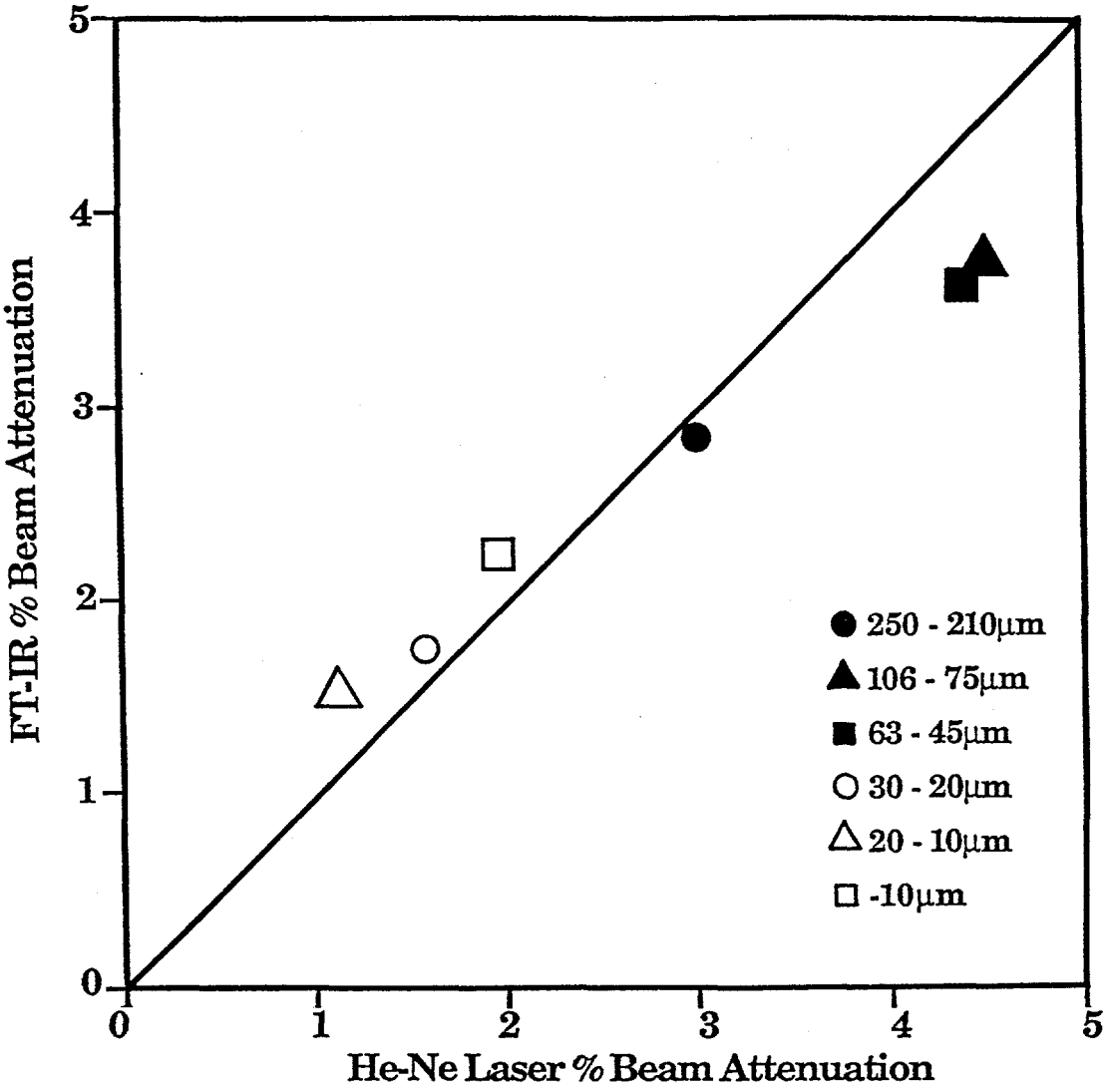

Figure II.A.6-17. FT-IR % Beam Attenuation at 6500 cm^{-1} vs. He-Ne Laser % Beam Attenuation for Different Particle Size Distributions of Smith Roland Subbituminous Coal.

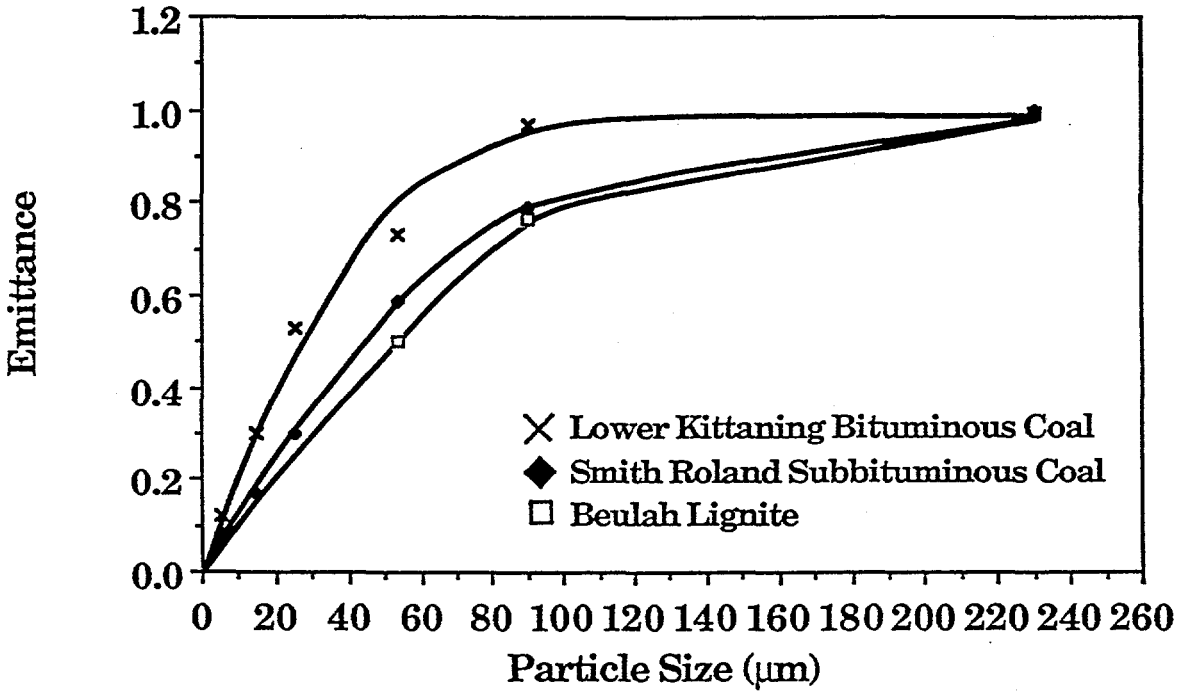

Figure II.A.6-18. Spectral Emittance (R_V^n / R_V^b) Calculated at 2500 cm^{-1} vs. Average Particle Size for Three Different Coal Samples.

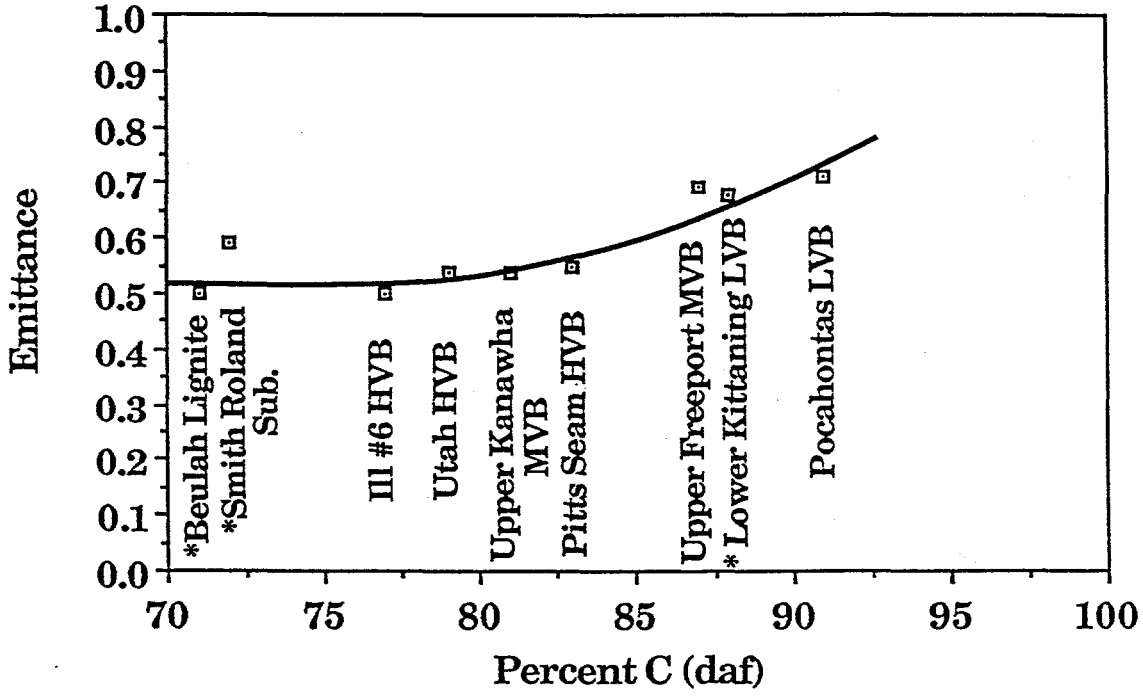

Figure II.A.6-19. Spectral Emittance (R_ν^n / R_ν^b) Calculated at 2500 cm^{-1} vs. Percent Carbon (daf) for Nine Coal Samples of Similar Particle Size Distribution (45-75 μm or *45-63μm).

should be well out of the diffraction and absorption regime for the samples used here, the ϵ_v values in regions of strong infrared absorption bands for various particle sizes of the same material begin to converge. The laser attenuation values, however, are not as accurate as necessary for these determinations due to: 1) laser power drift, 2) detector response drift, and 3) signal contribution from extraneous modulation of the laser beam due to the traversing coal particles.

Optical Properties Model

An outline of the proposed optical properties submodel is shown in Fig. II.A.6-20. In the case of the optical properties submodel, it is not clear yet how much impact this model will have on the predictions of PCGC-2. Consequently, a sensitivity analysis is now underway. The optical properties for different size particles of Zap lignite were calculated and sent to BYU for input into PCGC-2. The results from the study of BYU suggest that there is no need for a detailed submodel in PCGC-2 for coal optical properties.

II.A.7. Polymethylenes

There is present in coals varying amounts (typically 0-9%, but in some cases as high as 18%) of long-chain aliphatics (polymethylenes). These have recently been reported in pyrolysis products by Nelson (1987) and by Calkins and coworkers (1984a,b,c,d) and references quoted therein. The chains appear alone and attached to aromatic nuclei. During devolatilization, the smaller molecules may be released without bond breaking and the heavier molecules with bond breaking to contribute to the tar. The presence of these polymethylenes makes the tar more aliphatic than the parent coal. Further cracking of this material under more severe devolatilization conditions produces ethylene, propylene, and butadiene from which the concentration of polymethylenes may be determined (Calkins, 1984d). Originally, the polymethylenes were included in the FG model as part of the aliphatic functional group pool, which is assumed to decompose to produce gas products, not tar. This led to an error in determining the H/C ratio in the tar which can be important for low rank coals (Freihaut, et al., 1988).

A literature review was done on the occurrence of polymethylenes in coals in order to help formulate a strategy to address the problem. This was included in Appendix B in the Eleventh Quarterly Report. This information can be summarized as follows:

1. Polymethylenes, $(CH_2)_n$, are present in coals at a level of 0 – 18 wt.% depending on rank.

2. Very high rank coals (anthracites) contain very little $(CH_2)_n$ while low rank coals (lignites) generally contain at least 10 wt.%. The amounts for coals of intermediate rank are highly variable and depend on geochemical factors.

3. Exinite macerals are high in polymethylenes, followed by vintrinite and then inertinite.

4. A significant fraction of the $(CH_2)_n$ are attached to aromatic structures in the coal and are not readily extractable.

5. The $(CH_2)_n$ are the precursors for the ethylene, propylene, and butadiene produced from high temperature pyrolysis of coal. They are not precursors for methane, benzene or other light aromatic compounds.

6. The $(CH_2)_n$ appear to play an important role in donating hydrogen to stabilize the reactive aromatic fragments.

7. The $(CH_2)_n$ appear to decompose by a free radical chain reaction which is different than that observed for pure $(CH_2)_n$ in the gas phase. They also decompose differently than the main coal structure.

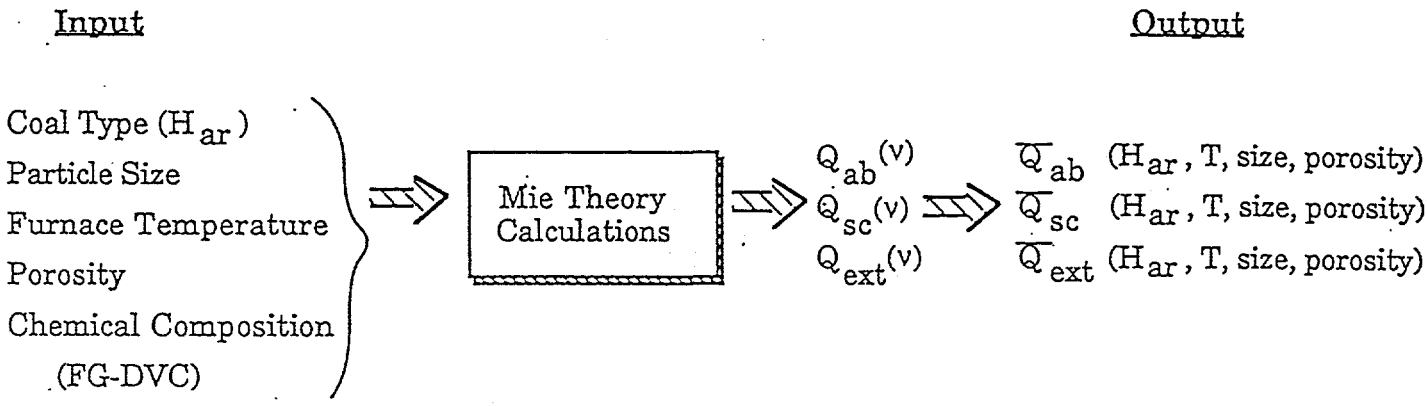

Figure II.A.6-20. Outline of Submodel for Optical Properties of Coals and Chars.

8. Some of the $(CH_2)_n$ are light enough to vaporize directly without bond breaking. The low temperature tars which evolve prior to the main decomposition peak and the low temperature extracts from coal are enriched in $(CH_2)_n$.

9. The vaporization laws which apply to $(CH_2)_n$ will be different than those which apply to the aromatic tars. For a given molecular weight, aliphatic compounds are more volatile than aromatic compounds.

10. The $(CH_2)_n$ will not participate in crosslinking reactions in the same way as the rest of the (aromatic) tar molecules.

All of these factors must be addressed to correctly deal with the occurrence of polymethylenes. However, some can be neglected in the first generation model.

If the amount of heavy polymethylenes is determined, these can be computed as a separate functional group pool with an appropriate release rate and added to the tar. However, strictly speaking, a certain fraction of the polymethylenes should also be included as a type of oligomer so that the smaller species can vaporize directly, without bondbreaking. This would also allow the polymethylenes to be included in the extractable species. The problem of vaporizing the small polymethylenes and including them in the extract yield are related. For most coals, there is a low temperature tar peak which is polymethylene-rich but also includes aromatic tars. Currently, the FG-DVC model uses an interactive procedure at the beginning of a simulation which adjusts the oligomer length to match the experimental pyridine extract yield with the molecular configuration in the computer. The model considers extract to be those molecules which are less than 3000 in molecular weight. However, this does not produce tar molecules which are light enough to vaporize at low temperatures.

The presence of these polymethylenes makes the tar more aliphatic than the parent coal. Also, for most coals, there is a low temperature tar peak which results from the vaporization of unattached small polymethylenes plus small aromatic ring clusters. This vaporization peak is illustrated in Fig. II.A.7-1. Polymethylene chains can also crack or be released into the second tar peak. Further cracking of this material under more severe devolatilization conditions produces ethylene, propylene, and butadiene from which the concentration of polymethylenes may be determined (Calkins et al., 1984d). Originally, the polymethylenes were included in the FG model as part of the aliphatic functional group pool, which is assumed to decompose to produce gas products, not tar. This leads to predicted H/C ratios in the tar for low rank coals which are lower than those measured by Freihaut et al. (1988).

Polymethylenes have now been added to the DVC part of the model as a second class of material whose molecular weight distribution and functional group composition are different from the main macromolecular network. The starting coal molecule now includes a distribution of oligomer sizes for polymethylenes and other guest molecules (with the chemical composition of the network). The vaporization of these molecules produces a peak which matches the early vaporization peak as shown in Fig. II.A.7-1. We also account for polymethylenes which are attached to the coal matrix and removed by bond breaking by including them as species in the FG model. Those polymethylenes are then added to the tar after vaporization.

The model requires a value for the total polymethylene content in the coal. Calkins determined that the yields of ethylene, butadiene, and propylene correlated well with the polymethylene content (1984d). It was decided that this is the most general and fruitful approach to take and we have used the coals which are in our set and Calkins' set to calibrate the method. As a first approximation, we arbitrarily chose to use polymethylene = 0.7 (C_2H_4). This gave -CH_2- contents slightly above Calkin's values, but within 15% of Calkin's. The model also assumes that 50% of the polymethylenes are small enough to vaporize and are included in the oligomer pool while the other 50% are not and are included in the FG pool.

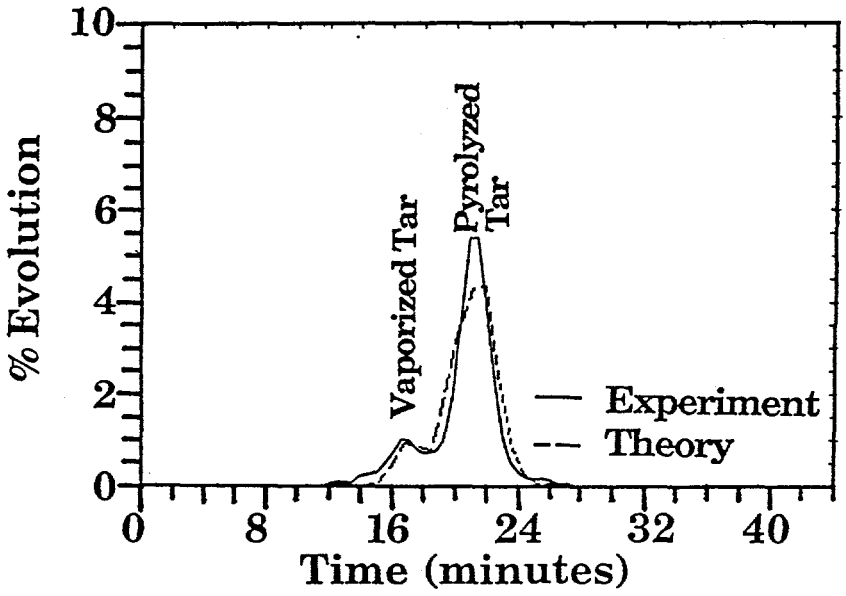

Figure II.A.7-1. Comparison of FG-DVC Model Predictions for Tar Evolution Rate from Upper Freeport Coal with TG-FTIR Data.

A prediction for the total tar yield including polymethylenes is compared in Fig. II.A.7-1 with measurements from a TG-FTIR experiment (Solomon et al., 1989a). The agreement is good. Comparisons between the predicted and measured (Freihaut et al., 1988) tar hydrogen compositions are shown in Fig. II.A.7-2. The prediction is good for high rank coals and shows the correct trend with rank. The tar hydrogen composition is, however, overpredicted for lower rank coals. This is due to an error in the way Freihaut plotted his data. The correct data compares well with the model. The relative contribution of polymethylenes is then more important. By improving the tar predictions with adjustments of DVC parameters, we should be able to obtain more accurate values of the tar hydrogen composition.

II.A.8. Crosslinking

The measurement and modeling of crosslinking phenomena in pyrolysis and how this process affects the evolved product distributions has been presented in Solomon, et al., (1990a). The abstract for this paper is presented below.

Abstract

During coal conversion, the breakup of the coal macromolecular network and resulting product formation are controlled by relative rates of bond breaking, crosslinking, and mass transport. The objective of this work was to systematically study the variations in crosslinking with several parameters (rank, temperature, heating rate, pretreatment, etc.), to identify the factors that control crosslinking, to try to identify the reactions responsible for crosslinking, and to determine the crosslinking rates. This paper describes a study of crosslinking behavior in which chars of a number of coals (including the Argonne premium coal samples) have been pyrolyzed under a variety of temperature histories and analyzed at intermediate extents of pyrolysis for solvent swelling behavior and functional group compositions. The variations in these properties were correlated with the tar molecular weight distribution measured by field ionization mass spectrometry and with the gas evolution. The study of crosslinking as a function of coal rank and pyrolysis temperature shows that there are at least two distinct crosslinking events: one occurs at low temperature prior to tar evolution (in low rank coals only) and the second occurs at moderate temperatures slightly above that for tar evolution. The low temperature crosslinking process results in low tar yields, low fluidity, (e.g., measured by Geissler plastometer), low extract yields, and low molecular weight tar. Low temperature crosslinking is increased by oxidation of the coal and reduced by methylation. Studies that compare char solvent swelling behavior to gas evolution have shown that low temperature crosslinking occurs simultaneously with CO_2 and H_2O evolution. Moderate temperature crosslinking appears to correlate best with methane formation. Studies that compare char swelling behavior to changes in char functional group concentrations have shown that crosslinking reactions occur with the loss of carboxyl groups present in the coal. A clear role for hydroxyl grups in low temperature crosslinking could not be established, nor could it be ruled out.

II.A.9. Char Reactivity Measurements

Introduction

Understanding char reactivity is important since the consumption of char is the slowest and, therefore, the controlling process in combustion or gasification. Reviews of char reactivity (Essenhigh, 1981; and Smth, 1982) demonstrate that there is a wide variation in observed reactivities. Work described by Wells, et al., (1982) highlights the very large variations (two orders of magnitude) in char reactivity with method of formation. Similarly, Ashu, et al., (1978) found an enhanced reactivity of char caused by rapid heating of the precursor coal. In work done in a vertical tunnel furnace, Essenhigh and Farzan (1982) measured very rapid burnout times for small coal particles. They ascribed this to the firing condition which gave rates of heating in the 10^6 K/s regime, compared with the more usual value of 10^4 K/s in slower burning flames. Nsakala has reported a wide variation in reactivity associated with rank (Nsakala, et al., 1982).

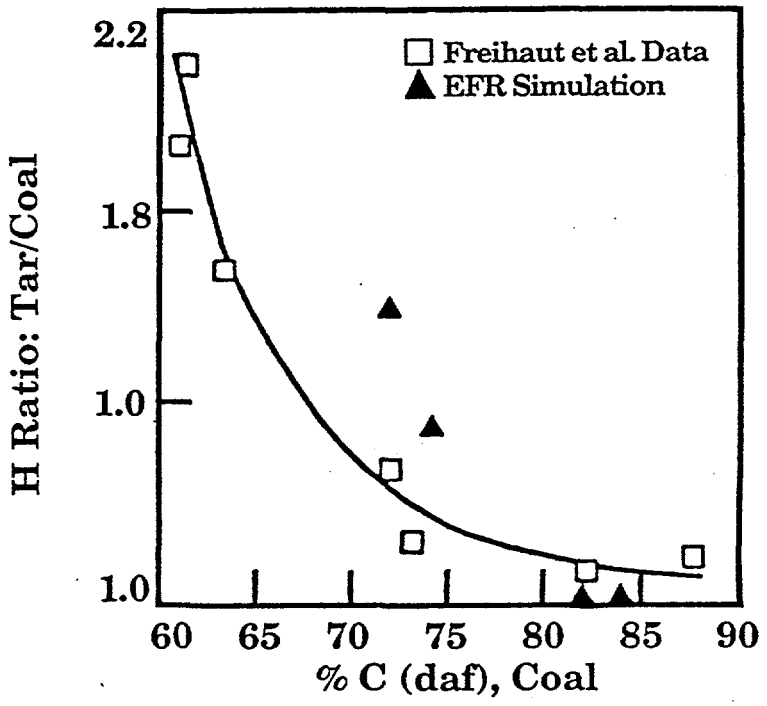

Figure II.A.7-2. Ratio of % H in Tar to % H in Coal as a Function of Coal Rank. (from Freihaut et al. (1988).

The intrinsic reactivity of the char is important in combustion experiments since most studies indicate that the char combustion at high temperatures occurs at less than the external diffusion limit (Field, 1970; Smith, 1971; Mitchell and McLean, 1982; Tichenor, et al., 1985; Waters, et al., 1988; and Leslie, et al., 1989). It has also been observed that char combustion exhibits a negative temperature coefficient (Essenhigh, 1981), which may be due to annealing which occurs during combustion at high temperatures. The effects of coal pyrolysis conditions on intrinsic combustion reactivity have not been studied over a wide range of conditions. One problem is the difficulty in making these measurements accurately at high temperatures. These experiments usually require a fairly complex apparatus and large quantities of coal, and the effects of heat and mass transport must be considered to back out intrinsic reactivity. A convenient experiment for measuring intrinsic reactivity is a thermogravimetric analyzer (TGA). However, two problems must be considered. One is how to develop a TGA test which can make measurements over a wide range of reactivities. The second problem is how to relate the low temperature reactivity measurements to the high temperature conditions of interest in pulverized fuel (p.f.) or fluidized bed combustion.

This section reports on a study of the combustion (oxidation) reactivity of a set of chars from five different coals prepared by pyrolysis at heating rates between 0.5 and 20,000°C/sec to temperatures between 400 and 1600°C. A new TGA technique was developed in which the weight loss was measured while the sample was heated at a constant heating rate in the presence of the reactive gas. The results for the present paper are for reactivity in air. This method has the advantage that the same conditions can be used for chars of widely varying reactivity. As discussed below, these low temperature measurements give reasonable predictions of high temperature char reactivities.

The development of the TGA reactivity measurement was done under previous DOE-METC Contracts (Nos. DE-AC21-84MC21004, DE-AC21-85MC22050) and applied to a larger set of coals and chars (including the Argonne Premium coals) under the current contract. The previous work is summarized below in order to provide background for the char reactivity model development that was the main focus of the current contract (see also Section II.A-10).

Experimental Procedure

Char Preparation - Chars for this study were prepared from the 200 x 325 mesh sieved fractions (~ 60 μm mean diameter) of coals and lignites listed in Table II.A.9-1. The chars were prepared by pyrolysis in an inert atmosphere in one of four reactors: 1) an atmospheric pressure entrained flow reactor (EFR) (Solomon, et al., 1982; and Solomon and Hamblen, 1985b) with coal particle temperatures between 650 and 1600°C at heating rates of ~ 10,000°C/sec; 2) a heated tube reactor (Solomon, et al., 1986c) with coal particle temperatures between 650°C and 950°C at heating rates of ~ 20,000°C/sec; 3) a thermogravimetric analyzer (TGA) with coal particle temperatures of 450°C to 900°C at heating rates of 0.5°C/sec; and 4) a high pressure entrained flow reactor (HPR) with coal temperatures of 600°C to 1400°C at heating rates of ~ 10,000°C/sec and pressures up to 200 psig (Solomon, et al., 1984).

Reactivity Measurements - Initial char reactivity measurements were made using the isothermal measurement technique developed at Pennsylvania State University (Mahajan, et al., 1978). In this method, the char is heated in a TGA in nitrogen to the desired temperature, usually 400-500°C. The temperature level is chosen to make sure no oxygen diffusion limitations are present, i.e., by varying the flow rate, bed depth and particle size. After the weight of the sample has stabilized at the selected temperature level, the nitrogen flow is switched to air and the weight loss is monitored. The time for 50% burnoff, $\tau_{0.5}$, is used as the reactivity index. Another group at Penn State has used the maximum rate of weight loss as a reactivity index, which is determined in a similar isothermal experiment (Jenkins, et al., 1973). In our char characterization work, we had difficulty applying the isothermal techniques to chars formed over a wide range of conditions. A temperature level selected for one char was inappropriate for another. The temperature was either too high for the rate to be chemically controlled or too low for the $\tau_{0.5}$ to be reached in a reasonable time period.

Table II.A.9-1.

SAMPLE PROPERTIES

	WT% DAF				
	Zap, North Dakota Lignite	Montana Rosebud Subbituminous	Illinois #6 Bituminous	Pittsburgh Seam Bituminous	Kentucky #9 Bituminous
Carbon	66.5	72.1	73.6	82.1	81.7
Hydrogen	4.8	4.9	4.7	5.6	5.6
Nitrogen	1.1	1.2	1.4	1.7	1.9
Sulfur	1.1	1.2	3.8	2.4	2.4
Oxygen (Diff.)	26.5	20.3	16.5	8.2	8.4
Ash (Dry Wt%)	7.1	10.0	11.0	9.2	14.1

In order to overcome this difficulty, a non-isothermal technique was developed. A Perkin-Elmer TGA 2 was initially used for this method. Recent measurements have been made using a Bomem TG/plus, which couples a Dupont 951 TGA with a Bomem Michelson 100 FT-IR spectrometer (Solomon, et al., 1989b). The sample size is about 1.5 mg. The sample is heated in air at a rate of 30 K/min until a temperature of 900°C is reached. The TGA records the sample weight continuously and, at the end of the experiment, the weight and derivative are plotted. Some representative curves for chars from the North Dakota (Zap) lignite and the Pittsburgh Seam bituminous coal are shown in Fig. II.A.9-1. The Zap and Pittsburgh chars were prepared in the EFR, in which it was calculated that the particles were heated at about 7000 K/s to 700°C before being quenched. The samples were oxidized with an air flow of 40 cc/min and a nitrogen purge flow of 400 cc/min. The derivative curve for the Zap lignite coal (Fig. II.A.9-1a) shows a sharp downward spike, indicating that the particle ignited. The Zap lignite also indicates burnout of several components of the char of different reactivity, while the Pittsburgh coal shows a more homogeneous burnout at higher temperatures.

The characteristics of the weight loss curve can be understood as follows: 1) At low temperature, there is an initial weight loss as moisture is removed, then a small weight gain due to oxygen chemisorption; 2) As the temperature is raised, the reactivity of the char increases until the fractional weight loss rate is sufficiently large to be observed. The sample size and oxygen flows are chosen so that the initial ~ 10-15% of the oxidation weight loss occurs under intrinsic reactivity control; 3) As the temperature continues to increase, the reactivity increases until eventually all the oxygen reaching the sample bed is consumed and the weight loss is controlled by the oxygen supply to the sample bed alone. Then the fractional weight loss rate becomes constant for all samples; 4) When the char has components of different reactivity, the weight loss can switch between being oxygen supply limited and being intrinsic reactivity limited as each component is consumed.

Figure II.A.9-2 compares the weight loss curves for the same char sample but with different sample sizes. The curves are identical for the initial weight loss which is controlled by the intrinsic reactivity. This is the region in which the reactivity measurements are made. As expected, the fractional rate of weight loss $df/dt = (1/m_o)\ (dm/dt)$ decreases with increasing sample size in the oxygen supply limited regime.

Theoretical Analysis

Comparison of Isothermal and Constant Heating Rate Reactivity Tests - The temperature (T_{cr}) at which the derivative of the fractional weight loss with respect to time reaches a value of 0.065 wt. fraction/min $\approx$ 0.001 wt. fraction/s was chosen as an index of reactivity to be compared with the $\tau_{0.5}$ values measured by the isothermal technique. The actual critical slope used is arbitrary. A value is chosen which is large enough to be unambiguously determined, but small enough so that reaction occurs in the chemically controlled regime. Values of $\ln \tau_{0.5}$ were plotted against $1/T_{cr}$ and a good correlation was observed.

It was subsequently decided that a comparison to $\tau_{0.1}$ (time for 10% burnoff) would be more relevant since the initial reactivity indicated by T_{cr} would be measured, rather than an integral reactivity over a large extent of conversion which could be affected by reactivity variations due to changes in the pore structure or sample inhomogeneity. A plot of $\ln \tau_{0.1}$ vs $1/T_{cr}$ is shown in Fig. II.A.9-3. This plot includes data for chars from three different coals (Lignite, Subbituminous, Bituminous) in four reactors. The experimental conditions covered the following ranges: heating rate = 0.5 to 20,000 K/sec; temperature = 400 to 1600°C; residence time = .020 s to 30 min; pressure = 0 to 1400 kPa.

It can be shown that a plot of $\ln \tau_{0.1}$ vs $1/T_{cr}$ will be linear with a slope equal to E/R, where E is the global activation energy for the intrinsic oxidation rate and R is the gas constant. For the reaction

$$C\ (solid) + O_2\ (gas) = CO_2\ (gas) \qquad (II.A.9\text{-}1)$$

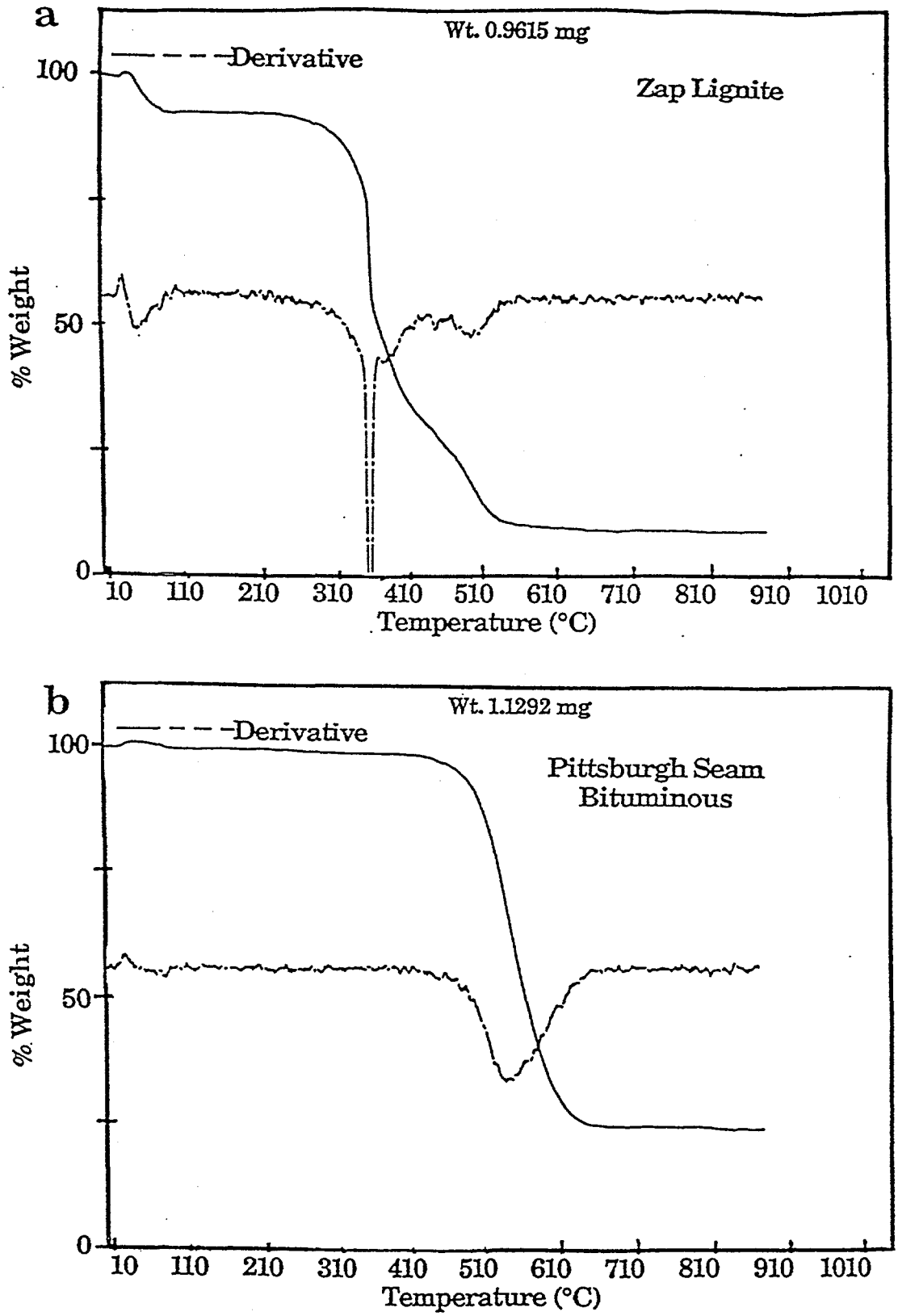

Figure II.A.9-1. Non-Isothermal TGA Reactivity Tests at 400 cc/min Air Flow; Heated at 30°C/min. a) High Reactivity Zap Lignite Char, b) Low Reactivity Pittsburgh Seam Bituminous Char.

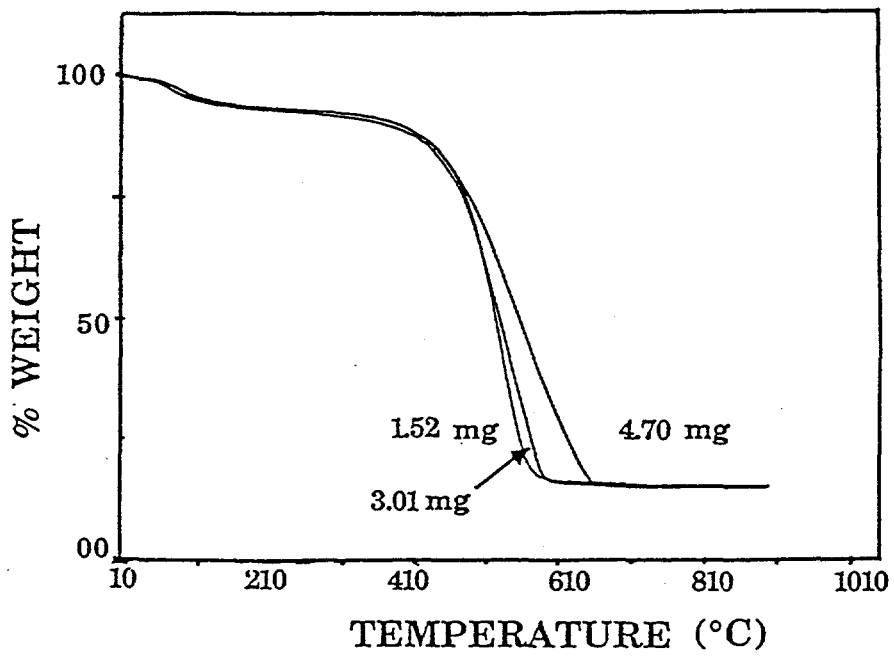

Figure II.A.9-2. TGA Weight Loss Curves for Zap Lignite Char at 3 Sample Weights.

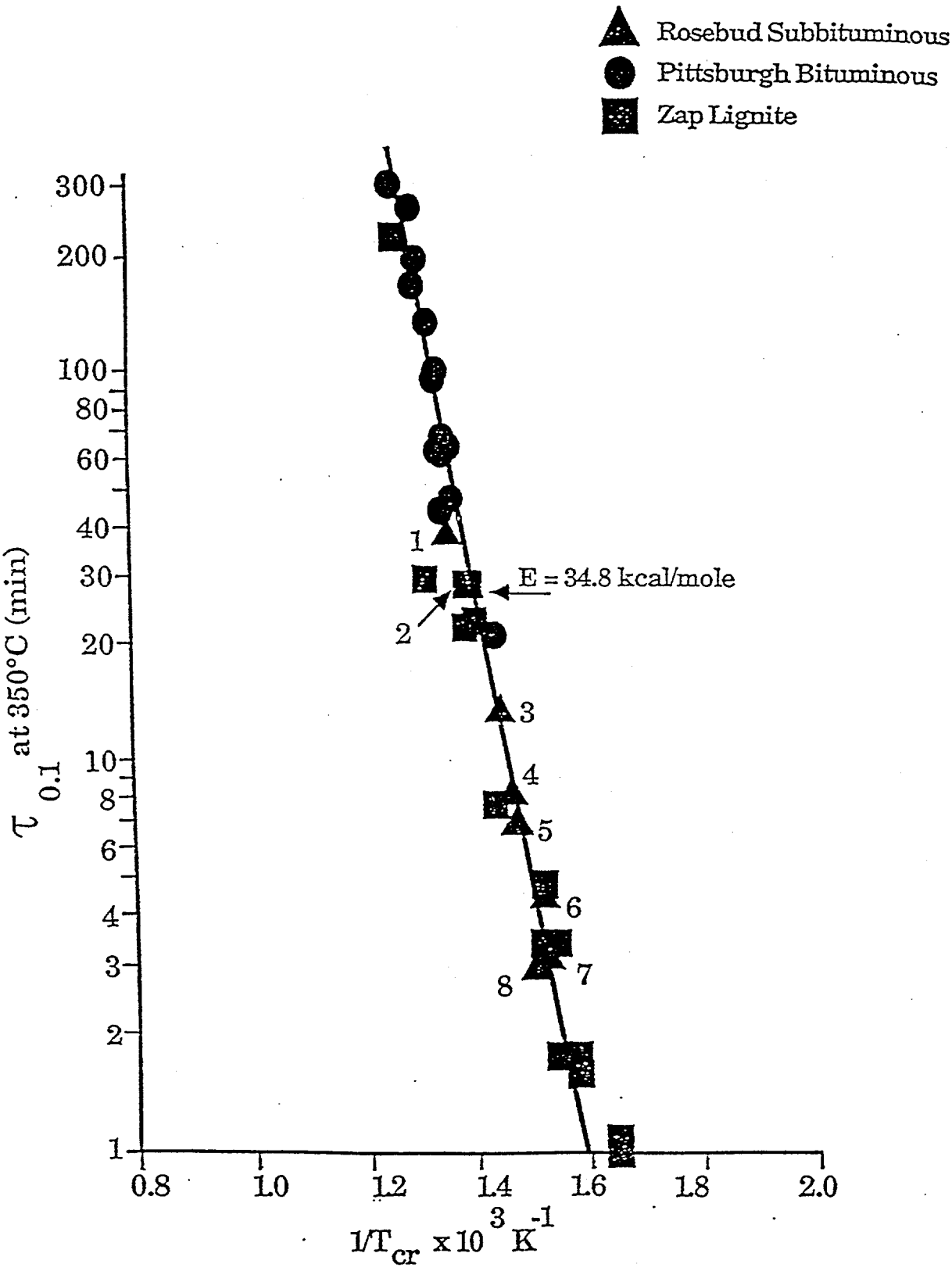

Figure II.A.9-3. $\tau_{0.1}$ (time for 10% burnoff) vs. $1/T_{cr}$. T_{cr} is the Temperature at which the Weight Loss Rate Equals −0.001 wt. Fraction/sec.

the initial fractional rate of disappearance of mass (under the condition of chemical reaction control) can be represented as follows (McKenzie, et al., 1974):

$$df/dt = 6\ R_e/(d_o\ \rho_o) \qquad \text{(II.A.9-2)}$$

where df/dt is the fractional loss of mass per particle in unit time (1/sec), R_e is the reaction rate based on external surface area (g/cm^{2}s), d_o is the initial particle diameter (cm), and ρ_o is the initial particle density. Following the treatment by Smith (1982), the relationship between the intrinsic and external reaction rate is as follows:

$$R_e = d_o\ \rho_o\ A_g\ R_i \qquad \text{(II.A.9-3)}$$

where R_i is the "intrinsic" reaction rate based on the internal surface area and A_g is the specific surface area in cm^2/g for the reaction. The parameter A_g can be thought of as the product of (βA_a), where β is the ratio of active area per unit accessible surface area (cm^2/cm^2) and A_a is the accessible surface area in cm^2 per gram. By making the above substitutions, one can arrive at a new expression for the initial fractional weight loss rate.

$$df/dt = 6\ A_g\ R_i = 6\ [\beta A_a]\ R_i \qquad \text{(II.A.9-4)}$$

In the isothermal experiment, the fractional burn-off rate is nearly constant up to ~ 10% weight loss:

$$df/dt \approx \Delta f/\Delta t \simeq -\ 0.1\ /\tau_{0.1} \qquad \text{(II.A.9-5)}$$

Substituting Eq. II.A.9-4 for df/dt:

$$6\ [\beta A_a]R_i = 0.1\ /\tau_{0.1} \qquad \text{(II.A.9-6)}$$

$$R_i = k_i C_s^{\ m} = k_i(T_o)C_s^{\ m} \qquad \text{(II.A.9-7)}$$

where T_o is the temperature of the experiment and C_s is the surface oxygen concentration.

Therefore:

$$6\ [\beta A_g]\ k_i(T_o)C_s^{\ m} = 0.1/\tau_{0.1} \qquad \text{(II.A.9-8)}$$

Solving for $\tau_{0.1}$:

$$\tau_{0.1} = 0.1/[6\ k_i(T_o)C_s^{\ m}] \cdot [1/[\beta A_a]] \qquad \text{(II.A.9-9)}$$

$$= K_1\ [1/\beta A_a] \qquad \text{(II.A.9-10)}$$

The quantities in the first set of brackets in Eq. II.A.9-9 are nearly constant for a given isothermal experiment (temperature = T_o) at low conversions and independent of coal type, while the second set of brackets contain quantities which vary with coal type and char formation conditions.

For the non-isothermal experiment, the relative rate of mass loss is constant at some critical temperature, T_{cr}:

$$df/dt = -\ 0.001 = 6\ [\beta A_a]\ k_i\ (T_{cr})C_s^{\ m} \qquad \text{(II.A.9-11)}$$

$$k_i(T_{cr}) = -0.001/[6\ C_s^{\ m}] \cdot [1/[\beta A_a]] \qquad \text{(II.A.9-12)}$$

$$= K_2\ [1/[\beta A_a]] \qquad \text{(II.A.9-13)}$$

The result obtained is that k_i (T_{cr}) is proportional to an experimental constant and inversely proportional to char properties.

For data collected on the same char sample, [βA_a] can be eliminated between Eqs. II.A.9-9 and II.A.9-12:

$$\tau_{0.1} = [0.1/[6\ k_i(T_o)C_s^m]] \cdot [k_i\ (T_{cr})\ 6\ C_s^m/-0.001] \qquad \text{(II.A.9-14)}$$

or

$$\tau_{0.1} = 100 \exp\ [-E/R\ [1/T_{cr} - 1/T_o]] \qquad \text{(II.A.9-15)}$$

assuming that k_i can be expressed as an Arrhenius expression $k_i(T) = k_o \exp(-E/RT)$.

Consequently, a plot of ln $\tau_{0.1}$ vs $1/T_{cr}$ will have a slope equal to -E/R of the intrinsic global oxidation rate. In the absence of catalytic effects, the value of E should be the same for chars from all coals and chars from the same coal prepared under a wide variety of conditions. The nearly linear data in Fig. II.A.9-3 appears to support this conclusion. A problem may arise if T_{cr} and T_o are significantly different. The mechanism of the oxidation reaction probably changes with temperature, as indicated by the wide range of activation energies and reaction orders reported for the char oxidation reaction in the literature (Larandeau, 1978). The best fit value of about 35 kcal/mole determined from Fig. II.A.9-3 is intermediate in reported values and close to the value of ~ 31 kcal/mole determined by Radovic et al. (1983), and Wells et al. (1982) for a wide range of chars from U.S. coals in TGA experiments. It also agrees with the value of 34 kcal/mole determined by Smith (1982) for the intrinsic global activation energy of several U.S. coals.

The formation conditions for the Montana Rosebud Chars which are labeled in Fig. II.A.9-3 are given in Table II.A.9-2. This provides an indication of the range of pyrolysis conditions required to provide the variation of $\tau_{0.1}$ and T_{cr} observed in Fig. II.A.9-3.

Results

Reactivity vs. Extent of Pyrolysis - Figure II.A.9-4 summarizes the results for chars from T_{cr} measurements on five coals produced over a wide range of pyrolysis conditions. The critical temperature (T_{cr}), which varies inversely with reactivity, is plotted as a function of the (daf) hydrogen content, which is used as a measure of the extent of pyrolysis. For each char type, there is a trend for increasing T_{cr} (decreasing reactivity) with decreasing hydrogen. Most of the change occurs below 2.5% hydrogen, after the evolution of aliphatic hydrogen is complete. That is, T_{cr} appears to vary primarily with the concentration of aromatic hydrogen. This variation could be due to a variation in the active site concentration (β), possibly correlated with the ring condensation accompanying the elimination of aromatic hydrogen. There does not appear to be any drastic effects due to heating rate for low rank coals containing minerals, as chars for a wide range of conditions all fell along the same curve. The results for bituminous coals and demineralized low rank coals do not show the same heating rate independence (Serio, et al., 1989). It should be noted that there is also ring oxygen in the char which is removed at about the same rate as the hydrogen and which may be related to the reactivity changes. Similar correlations were observed with oxygen concentration for chars produced from a single coal, i.e., the reactivity decreases with decreasing char oxygen concentration (Solomon, et al., 1984). However, it is thought that the hydrogen is a better indicator of reactivity, since it is present at about five times the level of oxygen on an atomic basis and can be more easily and accurately measured.

The upper solid line in Fig. II.A.9-4 is a "best fit" line drawn through the data for Kentucky No. 9 and Pittsburgh Seam bituminous chars. The lower solid line is a best fit line drawn through the Zap lignite chars. The differences in the values of T_{cr} with the extent of pyrolysis allows one to assess the importance of this parameter on reactivity. In the case of the Zap lignite, the range of T_{cr} from about 350°C to 525°C corresponds to a factor of ~ 500 in reactivity (assuming the 35 kcal/mole activation energy). In the case of the two bituminous coals, the range of T_{cr} from about 450°C to 575°C corresponds to a factor of ~ 40

Table II.A.9-2.

Key to Montana Rosebud Data in Figure II.A.9-3.

Datum No.	Reactor	Heating Rate[a] °C/s	Maximum Temperature °C	Residence Time[b] (s)	Pressure (psig)
1	TGA	0.5	900	---	0
2	EFR	10,000	1300	0.2	0
3	HPR	10,000	817	0.3	100
4	HTR	20,000	800	0.2	0
5	HPR	10,000	817	0.3	26
6	HTR	20,000	800	0.1	0
7	HTR	20,000	800	---	0
8	HTR	20,000	600	---	0

NOTES:

TGA Thermogravimetric Analyzer
EFR Atmospheric Pressure Entrained Flow Reactor
HPR High Pressure Entrained Reactor
HTR Heated Tube Reactor
a Heating rates are nominal
b Residence time at final temperature

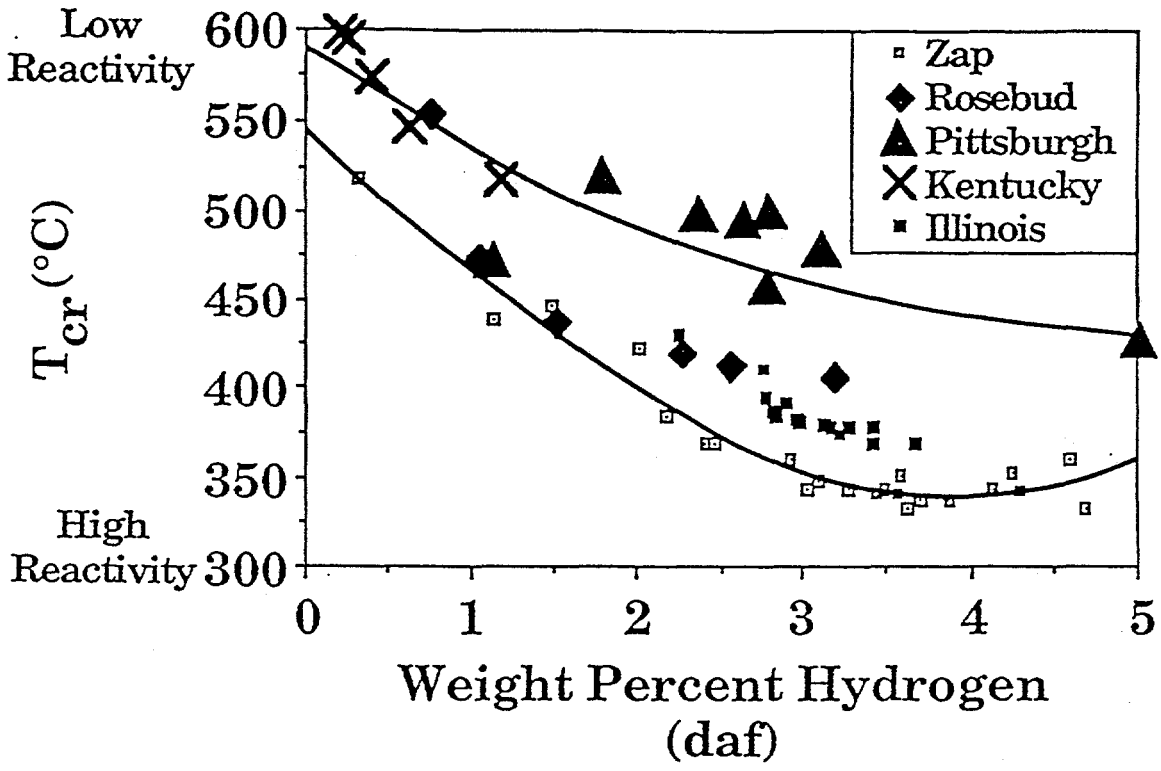

Figure II.A.9-4. Comparison of Reactivity for Chars from Five Various Ranks as a Function of Hydrogen Concentration. Tcr Varies Inversely with Reactivity.

in reactivity. Using the same method, one can track the maximum difference in reactivities with coal types as being a factor of 120 (350°C, 475°C) while the minimum difference is about a factor of 4 (525°C, 575°C).

Reactivity vs. Mineral Content - It is known that the vertical displacement of the curves in Fig. II.A.9-4. is at least partly due to the variations in catalytic activity of minerals. This effect has been observed in previous studies which have been reviewed by Mahajan and Walker (1978). The most reactive chars are for the Zap lignite which are known to have a high Na and Ca content. The results for T_{cr} versus daf hydrogen content for chars produced from demineralized Zap by the Bishop and Ward technique (Tichenor, et al., 1985) are similar to chars from bituminous coals (Serio, et al., 1989).

Reactivity vs. Surface Area - Our previous work has suggested that the rank differences in reactivity in Fig. II.A.9-4 are primarily due to differences in mineral content and not from differences in surface area (Solomon, et al., 1989b; Serio, et al., 1989; and Solomon, et al., 1988c). Similarly, the trends with the hydrogen concentration are due to changes in the molecular order (active site concentration) and not from changes in surface area.

The fact that reactivities differences between chars from different coals do not correlate well with BET surface area is not surprising. As discussed by Walker and coworkers (Radovic and Walker, 1983), it is the active surface area (ASA) as measured by oxygen chemisorption which is important. However, the utility of oxygen chemisorption as a technique for measuring the ASA of "young" chars in question (Suuberg, et al., 1986). In this work, we have not attempted to measure ASA's.

Reactivity vs. Burnout - Measurements have been made of T_{cr} versus the extent of burnout for chars from a Montana Rosebud and a Pittsburgh Seam coal (Solomon, et al., 1988d). In this case, the values of T_{cr} must be corrected for the increase in the ash content. The value of T_{cr} increases systematically with increasing burnout for both coals, which indicates that more reactive components are removed first (or that the burnout process anneals the remaining material).

Correlation of T_{cr} Measurements with High Temperature Combustion Reactivities - Of course the measurement of T_{cr} would not be of much good to those interested in p.f. combustion unless it can be shown that these measurements correlate with intrinsic reactivities measured at high temperatures. The T_{cr} measurement provides a temperature at which $df/dt = 0.001\ s^{-1}$. For a $\sim$ 60 μm mean diameter fraction of Montana Rosebud coal, the measured T_{cr} was 429°C (702K) while the measured initial CO_2 BET surface area was 152 m^2/g. The problems of using the BET surface area as a correlating parameter have been discussed previously (Serio, et al., 1989). However, since the intrinsic reactivity data in the literature have been derived using such measurements, this approach is consistent. The CO_2 area varies the least over a wide range of burnoffs, for most coal chars, and is used here. Using equation II.A.9-4, one would calculate $R_i = 1.1 \times 10^{-10} g/cm^2s$ at $T_p = 702K$. The most comprehensive compilation of intrinsic reactivity data for a range of carbons is that provided by Smith (1982). The correlation of Smith would predict a value of $R_i = 1.0 \times 10^{-11} g/cm^2s$. However, this correlation underpredicts the data for brown coal chars and lignites in this temperature range, so the agreement is actually within a factor of 2 of the relevant data in Fig. 9 of Smith (1982). The extrapolation to high temperatures can be done by using E = 35 kcal/mole which gives $R_i = 2 \times 10^{-4}\ g/cm^2s$ at $T_p = 1650K$. This estimate is about a factor of two lower than Smith's correlation and about a factor of two higher than his data for brown coal chars. A similar agreement is observed for the other chars that were studied. Consequently, it appears that the T_{cr} measurement is capable of giving meaningful results when extrapolated to high temperatures using an activation energy of E = 35 kcal/mole.

Recent work in our laboratory with a laminar coal flame experiment has shown a correlation of T_{cr} with the ignition point above the nozzle (Solomon, et al., 1988c) and with the interval of time required to achieve 100% burnout (Solomon, et al., 1989c).

Correlation of T_{cr} Measurements for Reactivity Modeling - As discussed in Section II.A.10, most of the work under the current contract has involved using the T_{cr} database to develop a char reactivity

submodel for use in a comprehensive entrained gasification and combustion code (Charpenay, et al. 1992 a,b, 1993). Since T_{cr} is inversely proportional to the reactivity, $1/T_{cr}$ was found to be a more appropriate quantity to use to develop correlations. Good linear correlations of $1/T_{cr}$ vs. the char hydrogen concentration were obtained for all of the coals examined, as shown in Fig. II.A.9-5. This includes some additional data which is not included in Fig. II.A.9-4. The points which fall below the bottom line for the Pittsburgh Seam coal are from chars which were produced at low heating rate in a TGA. For fluid coal, the pyrolysis heating rate can affect the reactivity by at least one order of magnitude.

Conclusion

A new reactivity test has been developed which allowed relative rates of reactivity to be determined for chars of widely varying reactivity. The method was applied to study the dependence of reactivity on coal properties and pyrolysis conditions. Reactivities are seen to decrease dramatically with decreasing aromatic hydrogen concentration. Reactivities were insensitive to pyrolysis heating rate for a lignite but were sensitive to heating rate for a bituminous coal. Mineral catalytic effects explain most of the rank variations. The test provides a measure of the reaction rate which agrees well with literature data for chars from similar coals. The measured intrinsic reactivities also extrapolate well to high temperature measurements if an activation energy of 35 kcal/mole is used. The test can also predict the reactivity differences between coals in a laminar coal flame experiment.

II.A.10. The Prediction of Coal Char Reactivity Under Combustion Conditions

The main objective of the char reactivity work under this contract was to develop a char reactivity submodel that could be used in a comprehensive code for entrained coal combustors and gasifiers. The requirement of a char reactivity model is to predict the reactivity of chars from a wide range of coals, over a wide range of temperatures, and for various degrees of burnoff. In order to predict intrinsic reactivity, correlations of reactivity with char hydrogen content, coal oxygen content and coal mineral content were used. A random pore model (high rank coals) and a volumetric model (low rank coals) were included to predict variations of intrinsic reactivity with burnoff. The correlations combined with those models gave good predictions of reactivity (within a factor of 2 to 4) and reactivity variations with burnoff (within 20%) for the range of chars studied.

In the pore diffusion regime, the model uses the Thiele modulus to calculate the reaction rates as a function of intrinsic rate (obtained using the correlations) and char properties such as porosity, tortuosity, and the mean pore radius. Predictions of reactivity required an estimate of the tortuosity and the mean pore radius. The tortuosity was kept constant at a value of 2. Using a value of 6Å (corresponding to the size of micropores) for the mean pore radius led to good predictions of the onset of diffusion limitations for low heating rate, fluid chars. For high heating rate chars, pore size distribution measurements showed that values of approximately 100Å were more appropriate. The corresponding predictions using this value gave a fairly good fit to the literature data investigated. This analysis shows that it may be possible to extend a low temperature reactivity model to high temperatures.

A complete description of this model appears in Charpenay et al. (1992a,b). The extension of the model to better account for the influence of char structure is discussed in Charpenay et al. (1993).

II.A.11. Analysis of the Argonne Premium Coal Samples by Thermogravimetric Fourier Transform Infrared Spectroscopy

We have developed a TG-FTIR instrument that combines thermogravimetric analysis (TGA) with evolved products analysis by Fourier Transform Infrared (FT-IR) spectroscopy. FT-IR analysis of evolved products has advantages over mass spectroscopy in allowing analysis of very heavy products and over gas chromatography in speed. The paper by Solomon et al. (1990a) describes the most recent improvements in the apparatus and presents is application in characterizing the Argonne premium coal samples. The TG-FTIR apparatus for pyrolysis, oxidation of pyrolysis products, and oxidation of the sample is described. To analyze coal, a sequence of drying, pyrolysis, and combustion is employed to

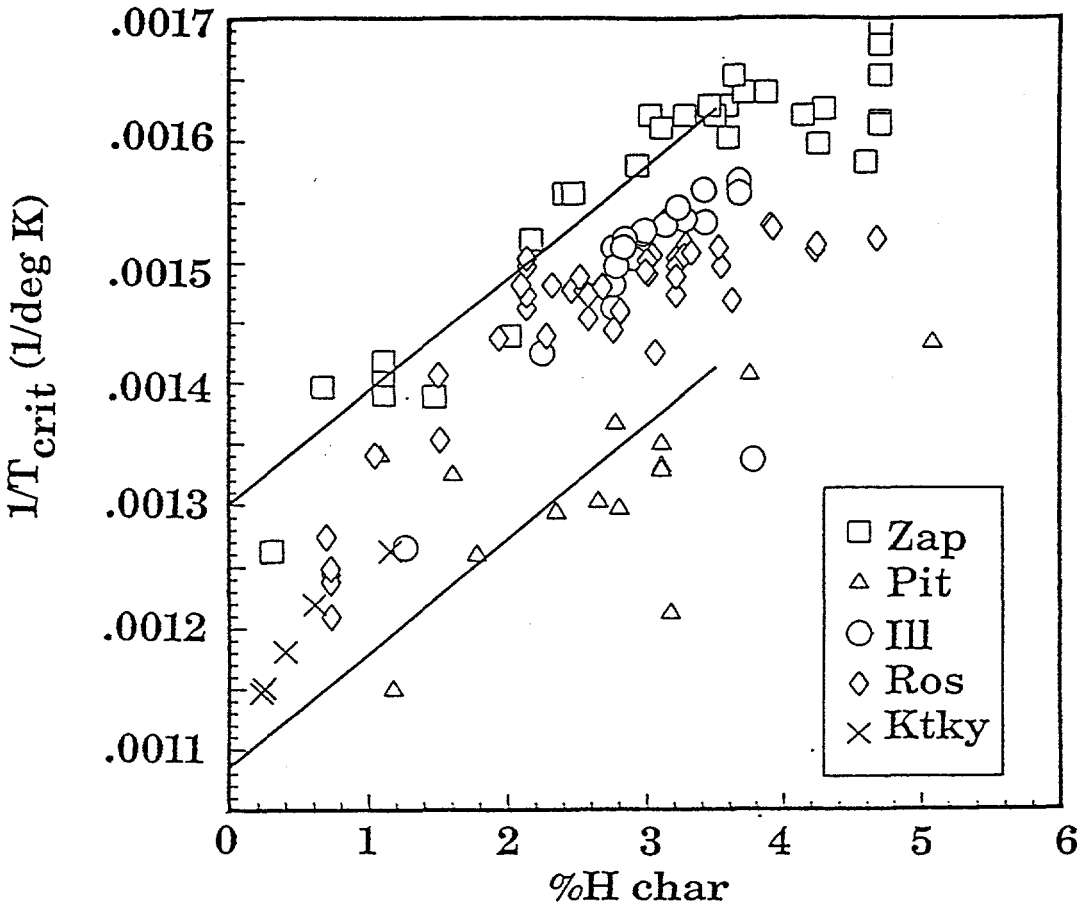

Figure II.A.9-5. Correlation of $1/T_{crit}$ with the Percent (daf) Hydrogen Content of the Char (H_{char}) for Zap, Rosebud, Illinois No. 6 and Pittsburgh No. 8 Coals.

obtain proximate analysis, volatile composition, volatile kinetics, and relative char reactivity. Pyrolysis results are presented for the eight Argonne coals, several demineralized coals, and two oxidized samples of Pittsburgh Seam coal. A kinetic analysis was applied to species evolution data collected at several different heating rates. There is a systematic variation in rate with rank. The rate for tar evolution from Pittsburgh Seam coal is in good agreement with that of Burnham et al. (1989) using a similar set of data. Analysis of the amounts of evolved products also show a systematic variation with rank consistent with the coal's elemental and functional group compositions. Postoxidation of the volatile products has been successful in providing elemental composition information on the volatile products as well as showing the evolution of H_2, which is not infrared active, and H_2S (in the postoxidized SO_2 profile), which is a weak infrared absorber. Oxidation of the char yields an ash amount as well as two measures of the char's reactivity, the oxygen absorbed by the char, and the temperature at which significant oxidation of the char occurs. This work is described in detail in Solomon et al. (1990a).

References for Subtask 2.a.

Annual Book of ASTM Standards, Sec. 5 Petroleum Products, Lubricants, and Fossil Fuels, Vol. 05.05 Gaseous Fuels; Coal and Coke, pp. 356-360 (1985)

Ashu, J.T., Nsakala, N.Y., Mahajan, O.P., and Walker, P.L., Jr.: Fuel, **57**, 251 (1978).

Baumann, H., and Moller, P., Erdol, Erdgas and Kohle, **44**, (1), 29-33 (1991).

Best, P.E., Carangelo, R.M., and Solomon, P.R., FT-IR Determination of Coal and Soot Particle Temperatures During Pyrolysis, ACS Div. of Fuel Chem. Preprtins, **29**, (6), 249 (1984).

Best, P.E., Carangelo, R.M., Markham, J.R., and Solomon, P.R., Extension of Emission-Transmission Technique to Particulate Samples Using FT-IR, Combustion and Flame, **66**, 47 (1986).

Bohren, C.F., and Huffman, D.R., Absorption and Scattering of Light by Small Particles, John Wiley & Sons, NY (1983).

Bose, A.C., Dannecher, K.M., and Wendt, J.O.L., Energy & Fuels, **2**, 301-308 (1988).

Boudou, J.P., Boulegue, J., Malechaux, L., Nip, M., de Leeuw, J.W., and Boon, J.J., Fuel, **66**, p 1558 (1987).

Burchill, P., Some Observations on the Variation of Nitrogen Content and Functionality with Coal Rank, Proceedings of the Int. Conf. on Coal Science, (J.A. Moulign, et. al., Eds.), Elsevier Science Publishers, BV Amsterdam, The Netherlands pp 5-8 (1987).

Burnham, A.K., Oh, M.S., Crawford, R.W., and Samoun, A.M., Energy & Fuels, **3**, 42 (1989).

Calkins, W.H., Hagaman, E., and Zeldes, H., Fuel, **63**, 1113 (1984a).

Calkins, W.H., Tyler, R.J., Fuel, **63**, 1119 (1984b).

Calkins, W.H., Fuel, **63**, 1125 (1984c).

Calkins, W.H., Hovsepian, B.K., Drykacz, G.R., Bloomquist, C.A.A., and Ruscic, L., Fuel, **63**, 1226 (1984d).

Calkins, W.H., Energy & Fuels, **1**, 59-64 (1987).

Carangelo, R.M., Solomon, P.R., and Gerson, D.J., Fuel, **66**, 960 (1987).

Charpenay, S., Serio, M.A., Solomon, P.R., The Prediction of Coal Char Reactivity Under Combustion Conditions, 24th Symposium (Int) on Combustion, The Combustion Institute, Pittsburgh, PA, 1189-1197 (1992).

Che, S.C., et al., Flash Pyrolysis Coal Liquefaction Process Development, Final Report for July 1976 to June 1978, DOE Report No. FE-2244-26 (1978).

Chen, S.L., Heap, M.P., Pershing, D.W., and Martin, G.B., Nineteenth Symposium (International) on Combustion, 1271-1280, The Combustion Institute, Pittsburgh, PA (1982).

Chiou, M.J. and Levine, H.B., Investigation of Structural Deformation of Coal Particles in Pyrolysis, Internal Report JAYCOR.

Essenhigh, R.H., *Chemistry of Coal Utilization*, (M.A. Elliott, Ed.), John Wiley & Sons, 2nd Supplementary Vol., p. 1162 (1981).

Essenhigh, R.H. and Farzan, H., Nineteenth Symposium (International) on Combustion, 1105-111, The Combustion Institute (1982).

Field, M.A., Combust. Flame, **14**, 237 (1970).

Foster, P.J. and Howarth, C.R. *Carbon*, **6**, 719, and references therein (1968).

Freihaut, J.D, Proscia, W.M., and Seery, D.J., ACS Div. Fuel Chem. Preprints, **33**(2), 262 (1988).

Gan, H., Nandi, S.P., and Walker, P.L., Jr., Fuel, **51**(4), 272 (1972).

Gorbaty, M.L. Kelemen, S.R., George, G.N., and Kwiatek, P.J., Fuel, **71**, 1255 (1992).

Huffman, G.P., Mitra, S., Hugguns, F.E., Shah, N., Vaidya, S., and Lu, F., Energy & Fuels, **5**, 574-581 (1991).

Jenkins, R.G., S.P. Nandi, and P.L. Walker, Jr., Fuel, **52**, 288 (1973).

Kelemen, S.R., Gorbaty, M.L., Vaughn, S.N., and George, G., Preprint, Am. Chem. Soc., Div. of Fuel Chem., **36** (3), 1225-1232 (1991).

Khan, M.R., Fuel, **68**, 1439 (1989).

Knight, R. A., Gissy, J., Onischak, M., Babu, S.P., Wooten, J.M., and Duthie, R.G., Development of an Advanced, Continuous Mild Gasification Process for the Production of Co-Products, Topical Report for Contract No. DE-AC21-87MC24266 (1990).

LaCount, R.B., Kern, D.G., King, W.P., Trulli, T.K., Walker, D.K., ASC Div. of Fuel Chem. Preprints, 1992, **37** (3), 1083 (1992).

Larandeau, N.M., Prog. Eng. Combust. Sci., **4**, 221 (1978).

Leslie, I.H., M. Jost, and C.H. Kruger, Combust. Flame, **78**, 195 (1989).

Litt, R.D., Paisely, M.A., and Tewksbury, T.L., Experimental Development of a Multi-Solid Fluidized-Bed Reactor Concept, Topical Report for Contract No. DE-AC21-87MC23293 (1990).

Mackie, J.C., Colket, M.B., and Nelson, P.F., Phys. Chem., **94**, 4099 (1990).

Mackie, J.C., Colket, M.B., Nelson, P.F., and Esler, M., Int. J. Chem. Kinetics, **23**, 733 (1991).

Mahajan, O.P., and Walker, P.J., Jr., *Analytical Methods for Coal and Coal Products*, (C. Karr, Ed.), Vol. II, Ch. 32, pp. 465-492, Academic Press (1978).

Mahajan, O.P., R. Yarzab, and P.L. Walker, Jr., Fuel, **57**, 643 (1978).

McKenzie, A., I.W. Smith, and G.A.D. Szpindler, J. Inst. Fuel, **47**, 75 (1974).

Mehldi Taghiei, M., Hugguns, F.E., Shah, N., and Huffman, G.P., Am. Chem. Soc., Div. Fuel Chem. Preprints, **36**, (2), 757-764 (1991).

Mitchell, R.E. and J.W. McLean, 19th Symposium (Int) on Combustion, The Combustion Institute, 1113 -1122 (1982).

Nelson, P.F., Fuel, **66**, 1264 (1987).

Nelson, P. F., Buckley, A. N. and Kelly, M. D., Twenty Forth Symposium (Int) On Combustion, The Combustion Institute, Pittsburgh, PA, 1259-1267 (1992).

Nsakala, N.Y., Patel, R.L., and Lao, T.C.: Final Report, Electric Power Research Institute, Report No. 1654-6 (1982).

Oh, M.S., Burnham, A.K., and Crawford, R.W., Am. Chem. Soc. Div. of Fuel Chem. Preprints, **33**. (1), 274 (1988).

Radovic, L.R., P.L. Walker, Jr., and R.G. Jenkins, Fuel, **62**, 849 (1983).

Scotti, L.J., et al., Char Oil Energy Development Interim Report No. 5, DOE Report No. FE-1212-5 (1975).

Serio, M.A., Hamblen, D.G., Markham, J.R., and Solomon, P.R., Kinetics of Volatile Product Evolution in Coal Pyrolysis: Experimental and Theory, Energy and Fuel, **1**, 138 (1987).

Serio, M.A., P.R. Solomon, R. Bassilakis, and E.M. Suuberg, ACS Div. of Fuel Chem. Prepr., **34**, (1), 9 (1989).

Smith, I.W, Combust. Flame, **17**, 421 (1971).

Smith, I.W., 19th Symposium (Int) on Combustion, The Combustion Institute, 1045-1065 (1982).

Solomon, P.R., Coal Structure and Thermal Decomposition, in *New Approaches in Coal Chemistry*, ACS Symposium Series, **169**, 61 (1981).

Solomon, P.R., Hamblen, D.G., Carangelo, R.M., and Krause, J.L., 19th Symposium (International) on Combustion/The Combustion Institute, Pittsburgh, PA, pp. 1139-1149 (1982).

Solomon, P.R., Hamblen, D.G., and Carangelo, R.M. Analytical Pyrolysis, (K.J. Voorhees, Ed.), Ch. 5, p. 121, Butterworths (1984).

Solomon, P.R., Hamblen, D.G., Carangelo, R.M., Markham, J.R., and Chaffee, M.R., Application of FT-IR Spectroscopy to Study Hydrocarbon Reaction Chemistry, ACS Div. of Fuel Chem. Preprints, **30** (1), 1 (1985a).

Solomon, P.R. and Hamblen, D.G. in *Chemistry of Coal Conversion*, (R.H. Schlosberg, Ed.), Ch. 5, p. 121, Plenum Press (1985b).

Solomon, P.R., Carangelo, R.M., Hamblen, D.G., and Best, P.E., Infrared Analysis of Particulates by FT-IR Emission/Transmission Spectroscopy, Applied Spectroscopy, **40** (6), 746 (1986a).

Solomon, P.R., Carangelo, R.M., Best, P.E., Markham, J.R., and Hamblen, D.G., Analysis of Particle Composition, Size and Temperature by FT-IR Emission/Transmission Spectroscopy, ACS Div. of Fuel Chem. Preprints, **31**, (1), 141 (1986b).

Solomon, P.R., Serio, M.A,. Carangelo, R.M., and Markham, J.R., Very Rapid Coal Pyrolysis, Fuel, **65**, 182, (1986c).

Solomon, P.R., Carangelo, R.M., Best, P.E., Markham, J.R., and Hamblen, D.G., The Spectral Emittance of Pulverized Coal and Char, 21st Symposium (Int) on Combustion, The Combustion Institute, Pittsburgh, PA, 437 (1986d).

Solomon. P.R., Carangelo, R.M., Best, P.E., Markham, J.R., and Hamblen, D.G., Analysis of Particle Emittance, Composition, Size, and Temperature for FT-IR Emission/Transmission Spectroscopy, Fuel, **66**, 897 (1987a).

Solomon, P.R., Hamblen, D.G., Serio, M.A., Smoot, L.D., and Brewster, S., Measurement and Modeling of Advanced Coal Conversion, First Annual Report, DoE/METC Contract No. DE-AC21-86MC23075 (1987b).

Solomon, P.R., Hamblen, D.G., Carangelo, R.M., Serio, M.A., and Deshpande, D.V., A General Model of Coal Devolatilization, Energy and Fuels, **2**, 405 (1988a).

Solomon, P.R., Hamblen, D.G., Carangelo, R.M., Serio, M.S., and Deshpande, D.V., Models of Tar Formation During Coal Devolatilization, Combustion and Flame, **71**, 137 (1988b).

Solomon, P.R., P.L. Chien, R.M. Carangelo, P.E. Best, and J.R. Markham, 22nd Symposium (Int) on Combustion, The Combustion Institute, 211-221 (1988c).

Solomon, P.R., Serio, M.A., Hamblen, D.G., Markham, J.R., Best, P.R., and Bassilakis, R., Chemical and Physical Develpoment of Char Particles During Devolatilization, DOE/METC Final Report under Contract No. DE-AC21-85MC22050 (1988b).

Solomon, P.R., Best, P.E., Yu, Z.Z., and Deshpande, G.V., ACS Div. of Fuel Chem. Prepr., **34,** (3), 895 (1989a).

Solomon, P.R., M.A. Serio, R.M. Carangelo, and R. Bassilakis, International Conference of Coal Science Proceedings, p. 67, IEA, Japan (1989b).

Solomon, P.R., M.A. Serio, D.G. Hamblen, L.D. Smoot, and B.S. Brewster, DOE/METC Third Annual Report under Contract No. DE-AC21-86MC23075 (1989c).

Solomon, P.R., Serio, M.A., Deshpande, G.V., and Kroo, E., Crosslinking Reactions During Coal Conversion, Energy and Fuel, **4**, 402 (1990a).

Solomon, P.R., Hamblen, D.G., Yu, Z., and Serio, M.A., Fuel, **69**, 754 (1990a).

Solomon, P.R., Serio, M.A., Carangelo, R.M., Bassilakis, R., Gravel, D., Bailargeon, M., Baudais, F., and Vail, G., Energy & Fuels, 4 (3), 319 (1990b).

Solomon, P.R., Best, P.E., Yu, Z.Z., and Charpenay, S., An Empirical Model for Coal Fluidity Based on a Macromolecular Network Pyrolysis Model, Energy and Fuel, **6**, 143 (1992).

Solomon, P.R., Hamblen, D.G., Serio, M.A., Yu, Z.Z., and Charpenay, S., A Characterization Method and Model for Predicting Coal Conversion Behavior, Fuel, **72** (4), 469 (1993).

Suuberg, E.M., Calo, J.M., and Mojtowciz, M.: ACS Div. of Fuel Chem. Prepr., **31**, (3), 186 (1986).

Tichenor, D.A., R.E. Mitchell, K.R. Hencken, and S. Niksa, 20th Symposium (Int) on Combustion, The Combustion Institute, 1213-1221 (1985).

Tyler, R.J., Flash Pyrolysis of Coals. Devolatilization of Bituminous Coals in a Small Fluidized Bed Reactor, Fuel, **59**, 218 (1980).

Users Guide for FG-DVC Model, PC version, Advanced Fuel Research, Inc., East Hartford, Connecticut, USA (February, 1992).

Usman Ghani, M., and Wendt, J.O.L. Twenty-Third Symposium (International) on Combustion, 1281-1288, The Combustion Institute, Pittsburgh, PA (1990).

Vorres, K.S., Users Handbook for the Argonne Coal Sample Program, (1989).

Wallace, S. Bartle, K.D., and Perry, D.L., Fuel, **68**, 1450 (1989).

Waters, B.J., R.E. Mitchell, R.G. Squires, and N.M. Laurendeau, 22nd Symposium (Int) on Combustion, The Combustion Institute, 17-27 (1988).

Wells, W.F., S.K. Kramer, L.D. Smoot, and A.U. Blackham, 19th Symposium (Int) on Combustion, The Combustion Institute, 1539-1546 (1982).

Whelan, J.K., Solomon, P.R., Deshpande, G.V., and Carangelo, R.M., Energy & Fuels, **2**, 65 (1988).

Zygourakis, K., Pyrolysis and Gasification of Coal Particles at High Temperatures, Proceedings of the Ninth Annual Gasification and Gas Stream Cleanup Systems Contractor's Review Meeting (1989).

II.B. SUBTASK 2.B. - FUNDAMENTAL HIGH-PRESSURE REACTION RATE DATA

Senior Investigators - Geoffrey J. Germane and Angus U. Blackham
Brigham Young University
Provo, Utah 84602
(801) 378-2355 and 6536

Student Research Assistants - Charles R. Monson, Gary Pehrson, and Kenneth Bateman

Introduction

Most of the coal currently being consumed is combusted in atmospheric pressure utility furnaces, but a large number of other processes are also being used and developed for either direct combustion of coal or conversion of coal into other products. A number of these processes, including coal gasification, operate at elevated pressure. Gas turbine and diesel engines, which typically use liquid petroleum fuels, operate at high pressures and prove to be candidates for coal fuel. Practical research is being conducted on the use of coal in these applications, yet little is known about the basic nature of coal combustion at elevated pressure. A great deal of research has been conducted on char combustion at atmospheric pressure but the data obtained by these experiments cannot be extrapolated to higher pressures because of the intricate coupling of transport phenomena and chemical kinetics during combustion. The effect of pressure on char reactions has been examined by only a few researchers during the past 25 years. These studies have been limited by experimental apparatus and have produced conflicting results. Careful research is needed to characterize the fundamental effects of pressure on char oxidation.

To this end a high pressure facility was designed and constructed for use in both preparing char and carrying out fundamental char oxidation experiments. Chars were prepared in sufficient quantities for oxidation tests and oxidation experiments were conducted at both atmospheric and elevated pressures. Simultaneous in-situ measurements of particle size, velocity and temperature in a controlled temperature environment were made for char particles for a range of oxygen partial pressures and total pressures.

Objectives

The overall objectives of this subtask are to determine the effects of pressure on the mass reactivities and reaction rates of coal chars combusting in oxidizing environments at high temperatures.

Specific objectives for the project included:

1. Design, construct and characterize a high-pressure, controlled-profile (HPCP) drop tube furnace for char preparation and oxidation studies at atmospheric and high pressure.

2. Prepare and characterize chars from the coals selected for this study, using the HPCP for char production.

3. Conduct high pressure and atmospheric oxidation tests in the HPCP reactor with chars produced from several of the coals selected for study.

Accomplishments

Three components of the subtask have been identified to accomplish the objectives outlined above: 1) design and construction of a laminar-flow, high-pressure, controlled-profile (HPCP) reactor, 2)

char preparation at high temperature and high pressure, and 3) determination of the kinetics of char-oxygen reactions at high pressure.

High Pressure Facility

The controlled conditions required for high temperature, pulverized coal char oxidation experiments place great demands on a test facility. Not only must the initial heating rates (10^4-10^5 K/s) and high particle temperatures (1700-2200 K) encountered in pulverized fuel combustors be simulated, but facility temperatures must be controllable over a wide range. It is also desired to maintain constant particle temperature during the oxidation process. The particle reaction must proceed in a consistent manner, with quenching occurring at various stages during the short time of particle burnout (<200 ms). The temperature and composition of the gas surrounding a particle must also be known and variable. The overall conditions of the oxidation process must allow subsequent correction for mass transfer effects, limiting experiments to single particles rather than group events. Also required is the ability to measure particle properties, especially temperature, during the reaction. The difficulties associated with implementing these requirements were compounded in the present study by the additional requirement of high-pressure operation.

A High-Pressure, Controlled temperature Profile (HPCP), drop-tube reactor was designed and constructed as part of this study for use in both devolatilization and char oxidation tests. The reactor has the following capabilities: pressure from 1 to 30 atm, gas temperature from 1000 to 1700 K, controllable temperature profile along the reaction tube length, particle residence times from 30 to 1000 ms, variable gas compositions of inert and oxidizing gases, and optical access ports for *in-situ* diagnostics. Fig. II.B-1 shows a cross-sectional view of the HPCP reactor. A particle imaging system, providing *in-situ* measurement of individual particle temperature, size and velocity was developed for use in conjunction with the reactor. The instrument was patterned after a pyrometer developed at Sandia National Laboratories (Tichenor et al., 1984; Niksa, et al., 1984), and further by Wells and Smoot (1989) with modifications made to allow the measurement of smaller (30 to 150 μm), cooler particles and to allow proper functioning with the heated wall reactor. Details of the HPCP reactor, the optical pyrometer and other components of the high-pressure facility were presented in progress reports for this study (Solomon et al.).

Char Oxidation Experiments

Approximately 100 oxidation experiments were performed with two bituminous coal chars. The bulk gas O_2 and total pressure ranges covered in the experiments were larger than any reported in the literature. Independent measurement of both particle temperature and reaction rates allowed an internal check of the data consistency and insight into the products of combustion. Details of the experiments and the results follow.

Char Preparation - Char oxidation experiments were performed with three fuels: two size fractions of UT Blind Canyon HVB coal (63-74 μm, 37-44 μm) and one size fraction of Pittsburgh HVA coal (63-74 μm). These are common U.S. coals that have been used in a number of char oxidation studies and are included in the Penn State, the Department of Energy and the Argonne National Laboratory coal banks. They are also standard ACERC coals. The UT coal was obtained from the Huntington power plant and the Pittsburgh coal was obtained from Argonne National Laboratories as tailings from the premium sample preparation process.

Samples of the coals were ground, dried and size-classified with a combination of sieving and aerodynamic classification (using a Vortec classifier) to produce tight size fractions of 200x230 mesh (63-74 μm) and 325x400 mesh (37-44 μm). The size fractions were verified by scanning electron microscope

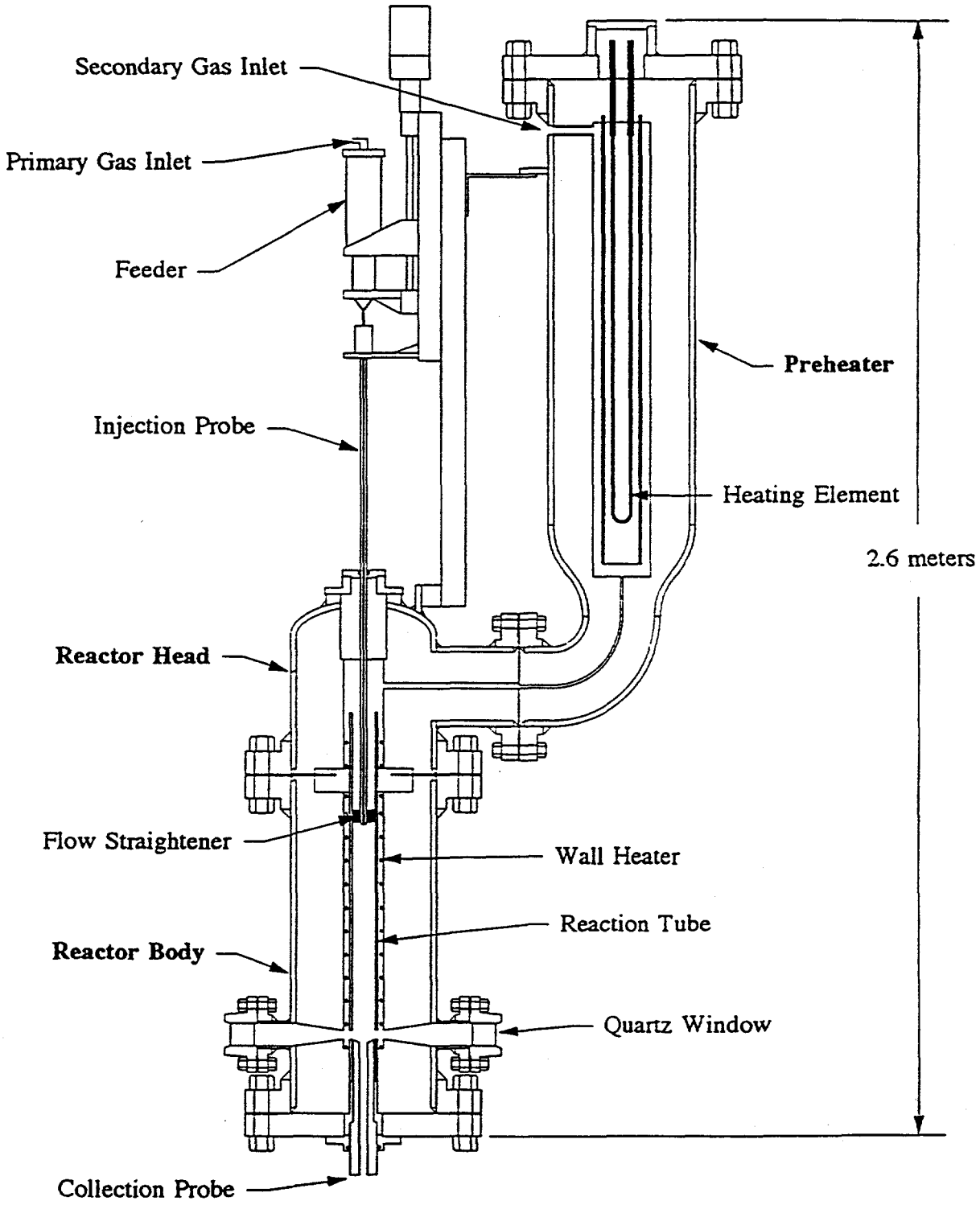

Figure II.B-1. Reactor cross section.

(SEM) and Coulter Counter measurements. Figure II.B-2 shows SEM photographs of each of the three coals along with their respective size histograms from the Coulter measurements. The sizing is seen to be excellent for the larger size fractions while the smaller size fraction exhibits a wider distribution, including a portion of smaller fines. Proximate and ultimate analyses, performed according to ASTM standards, are listed in Table II.B-1 for each of the coals.

Chars for the oxidation experiments were prepared in the HPCP furnace in a nitrogen environment. Since devolatilization conditions greatly affect char characteristics, all of the chars were prepared at the same reactor conditions. These conditions, chosen to produce complete devolatilization, were as follows: atmospheric pressure, wall and gas temperatures of 1500 K, an initial particle heating rate of 10^4 K/s (calculated using gas and wall temperature measurements), and a particle residence time of 300 ms. A number of properties for each of the resulting chars are listed in Table II.B-2 and SEM photographs and histograms are shown in Fig. II.B-3. In each case, the original coal softened during devolatilization, rounding the sharp edges and producing char particles that were quite spherical. The predominant structure for both UT chars was a 'lacy-cenosphere' type particle with no appreciable swelling. The mean size of the 70 μm UT char appears to have decreased somewhat, likely a result of the rounding of the nonspherical coal. The mean size of the 40 μm UT char was essentially unchanged, as were the distributions for both UT chars. The Pitt. char, on the other hand, exhibited thin and thick wall cenosphere formation with noticeable swelling. Its size distribution also widened substantially. While all of the raw coals had similar densities, the apparent density of the Pitt. char (0.43 g/cc) was about half that of the UT chars (0.80 and 0.86 g/cc).

Experimental Conditions - In order to obtain accurate results, a number of requirements pertaining to the particle temperature history had to be met. In the analysis of the results, it was assumed that the particle temperature was constant as it passed through the reaction zone. In order to approach this in the actual experiments, the gas temperature had to be carefully controlled. It was required that the preheated secondary flow enter the reaction zone somewhat hotter than the desired gas temperature to provide a rapid heatup of the primary gases and particles. Also, the temperatures of the gases and the particles were required to rapidly drop at the end of the reaction zone, upon entry into the collection probe. Conformance to these temperature requirements was monitored using a thermocouple probe to measure the gas temperature profiles before the experiments were performed.

The particle temperature history was also required to be similar for all particles during a given test. Because the gas motion was developing from plug flow to laminar flow, the gas and particle velocities at the reaction tube axis were greater than at some off-axis location. Particle dispersion was, therefore, held to a minimum so that all particles would experience approximately the same residence time. The particle dispersion was visually observed through the reactor windows and seldom ever approached 1 cm over a reaction length of 0.75 m.

Another requirement for reliable measurements was a constant oxygen concentration in the bulk gas. In order to ensure that this concentration was not affected by particle reactions, it was required that the char feed rate be at least 100 times smaller than the gas flow rate (Annamalai and Ramalingham, 1987). The char feedrate was 2 cc/hr (1.7 g/hr for the UT chars and 0.9 g/hr for the Pitt. char) for all of the tests and the slowest gas flow rate was 12 SLPM (850 g/hr), easily meeting the requirement. The low feedrate was also necessary to produce the small particle loading required by the optical pyrometer.

The plan for the char oxidation experiments consisted of a number of atmospheric pressure tests to both establish a baseline for the effect of pressure and to validate the procedure by comparison with other published data. These atmospheric tests then followed by higher pressure tests designed to allow examination of the effect of total pressure on the char oxidationprocess. The following parameters were varied during the experiments (with the corresponding number of levels shown in parentheses): fuel type (2), fuel size (2), total pressure (4), reactor temperature (3), bulk O_2 composition (3), and burnoff (3). An extensive test set was performed with the 70 μm UT char to provide a detailed description of the effects of

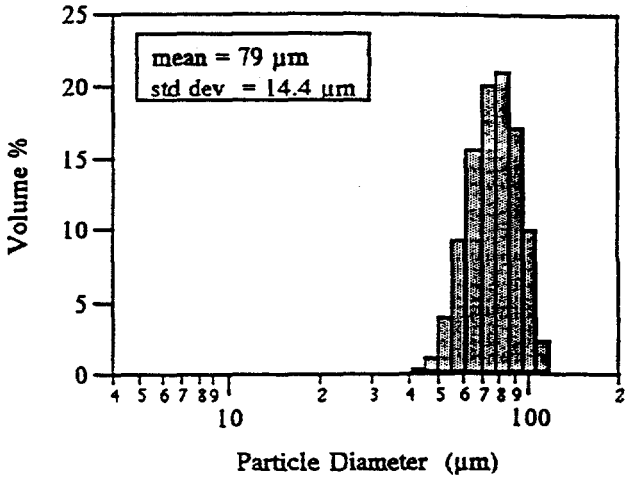

(a)

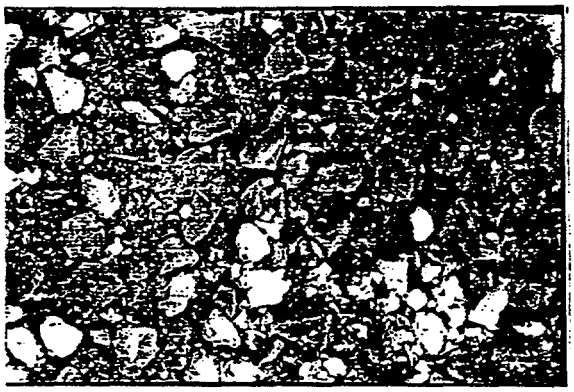

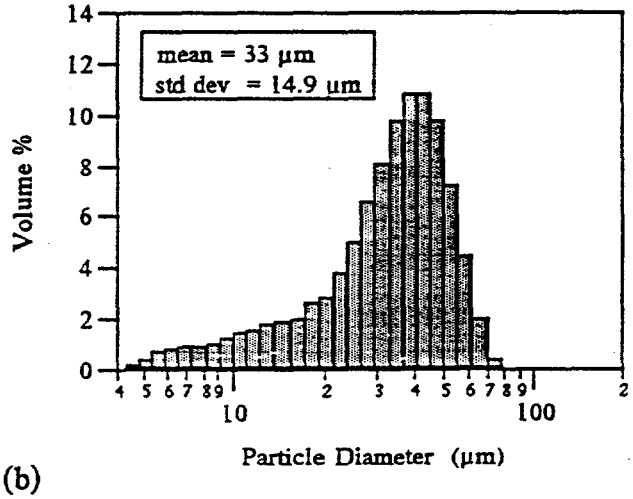

(b)

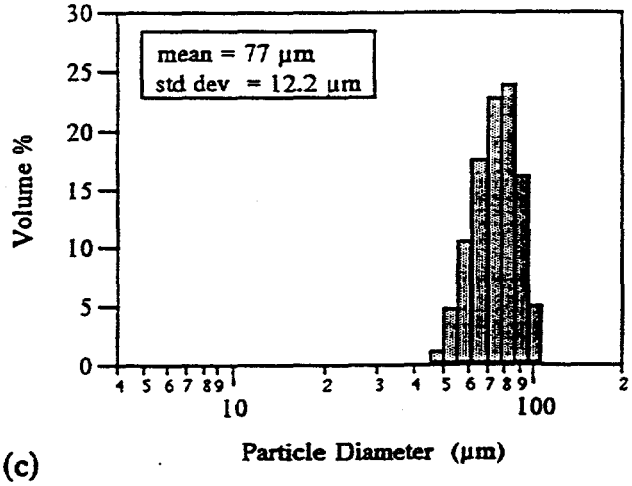

(c)

Figure II.B-2. SEM photographs and size histograms of the size- classified coals. a) 63-74 µm UT, b) 37-44 µm UT, c) 63-74 µm Pitt.

TABLE II.B-1
COAL ANALYSIS

Char	Proximate (%)				Ultimate (%)				
	Moisture	Volatiles	Carbon	Ash	C	H	N	S	O
UT (63-74 mm)									
UT (37-44 mm)									
Pitts. (63-74 mm)									

TABLE II.B-2

CHAR PROPERTIES

Char	Char Yield[1]	H/C	Ash Fraction (daf)	Apparent Density (g/cc)	Particle Diameter (mean, μm)[2]
UT (63-74 μm)	0.57	0.016	0.335	0.804	64
UT (37-44 μm)	0.57	0.016	0.236	0.860	36
Pitts. (63-74 μm)	0.64		0.248	0.431	73

1. m/mo

2. Calculated from $d_p = d_{p_o}\left(\frac{m/m_o}{\rho/\rho_o}\right)^{1/3}$

pressure on not only the reactivity and reaction rates of the char but also on the char's physical characteristics. The other chars were then tested at a limited number of conditions to observe their general pressure behavior. The experimental conditions for the three test sets are listed in Tables II.B-3 to II.B-5.

Because the burning behavior of the char was unknown over the wide range of conditions called for in the experimental plan, the particle residence length could not be specified beforehand. Determination of the length was made at the time of testing for each test condition in the following manner. The injection probe was initially positioned so its exit could be viewed through the optical access of the reactor. The probe was then raised until the ignition point of the particles was observed and this distance, referred to hereafter as the ignition distance, was recorded. The probe was then raised further until complete burnout of the particles was observed. Intermediate injection probe heights were then chosen to provide a range ofburnoffs. The ignition distance varied from near zero to several cm depending mainly on the reactor temperature and bulk O_2 concentration.

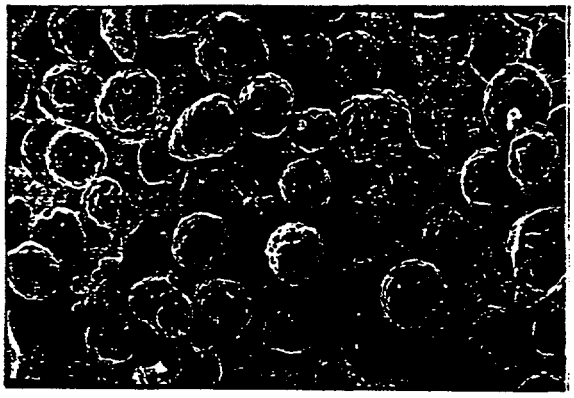

100 µm (x 130)

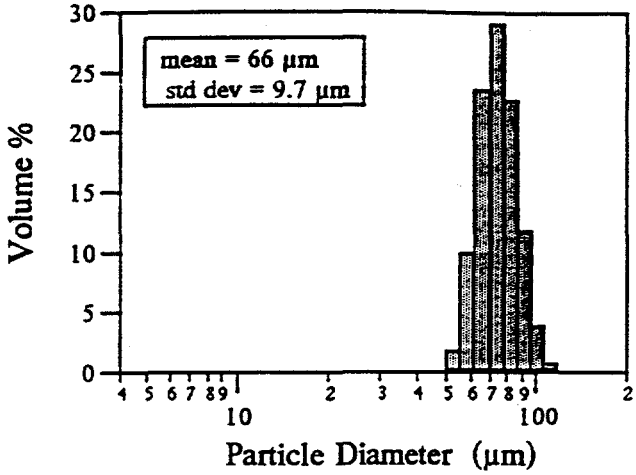

(a)

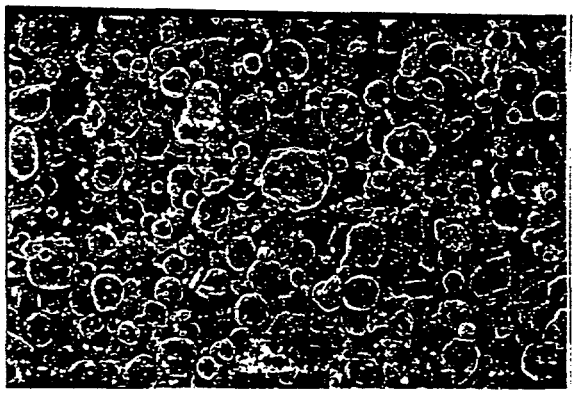

100 µm (x 130)

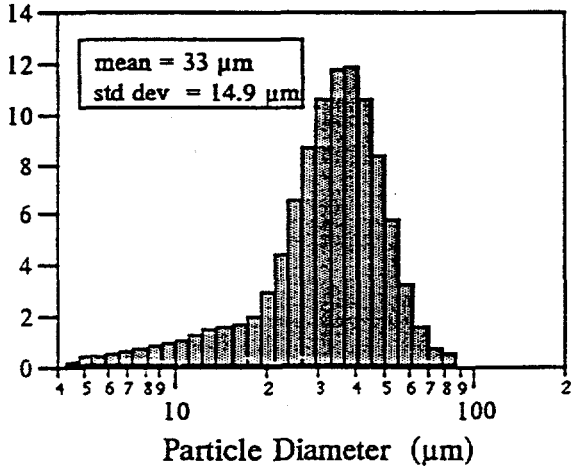

(b)

100 µm (x 130)

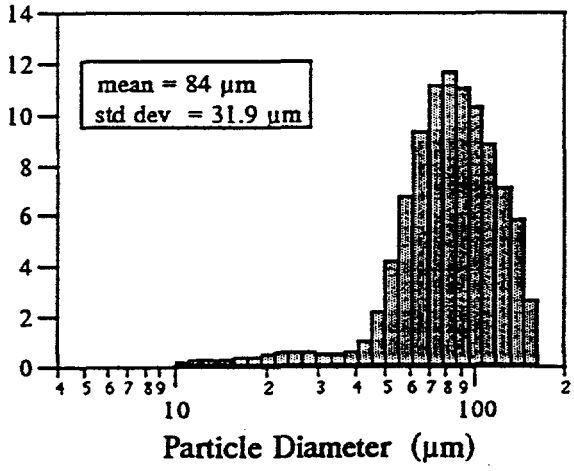

(c)

Figure II.B-3. SEM photographs and size histograms of the prepared chars. a) 63-74 µm UT, b) 37-44 µm UT, c) 63-74 µm Pitt.

TABLE II.B-3

70 μm UT CHAR EXPERIMENTAL CONDITIONS AND OVERALL RESULTS

Test	IP [1]	RL [2] (cm)	Pg (atm)	O_2 Conc (%)	T_p (K)	T_g (K)	T_w (K)	v_p (m/s)	t_r (ms)	B (%)	q_m [3]	q_a [4]	k_c [5]	χ	Sample
U1.1	U	7.5	0.92	4.40	—	1145	1143	1.1	68	9.2	1.43	—	—	—	1-53
U2.1	C	7.0	0.93	10.0	1550	1120	1100	1.19	59	15.4	2.84	2.50	9.54	0.14	1-8
.2	U	7.5	0.97	10.2	1621	1145	1143	0.94	80	38.2	5.92	4.68	19.7	0.26	1-25
.3	U	9.5	0.96	10.0	1646	1145	1143	1.00	95	49.2	6.87	5.13	22.5	0.29	1-24
U3.1	C	7.0	1.0	21.0	1827	1120	1100	1.08	64	57.3	12.4	8.85	22.9	0.22	1-7
.2	U	6.5	0.95	21.0	1853	1145	1143	1.10	59	75.3	20.4	13.0	37.7	0.32	1-22
.3	U	7.5	0.95	21.0	1819	1145	1143	1.13	66	63.0	13.9	9.59	25.9	0.24	1-20
.4	U	10.5	0.95	21.0	1815	1145	1143	1.19	88	70.3	12.3	8.12	21.2	0.20	1-21
.5	U	10.5	0.96	21.0	1804	1145	1143	1.05	100	83.4	14.3	8.66	22.9	0.21	1-23
.6	U	10.5	0.94	21.0	1953	1145	1143	1.12	94	73.6	12.4	8.02	21.0	0.20	1-47
.7	U	10.5	0.92	21.0	1942	1145	1143	1.11	95	78.1	13.5	8.47	22.7	0.21	1-50
.8	U	10.5	0.92	21.0	1962	1145	1143	1.07	98	68.4	10.6	7.08	18.4	0.18	1-51
.9	U	10.5	0.91	21.0	1962	1145	1143	1.08	97	74.1	12.1	7.80	20.7	0.19	1-52
U4.1	C	10.0	0.95	10.3	1672	1130	1130	1.21	83	45.6	7.15	5.44	23.3	0.29	1-5
U5.1	C	5.0	0.95	21.0	1892	1130	1130	1.19	42	46.6	14.5	11.0	30.0	0.27	1-4
.2	C	9.0	0.92	21.0	1812	1130	1130	1.23	87	64.6	15.1	9.41	25.9	0.23	1-12
.3	C	9.0	0.90	21.0	1812	1130	1130	1.04	73	79.1	13.0	8.89	24.0	0.22	1-9
.4	C	13.0	0.94	21.0	1846	1130	1130	1.23	106	70.4	10.3	6.79	17.2	0.17	1-3
U6.1	U	1.0	0.92	5.0	1659	1462	1462	1.35	78	0.0	—	—	—	—	1-48
.2	U	4.0	0.92	4.7	1704	1462	1462	1.51	26	23.3	10.0	8.49	—	0.90	1-49
U7.1	C	7.0	0.90	10.0	1769	1450	1428	0.98	71	57.0	11.2	8.00	38.7	0.39	1-11
.2	U	5.5	0.99	10.1	1817	1462	1469	0.87	63	65.3	15.3	10.4	52.9	0.49	1-29
.3	U	8.5	1.00	10.2	1865	1462	1469	0.86	99	59.9	—	—	—	—	1-30
.4	U	11.5	1.01	10.0	1829	1462	1469	0.94	122	85.8	12.3	7.32	30.3	0.34	1-31
U8.1	C	7.0	0.89	21.0	1970	1450	1428	0.96	73	87.0	21.1	12.4	35.0	0.27	1-10
.2	U	6.5	0.93	21.0	1951	1462	1469	1.23	52	68.4	19.7	13.2	36.9	0.29	1-26
.3	U	8.0	0.93	21.0	2014	1462	1469	0.96	83	86.7	18.4	10.9	28.9	0.24	1-27
.4	U	9.5	0.93	21.0	2017	1462	1469	1.00	95	89.5	17.1	9.91	25.9	0.21	1-28
U9.1	U	3.5	0.91	0.0	—	1143	1145	—	35	0.0	—	—	—	—	1-16
.2	U	3.5	0.95	0.0	—	1462	1469	—	35	0.0	—	—	—	—	1-19
U10.1	C	20.0	5.00	5.00	—	1100	1100	1	200	0.0	—	—	—	—	1-14
U11.1	C	10.0	4.84	9.95	1694	1100	1100	1.01	99	66.9	10.2	7.10	15.7	0.40	1-13
.2	U	8.5	5.12	10.2	1626	1131	1109	1.11	77	46.6	7.89	6.11	12.6	0.33	1-32
.3	U	11.5	5.15	10.1	1642	1131	1109	1.00	115	59.8	7.42	5.35	10.2	0.29	1-33
.4	U	14.5	5.15	10.1	1635	1131	1109	1.02	142	66.0	6.94	4.83	8.84	0.26	1-34
U12.1	U	6.5	5.21	21.0	1849	1131	1109	1.21	54	80.0	24.8	16.0	21.3	0.39	1-35
.2	U	8.0	5.32	21.0	1916	1131	1109	1.16	69	74.1	17.1	11.4	13.2	0.28	1-36
.3	U	9.5	5.38	21.0	1902	1131	1109	1.29	74	87.4	24.1	14.8	18.4	0.36	1-37
U13.1	U	8.5	5.30	4.20	1564	1136	1266	0.71	120	55.0	6.34	4.70	—	0.58	1-45
.2	U	12.5	5.00	4.00	1562	1136	1266	0.78	160	58.4	5.15	3.75	24.3	0.49	1-46
U14.1	U	7.5	5.26	10.1	1783	1336	1266	0.94	80	86.2	19.0	11.8	30.9	0.57	1-41
.2	U	9.5	5.26	10.1	1809	1336	1266	0.90	106	91.5	16.0	9.58	19.9	0.46	1-42
.3	U	11.5	5.26	10.0	1815	1336	1266	0.85	135	85.2	11.0	6.87	12.3	0.33	1-43
U15.1	U	6.5	5.25	21.0	2017	1336	1266	1.01	64	84.8	22.9	14.3	17.1	0.32	1-38
.2	U	8.0	5.33	21.0	2072	1336	1266	1.00	80	90.7	20.7	12.5	14.2	0.28	1-39
.3	U	9.5	5.31	21.0	2128	1336	1266	0.98	97	96.1	19.1	11.1	12.3	0.24	1-40
U16.1	U	3.5	4.88	0.0	—	1131	1109	—	35	0.0	—	—	—	—	1-17
.2	U	3.5	5.50	0.0	—	1336	1266	—	35	0.0	—	—	—	—	1-18
U17.1	U	6.5	9.86	5.0	1404	1006	726	0.49	133	41.7	3.97	3.14	8.68	0.40	1-58
.2	U	9.5	9.75	5.0	1424	1006	726	0.49	194	45.6	3.05	2.37	5.04	0.30	1-29
U18.1	U	6.5	9.84	10.0	1721	1006	726	0.52	125	51.8	5.59	4.22	5.22	0.25	1-56
.2	U	6.5	10.4	10.0	1622	1006	726	0.53	123	66.9	8.17	5.70	8.23	0.33	3-7
.3	U	6.5	10.4	10.0	1637	1006	26	0.49	133	60.2	6.48	4.69	6.12	0.28	3-8
.4	U	6.5	10.4	10.2	1643	1006	726	0.53	123	65.7	7.95	5.61	7.86	0.33	3-9
.5	U	6.5	10.4	10.0	1639	1006	726	0.52	125	69.3	8.48	5.84	8.38	0.34	3-10
.6	U	8.5	9.79	10.1	1687	1006	726	0.65	131	78.6	9.90	6.44	9.42	0.37	1-57
U19.1	U	5.5	10.0	21.0	1801	1006	726	0.65	85	52.5	—	—	—	—	1-54
.2	U	6.5	9.87	21.0	1938	1006	726	0.73	89	87.5	17.5	10.8	9.00	0.28	1-55
U20.1	U	7.5	10.2	5.0	1465	1173	858	0.49	153	39.8	3.25	2.59	5.48	0.30	1-61
.2	U	10.5	10.2	5.0	1540	1173	858	0.51	206	61.2	4.28	3.09	7.00	0.35	1-60

TABLE II.B-3 (CONTINUED)

Test	IP [1]	RL^2 [2] (cm)	Pg (atm)	O_2 Conc (%)	T_p (K)	T_g (K)	T_w (K)	v_p (m/s)	t_r (ms)	B (%)	q_m^3	q_a^4	k_c^5	χ	Sample
U21.1	U	8.5	10.2	10.0	1706	1173	858	0.63	135	82.6	10.4	6.60	9.24	0.35	1-62
.2	U	10.5	9.95	10.0	1759	1173	858	0.70	150	90.2	11.0	6.64	8.98	0.35	1-63
U22.1	U	6.5	10.0	21.0	1824	1173	858	0.56	116	—	—	—	—	—	1-65
.2	U	7.5	10.1	21.0	2025	1173	858	0.60	125	96.9	15.0	8.64	6.75	.20	1-64
U23.1	U	6.5	15.4	5.0	1328	987	631	0.24	271	23.4	0.98	0.84	1.07	0.11	3-6
.2	U	8.5	15.5	5.0	1376	987	631	0.25	340	43.0	1.61	1.27	1.72	0.16	3-5
U24.1	U	6.5	15.3	10.0	1545	987	631	0.25	260	70.2	4.16	2.84	2.74	0.17	3-3
.2	U	8.5	15.1	10.0	1592	987	631	0.30	283	80.7	4.77	3.06	2.98	0.18	3-4
U25.1	U	6.5	15.4	21.0	1864	987	631	0.29	224	73.0	5.13	3.45	2.03	0.09	3-1
.2	U	8.5	15.3	21.0	1914	987	631	0.34	250	92.8	6.93	4.11	2.45	0.11	3-2

1. Injection Probe: C - cooled, U - uncooled
2. Reaction Length
3. Mass Reactivity (g/g • s)
4. Area Reactivity($g/cm^2 \cdot s$) $\cdot 10^{-3}$
5. Reaction Rate Coefficient $(g/cm^2 \cdot s)(1/atm)^{0.5} \cdot 10^{-3}$

TABLE II.B-4

40 μm UT CHAR EXPERIMENTAL CONDITIONS AND OVERALL RESULTS

Test	IP [1]	RL^2 [2] (cm)	Pres (atm)	O_2 Conc (%)	T_p (K)	T_g (K)	T_w (K)	v_p (m/s)	t_r (ms)	B (%)	q_m^3	q_a^4	k_c^5	χ	Sample
U26.1	C	8.0	0.93	21.0	1820	1120	1100	1.22	66	57.7	12.4	5.41	12.9	0.08	2-2
.2	U	6.5	0.97	21.0	—	1145	1143	—	67	61.2	13.2	5.65	13.2	0.08	2-5
.3	u	9.5	0.96	21.0	1827	1145	1143	0.96	99	76.1	12.4	4.85	11.3	0.07	2-6
.4	u	12.5	0.96	21.0	1824	1145	1143	0.98	128	78.4	5.05	1.94	4.41	0.03	2-7
U27.1	C	4.5	0.90	21.0	1930	1428	1450	0.91	49	70.4	22.0	8.91	22.1	0.11	2-1
.2	u	6.5	0.90	21.0	1931	1469	1462	1.02	64	90.4	25.9	9.17	22.7	0.11	2-8
.3	u	7.5	0.97	21.0	1988	1469	1462	0.87	86	94.2	20.7	7.12	17.2	0.09	2-9
U28.1	U	6.0	5.16	21.0	1843	1131	1109	1.23	49	63.2	18.9	8.26	8.60	0.11	2-10
.2	U	8.5	5.04	21.0	1906	1131	1109	1.12	76	84.8	19.4	7.49	7.78	0.10	2-11
U29.1	U	6.5	5.32	21.0	1976	1336	1266	1.52	43	92.5	40.2	14.8	15.8	0.18	2-12
.2	U	9.5	5.32	21.0	2025	1336	1266	1.51	63	97.5	30.2	10.7	11.0	0.13	2-13

1. Injection Probe: C - cooled, U - uncooled
2. Reaction Length
3. Mass Reactivity (g/g • s)
4. Area Reactivity ($g/cm^2 \cdot s$) $\cdot 10^{-3}$
5. Reaction Rate Coefficient $(g/cm^2 \cdot s)(1/atm)^{0.5} \cdot 10^{-3}$

TABLE II.B-5

70 μm PITT. CHAR EXPERIMENTAL CONDITIONS AND OVERALL RESULTS

Test	IP [1]	RL [2] (cm)	Pres (atm)	O_2 Conc (%)	T_p (K)	T_g (K)	T_w (K)	v_p (m/s)	t_r (ms)	B (%)	q_m [3]	q_a [4]	k_c [5]	χ	Sample
P1.1	U	6.0	0.93	10.0	1755	1335	1330	1.26	48	24.0	5.68	4.80	19.4	0.25	1-3
.2	U	11.0	0.93	10.0	1780	1335	1330	1.40	79	46.0	7.56	5.74	23.9	0.29	1-4
P2.1	U	8.0	0.94	21.0	1900	1335	1330	1.24	65	66.3	15.4	10.4	28.0	0.24	1-1
.2	U	13.0	0.93	21.0	1893	1335	1330	1.37	95	78.8	13.7	8.56	22.3	0.20	1-2
P3.1	U	7.0	0.91	10.0	1757	1460	1450	1.39	50	12.3	—	—	—	—	1-7
.2	U	11.0	0.91	9.9	1799	1460	1450	1.35	81	—	—	—	—	—	1-8
P4.1	U	7.0	0.92	21.0	1971	1460	1450	1.51	46	60.4	18.7	13.1	36.9	0.29	1-5
.2	U	11.0	0.91	21.0	2012	1460	1450	1.42	77	80.9	17.6	10.8	29.2	0.24	1-6
P5.1	U	7.0	9.97	10.0	1746	1100	850	0.66	106	40.0	4.72	3.76	4.44	0.21	1-9
.2	U	11.0	10.1	9.9	1725	1100	850	0.64	172	29.5	—	—	—	—	1-10
P6.1	U	7.0	10.0	21.0	2011	1100	850	0.96	73	70.5	14.9	10.2	8.27	0.25	1-11
.2	U	10.0	10.0	21.0	2088	1100	850	0.84	119	86.4	12.8	7.93	6.15	0.19	1-12
P7.1	U	10.2	10.2	10.0	1669	1270	930	0.92	76	63.8	12.3	8.71	15.8	0.45	1-15
.2	U	10.3	10.3	10.0	1742	1270	930	0.87	115	78.4	11.2	8.30	10.2	0.37	1-16
P8.1	U	10.2	10.2	21.0	1936	1270	930	0.99	56	82.2	25.1	16.0	14.5	0.37	1-13
.2	U	10.2	10.2	21.0	2081	1270	930	0.98	77	92.2	22.2	13.2	11.0	0.30	1-14

1. Injection Probe: C - cooled, U - uncooled
2. Reaction Length
3. Mass Reactivity (g/g • s)
4. Area Reactivity (g/cm^2• s) •10^{-3}
5. Reaction Rate Coefficient(g/cm^2• s)(1/atm)$^{0.5}$ •10^{-3}

Experimental Results - Measurements taken during each test included reaction tube temperatures, bulk gas O_2 concentration, total pressure, reaction length, and individual particle temperature, size, and velocity. Gas temperatures were obtained for each reactor condition before the testing was performed. Subsequent analysis of the char residue included measurement of the ash content, elemental analysis of Ti, Al, C, and H, bulk density, true density, and N_2 surface area. Mass and area reactivities and apparent kinetic coefficients were determined for each of the fuels. The overall results for each of the tests are listed in Tables II.B-3 to II.B-5.

Analysis of Test Results

Detailed analyses of char oxidation measurements were conducted for the three fuels used. The analyses include char composition, char structure, char residence time and burnoff, and char reactivity.

Ash and Elemental Analyses - Ash and elemental analyses were performed on the residual char from each test. The fraction of ash in a given sample was determined by oxidizing the sample in a muffle furnace until only the ash component remained. Comparison was then made between the weight of the original sample and that of the final ash. The Ti and Al contents of the ash were determined by inductively-coupled plasma atomic emission spectroscopy (ICP). Elemental analysis of the char residue for the C and H contents were performed on a Leko instrument.

Particle Residence Time and Burnoff - The reaction length for a given test condition was determined as the difference between the injection-to-collection-probe length and the ignition distance. The average particle residence time was determined by dividing the reaction length by the measured, average particle velocity.

The carbon burnoff (dry, ash-free) of a sample was determined by following three tracers: ash, Ti and Al. Assuming that the given tracer does not react to form gaseous products during conversion, the burnoff can be calculated by (Pace, 1982)

$$B = \frac{x_{t_i}\left(1 - x_{a_f}\right)}{x_{t_f}\left(1 - x_{a_i}\right)} \qquad \text{II.B-1}$$

This formulation of the burnoff allows for ash loss (for minerals other than the specific tracer) when used with Ti or Al tracers. For each test, burnoffs were calculated using each of the tracers. In almost every case the three values agreed within a few percent, promoting confidence in the ash analyses. The three values were averaged to produce the burnoffs listed in the tables and used in subsequent calculations.

Particle Temperature, Velocity and Size Measurements - Approximately 50 to 100 individual particle traces were obtained from the optical system during each test. While valid measurements were obtained for the particle temperature and velocity in all cases, accurate particle size measurements were not obtained for the low temperature, 40 μm tests or the higher pressures of 10 and 15 atm, due to limitations of the optical pyrometer. With the collection probe located 5.5 cm below the optical control volume for nearly all of the tests, the optical measurements were typically obtained near the midpoint of the particle residence time. Mean temperature and velocity measurements for each test are listed in Tables II.B-3 to II.B-5.

Individual particle measurements for a typical 70 μm particle test, U3.2, are presented in Figs. II.B-4 and II.B-5. Particle-to-particle variations in minerals, macerals and structure resulted in wide distributions in temperature and size. The variation in combustion behaviors was also evidenced by SEM photographs of particle samples. Fig. II.B-4a shows a nearly normal particle temperature distribution that spans a range of 300 K. The mean and median temperature values were essentially equivalent for this and all of the oxidation tests. Fig. II.B-4b shows a 700 K difference in particle and gas temperatures. This is due to the high reactivity of the char and the high oxygen concentration of the combustion environment. Little particle size dependence is observed in the measured temperatures.

Measured particle velocities followed a normal distribution with a small standard deviation (Fig. II.B-5a). Because of the small size of the particles, slip velocity was very low (ca. a few percent of gas velocity) and very little difference in slip velocity for the particle size distribution was seen. Since the gas movement is a developing laminar flow with a maximum velocity at the center of the reaction tube, particles slightly off center would move a little slower than those flowing along the axis. Thus, the particle velocity distribution was mainly dependent on the gas velocity profile.

The measured particle size distribution, Fig. II.B-5b, exhibited a wide variance and a skewing to the smaller sizes. This is a result of differences in the combustion of individual particles. While most of the particles seemed to burn in a decreasing density mode, a small portion burning with decreasing diameter would result in the smaller sizes measured. Fragmentation would also contribute to the number of smaller particles.

Char Structure Results - Structural changes in the chars were followed by densities (bulk, apparent and true), SEM photographs, and N_2 BET adsorption surface area measurements. These results are tabulated in Appendix A.

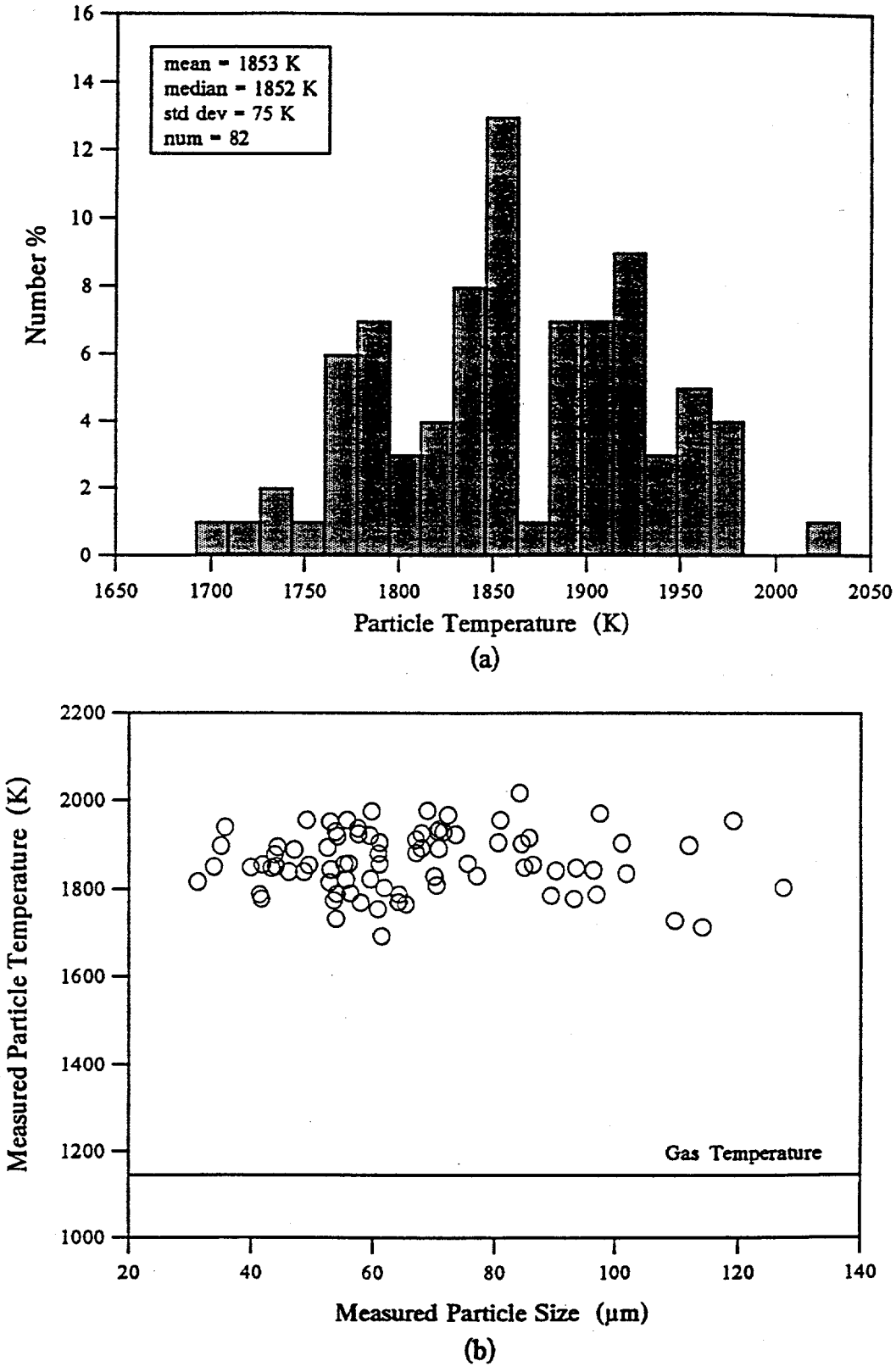

Figure II.B-4. Temperature measurement a) histogram and b) size dependence for a typical test (U3.2).

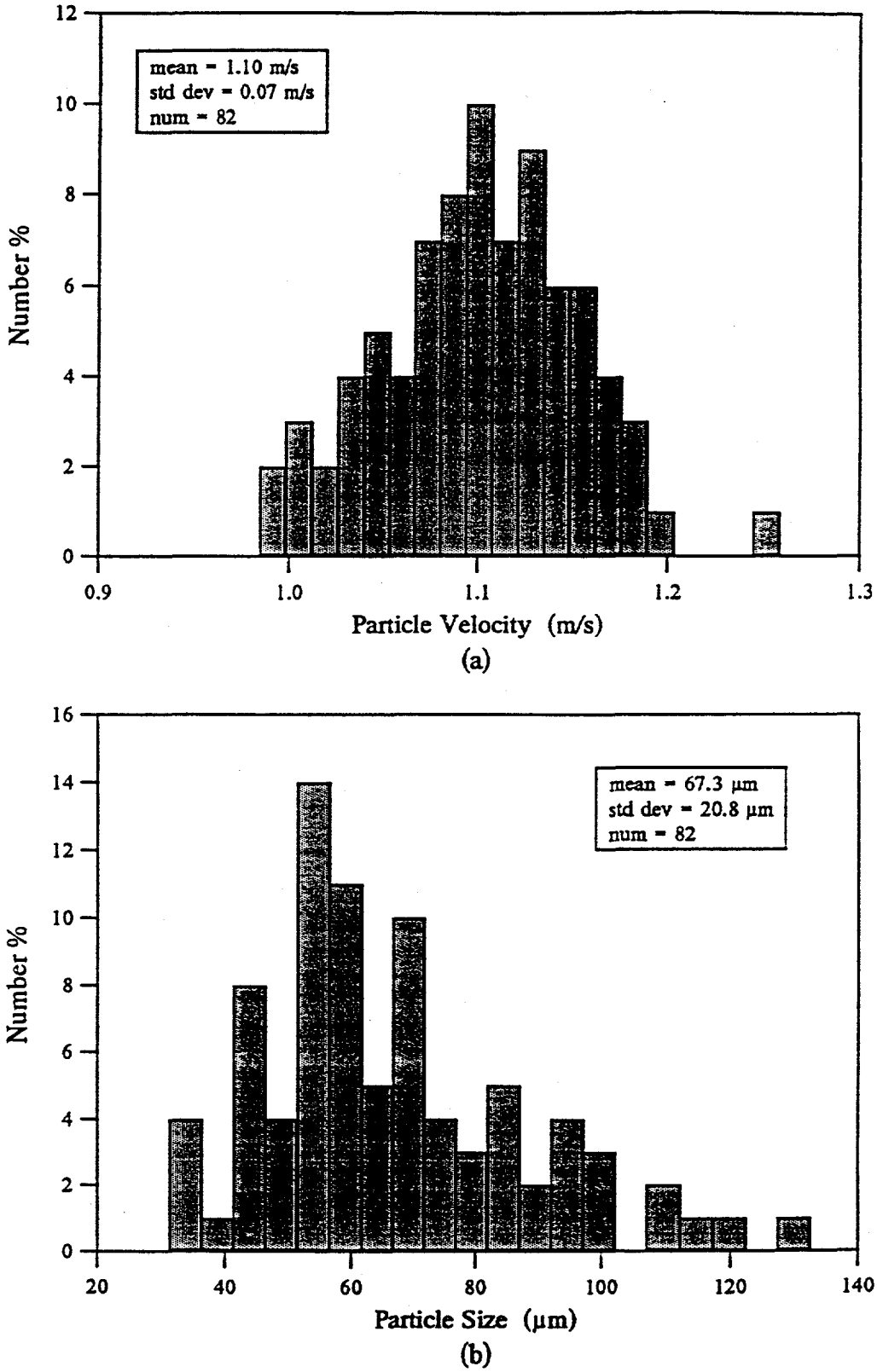

Figure II.B-5. Histograms of the a) velocity and b) size measurements for a typical test (U3.2).

Bulk densities were obtained for each test using a small graduated cylinder and a weight scale. The collected char residue was placed in the graduated cylinder and tapped until the minimum volume was obtained (typically 1-2 minutes). This volume, along with the weight of the sample, was used to calculate bulk density. Apparent densities were obtained from the bulk value by assuming the widely accepted interparticle void volume of 0.45 (Field, 1970).

$$\rho_{app} = \rho_b \frac{1}{(1-0.45)} \qquad \text{II.B-2}$$

The following correction was made for the ash content to yield the carbon apparent density, ρ_c (Hurt and Mitchell, 1992).

$$\rho_c = \frac{1-x_a}{\frac{1}{\rho_{app}} - \frac{x_a}{\rho_a}} \qquad \text{II.B-3}$$

The change in char density with burnoff is typically modelled by the burning mode parameter, α, as follows (Smith, 1982):

$$\frac{\rho_c}{\rho_{c0}} = \left(\frac{m}{m_o}\right)^{\alpha}_{daf} \qquad \text{II.B-4}$$

Figure II.B-6 shows the effect of conversion on the carbon apparent density and the predicted density change from the model. The burning mode parameter most consistent with the 1 atm data (Fig. II.B-6a), determined from least- squares regression (excluding outlying points), was 0.65, while the higher pressure data were best fit by a value of 0.5. The 5 atm outliers at high burnout can be explained by small errors in the burnout measurements. A small percentage increase in the burnout values brings these points into conformance with the other data. Figures II.B-6b - II.B-6c present the same information for the 40 μm UT char and the Pitt. char. These fuels also exhibited nearly the same changes in structure with conversion. This reducing density, and reducing diameter burning, indicates that significant reaction was occurring within the particle pores (Zone II burning). Higher gas pressures did not significantly alter this mode of burning.

The trends in char structure indicated by the density analyses were consistent with the SEM photographs. Selected char samples were chosen to provide a range of burnoffs at two pressures for each of the fuels. Photographs of these samples are shown in Figs. II.B-7 to II.B-9. The variety of char structures present in each of the fuel types was most likely a result of varying maceral content in the particle populations (Tsai and Scaroni, 1987). The predominate structure in both UT chars was lacy cenospheres, while that of the Pitt. char was thin and thick walled cenospheres. As the chars burned, pore combustion resulted in fragile lacy structures, nearly the same size as the original chars. At high levels of conversion, these appear to have fragmented into smaller pieces. It is apparent that the char population was composed of particles exhibiting a wide range of reactivities. In the 1 atm, 0.15 conversion photograph in Fig. II.B-7, for example, some particles show no signs of any reaction while others show significant pore development and other signs of substantial conversion. It is also interesting to note that a few particles retained their original coal-like shape even at high burnoff values. In agreement with the density results, no pressure dependence is apparent in the photographs.

N_2 and CO_2 surface area measurements were used to estimate the mesopore and micropore areas of the original UT chars. The mesopore areas were fairly small, about 1 m^2/g, while the micropore

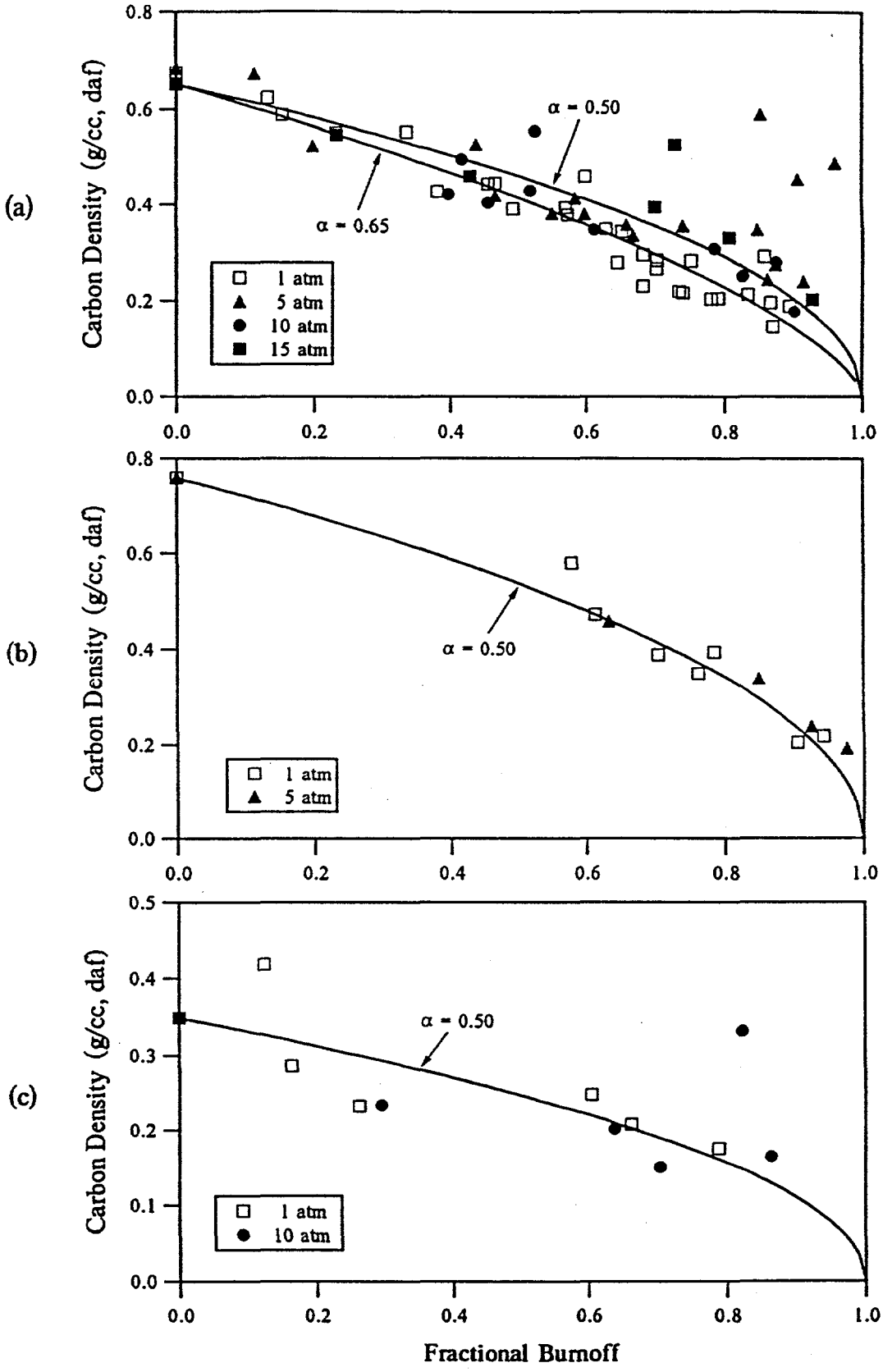

Figure II.B-6. The change in carbon density with burnoff for the a) 70 μm UT, b) 40 μm UT and c) 70 μm Pitt. Chars.

Raw Coal

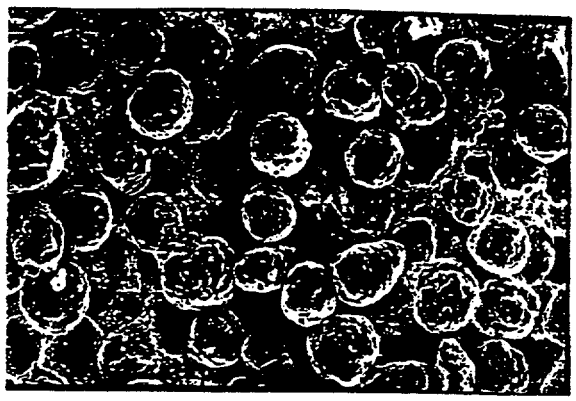

Original Char

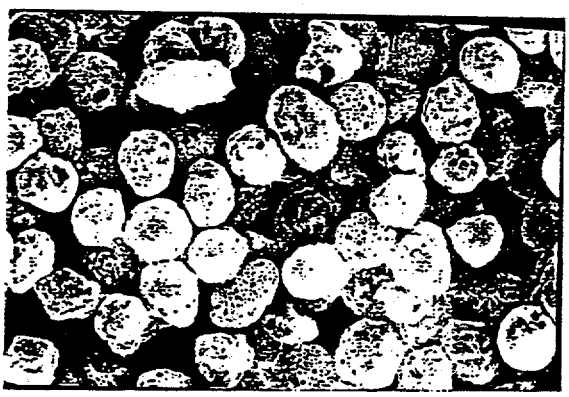

1 atm - 0.15 Conversion (U2.1)

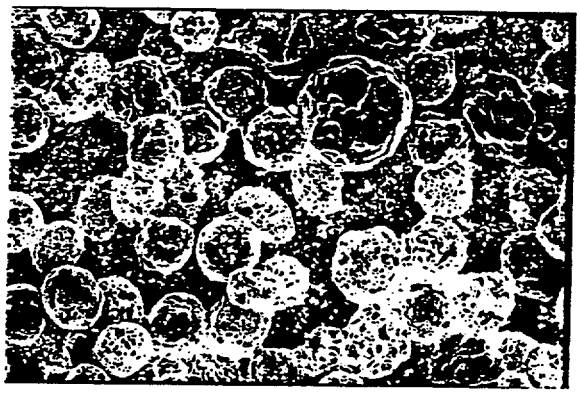

10 atm - 0.42 Conversion (U17.1)

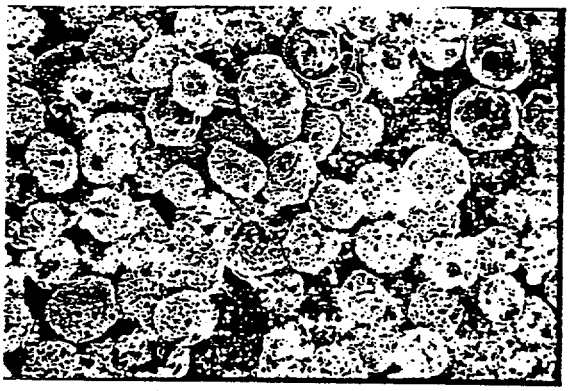

1 atm - 0.65 Conversion (U7.2)

10 atm - 0.83 Conversion (U21.1)

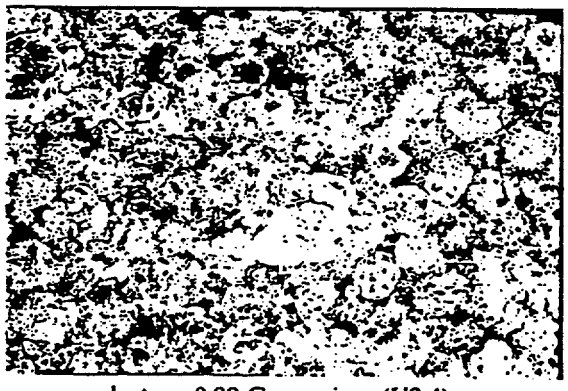

1 atm - 0.90 Conversion (U8.4)

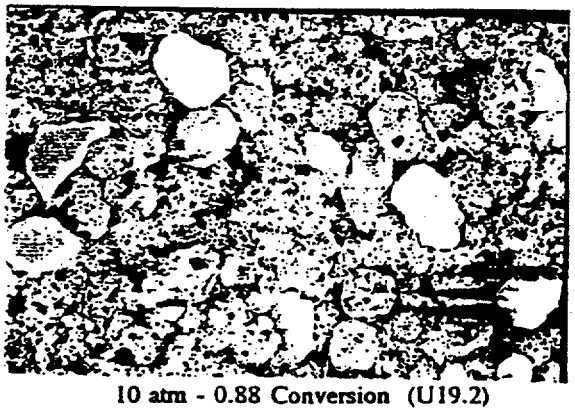

10 atm - 0.88 Conversion (U19.2)

Figure II.B-7. SEM photographs of the 70 μm UT char as a function of conversion at 1 and 10 atm total pressure.
———— 100 μm (x 130).

Raw Coal

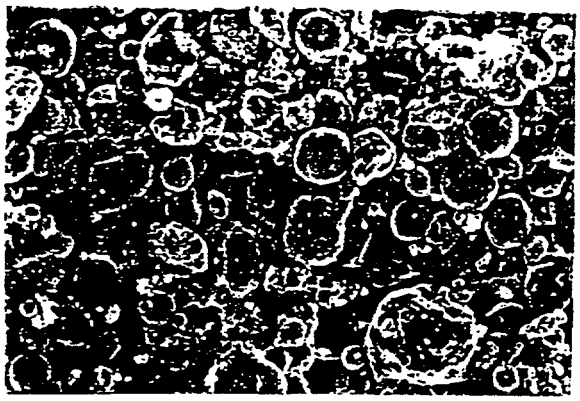

Original Char

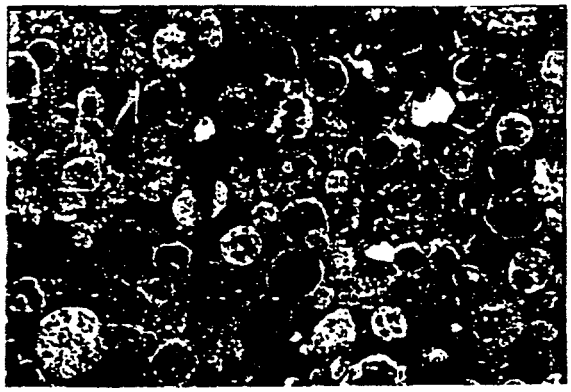

1 atm - 0.58 Conversion (U26.1)

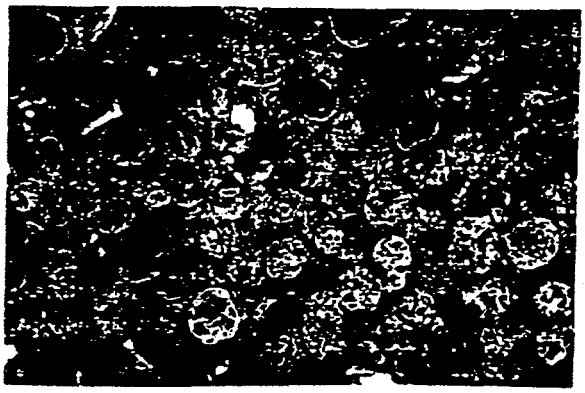

5 atm - 0.63 Conversion (U28.1)

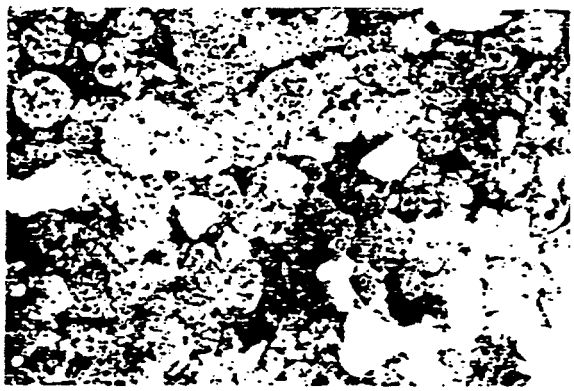

1 atm - 0.90 Conversion (U27.2)

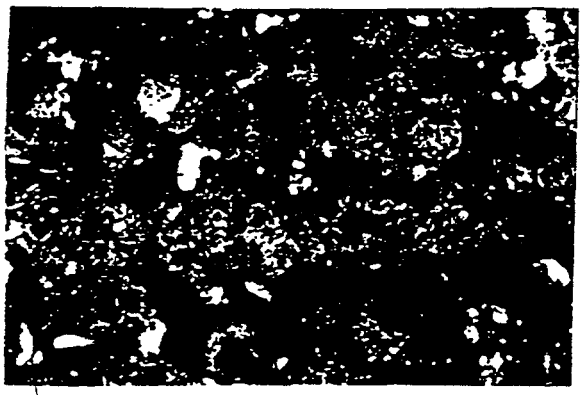

5 atm - 0.85 Conversion (U28.2)

Figure II.B-8. SEM photographs of the 40 μm UT char as a function of conversion at 1 and 10 atm total pressure.
———— 100 μm (x 200).

Raw Coal

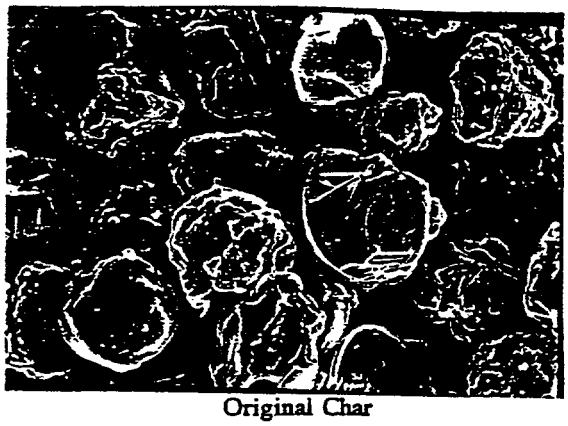

Original Char

1 atm - 0.16 Conversion (P1.1)

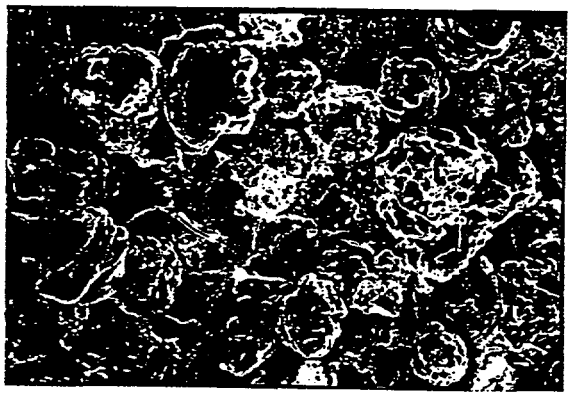

10 atm - 0.40 Conversion (P5.1)

1 atm - 0.35 Conversion (P3.2)

10 atm - 0.78 Conversion (P7.2)

1 atm - 0.81 Conversion (P4.2)

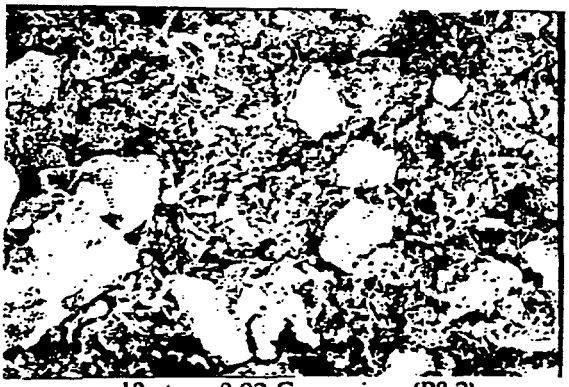

10 atm - 0.92 Conversion (P8.2)

Figure II.B-9. SEM photographs of the 70 μm Pitt. char as a function of conversion at 1 and 10 atm total pressure.
———— 100 μm (x 130).

areas where quite extensive, around 350 m^2/g. N_2 surface area measurements were also performed on selected chars as a function of burnoff and pressure. The samples used for these measurements corresponded to those used for the SEM photographs. These results are plotted in Fig. II.B-10. The pore evolution shows a maximum around mid-burnoff with little mesopore area in either the unoxidized or highly converted chars. Little pressure effect is seen in the surface areas.

All of the structure measurements are in agreement. The oxidation experiments occurred in a regime where internal burning was significant and the total pressure had no apparent effect on the char structure.

Char Reactivity - The overall chemical kinetics of char oxidation are usually described by the mass and area reactivities (Laurendeau, 1978). The mass reactivity, q_m, is defined by

$$q_m = \frac{1}{m}\frac{dm}{dt} \qquad \text{II.B-5}$$

Assuming the particle temperature remains constant during burnoff and taking the carbon mass at the midpoint of burnoff, the average mass reactivity can be determined from experimental measurement by

$$q_m = \frac{2B}{2-B}\frac{1}{t_r} \qquad \text{II.B-6}$$

In a manner similar to the mass reactivity, the overall reaction rate can also be described on a particle external surface area basis (assuming a spherical particle) by the area reactivity.

$$q_a = -\frac{1}{A_p}\frac{dm}{dt} \qquad \text{II.B-7}$$

Taking A_p at the midpoint of combustion, the time-averaged area reactivity can be determined from

$$q_a = -\frac{m_o}{A_{pm}}\frac{B}{t_r} \qquad \text{II.B-8}$$

The initial char apparent density and diameter can be used to calculate the initial particle mass, m_o, and A_{pm} can be calculated using Eqns. II.B-3, II.B-4, and geometry. Values for q_m and q_a for each test are listed in Tables II.B-3 - II.B-5. They are also plotted in Arrhenius form in Figs. II.B-11 to II.B-15.

Figure II.B-11 shows a comparison of area reactivities from the 1 atm UT char tests and from experiments conducted with UT chars at Sandia National Laboratories (Hurt et al., 1991) and Stanford University (Leslie et al., 1989). While the Sandia study did not report reactivities as a function of temperature, the basic measurements required to make these determinations (mass fractions of ash and tracers, residence time, diameter, density, and temperature) were reported. Thus, the Sandia reactivities shown in the figure were calculated from the reported measurements using the methods of this study. The Stanford reactivities in the figure are those reported by Leslie et al. (1989). It should be noted that the particle temperatures were calculated, not measured, in the Stanford study. Experiments at Sandia were carried out in laminar flows with gas O_2 pressures of 0.06 and 0.12 atm, while those at Stanford were performed in turbulent flows at 0.075 atm O_2 pressure. The data sets shown in the figure cover a particle size range of 40 to 116 μm.

Agreement between the similar-sized char data sets, 59 and 70 μm, is quite good and all the data sets agree within a factor of three. The differences could be attributed to a number of variables including

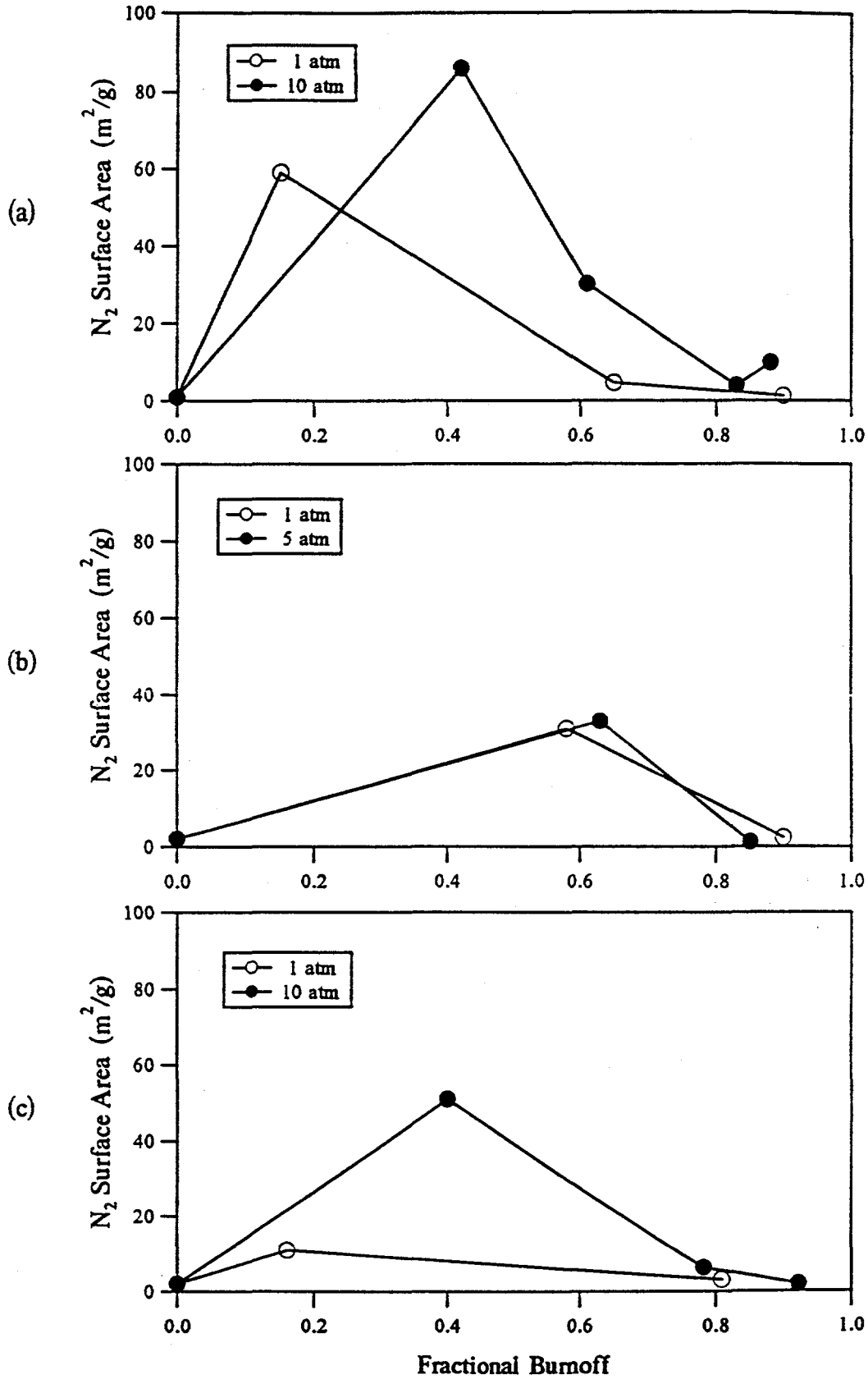

Figure II.B-10. The change in N2 surface area with burnoff for the a) 70 μm UT, b) 40 μm UT and c) 70 μm Pitts. chars.

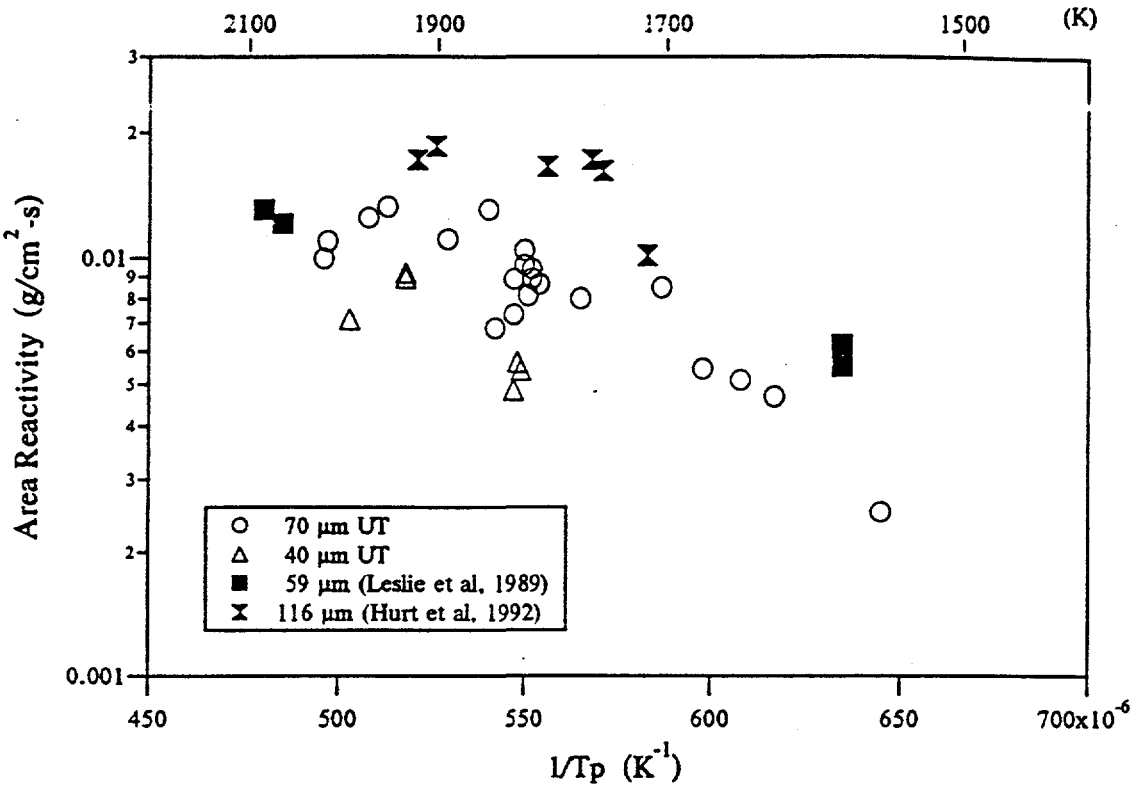

Figure II.B-11. Experimentally derived area reactivity for the UT Chars (at 1 atm) plotted with results from others' work with the same coal.

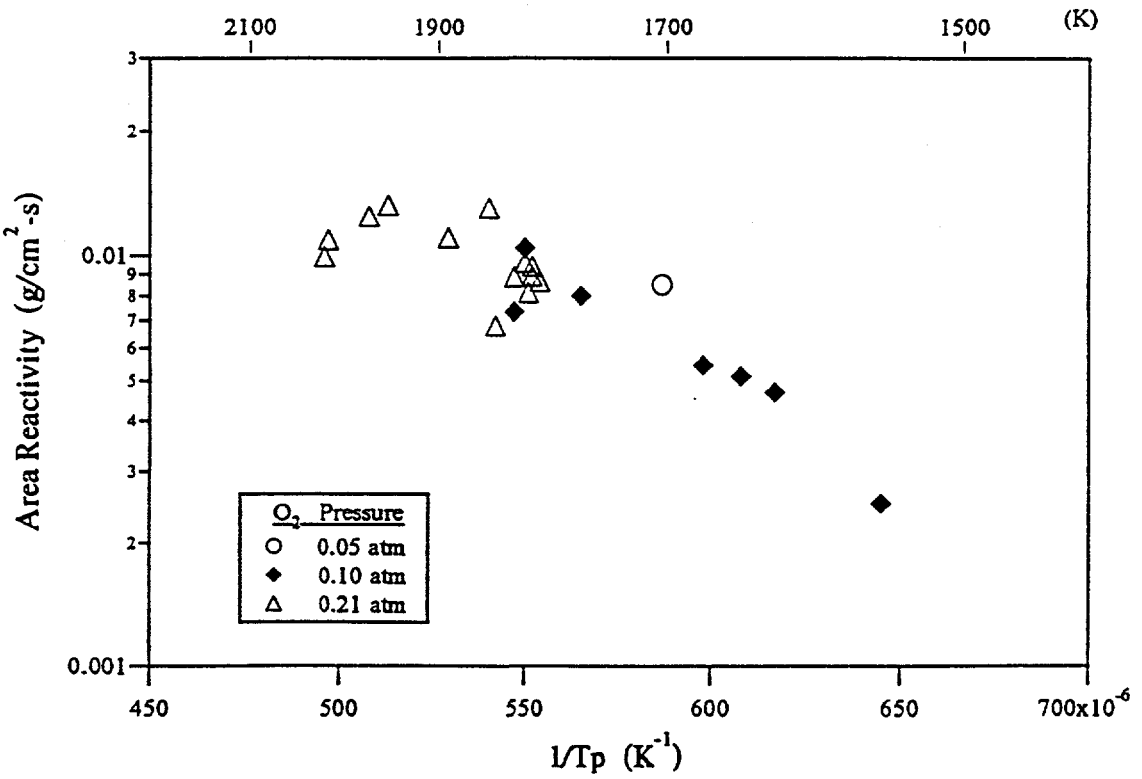

Figure II.B-12. Experimentally derived area reactivity for the 70 μm UT char (at 1 atm) as a function of bulk gas O_2 pressure.

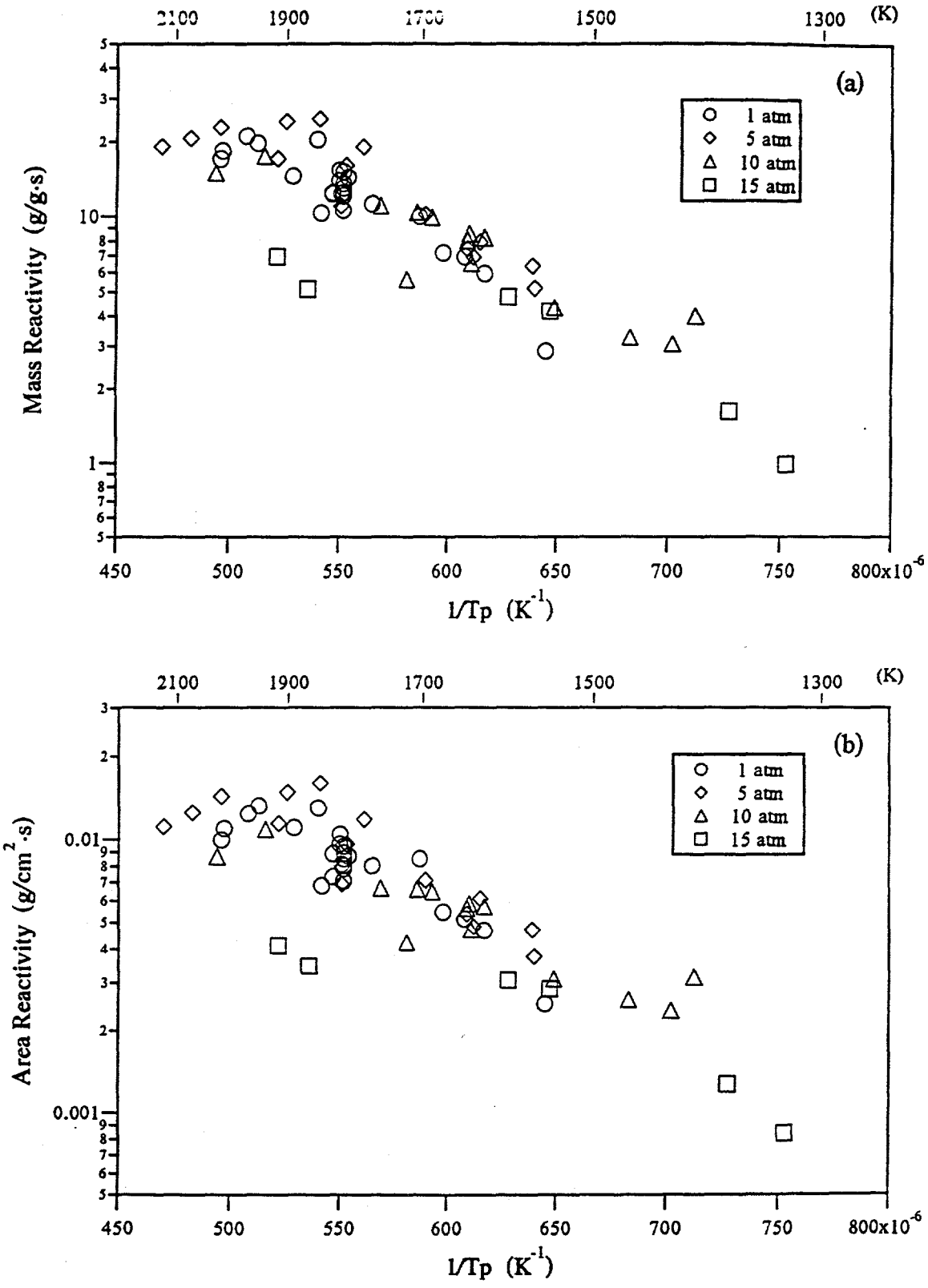

Figure II.B-13. Experimentally derived a) mass and b) area reactivities as functions of particle temperature for the 70 μm UT char.

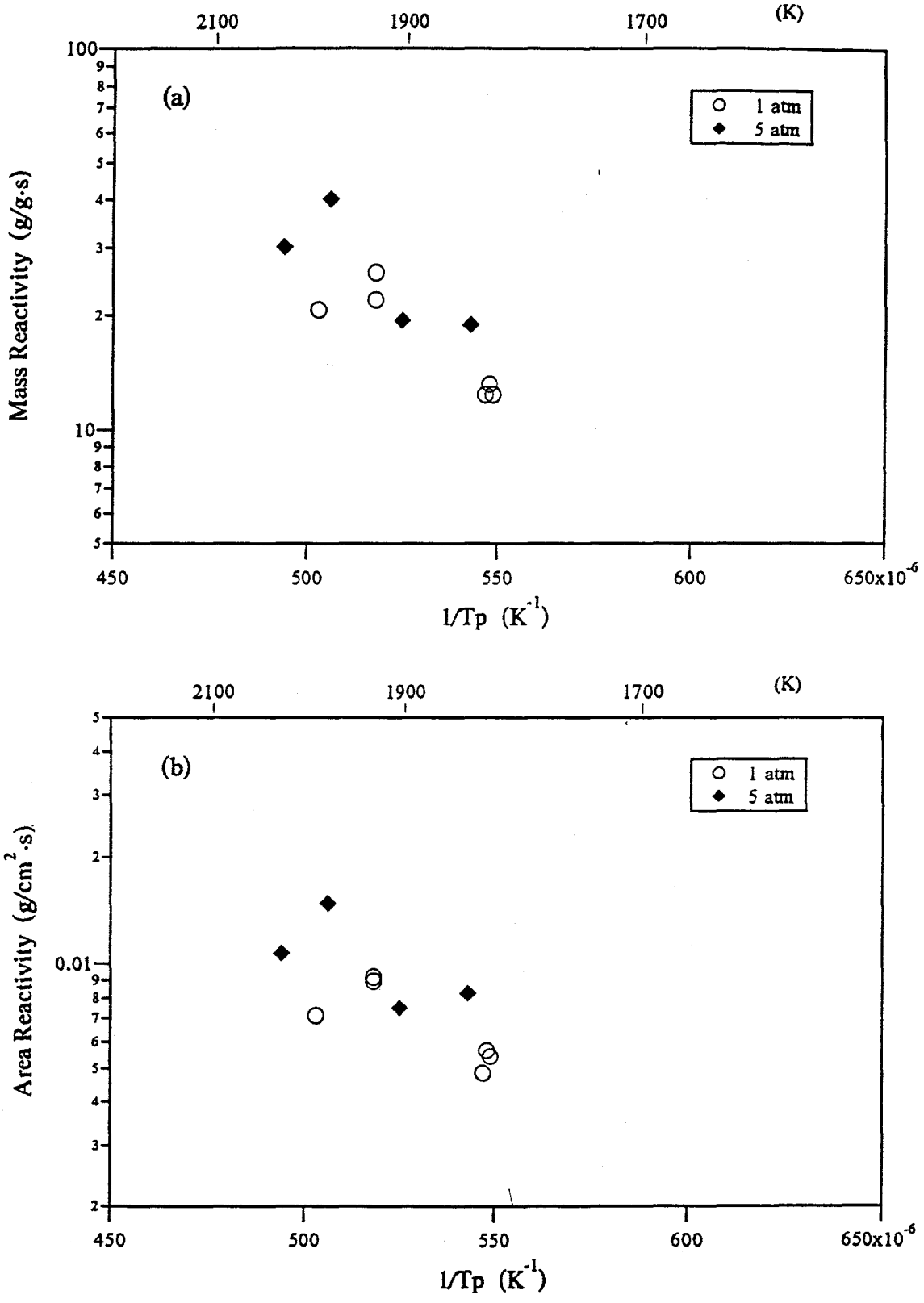

Figure II.B-14. Experimentally derived a) mass and b) area reactivities as functions of particle temperature for the 40 μm UT char.

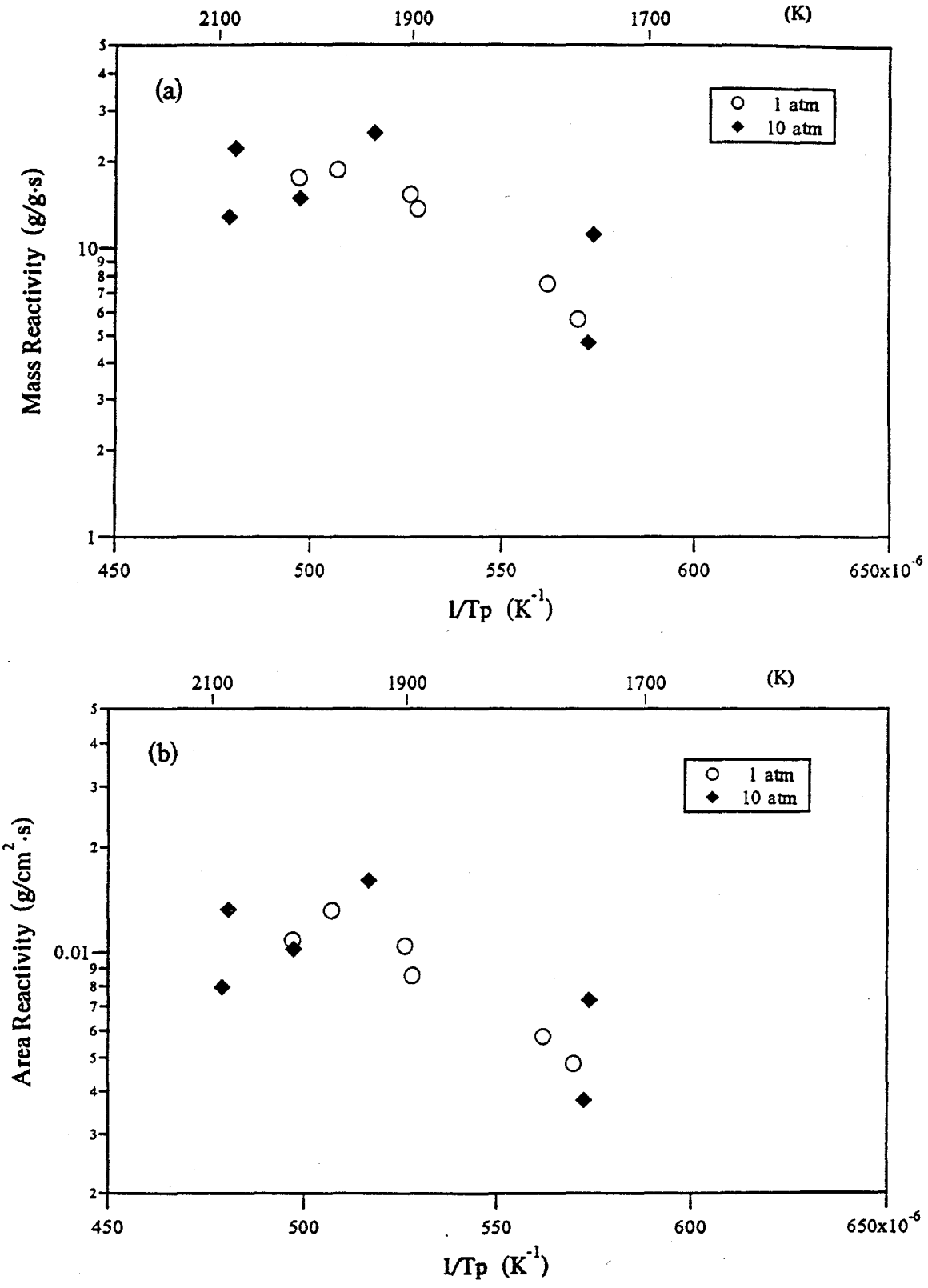

Figure II.B-15. Experimentally derived a) mass and b) area reactivities as functions of particle temperature for the 70 μm Pitt. char.

chars differing in chemical and structural properties as a result of coal variability and differing devolatilization conditions. Even if the starting chars were identical, differences between the data sets would be expected because of the dependence of the area reactivity on the diffusion rate and, hence, the particle size, gas O_2 concentration and flow characteristics. It was reported that the 116 μm char burned near the diffusion limit (Mitchell et al., 1992) and that the 59 μm char reacted in the pore diffusion regime(Leslie et al., 1989). While these two data sets were obtained at similar O_2 pressures, the smaller particle size and the turbulent flow of the Stanford experiments would move the combustion process away from the diffusion limit as compared to the Sandia study. The structural changes in the chars of this study indicate that combustion was occurring between the pore diffusion and kinetic regimes. This is plausible considering the small particle sizes and the higher O_2 pressures (0.21 atm) at the higher temperatures. The lower area reactivity of the 40 μm UT char as compared to the 70 μm UT char lends support to this burning regime. All of these results are consistent with the graphical position of the data sets in the Fig. II.B-11.

Figure II.B-12 shows the dependence of the area reactivity and particle temperature on the bulk gas O_2 pressure for the 70 μm UT char tests at 1 atm. As expected, higher O_2 pressures led to higher reaction rates. And thus, he various particle temperatures seen at the 10 and 21% O_2 concentrations resulted from varying the reactor temperature (gas and wall) from 1145 to 1460 K. Ignition was obtained in the 5% O_2 concentration environment at only the highest reactor temperature (this test turned out to be controlled by diffusion). Little temperature overlap is seen for the different oxygen concentration tests; the hottest reactor condition with 10% O_2 in the bulk gas produced particle temperatures equivalent to the lowest temperature reactor conditions with 21% O_2 in the bulk gas.

The mass and area reactivities for each of the three sets of chars are plotted in Figs. II.B-13 to II.B-15. Little difference is seen in the trends of the two reactivity types because of the use of common particle sizes for each fuel. Activation energies are slightly lower for the area reactivities because of the general trend of increasing burnoff with increasing temperature in the experiments. This results because a burning particle's mass decreases faster than its external surface area. Since an inverse relationship exists between these properties and the reactivities, the area reactivity decreases faster than the mass reactivity with burnoff.

Surprisingly, little total pressure effect is seen in the reactivities of any of the fuels. For the most part, the reactivities are grouped along the 1 atm line within the experimental error (about a factor of 1.5). The high temperature 15 atm points in Fig. II.B-13 are an exception to this, and low by about a factor of 3. This could be a pressure effect but is more likely a result of nonsteady particle temperatures at this extreme test condition. The combination of high pressure and high temperature resulted in a short reaction length for these tests. The assumption of a steadily burning particle would be invalid if the particle temperature peaked about halfway through the reaction zone (near the temperature measurement location) and then sharply fell during the remainder of the zone. The result would be a measured reactivity lower than expected for the measured temperature.

Pressure Effects on the Measured Particle Temperature - Measured particle temperature as a function of O_2 pressure and total pressure for the 70 μm UT char experiments is shown in Fig. II.B-16. Experiments performed at a fixed reactor temperature and pressure but with varying oxygen concentration (5, 10 and 21%) are joined by solid lines. Data from two reactor temperature settings are shown for all but the 15 atm pressure sets. Although the data points for the total pressures do not cover the same O_2 pressure range, strikingly large dependencies of the particle temperature on the total pressure and on oxygen partial pressure is apparent. At the same O_2 pressure and gas temperature, the particle temperature is typically several hundred degrees lower at the next higher total pressure level. The effect of the total pressure on the particle temperature was much larger than that due to changes in reactor temperature. Conversely, increasing oxygen partial pressure causes sharp increases in particle temperature at a fixed total pressure.

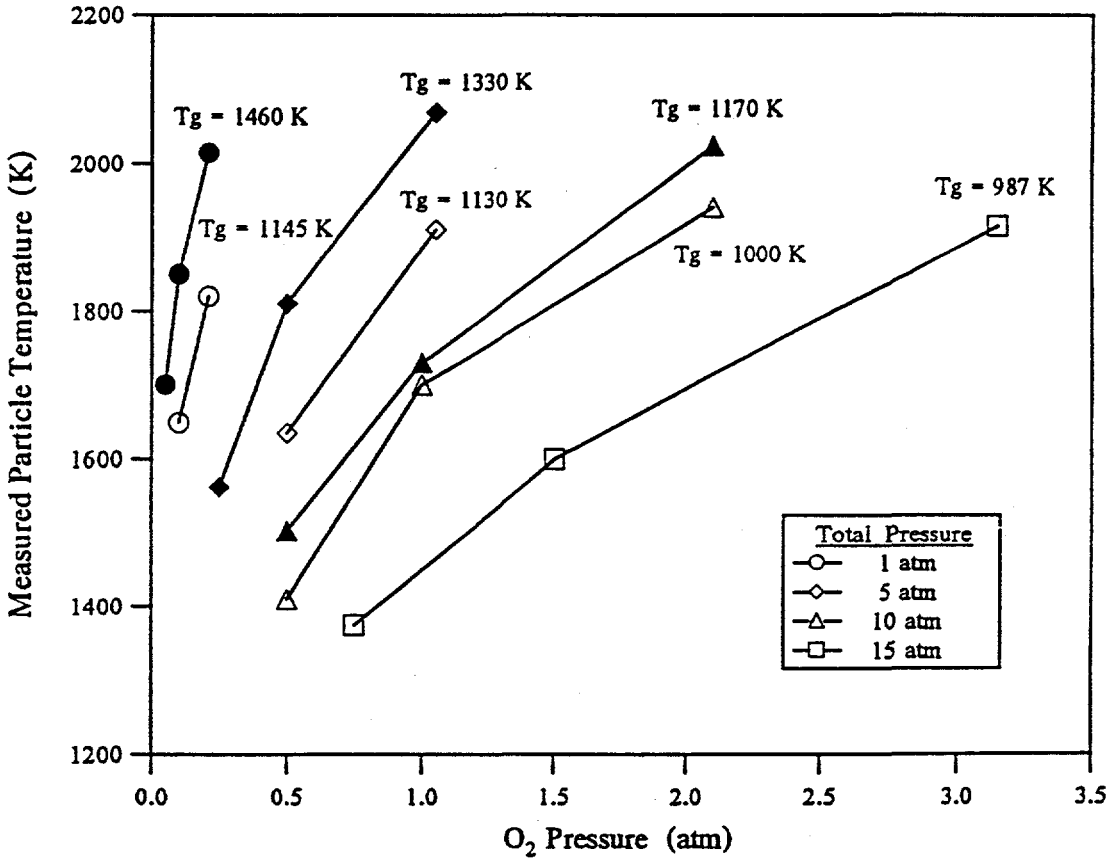

Figure II.B-16. The effects of O_2 pressure and total pressure on the measured particle temperature of the 70 μm UT char.

Global Char Oxidation Model

In high temperature char combustion processes, pore diffusion and internal reaction typically influence the overall reaction rate. Because the details of the complex particle pore structure and the accessibility of oxygen to these internal surfaces are usually not known, it has been common practice to relate the char reaction rate to the external surface area (Smith, 1982). In this model, diffusion across the boundary layer is treated but diffusion and burning within the particle pores is neglected. This global char oxidation model was used to correlate the results of this study. The wide range of conditions over which the oxidation experiments were performed provided a means of testing the validity of the n^{th} order rate equation.

Using the single film burning model and assuming a quasi-steady reaction, the global model equates the rate of carbon diffusion to the rate of carbon consumption. Using an n^{th} order power law, the following expression for the overall rate of carbon consumption per unit external surface area, q_a, is obtained:

$$q_a = k_c P_{os}^{\,n} \qquad \text{II.B-9}$$

he apparent chemical reaction rate coefficient, k_c, follows the Arrhenius form:

$$k_c = A\, e^{\frac{-E}{RT_p}} \qquad \text{II.B-10}$$

Experimental studies have indicated that, besides CO, some CO_2 is also a primary product of heterogeneous char oxidation (Mitchell, 1988, Waters *et al.*, 1988, Young and Niksa, 1988, Mitchell *et al.*, 1990b). This is significant because of the large heat of reaction (over 3 times greater than the CO reaction) and the stoichiometry of the CO_2 reaction (only half as much carbon consumed per oxygen molecule as compared to the CO reaction). The fraction of carbon converted to CO_2 is represented by ψ.

$$C + \frac{1}{2}(1+\psi)O_2 \rightarrow (1-\psi)CO + \psi CO_2 \qquad \text{II.B-11}$$

The rate of carbon diffusion on a particle-surface-area basis can be described by the following relation (Frank-Kamenetskii, 1969 and Mitchell, 1988). It allows for the formation of both CO and CO_2 and also accounts for the Stephan flow (the convective flow resulting from a change in the number of moles during the reaction).

$$q_a = \left(\frac{2}{1+\psi}\right)\frac{P}{R\,T_p}\,\frac{2\,M_c D_{ox}}{d_p\,\gamma}\ln\left(\frac{1-\gamma\frac{P_{os}}{P}}{1-\gamma\frac{P_{og}}{P}}\right) \qquad \text{II.B-12}$$

where γ is defined as

$$\gamma = \frac{\psi - 1}{\psi + 1} \qquad \text{II.B-13}$$

The rate of carbon consumption (Eqn. II.B-9) and the rate of carbon diffusion (Eqn. II.B-12) are combined to eliminate the unknown P_{os}, yielding an implicit equation for q_a in terms of the apparent kinetic coefficients (A, E and n), the gas and particle properties, and ψ.

The particle temperature is described by the energy equation. In this study the particle temperature is assumed to remain fairly constant during the oxidation process. Thus, the inertial component can be neglected and the energy equation can be written as

$$0 = -\frac{Nu\lambda(T_p - T_g)}{d_p}\left(\frac{B_f}{e^{B_f}-1}\right) + \varepsilon\sigma\left(T_p^4 - T_w^4\right) - q_a\Delta H \qquad \text{II.B-14}$$

The Stephan flow is accounted for by the blowing factor, B.

$$B_f = \frac{C_{pg}\, q_a}{M_c\, h}\left(\frac{\psi - 1}{2}\right) \qquad \text{II.B-15}$$

The heat of reaction is dependent on the fraction of CO_2 generated.

$$\Delta H = -26.4(1-\psi) - 94.1\psi \qquad \text{II.B-16}$$

The model requires a number of temperature- and pressure-dependent gas properties: ρ, C_{pg}, μ, λ, and D_{ox}. These values were determined at the film temperature assuming ideal gas behavior, using curve fits from the JANAF Thermochemical Tables, and relying on molecular theory. The pressure dependence of C_{pg} and μ is very slight over the range of test conditions and, therefore, neglected. The strong dependence of D_{ox} on both temperature and pressure greatly affects the balance between the diffusion and kinetic rates. The thermal conductivity shows an almost proportional dependence on temperature and an almost negligible dependence on pressure.

The complex interaction between the three main equations in the model (Eqns. II.B-9, II.B-12, and II.B-14) and the variable gas properties make it difficult to accurately identify trends without a numerical simulation. The computer model was used to perform a number of simulations with the aim of examining the effect of O_2 and total pressure changes on char oxidation behavior. In these simulations it was assumed that the model and its kinetic parameters were valid over a wide range of combustion conditions.

Figure II.B-17a shows the predicted effect of increasing O_2 pressure at a constant total pressure of 1 atm. The parameters held constant are listed on the plot. Values of χ (ratio of observed rate to diffusion-limited rate) range from 0.35 to 0.6, indicating that neither the diffusion nor the chemical reaction rate control the combustion process in this case. χ experiences a minimum at a pressure just below 0.2, where the maximum amount of kinetic control occurs. At lower and higher oxygen concentrations the diffusion process increases its control on the overall reaction and χ increases moderately, tending to flatten out at higher O_2 pressures. The moderate rate of increase in χ with increasing O_2 pressure is not as large as expected. Other simulations showed that the average value of χ and the position of the minimum in χ vary considerably with changes in the combustion conditions and kinetic parameters. Also shown on the plot are the particle reaction rate and the diffusion-limited reaction rate. Both rates start at 0 with no oxygen in the gas and then increase substantially with increasing oxygen concentrations.

Figure II.B-17b shows the effect of the total gas pressure on the reaction rate. The solid lines represent constant mole fractions (Y_{O2}) and the dashed lines represent constant O_2 pressures (P_{O2}). As the total pressure is increased above 1 atm at a constant gas mole fraction, the reaction rate first increases fairly rapidly and then flattens off at higher pressures. The initial rise is more pronounced for higher oxygen gas compositions. In general, an increase in the O_2 mole fraction produces a substantially larger increase in rate than an increase in the total pressure. The constant O_2 pressure lines show the same unexpected trend as the temperature measurements of Fig. II.B-16: a decrease in the reaction rate with increasing total pressure. The pressure effect on the rate is quite marked at higher O_2 pressures.

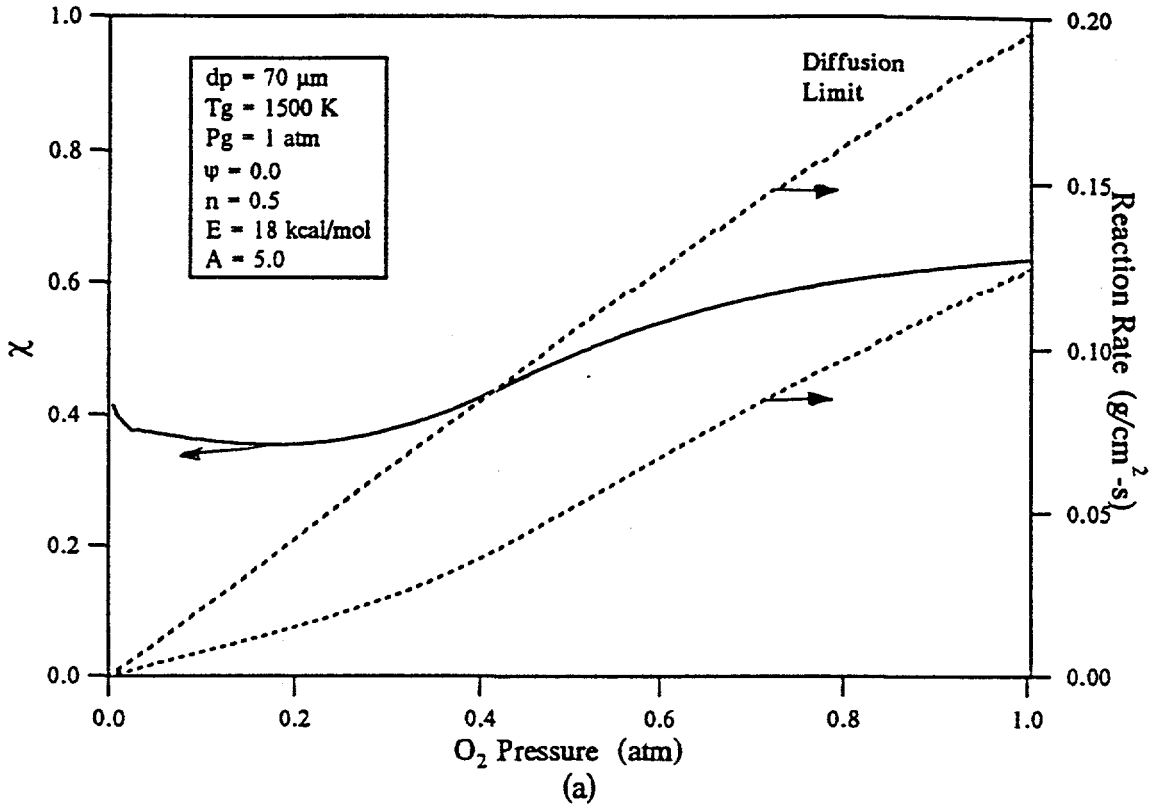

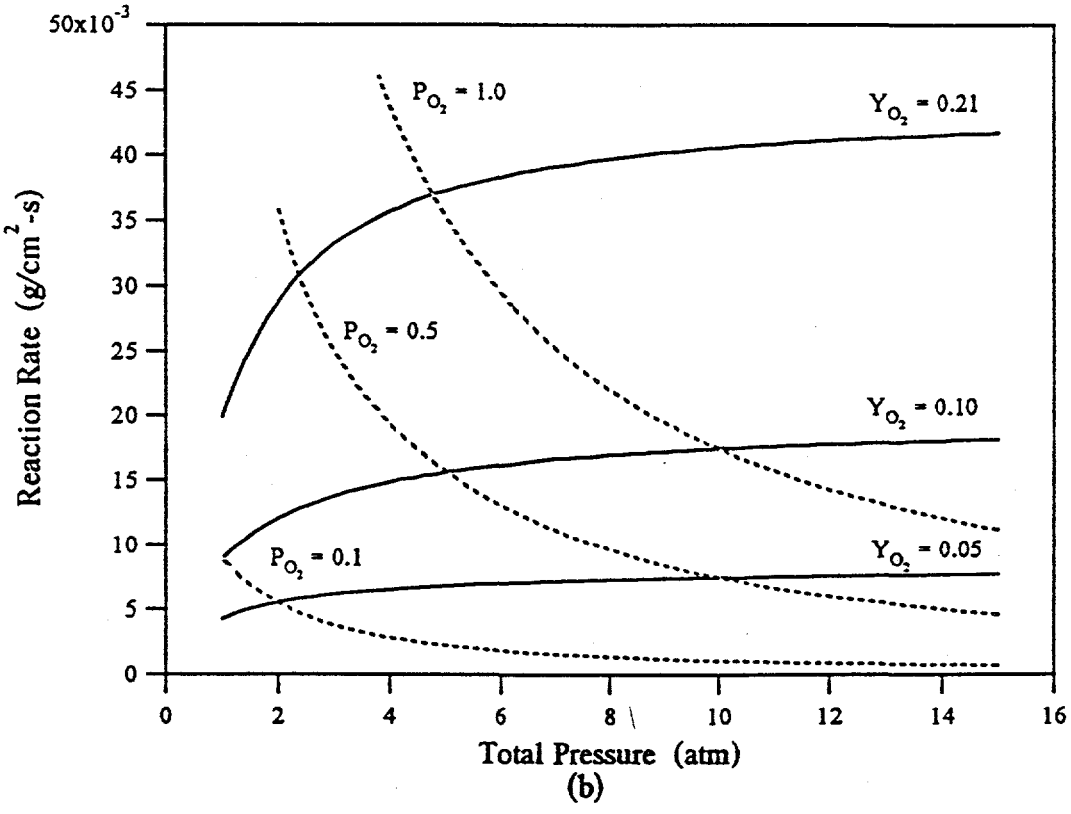

Figure II.B-17. Simulation results from the staeady state char oxidation model a) particle reactionr ate and χ at 1 atm total pressure b) particle reaction rate as a function of total pressure and gas composition.

These pressure effects on the reaction rate can be explained in the following manner. The decrease in diffusivity accompanying an increase in the total pressure slows the rate of O_2 diffusion to the particle, resulting in a lower O_2 pressure at the particle surface in the case of constant O_2 partial pressure. This decrease in the particle surface concentration slows the chemical reaction rate which, in turn, lowers the particle temperature and results in a further decrease in the oxygen diffusivity. The process of reducing reaction rate continues until a balance is obtained between the diffusion and kinetic rates and between the energy generated by the reacting particle and the energy lost by the particle through heat transfer. The final result is a decreasing particle reaction rate and temperature as the total pressure is increased. For the case of constant O_2 mole fraction, where the bulk O_2 pressure increases in proportion to the total pressure, the decrease in diffusivity leads to a very moderate increase in reaction rate and temperature. Most of changes due to pressure have occurred by 10 atm and further pressure increases produce little additional effect.

Elevated Pressure Data Analysis

Combustion Regime - Establishing the burning regime of the char experiments was an important step in analyzing the data. Had combustion occurred in the bulk diffusion controlled regime (Zone III) kinetic parameters could not have been determined. The ratio of the measured rate to the maximum rate, χ, was determined to help quantify the controlling processes. The maximum burning rate was calculated assuming complete conversion of carbon to CO at the diffusion limit, while allowing for the particle temperature increase due to the faster reaction. Hence, the diffusion and energy equations (Eqns. II.B-12 and II.B-14) were simultaneously solved for the given experimental conditions to determine the maximum rate. The value of χ determined from each test is listed in Tables II.B-3 to II.B-5. χ was typically in the range of 0.15-0.50 for the 70 μm char and somewhat lower for the 40 μm char. The decrease in χ with particle size was expected because the boundary layer depth also decreases with size, resulting in a faster diffusion rate. In only one test, U6.2, did the reaction occur near the diffusion limit. The effect of pressure on χ was masked by its dependence on the gas film temperature and O_2 pressure. χ seems to have slightly increased with pressure from 1 to 5 atm but further increases in pressure were accompanied by decreases in the film temperature and increases in O_2 pressure.

The χ values calculated for the tests, typically less than 0.5, indicate that the kinetic rates were exerting significant control over the combustion process. This result is consistent with the other experimental data. The slight decrease in the area reactivity of the smaller sized UT chars (Fig. II.B-11) indicates a burning regime between the kinetic (Zone I) and pore diffusion (Zone II) controlled zones (q_a is proportional to dp in zone I and independent of dp in Zone II). The particle density, SEM photographs, and calculated α's and activation energies also support this conclusion.

Interestingly, no significant total pressure effect on the burning regime was found. This result conflicts with the commonly held belief that higher pressures lead to complete diffusion control (zone III). Since the maximum (diffusion controlled) reaction rate is independent of pressure for a given gas composition (the diffusivity is inversely proportional and the O_2 pressure is directly proportional to the total pressure), the explanation must lie in the reaction rate behavior. Because the increase in overall rate with total pressure is much lower than expected, as a result of the pressure and temperature dependent diffusivity, the increase in χ with pressure is also much lower than expected. This leads to the conclusion that kinetic rates can exert significant control on the overall reaction rate at elevated pressures and that kinetic parameters can reasonably be extracted from the experimental data.

Reaction Products - CO/CO_2 - Although CO has commonly been accepted as the primary product of heterogeneous char oxidation, some researchers have found evidence for the formation of CO_2 as well. It was postulated by Arthur (1951) that the ratio of the CO to CO_2 formed was a function of the particle temperature and that it could be described by the Arrhenius law in the following manner.

$$\frac{\psi - 1}{\psi} = A_c \, e^{\frac{-E_c}{RT_p}} \qquad \text{II.B-17}$$

In drop tube experiments, independent measurement of both the particle temperature and the rate of reaction is required to allow calculation of the fraction of CO_2 produced. With increases in CO_2 production the particle temperature is increased and the reaction rate is decreased. Thus, an energy balance will be consistent only for the proper ψ. With known particle temperature, reaction rate, and reactor conditions, ψ is calculated by solving the energy equation, Eqn II.B-14. Only researchers at Sandia National Laboratories have reported high temperature oxidation experiments where sufficient information was collected to allow these determinations (Mitchell, 1988, Waters *et al.*, 1988, Mitchell *et al.*, 1990, Hurt and Mitchell, 1992a).

Results from the determination of ψ for the 70 μm UT char data are shown in Fig. II.B-18 as a function of particle temperature. The results are somewhat scattered because of the sensitivity of the calculation to errors; any errors introduced by experimental measurements or shortcomings in the global model are included in the calculated ψ. In spite of the scattering, there is clearly a transition from CO_2 to CO production as the particle temperature increases from approximately 1500 to 1900 K. At temperatures below about 1700 K, oxidation rates are much too slow to produce the measured particle temperatures if CO is the only product considered. The solid line in the figure represents the best fit Arrhenius model to the data; agreement is seen to be quite good considering the uncertainties associated with the ψ determination. Agreement is also good with the parameters determined by Hurt and Mitchell (1992) for a UT char, $A_c = 3 \cdot 10^8$ and $E_c = 60$ kcal/mol. Surprisingly, ψ seems to be independent of the total gas pressure over the range covered in the experiments.

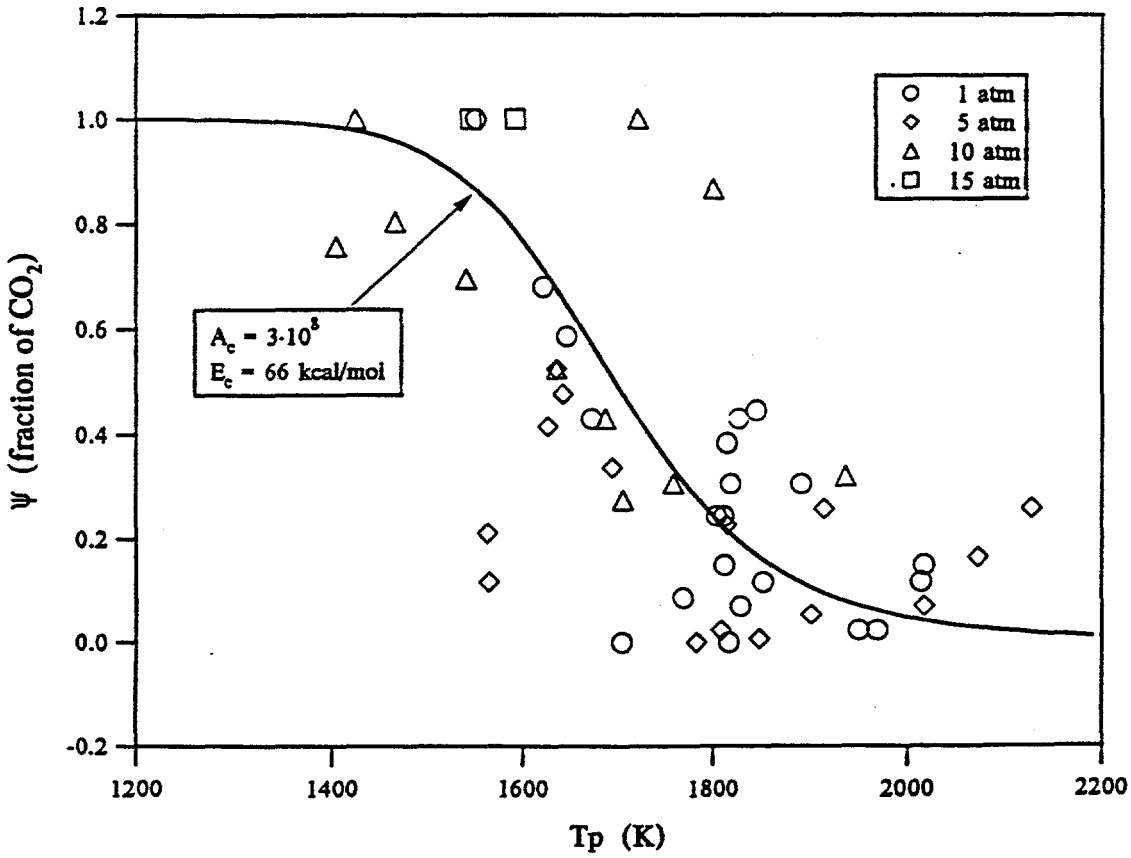

Figure II.B-18. Temperature dependence of φ for the 70 μm UT char.

It should be noted that while these results indicate that CO_2 may be formed heterogeneously, the global model is not sufficiently fundamental to prove this. Other explanations may also be plausible. For example, the same trend would be observed if only a portion of the particles ignited and temperature measurements were made on only burning particles. The collected char residue could contain a significant fraction of unreacted or partially reacted particles, resulting in a measured reaction rate lower than one corresponding to the measured temperatures.

Apparent Chemical Kinetics - The reaction rate coefficient, k_c, was determined from Eqn. II.B-9, using Eqns. II.B-10 and II.B-12 to determine P_{os}. Consistent with the previous work of other researchers (Young and Smith, 1981, Mitchell and McLean, 1982, and Hurt and Mitchell, 1992a) an apparent reaction order of 0.5 was used. Arrhenius plots of k_c are shown in Figs. II.B-19 and II.B-20. The activation energy and frequency factor at each total pressure were determined by a least squares regression of k_c vs. $1/T_p$, ignoring outlying points; these parameters are listed in Table II.B-6.

Interestingly, a significant pressure effect is seen on both the activation energy and frequency factor in each case. Both of these parameters are decreased at higher pressures. While the frequency factor decreases somewhat proportional to the pressure, the activation energy is significantly reduced at 5 atm and does not change with further pressure increases. This same pressure behavior is observed for each of the fuels.

The effect of fuel type on k_c is shown in Fig. II.B-20. The rate coefficients for all of the chars exhibit very similar temperature behavior and at any given pressure and temperature the rate coefficients for the chars agree within the experimental error. With this in mind, the larger 'best fit' Arrhenius parameters determined for the 40 μm UT char are most likely too high. A fairly large uncertainty was associated with the parameter determination for this fuel because of the small temperature range covered by the limited number of test conditions. The close agreement of the global rate coefficients for the three chars was expected because of their almost identical physical structures.

The large changes in Arrhenius parameters with pressure variations indicate an inadequacy in the model. Another observation further increases concern over the model adequacy. While little difference is seen in the overall reaction rates measured for a range of pressures (Figs. II.B-13 - II.B-15), after using the model to account for bulk diffusion effects, the reaction rate coefficients show a very pronounced pressure effect (Fig. II.B-19).

This could be a result of pressure related pore diffusion effects not accounted for in the global model if the pore area available to oxygen decreased with increasing pressure as Lester et al. (1981) conjectured. However, this would lead to an accompanying change in particle structure (a trend towards constant density burning with increasing pressure) and none of the structure measurements showed any significant effect of pressure. Also,unless the pore diffusion was also a complex function of temperature, a change in only the frequency factor, not the activation energy, would occur.

A more likely possibility is the inadequacy of the n^{th} order equation to predict changes with pressure. While it is commonly used and has proven adequate for predictive use at atmospheric pressure, the equation has no theoretical basis and has been shown to be invalid for atmospheric pressure char oxidation (Essenhigh, 1988 and 1991). Extrapolation of this empirical equation to elevated pressure would be valid only if it were consistent with experimental results. With the very limited research conducted at elevated pressures to date, the validity of the equation at these conditions has not been examined before. While the general trends of the model are consistent with the high pressure data obtained in this study, the variation in the kinetic coefficients with pressure indicate the inadequacy of the n^{th} order equation to model pressure changes. Use of a more fundamental rate equation, such as the Langmuir equation, may better describe the total pressure effects.

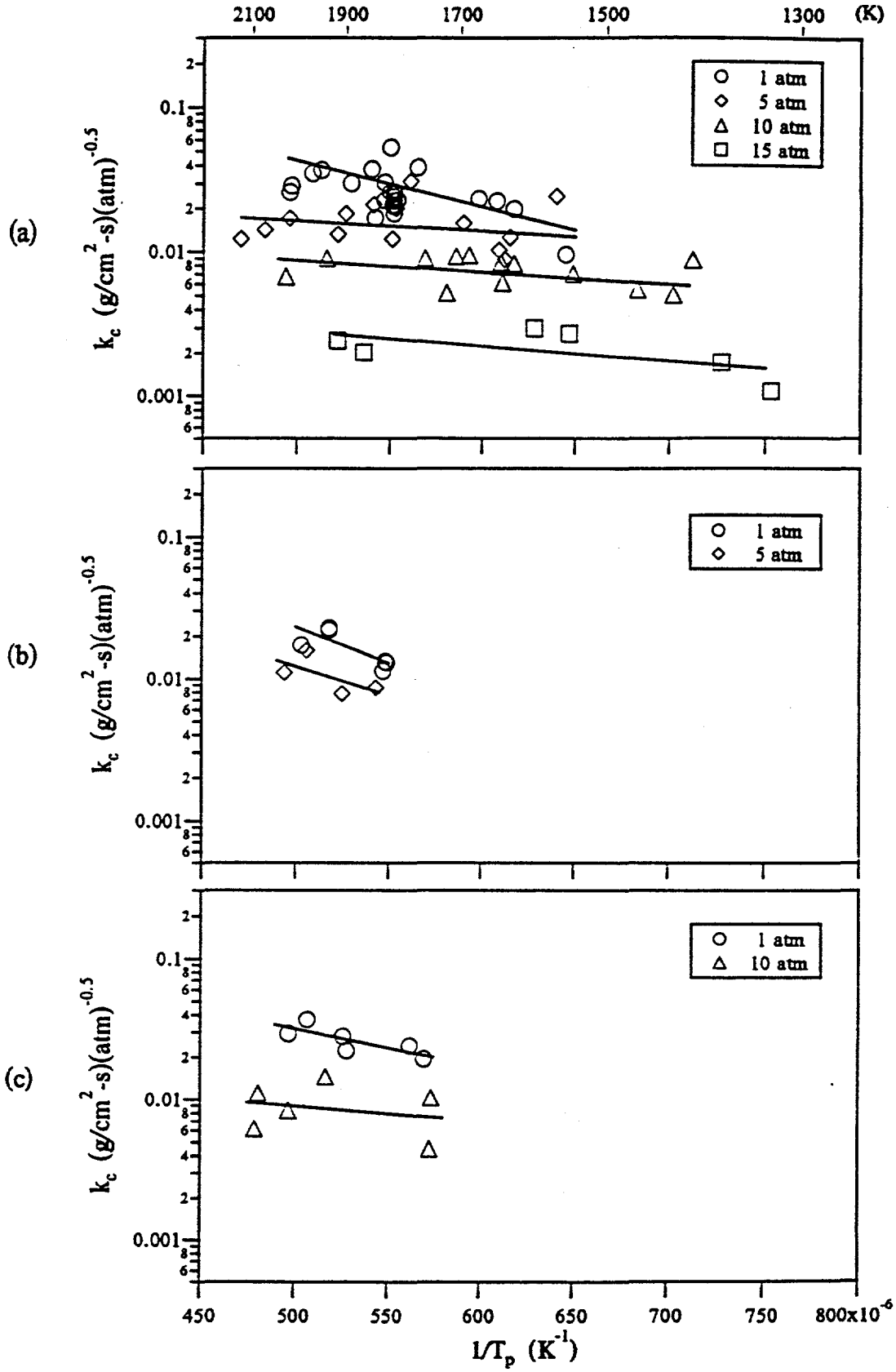

Figure II.B-19. Reaction rate coefficient as a function of particle temperature and total pressure for the a) 70 µm UT, b) 40 µm UT and c) 70 µm Pitt. Chars.

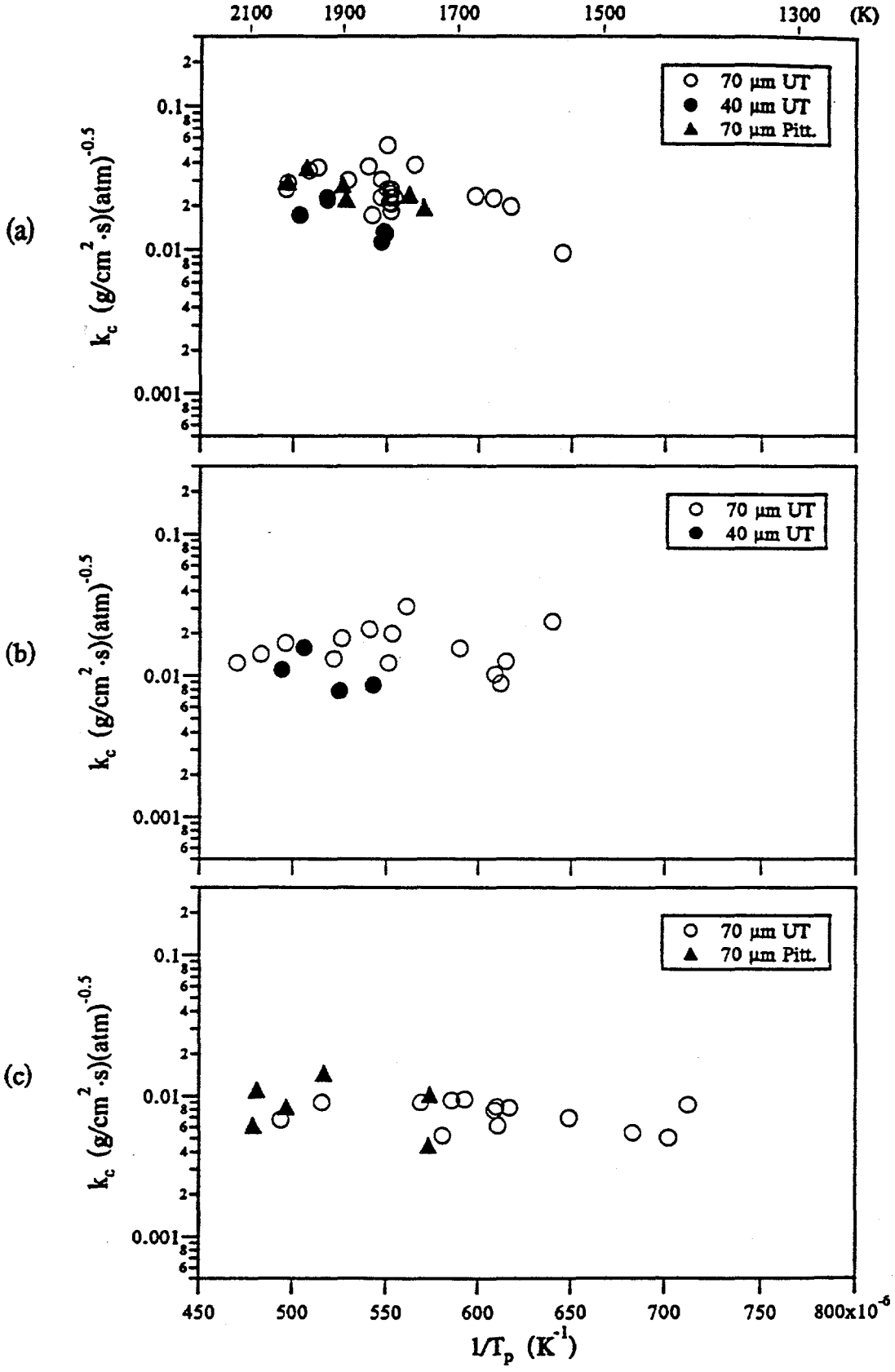

Figure II.B-20. Reaction rate coefficient as a function of particle temperature and char for a) 1 atm, b) 5 atm and c) 10 atm total pressures.

TABLE II.B-6

GLOBAL KINETIC PARAMETERS FOR AN APPARENT ORDER OF 1/2

Char	Pressure (atm)	A $(g/cm^2 \cdot s)(atm)^{-0.5}$	E (kcal/mol)
70 μm UT	1	1.780	14.8
	5	0.0382	3.4
	10	0.0227	3.8
	15	0.00981	4.9
40 μm UT	1	8.38	23.4
	5	1.38	18.8
70 μm Pitt.	1	0.700	12.3
	10	0.029	4.7

Because the choice of apparent order exerts a great influence on the determined Arrhenius parameters, the use of 0.5 for the order in this study must be rationalized. While an assumed order of 0 leads to no total pressure dependence of the Arrhenius parameters (the reaction rate coefficients are equivalent to the area reactivities), the 0^{th} order assumption is obviously erroneous as demonstrated by the unmistakable increase in experimentally observed reaction rates with increases in O_2 pressure. On the other hand, an assumed order of 1 leads to small and even negative activation energies. Model simulations have shown the predicted results to be fairly insensitive to the chosen order; assumed apparent orders from .5 to 1 lead to Arrhenius parameters that seem to fit the data equally well. Further, Essenhigh (1988) showed a smooth change in apparent order from 0 to 1 as char oxidation temperatures increased from 1000 to 2000 K. Thus the chosen order of 0.5 is a good average value and, as mentioned above, it has been used in recent atmospheric pressure char oxidation studies.

Model Predictions of the Elevated Pressure Data

The kinetic parameters derived from the data were used with the global model as a check on their predictive capabilities. Model simulations were performed for the conditions of the 70 μm UT char oxidation experiments. Fig. II.B-21 shows the model predictions.

The comparisons show that the model can be used to predict the data as long as adjustments are made in the kinetic parameters for differing total pressure (Table II.B-6). Assuming the chemistry of the carbon/oxygen reaction remains unchanged with pressure, the need to make adjustments in the kinetic parameters with pressure indicates some inadequacy in the model. Another observation increases concern over the model adequacy. While little difference is seen in the overall reaction rates measured for a range of pressures (Figs. II.B-13 - II.B-15), after using the model to account for bulk diffusion effects, the reaction rate coefficients show a very pronounced pressure effect (Fig. II.B-19).

This could be a result of pressure-related pore diffusion effects not accounted for in the global model such as the pore area available to oxygen decreasing with increasing pressure as Lester et al. (1981) conjectured. However, this would lead to an accompanying change in particle structure (a trend towards constant density burning with increasing pressure) and none of the structure measurements

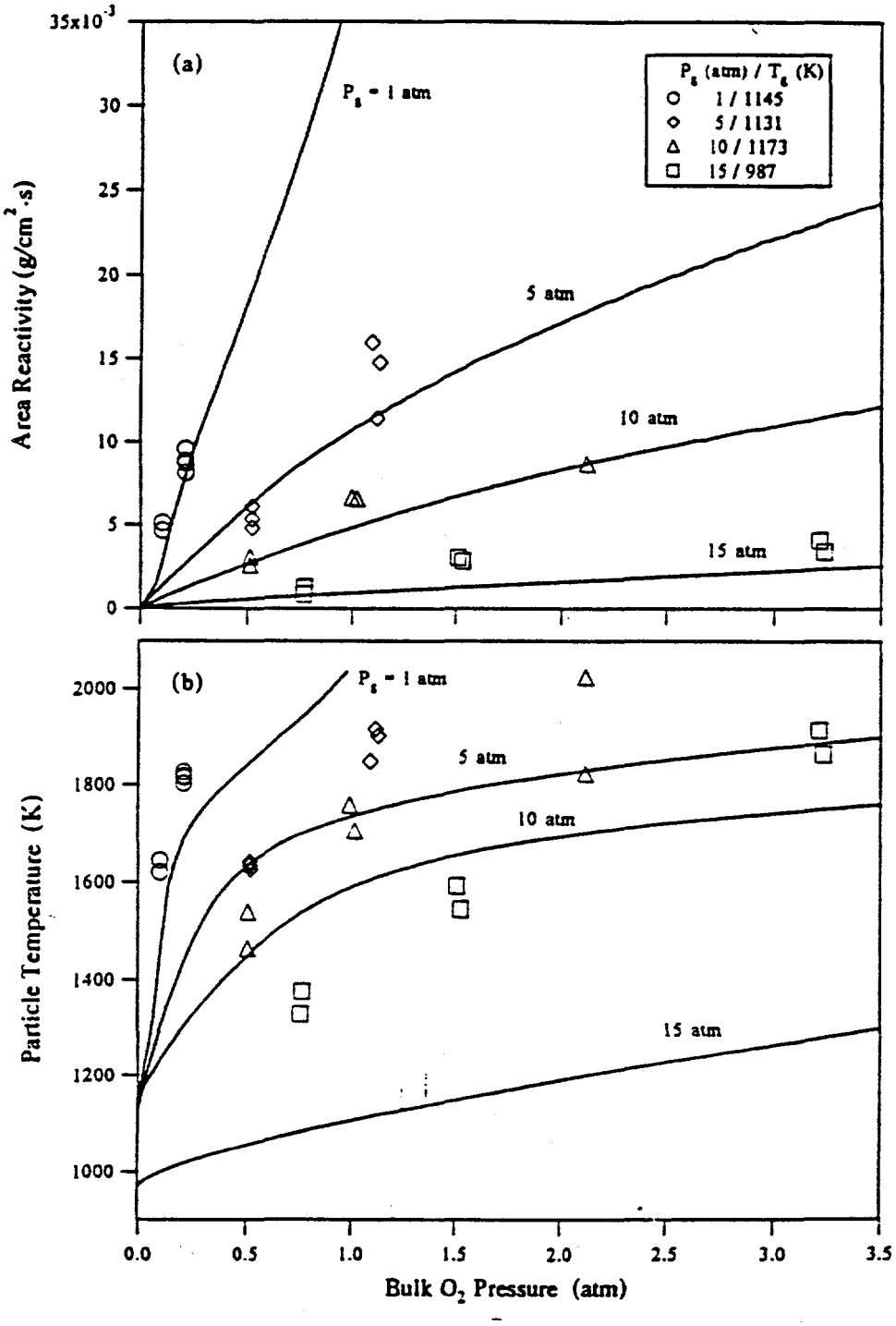

Figure II.B-21. Comparison of experimental data and model calculations for the 70 μm UT char. a) area reactivity and b) particle temperature. This is a check on consistency, not an independent prediction, since the model parameters were determined from these same data.

showed any significant effect of pressure. Also, unless the pore diffusion was also a complex function of temperature, a change in only the frequency factor, not the activation energy, would occur.

A more likely possibility is the inadequacy of the n^{th} order equation to predict changes with pressure. While it is commonly used and has proven adequate for predictive use at atmospheric pressure, the equation has no theoretical basis (Essenhigh, 1991). Extrapolation of this empirical equation to elevated pressure would be valid only if it were consistent with experimental results. With the very limited research conducted at elevated pressures to date, the validity of the equation at these conditions has not before been examined. While the general trends of the model are consistent with the high pressure data obtained in this study, the required variation of the kinetic coefficients with pressure to completely describe the data indicate the inadequacy of the n^{th} order equation to predict changes due to pressure effects. Use of a more fundamental rate equation, such as Langmuir- type kinetics, may better describe these total pressure effects.

Summary and Conclusions

The object of this study was to examine char oxidation at elevated pressure. To this end a high pressure facility was designed and constructed and char oxidation experiments were conducted at both atmospheric and elevated pressures.

The facility consists of a high pressure drop tube reactor, an optical pyrometer and support equipment. The electrically heated, computer controlled reactor has the following capabilities: pressure from 1 to 30 atm, temperature from 1000 to 1700 K, controllable temperature profile along the reaction tube length, particle residence times from 30 to 1000 ms, variable gas compositions of inert and oxidizing gases, and optical access ports for *in-situ* diagnostics. A particle imaging system providing *in-situ*, simultaneous measurement of individual particle temperature, size and velocity was developed for use in conjunction with the reactor. The pyrometer was shown to be both precise and accurate for the intended operating conditions (particles ranging from 30 to 150 μm at temperatures above 1500 K and velocities under 5 m/s). High quality temperature and velocity measurements were obtained over the entire design range, while high quality size measurements were obtained for all but the smallest particles and lowest temperatures. The size measurements were also limited to pressures below 10 atm.

Approximately 100 oxidation experiments were performed with two sizes of UT and Pitt. bituminous coal chars at 1, 5, 10, and 15 atm total pressure. Reactor temperatures were varied between 1000 and 1500 K and bulk gas compositions ranged from 5 to 21%, resulting in average particle temperatures ranged from 1400 to 2100 K with burnouts from 15 to 96%. Individual particle temperature, size and velocity were determined for approximately 75 particles at each test condition and overall reaction rates were independently determined from mass loss measurements. This allowed an internal check of the data consistency and insight into the products of combustion. Significant particle-to-particle variations were observed at each test condition. The results from the 1 atm UT char oxidation results were shown to be consistent with results obtained by other researchers using the same coal. The chars were found to be burning in mainly a reducing density mode in a regime intermediate between the kinetic and pore diffusion zones, irrespective of total pressure. While the global model was used to correlate the results of the study, the extrapolation of the n^{th} order rate equation to pressures higher than atmospheric was found to be invalid.

The effect of increasing total pressure on char oxidation at a constant gas composition can be summarized as follows. Raising total pressure also necessarily increases the bulk gas O_2 pressure, leading to an increase in the reaction rate. However, this increase is tempered by the decrease in oxygen diffusivity that also accompanies increases in pressure. The overall result is a slight increase in rate with increasing total pressure. Most of this change has occurred by 10 atm and further increases in total pressure produce little effect on the rate.

The major findings of the study are as follows:

1. In spite of careful size classification and char preparation, the resulting particle population exhibited substantial variation in combustion behavior.

2. Increasing total pressure in an environment of constant gas composition leads to modest increases in the reaction rate and particle temperature.

3. Significant kinetic control of the char oxidation process is exhibited at elevated pressures.

4. The global model kinetic parameters were found to be strongly dependent on the total pressure. This indicates that the empirical n^{th} order equation is not completely valid over the range of pressures covered in the experiments.

5. CO_2 formation must be accounted for at particle temperatures below about 1700 K. This is true regardless of the pressure.

6. Independent particle temperature and mass loss measurements are both experimental necessities to fully describe combustion behavior.

With little high pressure char oxidation data available in the literature, this study has begun to fill a much neglected area of coal combustion and gasification. Insight into the fundamentals of char oxidation at both atmospheric and elevated pressure has been gained. Practically, the results are directly applicable to pressurized coal combustion. Accurate high pressure oxidation predictions could be made using the nth order global model as long as the Arrhenius parameters were adjusted not only for coal types but for pressure as well. However, a number of issues still remain unresolved: Do Langmuir or other types of kinetics better explain the total pressure behavior?, Do other coal chars exhibit similar pressure effects?, How do pore diffusion characteristics change with pressure?, Do chars of different sizes behave similarly at elevated pressures?, can these trends be extrapolated to higher pressures?, What effects do different gas environments have at pressure? Further work is also necessary to quantify the effects of pressure on devolatilization as well as simultaneous devolatilization/oxidation before a complete understanding of the coal combustion process can be obtained.

NOMENCLATURE

A	apparent frequency factor	$(g_C/cm^2 \cdot s)(1/atm)^n$
A_c	CO/CO_2 apparent frequency factor	
A_p	particle external surface area	(cm^2)
A_{pm}	mean particle external surface area	(cm^2)
B	carbon burnoff	(%)
B_f	blowing factor	
C_{pg}	gas specific heat	(cal/mole·K)
D_{ox}	oxygen diffusivity	(cm^2/sec)
d_p	particle diameter	(cm)
E	apparent activation energy	(cal/mole)
E_c	CO/CO_2 activation energy	(cal/mole)
h	convection heat transfer coefficient	$(cal/cm^2 \cdot s \cdot K)$
ΔH	heat of reaction	(cal/g_C)
k_c	apparent chemical reaction rate coefficient	$(g_C/cm^2 \cdot s)(1/atm)^n$
k_d	film diffusion rate coefficient	$(g_C/cm^2 \cdot s)(1/atm)$
m	mass of carbon	(g)
M_C	carbon molecular weight (12)	(g/g·mole)
m_o	initial mass of carbon	(g)
n	apparent reaction order	
Nu	Nusselt number	
P	total gas pressure	(atm)
P_{og}	oxygen partial pressure in the bulk gas	(atm)
P_{os}	oxygen partial pressure at the particle surface	(atm)
q_a	overall rate of carbon consumption per unit external surface area (area reactivity)	$(g_C/cm^2 \cdot s)$
q_m	mass reactivity	(g/g·s)
Pr	Prandtl number	
R	gas constant (1.9859)	(cal/mole·K)
R'	gas constant (82.32)	$(atm \cdot cm^3/mole \cdot K)$
Re	Reynolds number	
t	time	(s)
T_g	gas temperature	(K)
T_p	particle temperature	(K)
t_r	particle residence time	(s)
T_w	wall temperature	(K)
v_p	particle velocity	(cm/s)
v_∞	particle terminal velocity	(cm/s)
x_a	mass fraction of ash	
α	burning mode parameter	
γ	intermediate factor based on ψ (Eq. 4)	
ε	particle emissivity	
λ	gas thermal conductivity	(cal/cm·s·K)
μ	gas viscosity	(g/cm·sec)
ρ	gas density	(g/cm^3)
ρ_a	ash apparent density (1.5)	(g/cc)
ρ_{app}	particle apparent density	(g/cc)
ρ_b	bulk density	(g/cc)

ρ_c	carbon density	(g/cc)
ρ_{co}	initial carbon density	(g/cc)
σ	Stefan-Boltzmann constant ($1.345 \cdot 10^{-12}$)	($cal/cm^2 \cdot s \cdot K^4$)
χ	fraction of measured to CO diffusion limited rate	
ψ	fraction of CO_2 production	

References for Section 2.b.

Annamalai K. and Ramalingham S.C., Group Combustion of Char/Carbon Particles, Combustion and Flame, **70**, 307 (1987).

Arthur, J.R., Reaction Between Carbon and Oxygen, Transactions of the Faraday Society, **47**, 164, (1951).

Essenhigh, R.H., An Integration Path for the Carbon-Oxygen Reaction with Internal Reaction, Twenty -Second Symposium on Combustion/The Combustion Institute, 89 (1988).

Essenhigh, R.H., Rate Equations for the Carbon-Oxygen Reaction: An Evaluation of the Langmuir Adsorption Isotherm at Atmospheric Pressure, Energy and Fuels, **5**, 41 (1991).

Field, M. A., Measurement of the Effect of Rank on the Combustion Rates of Pulverized Coal, Combustion and Flame, **14,** 237 (1970).

Frank-Kamenetskii, D.A., *Diffusion and Heat Transfer in Chemical Kinetics*, Plenum Press, New York - London, 1969.

Hurt, R.H and Mitchell, R.E., Unified High-Temperature Char Combustion Kinetics for a Suite of Coals of Various Ranks, Twenty Fourth International Symposium on Combustion, The Combustion Institute, Pittsburgh, PA, (1992a).

Laurendeau, N.M., Heterogeneous Kinetics of Coal Char Gasification and Combustion, Progress in Energy and Combustion Science, **4**, 221 (1978).

Leslie, I.H., Jost, M., Kruger, C.H., Measured and Predicted Char Reactivity of Three U.S. Coals, Combustion and Flame, **78**, 195 (1989).

Lester, T.W., Seeker, W.R. and Merklin, J.F. , The Influence of Oxygen and Total Pressure on the Surface Oxidation Rate of Bituminous Coal, Eighteenth Symposium on Combustion/The Combustion Institute, 1257 (1981).

Mitchell, R.E.and McLean, W.J., On the Temperature and Reaction Rate of Burning Pulverized Fuels, Nineteenth International Symposium on Combustion, The Combustion Institute, Pittsburgh, PA, 1113 (1982).

Mitchell, R.E., On the Products of the Heterogeneous Oxidation Reaction at the Surfaces of Burning Coal Char Particles, Twenty Second International Symposium on Combustion, The Combustion Institute, Pittsburgh, PA, 69 (1988).

Mitchell, R.E., Kee, R.J., Glarborg, P., and Coltrin, M.E. The Effect of CO Conversion in the Boundary Layers Surrounding Pulverized-Coal Char Particles, Twenty Third International Symposium on Combustion, The Combustion Institute, Pittsburgh, PA, (1990b).

Mitchell, R.E., Hurt, R.H., Baxter, L.L., Hardesty, D.R. Compilation of Sandia Coal Char Combustion Data and Kinetic Analyses, Milestone Report, Sand92-8208, Sandia National Laboratories at Livermore, September 1991.

Niksa, S., Mitchell, R.E., Hencken, K.R., and Tichenor, D.A., Optically Determined Temperatures, Sizes and Velocities of Individual Carbon Particles under Typical Combustion Conditions, Combustion and Flame, **60**, 183 (1984).

Pace, R.S., Titanium as a Tracer for Determining Coal Burnout, M.S. Thesis, Brigham Young University, Dept. of Chem. Eng., Provo, UT (1982).

Smith, I.W., The Combustion Rates of Coal Chars: A Review, Nineteenth International Symposium on Combustion, The Combustion Institute, Pittsburgh PA, 1045 (1982).

Solomon, P.R., Serio, M.A., Hamblen, D.G., Smoot, L.D. and Brewster, B.S., Measurement and Modeling of Advanced Coal Conversion Processes, 5th Annual Report, DOE-METC Contract No. DE-AC21-86MC23075, Advanced Fuel Research, Hartford, CT, (1991).

Solomon, P.R., Serio, M.A., Hamblen, D.G., Smoot, L.D. and Brewster B.S., Measurement and Modeling of Advanced Coal Conversion Processes, 5th Annual Report, DOE-METC Contract No. DE-AC21-86MC23075, Advanced Fuel Research, Hartford, CT, (1990).

Solomon, P.R., Serio, M.A., Hamblen, D.G., Smoot, L.D. and Brewster B.S., Measurement and Modeling of Advanced Coal Conversion Processes, 5th Annual Report, DOE-METC Contract No. DE-AC21-86MC23075, Advanced Fuel Research, Hartford, CT, (1991).

Tichenor, D.A., Mitchell, K.R., Hencken, K.R., Niksa, S., Simultaneous In Situ Measurement of the Size, Temperature and Velocity of Particles in a Combustion Environment, Twentieth International Symposium on Combustion, The Combustion Institute, Pittsburgh, PA, 1213 (1984).

Tsai, C.Y., Scaroni, A.W., The Structural Changes of Bituminous Coal Particles During the Initial Stages of Pulverized-Coal Combustion, Fuel, **66**, 200 (1987).

Waters, B.J., Squires, R.G., Laurendeau, N.M., and Mitchell, R.E., Evidence for Formation of CO_2 in the Vicinity of Burning Pulverized Carbon Particles, Combustion and Flame, **74**, 91 (1988).

Young, B.C. and Smith, I.W., The Kinetics of Combustion of Petroleum Coke Particles at 1000 to 1800 K: The Reaction Order, Eighteenth Symposium on Combustion/The Combustion Institute, 1249 (1981).

Young, B.C.and Niksa, S., Combustion Rates for Selected Low-Rank Coal Chars, Fuel, **67**, 155 (1988).

II.C. SUBTASK 2.c. - SECONDARY REACTION OF PYROLYSIS PRODUCTS AND CHAR BURNOUT SUBMODEL

Senior Investigators - Peter R. Solomon, James R. Markham, and Michael A. Serio
Advanced Fuel Research, Inc.
87 Church Street, East Hartford, CT 06108
(203) 528-906

Objective

The objective of this subtask was to develop and evaluate by comparison with laboratory experiments, an integrated and compatible submodel to describe the secondary reactions of volatile pyrolysis products and char burnout during coal conversion processes. Experiments on tar cracking, soot formation, tar/gas reactions, char burnout, and ignition were done in order to allow validation of submodels.

Summary of Accomplishments

The processes addressed under this subtask were:

- ignition
- soot formation
- soot radiation
- char burnout

These processes were studied using a new laminar coal flame experiment developed at AFR known as the Transparent Wall Reactor (TWR) and a novel diagnostic method known as Fourier Transform Infrared (FT-IR) Emission/Transmission (E/T) Tomography. This work is described in a number of publications and papers that resulted from this contract:

- Solomon, P.R., Chien, P.L., Carangelo, R.M., Best, P.E., and Markham, J.R., Application of FT-IR E/T Spectroscopy to Study Coal Combustion Phenomena, paper presented at the Int. Coal Combustion Symposium, Beijing, China (1987).
- Solomon, P.R., Chien, P.L., Carangelo, R.M., Best, P.E., and Markham, J.R., Application of FT-IR Emission/Transmission (E/T) Spectroscopy to Study Coal Combustion Phenomena, The 22nd Symposium (Int) on Combustion, The Combustion Institute, Pittsburgh, PA, p. 211 (1988).
- Solomon, P.R., Best, P.E., Markham, J.R., and Klapheke, J., The Study of Coal Flames Using FT-IR Emission/Transmission Tomography, Int. Conference on Coal Science Proceedings, IEA, Tokyo, Japan, p. 329 (October 23-27, 1989).
- Solomon, P.R., Serio, M.A., and Markham, J.R., Kinetics of Coal Pyrolysis, Int. Conference on Coal Science Proceedings, IEA, Tokyo, Japan, p. 575, (October 23-27, 1989).
- Brewster, B.S., Smoot, L.D., and Solomon, P.R., Structure of a Near Laminar Coal Jet Diffusion Flame, Poster Session, 23rd Symposium (Int) on Combustion, The Combustion Institute, Orleans, France (1990).
- Solomon, P.R., Chien, P.L., Carangelo, R.M., Serio, M.A., and Markham, J.R., New Ignition Phenomenon in Coal Combustion, Combustion & Flame, 79, 214 (1990a).

- Solomon, P.R., Markham, J.R., Zhang, Y.P., and Carangelo, R.M., FT-IR Emission/Transmission Tomography of Coal Flames, ACS Div. of Fuel Chem. Preprints, **35**, (3), 746, (1990).

- Markham, J.R., Zhang., Y.P., Carangelo, R.M., and Solomon, P.R., FT-IR Emission/Transmission Tomography of a Coal Flame, 23rd Symposium (Int) on Combustion, The Combustion Institute, Orleans, France, pp 1869-1875 (1990).

- Solomon, P.R., and Best, P.E., Fourier Transform Infrared Emission/Transmission Spectroscopy in Flames, in *Combustion Measurements*, (N. Chigier, Ed.), Hemisphere Publishing Corp. pp. 385-344 (1991).

- Brewster, B.S., Smoot, L.D., Solomon, P.R., and Markham, J.R., Structure of a Near-Laminar Coal Jet Flame, Energy and Fuels 7 (6), 884 (1993).

- Solomon, P.R., On-Line Fourier Transform Infrared Spectroscopy in Coal Research, in *Advances in Coal Spectroscopy*, (H.L.C. Meuzelaar, Ed.), Plenum Publishing Corp. pp. 341-371 (1992).

The work done under this subtask is described below. In cases where the work has been well documented in the open literature, reference has been made to the appropriate publications and only the abstracts are included. Details of the work can also be found in the Quarterly and Annual reports for this contract. Additional studies of char burnout were performed under Subtasks 2.a., 2.b., and 2.f. Studies of tar cracking were also made under Subtask 2.e.

II.C.1. Application of FT-IR Emission/Transmission (E/T) Spectroscopy to Study Coal Combustion Phenomena

This work was described in Solomon et al. (1988). The abstract for this paper is given below.

Abstract

This paper describes the application of a recently described Fourier Transform Infrared (FT-IR) Emission and Transmission (E/T) technique to study coal flames produced in a transparent wall reactor. Comparisons are made for the ignition, soot formation, particle temperature and gas temperature for a number of coals varying in rank from lignite to low volatile bituminous. Samples of chars prepared at different temperatures and demineralized coals were also studied. Flame properties were compared with characteristics of the samples to determine the factors which control flame behavior. A comparison of the ignition of several samples suggests that the rate of ignition correlates with the initial rate of weight loss in air in a TGA experiment at lower temperatures. Ignition of chars is heterogeneous; ignition of high rank coals is homogeneous; but low rank coals exhibit both homogeneous and heterogeneous contributions to ignition. Soot formation in combustion correlates well with the tar yield in pyrolysis, suggesting that tar is the chief precursor of soot.

This work is also discussed in a paper by Solomon et al. (1987) and in review articles by Solomon and Best (1991) and Solomon (1992).

II.C.2. FT-IR E/T Tomography of a Coal Flame

This work is discussed briefly in Solomon et al. (1989) and in more detail by Markham et al. (1990). The abstract for the latter paper is given below:

Abstract

Fourier Transform Infrared (FT-IR) Emission/Transmission (E/T) spectroscopy has recently been shown

to be a versatile technique for coal combustion diagnostics by allowing for measurements of particle concentrations and temperatures, and gas compositions, concentrations, and temperatures. These measurements are for the ensemble of particles and gases along a line-of-sight in the flame. In this paper, tomographic reconstruction techniques have been applied to line-of-sight FT-IR E/T measurements to derive spectra that correspond to small volumes within a coal flame. From these spectra, spatially resolved point values for species temperature and relative concentrations can be determined. The technique was used to study the combustion of Montana Rosebud subbituminous coal burned in a transparent wall reactor. The coal is injected into the center of an up-flowing preheated air stream to create a stable flame. Values for particle temperature, relative radiance intensity, the relative CO_2 concentrations and the CO_2 temperature have been obtained as functions of distance from the flame axis and height above the coal injector nozzle. The spectroscopic data are in good agreement with visual observations and thermocouple measurements. The data present a picture of the coal burning in a shrinking region which collapses to the center at the tip of the flame. The highest CO_2 temperatures are 2200 to 2600 K. The highest particle temperatures are 1900 to 2000 K with occasional temperatures up to 2400 K.

This work is discussed further Solomon et al. (1990), where a second Rosebud subbituminous coal flame was studied which was produced using a slower flow of preheated gas, along with a third flame produced from Pittsburgh Seam bituminous coal under the same conditions. The three flames showed both coal and flow dependent phenomena. The slow flow cases showed reduced mixing (more soot and more variations in flame properties with radius) compared to the fast flow case. The Pittsburgh Seam coal produced higher soot yields, higher particle swelling, lower particle temperatures and lower char reactivity when compared to the Rosebud coal.

II.C.3. New Ignition Phenomenon in Coal Combustion

A new ignition phenomenon has been observed during the studies of coal combustion in the TWR. The experiment, which was described in several publications (Solomon et. al., 1988; Markham el al., 1990), injects coal particles suspended in a room-temperature carrier gas as a jet into a flowing preheated air stream. The new phenomenon is shown in Fig. II.C-1, which is a photograph of several ignited coal or char particles traveling upward. The particles of interest are at the edge of the cold particle stream and have first contact with the surrounding hot preheated gas stream. They ignite and appear to burn on the particle's surface, as indicated by the fact that the width of the luminosity is roughly that of the particle diameter. The particles become hotter with increasing distance.

The new ignition phenomenon occurs after the particles have burned for a short time. Under these conditions there is often a secondary ignition event. To the unaided eye, it looks like a bright flash of light at the end of a long luminous trajectory. When viewed through a microscope, this event has the following characteristics.

1. The dimension of the second flame zone increased to about 3 times the original dimension.

2. The second flame appears to be hotter than the original.

3. The second flame often ends with particle fragmentation, suggesting burnout of the char.

4. The duration of the flame is on the order of a few milliseconds.

5. The flame appears to oscillate or spiral around the particle in almost all (90%) cases.

The effect has been observed for chars as well as coals, so it is not associated with volatiles. The effect has been observed for demineralized coals and thus is not a mineral effect.

One possibility is that the flame results from CO burning in a sheath surrounding the particle rather than well away from the particle. This would transfer the heat from the $CO \rightarrow CO_2$ flame back to the particle

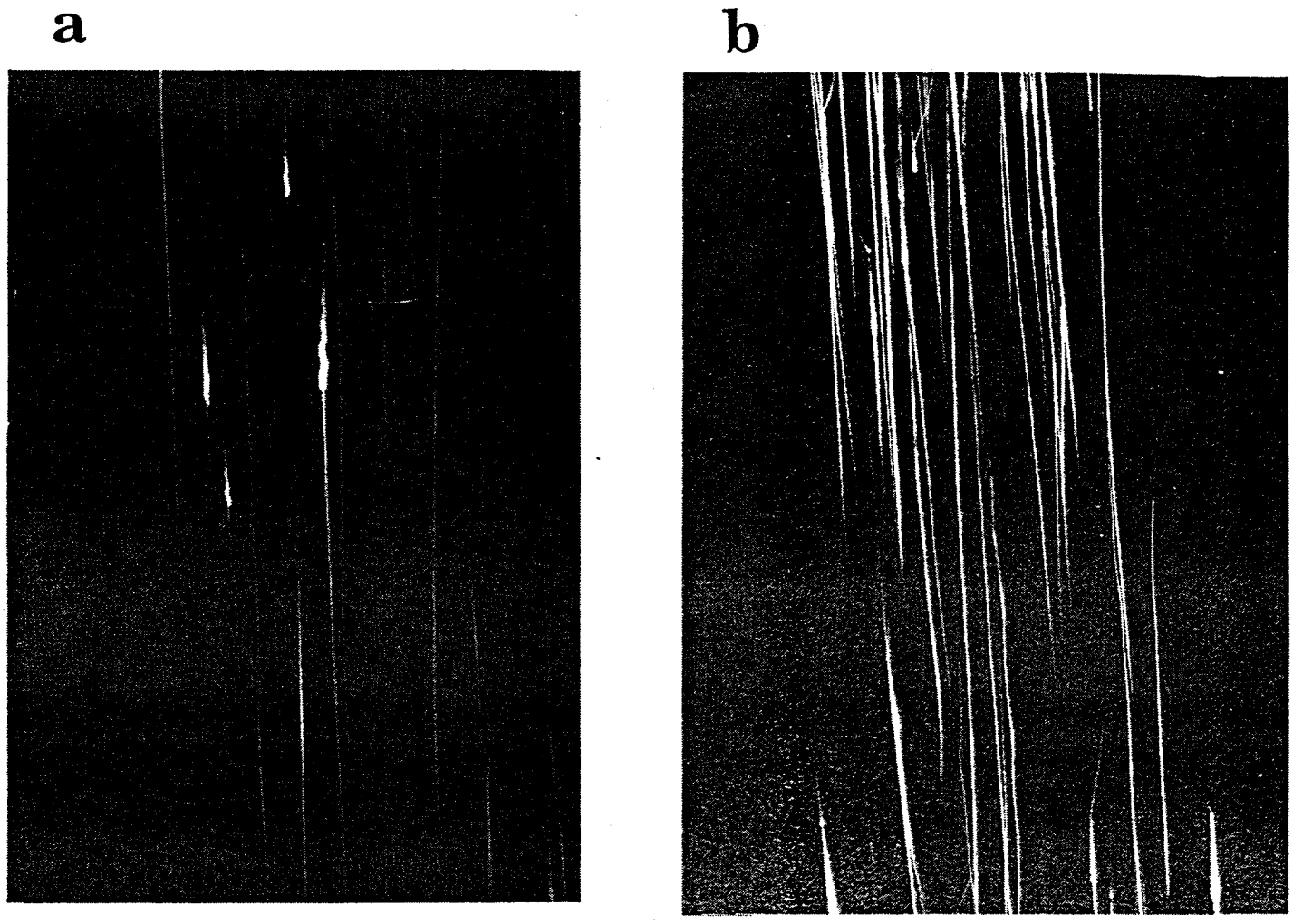

Figure II.C-1. Secondary Ignition Observed for a) Coal and b) Char Particles.

and result in a more intense flame with the possibility of more rapid burnout. However, this mechanism requires that the chief heterogeneous reaction be CO_2 gasification on the coal particles surface. The higher temperature may make this slower reaction possible.

This work is discussed further in Solomon et al. (1990a). Further work is required to more fully characterize and explain this new phenomenon.

II.C.4. Pyrolysis Experiments with In-Situ FT-IR Diagnostics in the TWR

Introduction

In the literature, there are orders of magnitude discrepancies in the reported rates for coal pyrolysis weight loss or tar loss. The conflict in values and the reasons for the conflict have been discussed previously (Solomon and Hamblen, 1985; Solomon and Serio, 1987; Solomon et. al., 1992). These studies concluded that inaccurate knowledge of coal particle temperatures was the chief cause of the variations.

To improve the knowledge of particle temperatures, a new method was developed which employs a Fourier Transform Infrared (FT-IR) spectrometer to measure the emission and transmission (E/T) in a reacting particle stream (Solomon and Hamblen, 1985; Serio et al., 1987). This technique has been applied to measure the temperature of coal particles in an entrained flow reactor (EFR) (Best et al., 1986; Solomon et al., 1987a) and a heated tube reactor (HTR) (Solomon et al. 1986). The kinetic rate, determined from these experiments for a number of coals and lignites was 8.6×10^{14} exp (-228,500/RT) sec^{-1} for tar loss (or approximately half this value for weight loss) and was the highest ever reported at temperatures above 600°C. There were, however, some limitations to these experiments. The EFR experiments only allowed optical access for temperature measurement at one position and the HTR was limited to non-swelling coals. Recent experiments by Fletcher (1989) in an apparatus which does not have these limitations and which employs temperature measurements by 2-color pyrometry have confirmed these high rates within a factor of 2 for both low and high rank coals.

Under this subtask, kinetic rate measurements were made on a Zap North Dakota lignite and a Pittsburgh Seam bituminous coal in the transparent wall reactor (TWR) which does not have the limitations of the HTR or EFR. The temperature measurements were made with the FT-IR E/T technique. This reactor, with the in-situ FT-IR diagnostics, was used under this subtask to make spatially resolved measurements on coal flames using a tomographic technique, as discussed above. These measurements provide fundamental data on the processes of ignition, soot formation, and char burnout for submodel validation. The pyrolysis experiments allow a test of the experimental and optical systems for a simpler set of conditions.

Experimental

The measurement of particle temperatures from the particle's emitted radiation is difficult if the pyrolysis reactor has hot walls. In this case, wall radiation scattered by the particles interferes with the emitted radiation. To overcome this problem, the pyrolysis experiments in this study were performed in a reactor with relatively cold walls. The apparatus is a transparent wall reactor (TWR) which has been discussed above and in the literature (Solomon et al., 1989c). Nitrogen is passed through a heat exchanger and enters a reaction section at approximately 850°C. Coal entrained in cold nitrogen carrier gas is injected through a co-axial 7 mm diameter tube into the preheated stream. An octagonal glass enclosure shields the pyrolyzing stream from room air currents. The glass enclosure has movable KBr windows to allow access to the flame for radiation measurements. Particle velocities were measured using a video camera under slightly oxidizing conditions which allowed a small percentage of the particles to ignite.

To measure temperatures of pyrolyzing coal particles, several other problems had to be overcome.

Because pyrolysis in this reactor occurs at relatively low temperatures (600-800°C), the measurements are made in the mid-infrared where sufficient energy is emitted. In addition, coal is not a gray-body and its emissivity changes during pyrolysis. To overcome this problem, the temperature has been measured using the amplitude of the radiated energy in a frequency range where the emissivity is close to one and independent of the extent of pyrolysis. The transmission is used to determine the emitting surface area of the particles. Finally, soot radiation can make the particle temperature appear much higher than it really is. Measurements have been made with a gas temperature of 850°C, so soot formation did not occur.

The coals studied in this work were a dried Zap North Dakota lignite and a Pittsburgh Seam bituminous coal. The ultimate analyses are approximately those reported in Serio et al. (1987). Both samples were sized to 200 x 325 mesh. Weight loss was determined from captured char particles, by ash tracer analysis, using a Perkin Elmer TGA.

Results and Discussion

The emission spectra for the pyrolyzing particles at 15 cm above the injector are presented in Solomon et al. (1989) and Solomon (1992). The spectra are normalized by the emitting surface area using the measured attenuation at 3500 cm^{-1} assuming a total extinction efficiency of 1.2. The spectra are not gray-body. They reveal the infrared absorption bands in the char, such as the higher hydroxyl and carbonyl bands in the lignite and the higher aliphatic and aromatic C-H bands in the bituminous coal. Bands for pyrolysis water, CO_2, and CO are also apparent. Particle temperatures were determined by matching the theoretical black-body curves curves to the radiance at 1600 cm^{-1}, where the emissivity is approximately 1.0 (Best et al., 1986).

Spectra such as these were obtained for both coals at positions between 5 and 40 cm. In addition, char samples were captured at a number of locations and the FT-IR E/T technique was used to determine both particle and CO_2 temperatures (Solomon et al., 1987a,1989c). The CO_2 and particle temperatures agree to within 100°C. The thermocouple temperature measurements averaged across the estimated width of the particle stream are also in reasonable agreement, except early in the early stages when the particles are heating and in the later stages when the gas is cooling. The particle's heating rate is about 5000°C/sec. Data were also obtained for the weight loss determined by ash tracer analysis, which are compared to predictions of the FG-DVC model (Solomon et al., 1988).

As discussed in Solomon et al. (1989) and Solomon (1992), the high kinetic rates for tar evolution or weight loss recently reported by Solomon et al. (1985,1986a), Serio et al. (1987) and Fletcher (1989) are supported by these TWR measurements. At high heating rates, significant pyrolysis occurs within 100 ms at temperatures between 700 and 1000 K for both a lignite and a bituminous coal. At lower heating rates, the differences in rate between coals of different rank are more readily apparent (see subtask 2.a.).

II.C.5. Gas Flow Characteristics and Sample Burnout Profiles in the TWR

Introduction

In order to provide data for validation of the PCGC-2 code predictions (reported under Subtask 3.a.) and discussed in Brewster et al. (1990, 1993) an effort was directed at characterizing the TWR with regard to air and particle velocities, gas temperature profiles, particle spreading, and char burnout as a function of distance from the nozzle.

Results and Discussion

Radial gas temperature measurements were taken by thermocouples with and without coal being injected. Figure II.C-2, for the no coal case, shows measurements done from 2 mm above the nozzle to 70 cm above the nozzle. The measurements were taken with a bare 0.005" diameter bead chromel-alumel thermocouple, which was corrected for radiation loss to the cold walls, and for thermocouple surface

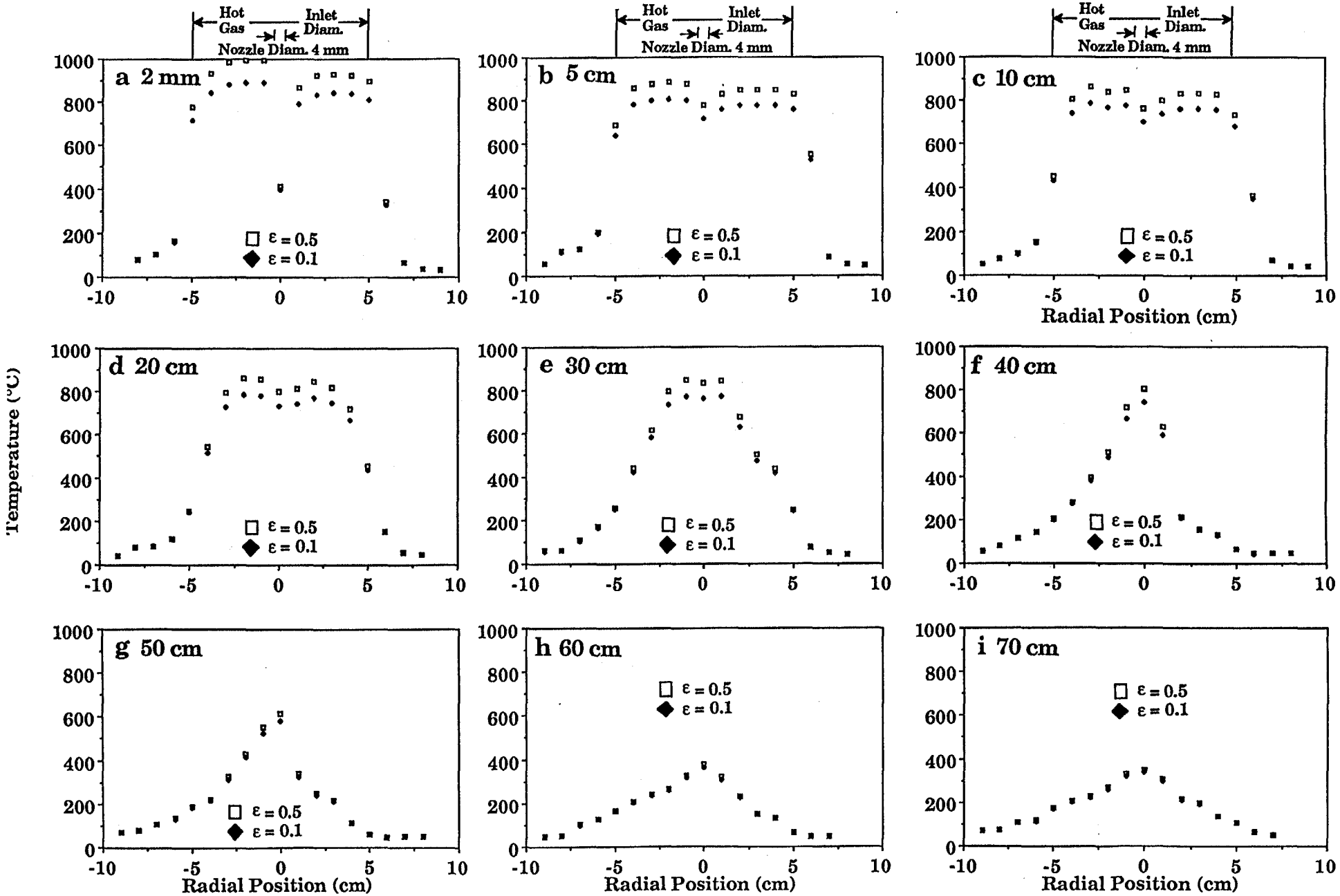

Figure II.C-2. Radial Gas Temperature Profile in the TWR, No Coal Case.

emissivity. Emissivity values of 0.1 and 0.5 were used, based on a literature value range for shiny to oxidized surfaces of this material. The figure clearly shows the region where cold gas is injected through the nozzle and that the integrity of the hot gas column is maintained through 20 cm.

Figure II.C-3 again profiles the gas temperature, but with 200 x 325 mesh Montana Rosebud coal injected into the TWR. For this case a 0.015" diameter platinum - 13% rhodium/platinum thermocouple was used. Surface emissivity values of 0.1 and 0.9 were used, based on the extremes of shiny metal to a soot/carbon coated surface. Profiles similar to the no coal case were observed, except for in the coal region, where the temperature greatly increases upon ignition of the coal at 10 cm above the nozzle.

The dimensions of the particle stream for the Rosebud flame were measured with a video camera. A schematic is shown in Fig. II.C-4. Above the ignition point, direct recording of the flame width was possible; below the ignition point, a He-Ne laser was directed through the particle stream and the laser light that was scattered by the particles was used to define the stream boundaries. The dimensions determined by the video camera were in agreement with spectroscopic detection of particles during the tomography measurements, and for detection of trace amounts of SO_2 fed through the nozzle.

Particle velocities as a function of distance from the nozzle are shown in Fig. II.C-5 for pyrolysis (N_2) and combustion (air) conditions. These were measured from particle tracks that were recorded with the video camera at a known shutter speed. For pyrolysis conditions, a small amount of oxygen was added to the gas stream to allow a small percentage of the particles to ignite. The particle velocities for each case are similar until beyond 20 cm above the nozzle. At this point the pyrolyzing stream approaches the calculated velocity of the hot gas at the nozzle region. Under combustion conditions, however, the energy released upon ignition drives the particles to higher velocities.

Particle burnouts as a function of distance from the nozzle were measured for 200 x 325 mesh samples of a dry Zap lignite, dry Rosebud subbituminous coal, and Pittsburgh Seam bituminous coal. Char collections were achieved with a 5/8" diameter water cooled extractor that adds cold helium gas to the removed hot particle stream as it is aspirated to a cyclone separator. The extractor inlet temperature was maintained below 300°C by the helium addition

Percent burnout was determined by ash tracer analysis of the collected char. The results are presented in Fig. II.C-6. One observation is the rank dependent effect on char reactivity, as indicated by the interval of time necessary to achieve 100% burnout: Zap < Rosebud < Pittsburgh.

II.C.6 In-Situ FT-IR Diagnostics in BYU Gasifier

An optical path was added to the BYU gasifier to allow the FT-IR transmission and emission measurements, as shown in Figs. II.C-7 and II.C-8. Figure II.C-7 shows the location of the optical path for the gasifier, while Fig. II.C-8 shows the schematic details of the spectrometer optics. The method requires two basic measurements: an emission spectrum from the flame through the spectrometer to the emission detector, and a transmission spectrum using the IR source within the spectrometer through the flame to the transmission detector. Several calibration spectra are also required: 1) a background emission spectra from the hot gasifier without a flame (to correct the emission spectra for gasifier wall radiation); 2) an emission spectrum from a black-body source (to correct the emission spectrum from instrument losses and detector sensitivity, etc.); and 3) a transmission spectrum without a flame (to correct the transmission spectrum from instrument and optical path effects).

An example of the corrected transmission ($1-\tau$) and emission (E) spectra are shown in Fig. II.C-9a,b. The emission (radiance) curve represents the radiation per unit area of the flame. The normalized emission, $E/(1-\tau)$, has the effect of normalizing to effective area of the radiating particles to provide the radiation per unit area of radiating particles and gases (Fig. II.C-9c). In the regions of the spectrum in Fig. II.C-9c where there are no gas absorptions, the curve can be fit by a black-body Planck function, scaled

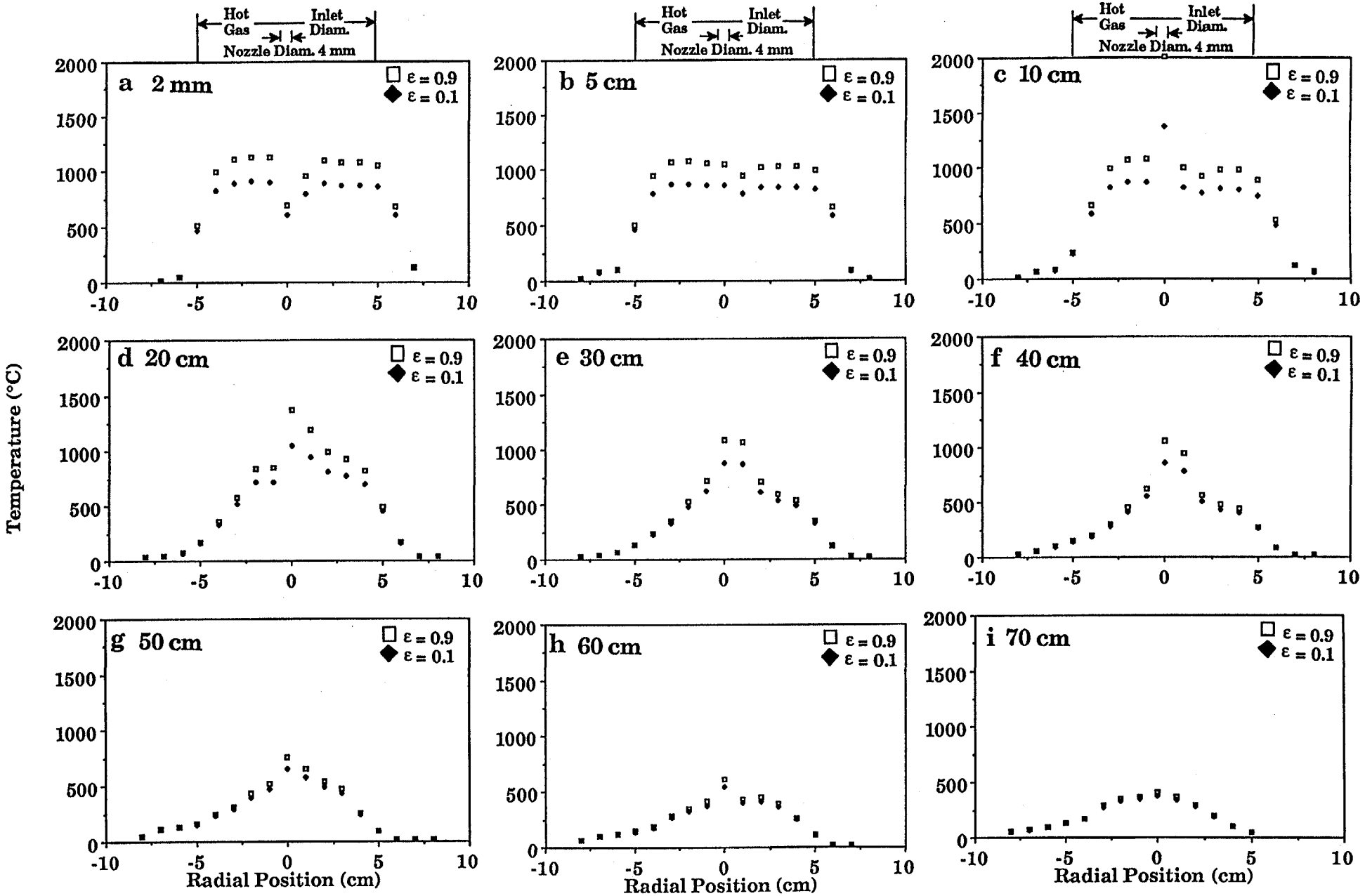

Figure II.C-3. Radial Gas Temperature Profile in the TWR During Combustion of Montana Rosebud Coal.

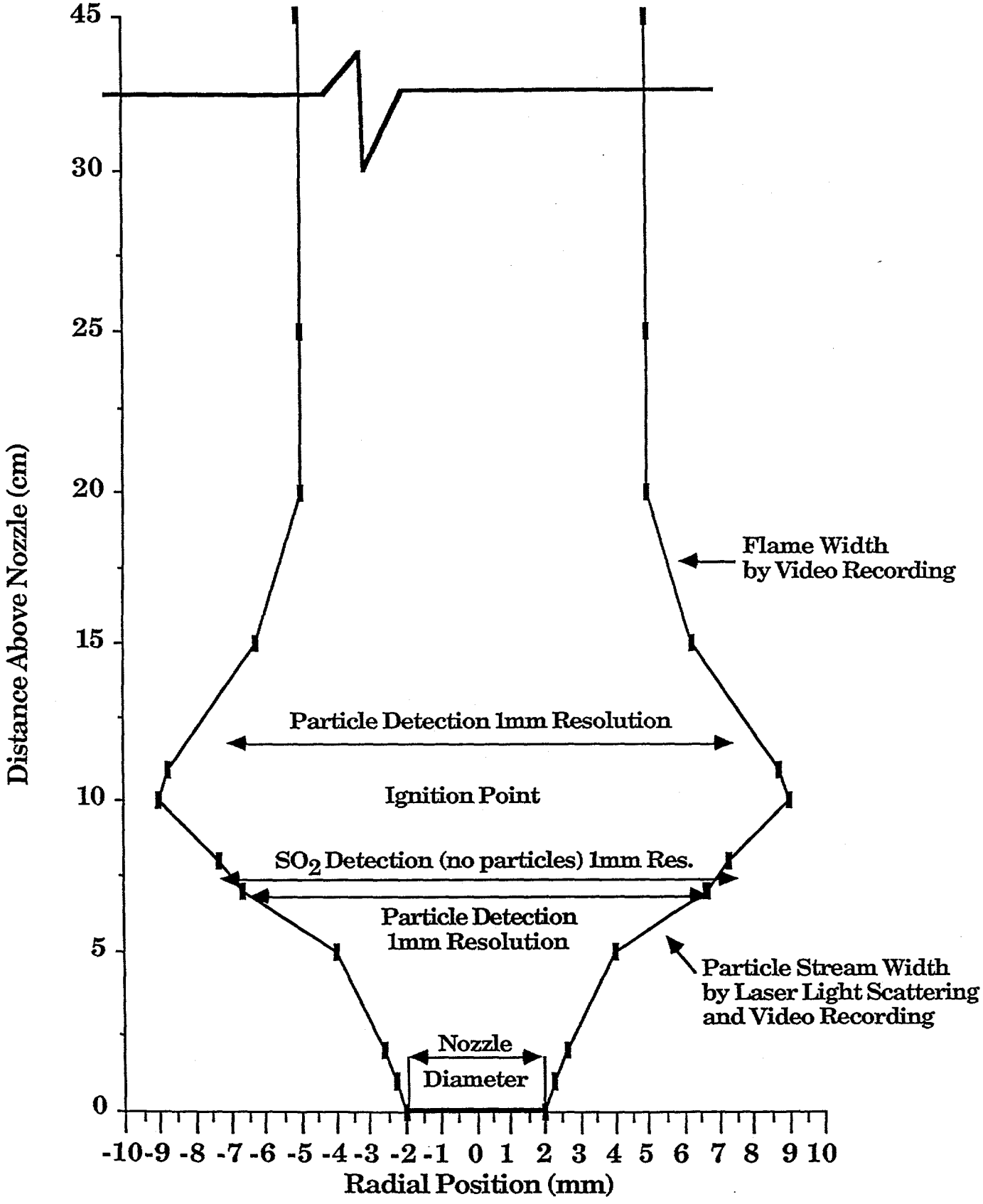

Figure II.C-4. Schematic of Montana Rosebud Particle Stream Boundaries before and after Ignition.

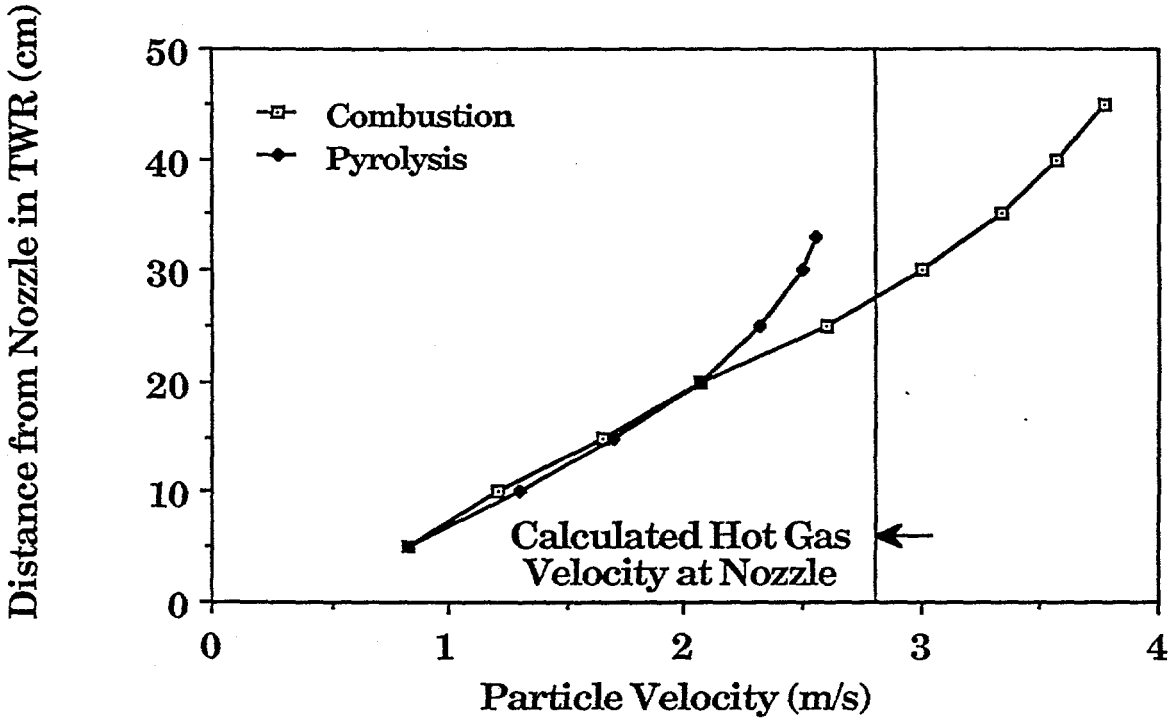

Figure II.C-5. Velocity of 200 x 325 mesh Montana Rosebud Particles in the TWR. Velocities were Measured by a Video Recording of Particle Tracks.

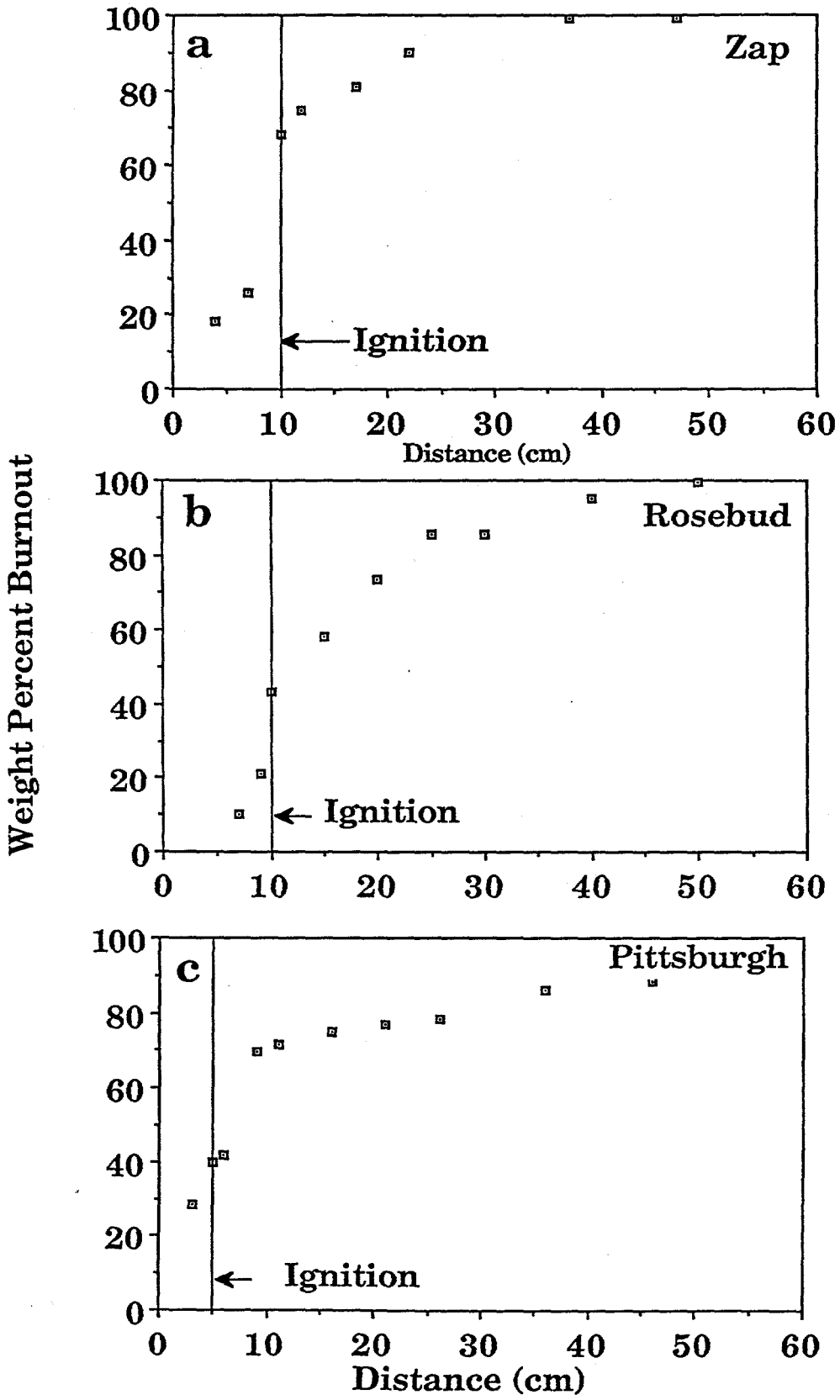

Figure II.C-6. Particle Burnout for Combustion of a) Zap Lignite, b) Montana Rosebud SubbituminousCoal and c) Pittsburgh Seam Bituminous Coal in the TWR.

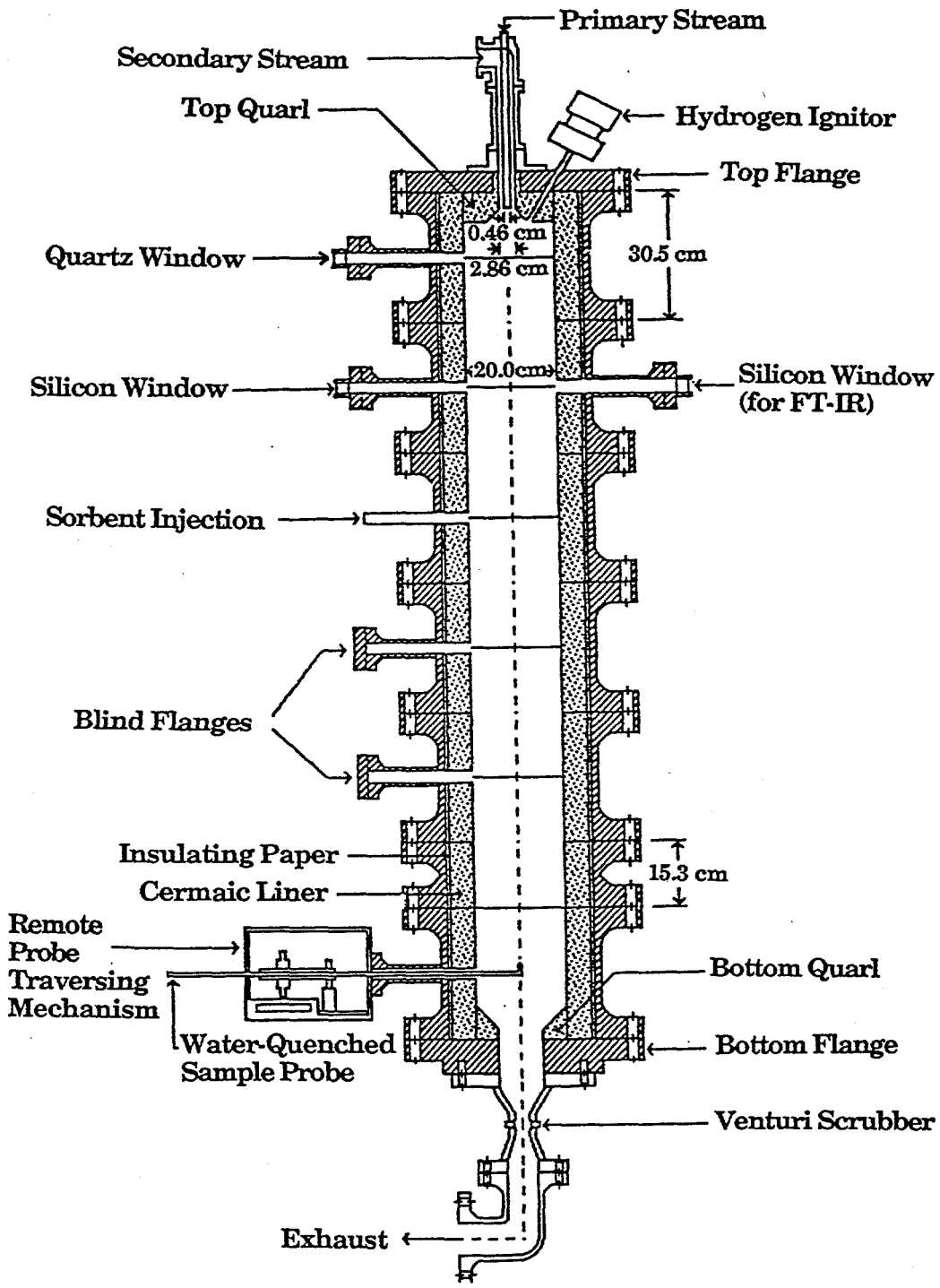

Figure II.C- 7. Modified Gasifier for Sorbent Injection and FT-IR Measurements.

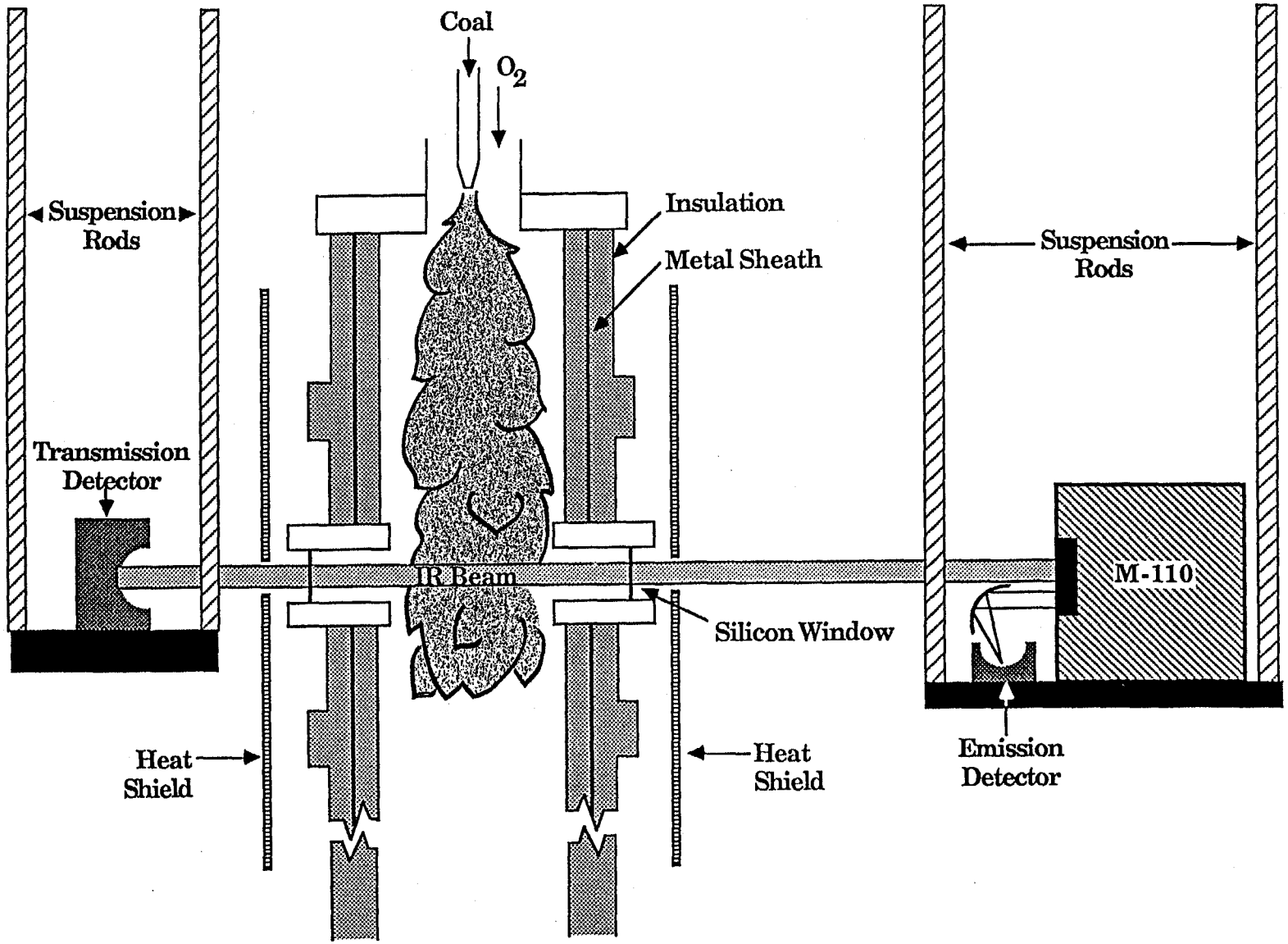

Figure II.C-8. Schematic of BYU Gasifier with In-Situ FT-IR Diagnostics.

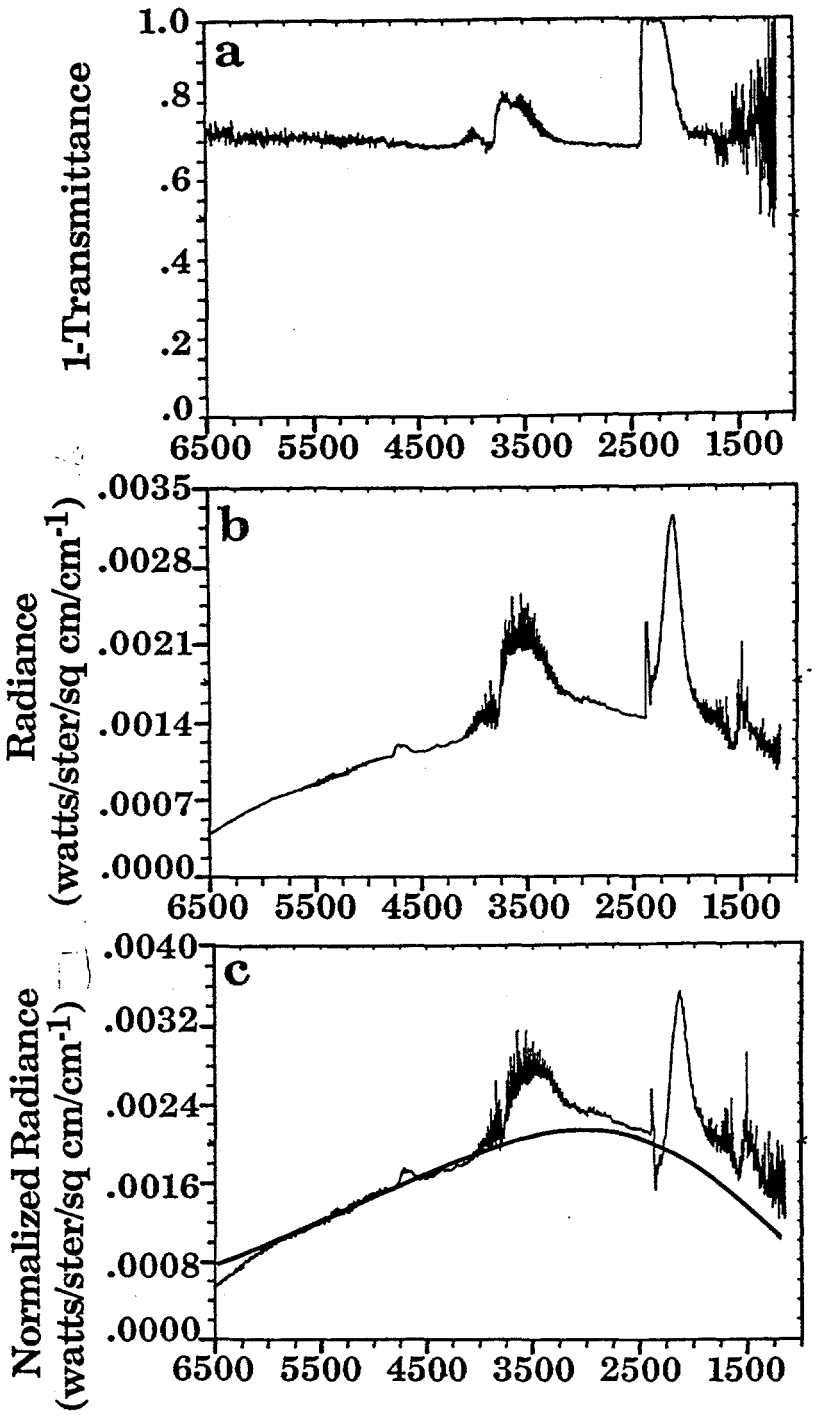

Figure II.C-9. Transmission, Emission and Normalized Emission Spectra through the Flame of the BYU Pilot Flame for the Combustion of Pulverized Coal.

by the emissivity of the particles and by the fraction of ignited particles, and therefore the shape can be used to determine the particle temperature. As discussed above, the scale factor is the product of the emissivity times the ignited fraction. Table II.C-1 shows the average particle temperatures for different runs. A scale factor was not determined since it appears all the particles are ignited.

In the region where there are absorbing gases (e.g., H_2O and CO_2) the gas emission is partially blocked by the particles, and vice versa. To deconvolute the gas and particle contributions in these regions, we use the fact that the absorbances (=-log(transmission)) add linearly (Beer's Law).

$$A(total) = A(gas) + A(particles) \qquad (II.C-1)$$

so that the fraction of the emission due to gases is

$$f_g = 1 - A(particles)/A(total) \qquad (II.C-2)$$

The particle absorbance spectrum is assumed to be relatively structureless, so the first step is to compute the absorbance from Fig. II.C-9a as shown in Fig. II.C-10a, and fit a smooth baseline to the resulting spectrum A(total) to obtain A(particles). Fig. II.C-10b shows the fraction of absorbance due to gases, f_g. The total normalized emission is given by

$$E_T = f_g*E_g + (1-f_g)*E_p \qquad (II.C-3)$$

where E_g is the gas emission and E_p is the particle emission. Solving this for the gas emission (for which the emissivity is unity) we find

$$E_g = (E_T - (1-f_g)*E_p)/f_g \qquad (II.C-4)$$

which is shown in Fig. II.C-10c. From Fig. II.C-10b and c, we show the regions where the water and CO_2 emission occurs, and note that in the cross-hatched region the CO_2 is totally opaque, so that the emission can be seen only from an unknown depth into the flame. Thus, as indicated by the emission curves of Fig. II.C-10c, we can determine the gas temperatures for water and CO_2 by comparison with the black-body curves. At high temperatures, CO is in equilibrium with CO_2. Shown in Table II.C-1 are the gas temperatures computed in this manner, from a few wavelength regions.

Note that the gases are not all at one temperature. Since this is a line of sight measurement, the instrument is seeing a distribution of gas temperature; cold gases near the reactor walls and hot gases in the center of the combustion zone. These different temperature gases have specific regions in the infrared where their effect is maximized since different populations of rotational states are produced. Thus, water at 3150 cm^{-1} and CO/CO_2 near 2000 cm^{-1} is representative of the hotter zones while water at 4100 cm^{-1} and CO_2 at 2350 cm^{-1} represent colder regions. A more exact mathematical deconvolution of temperatures across a line of sight is given by Krakow (1966) and may be used in future measurements.

Gas temperatures were distributed over a 1500 K range and were up to around 1400 K hotter than the particles which were between 1500 K to 1600 K for all the runs. Given the noise level in the data, particle temperatures appear to be accurate to 25°C and gas temperatures (at specific wavelengths) to 50°C.

II.C.7. Submodel for Soot Radiative Properties

Under this subtask, work was done on developing a radiative model for soot as part of the soot submodel and the results were sent to BYU. The inputs will be the volume fraction of soot and the temperature. The output will be the average soot emissivity. The main difficulty will be to correct for the

Table II.C-1. Summary of Experimental Results from Application of FT-IR Diagnostics to BYU Gasifier.

Run #	Coal	O_2/Coal	Avg. Particle Temperature (K)	CO/CO_2 Temperature (K)			H_2O Temperature (K)		
				2350 cm^{-1}	2000 cm^{-1}	2200 cm^{-1}	4100 cm^{-1}	3150 cm^{-1}	3700 cm^{-1}
24	Alberta	1.06	1500	1300	2800	2100	1750	2700	1900
27	Alberta	.92	1525	1350	2700	2150	1700	2700	1900
36	Utah	1.65	1550	1400	2950	2000	1800	2850	1950
37	Utah	1.17	1525	1400	2700	2050	1750	2800	1850
38	Utah	.96	1575	1400	2900	1950	1650	2600	1800
39	Utah	.50	1550	1400	2550	1900	1500	2300	1850

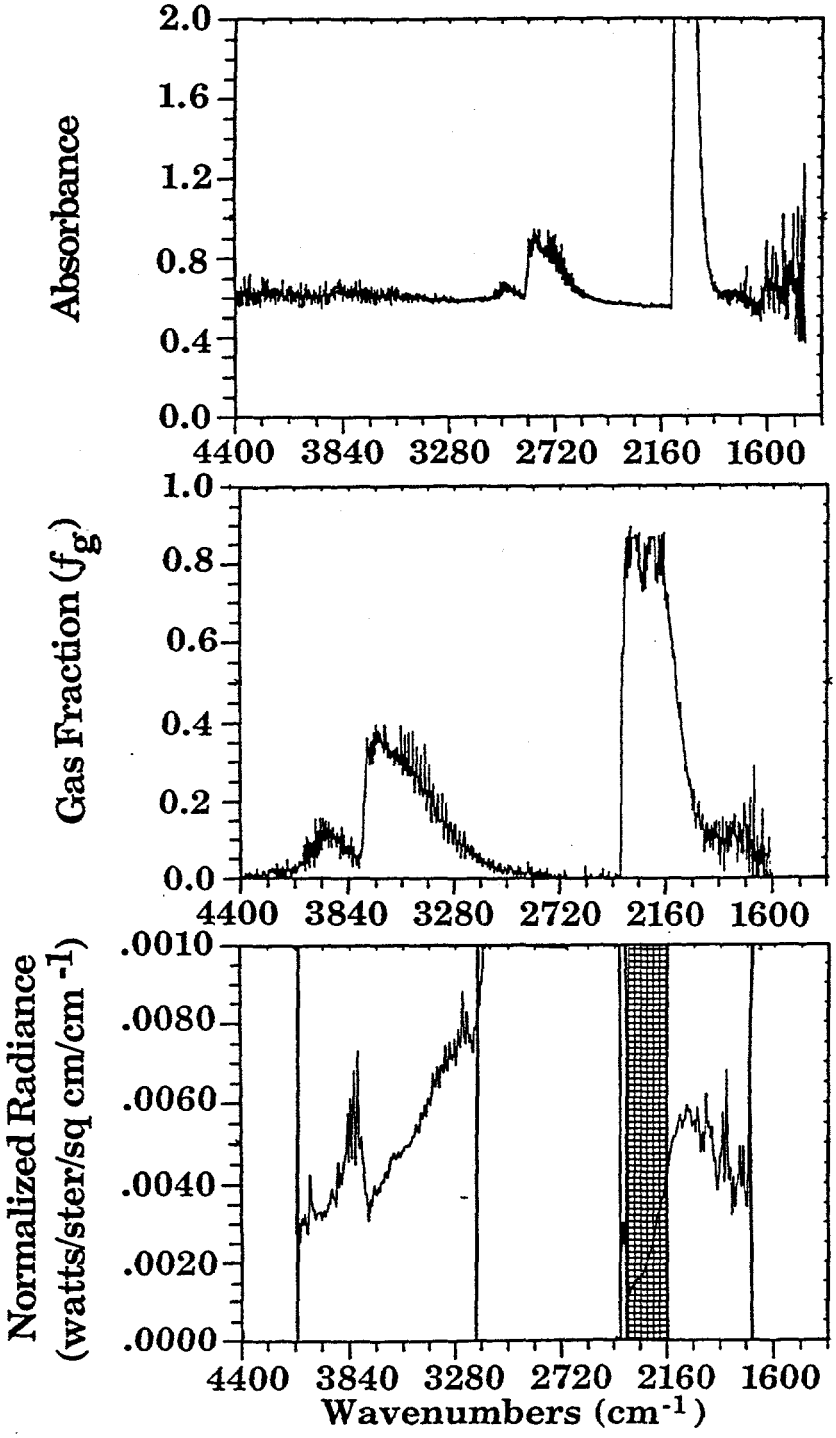

Figure II.C-10. Absorbance, Gas Fraction and Normalized Radiance for Gas Obtained from Utah Blind Canyon Bituminous Coal in the BYU Pilot Flame.

presence of CO_2 and H_2O. This work is being done jointly with BYU since the radiation model is an integral part of PCGC-2. A literature correlation is being used (Kent and Honnery) to make predictions of the average soot emissivity. Correlations from Hottel and Sarofim (1967) are being used to correct for the contributions of water and CO_2. Based on comparisons to an actual measured soot, water and CO_2 spectra, it appears that these corrections are accurate to within 5%.

A primary concern was to correct for the effect of the water and CO_2 bands. It turns out that these bands are sufficiently close to the location of the average wavelength of the soot radiation that the soot acts like a grey body.

The work on the soot radiative properties submodel was completed and these changes have already been implemented into PCGC-2. This includes a correction factor due to the overlap of the soot continuum with spectral lines for H_2O and CO_2.

In previous work, equations II.C-5a and 5b were developed to describe the soot radiative properties as a function of temperature. However, these equations did not have a correction factor due to the overlap of the soot continuum with H_2O and CO_2 lines. The equations were of extinction coefficients, as follows:

$$K_{soot\ em} = (1.9 \times 10^3 \times f_v \times T_e\ (m^{-1}) \qquad \text{(II.C-5a)}$$

$$K_{soot\ abs} = (1.9 \times 10^3 \times f_v \times T_b\ (m^{-1}) \qquad \text{(II.C-5b)}$$

where f_v is the volume fraction, and T_e, T_b are the appropriate temperatures, in Kelvin, for emission and absorption, respectively. The correction terms for the overlap of soot and vapor radiation features are described below.

Hottel and Sarofim (1967) describe a correction due to such overlap, $\Delta\epsilon$, (their Eq. 6-58) as

$$\Delta\epsilon \doteq \sum_i \epsilon_i - [1 - \pi_i (1-\epsilon_i)] \qquad \text{(II.C-6)}$$

With a three component model for flame radiation (soot, H_2O, and CO_2), and with the correction due to the overlap of CO_2 and H_2O lines already included in PCGC-2, the additional correction simplifies to two pairwise corrections, for soot-CO_2 and soot-H_2O, respectively.

In that case, Eq. II.C-6 simplifies to

$$\Delta\epsilon_{soot,\ CO2} = \epsilon_{soot} \times \epsilon_{CO2} \qquad \text{(II.C-7)}$$

and

$$\Delta\epsilon_{soot,\ H2O} = \epsilon_{soot} \times \epsilon_{H2O} \qquad \text{(II.C-8)}$$

However, Eq. II.C-6 only applies if all but one of the species is a grey-body radiator; not the case for soot. In this section, the proper calculation for the correction term is described, and it is shown that Eqs. II.C-7 and II.C-8 calculate the correction to within 4% for all temperatures and concentrations of interest.

The optical constants of soot from Habib and Vervisch (1988) were used them to calculate the soot absorption constant, k

$$k_{v,s} = \frac{36\pi \; x \; n_v \; K_v \; \nu}{(n_v^2 - k_v^2 + 2)^2 + 4 \; n_v^2 \; k_v^2} \qquad \text{(II.C-9)}$$

and the emissivity, ϵ for eight values of f_v between 5 X 10^{-6} and 5 X 10^{-4}.

$$\epsilon_{v,s}(f) = 1 - e\,[\,- k_{v,s} \; x \; f_v] \qquad \text{(II.C-10)}$$

For each f_v, "average" (as opposed to "spectral") quantities were calculated.

$$\epsilon_s(F) = \frac{\int \epsilon_{v,s}(f) \; R^b{}_v \; d_v}{\int R^b{}_v \; dv} \qquad \text{(II.C-11)}$$

where $R^b{}_v$ is the Planck function. These ϵ's were calculated for temperatures of 1500 K, 1800 K and 2100 K.

From measured absorbance spectra of water, A_v, and seven values of water concentration, X_ω, the emissivity of water vapor was calculated.

$$\epsilon_{v,s-w} = 1 - \exp\,[- K_{v,s} f_v + A_{v,\omega} \; X_\omega] \qquad \text{(II.C-12)}$$

and hence average emissivity

$$\frac{\epsilon_\omega = \int \epsilon_{v,\omega} \; R^b{}_v \; d_v}{\int R^b{}_v \; d_v} \qquad \text{(II.C-13)}$$

In similar fashion $\epsilon_{v,\,CO2}$ and ϵ_{CO2} for carbon dioxide were calculated. Finally, the emissivities, $\epsilon_{s,\omega}$ and $\epsilon_{s,CO2}$, for soot-water and soot-CO_2, respectively, were calculated.

For soot-water:

$$\epsilon_{v,s-w} = 1 - \exp\,[- K_{v,s} \; f_v + A_{v,\omega} \; X_\omega] \qquad \text{(II.C-14)}$$

$$\epsilon_{av,s-w} = \frac{\int \epsilon_{v,s-w} \; R^b{}_v \; d_v}{\int R^b{}_v \; d_v} \qquad \text{(II.C-15)}$$

$$\Delta \; \epsilon_{s-w} = \epsilon_{av,s-w} - \epsilon_{soot} - \epsilon_{water} \qquad \text{(II.C-16)}$$

The correction, and this correction was compared with the prediction of Eq. II.C-4 by taking the ratio

$$\Delta\epsilon_{s-w} \,/\, \Delta \; \epsilon_{soot\text{-}H2O} = \Delta\epsilon_{s-w} \,/\, \epsilon_{CO2} \; X \; \epsilon_{soot} \qquad \text{(II.C-17)}$$

A similar calculation was done for soot-H_2O.

The ratios are plotted as "spectra" with the x-value representing different combinations of f_v, X (or ϵ_{soot}, ϵ_{CO2}) in Figs. II.C-11 and II.C-12 For one value of X_{CO2}, f_v is changed over its range, giving rise to the down sloping line at the left of Fig. II.C-11. Then a new value of X_{CO2} is chosen, and the cycle of f_v repeated for this value, and so on for the seven values of X_{CO2}. The results show that the simple correction of Eqs. II.C-7 and II.C-8 is correct to within 5%, and that is the correction which we recommend. It turns out that the water and CO_2 bands are sufficiently close to the location of the average wavelength of the soot radiation that the soot acts like a grey-body.

II.C.8. Submodels for Ignition and Soot Formation

Under this subtask, models for ignition and soot formation were developed. An outline of the proposed particle ignition submodel is shown in Fig. II.C-13. The essential ingredients of the ignition model are already in PCGC-2. What is needed is to refine the assumptions regarding the fraction of CO_2 formed at the surface, as opposed to the gas phase, and the amount of energy feedback to the particle from the oxidation reaction of CO. These are related questions. The results of changing these assumptions on the PCGC-2 predictions of the laminar coal flame experiments are discussed in Brewster et al. (1993).

An outline of the proposed soot submodel is shown in Fig. II.C-14. The current soot formation model includes a calculation of the equilibrium amount of condensed carbon. This does a good job of predicting the location of the soot maximum but not the magnitude or the burnout. What is needed is an improved kinetic model for soot formation and destruction. This will require additional work.

These issues are also discussed under Subtask 3.a.

References for Subtask 2.c.

Best, P.E., Carangelo, R.M., Markham, J.R., and Solomon, P.R., Combustion and Flame, **66**, 47 (1986).

Brewster, B.S., Smoot, L.D., and Solomon, P.R., Structure of a Near Laminar Coal Jet Diffusion Flame, Poster Session, 23rd Symposium (Int) on Combustion, The Combustion Institute, Orleans, France (1990).

Brewster, B.S., Smoot, L.D., Solomon, P.R., and Markham, J.R., Structure of a Near-Laminar Coal Jet Flame, Energy and Fuels, 7 (6), 844 (1993).

Fletcher, T.H., Time-Resolved Particle Temperature Measurements and Mass Loss Measurements of a Bituminous Coal during Devolatilization, Combustion and Flame, 78, 223 (1989).

Habib, Z.G. and Vervisch, P. Comb. Sci. & Technol., **59**, 261 (1988).

Hottel, H.C. and Sarofim, A.F. *Radiative Transfer*, McGraw Hill, NY (1967).

Krakow, B., Spectroscopic Temperature Profile Measurements in Inhomogeneous Hot Gases, Applied Optics, **5**(2), 201, (1966).

Markham, J.R., Zhang., Y.P., Carangelo, R.M., and Solomon, P.R., FT-IR Emission/Transmission Tomography of a Coal Flame, 23rd Symposium (Int) on Combustion, The Combustion Institute, Orleans, France, pp 1869-1875 (1990).

Serio, M.A., Hamblen, D.G., Markham, J.R., Solomon, P.R., Energy & Fuels, **1**, 138 (1987).

Solomon, P.R., and Hamblen, D.G., Pyrolysis, in *Chemistry of Coal Conversion*, Plenum Press, (R.H. Schlosberg, Ed.), New York, 1985, ch. 5, p. 121.

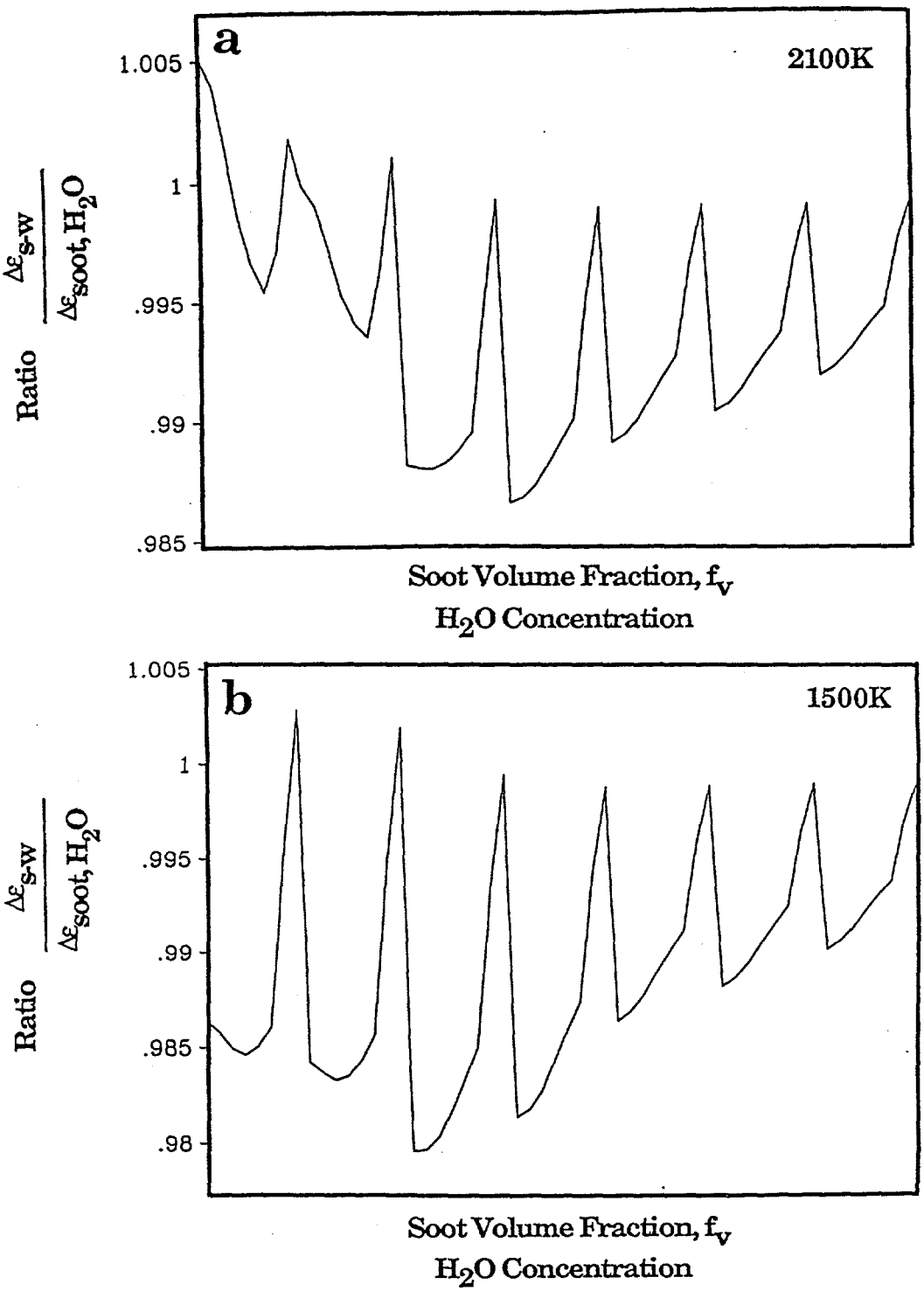

Figure II.C-11. Ratio of Correction Factors for Soot and H_2O at a) 2100K and b) 1500K.

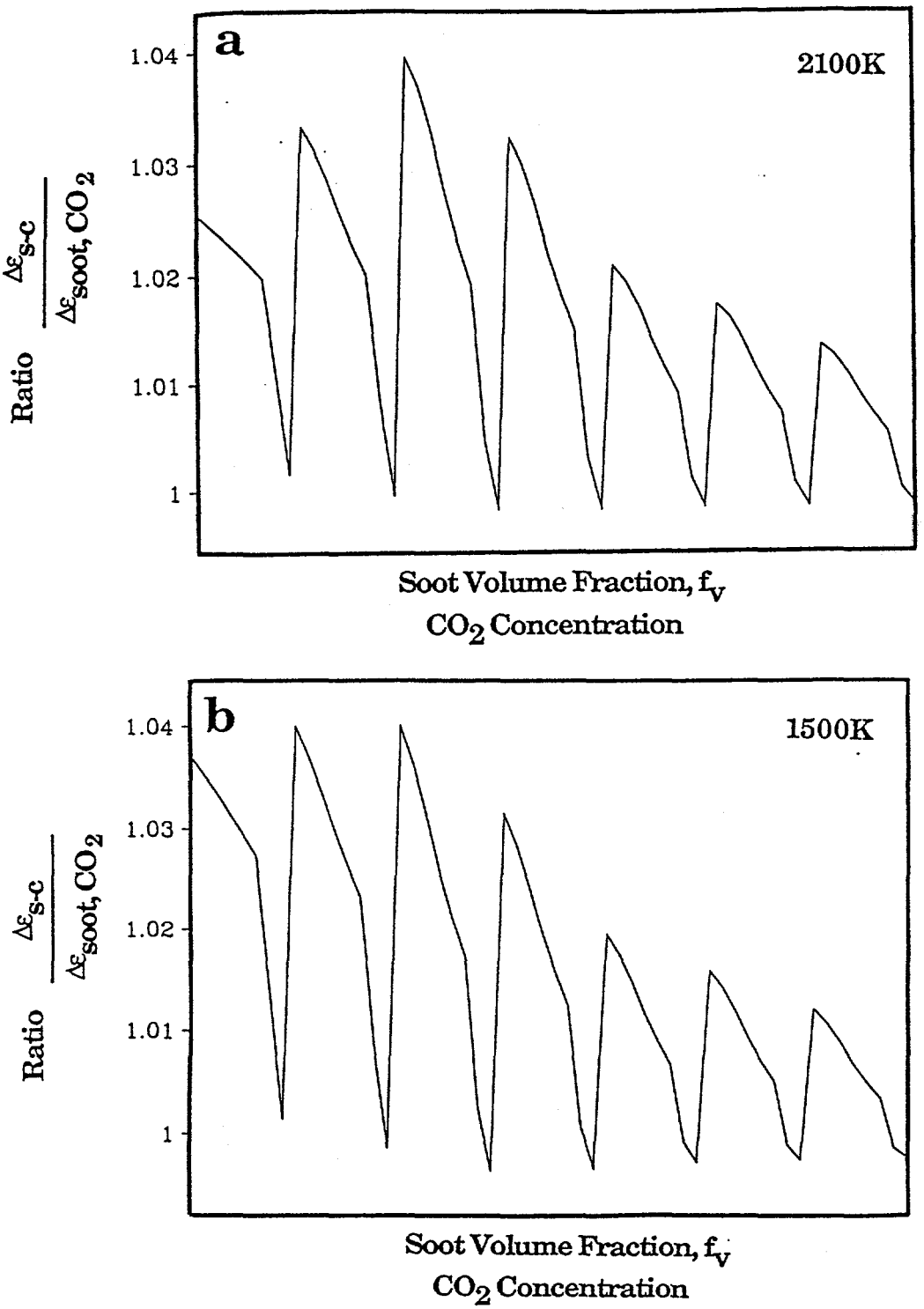

Figure II.C-12. Ratio of Correction Factors for Soot and CO_2 at a) 2100K and b) 1500K.

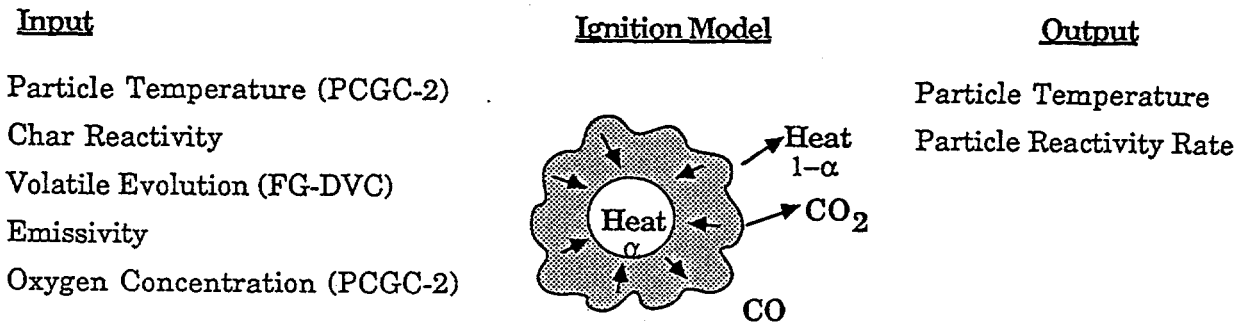

Figure II.C-13. Outline of Particle Ignition Submodel.

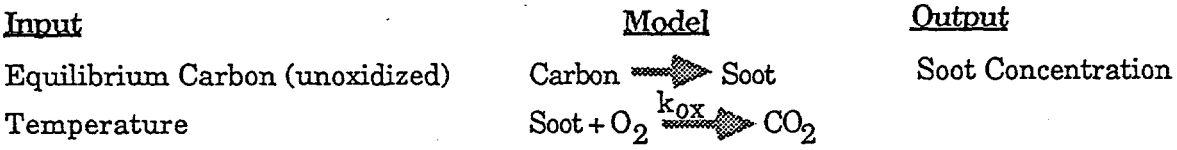

Figure II.C-14. Outline of Soot Formation Submodel.

Solomon, P.R., Serio, M.A., Carangelo, R.M., and Markham, J.R., Very Rapid Coal Pyrolysis, Fuel, **65**, 182-194 (1986).

Solomon, P.R., Carangelo, R.M., Best, P.E., Markham, J.R., and Hamblen, D.G., Fuel, **66**, 897 (1987a).

Solomon, P.R., Chien, P.L., Carangelo, R.M., Best, P.E., and Markham, J.R., Application of FT-IR E/T Spectroscopy to Study Coal Combustion Phenomena, paper presented at the Int. Coal Combustion Symposium, Beijing, China (1987).

Solomon, P.R., and Serio, M.A., in *Fundamentals of the Physical-Chemistry of Pulverized Coal Combustion*, Martinus Nijhoff Publishers, (J. Lahaye and G. Prado, Eds.), p. 126 (1987).

Solomon, P.R., Chien, P.L., Carangelo, R.M., Best, P.E., and Markham, J.R., Application of FT-IR Emission/Transmission (E/T) Spectroscopy to Study Coal Combustion Phenomena, The 22nd Symposium (Int) on Combustion, The Combustion Institute, Pittsburgh, PA, p. 211 (1988).

Solomon, P.R., Best, P.E., Markham, J.R., and Klapheke, J., The Study of Coal Flames Using FTIR Emission/Transmission Tomography, Int. Conference on Coal Science Proceedings, IEA, Tokyo, Japan, p. 329 (October 23-27, 1989).

Solomon, P.R., Chien, P.L., Carangelo, R.M., Best, P.E., and Markham, J.R., Application of FT-IR Emission/Transmission (E/T) Spectroscopy to Study Coal Combustion Phenomena, 22nd Symposium (Int) on Combustion, The Combustion Institute, Pittsburgh, PA (1989c).

Solomon, P.R., Serio, M.A., Hamblen, D.G., Smoot, L.D., and Brewster, B.S., Measurement and Modeling of Advanced Coal Conversion Processes, 11th Quarterly Report, Advanced Fuel Research, Hartford, CT, DOE-METC Contract No. DE-AC21-86MC23075, (1989c).

Solomon, P.R., Serio, M.A., and Markham, J.R., Kinetics of Coal Pyrolysis, Int. Conference on Coal Science Proceedings, IEA, Tokyo, Japan, p. 575, (October 23-27, 1989).

Solomon, P.R., Chien, P.L., Carangelo, R.M., Serio, M.A., and Markham, J.R., New Ignition Phenomenon in Coal Combustion, Combustion & Flame, 79, 214 (1990).

Solomon, P.R., Markham, J.R., Zhang, Y.P., and Carangelo, R.M., FT-IR Emission/Transmission Tomography of Coal Flames, ACS Div. of Fuel Chem. Preprints, **35**, (3), 746, (1990).

Solomon, P.R., and Best, P.E., Fourier Transform Infrared Emission/Transmission Spectroscopy in Flames, in *Combustion Measurements*, (N. Chigier, Ed.), Hemisphere Publishing Corp. pp. 385-344 (1991).

Solomon, P.R.,On-Line Fourier Transform Infrared Spectroscopy in Coal Research, in *Advances in Coal Spectroscopy*, (H.L.C. Meuzelaar, Ed.), Plenum Publishing Corp. pp. 341-371 (1992).

Solomon, P.R., Serio, M.A., and Suuberg, E.M., Coal Pyrolysis: Experiments, Kinetic Rates, and Mechanisms, Progress in Energy and Combustion Science, **18**, pp 133-220 (1992).

II.D. SUBTASK 2.d. - ASH PHYSICS AND CHEMISTRY SUBMODEL

Senior Investigators - Michael A. Serio, Peter R. Solomon, and Marek A. Wójtowicz
Advanced Fuel Research, Inc.
87 Church Street, East Hartford, CT 06108
(203) 528-9806

Objectives

The overall objective of this subtask was to determine and describe the ash physics and chemistry during coal conversion processes. Mineral matter in coal is a source of slagging and deposits on reactor or downstream component walls, causing corrosion of equipment. Minerals can also catalyze reactions or poison process catalysts. To accomplish the overall objective, the following specific objectives were formulated: 1) to develop an understanding of the mineral matter phase transformations during ashing and slagging in coal conversion. This information will be used for the eventual development of a predictive model of ash behavior based on the original mineral matter composition, particle size, and physical properties as well as the process conditions. It was determined based on the laboratory experiments and literature review that the completion of such a model would require more resources than were available in this study and may duplicate ongoing DOE sponsored work. Consequently, the original objective was scaled back to include only the identification of the key mineral transformation processes that need to be modeled in advanced coal conversion systems. 2) to investigate the catalytic effect of mineral matter on coal conversion processes and develop a model to include this effect on char reactivity.

Summary of Accomplishments

Under this subtask, work was performed in four areas:

- laboratory studies of mineral matter transformations
- laboratory studies of catalytic effects of minerals on char reactivity
- modeling of mineral effects on char reactivity
- literature reviews of mineral matter transformations

The modeling of mineral effects on char reactivity was integrated into the overall char reactivity model and is reported in Section II.A.10.

II.D.1. Laboratory Studies of Mineral Matter Transformations

Elemental Analysis of Coals by SEM/Dispersive Energy X-Ray

The elemental composition of the minerals in the ampoule coal samples was characterized by a Scanning Electron Microscope (SEM) with dispersive energy x-ray analysis. The samples were received in glass ampoules under an inert gas blanket and analyzed on an as received basis without further treatments. The particle size of coal samples are -100 mesh for 5 gm ampoules and -20 mesh for 10 gm ampoules. All the raw coals, except for the Wyodak samples, were received in the -100 mesh size. All the samples were reground into very fine particles using a ball-mill for 20 minutes and then pressed into a flat pellet containing about 300 mg of coal. This was done to ensure a representative sample was obtained. The samples were coated with graphite to prevent charging and then the resulting pellet was mounted in the SEM. The analysis of the elemental composition was based on the measurement of the x-ray intensities of the major elements (Fe, S, Ca, Ti, Mg, Na, Sl, and Si) from 121 subsamples, where a subsample is defined as a surface portion of the sample surface (typically 20 to 200 microns square). The electron beam was scanned from one subsample to another, and the x-ray intensities for all elements of interest were recorded. The data acquisition process was completely automated and takes about 10 minutes.

In order to compare the obtained elemental analysis of coal mineral impurities with the ASTM high temperature ashing sample measurements, the elemental compositions of the coals were recalculated and converted into the oxide form (MgO, Na_2O, Al_2O_3, SiO_2, K_2O, CaO, TiO_2, and Fe_2O_3). The amount of SO_3 was calculated in the ash as that portion of total sulfur could react with CaO to form $CaSO_4$. Therefore, the total number of moles of SO_3 present in the ash could not exceed the total number of moles of CaO presented in the coal. The excess amount of sulfur analyzed in raw coal was assumed to be released into the gas product stream during the coal conversion process. The iron content in the elemental composition are included only as iron in oxide form. The total iron contents were recalculated to include the iron existing in the pyrite form, based on the relative stoichiometry ratio.

The results of the mineral impurities analysis and other characteristics of raw coals are shown in Tables II.D.1-1 to II.D.1-3. Table II.D.1-1 shows the ultimate, proximate, and sulfur analyses of all raw coal samples. Most of these data were provided by Argonne, except the sulfur content and form which was analyzed at AFR. Argonne's data are also listed for comparison. The agreement is good in most cases. Table II.D.1-2 shows the results of mineral elemental composition analyses by SEM/dispersive energy x-ray analyses of nine raw coals. Table II.D.1-3 shows the results similar to those in Table II.D.1-2 but expressed in the oxide form in the ash. A comparison with the results of HTA samples analyses provided by Argonne is also presented, and the two methods show reasonable agreement.

When comparing the ash composition data obtained from AFR with Argonne's data, good agreement is found for the total ash content. For example, our data for the ash content of Upper Freeport bituminous and Wyodak subbituminous coals were 12.46 and 8.9 wt%, respectively, as compared with 13.03 and 8.83 wt% obtained from Argonne for these two coals. However, some discrepancies were observed for the sulfur and iron content. This may be due to our assumption that the CaO will react stoichiometrically to form SO_3. In the real ashing procedure, this may not be the case.

To collect ash samples under coal conversion conditions, two sample collection probes were constructed. They were inserted into the transparent wall reactor (TWR) to allow for the collection of char with its transforming mineral matter from the flame at various stages of burnoff. Mineral matter associated with the char as well as fly ash from above the flame were also collected. Both probes result in no visual disruption of the stability, size, or ignition delay time of the flames. Sample collections were performed using these probes from Zap lignite and Montana Rosebud coal flame experiments. SEM/dispersive x-ray analysis was performed on individual ash spheres that were recovered from the preseparator and the eight stages of the cascade impactor for an "in-stack" ash collection from 200 x 325 mesh Zap lignite.

The fly ash collector (in stack) consists of an inlet nozzle, large particle preseparator, cascade impactor and adjustable air pump. The char collector (in flame) consists of a water cooled nozzle that adds cold helium to the hot particle stream. After quenching, the particle stream passes through a large particle cyclone separator, and then through the preseparator and cascade impactor. A schematic of the system, as installed in the transparent wall reactor (TWR), is shown in Fig. II.D.1-1.

The char collector nozzle inlet temperature was maintained below 300°C by the He addition. The fly ash collector nozzle was placed in the flame exhaust stack having a typical radial temperature profile as presented in Fig. II.D.1-2.

Table II.D.1-4 and Fig. II.D.1-3 show collection and separation data for a Rosebud subbituminous coal and a Zap lignite under similar collection conditions. TGA weight loss measurements on the in-flame collected samples indicate that both cyclone fractions have a large amount of combustible material remaining (~ 60%). SEM photomicrographs (Figs. II.D.1-4 and II.D.1-5) show that both materials contain etched particles of the same size range as the starting materials, with some particles having discrete globules of ash stuck to the particle surface and others with a more uniform coating (possibly smaller globules) of ash as indicated by the bright (charging) areas. The Zap cyclone fraction appears to contain more particles with ash globules on particle surfaces, and more ash that has apparently been released from the char. This is also indicated in the size separation data presented in Fig. II.D.1-3. For the Zap

Table II.D.1-1. Properties of Coals to be used in Mineral Transformation Testing.

	Upper Freeport bituminous	Wyodak subbituminous	Illinois No.6 bituminous	Pittsburgh No.8 bituminous	Pocohontas No.3 bituminous	Utah Blind Canyon bituminous	Upper Knawha bituminous	North Dakota Zap lignite	Montana Rosebud subbituminous
Proximate Analysis, wt%									
Moisture	0.83	28.84	2.94	1.80	0.61	4.71	2.60	32.84	---
Volatile Matter	27.56	33.95	30.92	---	---	---	---	---	---
Fixed Carbon	58.56	30.84	42.72	---	---	---	---	---	---
Ash	13.05	6.37	23.42(16.2)++	9.27	4.87	4.68	19.81*	6.53**	---
Ultimate Analysis, wt%,maf.									
C	87	74	77	83	91	79	81	73	72.1
H	5.5	5.1	5.7	5.8	4.7	6.0	5.5	5.3	4.9
S**	2.8	0.5	5.4	1.6	0.9	0.5	0.6	0.8	1.2
N	1.4	1.3	1.2	1.5	0.9	1.3	1.0	0.5	1.2
O	4	19	10	8	3	13	11	21	20.3
Forms of S, wt%** +									
Inorganic	0.65(1.96)	0.29(0.14)	2.58(2.72)	1.38(1.33)	0.06(0.18)	0.14(--)	0.25(--)	0.27(--)	1.60(--)
Organic	0.71(0.49)	0.45(0.42)	1.90(2.08)	0.70(0.81)	0.50(0.42)	0.24(--)	0.48(--)	0.45(--)	0.47(--)
Total:	1.36(2.46)	0.74(0.56)	4.48(5.03)	2.08(2.14)	0.56(0.60)	0.38(--)	0.73(--)	0.72(--)	2.07(--)

Notes:

** Moisture free basis
* Analyzed by SEM/dispersive energy x-ray technique of raw coals on a dry basis.
+ Values in parenthesis represent Argonne's data on a dry basis.
++ Value from a second laboratory

Table II.D.1-2. Mineral Distribution, Elemental Composition.

Metal	Upper Freeport	Wyodak	Illinois No.6	Pittsburgh No.8	Pocahontas No.3	Utah Blind Canyon	Upper Knawha	North Dakota Lignite	Montana Rosebud
Na	0.03	0.11	0.12	0.02	0.07	0.08	0.11	0.36	0.02
Mg	0.22	0.37	0.16	0.13	0.11	0.11	0.33	0.54	0.35
Al	1.67	0.73	1.35	0.94	0.57	0.3	3.57	0.49	1.08
Si	2.92	1.12	2.88	1.72	0.69	0.49	5.47	0.82	0.49
K	0.24	0.02	0.16	0.07	0.02	0.03	0.42	0.03	0.03
Ca	0.19	1.3	0.71	0.16	0.26	0.28	0.08	1.56	1.17
Ti	0.11	0.09	0.07	0.01	0.05	0.01	0.26	0.05	0.07
S(o)	0.71	0.45	1.9	0.7	0.5	0.24	0.48	0.45	0.47
S(m)	0.65	0.22	2.58	1.38	0.06	0.14	0.25	0.27	1.6
Fe	0.47	0.29	0.6	0.3	0.28	0.14	0.47	0.4	0.32
Ash	12.49	9.02	16.14	8.51	4.4	3.41	21.48	9.6	12.33

Table II.D.1-3. Mineral Distribution in Raw Coal Ash (oxide form).

Metal	Upper Freeport	Argonne's Data	Wyodak	Argonne's Data	Illinois No.6	Pittsburgh No.8	Pocohontas No.3	Utah Blind Canyon	Upper Knawha	North Dakota Lignite	Montana Rosebud
Na_2O	0.32	0.44	1.67	2.15	1.01	0.32	2.19	3.28	0.69	5.35	0.22
MgO	2.93	1.07	6.90	6.11	1.66	2.53	4.24	5.54	2.55	9.86	4.67
Al_2O_3	25.33	23.97	15.50	17.26	15.98	20.88	25.05	17.23	31.48	10.20	16.43
SiO_2	50.16	42.82	26.93	32.91	38.60	43.27	34.34	31.87	54.63	19.33	25.68
K_2O	2.71	2.46	0.32	0.33	1.41	1.16	0.66	1.29	2.76	0.47	0.34
CaO	2.13	4.60	20.44	21.81	6.22	2.63	8.46	11.91	0.52	24.04	13.18
TiO_2	1.47	1.02	1.69	1.29	0.73	0.20	1.94	0.51	2.02	0.92	0.94
SO_3	3.04	1.32	18.82	10.69	8.88	3.75	12.07	16.99	0.75	19.83	18.81
Fe_2O_3	11.89	21.35	7.74	6.77	25.50	25.25	11.05	11.38	4.59	10.00	19.73
Total:	100.00	99.05	100.00	99.32	100.00	100.00	100.00	100.00	100.00	100.00	100.00
Ash	12.46	13.03	8.9	8.83	15.97	8.51	4.30	3.29	21.43	9.08	12.42

Table II.D.1-4. Sample Collection Data for Zap and Rosebud Flames.

Run #	Sample	% Ash	Collection Point	Collection Time Minutes	Wt. of Sample Collected (mg)	Percent Weight Loss in TGA* Cyclone Fraction	Percent Weight Loss in TGA* Preseparator Fraction
1	200 x 325 Dry Rosebud	12.7	7 cm above Ignition Point (in flame)	2	356.0	62.24	---
4	200 x 325 Dry Zap	7.3	7 cm above Ignition Point (in flame)	3	158.8	59.42	---
2	200 x 325 Dry Rosebud	12.7	In Stack 75 cm above Injector	10	81.5	---	6.10
10	200 x 325 Dry Zap	7.3	In Stack 75 cm above Injector	20	22.1	---	3.43

* TGA analysis in air at 30K/min to 900°C

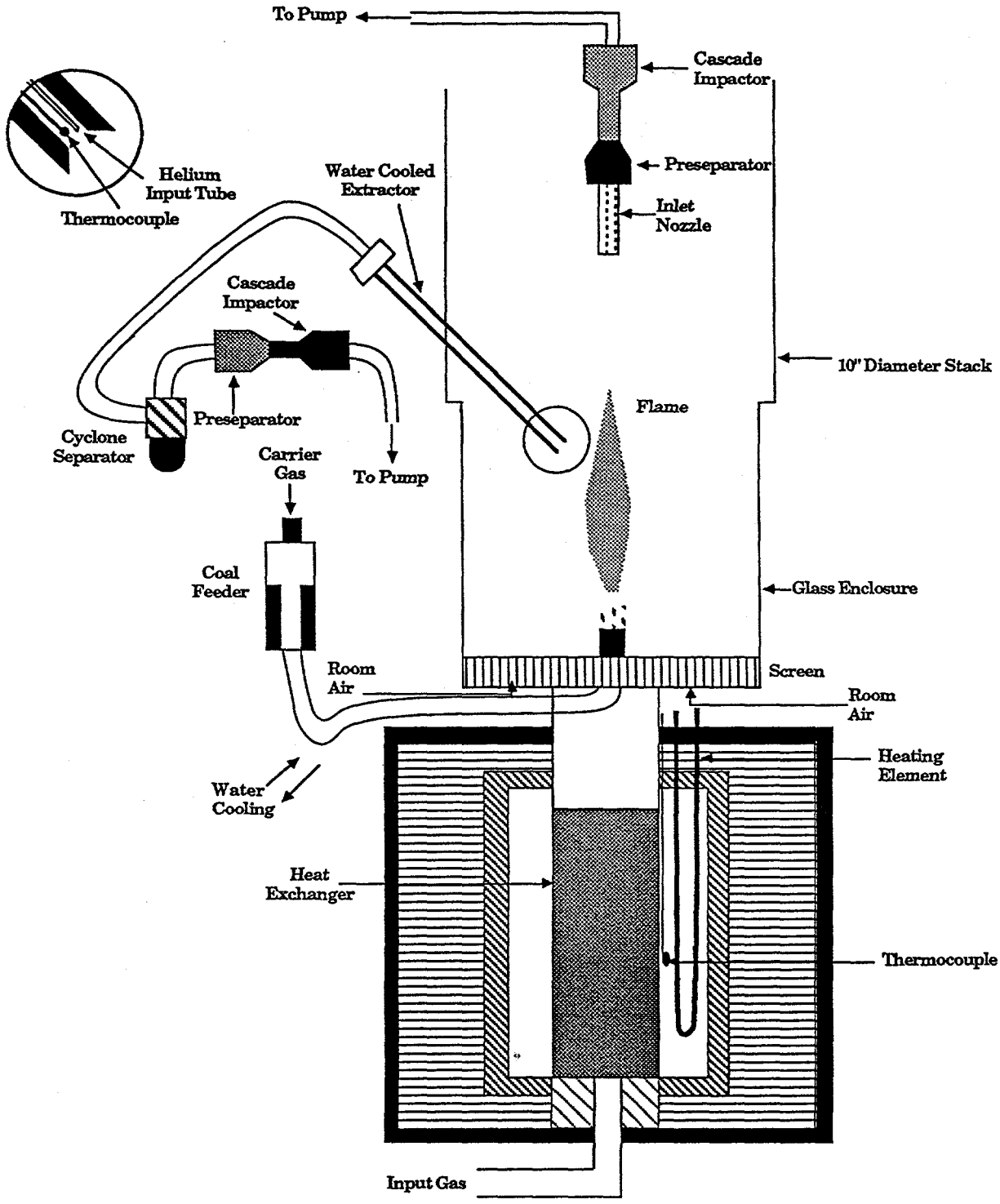

Figure II.D.1-1. Probes for Char and Ash Collection from the Transparent Wall Reactor.

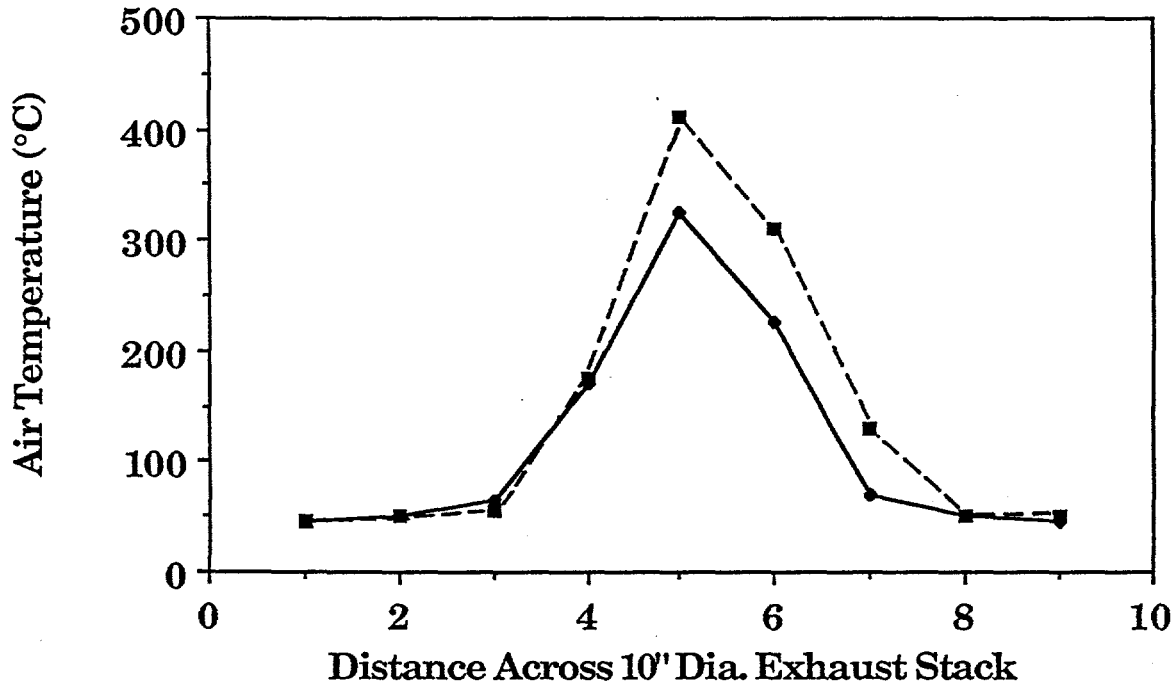

Figure II.D.1-2. Air Temperature Profile Across TWR Exhaust Stack with Rosebud (200x325) Flame On. Distance Above Injector: ■ , 70 cm; ◆ , 75 cm.

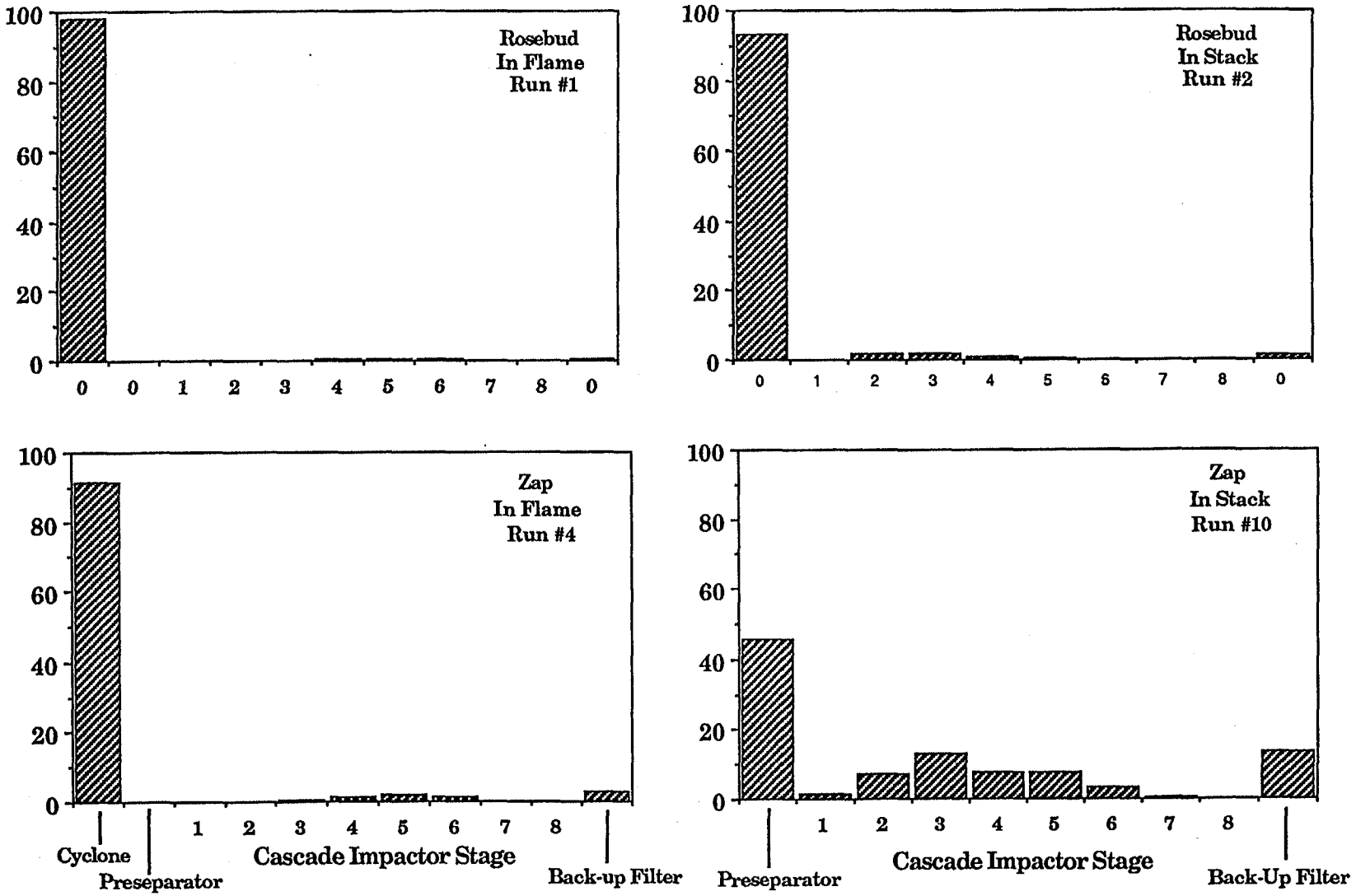

Figure II.D.1-3. Particle Separation Distributions for In Flame and In Stack Collections for Rosebud Subbituminous Coal and Zap Lignite.

Figure II.D.1-4. SEM Microphotograph of Cyclone Fraction of In Flame Collection for Rosebud Coal. Magnification: X400.

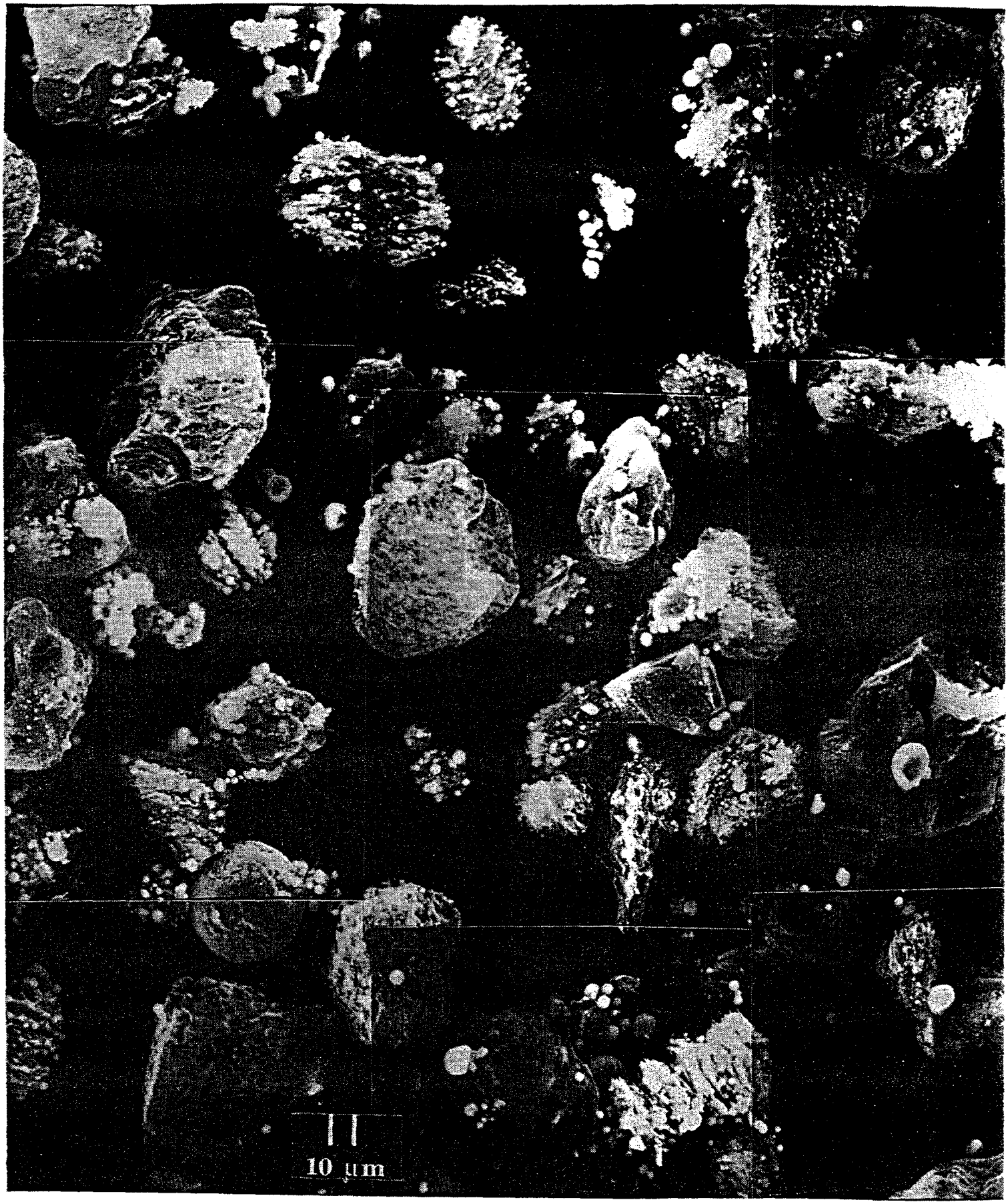

Figure II.D.1-5. SEM Microphotograph of Cyclone Fraction of In Flame Collection for Zap Lignite. Magnification: X400.

lignite sample, there is more material collected downstream of the large particle separators than for the Rosebud. Figure II.D.1-6 compares two stages of in-stack collection for the Zap, and clearly shows the individual and spheres. These photomicrographs also indicate the particle sizing ability of the cascade impactor.

To verify a difference in the ability of the starting material to "shed" ash, samples of Zap and Rosebud pyrolysis chars were quantitatively combusted in the entrained flow reactor to various levels of burnoff. The partially combusted material was collected in a cyclone separator that would clean the char of the smaller released ash and any fragmented particles. TGA weight loss analysis was then performed on the combustion char to indicate the fraction of ash present in the particles, and from this, the percent ash retained from the starting material can be calculated by

$$\text{percent ash retained} = \frac{\text{percent combustion sample} \times \text{percent ash in combustion sample}}{\text{percent ash in starting material}}$$

Table II.D.1-5 presents the percent ash retained values for several levels of combustion. The data appear to indicate two points: 1) the samples shed to a relatively constant ash level early in the combustion process, and 2) the Zap initially sheds more of its ash than the Rosebud.

To study the mineral matter to fly ash transformation, a comparison was made by SEM/dispersive x-ray analysis of the solidified ash spheres on the Zap char's surface with particles collected in the preseparator above the flame in the TWR. The ash spheres on the chars surface are rich in Ca, moderately rich in Al, and Si and have varying amounts of Fe, K and Mg. Representative qualitative analyses for these particles are presented in Table II.D.1-6. It appears that the coal's organically bound calcium accumulates in the form of molten liquids, along with the fine clay and pyrite particles.

Figure II.D.1-7a shows a photomicrograph of particles collected above the flame. Some of these particles have melted to form spheres and some have not. Qualitative analyses of the numbered particles are presented in Table II.D.1-7. In the figure, samples 1 and 2, which appear to have melted and crystallized, are almost pure iron oxide. Figure II.D.1-7b shows a close-up of the highly crystallized surface structure for these kinds of particles. Sample 3, which has not melted, is almost pure calcite. Sample 4 shows a region which has not melted and which is almost pure quartz, (like sample 5), and a part which has melted and which is a mixture of elements. Particles 1-5 appear to have been derived from individual extraneous mineral grains (pyrite, calcite, and quartz) without significant contamination by other mineral components. Small spheres (6 and 7, and those captured on the stages of the cascade impactor) as well as larger spheres (8 and 9) are mixtures of Si, Al, Ca, Fe, K, and Mg, like the particles attached to the chars surface captured in the flame.

Also of interest is that many of the pure mineral particles are of the same size (some larger) than the starting coal particles. Differences in color, magnetic attraction, and density (hollow vs solid) have also been observed.

SEM/dispersive x-ray analysis was also performed on individual ash spheres that were recovered from the eight stages of the cascade impactor for an "in-stack" ash collection from 200 x 325 mesh Zap lignite. The small spheres (< 10 μm in diameter) apparently are shed from the coal particles during the combustion process and contain inorganic components that are intrinsic to the coal.

Ash collection experiments were also performed in the entrained flow reactor (EFR), a schematic of which is shown in Fig. II.D.1-8. This system allows the use of smaller quantities of coal and provides for more complete collection of the ash. Experiments were done at different residence times to achieve a range of char burnouts. The products were collected in a cyclone/cascade impactor system for analysis by TGA for char burnout, SEM/x-ray for mineral analysis, and Quantimet for particle size distribution.

Table II.D.1-5. Percent Ash Retained in Partially Combusted Samples.

Sample	% Sample Recovered after Partial Combustion	% Ash Retained
Zap*	39.0	44.7
	27.0	37.2
	16.5	40.0
	7.6	35.0
Rosebud**	66.7	66.1
	28.0	71.0
	22.3	75.4
	21.1	67.1

* 900°C Zap Char

** 1500°C Rosebud Char

Table II.D.1-6.

REPRESENTATIVE QUALITATIVE* X-RAY ANALYSIS FOR ASH SPHERES ON CHAR PARTICLE SURFACES AS SHOWN IN FIG. II.D-5

Values are in weight percent

Mineral Component	A	B	C	D	E	F
Al	4.89	0.93	0.69	1.21	1.37	1.86
Si	6.10	0.85	5.05	0.56	1.78	1.49
Fe	0.65	3.47	0.73	0	0	1.21
Mg	2.70	1.45	1.21	1.53	1.53	3.31
Ca	5.86	11.71	3.31	2.22	2.66	6.62
Ti	0.52	0.08	0.04	0.04	0	0.20
Na	-	0	0	0	0.65	0
K	0	0	0.04	0.04	0.04	0
Sulfur (O)	0.16	0.12	1.05	0.08	0.56	0.48
Sulfur (M)	0	0	0	2.14	1.53	0
x in FeS_x	0	0	0	2	2	0
Total Ash	35.86	25.73	19.06	11.87	16.44	22.45

* Not matrix-corrected for coefficient of x-ray absorption for each component.

Table II.D.1-7.

QUALITATIVE* X-RAY ANALYSIS OF ASH PARTICLES PRESENTED IN FIG. II.D-7

Values are in weight percent

Mineral Component	1	2	3	4 (melted)	4 (not melted)	5	6	7	8	9
Al	0.23	0.19	0.36	12.18	2.52	2.20	9.78	0.84	9.13	9.55
Si	1.21	0.79	0.66	38.28	33.96	65.44	29.82	1.50	29.81	32.07
Fe	86.05	90.16	0.30	1.38	0.54	0.15	0.84	0.72	0.41	0.38
Mg	0.56	0.47	1.08	1.80	1.14	0.78	1.86	2.1	1.02	0.80
Ca	2.75	0.37	78.54	0.66	-	0.10	1.68	3.66	0.38	0.41
Ti	0	0	0.18	0.18	0.06	0	0.06	0.06	0.19	0.03
Na	0	0	0	2.04	0	0	4.14	0	1.18	2.70
K	0	0.09	0	7.14	0.90	0	0.84	0	6.81	5.15
Sulfur (O)	0	0	0	0.06	0	0.05	0.06	0	0	0
Sulfur (M)	0	0	0.60	0	0	0	0	0	0	0
x in FeS_x	0	0	2	0	0	0	0	0	0	0
Total Ash	129.69	131.41	113.46	125.22	79.98	145.48	101.10	12.36	95.55	102.60

* Not matrix-corrected for coefficient of x-ray absorption for each component.

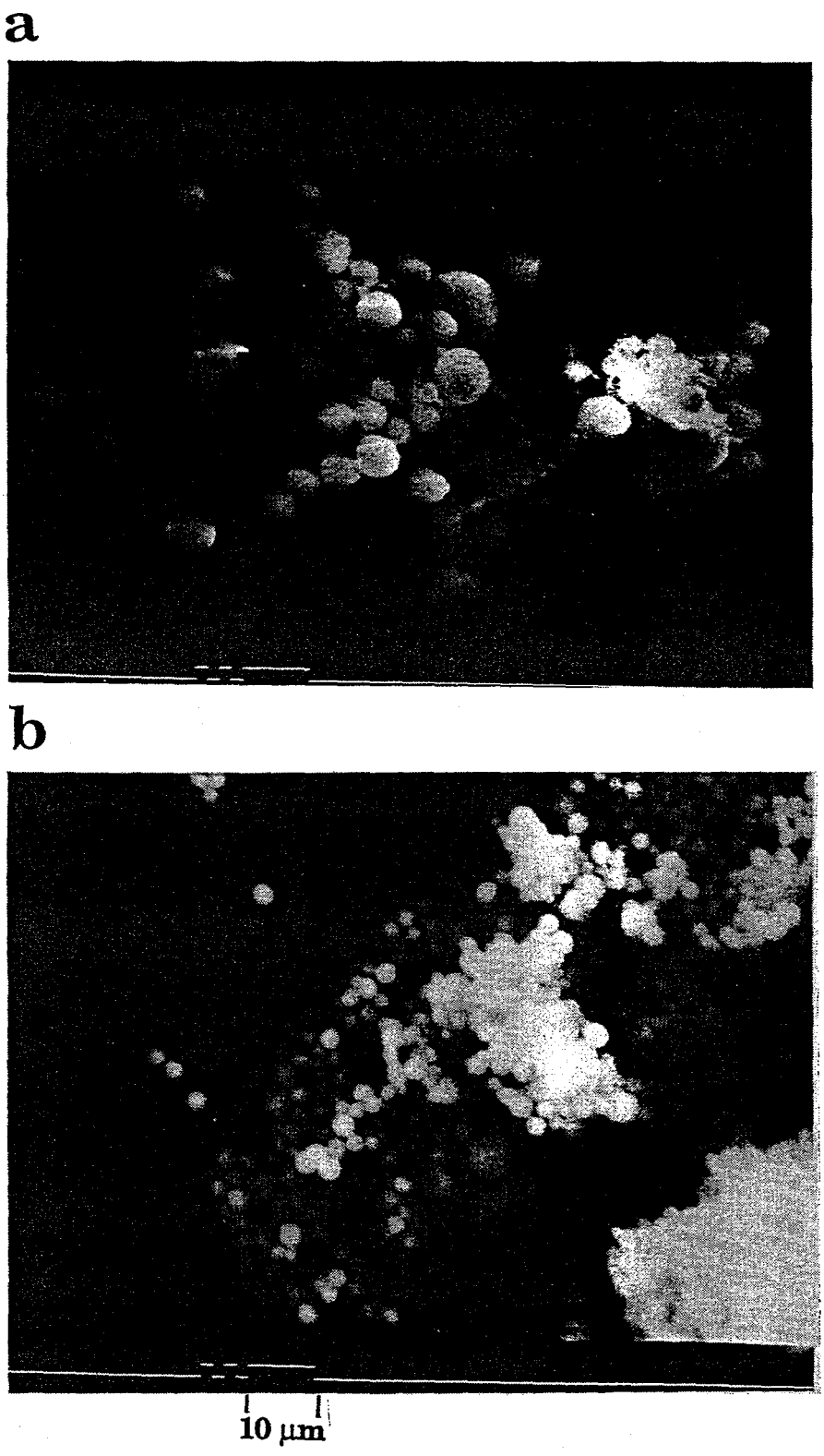

Figure II.D.1-6. SEM Photomicrographs of Fly Ash Collected Above a Zap Lignite Flame. a) Stage #2 and b) Stage #4 of Cascade Impactor. Magnification: X910.

a

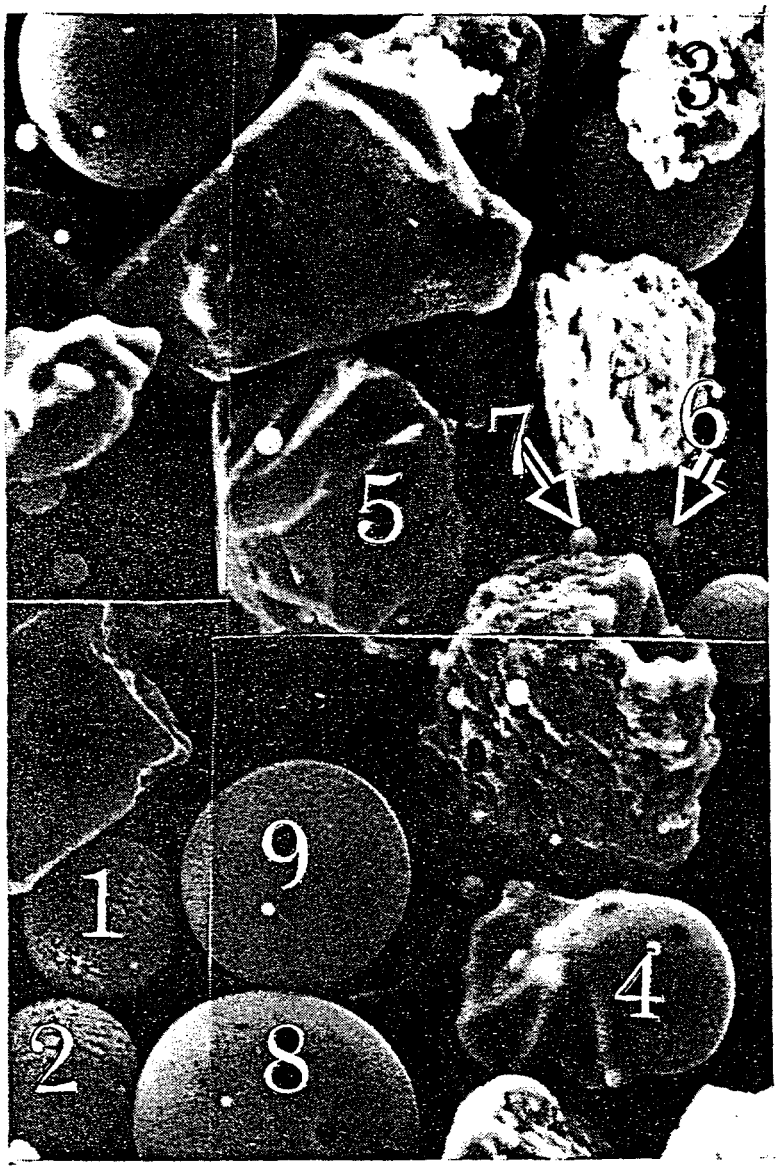

b

Figure II.D.1-7. SEM Micro Photograph of Fly Ash Collected Above a Zap Lignite Flame, Preseparator Fraction. a) X400 and b) Close-Up of Sample 1, X2,670.

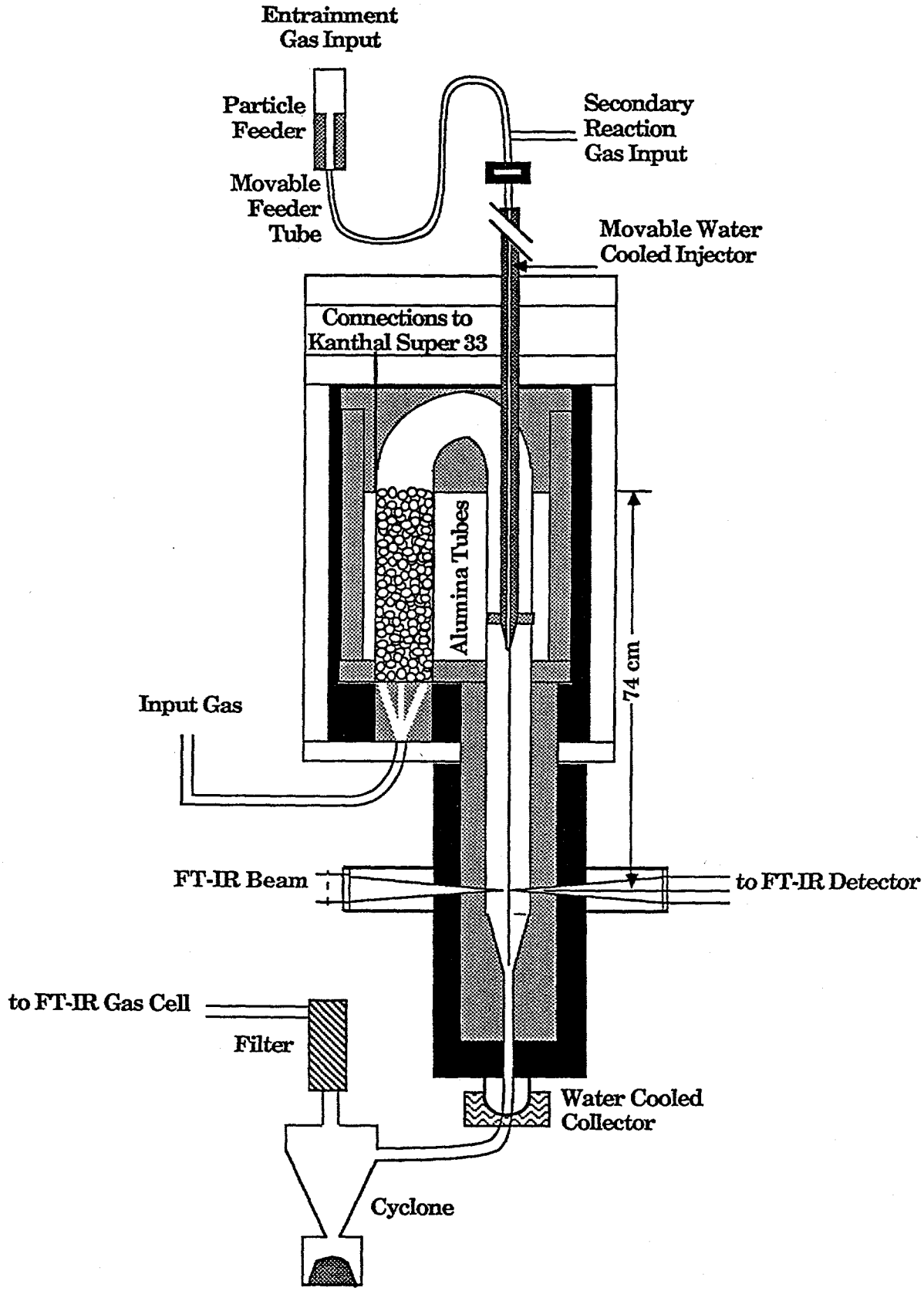

Figure II.D.1-8. Schematic of Ash Collection System Installed on the Entrained Flow Reactor.

A series of ash collection experiments was done in the entrained flow reactor. Five of the eight coals have been run over a series of burnouts ranging from 25 to 100% (see Table II.D.1-8). The results for ash collection are shown in Figs. II.D.1-9 to II.D.1-13. It is apparent that most of the ash is collected in the cyclone rather than the cascade impactor.

Elemental ash recoveries for the Upper Kanawha are shown in Figs. II.D.1-14 to II.D.1-17. These figures indicate that sodium is essentially completely lost, while magnesium is retained only until between 30% and 50% burnout. The unexpectedly high magnesium value for the 30% burnout case is consistent with the range of magnesium contents determined (up to 0.08%). Sulfur is progressively lost as burnout increases. The remaining elements appear to be well recovered (titanium is also consistent with the observed range of up to 0.44%).

In most cases, the extractor material and the cyclone collection appear to have similar compositions, with the cyclone collection possibly somewhat enriched in silicon and iron as compared to the extractor material.

In order to gain a better understanding of the mineral matter distributions, work was performed on density separations of the original feedstocks. Results for the Upper Kanawha are shown in Figs. II.D.1-18 and II.D.1-19. The results indicate that the sink fraction is enriched in silicon and iron, while the remaining elements are fairly uniformly distributed between the float and sink fractions.

II.D.2 Effects of Minerals on Char Reactivity

The reactivity of chars prepared from both raw and demineralized coals was measured. The chars were prepared by heating in N_2 at 30°C/min until 900°C was achieved. The char reactivity measurements were made by employing a non-isothermal technique using a TGA. With an air flow of 40 cc/min and a N_2 purge flow of 40 cc/min, the samples were heated at a rate of 30°C/min until 900°C was reached. The resulting critical temperatures (defined as the temperature at which the derivative of the weight loss reaches 0.11 weight fraction/min) are plotted in Fig. II.D.2-1 as a function of oxygen in the parent coal.

The trend for the raw samples is an increase in reactivity (decreasing T_{cr}) with increasing coal oxygen content, while the slope for the demineralized samples seems to flatten out at approximately 520°C. Above 10% oxygen, the mineral content of the coal dominates the char reactivity, increasing the char's reactivity (lower T_{cr}) compared to the demineralized samples. The reason for this increase appears to be the catalytic activity of the organically bound alkali metals, particularly the Ca, since Ca is naturally abundant in coals. Below 10% oxygen content, the raw coals have a lower reactivity (higher T_{cr}) than the demineralized samples. The reason for this is oxidation due to the demineralization process.

In order to ascertain why there is a systematic increase in reactivity with coal oxygen content when reactivity is thought to depend on calcium content, the calcium concentration of coals from the Exxon sample bank were plotted as a function of oxygen concentrations in Fig. II.D.2-2. Above 8% oxygen, there is a systematic increase in Ca with increasing oxygen.

Eight percent is the level at which carboxyl groups appear in coal (Blom, et al., 1957). This suggests that, above 8% oxygen content, there is a systematic increase in the amount of calcium ion-exchanged on the carboxyl groups and it is this calcium component which acts as a catalyst.

In order to further understand the roles played by the ion-exchangeable cations in char reactivity, a 200 x 325 mesh sieved fraction of Zap Indian Head, demineralized according to the standard Bishop and Ward (1958) technique, was subjected to ion-exchange with Ca, Mg, K, and Na using a modification of the procedure by Hengel and Walker (1984). The amount ion-exchanged onto the demineralized Zap lignite was controlled by using different molar solutions of the acetate salt. In the case of Ca, 1.5 M; 1.0 M; 0.5 M; 0.3 M; 0.1 M; and 0.05 M acetate salt solutions were employed. In the case of Mg, 1.5 M; and 0.05 M acetate salt solutions were employed. In the case of K, 1.5 M; 0.3 M; 0.1 M; and 0.04 M acetate

Table II.D.1-8. Actual Burnouts For Runs Completed

	Burnout Desired			
	25%	50%	75%	100%
Pocahontas #3 (PC)	22	(43)	(70)	(100)
Upper Freeport (UF)	22	(48)	(80)	100
Pittsburgh #8 (PT)	15	61	(75)	(100)
Upper Kanawha (UK)	30	50	87	100
Rosebud (RB)	---	---	---	100

( ) Without Extractor Washings

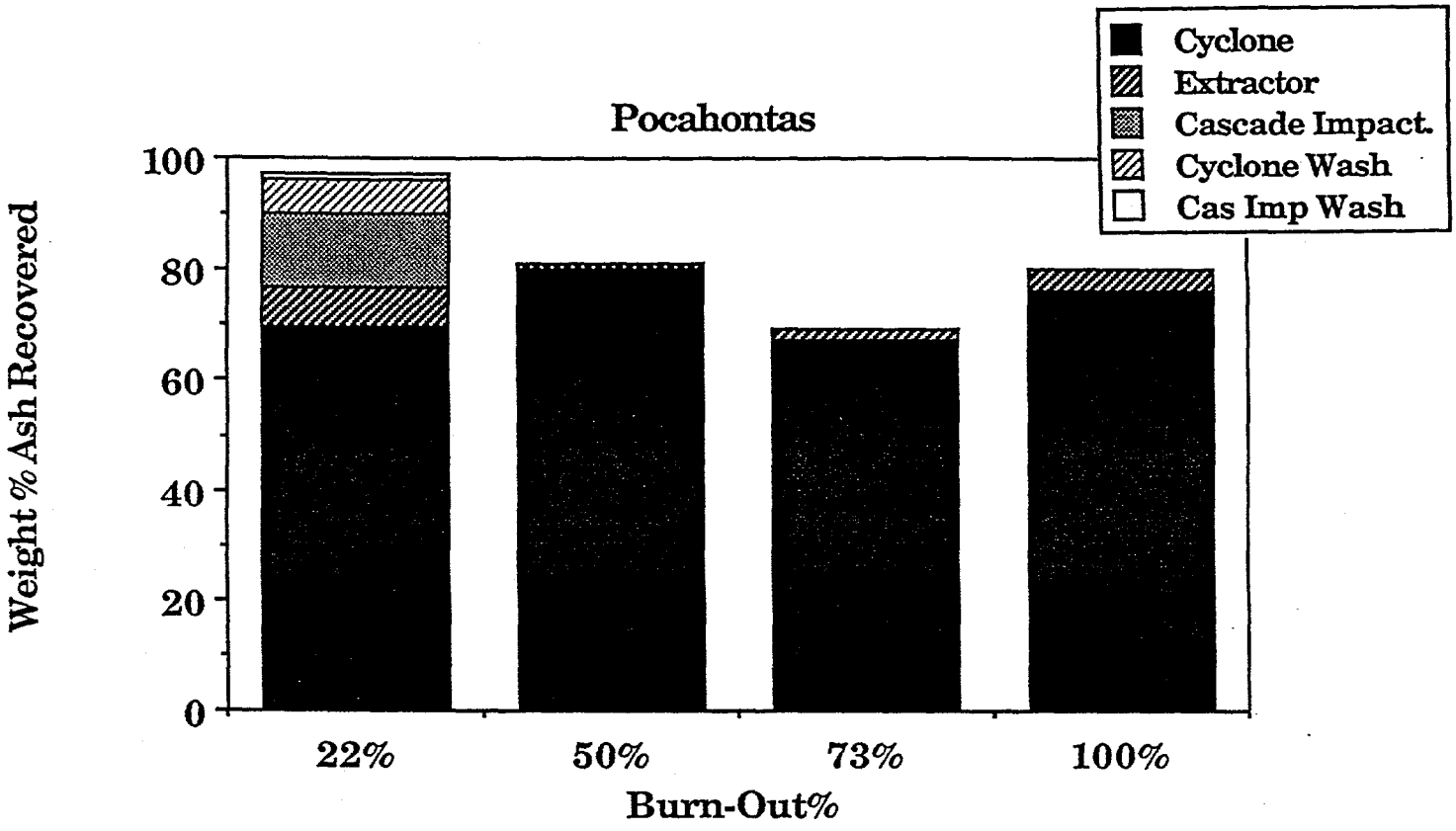

Figure II.D.1-9. Ash Recovery from Experiments over a Range of Burn-outs for Pocahontas Coal.

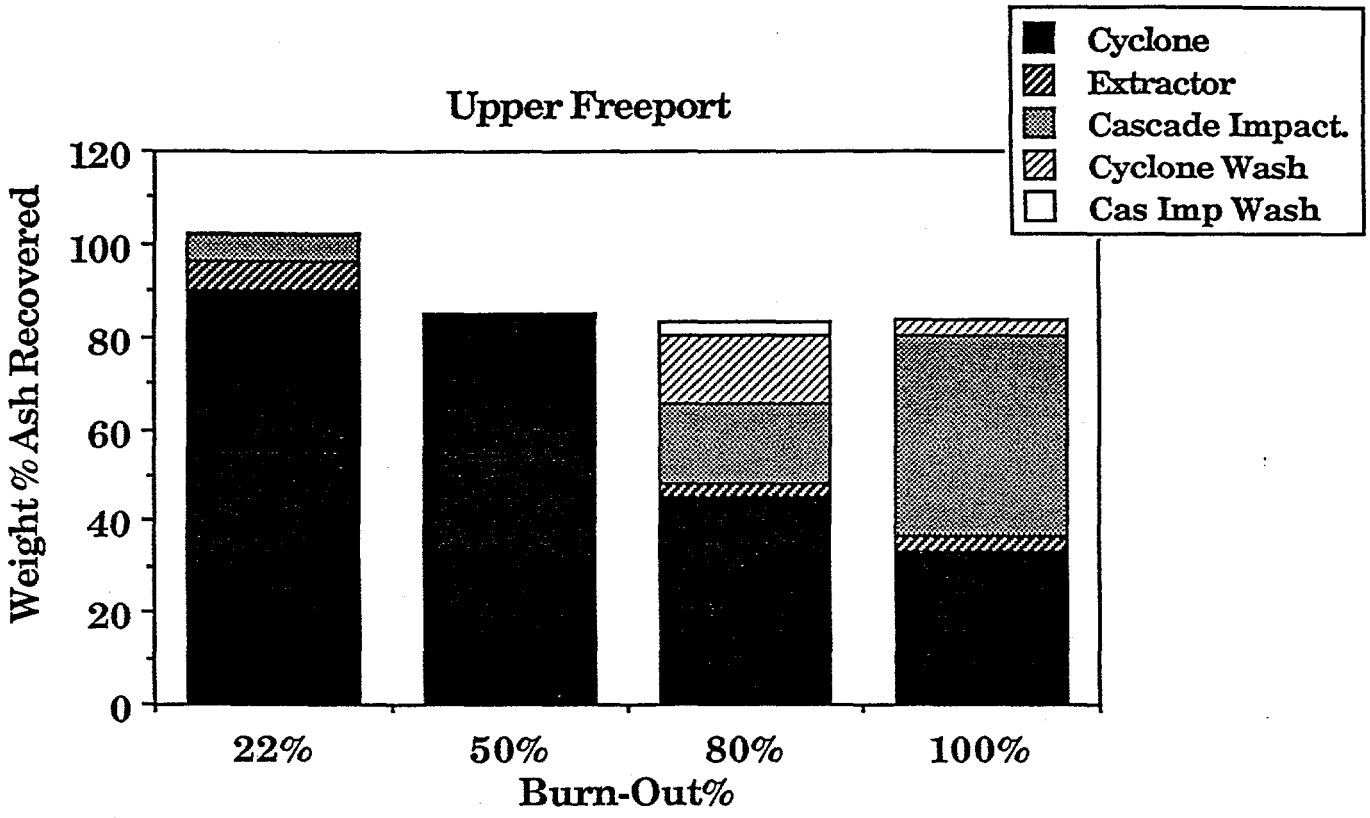

Figure II.D.1-10. Ash Collection from Experiments over a Range of Burn-outs for Upper Freeport Coal.

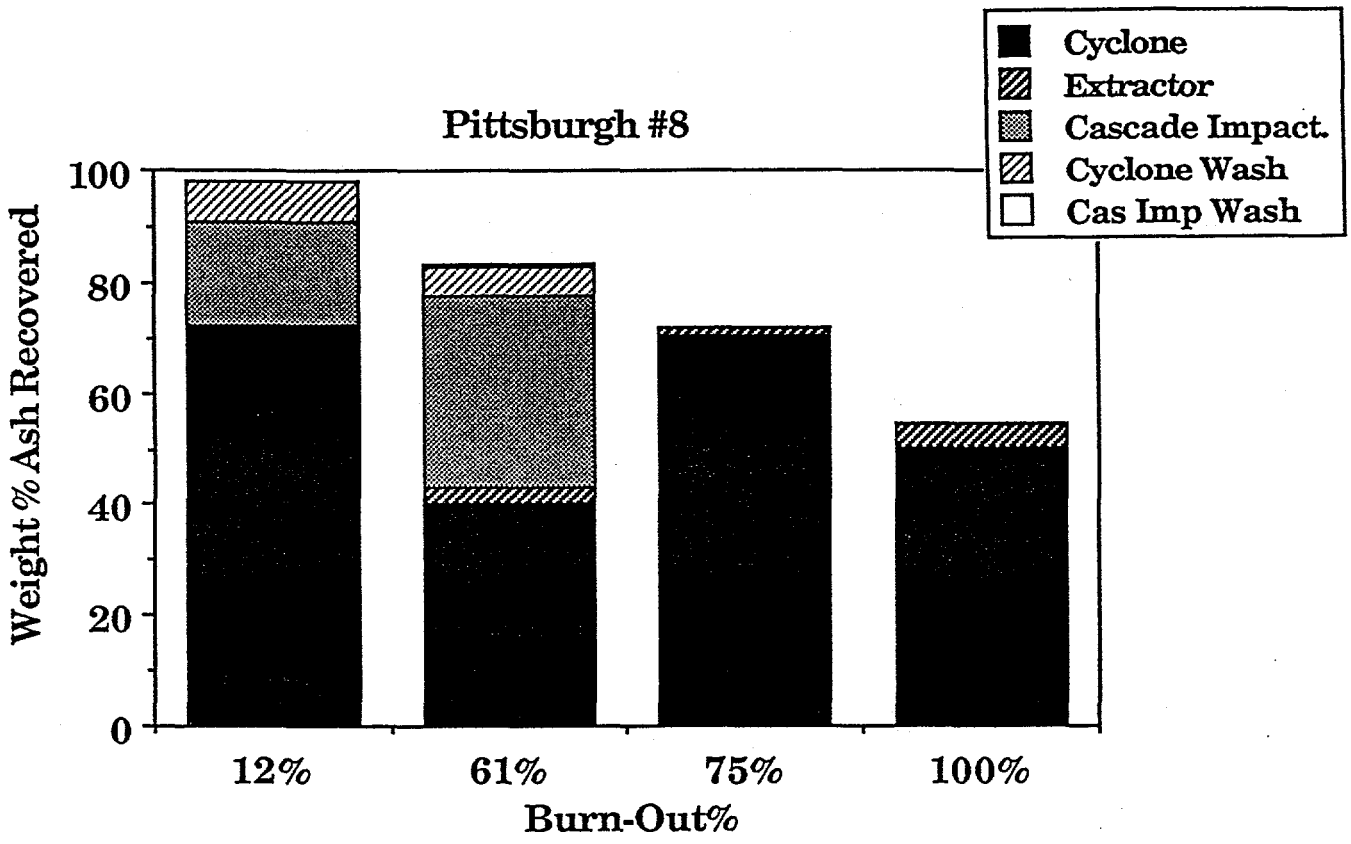

Figure II.D.1-11. Ash Collection from Experiments over a Range of Burn-outs for Pittsburgh No. 8 Coal.

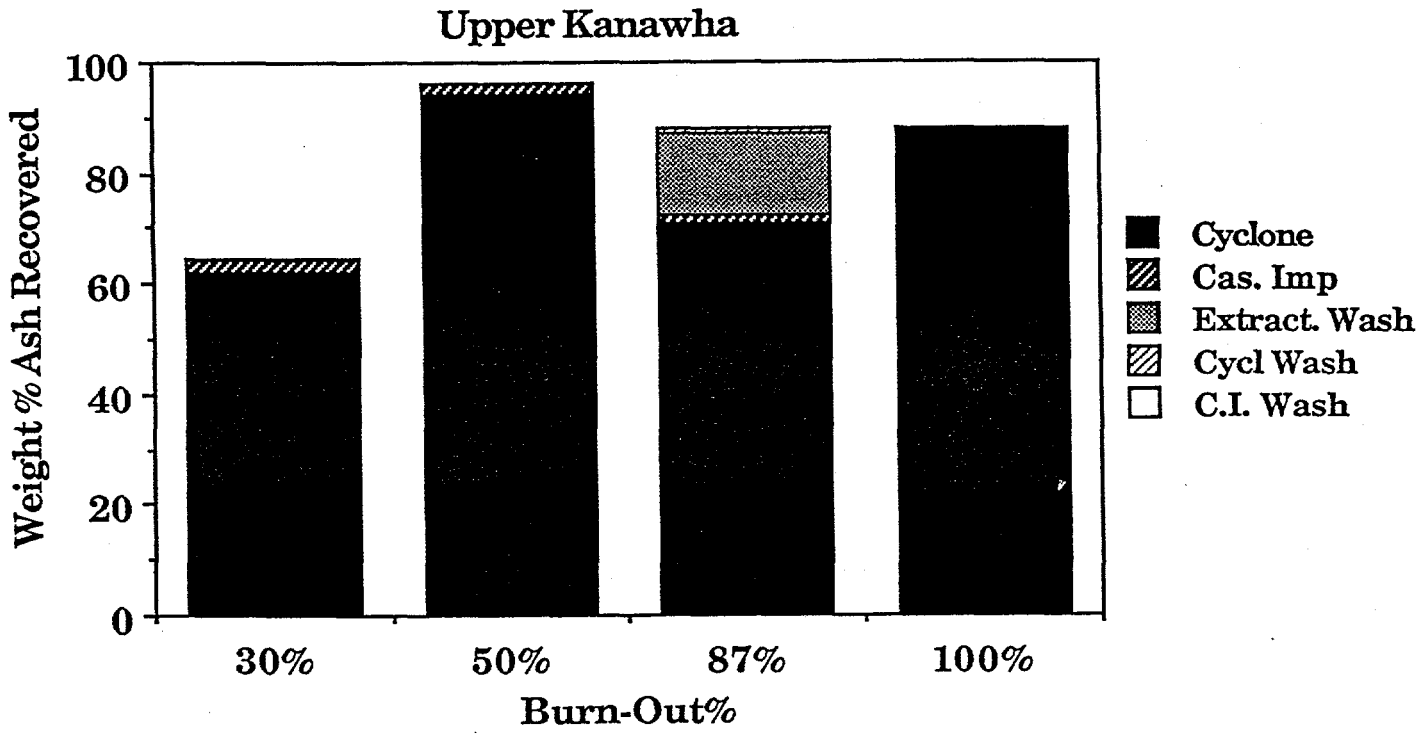

Figure II.D.1-12. Ash Collection from Experiments over a Range of Burn-outs for Upper Kanawha Coal.

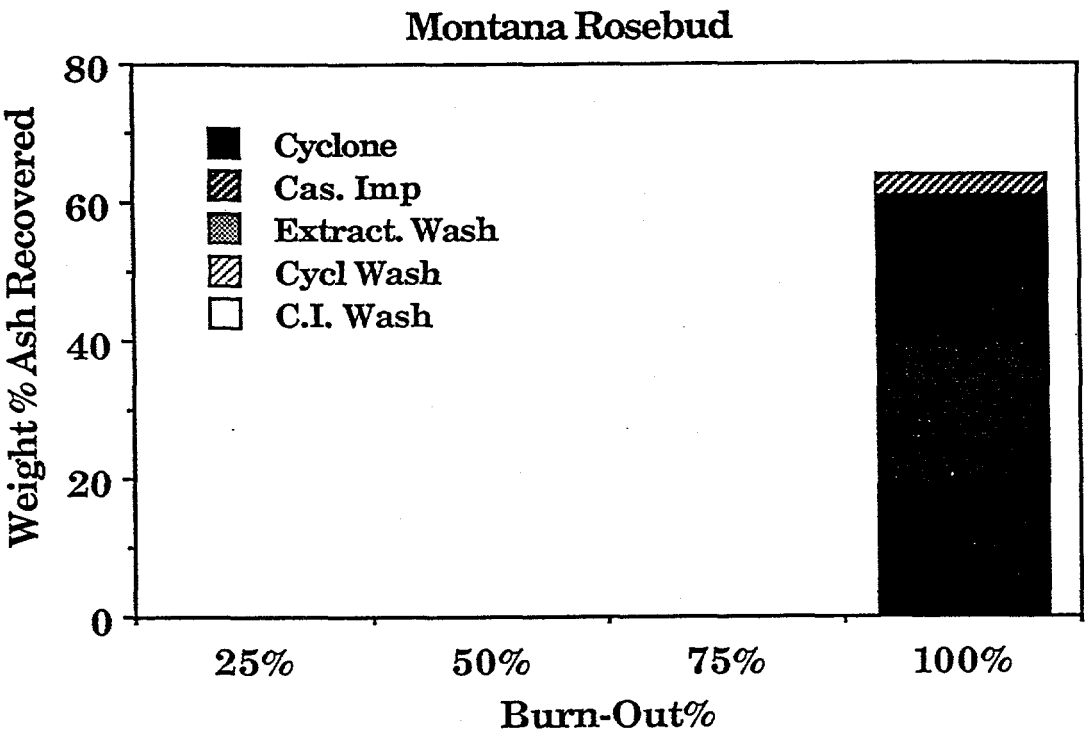

Figure II.D.1-13. Ash Collection from Experiments over a Range of Burn-outs for Montana Rosebud Coal.

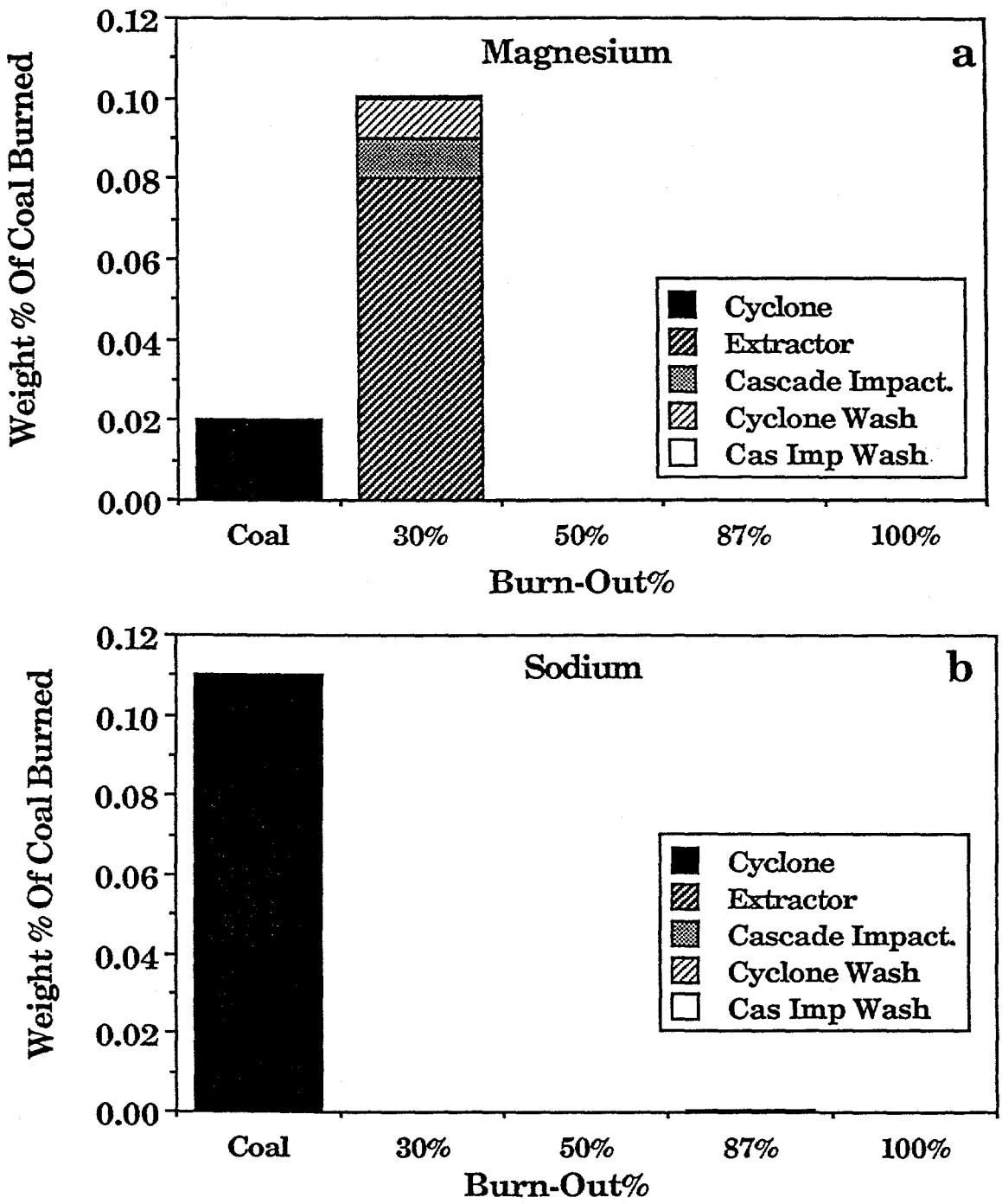

Figure II.D 1-14. Elemental Recoveries for Experiments over a Range of Burn-outs for Upper Kanawha Coal.

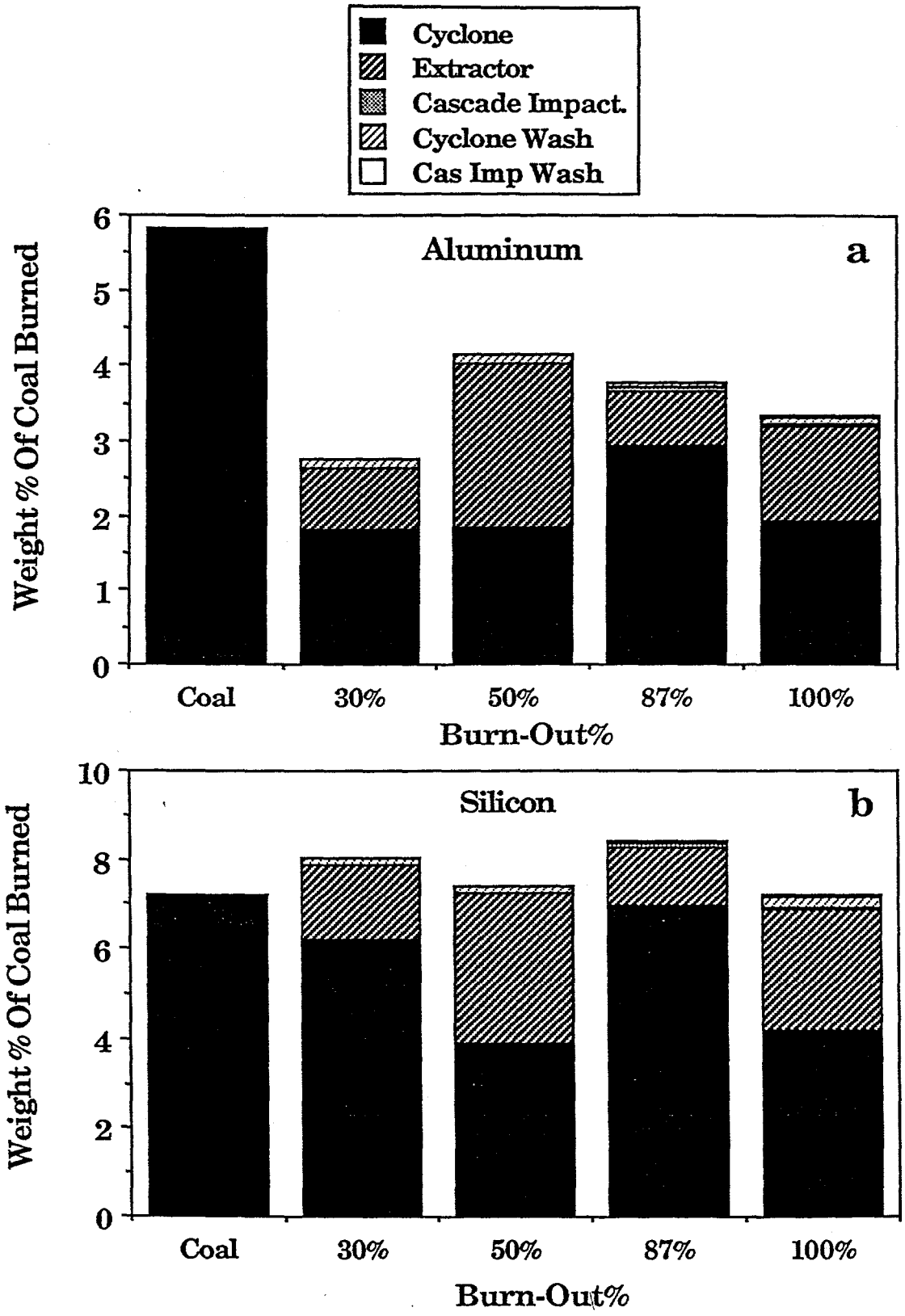

Figure II.D.1-15. Elemental Recoveries for Experiments over a Range of Burn-outs for Upper Kanawha Coal.

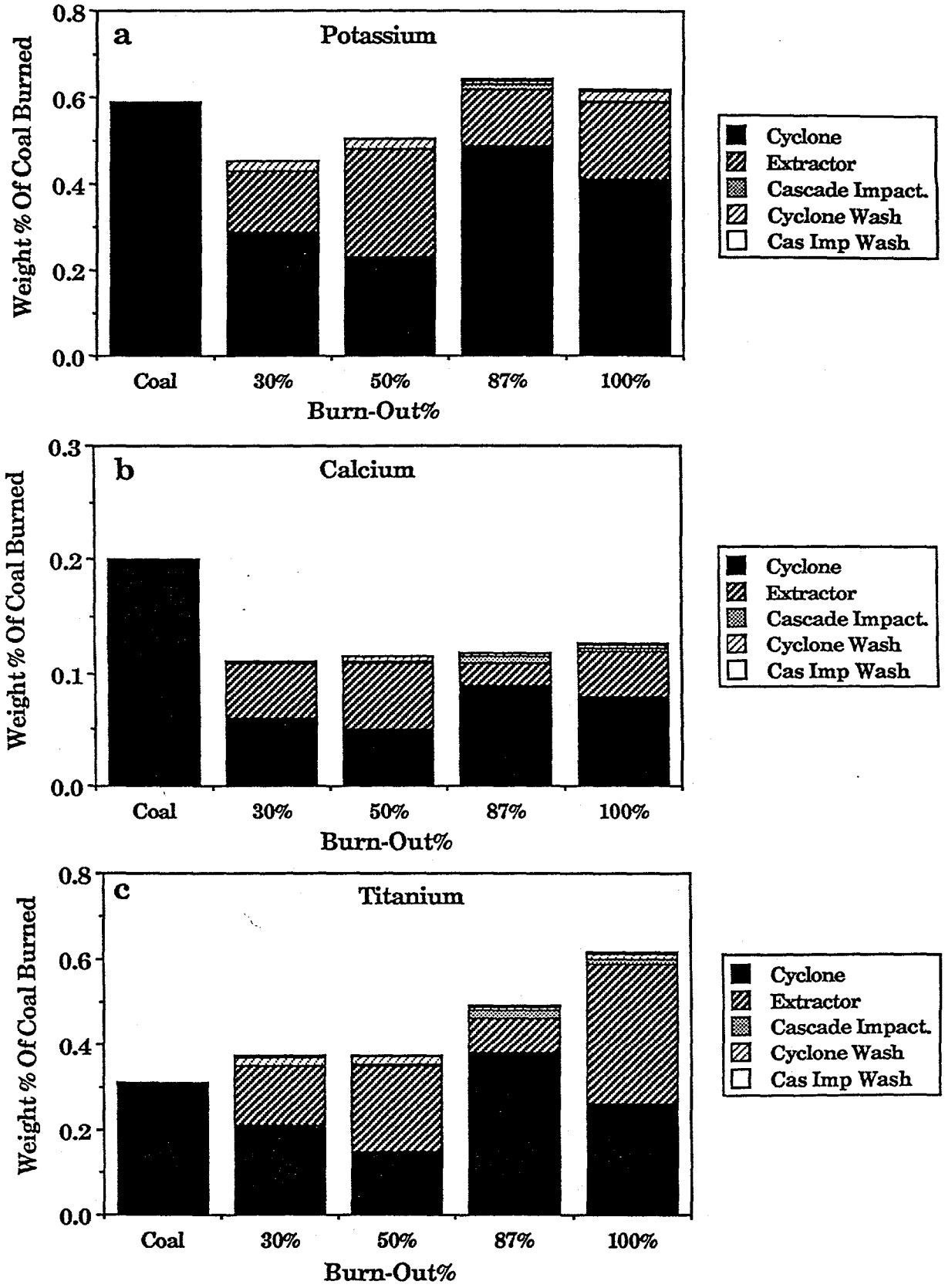

Figure II.D.1-16. Elemental Recoveries for Experiments over a Range of Burn-outs for Upper Kanawha Coal.

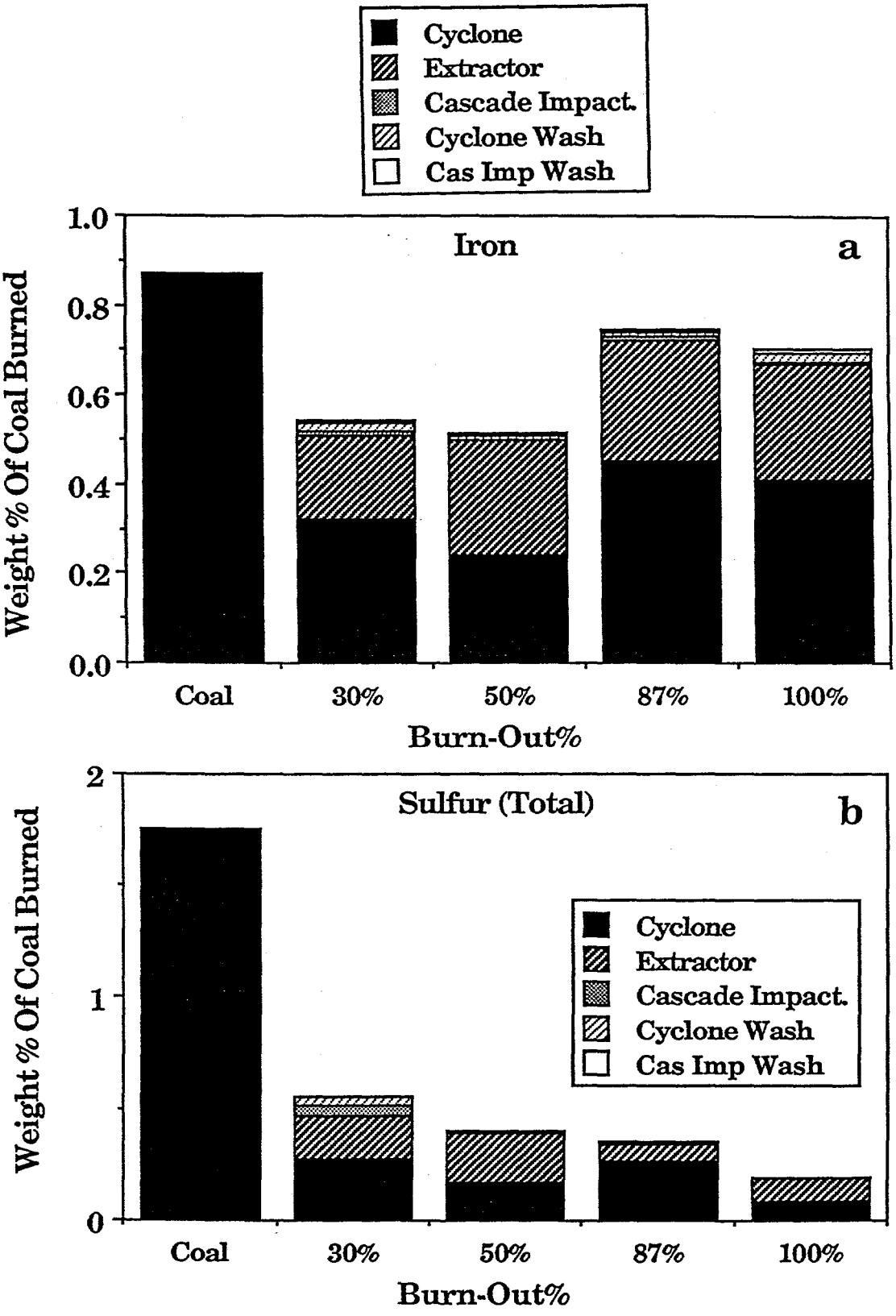

Figure II.D.1-17. Elemental Analysis of Upper Kanawha Density Separation (1.65 SG).

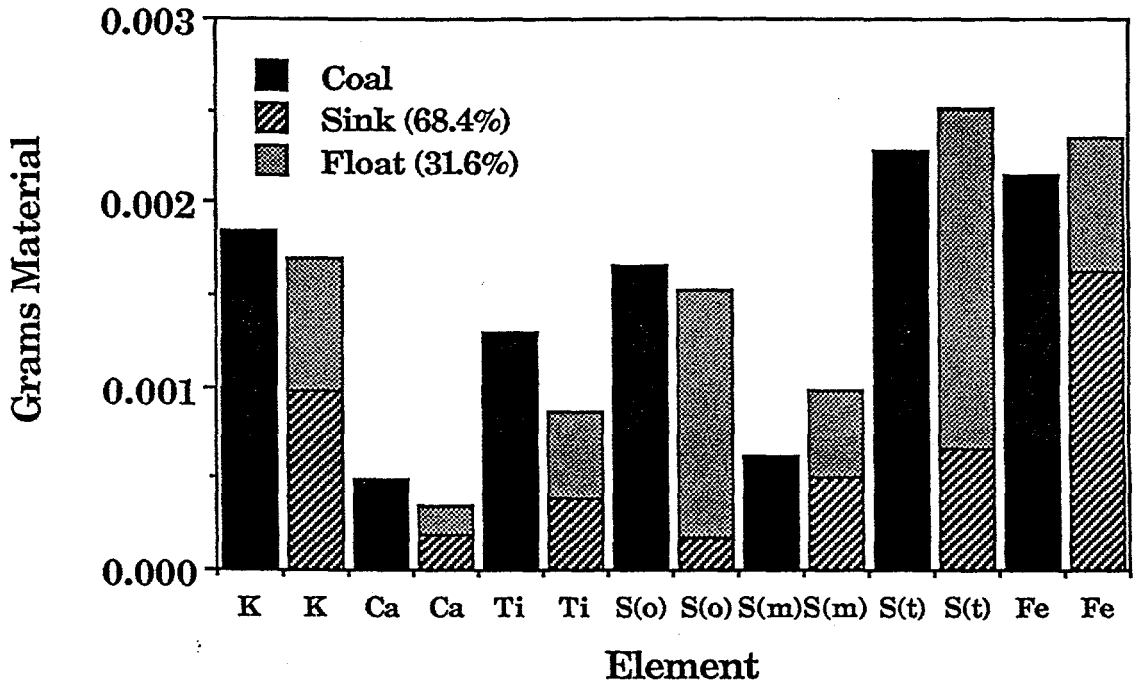

Figure II.D.1-18. Elemental Analysis of Upper Kanawha Density Separation (1.65 SG).

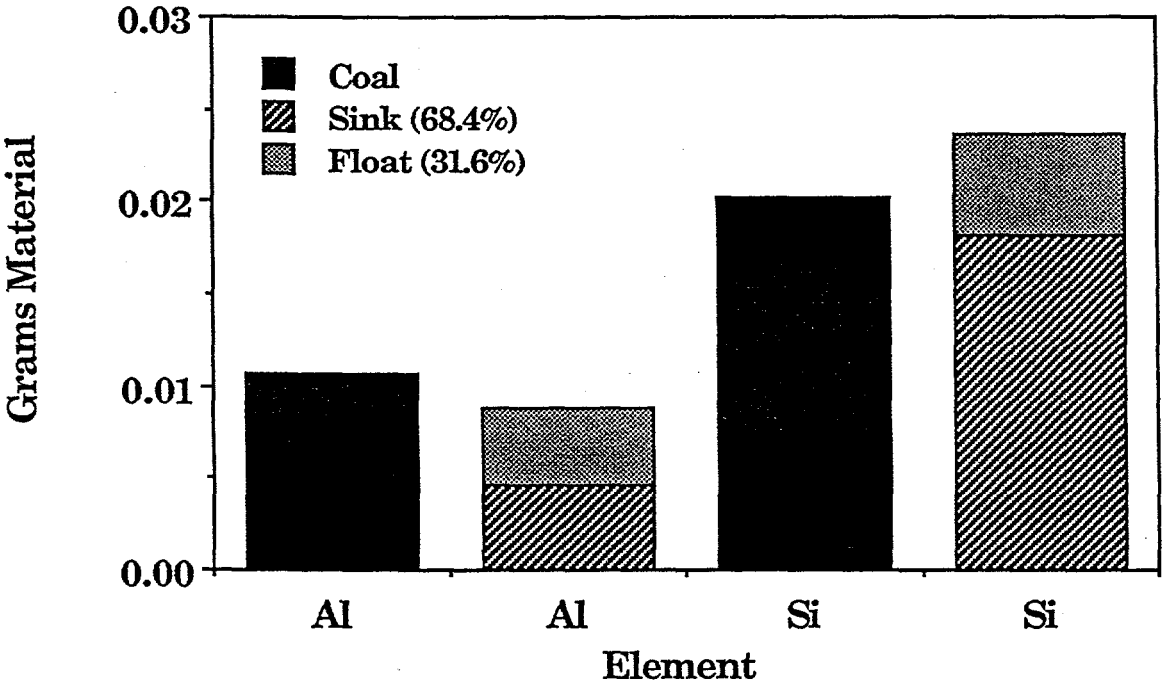

Figure II.D.1-19. Elemental Analysis of Upper Kanawha Density Separation (1.65 SG).

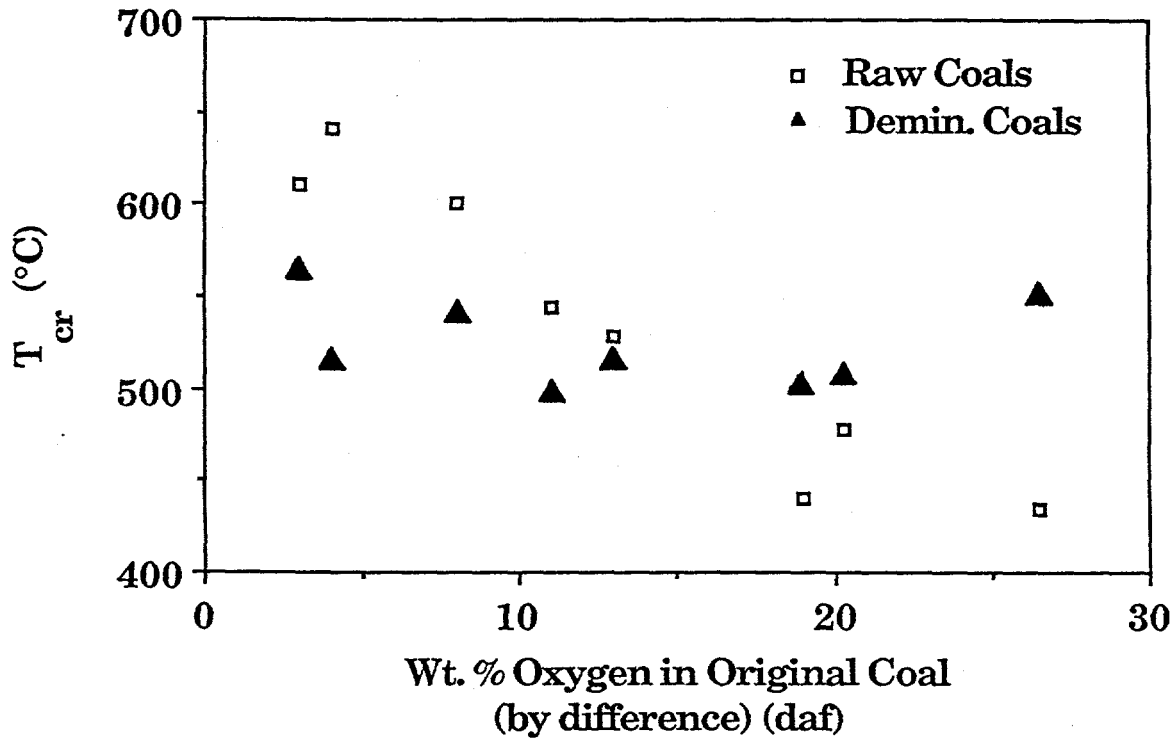

Figure II.D.2-1. Variation of Reactivity with Coal Oxygen Content for Raw and Demineralized Argonne Coals.

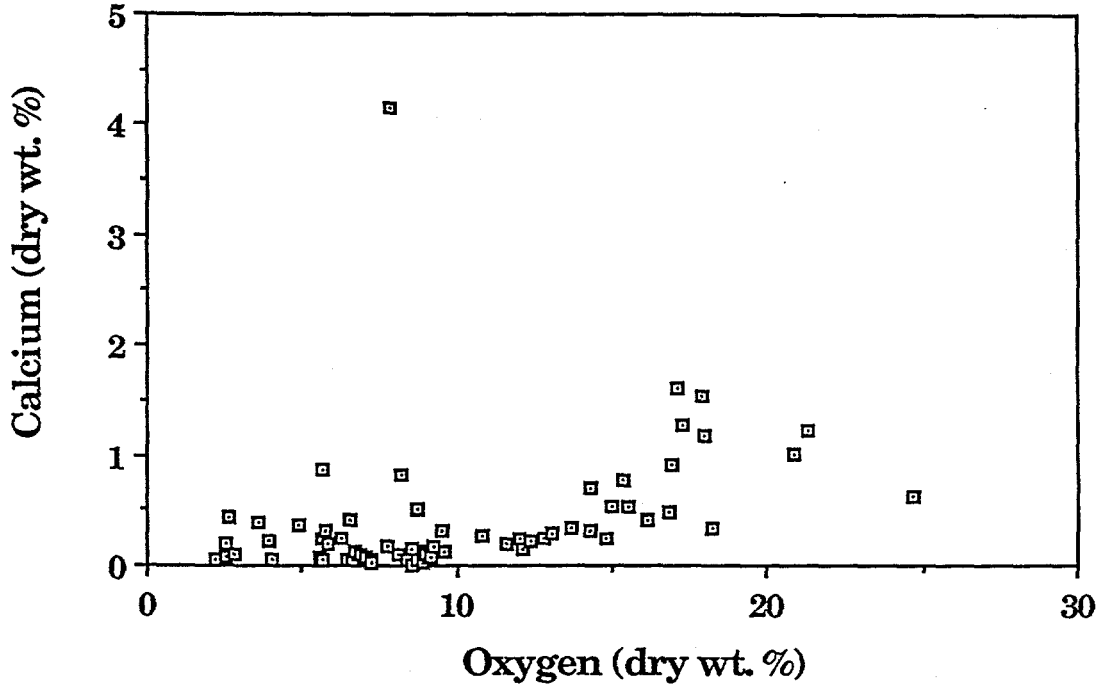

Figure II.D.2-2. Weight Percent Calcium as a Function of Oxygen in Coal.

salt solutions were employed, and in the case of Na, 1.5 M; 0.3 M; 0.1 M; and 0.05 M acetate salt solutions were used. Slurries of 5 grams of demineralized Zap and 125 ml of the desired loading solution were stirred at 57°C for 5½ hours. The solution was allowed to cool at room temperature and stirring was continued for an additional 22½ hours. The slurry was filtered, washed with deionized water and dried at 105°C in a vacuum oven for approximately two hours. The amount of cation exchanged was determined by x-ray analysis.

Chars were prepared from the cation loaded coals by heating in N_2 at 30°C/min to 900°C and these were subjected to the non-isothermal reactivity test in air. The char from demineralized Zap coal is far less reactive (higher T_{cr}) than the raw Zap char. As previously discussed, this is probably due to the removal of the organically bound alkali metals which are thought to dominate char reactivity in coals possessing more than 10% oxygen. If this is true, then cation loading should result in the resortation of char reactivity.

Plotted in Fig. II.D.2-3 is the variation of reactivity with the cation loadings. The Ca and Mg loadings effectively restored the reactivity of the demineralized Zap. In the case of Ca, the only significant change in reactivity occurs when the Ca level increase from the 0.01 wt% in the raw demineralized Zap to 1.65 wt% in the 00.5 M loading. Further increase in Ca does not cause any marked increases in reactivity. The low Na and K loadings were so effective in promoting the demineralized Zap char reactivity that the loaded samples yielded values of T_{cr} that were 45°C and 30°C, respectively, less than the T_{cr} of the raw Zap char itself. With high loadings, however, both Na and K lost their ability to increase char reactivity (lower the T_{cr}) and actually demonstrated hindering effects. The 1.5 M Na and K loadings gave values of T_{cr} which were higher by 129°C and 85°C, respectively, then the demineralized Zap sample. Surface area measurements on the raw and cation-loaded samples were done in these cases. However, significant differences were not observed between the raw and cation-loaded coals in either case. Consequently, the hindering effect must manifest itself either during the char formation process or the gasification process.

CO_2 char reactivity measurements were done on chars produced from raw, demineralized and loaded demineralized Zap samples by heating in N_2 at 30°C/min until 1000°C was achieved. The CO_2 reactivity followed similar trends as the air reactivities as shown in Fig. II.D.2-4.

A model was developed to predict the intrinsic reactivity (T_{cr}) of char based on calcium content for coals greater than 10% oxygen, while holding the extent of pyrolysis and heating rate constant. For a standard test:

$$T_{cr} = 520 + \alpha\ (Ca\ wt\% - (\beta * carbonate)) \qquad \text{(II.D-1)}$$

where, 520 represents the approximate T_{cr} for demineralized coals, α is the slope from the plot of T_{cr} vs Ca wt% in Fig. II.D.2-3a, β is a constant and the carbonate value is that obtained from quantitative FT-IR analysis.

Figure II.D.2-5a displays the correlation between actual T_{cr} and predicted T_{cr} with $\beta = 0$. Since it is the organically bound Ca which is thought to be catalytically active, a much better correlation is obtained when calcite corrections are included in the model (Fig. II.D.2-5b).

In order to better understand why the organically bound Ca offers catalytic activity and calcite does not, SEM Ca dot maps were done for a calcium loaded demineralized. Zap coal and an Exxon sample which, from FT-IR analysis, was known to be abundant in calcite. The maps in Fig. II.D.2-6 indicate that the organically bound Ca is very well distributed throughout the Zap coal while the calcite in the Exxon coal exists in large clusters. This is consistent with the fact that the Ca in the calcite form is not nearly as effective as a catalyst when compared to the ion-exchanged Ca.

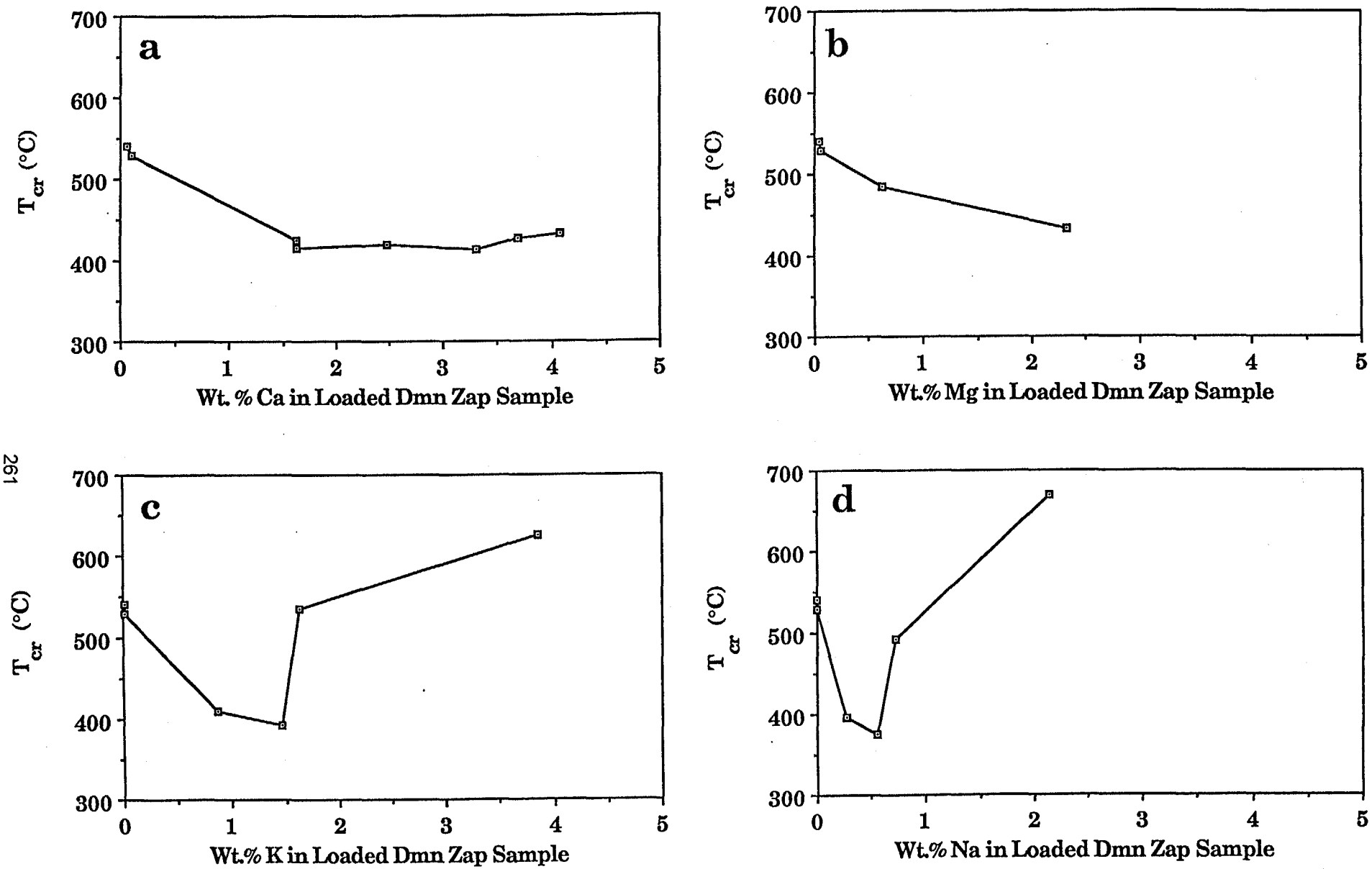

Figure II.D.2-3. Variation of Reactivity with Cation Loadings for Demineralized Zap Coal. a) Calcium; b) Magnesium; c) Potassium; d) Sodium.

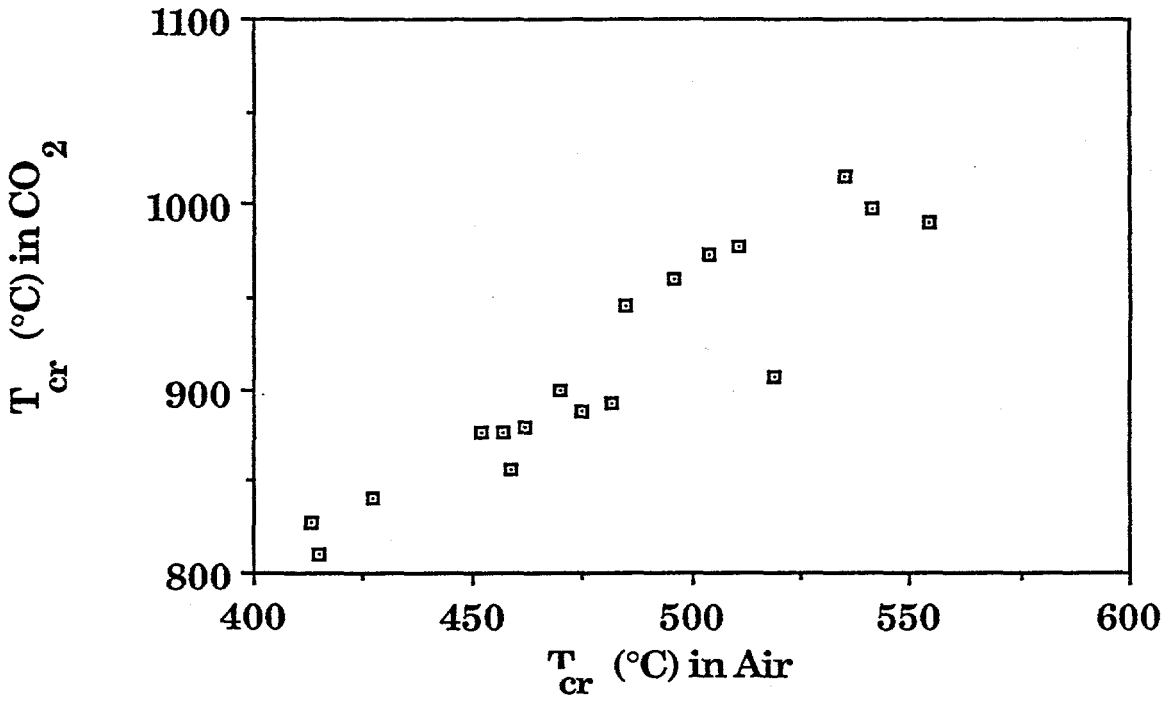

Figure II.D.2-4. Correlation Between CO_2 and Air Reactivity Parameters

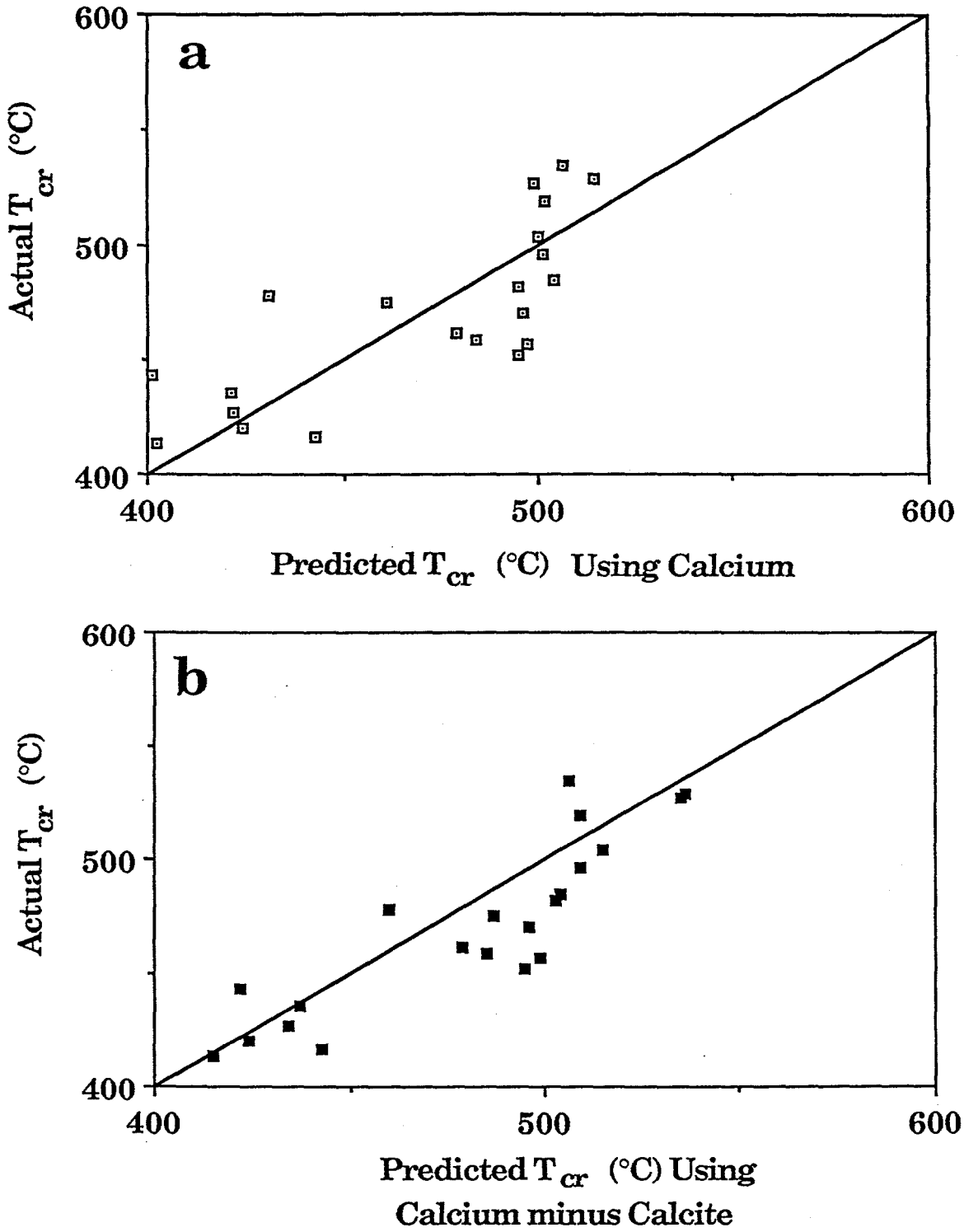

Figure II.D.2-5. Correlation Between Actual Reactivity and Predicted Reactivity Based on Ca Content. a) with Calcite; b) Without Calcite.

a

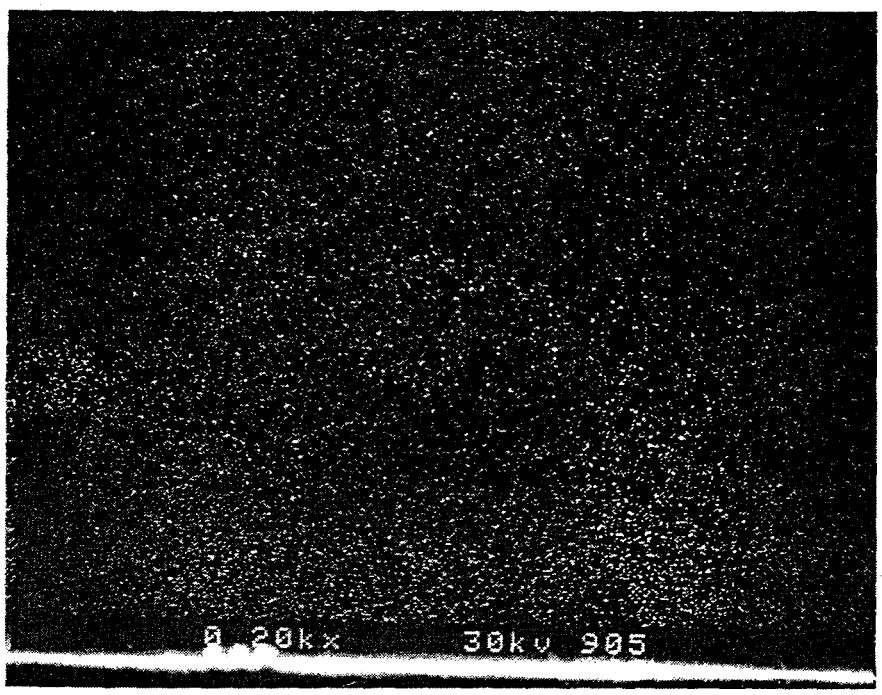

No Calcite

b

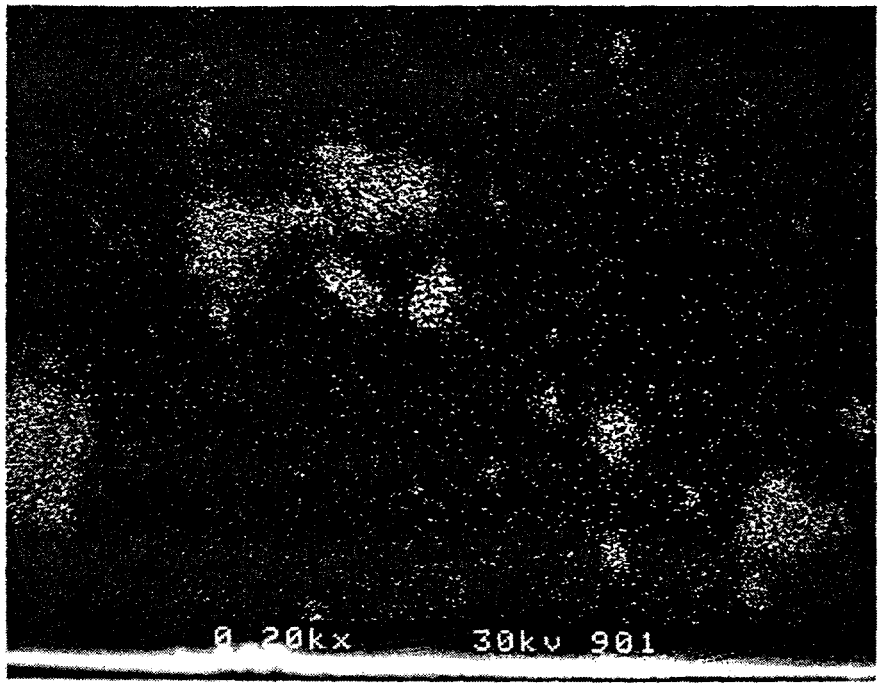

High Calcite

Figure II.D.2-6. SEM Calcium Dot Maps. a) Ca Loaded Demineralized Zap Coal, No Calcite; b) Exxon #6, High Calcite.

II.D.3. The Modeling of Mineral Matter Effects on Char Reactivity

The data from Section II.D-2 were used to develop a model for the effects of ion-exchanged alkali and alkaline earth metals on char reactivity. The model is discussed in Section II.A.10 and is described in Charpenay, et al., (1992).

II.D.4. Literature Review

To fully develop a mineral matter model for integration into PCGC-2, a number of effects must be included. The inputs will be the starting mineral concentrations and size distributions while the outputs will be the composition and size distribution of the fly ash. An outline of the proposed submodel for ash chemistry and physics is shown in Fig. II.D.4-1. Because of the complexity of this problem and the large amount of DoE and NSF supported work being done elsewhere, the eventual submodel will primarily be an integration of work done outside AFR. A brief summary of the most relevant studies appears below.

Although considerable progress has been made in understanding the underlying principles of ash formation and deposition, these processes, predictive modeling of ash behavior in the combustor still remains at the early stage of development. The ultimate objective is to provide a powerful tool for combustor design by identifying the régimes in which the fouling of heat-transfer surfaces is minimal. Three research groups have made important contributions to the study of coal-ash behavior during combustion: Energy and Environmental Research Center (EERC), University of North Dakota, Grand Forks, ND; PSI Technology Company, Andover, MA; and Massachusetts Institute of Technology (MIT), Cambridge, MA. The recent advances in characterization of mineral matter in coal as well as in the study of ash formation and deposition will be reviewed below. Unless stated otherwise, the presented material is based on references [Benson et al., 1993; Helble, 1992) and on the recent Short Course on Ash Formation and Deposition during Coal Combustion which was sponsored by EERC and the U.S. Department of Energy (St. Louis, MO, 10th May, 1993).

Review of Work Performed at EERC (and some other centers)

Precise, quantitative prediction of the fate of inorganic coal constituents during combustion is currently impossible due to an enormous complexity of the process, and due to inadequate mineral-matter characterization in the starting material. In general, the extent of ash-related problems depends upon the quantity and association of inorganic constituents in coal, the combustion conditions, and the system geometry. A detailed understanding of the critical phenomena is necessary to develop models that will accurately predict ash deposition as a function of coal characteristics and combustion conditions. The following key areas have been identified:

1. The chemical and physical characterization of inorganic matter in coal
2. The mechanisms of mineral-matter transformation into inorganic vapors, liquids and solids
3. The physical properties of the intermediate ash species as a function of temperature, atmosphere, and residence time
4. The mechanisms of ash transport to heat-transfer surfaces as a function of particle size and flow patterns in the combustor
5. The heat-transfer characteristics coupled with the reactivity and melting behavior of the deposited ash material
6. The characteristics of the liquid components in the deposit with respect to deposit growth and strength development
7. The physical characteristics of the deposit that influence its ability to be removed by conventional processes (e.g., by soot blowing).

Inorganic Constituents In Coals

Mineral matter can be present in coal in one of the three forms: (1) organically associated elements; (2) included minerals; and (3) excluded minerals. This division is illustrated in Figure II.D.4-2

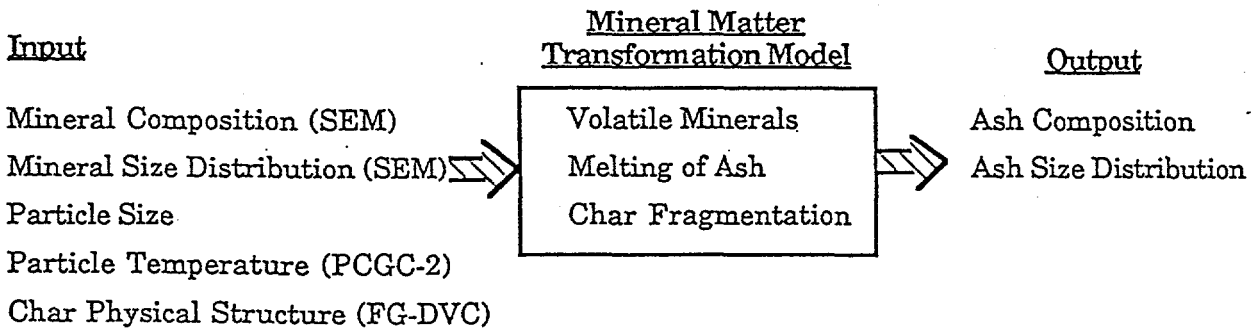

Figure II.D.4-1. Outline of Ash Physics And Chemistry Submodel.

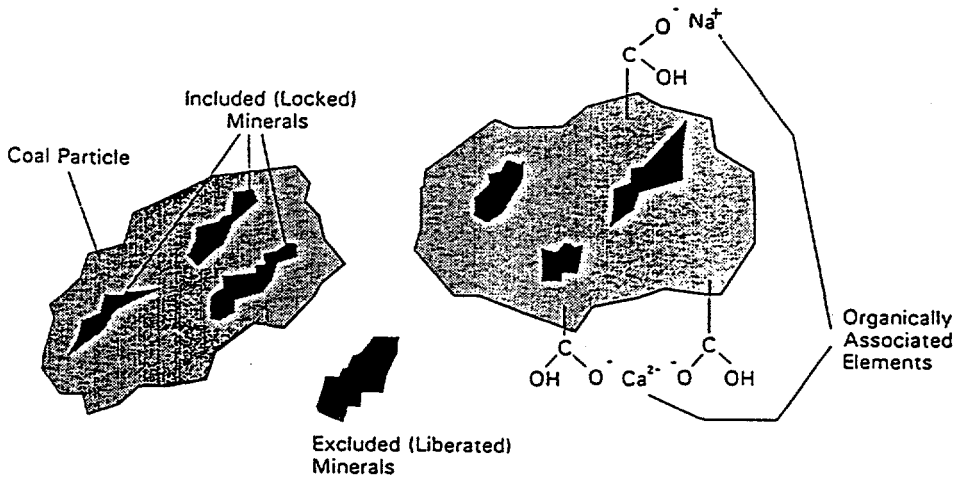

Figure II.D.4-2. Coal and associated inorganic components.

The fraction of inorganic components that are organically associated varies with coal rank. Lower-rank coals (subbituminous and lignitic) have high levels of oxygen. Approximately 25% of the oxygen is in the form of a carboxylic acid group. These groups act as bonding sites for cations such as sodium, magnesium, calcium, potassium, strontium, and barium (other minor and trace elements may also be associated in the coal in this form). In addition, some elements may be in the form of chelate coordination complexes with pairs of adjacent organic oxygen functional groups. The cations originate from the plant material from which the coal was formed and from groundwater filtering though the coal seam. In some low-rank coals, the organically associated inorganic components can comprise up to 60% of the total inorganic content of the coal (Benson and Holm, 1985). In higher-ranked coals, bituminous and anthracite, the inorganic components consist mainly of minerals.

Mineral grains are usually the most abundant inorganic component in coals. The minerals associated with coals are classified by coal geologists based on their origins as summarized by Stach *et al.* (1982). The major mineral groups found in coals include silicates and oxides, carbonates, sulfides, sulfates, and phosphates. In order to predict the behavior of the inorganic constituents during combustion, detailed information must be obtained on the abundance, size, and association of mineral grains in the coal.

The methods used to determine the association of inorganic components in coals have evolved significantly over the past 80 years. Ashing and gravity separation techniques are very common. These methods have inherent limitations and do not provide quantitative information on the association and abundance of inorganic components in coals. Recently, more advanced methods such as computer-controlled scanning electron microscopy (CCSEM) and chemical fractionation are being used to more quantitatively determine the abundance, size, and association of inorganic components in coals. Detailed information from the CCSEM and chemical fractionation allows for more effective prediction of the behavior of the inorganic components during combustion.

High-temperature ashing is a standard method that is routinely used to determine the quantity of inorganic constituents present in coal. This technique involves oxidizing the coal at 1023 K (750°C) followed by chemical analysis of the resultant ash. There are several limitations involved in this type of analysis. First, significant transformations and reactions of the inorganic components occur during the ashing process. The loss of mass due to water loss from clay minerals, carbon dioxide loss from carbonates, and sulfur loss from pyrite can significantly influence the determination of the inorganic content of coal. These species (H_2O, CO_2 and SO_2) are usually included as volatiles in the proximate analysis,

leading to erroneous results. In addition, the organically associated inorganic elements such as the alkali and alkaline earth elements absorb oxygen and SO_2 during the ashing processes, further complicating the determinations. Several investigators have developed empirical methods based on the composition of the ash and losses due to decomposition of minerals to estimate the inorganic content of coals as summarized by Given and Yarzab (1978).

Two other methods that have been used to concentrate the inorganic components in coal include gravity fractionation and low-temperature oxygen plasma ashing (LTA). Gravity separation only provides a partial separation of the minerals from the coal matrix, since some of the minerals that are small and included in the coal particles remain in the lighter fraction. In addition, the organically associated cations remain in the lighter organic-rich fraction. Therefore, gravity fractionation of the minerals is only a qualitative estimation of the minerals present in the coal. Low-temperature ashing is another technique that has been used to concentrate the inorganic species. This technique works quite well with higher-rank coal, but requires very long ashing times with lower-ranked coals containing high levels of organically associated cations.

Identification of the specific mineral species in coals (as opposed to chemical analysis) has been performed by several techniques. Jenkins and Walker (1978) provide a good summary of the techniques and applications prior to 1978. These include x-ray diffraction, infrared spectroscopy, differential thermal analysis, scanning electron microscopy, microprobe analysis, and ^{57}Fe Mössbauer. Unfortunately, the x-ray diffraction and infrared spectroscopy methods require low-temperature ashing prior to analysis. The technique that shows the most promise for quantitative determination of the mineral portion of the inorganic components in coal is scanning electron microscopy and microprobe (energy dispersive x-ray) analysis. Over the past ten years, this technique has been used much more rigorously to determine the mineral component in coal.

In order to determine the size, abundance, and association of mineral grains in both high- and low-rank coals, computer-controlled scanning electron microscopy (CCSEM) and automated image analysis (AIA) are the preferred techniques used to analyze polished cross sections of coal epoxy plugs (Zygarlick and Steadman, 1990). The CCSEM technique is used to determine the size, shape, quantity, and semi-quantitative composition of mineral grains in coals (Steadman et al., 1990 and Steadman et al., 1991). The key components of the CCSEM system that make it possible to image, size, and analyze inorganic particles are the backscatter electron detector, digital beam control, and the ultrathin window energy-dispersive x-ray detector. Backscatter electron imaging is used for CCSEM because the intensity of the backscattered electrons is a function of the average atomic number of the features on or near the surface. Since the mineral particles appear brighter relative to the lower atomic number background of the matrix, a distinction can be made between coal, mounting media, and mineral grains. In a typical CCSEM analysis the electron beam is programmed to scan over the field of view and locate the bright inclusions that correspond to mineral species. On finding a bright inclusion, the beam performs eight diameter measurements of the inclusion, finds the center of the inclusion, and collects and energy-dispersive spectrum (EDS) at the point for 2 seconds. Software classifies the mineral grains based on the EDS elemental composition and size. The parameters used to identify the minerals are based on published compositions of known minerals. A mineral association, such as aluminosilicate/gypsum, is a discrete particle that contains at least two adjacent or intimately associated minerals. The EDS spectra will reveal a combination of the proper elemental ratios for these associated minerals.

The differences in the chemical information provided by the ASTM versus CCSEM methods are illustrated in Figure II.D.4-3. In contrast to CCSEM, the ASTM analysis provides only a single data point which does not represent the true heterogeneity of the ash.

Quantification of the type and abundance of organically associated inorganic elements in lower-ranked subbituminous and lignitic coals is currently performed by chemical fractionation (Benson and Holm, 1985). Chemical fractionation is used to selectively extract elements from the coal based on solubility, which reflects their association in the coal. Briefly, the technique involves extracting the coal with water

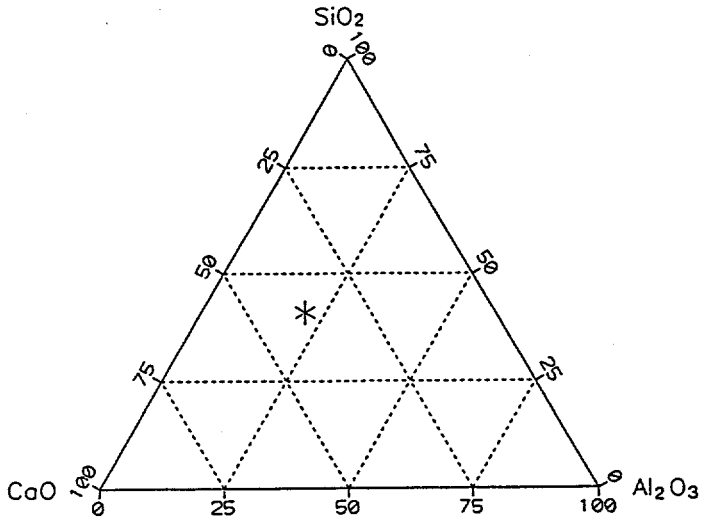

(a)

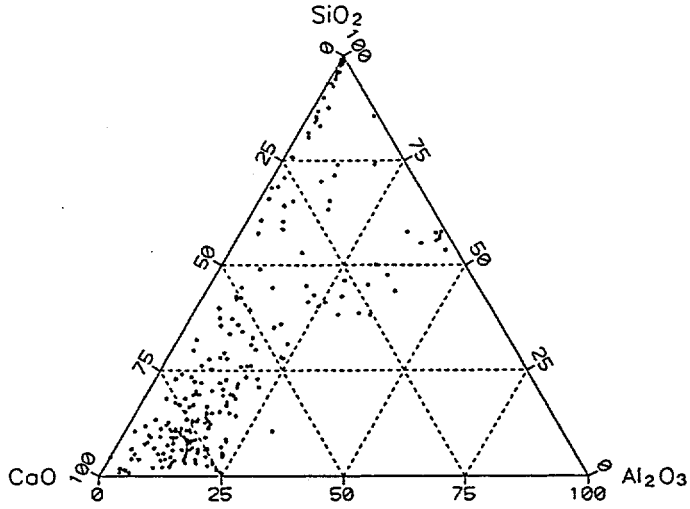

(b)

Figure II.D.4-3. Chemical information in coal ash provided by various types of chemical analysis: (a) ASTM ash analysis, and (b) CCSEM analysis of fly ash.

to remove water-soluble elements such as Na in sodium sulfate or those elements that were most likely associated with the groundwater in the coal. This is followed by extraction with 1M ammonium acetate to remove elements such as Na, Ca, and Mg that may be bound as salts of organic acids. The residue of the ammonium acetate extractions is then extracted with 1M HCl to remove acid-soluble species such as Fe and Ca which may be in the form of hydroxides, oxides, carbonates, and organically coordinated species. The components remaining in the residue after all three extractions are assumed to be associated with the insoluble mineral species such as clays, quartz, and pyrite. A number of Argonne Premium Coals have been analyzed by CCSEM and chemical fractionation, and the available data base is growing (Helbe et al., 1992 and Zygarlicke et al., 1990).

Formation Of Ash Intermediates

The inorganic coal components undergo complex chemical and physical transformations during combustion to produce intermediate ash species (gases, liquids, and solids). The physical transformation of inorganic constituents depends on the inorganic composition of the coal and on combustion conditions. There exists a wide range of combinations of mineral-mineral, mineral-coal, mineral-cation-coal, and mineral-mineral-cation-coal associations in coal. These associations are unique to each coal sample and they include: (1) coalescence of individual mineral grains within a char particle; (2) shedding of the ash particles from the surface of the chars; (3) incomplete coalescence due to disintegration of the char; (4) convective transport of ash from the char surface during devolatilization; (5) fragmentation of the inorganic mineral particles; (6) formation of cenospheres; and (7) vaporization and subsequent condensation of the inorganic components upon gas cooling. As a result of these interactions, the fly ash usually has a bimodal size distribution, with maximum at particle sizes of ~0.1 μm and ~10 μm. The submicron component is largely a result of the condensation of flame-volatilized inorganic components. The larger size particles have been called the residual ash by some investigators (Sarofim et al., 1977) because these ash particles resemble, to a limited degree, the original minerals in the coals.

The transformations of excluded minerals are dependent upon the physical characteristics of the mineral. Excluded minerals such as quartz (SiO_2) can be carried through the combustion system with its angular structure still intact. Excluded clay minerals can fragment during dehydration, melt, and form cenospheres. The behavior of excluded pyrite depends upon its morphology. Some of the pyrite may be present as framboids. Framboidal pyrite fragments more easily than massive pyrite particles. In addition, pyrite transforms to pyrrhotite and oxidizes to FeO, Fe_3O_4, and Fe_2O_3 during combustion. The transformations of pyrite have been examined and modeled in detail by Srinivasachar et al. (1990). The carbonate minerals will fragment during the loss of carbon dioxide. According to Raask (1985), some of the carbonate minerals fragment and produce submicron-sized particles.

There are two extreme kinds of behavior that the inorganic constituents may exhibit during combustion (Field et al., 1967): (1) Each mineral grain forms a single ash particle; (2) One ash particle is formed per coal particle. Some of the differences in the fly ash size distribution exhibited for different coals are probably due to the burning char characteristics of the chars. For example, some coal particles swell and become hollow and porous during combustion. The degree of swelling depends on coal composition or maceral distribution and the combustion conditions.

Depending upon the distribution of minerals and other inorganic components, coalescence may occur to a larger or smaller extent. If the ash particles are similar in size to the original minerals in the coal, coalescence is insignificant and one ash particle per mineral grain is formed. In contrast, coalescence of minerals into a large particle occurs when the receding carbon surface brings the ash particles together. Thus, shrinking sphere represents the limiting case where one fly ash particle is produced per coal particle. In most cases, the actual fly ash size falls between the fine limit of one ash particle per mineral grain and the coarse limit of one ash particle per coal particle. In cases where mineral fragmentation occurs, the fine limit on size may be exceeded. In addition, shedding or convective transport of small ash particles originating from organic associations or submicron mineral grains can contribute to fine particle formation.

Vaporization and condensation of inorganic elements also contribute to the formation of fine particulate when the vapors condense homogeneously. In lower-rank coals, organically associated inorganic elements such as sodium, calcium, magnesium, and potassium have the potential to vaporize during combustion. The evidence for vaporization and condensation of sodium and potassium is abundant. The reactions of calcium and magnesium are less clear.

The chemical composition of the intermediate ash particles will influence their melting behavior in combustion systems. Figure II.D.4-4 illustrates the composition evolution of Upper Freeport fly ash. The figure shows that the major minerals such as pyrite, aluminosilicates, and K-aluminosilicates are transformed during the combustion process. The result is the formation of iron oxides, iron aluminosilicates, and other complex glass phases. These fly ash particles vary widely in size and chemical composition.

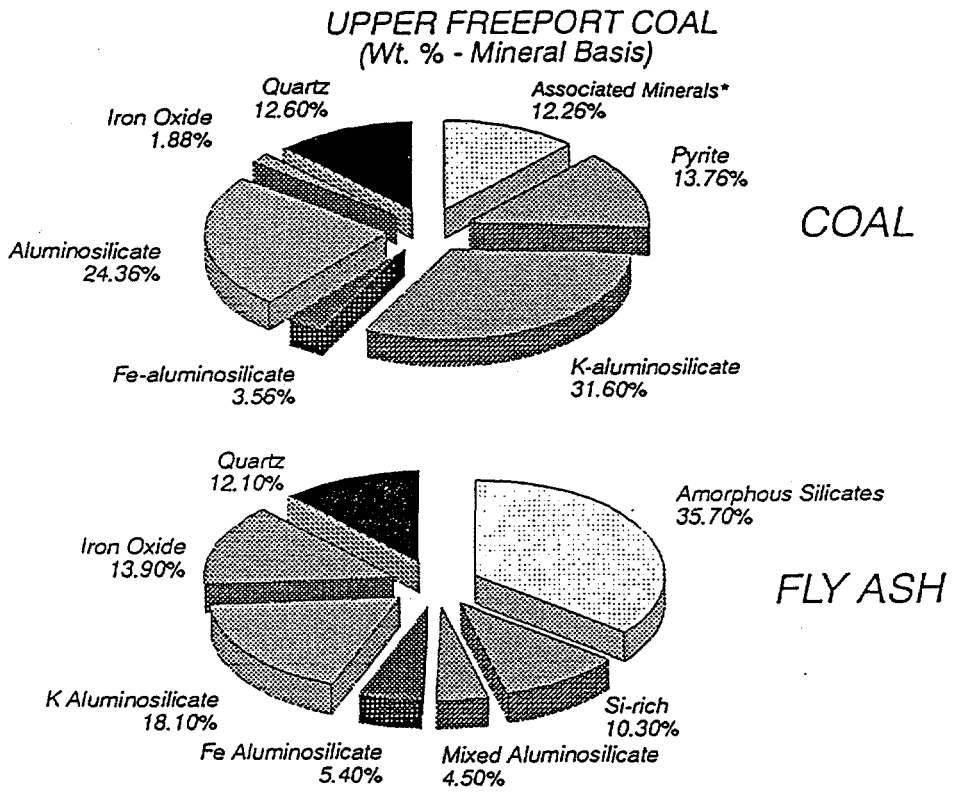

Figure II.D.4-4. Composition evaluation of Upper Freeport Bituminous coal ash during combustion (wt % mineral basis): (a) coal composition, (b) fly ash composition. * Mixed minerals such as quartz and pyrite.

In general, fly ash produced during pulverized coal combustion is approximately 90 to 95% amorphous and consists mainly of silicate glass. The conditions for glass formation have been discusses by Kingery et al. (1976). Glass-forming oxides, sometimes referred to as network formers, have the ability to build and form three-dimensional, random networks. The oxides that are good network formers include SiO_2, B_2O_3, GeO_2, P_2O_5, and AsO_4. These network formers form highly covalent bonds with the oxygen atoms. In contrast, a network-modifying oxide is incapable of building a continuous network. The addition of such a modifying oxide to a network causes weakening of the network. Good examples of network modifiers are oxides of sodium, magnesium, calcium, and potassium.

An element that can act as either a network modifier or an intermediate oxide is iron. In coal ash systems, the effect of iron on the silicate glasses is extremely important. The oxidation state of the iron dictates whether iron will exist as a network modifier or an intermediate. Iron present as FeO (Fe^{2+}) will act as a network modifier, resulting in the formation of nonbridging oxygens and weakening the network. Iron present as Fe_2O_3 (Fe^{3+}) will act as an intermediate oxide and may take part in the glass network.

Liquid sulfate phases also contribute to the formation of depositions in combustion systems. These phases have very little tendency to form chains, rings, and network structures typical of silicates. The sulfate phases form as a result of the reaction of sulfur oxides with alkali and alkaline earth oxides such as sodium and calcium, respectively. The sulfur oxides form from the oxidation of sulfides and organic sulfur during combustion. These oxides can then react with ash in the combustor. It has been shown that the maximum amount of reaction between sulfur oxides and ash occurs at approximately 830 K and is dependent upon the quantity of alkali and alkaline earth oxides in the ash (Reid, 1981). The exact manner in which sulfates form is not well understood.

The behavior of alkali species such as sodium is extremely important with respect to the formation of convective pass fouling deposits. The mechanisms by which sodium forms deposits have been investigated by a number of researchers (Jones and Benson, 1987 and Sondreal et al., 1977). Sodium present as salts of organic acid groups in the coal will readily volatilize in a pulverized coal flame. According to Raask (1985), volatile sodium can easily dissolve in the surfaces of silicate particles or become sulfated. Sodium silicate ($Na_2Si_2O_5$) was found to be thermodynamically more stable than sulfates at temperatures from 1470 - 1870 K, while sodium sulfate was stable below approximately 1370 K. In fact, the formation of Na_2SO_4 at temperatures less than approximately 1300 K inhibited the formation of sodium silicate (Wibberley and Wall 1982). Therefore, the distribution of volatile sodium between silicate components of the ash and sulfate is influenced by temperature, as well as the residence time, of the particle in the flame.

Deposit Initiation

The transport of intermediate ash species is a function of the state and size of the species and system conditions such as gas flow patterns, gas velocity, and temperature. Several processes are involved as described by Raask (1985) and Rosner et al. (1992).

The primary transport mechanisms are illustrated in Fig. II.D.4-5. The small particles (<1 μm) and vapor phase species are transported by vapor phase and small particle diffusion. These particles are characteristically rich in flame-volatilized species that condense upon cooling in the bulk gas or in the gas boundary layer next to the tube.

An additional transport mechanism which is important for the intermediate size range of particles is that of thermophoresis, as illustrated in Fig. II.D.4-5. This transport mechanism is important for particles <10 μm. Electrophoresis is another transport mechanism that may be important with respect to the formation of deposits (Raask, 1985).

Larger particles, greater than 10 μm in diameter, may impact a heat transfer surface due to their inertia which prevents them from following the gas streamlines (e.g. around a tube). Inertial impaction accounts for the bulk of the deposit growth.

The factors that influence the adhesion of an ash deposit to a heat-transfer surface include:

1. Temperature of the steel surface.
2. Thermal compatibility between the deposited material and the heat transfer surface.
3. Chemical compatibility between the initiating particles and the heat transfer surface.
4. Surface tension of the initiating ash droplet.

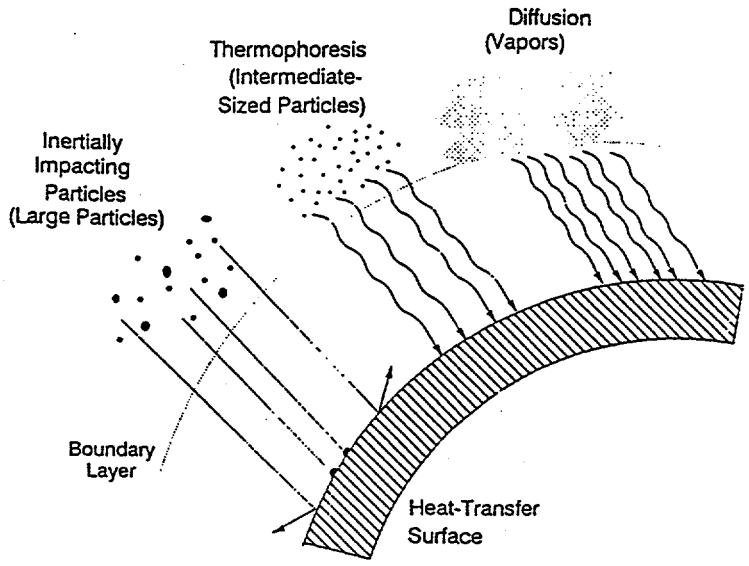

Figure II.D.4-5. Ash transport mechanisms to heat-transfer surfaces.

In the high-temperature radiant section of a utility boiler, molten ash particles may impact on the waterwalls resulting in the formation of a deposit. The initiating layers next to the heat-transfer surface may contain condensed, flame-volatilized species, in the form of small particles, that are rich in alkali and alkaline earth sulfates. These particles are held in place by van der Waals and electrostatic forces (Raask, 1985). Particles impacting this layer may incorporate some alkali and alkaline earth elements. The alkali and alkaline elements will cause the formation of lower melting point phases that can contribute to increased bonding to the surface.

If the thermal characteristics (i.e., thermal expansion coefficients) of the heat-transfer surface and the depositing material are similar, the deposit will not shed easily when the unit is cycled. One the other hand, if the thermal expansion coefficients of the ash and the surface are different, the deposits will shed much more easily during cycling.

Detailed fundamental studies of factors that influence the sticking of coal ash slags to heat-transfer surfaces were conducted by Austin et al. (1981 and Abbot and Austin, 1985). They developed a simplified apparatus to produce molten droplets of slag and allow them to fall and stick to a boiler steel coupon that was held at a controlled temperature. The information generated with this apparatus lead to an improved understanding of the factors that influence the sticking behavior of slag droplets on boiler steel surfaces. The factors include slag droplet composition, droplet temperature, nature of the steel surface, steel temperature, and the contact of angle of the droplet.

Deposit Characteristics And Growth

The characteristics of a deposit depend upon the chemical and physical characteristics of the intermediate ash species, geometry of the system (gas flow patterns), gas temperature, gas composition, and gas velocity. Figure II.D.4-6 illustrates ash deposition phenomena in utility boilers. Deposits that form in the radiant section are called slag deposits. Deposits that form in the convective pass on steam tubes are called fouling deposits. Slag deposits are exposed to radiation from the flame, and are usually associated with a high level of liquid phase components. Silicate liquid phases are typically the most

prevalent, although the deposit may also contain moderate to high levels of reduced iron phases. Initial layers of slag deposits may consist of very fine particulate which can be highly reflective. Fouling deposits form in the convective passes of utility boilers and, in most cases, do not contain the high levels of liquid phases that are usually associated with slagging type deposits. Rather, fouling deposits contain low levels of liquid phases (e.g. a combination of silicates and sulfates) that bind the particles together. The formation of these deposits on heat-transfer surfaces can significantly reduce heat transfer. The heat transfer through a deposit is related to the temperature, thermal history, and physical and chemical properties of the deposited material. Properties which have a significant effect on heat transfer include the thermal conductivity, emissivity, and absorptivity.

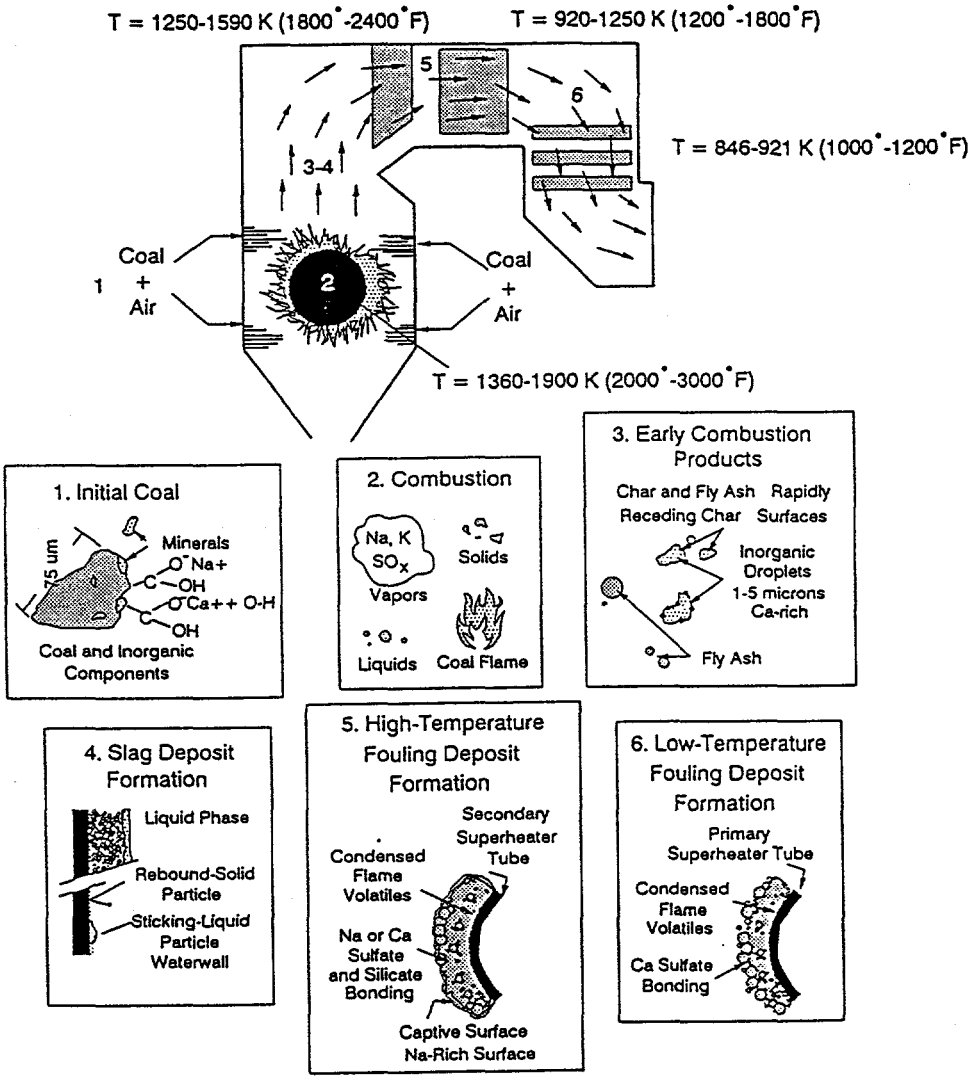

Figure II.D.4-6. Ash deposition phenomena in utility boilers.

The factors that contribute to the formation of slag deposits include (1) gas flow patterns resulting in impacting and sticking of the particles, (2) low-excess air conditions (3) the formation of a molten captive deposit that becomes an efficient collector of impacting particles, and (4) an increase in gas temperature

caused by less efficient heat transfer. Hatt et al. (1990) have classified slag deposits from utility boilers into four principal types which include (1) metallic slags that have a metallic luster and are usually associated with the combustion of pyrite-rich coals (reducing conditions cause the separation of the metallic portion from the other slag components), (2) amorphous, glassy slag that is relatively homogeneous with a high degree of assimilated ash particles, (3) vesicular slags that consist of amorphous slag that contain trapped bubbles and have a sponge- like appearance, and (4) sintered slag deposits that are only partially fused.

Fouling problems in utility boilers have been classified into two principal types: high temperature fouling and low temperature fouling (Hurley et al., 1991). This distinction is needed since the bonding mechanism of the deposits differ. In high-temperature fouling, the bonding of particles is due to silicate liquid phases, whereas in low-temperature fouling, the bonding is a result of the formation of sulfates. Condensed sulfur species, principally in the form of CaSO4, are stable and form the matrix or bonding material in the low-temperature deposits.

In combustors burning coals that contain high levels of alkali and alkaline earth elements, high-temperature fouling can be a significant problem. In most cases, the innermost layers consist primarily of small particles, rich in flame-volatilized species such as sodium and sulfur, which are transported to the surface by vapor phase diffusion and thermophoresis.

Properties Of Deposits

The development of deposit strength is due primarily to sintering or densification of the deposit. Sintering may occur by several mechanisms, as discussed in Kingery et al. (1976). Liquid phase or viscous flow sintering appears to be the dominant mechanism but other mechanisms, such as solid state sintering, may also be involved.

The driving force for densification is derived from capillary pressure of the liquid phase between particles. When two particles that are coated with a liquid phase are in contact with each other, the interparticle space becomes a capillary in which substantial capillary pressure can develop. For example, in silicate systems containing capillary diameters between 0.1 and 1 μm can range from 1.2-12.1 MPa (Kingery et al., 1976).

The capillary pressure increases densification by:

1. Rearranging the particles to increase packing effectiveness
2. Increasing the number of contact points between particles
3. Promoting the dissolution of smaller particles to produce large particles (Ostwald ripening)
4. Transferring material away from particle contact points to bring particle centers closer together.

The reactivity and liquid forming propensity of the deposited ash particles can be approximated from the base-to-acid ratio distribution of the particles. Basic components include network modifiers such as calcium or sodium. Acidic components include species such as silica which are network formers. A mixture of acidic and basic components tend to react to form low melting point species. Therefore, deposit which contains both acidic and basic particles has a high potential for liquid phase formation. In contrast, a deposit consisting of particles which are either all basic or all acidic has less potential for liquid phase formation. Crystallization is another factor which may affect the densification process. In general, crystallization tends to slow the densification process and weaken the deposit. Relationships are currently being developed between the chemical composition and physical properties of coal ash slags (Nowak and Benson, 1992).

The properties of the deposit that influence the heat transfer in a utility boiler are the emissivity and the thermal conductivity. Wall et al. (1979) reviewed the effect of deposit properties on the emissivity and thermal conductivity of the deposit. The emissivity was affected by the physical structure, shape, and

chemical composition (color) of the deposit. Emissivity of coal ashes decreased with temperature at lower temperatures, and then increased sharply at higher temperatures as sintering and fusion occurred. Particle size was the most dominant variable which affected the emissivity of unsintered samples.

The thermal conductivity of the deposit is also related to the physical structure and chemical composition of the deposit. A deposit that is highly porous and composed of insulating materials will have a low thermal conductivity, while low-porosity materials containing iron will have higher thermal conductivities. Figure II.D.4-7 shows thermal conductivities for deposits as measured by Wall et al. (1979) and Benson et al. (1990).

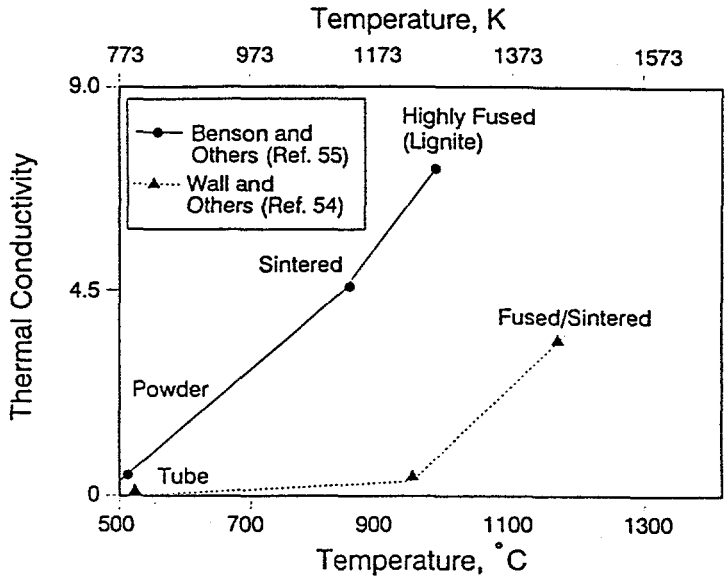

Figure II.D.4-7. Thermal conductivity of deposits having different characteristics.

Model Development

Modeling of ash formation and deposition has a goal of producing the following information as an end-product:

1. Deposition rate, which will provide information as to the frequency of soot blowing or load shedding required to operate the unit
2. Heat-transfer recovery after cleaning by soot blower or load-drop methods
3. Potential for catastrophic deposition.

This information will provide users with the ability to ascertain the limits on system performance due to ash deposit formation. Utility operators want to determine when the deposition rate is less than or equal to the heat-transfer recovery due to soot blowing (Case 1 in Fig. II.D.4-8). Under Case 1, the unit can operate continuously at the current conditions. If the deposition rate becomes greater than the heat-transfer recovery due to soot blowing, as illustrated for Case 2, load must be dropped in order to shed deposits.

The approach required to develop a model that can predict the deposition index illustrated in Fig. II.D.4-8 is shown in Fig. II.D.4-9. This is an overview diagram representing a phenomenological approach. The diagram does not illustrate the effects of boiler design and localized deposition in the radiative and convective passes of a utility boiler. A model is needed to predict the deposition index shown in Fig. II.D.4-8 as a function of the operating conditions, coal composition, and boiler geometry.

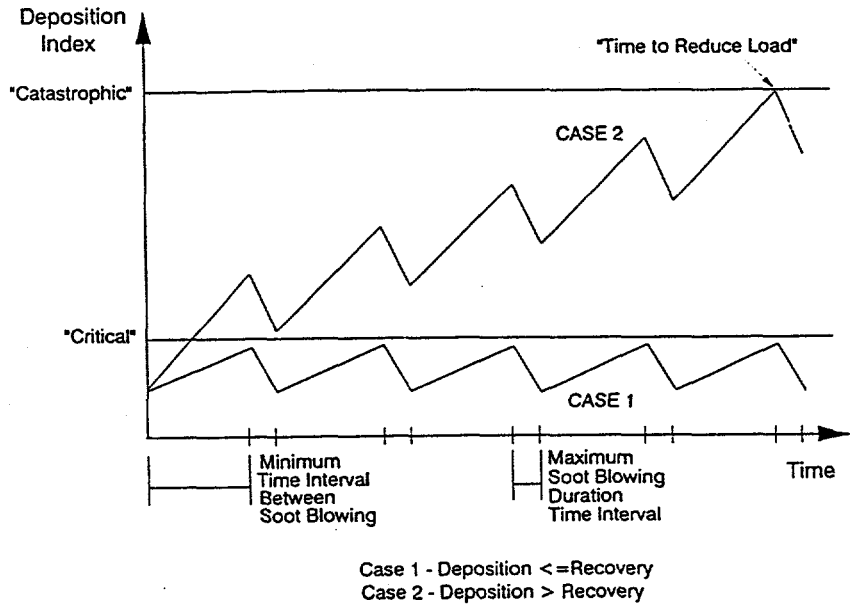

Figure II.D.4-8. Deposition index versus time for ash growth in utility boilers (Pavlish et al., 1991).

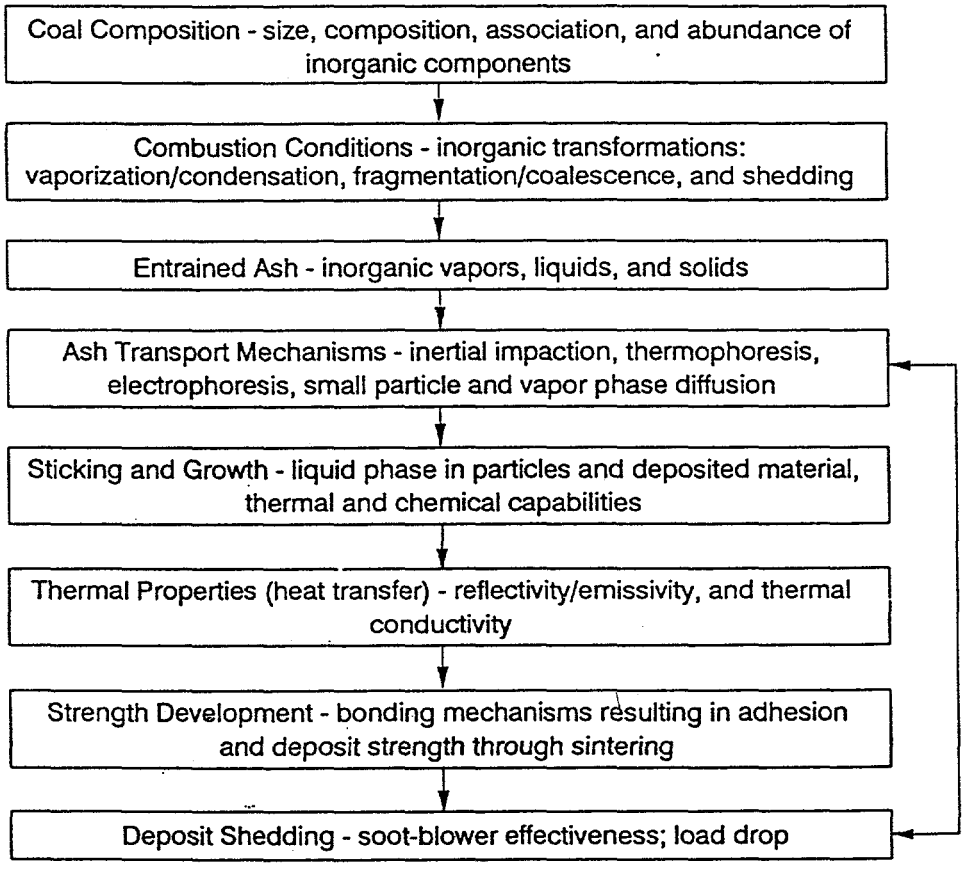

Figure II.D.4-9. Description of Coal Inorganic Components.

Modeling the behavior of inorganic constituents during combustion is limited, to a large extent, by the description of the coal inorganic components that is provided as input to the model. Model input parameters should include: (1) chemical information on both the coal and coal minerals, (2) the particle-size distribution of the coal and minerals, (3) information on the association between the coal and mineral phases, and (4) the abundance of organically associated inorganic components. Chemical information may be obtained from standard ASTM procedures, CCSEM and chemical fractionation, as discussed before.

One method of describing ash transformations is to follow the mineral behavior during combustion of a single coal particle. In order to do this, it is necessary to know the mineral composition of the coal on a particle-by-particle basis. In other words, a knowledge of the particular minerals associated with a given coal particle is required. CCSEM typically gives the size and composition of only the mineral particles that are greater than 1 μm, but does not associate particular mineral particles with coal particles. Therefore, it is necessary to randomly redistribute the minerals (as measured by CCSEM) back into the coal in order to approximate the particle-by-particle mineral composition of the coal.

Methods for mineral redistribution have been discussed by Wilemski et al. (1992) and Beer et al. (1992). Redistribution techniques usually involve a Monte Carlo simulation and/or the use of Poisson distribution functions to represent the distribution of mineral particles in coal.

Modeling of Ash Formation

Two previously mentioned limiting cases have been extensively studied. The first of these is the coarse limit or full coalescence limit that assumes all of the ash in the char coalesces to form a single ash particle. The second limiting case is the fine limit in which no coalescence occurs and each mineral inclusion forms one ash particle. The actual fly ash distribution probably lies between these two extremes. These two limiting cases were recently used to predict the size and composition of fly ash from three bituminous and one lignitic coal (Wilemski et al., 1992). Predictions with the full coalescence model compared well with experimentally measured size and composition. In contrast, predictions with the no-coalescence assumption did not compare well with either the size or composition for the coals examined. Less satisfactory agreement between the full-coalescence model and experimental data was observed by Loehden et al. (1989), who found that the no-coalescence model gave a better estimate of the fly ash size distribution. Other studies have shown that the fly ash particle-size distribution approaches that of the mineral inclusions (i.e., no coalescence) for high-rank coals (Beer et al., 1990). However, even when the no-coalescence model approximates the fly ash particle-size distribution, the predicted composition distribution may be very inaccurate as discussed by Beer et al. (1992). The above results indicate that the simple "limiting case" models lack the sophistication necessary to describe inorganic transformation for a variety of coals and operating conditions. This is why partial coalescence models have been developed.

There are two basic types of partial coalescence models found in the literature. The first type makes the transition from coal inorganic components to fly ash by modeling char combustion explicitly and tracking the inorganic transformations as the char burns. The second type uses random combinations of the coal minerals to form the fly ash without explicitly considering char combustion. Both types of models require the detailed chemical data available from CCSEM.

Sample results from the latter procedure are shown in Fig. II.D.4-10. This method has the distinct advantage of eliminating the need to redistribute the mineral grains back into the coal matrix; the fly-ash distribution is generated directly from the CCSEM data. Excluded minerals are known to behave differently from included minerals which are intimately associated with the char combustion process. Srinivasachar and Boni (1989) recently developed a mathematical model to describe the transformations of excluded pyrite, a mineral form that is important in the slagging of boilers burning eastern coals. They found that, for the simulated conditions, approximately 80% of the total time required to oxidize pyrite to solid magnetite was spent in the molten phase. Clearly, the presence of the molten phase is significant with

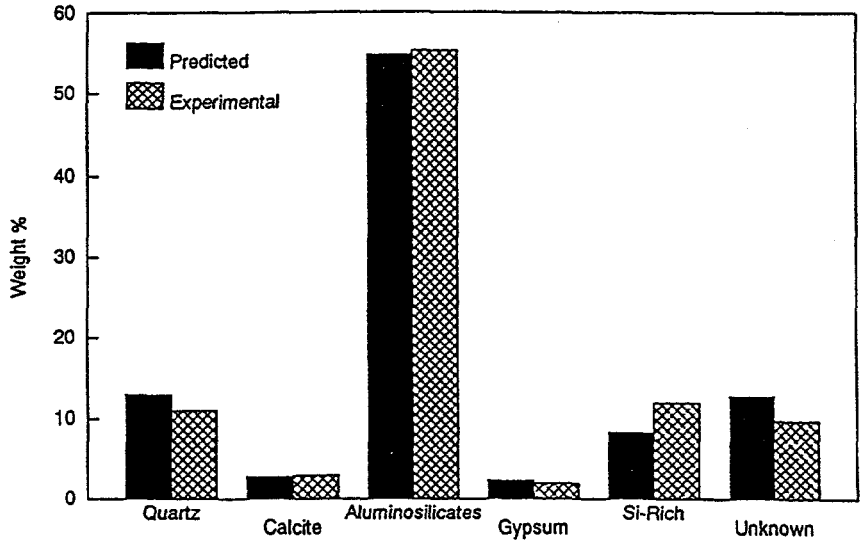

(a)

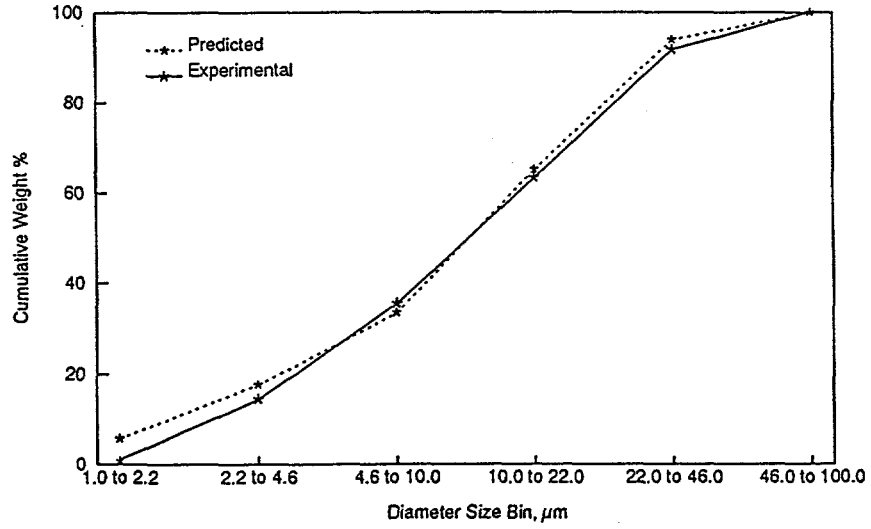

(b)

Figure II.D.4-10. Particle-size and composition distribution predictions using the EERC model for Kentucky #9 on an iron-free basis: (a) predicted and experimental phase distribution, and (b) predicted and experiment size distribution (Zygarlicke et al., 1992).

respect to deposit formation. Other excluded minerals of interest include illite, which melts under typical combustion conditions (Srinivasachar et al., 1990), and silica which reacts with vaporized alkali or alkaline earth metals.

Simulation of the behavior of vaporizable species should consider the following areas:

1. Release of the species into the vapor phase
2. Chemistry of the species in the vapor phase
3. Transport of vapor species to locations where reaction or condensation may take place
4. Reaction or condensation of the vapor species

Equilibrium calculations have been used by a variety of investigators to determine the behavior of inorganic elements in the vapor phase (Wilson and Redifer 1973, Wibberley and Wall 1982, and Benson 1987). These calculations appear to adequately represent the species present in the vapor phase, with the exception of species like sodium sulfate that are thermodynamically stable, but are not readily formed due to kinetic constraints (Srinivasachar et al., 1990 and Steinberg and Kchofield, 1990).

Transport Processes

A single cylinder in cross-flow most closely represents a leading heat-exchanger tube in the convective pass. Quantitative impaction rates have been determined for particles transported by both inertial impaction and thermophoresis. The most frequently cited correlation of inertial impaction rates is perhaps that of Israel and Rosner (1983) who correlated the impaction efficiency in terms of a generalized Stokes number for a clean tube (free of deposit). Thermophoresis may also significantly impact the transport rates of small particles (<10 μm) as discussed before. Both Eulerian (Rosner, 1986) and Lagrangian (Wessel and Righi, 1988 and Jacobsen and Brock, 1965) approaches have been used to simulate thermophoretic transport for a cylinder in cross-flow.

There are locations in a boiler or combustor where the gas flow is predominantly parallel to the surface, as opposed to the perpendicular or impinging flow of the cylinder in cross-flow. In such cases, eddy impaction due to turbulence may play an important role in particle transport. Methods for calculations of particle deposition from turbulent flows were reviewed with regard to assumptions, accuracy, and range of application by Papavergos and Hedley (1984). These authors identified two basic types of models: (1) models based on theories of classical turbulence, and (2) stochastic models. Models based on the classical concepts of turbulence possessed the following characteristic: (1) incorporation of the "stopping distance" concept, (2) use of the multilayer fluid model adjacent to the wall (laminar sublayer, buffer layer, and turbulent core), (3) a particle diffusivity which is equal or proportional to the eddy diffusivity of momentum, (4) use of the r.m.s. radial fluid velocity to approximate the free flight velocity of the particle. It was concluded that theories based on the classical concepts of turbulence were "of limited application and accuracy, but easy to use in design calculations" (Papavergos and Hedley, 1984). Stochastic models are generally more accurate, but also more complex. A recent example of the stochastic approach is the study of Kallio and Reeks (1989), who used a Lagrangian random-walk approach to model particle deposition in turbulent ducts.

Particle Capture and Deposit Growth

Several different factors influence the sticking probability of a given particle, including the particle velocity, viscosity, surface tension, temperature, size, and impact angle, as well as the condition of the substrate upon which the particle impacts. In theory, it should be possible to describe quantitatively all of the above factors and simulate deposit growth on a particle-by-particle basis. However, the excessive amount of computer time that would be required and the inherent complexity of the deposition process itself preclude the use of such simulations for practical systems. Consequently, models of particle capture and deposit growth have focused on the factors considered most important to the particular system of interest. A significant amount of work remains to be done before it will be possible to quantitatively predict

particle capture and deposit growth. In order for this to be successful, theoretical work must be coupled with experiments at every stage of development.

Thermal Properties of Deposits

Two key physical properties are the emissivity and the thermal conductivity, both of which vary with the particle size, chemical composition, temperature, and thermal history of the deposit.

Wall et al. (1979) reviewed the influence of ash deposits on wall emissivities. Methods for laboratory measurement of emissivity were discussed and problems identified. Problems included the fact that boiler deposits are not flat, and that rough deposits have effective emissivities that are well above laboratory values. The chemistry of the deposits also has an effect on emissivity. The authors recommend in-situ measurement of this important physical property.

Ash deposits are often characterized by an effective thermal conductivity (keff) which is a single value used to represent the entire thickness of the deposit. Measurements of effective thermal conductivities have been made for both particulate and fused deposits. They clearly show that the magnitude of the effective conductivity varies significantly with the type of deposit formed. Caution should be exercised when using keff values measured in the laboratory since these measurements are typically made by grinding a sample of ash into a powder and pressing it into a pellet for the measurements. Consolidation and sintering invariably occur to one degree or another in boiler deposits, leading to an effective conductivity which is greater than values generally derived from laboratory measurements (Wall et al., 1979). In the absence of other information, a reasonable value for the effective thermal conductivity of deposits which are not highly fused is 0.5 W/m K (Creek, 1985 and Anderson et al., 1987).

Review of Work Performed at PSI

Between 1986 and 1992 PSI Technology Company (PSIT) conducted a mineral and ash study for DoE/PETC. The goal of the study "was the development of a comprehensive model to predict the size and chemical composition distributions of ash produced during pulverized coal combustion". The results of the study are reported in Phase I and Phase II Final Reports (Boni, et al., 1990; and Helble, et al., 1992).

The study developed techniques for characterizing the size and composition of both minerals included in coal particles as well as fly ash. The most important characterization technique was (CCSEM) in which sample of each coal fly ash was analyzed by Computer Controlled Scanning Electron Microscopy to determine the type, composition, and size of the coal mineral matter. This technique was eventually employed as the primary input for the engineering model.

The engineering model is illustrated in Fig. II.D.4-11. The model starts with the evaluation of the mineral inclusion compositions and sizes. This analysis is performed once for any coal and a mineral redistribution model is used to determine how the minerals are distributed among particles for any coal grind. This statistically calculated mix of particles with their included and excluded minerals is used to predict the ash particle distribution. To do this requires answers to specific questions on the chemical and physical transformation of the minerals such as:

- Do mineral grains coalescence?
- What happens to the organically bound alkali metals?
- What happen to the pyrite?

To answer these questions, the PSI Technology study included a wide range of experiments. For the purpose of the engineering model, the most important findings were as follows:

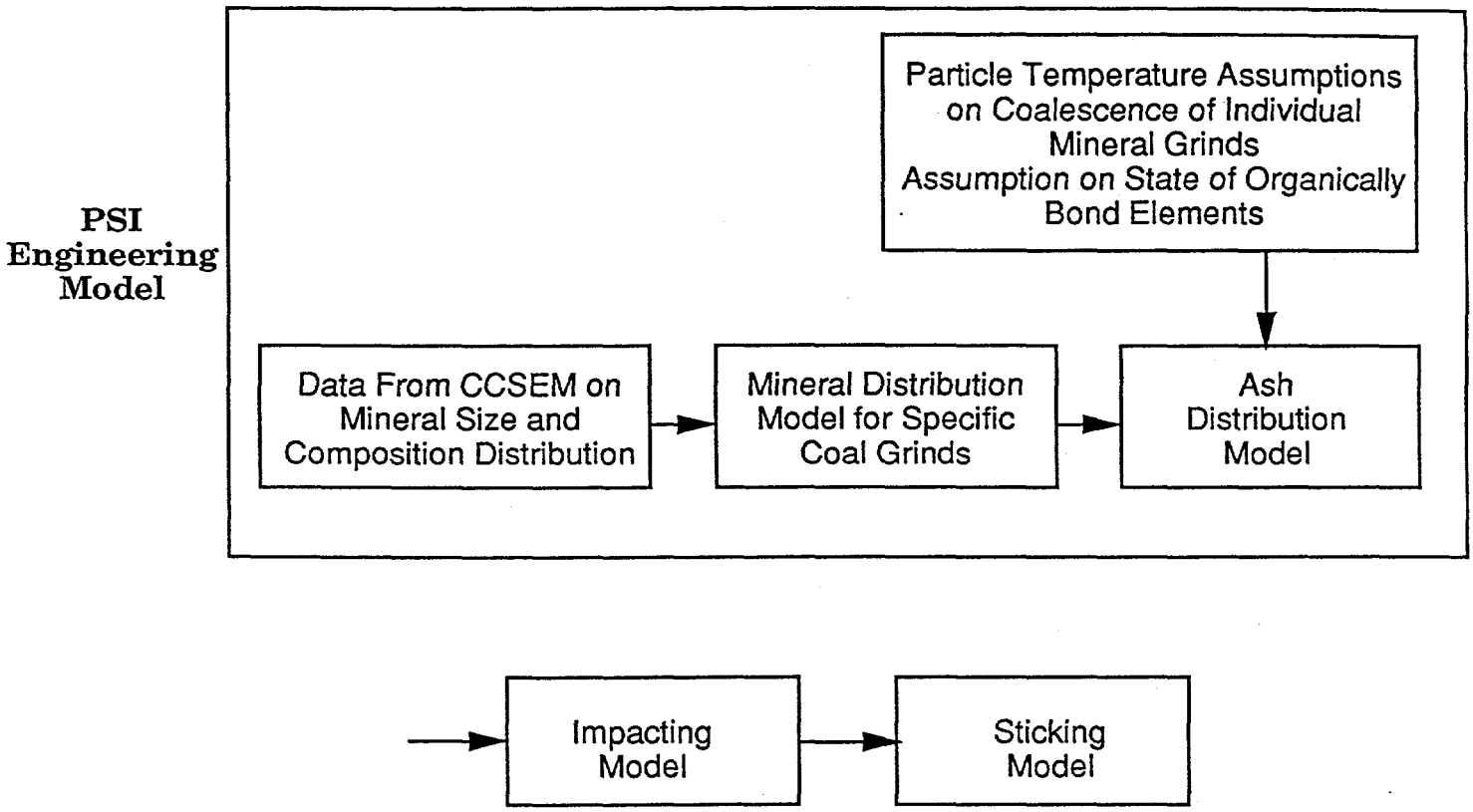

Figure II.D.4-11. PSI Technology Engineering Model for Ash Particle Size and Composition.

- "The full coalescence model gives generally acceptable predictions of ash composition and size distributions. On the other hand, the no coalescence model fails to identify several ash composition categories and consistently predicts too fine an ash size distribution in the smaller size range".

- "Calcium aluminosilicate ash results mainly from the interaction of organically-bound calcium with aluminosilicate minerals. Calcium, present as calcite, does not interact with other minerals, unless it is present as very fine inclusions. The compositions and concentrations of calcium-containing ash particles are sensitive to the amount of organically-bound calcium in the coal".

- "Char fragmentation, was found to have little influence on the ash distributions for all but the lowest ash (< 5%) coals".

- "Alkali vaporization (mainly sodium) was found to be affected by the presence of aluminosilicate minerals, with the formation of alkali aluminosilicates retarding alkali vaporization".

- "Calcium-rich aluminosilicates were found to lead to significant particle deposition under a wide range of conditions".

- "Pyrite-derived ash particles were also found to deposit over a wide range of conditions, provided that a molten phase was present".

- "Coalescence of ash particles during char combustion is enhanced by the presence of alkali and alkaline earth metals in the coal".

- "Coal mineralogy and combustion temperature (not combustion scale) are the most important parameters determining the composition distribution of combustion-derived fly ash particles".

- "Traditional indices for slagging and fouling based on mean ASTM ash compositions are inadequate because they fail to account for the wide variability in compositions and sizes of ash particles".

General Modeling Issues and Concluding Remarks

Previous sections have discussed several aspects of mineral matter behavior, all of which are relevant to the development of a complete model of inorganic transformations and ash deposition. The quantitative description of each of these aspects alone requires a relatively complex mathematical model. In fact, it is still not possible to accurately predict some of the key aspects (e.g., deposition rate). Clearly, then, the combination of all the different aspects of mineral behavior into a single submodel represents a formidable task.

As this task is approached, it is important to realize that different fuel and boiler combinations require different aspects of mineral behavior in order to predict ash formation and deposition. Therefore, the sophistication of the mineral matter submodel should be reduced to the key aspects needed to solve the problem set of interest. In addition, the type of information needed by the user will determine the level of simulation which must be performed. With this in mind, there is a need for at least two principal levels of modeling, namely, (1) simple simulations to determine the relative behavior of different fuels, and (2) comprehensive simulations with localized resolution in the boiler. The simple model (1) should be designed to run efficiently on a low-level platform, such as a personal computer. The second level of modeling is a mineral matter submodel incorporated into a comprehensive combustion code. The development of a first-generation submodel is currently in progress.

During the past several years, significant advances have been made in our understanding of the fundamental mechanisms of ash formation, transport, growth, and strength development. Many of these advances are related to the development of analytical techniques, such as CCSEM, which enable determination of the size, composition, abundance, and association of mineral grains in coal. This detailed analytical information has been an important factor in the identification of the key mechanisms which govern ash behavior, and has led to the development of mechanistic models to describe ash transformations and depositions. These models provide the basis for predictive tools which can be applied to practical systems.

Although considerable progress has been made, there is still much work to be done. For example, there is a need to develop quantitative relationships between the characteristics of the entrained ash (e.g. fly-ash chemistry and morphology) and the physical properties of ash deposits that influence deposit growth, strength development, and cleanability. Also, data from bench-scale, pilot-scale, and full-scale units are needed for verification of mechanistic models. Once verification is complete, the predictive models will be available for simulation of practical systems in order to determine operating conditions which will minimize deposition problems, maximize efficiency, and reduce emissions.

References for Subtask 2.d.

Abbott, M.F., Moza, A.K., and Austin, Studies on Stag Deposit Formation in Pulverized Coal Combustors: 2. Results on the Wetting and Adhesion of Synthetic Ash Drops on Different Steel Substrates, Fuel, Vol. 60, pp. 1065-1072 (1981).

Abbott, M.F., and Austin, L.G., Studies on Slag Deposit Formation in Pulverized-Coal Combustors: 4. Comparison of Sticking Behavior of Minerals and Low-Temperature and ASTM High-Temperature Coal Ash on Medium Carbon Steel Substrates, Fuel, Vol. 61, pp. 765-770 (1982).

Abbott, M.F., Conn, R.E., and Austin, L.G., Studies on Slag Deposit Formation in Pulverized Coal Combustors: 5. Effect of Flame Temperature, Thermal Cycling of The Steel Substrate, and Time on the Adhesion of Slag Drops to Oxidized Boiler Steels, Fuel, Vol. 64, pp. 827-831 (1985).

Abbott, M.F., and Austin, L.G., Studies on Slag Deposit Formation in Pulverized-Coal Combustors: 6. Stricking Behavior of Slag Drops form Three Pennsylvania Steam Coals, Fuel, Vol. 64, No. 6, pp. 832-838 (1985).

Anderson, D.W., Viskanta, R., and Incropera, F.P., Effective Thermal Conductivity of Coal Ash Deposits at Moderate to High Temperature, Trans. ASME, J.Eng., Gas Turbine Power, Vol. 109, p. 215 (1987).

Beer, J.M., Sarofim, A.F., Barta, L.E., From Coal Mineral Properties to Fly Ash Deposition Tendencies: A Modeling Route, in S.A. Benson (Editor), Inorganic Transformations and Ash Deposition During Combustion, Engineering Foundation Press, ASME, New York, NY (1992).

Benson, S.A., Jones, M.L. and Harb, J.N., Ash Formation and Deposition, in *Fundamentals of Coal Combustion for Clean and Efficient Use*, (L. D. Smoot, Ed.), Elsevier, Amsterdam, pp. 299-373 (1993).

Benson, S.A., and Holm, P.L., Comparison of Inorganic Constituents in three Low-Rank Coals, Ind. Eng. Chem. Prod. Res. Dev., Vol. 24, p. 137 (1985).

Benson, S.A., Laboratory Studies of Ash Deposit Formation During the Combustion of Western U.S. Coals, PhD. Thesis, The Pennsylvania State University, University Park, PA , p. 266 (1987).

Bishop, M. and Ward, D.L., Fuel, 37. 191 (1958).

Blom, L., Edelhausen, L., and van Krevelen, D.W., Fuel, 36 (1957).

Boni, A.A., Beér, J.M., Bryers, R.W., Flagan, R.C., Helble, J.J., Huffman, G.P., Huggins, F.E., Peterson, T.W., Sarofim, A.F., Srinivasachar, S., and Wendt, J.O.L., Transformations of Inorganic Coal Constituents in Combustion Systems, Phase I Final Report for U.S. DOE Contract No. DE-AC22-86PC90751 (1990).

Charpenay, S., Serio, M.A., and Solomon, 24th Symposium (Int) on Combustion, The Combustion Institute, Pittsburgh, PA, 1189-1197 (1992).

Creek, R.C., Thermal Properties of Boiler Ash Deposits, State Electricity Commission of Victoria, Research and Development Dept., Brown Coal Research Division, Rep. No. ND/85/014, (May 1985).

Field, M.A., Gill, D.W., Morgan, B.B., and Hawksley, P.G.W., *Combustion of Pulverized Coal*, BCURA, Leatherhead, p 186 (1967).

Given, P.H., and Yarzab, R.F., Analysis of the Organic Substance of Coals: Problems Posed by the Presence of Mineral Matter, in C.J. Karr (Editor), Analytical Methods for Coal and Coal Products, 2nd ed., Academic Press, New York, NY, Chapter 20, pp 3-41 (1978).

Hatt, R.M., Fireside Deposits in Coal-Fired Utility Boilers, Prog. Energy Combust. Sci., Vol. 16, pp. 235-241 (1990).

Helble, J.J. (Ed.), Transformations of Inorganic Coal Constituents in Combustion Systems, Final Report (Contract No. DE-AC22-86PC90751), PSI, MIT, University of Arizona and University of Kentucky, Vol. I—III (Nov. 1992).

Helble, J.J., Srinivasachar, S., Wilemski, G., Boni, A.A., Kang, S-G., Sarofim, A.F., Graham, K.A., Beér, J.M., Peterson, T.W., Wendt, J.O.L., Gallagher, N.B., Bool, L., Huggins, F.E., Huffman, G.P., Shah, N., and Shah, A., Transformations of Inorganic Coal Constituents in Combustion Systems, Phase II Final Report for U.S. DoE Contract No. DE-AC22-86PC90751, (Vols. I, II, and III) (1992).

Hengel, T.D. and Walker, P.L., Jr., Fuel, 63, 1214 (1984).

Hurley, J.P., Erickson, T.A., Benson, S.A., and Brobjorg, J.N., Ash Deposition at Low Temperatures in Boilers Firing Western U.A. Coals, International Joint Power Generation Conference, San Diego, CA (1991).

Israel, R., and Rosner, D.E., Use of a Generalized Strokes Number to Determine the Aerodynamic Capture Efficiency of Non-Stokesian Particles form a Compressible Gas Flame, Aerosol Sci, and Tech., Vol. 2, pp. 45-51 (1983).

Jacobsen, S., and Brock, J.R., The Thermal Force on Spherical Sodium Chloride Aerosols, J.Colloid Sci., Vol. 20, pp. 544-554 (1965).

Jenkins, R.G., and Walker, P.L., Analysis of Mineral Matter in Coal, in C. Karr Jr. (Editor), *Analytical Methods for Coal and Coal Products*, 2nd ed., Academic Press, New York, NY, Chapter 26, pp. 265-292 (1978).

Jones, M.L., and Benson, S.A., An Overview of Fouling/Slagging with Western Coals, Presented at the EPRI-Sponsored Conference on Effects of Coal Quality on Power Plants, Atlanta, GA, p.22, October 13-15 (1987).

Kallio, G.A., and Reeks, M.W., A Numerical Simulation of Particle Deposition in Turbulent Boundary Layer, J. Multiphase Flow, Vol. 15, pp. 433-446 (1989).

Kingery, W.D., Bowen, H.K., Uhlmann, D.R., *Introduction to Ceramics*, 2nd ed., John Wiley & Sons, New York, NY, p. 1032 (1976).

Loehden, D., Walsh, P.M., Sayre, A.N., Beer, J.M., and Sarofim, A.F., Generation and Deposition of Fly Ash in the Combustion of Pulverized Coal, J. Inst. Energy, pp. 119-127 (June 1989).

Moza, A.K. and Austin, L.G., Studies on Slag Deposit Formation in Pulverized Coal Combustors: 1. Results on the Wetting and Adherence of Synthetic Coal Ash Drops on Steel, Fuel, Vol. 60, pp. 1057-1064 (1981).

Moza, A.K., and Austin, L.G., Studies on Slag Deposit Formation in Pulverized-Coal Combustors: 3. Preliminary Hypothesis for the Sticking Behavior of Slag Drops on Steels, Fuel, Vol. 61, pp. 161-165 (1982) .

Nowok, J.W., and Benson, S.W., Correlation of Interfacial Surface Tension/Viscosity Ratio with Base/Acid Ratio, Nonbridging Oxygen Factor, and Compressive Strength Development in Coal Ashes, in S.A. Benson (Editor), Inorganic Transformation and Ash Deposition During Combustion, Engineering Foundation Conference, ASME, New York, NY (1992).

Papavergos, P.G., and Hedley, A.B., Particle Deposition Behavior from Turbulent Flows, Chem. Eng. Res. Dev., Vol. 62, p.275 (1984).

Raask, E. ,*Mineral Impurities in Coal Combustion*, Hemisphere Publishing Company, Washington, (1985).

Reid, W.T., Coal Ash--Its Effect on Combustion Systems, in M.A. Elliot (Editor), *Chemistry of Coal Utilization*, 2nd ed., John Wiley & Sons, New York, NY, pp. 1389-1445 (1981).

Rosner, D.E., Konstandopoulos, A.G., Tassopoulos, M., and Mackowski, D.W., Deposition Dynamics of Combustion-Generated Particles: Summary of Recent Studies of Particle Transport Mechanisms, Capture Rates, and Resulting Deposit Microstructure/Properties, in S.A. Benson (Editor), Inorganic Transformations and Ash Deposition During Combustion, Engineering Foundation, ASME, New York (1992).

Rosner, D.E., *Transport Processes in Chemically Reacting Flow Systems*, Butterworth, Stoneham, MA, (1986), p. 539.

Sarofim, A.F., Howard, J.B., and Padia, A.S., The Physical Transformation of the Mineral Matter in Pulverized Coal Under Simulated Combustion Conditions, Combust. Sci. Technol., Vol. 16, pp. 187-204 (1977).

Sondreal, E.A., Tufte, P.H., and Beckering, W., Ash Fouling in the Combustion of Low-Rank Western U.S. Coals, Combustion Science and Technology, Vol. 16, p. 95 (1977).

Srinivasachar, S., Helble, J.J., and Boni, A.A., Mineral Behavior During Coal Combustion: 1. Pyrite Transformations, Prog. Energy Combust. Sci., Vol. 16, pp 281-292 (1990).

Srinivasachar, S., and Boni, A.A., A Kinetic Model for Pyrite Transformations in a Combustion Environment, Fuel, Vol. 68, p. 829 (1989).

Srinivasachar, S. Helble, J.J., Boni, A.A., Shah, N. Huffman, G.P., and Huggins, F.E., Mineral Behavior During Coal Combustion: 2. Illite Transformations, Prog. Energy Combust. Sci., Vol. 16, p. 293 (1990).

Srinivasachar, S., Helble, J.J., Ham, D.O., and Domazetis, G., A Kinetic Description of Vapor Phase Alkali Transformations in Combustion Systems, Prog. Energy Combsut. Sci., Vol. 16, p. 303 (1990).

Stach, E., Mackowski, M.-th, Teichmuller, M., Taylor, G.H., Chandra, D., and Teichmuller, R., *Coal Petrography*, 3rd Edition, Gebruder Borntraeger, Berlin, (1982).

Steadman, E.N., Zygarlicke, C.J., Benson, S.A., and Jones, M.L., A Microanalytical Approach to the Characterization of Coal, Ash, and Deposits, in Seminar on Fireside Fouling Problems, ASME Research Comm. on Corrosion & Deposits from Combustion Gases, Washington, DC (1990).

Steadman, E.N., Benson, S.A., and Zygarlicke, C.J., Digital Scanning Electron Microscopy Techniques for the Characterization of Coal Minerals and Coal Ash, Presented at the Low-Rank Fuels Symposium, Billings, MT, p.16, May 20-23 (1991).

Steinberg, M., and Schofield, K., The Chemistry of Sodium with Sulfur in Flames, Prog. Energy Combsut, Sci., Vol. 16, p 311 (1990).

Wall, T.F., Lowe, A., Wibberley, L.J., and Stewart, I., Mineral Matter Redistribution and Ash Formation in Pulverized Coal Combustion, in S.A. Benson (Editor), Inorganic Transformations and Ash Deposition During Combustion, Engineering Foundation Press, ASME, New York, NY (1992).

Wessel, R.A., and Righi, J., Generalized Correlations for Inertial Impaction of Particles on a Circular Cylinder, Aerosol Sci. Tech., Vol. 9 (1988) pp. 29-60.

Wilson, J.S., and Redifer, M.W., Equilibrium Composition of Simulated Coal Combustion Products: Relationship to Fireside Corrosion and Ash Fouling, Paper No. 73-WA/CD-6, ASME, (1973).

Wibberley, L.J., and Wall, TIF., Alkali-Ash Reactions and Deposit Formation in Pulverized Coal-Fired Boilers: Thermodynamic Aspects Involving Silica, Sodium, Sulphur and Chlorine, Fuel, Vol. 61 (1982) p. 87.

Wibberley, L.J., and Wall, T.F., Alkali-Ash Reactions and Deposit Formation in Pulverized Coal -Fired Boilers: Experimental Aspects of Sodium Silicate Formation and the Formation of Deposits, Fuel, Vol. 61, p. 93 (1982).

Zygarlicke, C.J., and Steadman, E.N., Advanced SEM Techniques to Characterize Coal Minerals, Scanning Electron Microsc., Vol. 4, No. 3, pp. 579-590 (1990).

Zygarlicke, C.J., Jones, M.L., Steadman, E.N., and Benson, S.A., Characterization of Mineral Matter in ACERC Coals, Prepared for the Advanced Combustion Engineering Research Center, Brigham Young University, Provo, UT (1990).

Zygarlicke, C.J., Ramanathan, M., and Erickson, T.A., Fly Ash Distribution and Composition: Experimental and Phenomenological Approach, in S.A. Benson (Editor), *Inorganic Transformations and Ash Deposition During Combustion*, Engineering Foundation Press, ASME, New York, NY (1992).